JUNE 2018

AJNR

VOLUME 39 • PP 993–1191

AJNR

AMERICAN JOURNAL OF NEURORADIOLOGY

JUNE 2018
VOLUME 39
NUMBER 6
WWW.AJNR.ORG

THE JOURNAL OF DIAGNOSTIC AND INTERVENTIONAL NEURORADIOLOGY

Multisite concordance of DSC for brain tumors
Comparison of 3T intracranial vessel wall sequences
Ophthalmic artery collaterals in Moyamoya disease

Official Journal ASNR • ASFNR • ASHNR • ASPNR • ASSR

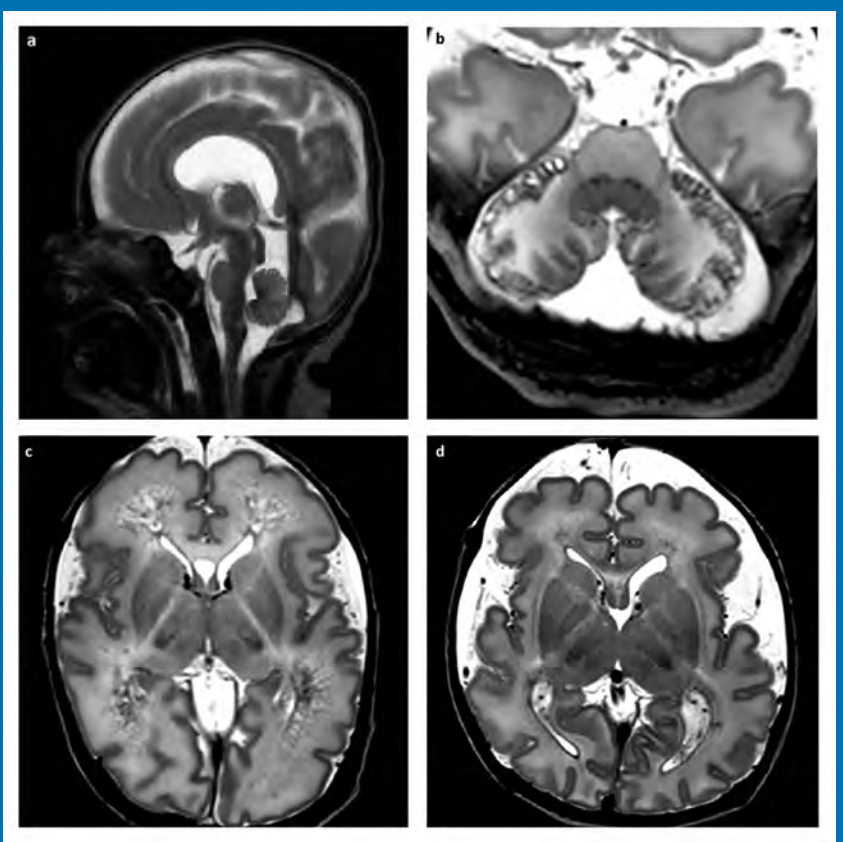

MicroVention
TERUMO

LVIS®

Intraluminal Support Device

Low-profile **V**isualized **I**ntraluminal **S**upport

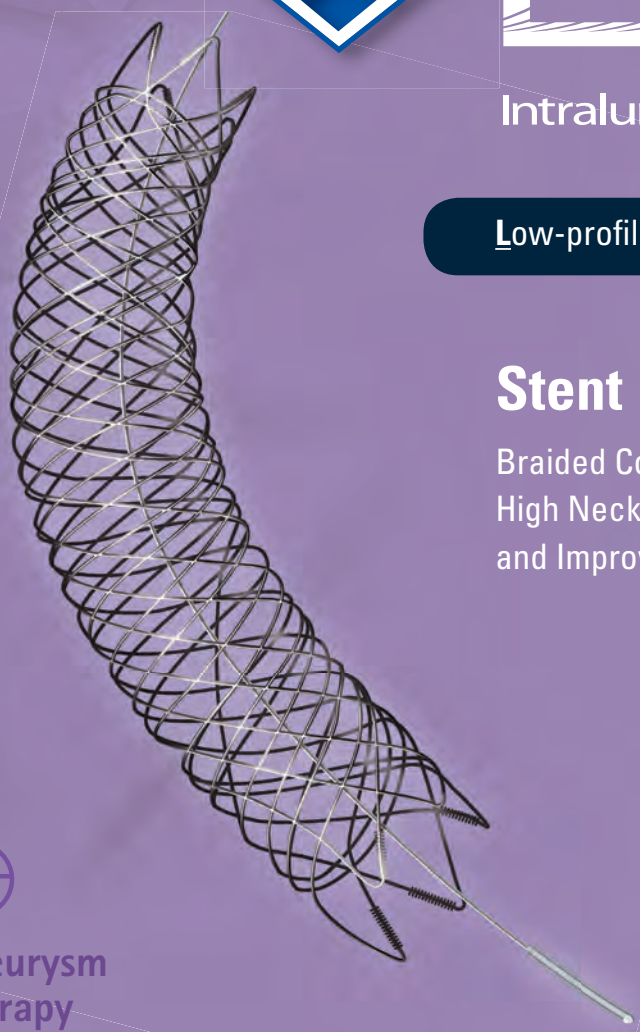

Stent Deployment. Refined.

Braided Coil Assist Stents with
High Neck Coverage, Excellent Visibility
and Improved Conformability*

Aneurysm
Therapy
Solutions

For more information or a product demonstration, contact your local MicroVention representative:

MicroVention Worldwide
Innovation Center PH +1.714.247.8000
35 Enterprise
Aliso Viejo, CA 92656 USA
MicroVention UK Limited PH +44 (0) 191 258 6777
MicroVention Europe, S.A.R.L. PH +33 (1) 39 21 77 46
MicroVention Deutschland GmbH PH +49 211 210 798-0
microvention.com

**Humanitarian Device: Authorized by Federal Law for use with bare platinum embolic coils for the treatment of unruptured, wide neck (neck ≥ 4 mm or dome to neck ratio < 2), intracranial, saccular aneurysms arising from a parent vessel with a diameter ≥ 2.5 mm and ≤ 4.5 mm. The effectiveness of this device for this use has not been demonstrated.*

MICROVENTION and LVIS are registered trademarks of MicroVention, Inc. • Refer to Instructions for Use, contraindications and warnings for additional information. Federal (USA) law restricts this device for sale by or on the order of a physician. ©2018 MicroVention, Inc. Jan. 2018

CE 0297

stryker

Now you have **24 hours** to make a lifetime of difference in stroke patients like Nora

The Trevo Retriever is the only device cleared to **reduce disability in stroke patients up to 24 hours** from time last seen well.

For more information, visit strykerneurovascular.com/trevo24hours

Trevo® XP
PROVUE RETRIEVER

Copyright © 2018 Stryker
AP002078 v1.0

Balt USA.
The Future of Innovation is Here.

Introducing

Pushing Beyond the Boundaries of

Softness and Speed

Visit balt-usa.com to learn more

29 Parker, Irvine, CA 92618
P 949.788.1443 **F** 949.788.1444
© 2018 BALT USA MKTG-101 Rev. A

balt
inspiring innovation

A Complete Coil Portfolio

MicroVention's comprehensive portfolio features clinically proven Hydrogel coils, which can be used exclusively or in combination with our trusted Platinum coils to treat a wide range of aneurysms and neurovascular lesions.

Aneurysm Therapy Solutions

Breakthrough Hydrogel Technology

- Less Recurrence
- Less Retreatment
- More Progressive Occlusion

Compared to platinum coils with comparable safety[1]

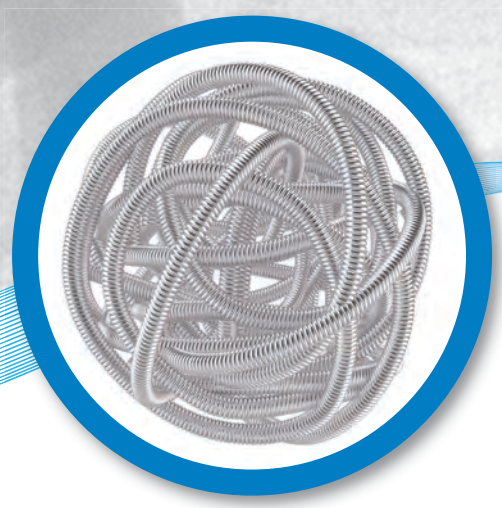

REFERENCES:

1. Taschner et al. Second-Generation Hydrogel Coils for the Endovascular Treatment of Intracranial Aneurysm; A Randomized Controlled Trial. 2018;49:00-00. DOI:10.1161/STROKEAHA.117.018707

INDICATIONS FOR USE:

The HydroCoil® Embolic System (HES) and MicroPlex® Coil System (MCS) are intended for the endovascular embolization of intracranial aneurysms and other neurovascular abnormalities such as arteriovenous malformations and arteriovenous fistulae. The HES and MCS are also intended for vascular occlusion of blood vessels within the neurovascular system to permanently obstruct blood flow to an aneurysm or other vascular malformation and for arterial and venous embolizations in the peripheral vasculature.

CE 0297

The device should only be used by physicians who have undergone pre-clinical training in all aspects of HES/MCS procedures as prescribed by MicroVention.

For more information or a product demonstration, contact your local MicroVention representative:

MicroVention® TERUMO

MicroVention Worldwide
Innovation Center PH +1.714.247.8000
35 Enterprise
Aliso Viejo, CA 92656 USA
MicroVention UK Limited PH +44 (0) 191 258 6777
MicroVention Europe, S.A.R.L. PH +33 (1) 39 21 77 46
MicroVention Deutschland GmbH PH +49 211 210 798-0
microvention.com

MICROVENTION, MicroPlex and HydroCoil are registered trademarks of MicroVention, Inc. • Refer to Instructions for Use, contraindications and warnings for additional information. Federal (USA) law restricts this device for sale by or on the order of a physician. ©2018 MicroVention, Inc. Jan. 2018

stryker

Bending expectations of conformability and stability.

Enhanced conformability – The hybrid cell structure is designed to enhance stent opening and conformability in bifurcations and tight curves.

Ease of use – All sizes of the Neuroform Atlas Stent are deliverable through Excelsior® SL-10® and Excelsior XT-17™ Microcatheters.

Higher deployment accuracy – The Neuroform Atlas Stent is designed to have very low foreshortening, which enables very high deployment accuracy.

Neuroform Atlas™
STENT SYSTEM

The Neuroform Atlas Stent System is authorized under a Humanitarian Device Exemption (HDE). IRB approval is required prior to use.

Copyright © 2017 Stryker

NEURORADIOLOGY
Adding Value & Improving Healthcare

ASNR 2018 ▪ VANCOUVER

ASFNR ASHNR ASPNR ASSR SNIS

THE FOUNDATION OF THE ASNR

Thank You

to the ASNR 56th Annual Meeting & The Foundation of the ASNR Symposium 2018 Partners:

Sustaining Partner

BAYER

Collaborating Partners

BRACCO
LIFE FROM INSIDE

Canon

Guerbet
Contrast for Life

PHILIPS

RAPID

SIEMENS
Healthineers

American Society of Pediatric Neuroradiology

SAVE THE DATE

1st Annual Meeting of the

AMERICAN SOCIETY OF

Pediatric Neuroradiology

January 18-20, 2019

Royal Sonesta Hotel - New Orleans • New Orleans, Louisiana

Please contact Educational Symposia, at 813-806-1000 or ASPNR@edusymp.com or visit www.ASPNR.org for additional information.

Neuroform Atlas™ Stent System

See package insert for complete indications, contraindications, warnings and instructions for use.

Humanitarian Device. Authorized by Federal law for use with neurovascular embolic coils in patients who are ≥ 18 years of age for the treatment of wide neck, intracranial, saccular aneurysms arising from a parent vessel with a diameter of ≥ 2 mm and ≤ 4.5 mm that are not amenable to treatment with surgical clipping. Wide neck aneurysms are defined as having a neck ≥ 4 mm or a dome-to-neck ratio < 2. The effectiveness of this device for this use has not been demonstrated.

INDICATIONS FOR USE

The Neuroform Atlas™ Stent System is indicated for use with neurovascular embolic coils in patients who are ≥ 18 years of age for the treatment of wide neck, intracranial, saccular aneurysms arising from a parent vessel with a diameter of ≥ 2 mm and ≤ 4.5 mm that are not amenable to treatment with surgical clipping. Wide neck aneurysms are defined as having a neck ≥ 4 mm or a dome-to-neck ratio of < 2.

CONTRAINDICATIONS

Patients in whom antiplatelet and/or anticoagulation therapy is contraindicated.

POTENTIAL ADVERSE EVENTS

The potential adverse events listed below, as well as others, may be associated with the use of the Neuroform Atlas™ Stent System or with the procedure:

Allergic reaction to nitinol metal and medications, Aneurysm perforation or rupture, Coil herniation through stent into parent vessel, Death, Embolus, Headache, Hemorrhage, In-stent stenosis, Infection, Ischemia, Neurological deficit/intracranial sequelae, Pseudoaneurysm, Stent fracture, Stent migration/embolization, Stent misplacement, Stent thrombosis, Stroke, Transient ischemic attack, Vasospasm, Vessel occlusion or closure, Vessel perforation/rupture, Vessel dissection, Vessel trauma or damage, Vessel thrombosis, Visual impairment, and other procedural complications including but not limited to anesthetic and contrast media risks, hypotension, hypertension, access site complications.

WARNINGS

- Contents supplied STERILE using an ethylene oxide (EO) process. Do not use if sterile barrier is damaged. If damage is found, call your Stryker Neurovascular representative.
- For single use only. Do not reuse, reprocess or resterilize. Reuse, reprocessing or resterilization may compromise the structural integrity of the device and/or lead to device failure which, in turn, may result in patient injury, illness or death. Reuse, reprocessing or resterilization may also create a risk of contamination of the device and/or cause patient infection or cross-infection, including, but not limited to, the transmission of infectious disease(s) from one patient to another. Contamination of the device may lead to injury, illness or death of the patient.
- After use, dispose of product and packaging in accordance with hospital, administrative and/or local government policy.
- This device should only be used by physicians who have received appropriate training in interventional neuroradiology or interventional radiology and preclinical training on the use of this device as established by Stryker Neurovascular.
- Select a stent size (length) to maintain a minimum of 4 mm on each side of the aneurysm neck along the parent vessel. An incorrectly sized stent may result in damage to the vessel or stent migration. Therefore, the stent is not designed to treat an aneurysm with a neck greater than 22 mm in length.
- If excessive resistance is encountered during the use of the Neuroform Atlas™ Stent System or any of its components at any time during the procedure, discontinue use of the stent system. Continuing to move the stent system against resistance may result in damage to the vessel or a system component.
- Persons allergic to nickel titanium (Nitinol) may suffer an allergic response to this stent implant.
- Purge the system carefully to avoid the accidental introduction of air into the stent system.
- Confirm there are no air bubbles trapped anywhere in the stent system.

CAUTIONS / PRECAUTIONS

- Federal Law (USA) restricts this device to sale by or on the order of a physician.
- Use the Neuroform Atlas Stent System prior to the "Use By" date printed on the package
- Carefully inspect the sterile package and Neuroform Atlas Stent System prior to use to verify that neither has been damaged during shipment. Do not use kinked or damaged components; contact your Stryker Neurovascular representative.
- The stent delivery microcatheter and the Neuroform Atlas Stent delivery wire should not be used to recapture the stent.
- Exercise caution when crossing the deployed stent with adjunctive devices.
- After deployment, the stent may foreshorten from up to 6.3%.
- The max OD of the coiling microcatheter should not exceed the max OD of the stent delivery microcatheter.
- Standard interventional devices with distal tips > 1.8 F may not be able to pass through the interstices of the stent.
- Safety of the Neuroform Atlas Stent System in patients below the age of 18 has not been established.
- In cases where multiple aneurysms are to be treated, start at the most distal aneurysm first.

MAGNETIC RESONANCE IMAGING (MRI)

Safety Information Magnetic Resonance Conditional

Non-clinical testing and analysis have demonstrated that the Neuroform Atlas Stent is MR Conditional alone, or when overlapped with a second stent, and adjacent to a Stryker Neurovascular coil mass. A patient with the Neuroform Atlas Stent can be safely scanned immediately after placement of this implant, under the following conditions:

- Static magnetic field of 1.5 and 3.0 Tesla
- Maximum spatial gradient field up to 2500 Gauss/cm (25 Tesla/m)
- Maximum MR system reported whole body averaged specific absorption rate of 2 W/kg (Normal Operating Mode) and head averaged specific absorption rate of 3.2 W/kg.

Under the scan conditions defined above, the Neuroform Atlas Stent is expected to produce a maximum temperature rise of 4°C after 15 minutes of continuous scanning. The Neuroform Atlas Stent should not migrate in this MRI environment.

In non-clinical testing, the image artifact caused by the device extends approximately 2 mm from the Neuroform Atlas Stent when imaged with a spin echo pulse sequence and 3 Tesla MRI System. The artifact may obscure the device lumen. It may be necessary to optimize MR imaging parameters for the presence of this implant.

Excelsior® XT-17™ Microcatheter

See package insert for complete indications, contraindications, warnings and instructions for use.

INTENDED USE / INDICATIONS FOR USE

Stryker Neurovascular's Excelsior XT-17 Microcatheters are intended to assist in the delivery of diagnostic agents, such as contrast media, and therapeutic agents, such as occlusion coils, into the peripheral, coronary and neuro vasculature.

CONTRAINDICATIONS

None known.

POTENTIAL ADVERSE EVENTS

Potential adverse events associated with the use of microcatheters or with the endovascular procedures include, but are not limited to: access site complications, allergic reaction, aneurysm perforation, aneurysm rupture, death, embolism (air, foreign body, plaque, thrombus), hematoma, hemorrhage, infection, ischemia, neurological deficits, pseudoaneurysm, stroke, transient ischemic attack, vasospasm, vessel dissection, vessel occlusion, vessel perforation, vessel rupture, vessel thrombosis

WARNINGS

- The accessories are not intended for use inside the human body.
- Limited testing has been performed with solutions such as contrast media, saline and suspended embolic particles. The use of these microcatheters for delivery of solutions other than the types that have been tested for compatibility is not recommended. Do not use with glue or glue mixtures.
- Carefully inspect all devices prior to use. Verify shape, size and condition are suitable for the specific procedure.
- Exchange microcatheters frequently during lengthy procedures that require extensive guidewire manipulation or multiple guidewire exchanges.
- Never advance or withdraw an intravascular device against resistance until the cause of the resistance is determined by fluoroscopy. Movement of the microcatheter or guidewire against resistance could dislodge a clot, perforate a vessel wall, or damage microcatheter and guidewire. In severe cases, tip separation of the microcatheter or guidewire may occur.
- Contents supplied STERILE using an ethylene oxide (EO) process. Do not use if sterile barrier is damaged. If damage is found, call your Stryker Neurovascular representative.
- For single use only. Do not reuse, reprocess or resterilize. Reuse, reprocessing or resterilization may compromise the structural integrity of the device and/or lead to device failure which, in turn, may result in patient injury, illness or death. Reuse, reprocessing or resterilization may also create a risk of contamination of the device and/or cause patient infection or cross-infection, including, but not limited to, the transmission of infectious disease(s) from one patient to another. Contamination of the device may lead to injury, illness or death of the patient.
- After use, dispose of product and packaging in accordance with hospital, administrative and/or local government policy.
- These devices are intended for use only by physicians trained in performing endovascular procedures.
- Inspect product before use for any bends, kinks or damage. Do not use a microcatheter that has been damaged. Damaged microcatheters may rupture causing vessel trauma or tip detachment during steering maneuvers.
- The shaping mandrel is not intended for use inside the human body.
- Discontinue use of microcatheter for infusion if increased resistance is noted. Resistance indicates possible blockage. Remove and replace blocked microcatheter immediately. DO NOT attempt to clear blockage by over-pressurization. Doing so may cause the microcatheter to rupture, resulting in vascular damage or patient injury.
- Do not exceed 2,070 kPa (300 psi) infusion pressure. Excessive pressure could dislodge a clot, causing thromboemboli, or could result in a ruptured microcatheter or severed tip, causing vessel injury.

CAUTIONS / PRECAUTIONS

- To reduce the probability of coating damage in tortuous vasculature, use a guide catheter with a minimum internal diameter as specified in Table 1 above, and is recommended for use with Stryker Neurovascular hydrophilically coated microcatheters.
- To control the proper introduction, movement, positioning and removal of the microcatheter within the vascular system, users should employ standard clinical angiographic and fluoroscopic practices and techniques throughout the interventional procedure.
- Exercise care in handling of the microcatheter during a procedure to reduce the possibility of accidental breakage, bending or kinking.
- Use the product prior to the "Use By" date printed on the label.
- Limited testing indicates that Excelsior XT-17 Microcatheter is compatible with Dimethyl Sulfoxide (DMSO). The compatibility of Excelsior XT-17 Microcatheter with individual agents suspended in DMSO has not been established.
- Federal Law (USA) restricts this device to sale by or on the order of a physician.
- Wet dispenser coil or packaging tray and hydrophilically coated outer shaft of microcatheters prior to removal from packaging tray. Once the microcatheter has been wetted, do not allow to dry.
- The packaging mandrel is not intended for reuse. The packaging mandrel is not intended for use inside the human body.
- Check that all fittings are secure so that air is not introduced into guide catheter or microcatheter during continuous flush.
- In order to achieve optimal performance of Stryker Neurovascular Microcatheters and to maintain the lubricity of the Hydrolene® Coating surface, it is critical that a continuous flow of appropriate flush solution be maintained between the Stryker Neurovascular Microcatheter and guide catheter, and the microcatheter and any intraluminal device. In addition, flushing aids in preventing contrast crystal formation and/or clotting on both the intraluminal device and inside the guide catheter and/or the microcatheter lumen.
- Do not position microcatheter closer than 2.54 cm (1 in) from the steam source. Damage to the microcatheter may result.
- Excessive tightening of a hemostatic valve onto the microcatheter shaft may result in damage to the microcatheter. Removing the peel away introducer without a guidewire inserted in the microcatheter lumen might result in damage to the microcatheter shaft.
- To facilitate microcatheter handling, the proximal portion of the microcatheter does not have the hydrophilic surface. Greater resistance may be encountered when this section of the microcatheter is advanced into the RHV.

Excelsior® SL-10® Microcatheter

See package insert for complete indications, contraindications, warnings and instructions for use.

INTENDED USE / INDICATIONS FOR USE

Stryker Neurovascular Excelsior SL-10 Microcatheter is intended to assist in the delivery of diagnostic agents, such as contrast media, and therapeutic agents, such as occlusion coils, into the peripheral, coronary, and neurovasculature.

CONTRAINDICATIONS

None known.

POTENTIAL ADVERSE EVENTS

Potential adverse events associated with the use of microcatheters or with the endovascular procedures include, but are not limited to: access site complications, allergic reaction, aneurysm perforation, aneurysm rupture, death, embolism (air, foreign body, plaque, thrombus), hematoma, hemorrhage, infection, ischemia, neurological deficits, pseudoaneurysm, stroke, transient ischemic attack, vessel dissection, vessel occlusion, vessel perforation, vessel rupture, vessel thrombosis.

WARNINGS

- Contents supplied STERILE using an ethylene oxide (EO) process. Do not use if sterile barrier is damaged. If damage is found, call your Stryker Neurovascular representative.
- For single patient use only. Do not reuse, reprocess or resterilize. Reuse, reprocessing or resterilization may compromise the structural integrity of the device and/or lead to device failure which, in turn, may result in patient injury, illness or death. Reuse, reprocessing or resterilization may also create a risk of contamination of the device and/or cause patient infection or cross-infection, including, but not limited to, the transmission of infectious disease(s) from one patient to another. Contamination of the device may lead to injury, illness or death of the patient.
- After use, dispose of product and packaging in accordance with hospital, administrative and/or local government policy.
- **These devices are intended for use only by physicians trained in performing endovascular procedures.**
- Limited testing has been performed with solutions such as contrast media, saline and suspended embolic particles. The use of these catheters for delivery of solutions other than the types that have been tested for compatibility is not recommended. Do not use with glue or glue mixtures.
- The accessories are not intended for use inside the human body.
- Carefully inspect all devices prior to use. Verify shape, size and condition are suitable for the specific procedure.
- Exchange microcatheters frequently during lengthy procedures that require extensive guidewire manipulation or multiple guidewire exchanges.
- Never advance or withdraw an intravascular device against resistance until the cause of the resistance is determined by fluoroscopy. Movement of the microcatheter or guidewire against resistance could dislodge a clot, perforate a vessel wall, or damage microcatheter and guidewire. In severe cases, tip separation of the microcatheter or guidewire may occur.
- Inspect product before use for any bends, kinks or damage. Do not use a microcatheter that has been damaged. Damaged microcatheters may rupture causing vessel trauma or tip detachment during steering maneuvers.
- Shaping mandrel is not intended for use inside the human body.
- Discontinue use of microcatheter for infusion if increased resistance is noted. Resistance indicates possible blockage. Remove and replace blocked microcatheter immediately. DO NOT attempt to clear blockage by over-pressurization. Doing so may cause the microcatheter to rupture, resulting in vascular damage or patient injury.
- Do not exceed 2,070 kPa (300 psi) infusion pressure. Excessive pressure could dislodge a clot, causing thromboemboli, or could result in a ruptured microcatheter or severed tip, causing vessel injury.

CAUTIONS / PRECAUTIONS

- Federal Law (USA) restricts this device to sale by or on the order of a physician.
- To facilitate microcatheter handling, the proximal portion of the microcatheter does not have the hydrophilic surface. Greater resistance may be encountered when this section of the microcatheter is advanced into the RHV.
- Exercise care in handling of the microcatheter during a procedure to reduce the possibility of accidental breakage, bending or kinking.
- To reduce the probability of coating damage in tortuous vasculature, use a guide catheter with a minimum internal diameter that is ≥ 1.00 mm (0.038 in) and is recommended for use with Stryker Neurovascular hydrophilically coated microcatheters.
- To control the proper introduction, movement, positioning and removal of the microcatheter within the vascular system, users should employ standard clinical angiographic and fluoroscopic practices and techniques throughout the interventional procedure.
- Flush dispenser coil of hydrophilically coated microcatheters prior to removal from dispenser coil. Once the microcatheter has been wetted, do not allow to dry. Do not reinsert the microcatheter into dispenser coil.
- Do not position microcatheter closer than 2.54 cm (1 in) from the steam source. Damage to the microcatheter may result.
- Check that all fittings are secure so that air is not introduced into guide catheter or microcatheter during continuous flush.
- In order to achieve optimal performance of Stryker Neurovascular Microcatheters and to maintain the lubricity of the Hydrolene® Coating surface, it is critical that a continuous flow of appropriate flush solution be maintained between the Stryker Neurovascular Microcatheter and guide catheter, and the microcatheter and any intraluminal device. In addition, flushing aids in preventing contrast crystal formation and/or clotting on both the intraluminal device and inside the guide catheter and/or the microcatheter lumen.
- Excessive tightening of a hemostatic valve onto the microcatheter shaft may result in damage to the microcatheter.

Stryker Neurovascular
47900 Bayside Parkway
Fremont, CA 94538

strykerneurovascular.com

Date of Release: NOV/2017

EX_EN_US

Copyright © 2017 Stryker

Trevo® XP ProVue Retrievers

See package insert for complete indications, complications, warnings and instructions for use.

INDICATIONS FOR USE

1. The Trevo Retriever is indicated for use to restore blood flow in the neurovasculature by removing thrombus for the treatment of acute ischemic stroke to reduce disability in patients with a persistent, proximal anterior circulation, large vessel occlusion, and smaller core infarcts who have first received intravenous tissue plasminogen activator (IV t-PA). Endovascular therapy with the device should start within 6 hours of symptom onset.
2. The Trevo Retriever is intended to restore blood flow in the neurovasculature by removing thrombus in patients experiencing ischemic stroke within 8 hours of symptom onset. Patients who are ineligible for intravenous tissue plasminogen activator (IV t-PA) or who fail IV t-PA therapy are candidates for treatment.
3. The Trevo Retriever is indicated for use to restore blood flow in the neurovasculature by removing thrombus for the treatment of acute ischemic stroke to reduce disability in patients with a persistent, proximal anterior circulation, large vessel occlusion of the internal carotid artery (ICA) or middle cerebral artery (MCA)-M1 segments with smaller core infarcts (0-50cc for age < 80 years, 0-20cc for age ≥ 80 years). Endovascular therapy with the device should start within 6-24 hours of time last seen well in patients who are ineligible for intravenous tissue plasminogen activator (IV t-PA) or who fail IV t-PA therapy.

COMPLICATIONS

Procedures requiring percutaneous catheter introduction should not be attempted by physicians unfamiliar with possible complications which may occur during or after the procedure. Possible complications include, but are not limited to, the following: air embolism; hematoma or hemorrhage at puncture site; infection; distal embolization; pain/headache; vessel spasm, thrombosis, dissection, or perforation; emboli; acute occlusion; ischemia; intracranial hemorrhage; false aneurysm formation; neurological deficits including stroke; and death.

COMPATIBILITY

3x20mm retrievers are compatible with Trevo® Pro 14 Microcatheters (REF 90231) and Trevo® Pro 18 Microcatheters (REF 90238). 4x20mm retrievers are compatible with Trevo® Pro 18 Microcatheters (REF 90238). 4x30mm retrievers are compatible with Excelsior® XT-27® Microcatheters (150cm x 6cm straight REF 275081) and Trevo® Pro 18 Microcatheters (REF 90238). 6x25mm Retrievers are compatible with Excelsior® XT-27® Microcatheters (150cm x 6cm straight REF 275081). Recommended minimum vessel ID for all Retriever sizes is 2.5mm. Compatibility of the Retriever with other microcatheters has not been established. Performance of the Retriever device may be impacted if a different microcatheter is used.

Balloon Guide Catheters (such as Merci® Balloon Guide Catheter and FlowGate® Balloon Guide Catheter) are recommended for use during thrombus removal procedures.

Retrievers are compatible with the Abbott Vascular DOC® Guide Wire Extension (REF 22260).

Retrievers are compatible with Boston Scientific Rotating Hemostatic Valve (Ref 421242).

SPECIFIC WARNINGS FOR INDICATION 1

- The safety and effectiveness of the Trevo Retrievers in reducing disability has not been established in patients with large core infarcts (i.e. ASPECTS ≤ 7). There may be increased risks, such as intracerebral hemorrhage, in these patients.
- The safety and effectiveness of the Trevo Retrievers in reducing disability has not been established or evaluated in patients with occlusions in the posterior circulation (e.g., basilar or vertebral arteries) or for more distal occlusions in the anterior circulation.

SPECIFIC WARNINGS FOR INDICATION 2

- To reduce risk of vessel damage, take care to appropriately size Retriever to vessel diameter at intended site of deployment.

SPECIFIC WARNINGS FOR INDICATION 3

- The safety and effectiveness of the Trevo Retrievers in reducing disability has not been established in patients with large core infarcts (i.e., ASPECTS ≤ 7). There may be increased risks, such as intracerebral hemorrhage, in these patients.
- The safety and effectiveness of the Trevo Retrievers in reducing disability has not been established or evaluated in patients with occlusions in the posterior circulation (e.g., basilar or vertebral arteries) or for more distal occlusions in the anterior circulation.
- Users should validate their imaging software analysis techniques to ensure robust and consistent results for assessing core infarct size.

WARNINGS APPLIED TO ALL INDICATIONS

- Administration of IV t-PA should be within the FDA-approved window (within 3 hours of stroke symptom onset).
- To reduce risk of vessel damage, adhere to the following recommendations:
  - Do not perform more than six (6) retrieval attempts in same vessel using Retriever devices.
  - Maintain Retriever position in vessel when removing or exchanging Microcatheter.
- To reduce risk of kinking/fracture, adhere to the following recommendations:
  - Immediately after unsheathing Retriever, position Microcatheter tip marker just proximal to shaped section. Maintain Microcatheter tip marker just proximal to shaped section of Retriever during manipulation and withdrawal.
  - Do not rotate or torque Retriever.
  - Use caution when passing Retriever through stented arteries.
- The Retriever is a delicate instrument and should be handled carefully. Before use and when possible during procedure, inspect device carefully for damage. Do not use a device that shows signs of damage. Damage may prevent device from functioning and may cause complications.
- Do not advance or withdraw Retriever against resistance or significant vasospasm. Moving or torquing device against resistance or significant vasospasm may result in damage to vessel or device. Assess cause of resistance using fluoroscopy and if needed resheath the device to withdraw.
- If Retriever is difficult to withdraw from the vessel, do not torque Retriever. Advance Microcatheter distally, gently pull Retriever back into Microcatheter, and remove Retriever and Microcatheter as a unit. If undue resistance is met when withdrawing the Retriever into the Microcatheter, consider extending the Retriever using the Abbott Vascular DOC guidewire extension (REF 22260) so that the Microcatheter can be exchanged for a larger diameter catheter such as a DAC® Catheter. Gently withdraw the Retriever into the larger diameter catheter.
- Administer anti-coagulation and anti-platelet medications per standard institutional guidelines.
- Users should take all necessary precautions to limit X-radiation doses to patients and themselves by using sufficient shielding, reducing fluoroscopy times, and modifying X-ray technical factors where possible.

PRECAUTIONS

- Prescription only – device restricted to use by or on order of a physician.
- Store in cool, dry, dark place.
- Do not use open or damaged packages.
- Use by "Use By" date.
- Exposure to temperatures above 54°C (130°F) may damage device and accessories. Do not autoclave.
- Do not expose Retriever to solvents.
- Use Retriever in conjunction with fluoroscopic visualization and proper anti-coagulation agents.
- To prevent thrombus formation and contrast media crystal formation, maintain a constant infusion of appropriate flush solution between guide catheter and Microcatheter and between Microcatheter and Retriever or guidewire.
- Do not attach a torque device to the shaped proximal end of DOC® Compatible Retriever. Damage may occur, preventing ability to attach DOC® Guide Wire Extension.

DOC is a trademark of Abbott Laboratories.

Stryker Neurovascular
47900 Bayside Parkway
Fremont, CA 94538

strykerneurovascular.com

Date of Release: APR/2018

EX_EN_US

Copyright © 2018 Stryker

AJNR

AMERICAN JOURNAL OF NEURORADIOLOGY

JUNE 2018
VOLUME 39
NUMBER 6
WWW.AJNR.ORG

Publication Preview at www.ajnr.org features articles released in advance of print. Visit www.ajnrblog.org to comment on AJNR content and chat with colleagues and AJNR's News Digest at http://ajnrdigest.org to read the stories behind the latest research in neuroimaging.

993 **PERSPECTIVES** *E. Attaya*

REVIEW ARTICLE

994 **What Have We Learned from Perfusion MRI in Multiple Sclerosis?** *E. Lapointe, et al.* — ADULT BRAIN

RESEARCH PERSPECTIVES

1001 **Who's Contributing Most to American Neuroscience Journals: American or Foreign Authors?** *P. Charkhchi, et al.*

GENERAL CONTENTS

1008 **Multisite Concordance of DSC-MRI Analysis for Brain Tumors: Results of a National Cancer Institute Quantitative Imaging Network Collaborative Project** *K.M. Schmainda, et al.* — ADULT BRAIN

1017 **Edge Contrast of the FLAIR Hyperintense Region Predicts Survival in Patients with High-Grade Gliomas following Treatment with Bevacizumab** *N. Bahrami, et al.* — ADULT BRAIN

1025 **Postcontrast T1 Mapping for Differential Diagnosis of Recurrence and Radionecrosis after Gamma Knife Radiosurgery for Brain Metastasis** *B. Wang, et al.* — ADULT BRAIN

1032 **Comparative Analysis of Diffusional Kurtosis Imaging, Diffusion Tensor Imaging, and Diffusion-Weighted Imaging in Grading and Assessing Cellular Proliferation of Meningiomas** *L. Lin, et al.* — ADULT BRAIN

1039 **Sequential Apparent Diffusion Coefficient for Assessment of Tumor Progression in Patients with Low-Grade Glioma** *I.E. Chen, et al.* — ADULT BRAIN

1047 **MRI Planimetry and Magnetic Resonance Parkinsonism Index in the Differential Diagnosis of Patients with Parkinsonism** *V.C. Constantinides, et al.* — ADULT BRAIN

1052 **Dark Rims: Novel Sequence Enhances Diagnostic Specificity in Multiple Sclerosis** *J.-M. Tillema, et al.* — ADULT BRAIN

1059 **Association of Quantified Location-Specific Blood Volumes with Delayed Cerebral Ischemia after Aneurysmal Subarachnoid Hemorrhage** *W.E. van der Steen, et al.* — ADULT BRAIN

AJNR (Am J Neuroradiol ISSN 0195–6108) is a journal published monthly, owned and published by the American Society of Neuroradiology (ASNR), 800 Enterprise Drive, Suite 205, Oak Brook, IL 60523. Annual dues for the ASNR include $170.00 for journal subscription. The journal is printed by Cadmus Journal Services, 5457 Twin Knolls Road, Suite 200, Columbia, MD 21045; Periodicals postage paid at Oak Brook, IL and additional mailing offices. Printed in the U.S.A. POSTMASTER: Please send address changes to American Journal of Neuroradiology, P.O. Box 3000, Denville, NJ 07834, U.S.A. Subscription rates: nonmember $400 ($470 foreign) print and online, $320 online only; institutions $460 ($530 foreign) print and basic online, $915 ($980 foreign) print and extended online, $380 online only (basic), extended online $825; single copies are $35 each ($40 foreign). Indexed by PubMed/Medline, BIOSIS Previews, Current Contents (Clinical Medicine and Life Sciences), EMBASE, Google Scholar, HighWire Press, Q-Sensei, RefSeek, Science Citation Index, SCI Expanded, and Meta/CZI. Copyright © American Society of Neuroradiology.

1065 **Blood Flow Mimicking Aneurysmal Wall Enhancement: A Diagnostic Pitfall of Vessel Wall MRI Using the Postcontrast 3D Turbo Spin-Echo MR Imaging Sequence** *E. Kalsoum, et al.* — ADULT BRAIN

1068 **Use of Diffusional Kurtosis Imaging and Dynamic Contrast-Enhanced MR Imaging to Predict Posttraumatic Epilepsy in Rabbits** *W. Li, et al.* — ADULT BRAIN

1074 **Value of Quantitative Collateral Scoring on CT Angiography in Patients with Acute Ischemic Stroke** *A.M.M. Boers, et al.* — INTERVENTIONAL ADULT BRAIN

1083 **Clinical Outcomes of Endovascular Treatment within 24 Hours in Patients with Mild Ischemic Stroke and Perfusion Imaging Selection** *X. Shang, et al.* — INTERVENTIONAL

1088 **Slow Collateral Flow Is Associated with Thrombus Extension in Patients with Acute Large-Artery Occlusion** *R. Zhang, et al.* — INTERVENTIONAL

1093 **Multicentric Experience in Distal-to-Proximal Revascularization of Tandem Occlusion Stroke Related to Internal Carotid Artery Dissection** *G. Marnat, et al.* — INTERVENTIONAL

1100 **Treatment of Distal Anterior Cerebral Artery Aneurysms with Flow-Diverter Stents: A Single-Center Experience** *F. Cagnazzo, et al.* — INTERVENTIONAL

1107 **Surpass Streamline Flow-Diverter Embolization Device for Treatment of Iatrogenic and Traumatic Internal Carotid Artery Injuries** *M. Ghorbani, et al.* — INTERVENTIONAL

1112 **Comparison of 3T Intracranial Vessel Wall MRI Sequences** *A. Lindenholz, et al.* — EXTRACRANIAL VASCULAR

1121 **Anatomic and Angiographic Analyses of Ophthalmic Artery Collaterals in Moyamoya Disease** *T. Robert, et al.* — EXTRACRANIAL VASCULAR

1127 **Segmentation of the Globus Pallidus Internus Using Probabilistic Diffusion Tractography for Deep Brain Stimulation Targeting in Parkinson Disease** *E.H. Middlebrooks, et al.* — FUNCTIONAL

1135 **Cavitary Plaques in Otospongiosis: CT Findings and Clinical Implications** *P. Puac, et al.* — HEAD & NECK

1140 **Submandibular Gland Transfer: A Potential Imaging Pitfall** *X. Wu, et al.* — HEAD & NECK

1146 **Characteristic MR Imaging Findings of the Neonatal Brain in RASopathies** *M.N. Cizmeci, et al.* — PEDIATRICS

1153 **Clival Malformations in CHARGE Syndrome** *E.S. Mahdi, et al.* — PEDIATRICS

1157 **Noninvasive Assessment of Hemodynamic Stress Distribution after Indirect Revascularization for Pediatric Moyamoya Vasculopathy** *D. Tortora, et al.* — PEDIATRICS

1164 **Volumetric Brain MRI Study in Fetuses with Congenital Heart Disease** *H. Olshaker, et al.* — PEDIATRICS

1170 **Postnatal Brain Growth Assessed by Sequential Cranial Ultrasonography in Infants Born <30 Weeks' Gestational Age** *R. Cuzzilla, et al.* — PEDIATRICS

1177 **Altered White Matter Microstructure in the Corpus Callosum and Its Cerebral Interhemispheric Tracts in Adolescent Idiopathic Scoliosis: Diffusion Tensor Imaging Analysis** *C. Xue, et al.* — PEDIATRICS

1185 **CSF Pressure Change in Relation to Opening Pressure and CSF Volume Removed** *B. Griffith, et al.* — SPINE

MEMORIAL

1191 **Brian C. Bowen, MD, PhD** *R.M. Quencer*

ONLINE FEATURES

CONSENSUS STATEMENT

E61 **Multisociety Consensus Quality Improvement Revised Consensus Statement for Endovascular Therapy of Acute Ischemic Stroke**
D. Sacks, et al.

LETTERS

E77 **Targeting the Clot in Acute Stroke** *K.-O. Lövblad*

E78 **Consensus Needed for Noncontrast CT Markers in Intracerebral Hemorrhage** *G. Boulouis, et al.*

E80 **Increasing the Accuracy of Optic Nerve Measurement Using 3D Volumetry** *A. Lecler, et al.*

E81 ***Reply*** *C.E. Al-Haddad, et al.*

BOOK REVIEWS *R.M. Quencer, Section Editor*
Please visit www.ajnrblog.org to read and comment on Book Reviews.

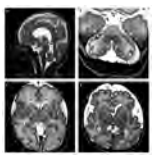

Characteristic MR imaging findings of neonates with RASopathy. *A*, T2-weighted sagittal image shows a vertical tentorium and splenium of the corpus callosum. *B*, T2-weighted axial MRI demonstrates the hemorrhagic and cystic lesions in the peripheral regions of the cerebellum. *C*, T2-weighted axial MRI shows a mildly enlarged extracerebral space with severe white matter injury. *D*, Axial T2-weighted MRI shows a severely enlarged extracerebral space, punctate white matter lesions, and a small amount of blood in the lateral ventricles.

Indicates Editor's Choices selection
Indicates Fellows' Journal Club selection
Indicates open access to non-subscribers at www.ajnr.org
Indicates article with supplemental on-line table
Indicates article with supplemental on-line photo
Indicates article with supplemental on-line video
Evidence-Based Medicine Level 1
Evidence-Based Medicine Level 2

AJNR

AMERICAN JOURNAL OF NEURORADIOLOGY

Publication Preview at www.ajnr.org features articles released in advance of print. Visit www.ajnrblog.org to comment on AJNR content and chat with colleagues and AJNR's News Digest at http://ajnrdigest.org to read the stories behind the latest research in neuroimaging.

JUNE 2018 • VOLUME 39 • NUMBER 6 • WWW.AJNR.ORG

Official Journal:
American Society of Neuroradiology
American Society of Functional Neuroradiology
American Society of Head and Neck Radiology
American Society of Pediatric Neuroradiology
American Society of Spine Radiology

EDITOR-IN-CHIEF

Jeffrey S. Ross, MD
Professor of Radiology, Department of Radiology, Mayo Clinic College of Medicine, Phoenix, AZ

SENIOR EDITORS

Harry J. Cloft, MD, PhD
Professor of Radiology and Neurosurgery, Department of Radiology, Mayo Clinic College of Medicine, Rochester, MN

Thierry A.G.M. Huisman, MD
Professor of Radiology, Pediatrics, Neurology, and Neurosurgery, Chairman, Department of Imaging and Imaging Science, Johns Hopkins Bayview, Director, Pediatric Radiology and Pediatric Neuroradiology, Johns Hopkins Hospital, Baltimore, MD

Yvonne W. Lui, MD
Associate Professor of Radiology, Chief of Neuroradiology, New York University School of Medicine, New York, NY

C.D. Phillips, MD, FACR
Professor of Radiology, Weill Cornell Medical College, Director of Head and Neck Imaging, New York-Presbyterian Hospital, New York, NY

Pamela W. Schaefer, MD
Clinical Director of MRI and Associate Director of Neuroradiology, Massachusetts General Hospital, Boston, Massachusetts, Associate Professor, Radiology, Harvard Medical School, Cambridge, MA

Charles M. Strother, MD
Professor of Radiology, Emeritus, University of Wisconsin, Madison, WI

STATISTICAL SENIOR EDITOR

Bryan A. Comstock, MS
Senior Biostatistician, Department of Biostatistics, University of Washington, Seattle, WA

EDITORIAL BOARD

Ashley H. Aiken, *Atlanta, GA*
Lea M. Alhilali, *Phoenix, AZ*
John D. Barr, *Dallas, TX*
Ari Blitz, *Baltimore, MD*
Barton F. Branstetter IV, *Pittsburgh, PA*
Jonathan L. Brisman, *Lake Success, NY*
Julie Bykowski, *San Diego, CA*
Keith Cauley, *Danville, PA*
Asim F. Choudhri, *Memphis, TN*
Alessandro Cianfoni, *Lugano, Switzerland*
J. Matthew Debnam, *Houston, TX*
Seena Dehkharghani, *New York, NY*
Colin Derdeyn, *Iowa City, IA*
Rahul S. Desikan, *San Francisco, CA*
Yonghong Ding, *Rochester, MN*
Clifford J. Eskey, *Hanover, NH*
Saeed Fakhran, *Phoenix, AZ*
Massimo Filippi, *Milan, Italy*
Allan J. Fox, *Toronto, Ontario, Canada*
Wende N. Gibbs, *Los Angeles, CA*
Christine M. Glastonbury, *San Francisco, CA*
John L. Go, *Los Angeles, CA*
Allison Grayev, *Madison, WI*
Brent Griffith, *Detroit, MI*
Wan-Yuo Guo, *Taipei, Taiwan*
Ajay Gupta, *New York, NY*
Rakesh K. Gupta, *Lucknow, India*
Lotfi Hacein-Bey, *Sacramento, CA*
Christopher P. Hess, *San Francisco, CA*
Andrei Holodny, *New York, NY*
Benjamin Huang, *Chapel Hill, NC*
George J. Hunter, *Boston, MA*
Mahesh V. Jayaraman, *Providence, RI*
Valerie Jewells, *Chapel Hill, NC*
Christof Karmonik, *Houston, TX*
Timothy J. Kaufmann, *Rochester, MN*
Hillary R. Kelly, *Boston, MA*
Toshibumi Kinoshita, *Akita, Japan*
Kennith F. Layton, *Dallas, TX*
Michael M. Lell, *Nürnberg, Germany*
Michael Lev, *Boston, MA*
Karl-Olof Lovblad, *Geneva, Switzerland*
Franklin A. Marden, *Chicago, IL*
M. Gisele Matheus, *Charleston, SC*
Joseph C. McGowan, *Merion Station, PA*
Stephan Meckel, *Freiburg, Germany*
Christopher J. Moran, *St. Louis, MO*
Takahisa Mori, *Kamakura City, Japan*
Suresh Mukherji, *Ann Arbor, MI*
Amanda Murphy, *Toronto, Ontario, Canada*
Alexander J. Nemeth, *Chicago, IL*
Sasan Partovi, *Cleveland, OH*
Laurent Pierot, *Reims, France*
Jay J. Pillai, *Baltimore, MD*
Whitney B. Pope, *Los Angeles, CA*
M. Judith Donovan Post, *Miami, FL*
Tina Young Poussaint, *Boston, MA*
Joana Ramalho, *Lisbon, Portugal*
Otto Rapalino, *Boston, MA*
Álex Rovira-Cañellas, *Barcelona, Spain*
Paul M. Ruggieri, *Cleveland, OH*
Zoran Rumboldt, *Rovinj-Rovigno, Croatia*
Amit M. Saindane, *Atlanta, GA*
Erin Simon Schwartz, *Philadelphia, PA*
Lubdha M. Shah, *Salt Lake City, UT*
Aseem Sharma, *St. Louis, MO*
J. Keith Smith, *Chapel Hill, NC*
Maria Vittoria Spampinato, *Charleston, SC*
Gordon K. Sze, *New Haven, CT*
Krishnamoorthy Thamburaj, *Hershey, PA*
Cheng Hong Toh, *Taipei, Taiwan*
Thomas A. Tomsick, *Cincinnati, OH*
Aquilla S. Turk, *Charleston, SC*
Willem Jan van Rooij, *Tilburg, Netherlands*
Arastoo Vossough, *Philadelphia, PA*
Elysa Widjaja, *Toronto, Ontario, Canada*
Max Wintermark, *Stanford, CA*
Ronald L. Wolf, *Philadelphia, PA*
Kei Yamada, *Kyoto, Japan*
Carlos Zamora, *Chapel Hill, NC*

EDITORIAL FELLOW

Vahe Zohrabian, *New Haven, CT*

SPECIAL CONSULTANTS TO THE EDITOR

AJNR Blog Editor
Neil Lall, *Denver, CO*
Case of the Month Editor
Nicholas Stence, *Aurora, CO*
Case of the Week Editors
Juan Pablo Cruz, *Santiago, Chile*
Sapna Rawal, *Toronto, Ontario, Canada*
Classic Case Editor
Sandy Cheng-Yu Chen, *Taipei, Taiwan*
Health Care and Socioeconomics Editor
Pina C. Sanelli, *New York, NY*
Physics Editor
Greg Zaharchuk, *Stanford, CA*
Podcast Editor
Wende N. Gibbs, *Los Angeles, CA*
Twitter Editor
Jennifer McCarty, *Atlanta, Georgia*

YOUNG PROFESSIONALS ADVISORY COMMITTEE

Asim K. Bag, *Birmingham, AL*
Anna E. Nidecker, *Sacramento, CA*
Peter Yi Shen, *Sacramento, CA*

Founding Editor
Juan M. Taveras
Editors Emeriti
Mauricio Castillo, Robert I. Grossman, Michael S. Huckman, Robert M. Quencer

Managing Editor
Karen Halm
Assistant Managing Editor
Laura Wilhelm
Digital Publications and Social Media Coordinator
Kylie Mason
Executive Director, ASNR
Mary Beth Hepp

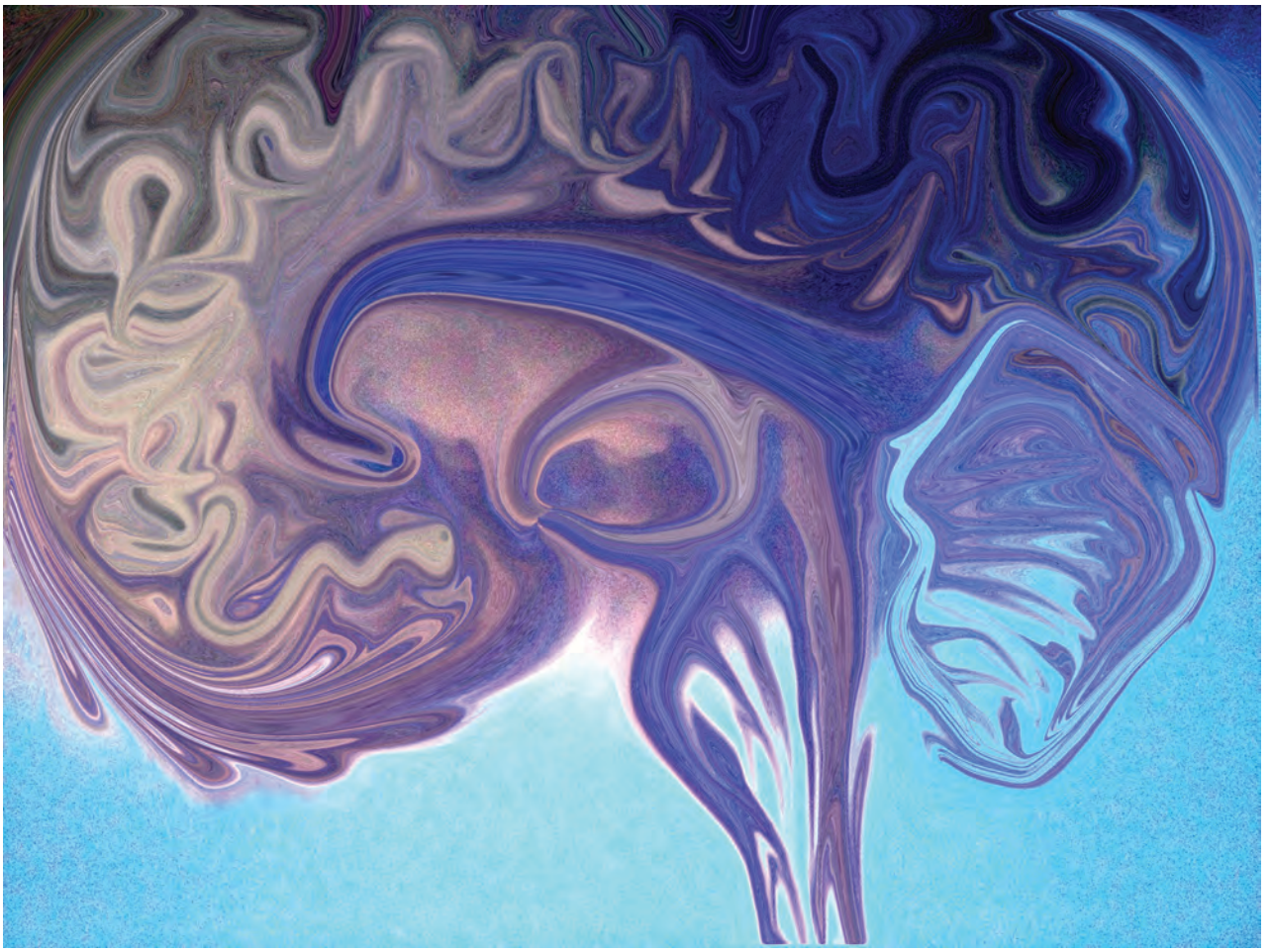

Title: Clouds. This is a photograph of cumulus clouds. I used a distortion filter to move parts of the image around to create this sagittal image of the brain.

Eman Attaya, MD, University Medical Center, Lubbock, Texas

What Have We Learned from Perfusion MRI in Multiple Sclerosis?

E. Lapointe, D.K.B. Li, A.L. Traboulsee, and A. Rauscher

ABSTRACT

SUMMARY: Using MR imaging, perfusion can be assessed either by dynamic susceptibility contrast MR imaging or arterial spin-labeling. Alterations of cerebral perfusion have repeatedly been described in multiple sclerosis compared with healthy controls. Acute lesions exhibit relative hyperperfusion in comparison with normal-appearing white matter, a finding mostly attributed to inflammation in this stage of lesion development. In contrast, normal-appearing white and gray matter of patients with MS has been mostly found to be hypoperfused compared with controls, and correlations with cognitive impairment as well as fatigue in multiple sclerosis have been described. Mitochondrial failure, axonal degeneration, and vascular dysfunction have been hypothesized to underlie the perfusion MR imaging findings. Clinically, perfusion MR imaging could allow earlier detection of the acute focal inflammatory changes underlying relapses and new lesions, and could constitute a marker for cognitive dysfunction in MS. Nevertheless, the clinical relevance and pathogenesis of the brain perfusion changes in MS remain to be clarified.

ABBREVIATIONS: ASL = arterial spin-labeling; DCE = dynamic contrast-enhanced; NAWM = normal-appearing white matter; RRMS = relapsing-remitting MS

Multiple sclerosis is considered an immune-mediated disease characterized by inflammation and neurodegeneration.[1] However, the pathogenesis of the disease is incompletely understood.[1] Advanced imaging techniques have been used to better characterize and understand the disease. Interest in vascular pathology contributing to MS pathogenesis has grown following several observations: Lesions are known to predominantly develop around small central veins,[2] and there is lymphocytic infiltration of the vein walls, perhaps preceding perivenular inflammatory infiltration.[2,3] Microvascular occlusive changes have occasionally been described, suggesting that ischemia could occur in MS.[4]

Positron-emission tomography and single-photon emission CT were first used to evaluate brain perfusion in MS. Early studies found white and gray matter oxygen hypometabolism and reduced blood flow in comparison with healthy controls, with some correlations with cognitive dysfunction.[5-7] MR imaging is a non-ionizing radiation technique that offers faster acquisition and better signal-to-noise and contrast-to-noise ratios than these techniques, and it allows unlimited repeat measurements in the same patients.[8]

This review summarizes the perfusion MR imaging literature in MS, important clinical correlations, and presumed underlying mechanisms.

Perfusion MR Imaging Techniques

Using MR imaging, perfusion can be assessed by either measuring the effects of a paramagnetic contrast agent or labeling inflowing spins with a radiofrequency pulse. The former approach includes dynamic susceptibility contrast and dynamic contrast-enhanced (DCE) MR imaging; the latter is called arterial spin-labeling (ASL).

Dynamic Susceptibility Contrast MR Imaging

In DSC, an intravenous paramagnetic contrast agent is administered, and the brain is scanned with a rapid imaging technique, typically T2*-weighted single-shot gradient-echo-planar imaging[9] or a T2-weighted spin-echo-planar scan. When the contrast agent reaches the tissue vasculature, it makes the vessels more paramagnetic, creating field inhomogeneities around the vessels. These lead to accelerated dephasing of magnetization (ie, a signal reduction via accelerated R2* relaxation). By measuring the signal dynamically with a temporal resolution of typically 1–2 seconds and knowing the relaxivity of the contrast agent, one can measure

From the Division of Neurology (E.L., A.L.T.), Department of Medicine (E.L., A.L.T.), MRI Research Center (A.R.), and Departments of Pediatrics (A.R.) and Radiology (D.K.B.L.), University of British Columbia, Djavad Mowafaghian Center for Brain Health, Vancouver, British Columbia, Canada.

Please address correspondence to Emmanuelle Lapointe, MD, Division of Neurology and Department of Medicine, DM Center for Brain Health, 2215 Wesbrook Mall, Vancouver, BC, V6T 2B5 Canada; e-mail: emmanuelle.lapointe@usherbrooke.ca

Indicates open access to non-subscribers at www.ajnr.org

http://dx.doi.org/10.3174/ajnr.A5504

the contrast agent concentration across time. This function can be converted into maps of cerebral blood flow, cerebral blood volume, and temporal parameters such as mean transit time.[9] However, this step requires a deconvolution with the concentration function in a feeding artery, the arterial input function, which has its limitations. Deconvolution is an inherently ill-posed mathematic operation, and accurate measurement of the arterial input function is hampered by partial volume effects.[9]

A variant of gradient-echo DSC is spin-echo DSC, which uses a spin-echo-planar scan. The effects of a contrast agent on the spin-echo signal are much weaker than on the gradient-echo signal. In the former, the signal loss is mainly mediated by diffusion of spins within a magnetically inhomogeneous environment. In the latter, there is additional static dephasing of spins in the same inhomogeneous environment. Due to the stronger effect of the contrast agent on the gradient-echo signal, most studies use gradient-echo signal planar imaging. Numerical simulations[10,11] and experiments[10] have shown that spin-echo DSC is particularly sensitive to capillary-sized vessels, whereas the sensitivity of gradient-echo DSC is similar for a broad range of vessel sizes. Both techniques benefit from higher field strengths due to increased susceptibility effects from the contrast agent.

Typical parameters of a gradient-echo DSC scan are a voxel size of 3 × 3 mm and a slice thickness of 3–5 mm. At 3T, the TE is in a range of 30–50 ms for gradient-echo DSC and around 50–70 ms for spin-echo DSC. The TR is as short as possible, typically between 1 and 2 seconds. Because the DSC scan needs to capture the dynamics of the contrast agent entering and exiting the brain tissue, scan times are typically in the range of 1–3 minutes.[8,12,13] The cortical ribbon is thinner than the typical voxel size of DSC MR imaging. Recent developments in rapid imaging using multiband MR imaging[14] will allow further reduction of TR and/or reduction of voxel size. The reduced TR increases the temporal signal-to-noise ratio,[15] and the smaller voxel size reduces partial volume effects between cortical gray matter and underlying white matter, allowing improved assessment of cortical perfusion.

Dynamic Contrast-Enhanced Imaging

Dynamic contrast-enhanced imaging uses T1-shortening due to a contrast agent[16] to detect areas of disrupted blood-brain barrier. DCE-MR imaging is performed by acquiring repeat T1-weighted scans after intravenous injection of a contrast agent. The signal enhancement across time can be used to compute maps of blood-brain barrier integrity. Therefore, DCE is the standard approach for the measurement of permeability. However, high-temporal-resolution DCE can also assess perfusion information. DCE is mainly used for tumor imaging, and applications to MS are rare though it has been used to characterize the spatiotemporal enhancement patterns of active lesions.[17] Typical scan times are in the range of 4–8 minutes.[17]

Arterial Spin-Labeling

In ASL, 2 images are acquired, 1 with and 1 without a labeling pulse.[18] In both images, blood is allowed a certain delay time to flow into the imaging volume. The difference between the 2 images shows only signal from spins that have moved into the tissue and is therefore a measure of CBF. The delay time ranges between 1 and 3 seconds to allow the blood to reach the capillary bed. In principle, longer delay times would allow the spins to reach the venous system. However, the T1-relaxation time is short relative to the arterial-venous transit time, and the labeling has decayed before spins reach the venous system. The postlabeling delay poses a trade-off. For short delays, the blood may not have reached all brain regions. For long delays, the labeling has decayed due to T1 relaxation, resulting in a reduced signal-to-noise ratio. Because of the prolonged T1, ASL benefits from higher field strengths. Scan times are between 2 and 4 minutes for this technique.[19] The recently published consensus guidelines recommend the use of pseudocontinuous ASL labeling.[19] Due to the lower signal-to-noise ratio of ASL compared with DSC, spatial resolution is sometimes lower than in DSC, further complicating the evaluation of cortical gray matter and small lesions, so ALS is currently not recommended for use in WM.[19] There are several additional pitfalls with ASL. The labeling may be inefficient, resulting in low apparent CBF in the insufficiently labeled vascular territory. Motion between the 2 scans may be present but can be mitigated by image registration and by suppressing nonmoving spins (ie, background tissue). Areas more distal to the labeling plane have longer transit times during which some of the labeling has decayed. This effect may be erroneously interpreted as reduced CBF.

Perfusion in MS Lesions

Wuerfel et al[20] first analyzed the evolution of the perfusion of gadolinium-enhancing lesion formation in 20 patients with relapsing-remitting multiple sclerosis (RRMS) using spin-echo DSC. They observed a 20% increase in CBF and CBV from baseline up to 3 weeks before enhancement, a 25% increase at the time of enhancement, and a slow decline to baseline during 20 weeks after initial gadolinium enhancement. Ring-enhancing lesions showed similar changes only in the enhancing periphery, the site of maximal inflammation on pathology.[21] Indeed, clustering of macrophages and active demyelination are present at the edge of active MS ring-enhancing lesions.[21] These findings suggest that perfusion MR imaging is highly sensitive to inflammatory activity and able to show changes long before and after blood-brain barrier disruption can be detected with gadolinium enhancement.

DCE-MR imaging permits observation of enhancement patterns across more time.[17] Gaitán et al[17] found that smaller nodular contrast-enhancing lesions enhance centrifugally, whereas larger ring-enhancing or expanding nodular enhancing lesions enhance centripetally; this feature likely reflects the outward expansion of the lesions from the central vein during their formation.

Observations from cross-sectional studies also suggested that perfusion in lesions is dynamic and related to inflammation. Studies using either gradient-echo DSC or DCE MR imaging found increased CBV and CBF in contrast-enhancing lesions compared with normal-appearing white matter (NAWM) (Table).[12,22,23] However, Ge et al[12] found no difference between CBV and CBF in contrast-enhancing MS lesions compared with the WM in healthy controls. They also described 2 perfusion patterns in nonenhancing lesions: A subset of these lesions exhibited lower CBF than WM in healthy controls as well as lower CBF and

Summary of the main perfusion MRI study findings in MS

	Active Lesions	Chronic Lesions	NAWM	Deep Gray Matter
CBF	↑ (Compared with NAWM)	↓ (Compared with NAWM and WM in controls)	↓ (Compared with WM in controls)	↓ (Compared with controls)
CBV	↑ (Compared with NAWM)	↓ (Compared with NAWM)	↓ (Compared with WM in controls)	↓ (Compared with controls)
MTT	No significant change	↑ (Compared with WM in controls)	↑ (Compared with WM in controls)	↑ (Compared with controls)

Note:— ↑ indicates increased; ↓, decreased.

CBV than NAWM in subjects with MS. The remaining lesions were more like enhancing lesions and presumably also in an inflammatory state, with increased CBV in comparison with MS NAWM but not increased compared with healthy control WM.

On the other hand, T1-hypointense lesions (black holes) were found to have lower CBV values than T1-isointense lesions and healthy control WM.[23,24] In contrast, T1-isointense lesions did not differ from healthy control WM.[24] Black holes are characterized by axonal loss and thus are likely to be less perfused and metabolically less active.[23,24]

Cortical lesions were also evaluated using DSC-MR imaging in 44 patients with RRMS.[13] Most exhibited significantly lower CBF and CBV than normal-appearing gray matter. Nonetheless, like WM lesions, some cortical lesions showed increased CBF and/or CBV, again thought to reflect acute inflammation. Accurate cortex delineation on perfusion imaging can be challenging. However, in that study, double inversion recovery images were registered to DSC, and every voxel was individually analyzed to reduce bias due to noise, partial volume, and nonuniformity.[13]

Perfusion in Normal-Appearing Tissue

Most cross-sectional studies assessing perfusion in NAWM identified altered perfusion parameters with different combinations of either reduced CBF or reduced CBV and CBF and elevated mean transit time in patients with MS compared with healthy controls.[3,8,12,25-28] Only 1 report identified an overall increased WM perfusion in 60 patients with MS with mixed phenotypes, but heterogeneous WM perfusion.[29]

In 17 subjects with RRMS, Law et al[3] found overall reduced CBF and prolonged mean transit time but no changes in CBV in the NAWM of patients compared with controls. Controls but not patients with MS had higher periventricular CBV and CBF relative to the adjacent WM. Consistently, evaluation of WM perfusion revealed a decreased CBF in periventricular WM in 12 patients with clinically isolated syndrome compared with controls, whereas patients with early RRMS also had decreased CBF in deep gray matter.[30] This finding suggests that periventricular WM is affected early and is distinctively susceptible to the changes leading to a perfusion defect. Periventricular WM is vulnerable to microvascular injury, which has been hypothesized to underlie the hypoperfusion.[3]

Decreased perfusion has also been observed in deep and cortical gray matter of patients with MS compared with healthy controls.[26,27,29-33] In early RRMS, reduced perfusion but no atrophy was described in multiple cortical areas and deep gray matter structures including the thalamus, caudate, putamen, and hippocampus.[26,30] Moreover, Debernard et al[26] found that these findings correlated to visual and verbal memory impairment in 25 patients with early RRMS. Hence, perfusion changes may constitute a clinically relevant biomarker in early MS, especially because they could precede detectable structural atrophy.[26,30]

Using DCE-MR imaging, a more recent study with high projected statistical power based on calculation using means and SDs derived from a Monte Carlo simulation found much lower CBF and CBV values than the aforementioned reports, with no difference in CBF, CBV, or mean transit time between 16 controls and 24 patients with RRMS.[34] DCE-MR imaging is rarely used to assess perfusion in MS, and the impact of the differences in technical factors compared with DSC-MR imaging remains to be clarified.

Perfusion in MS Subtypes

Potential differences in perfusion across MS subtypes are predominately based on the small numbers of subjects in each investigation, precluding definitive conclusions.

In 3 early (4- to 5-year disease duration) RRMS cohorts, low perfusion in NAWM and gray matter was reported.[26,30,32] Two studies in patients with clinically isolated syndrome reported regional CBF decreases in either periventricular NAWM or deep gray matter compared with healthy controls.[30,35] CBV and mean transit time were found to be elevated relative to healthy controls in NAWM and deep gray matter in 1 of the 2 studies.[35] Differences in perfusion between progressive and relapsing-remitting subgroups have not been consistently demonstrated. Patients with primary-progressive MS have been found to have significantly or trending lower perfusion in normal-appearing gray matter and periventricular NAWM than patients with RRMS.[8,25,29,31] In fact, Adhya et al[25] identified significantly lower CBF and CBV in periventricular NAWM and lower CBV in frontal WM, without any significant difference in other WM regions. This finding is in line with the aforementioned observations in clinically isolated syndrome and early RRMS cohorts and implies a unique susceptibility of periventricular WM to declining perfusion in progressive disease as well. Mean cortical gray matter CBF has also been described as lower in secondary-progressive MS than in RRMS in a large MS cohort, but significance was lost after adjusting for other accounting factors such as T2 lesion volume, age, sex, and disease duration.[36]

Clinical Correlations

Despite compelling and reproducible perfusion abnormalities in MS, their relation to clinical measures of disability and disease severity has not been strongly established. No association between the Expanded Disability Status Scale or disease duration and perfusion parameters in NAWM or gray matter has been identified in clinically isolated syndrome and early RRMS cohorts, or in most mixed MS phenotype cohorts.[8,23,26,27,29-31,33,35] Two studies revealed a negative correlation between the Expanded Disability Status Scale and CBF and CBV in NAWM.[25,37] One study of 23 subjects with RRMS found a significant negative association between hypoperfusion in the nonatrophic bilateral median thalami

and time to complete the 9-Hole Peg Test.[32] No correlation between perfusion in white matter lesions and disability has been found, though these were assessed in only 1 article.[23] Likewise, although they were evaluated in most publications, relationships between perfusion measurements and either T2 or T1 or contrast-enhancing lesion volumes or white and gray matter atrophy were not identified in most reports.[8,25,26,30,31,35,37]

The absence of a correlation between perfusion alterations and gross measures of disability may be due to the lack of sensitivity of these outcome measures to predict disability.[38] The Expanded Disability Status Scale mostly reflects gait disability related to spinal cord disease and has been criticized for its variability among examiners.[38] The 9-Hole Peg Test reliably detects progression in patients with MS but is a measure specific to upper extremity motor function.[39] Moreover, MR imaging gadolinium-enhancing or T2 lesion load is not a good predictor of long-term disability.[38] Nevertheless, the usefulness of perfusion MR imaging probably lies more in its ability to detect acute inflammatory changes earlier than conventional MR imaging as detailed above.[20] This ability could lead to earlier identification of symptomatic and asymptomatic disease activity underlying relapses and new T2 lesions, which are known to impact disability.[38]

D'haeseleer et al[40] found that Paced Auditory Serial Addition Test scores in 10 patients with RRMS and 10 with primary-progressive MS correlated strongly with reduced CBF in the left centrum semiovale, an area involved in processing speed and verbal working memory. In an early RRMS cohort, visual and verbal memory impairment was related to perfusion reduction in many cortical and deep gray matter areas.[26] Moreover, Inglese et al[8] reported a moderate-to-strong positive association between deep gray matter CBF and visuoperceptual ability in 18 patients with RRMS and 14 with primary-progressive MS. They also measured inhibition switching, which was also moderately correlated to deep gray matter CBV. The same group identified Multidimensional Fatigue inventory reduced activity and reduced motivation scores as correlates to deep gray matter perfusion.[31] Furthermore, perfusion analysis in 25 cognitively impaired versus 20 unimpaired subjects with secondary-progressive MS revealed, in the former, lower quantitative CBV in the bilateral superior medial frontal cortex and lower quantitative CBV and CBF in the thalami and caudate nuclei.[41] Overall impairment in the Minimal Assessment of Cognitive Function battery as well as subscores of processing speed, verbal fluency, and visuospatial memory showed a moderate positive correlation with these perfusion findings. It is unknown whether a common factor alters both perfusion and cognition or whether one influences the other, but decreased brain perfusion could be a marker of cognitive impairment and fatigue in MS, 2 prevalent and disabling symptoms.[42] However, the impact of perfusion normalization on cognitive dysfunction in MS is still to be assessed.

Limitations to the Interpretation of the Data

Interpretation of the summarized data is limited by several factors. First, although longitudinal studies would provide valuable data on how the perfusion characteristics of brain tissue change due to MS, only 1 study assessed changes in perfusion across time.[20] There is evidence that contrast agents accumulate in the brain[43]; this finding hampers their repeat administration in longitudinal studies using DSC. Furthermore, the ill-posed deconvolution and the selection of the arterial input function required in DSC make serial studies particularly difficult to perform.[9]

Second, analysis of perfusion imaging requires many technical steps that are each susceptible to measurement error. Imaging protocols and techniques are also heterogeneous, with most studies using DSC-MR imaging but some using ASL.[26-29,32,33,36,40,44] As explained above, ASL is not recommended to evaluate WM because of its low signal-to-noise ratio.[19] Delineation of ROIs also varies greatly, from specific gyri to global white or gray matter. The spatial resolution of perfusion MR images, typically 8–27 mm^3, does not always allow a clear distinction between gray and white matter, making accurate cortex delineation and evaluation of MS lesions with diameters of <3–4 mm challenging. External factors, such as the degree of hydration and substances such as caffeine or ethanol, can also influence cerebral perfusion[45-47] but have not been accounted for in any MS perfusion study. Furthermore, although technical factors can alter the comparison among subjects, analysis of lesion perfusion has been performed using NAWM as a comparator, which is known to be abnormal in MS.

There is also an issue with using any area of the brain to normalize perfusion maps. Indeed, CBF maps obtained after deconvolution are dependent on the arterial input function, which is influenced by contrast agent properties, partial volume effects, and bolus delay and dispersion.[48] A way to reduce the contribution of these artifacts is to normalize the values using a reference area of the brain, but this is rarely done.[35] Normalization however introduces another potential bias because no part of the brain is entirely normal at a pathological level in the MS brain.[49]

Additionally, it has been recently demonstrated that gradient-echo DSC perfusion measurements are strongly influenced by the anisotropic nature of the WM vasculature, with angle-dependent variations of up to 130% in CBF and CBV.[50] This orientation dependency is caused by blood vessels running in parallel to WM tracts, the effect being much weaker for vessels parallel to the main magnetic field than for vessels perpendicular to the main magnetic field. Both CBF and CBV in lesions that are traversed by a vein parallel to the orientation of the main magnetic field, such as Dawson fingers, may appear lower than in lesions traversed by a vein perpendicular to the main magnetic field.[50] To our knowledge, tissue orientation was not accounted for in any of the previous studies. For studies comparing nonlesional tissue among groups on the other hand, this limitation may be less relevant. Moreover, spin-echo DSC is much less affected by orientation effects,[51] but gradient-echo was used in all the aforementioned DSC assessments. Gradient-echo DSC also has signal drop-out near tissue-air and tissue-bone interfaces, making these brain areas difficult to evaluate.[52]

Third, groups of subjects are widely heterogeneous in their disease duration, disability, presence or absence of MS disease-modifying therapy, and disease subtype.[8,22,23,25,27,29,31,33,36] Inflammation is generally less prominent with longer disease duration and in progressive forms of MS.[21] Disease-modifying therapies can also reduce inflammation.[1] Consequently, these factors are likely to influence perfusion, with lower brain CBF and CBV in less inflammatory conditions, such as in progressive dis-

ease[8,25,29,31] and as evidenced by higher NAWM CBV and CBF in patients with MS with repeat new contrast-enhancing lesions.[37]

Hypotheses Underlying Perfusion Modifications

Increased perfusion in active lesions most likely represents vasodilation secondary to inflammation of the involved gray or white matter.[20] More uncertainties surround the explanation for the diffuse perfusion decrease in NAWM and gray matter, a phenomenon attributed to either a primary vascular insult or reduced tissue metabolic function from neuronal loss.[53] Evidence of cerebral vascular dysfunction has been brought forward in MS but is not sufficient to explain alterations of brain perfusion. A combination of factors is more likely at play.

Vascular Involvement

Initially, the controversial and now refuted theory of chronic cerebrospinal vascular insufficiency underlying MS caused a lot of attention. Nonetheless, epidemiologic studies have identified a small excess of strokes in patients with MS,[54] though lifestyle factors such as smoking were not accounted for. Moreover, some pathologic findings support vascular involvement in MS.[3,4] It is well-accepted that plaques occur around a central vein and DCE-MR imaging findings support the formation and expansion of newly formed lesions around that central vein.[2,17] Vasculitic changes, reflected by lymphocytic infiltration of the vein walls, have been hypothesized to predate plaque development.[3] Indeed, type III demyelinating MS lesions have pathologic findings common to WM lesions occurring on an ischemic background.[49,55] There is preferential loss of myelin-associated glycoprotein and oligodendrocyte apoptosis with preservation of other myelin proteins.[49,55] Upregulation of hypoxia inducible factor-1α, a transcription factor involved in response to hypoxia, is present in type III lesion glial cells,[49] and expression of *hypoxia inducible factor-1*α and its downstream genes has been found to be enhanced in secondary-progressive MS.[49,53,55] However, this gene is also upregulated in states of nonhypoxic energy failure, such as decreased mitochondrial adenosine triphosphate production,[55] which occurs in MS.

Marshall et al[44] have found CBF modulation in gray matter to be less responsive to hypercapnia in subjects with MS than in controls, suggesting dysfunction of cerebrovascular reactivity in MS. This lack of cerebrovascular reactivity was correlated to WM lesion volume and global gray matter atrophy.[38] Dysfunctional vasoactivity of the cerebral vasculature has been further evidenced by elevated jugular levels of endothelin-1, a potent vasoconstrictor, measured in 15 patients with MS compared with controls.[56] An increase of their CBF by 20% after administration of bosentan, an endothelin-1 antagonist, confirmed the mechanistic impact of endothelin-1 on brain perfusion and suggested potential reversibility of CBF impairment.

Despite evidence of vascular dysfunction in MS, it is unclear whether brain damage results from or engenders the perfusion defect. Looking at perfusion and diffusion tensor imaging in a small cohort of patients with RRMS, Saindane et al[57] found that decreasing CBF and CBV in the corpus callosum significantly correlated with decreasing mean diffusivity but not fractional anisotropy. This pattern was recognized as consistent with a primary ischemic insult rather than hypoperfusion resulting from axonal degeneration, which would translate into increased mean diffusivity and decreased fractional anisotropy.[57] However, alternative explanations, namely a reduced axonal energy state without irreversible axonal degeneration, are not excluded. Some findings suggest that reduced perfusion could limit repair and remyelination. In fact, chronic T2 lesions and T1-hypointense lesions seem to occur predominantly in areas of reduced CBF, as indicated by perfusion maps on imaging[28,58] or anatomic watershed areas on pathology.[59] Moreover, in a very large MS cohort, Holland et al[58] found that preferential occurrence of lesions in areas of low perfusion was more frequent in secondary-progressive MS than in RRMS.

Certain observations argue against a primary vascular pathology in MS.[49] The increased perfusion observed in acute lesions indicates inflammation rather than primary ischemia. The diffuse rather than regional abnormal perfusion is also not in agreement with presumed focal vasculitic involvement. In addition, microvessel thrombosis is only rarely identified on pathology, and MS-like lesions are not typically induced by stroke, the prototypical example of brain ischemia.[49]

Metabolic Dysfunction

Neuronal loss has been hypothesized to explain the diffuse reduction in perfusion in MS by reducing the demand for energy.[26] Nonetheless, the presence of a tissue perfusion decrease despite the absence of atrophy, as described above, argues against this sole mechanism.[26] Oxidative stress and deficient energy production resulting from mitochondrial dysfunction are thought to be important factors behind neurodegeneration in MS.[60] The mechanisms leading to mitochondrial injury following demyelination are not fully understood.[60] Virtual hypoxia refers to reduced adenosine triphosphate production secondary to mitochondrial dysfunction coupled with increased energy demand in demyelinated axons. Virtual hypoxia could lead to axon necrosis.[60] This metabolic failure could be reflected through reduced perfusion in noninflammatory tissue without actual ischemia. On the other hand, decoupling between the *N*-acetylaspartate-to-creatine ratio, reflecting axonal metabolism, and CBF has been observed in the corpus callosum of 25 patients with MS and suggested that metabolic dysfunction or axonal loss alone is unlikely to account for the perfusion modifications.[27] Alternatively, reduced energy production by astrocytes in MS could contribute to reduced demand in blood flow, which would also manifest as reduced perfusion on MR imaging.[49] Astrocytes in MS lesions lack β2-adrenergic receptors. Norepinephrine-mediated activation of these receptors is important, notably for energy production and vasodilation; default of this pathway would thus lead to reduced CBF.[49]

Conclusions and Future Directions

There is a large body of limited-quality-but-concordant evidence demonstrating alteration of cerebral perfusion in MS. Perfusion MR imaging appears to be a sensitive tool, perhaps more than conventional MR imaging, for detecting focal inflammatory activity in the brain. Its usefulness to improve early detection of relapses and new lesions and the impact on treatment decision-

making should be clarified. The effect of disease-modifying therapy on brain perfusion should also be characterized. This characterization would allow assessment of the potential role of perfusion MR imaging as a marker of treatment response through monitoring of inflammatory activity. Diffuse hypoperfusion of white and gray matter is found and could be a clinically relevant marker of cognitive dysfunction and fatigue. The potential for reliable identification of cognitively impaired patients or patients at risk of cognitive dysfunction should be explored. Furthermore, defining the impact of reversing normal-appearing tissue hypoperfusion on cognition and disability could lead to a better understanding of the disease pathogenesis and potentially to novel treatment options for symptoms. Alteration of cerebral perfusion in patients with MS compared with controls certainly raises questions about the pathogenesis of the disease. Reduction of energy demand and blood supply resulting from mitochondrial and astrocytic dysfunction as well as from axonal degeneration perhaps does not fully explain the diffuse reduction in perfusion. Some evidence of hypoxic-mediated injury in MS exists, and dysfunction of cerebrovascular vasoactivity could contribute to hypoperfusion. However, a combination of inflammatory, metabolic, and vascular factors is more likely than a sole primary vascular pathology. Advanced techniques, such as the measurement of the cerebral metabolic rate of oxygen, along with the oxygen extraction fraction, may shed further light on these issues.[61]

Disclosures: Emmanuelle Lapointe—*UNRELATED*: *Consultancy*: EMD Serono and Hoffmann-La Roche. Anthony L. Traboulsee—*UNRELATED*: *Grant*: Canadian Institute for Health Research*; *UNRELATED*: *Consultancy*: Biogen Idec, Hoffman-La Roche, Sanofi Genzyme, Novartis, Teva Canada Innovation; *Grants/Grants Pending*: MS Society of Canada, Chugai Pharmaceutical Co, Biogen Idec, Sanofi Genzyme, Hoffman-La Roche*; *Payment for Lectures Including Service on Speakers Bureaus*: Sanofi Genzyme, Hoffman-La Roche; *Travel/Accommodations/Meeting Expenses Unrelated to Activities Listed*: Sanofi Genzyme. Alexander Rauscher—*UNRELATED*: *Payment for Lectures Including Service on Speakers Bureaus*: Philips Healthcare, *Comments*: fees for a keynote lecture at a Philips MRI Lunch Symposia. *Money paid to the institution.

REFERENCES

1. Grigoriadis N, van Pesch V, Paradig MS; Paradig MS Group. **A basic overview of multiple sclerosis immunopathology.** *Eur J Neurol* 2015;22(suppl 2):3–13 CrossRef Medline
2. Sati P, Oh J, Constable RT, et al. **The central vein sign and its clinical evaluation for the diagnosis of multiple sclerosis: a consensus statement from the North American Imaging in Multiple Sclerosis Cooperative.** *Nat Rev Neurol* 2016;12:714–22 CrossRef Medline
3. Law M, Saindaine AM, Ge Y, et al. **Microvascular abnormality in relapsing-remitting multiple sclerosis: perfusion MR imaging findings in normal-appearing white matter.** *Radiology* 2004;231:645–52 CrossRef Medline
4. D'haeseleer M, Hostenbach S, Peeters I, et al. **Cerebral hypoperfusion: a new pathophysiologic concept in multiple sclerosis?** *J Cereb Blood Flow Metab* 2015;35:1406–10 CrossRef Medline
5. Sun X, Tanaka M, Kondo S, et al. **Clinical significance of reduced cerebral metabolism in multiple sclerosis: a combined PET and MRI study.** *Ann Nucl Med* 1998;12:89–94 CrossRef Medline
6. Lycke J, Wikkelsö C, Bergh AC, et al. **Regional cerebral blood flow in multiple sclerosis measured by single photon emission tomography with technetium-99m hexamethylpropyleneamine oxime.** *Eur Neurol* 1993;33:163–67 Medline
7. Brooks DJ, Leenders KL, Head G, et al. **Studies on regional cerebral oxygen utilisation and cognitive function in multiple sclerosis.** *J Neurol Neurosurg Psychiatry* 1984;47:1182–91 CrossRef Medline
8. Inglese M, Adhya S, Johnson G, et al. **Perfusion magnetic resonance imaging correlates of neuropsychological impairment in multiple sclerosis.** *J Cereb Blood Flow Metab* 2008;28:164–71 CrossRef Medline
9. MacDonald ME, Frayne R. **Cerebrovascular MRI: a review of state-of-the-art approaches, methods and techniques.** *NMR Biomed* 2015; 28:767–91 CrossRef Medline
10. Boxerman JL, Hamberg LM, Rosen BR, et al. **MR contrast due to intravascular magnetic susceptibility perturbations.** *Magn Reson Med* 1995;34:555–66 CrossRef Medline
11. Weisskoff RM, Zuo CS, Boxerman JL, et al. **Microscopic susceptibility variation and transverse relaxation: theory and experiment.** *Magn Reson Med* 1994;31:601–10 CrossRef Medline
12. Ge Y, Law M, Johnson G, et al. **Dynamic susceptibility contrast perfusion MR imaging of multiple sclerosis lesions: characterizing hemodynamic impairment and inflammatory activity.** *AJNR Am J Neuroradiol* 2005;26:1539–47 Medline
13. Peruzzo D, Castellaro M, Calabrese M, et al. **Heterogeneity of cortical lesions in multiple sclerosis: an MRI perfusion study.** *J Cereb Blood Flow Metab* 2013;33:457–63 CrossRef Medline
14. Barth M, Breuer F, Koopmans PJ, et al. **Simultaneous multislice (SMS) imaging techniques.** *Magn Reson Med* 2016;75:63–81 CrossRef Medline
15. Todd N, Moeller S, Auerbach EJ, et al. **Evaluation of 2D multiband EPI imaging for high-resolution, whole-brain, task-based fMRI studies at 3T: sensitivity and slice leakage artifacts.** *Neuroimage* 2016;124(Pt A):32–42 CrossRef Medline
16. Tofts PS, Brix G, Buckley DL, et al. **Estimating kinetic parameters from dynamic contrast-enhanced T(1)-weighted MRI of a diffusable tracer: standardized quantities and symbols.** *J Magn Reson Imaging* 1999;10:223–32 Medline
17. Gaitán MI, Shea CD, Evangelou IE, et al. **Evolution of the blood-brain barrier in newly forming multiple sclerosis lesions.** *Ann Neurol* 2011;70:22–29 CrossRef Medline
18. Williams DS, Detre JA, Leigh JS, et al. **Magnetic resonance imaging of perfusion using spin inversion of arterial water.** *Proc Natl Acad Sci U S A* 1992;89:212–16 CrossRef Medline
19. Alsop DC, Detre JA, Golay X, et al. **Recommended implementation of arterial spin-labeled perfusion MRI for clinical applications: a consensus of the ISMRM perfusion study group and the European consortium for ASL in dementia.** *Magn Reson Med* 2015;73:102–16 CrossRef Medline
20. Wuerfel J, Bellmann-Strobl J, Brunecker P, et al. **Changes in cerebral perfusion precede plaque formation in multiple sclerosis: a longitudinal perfusion MRI study.** *Brain* 2004;127(Pt 1):111–19 CrossRef Medline
21. Lassmann H. **The pathologic substrate of magnetic resonance alterations in multiple sclerosis.** *Neuroimaging Clin N Am* 2008;18:563–76, ix CrossRef Medline
22. Ingrisch M, Sourbron S, Morhard D, et al. **Quantification of perfusion and permeability in multiple sclerosis: dynamic contrast-enhanced MRI in 3D at 3T.** *Invest Radiol* 2012;47:252–58 CrossRef Medline
23. Haselhorst R, Kappos L, Bilecen D, et al. **Dynamic susceptibility contrast MR imaging of plaque development in multiple sclerosis: application of an extended blood-brain barrier leakage correction.** *J Magn Reson Imaging* 2000;11:495–505 Medline
24. Li L, Chopp M, Nejad-Davarani SP, et al. **Perfusion and diffusion abnormalities of multiple sclerosis lesions and relevance of classified lesions to disease status.** *J Neurol Neurophysiol* 2014;2014(Suppl 12):12 CrossRef Medline
25. Adhya S, Johnson G, Herbert J, et al. **Pattern of hemodynamic impairment in multiple sclerosis: dynamic susceptibility contrast perfusion MR imaging at 3.0 T.** *Neuroimage* 2006;33:1029–35 CrossRef Medline
26. Debernard L, Melzer TR, Van Stockum S, et al. **Reduced grey matter perfusion without volume loss in early relapsing-remitting multiple sclerosis.** *J Neurol Neurosurg Psychiary* 2014;85:544–51 CrossRef Medline
27. Steen C, D'haeseleer M, Hoogduin JM, et al. **Cerebral white matter**

blood flow and energy metabolism in multiple sclerosis. *Mult Scler* 2013;19:1282–89 CrossRef Medline
28. Narayana PA, Zhou Y, Hasan KM, et al. **Hypoperfusion and T1-hypointense lesions in white matter in multiple sclerosis.** *Mult Scler* 2014;20:365–73 CrossRef Medline
29. Rashid W, Parkes LM, Ingle GT, et al. **Abnormalities of cerebral perfusion in multiple sclerosis.** *J Neurol Neurosurg Psychiary* 2004; 75:1288–93 CrossRef Medline
30. Varga AW, Johnson G, Babb JS, et al. **White matter hemodynamic abnormalities precede sub-cortical gray matter changes in multiple sclerosis.** *J Neurol Sci* 2009;282:28–33 CrossRef Medline
31. Inglese M, Park SJ, Johnson G, et al. **Deep gray matter perfusion in multiple sclerosis: dynamic susceptibility contrast perfusion magnetic resonance imaging at 3 T.** *Arch Neurol* 2007;64:196–202 CrossRef Medline
32. Doche E, Lecocq A, Maarouf A, et al. **Hypoperfusion of the thalamus is associated with disability in relapsing remitting multiple sclerosis.** *J Neuroradiol* 2017;44:158–64 CrossRef Medline
33. Ota M, Sato N, Nakata Y, et al. **Abnormalities of cerebral blood flow in multiple sclerosis: a pseudocontinuous arterial spin labeling MRI study.** *Magn Reson Imaging* 2013;31:990–95 CrossRef Medline
34. Ingrisch M, Sourbron S, Herberich S, et al. **Dynamic contrast-enhanced magnetic resonance imaging suggests normal perfusion in normal-appearing white matter in multiple sclerosis.** *Invest Radiol* 2017;52:135–41 CrossRef Medline
35. Papadaki EZ, Mastorodemos VC, Amanakis EZ, et al. **White matter and deep gray matter hemodynamic changes in multiple sclerosis patients with clinically isolated syndrome.** *Magn Reson Med* 2012; 68:1932–42 CrossRef Medline
36. Amann M, Achtnichts L, Hirsch JG, et al. **3D GRASE arterial spin labelling reveals an inverse correlation of cortical perfusion with the white matter lesion volume in MS.** *Mult Scler* 2012;18:1570–76 CrossRef Medline
37. Bester M, Forkert ND, Stellmann JP, et al. **Increased perfusion in normal appearing white matter in high inflammatory multiple sclerosis patients**. *PLoS One* 2015;10:e0119356 CrossRef Medline
38. Hyland M, Rudick RA. **Challenges to clinical trials in multiple sclerosis: outcome measures in the era of disease-modifying drugs.** *Curr Opin Neurol* 2011;24:255–61 CrossRef Medline
39. Feys P, Lamers I, Francis G, et al; Multiple Sclerosis Outcome Assessments Consortium**. The Nine-Hole Peg Test as a manual dexterity performance measure for multiple sclerosis.** *Mult Scler* 2017;23: 711–20 CrossRef Medline
40. D'haeseleer M, Steen C, Hoogduin JM, et al. **Performance on Paced Auditory Serial Addition Test and cerebral blood flow in multiple sclerosis.** *Acta Neurol Scand* 2013;128:e26–29 CrossRef Medline
41. Francis PL, Jakubovic R, O'Connor P, et al. **Robust perfusion deficits in cognitively impaired patients with secondary-progressive multiple sclerosis.** *AJNR Am J Neuroradiol* 2013;34:62–67 CrossRef Medline
42. Penner IK. **Evaluation of cognition and fatigue in multiple sclerosis: daily practice and future directions.** *Acta Neurol Scand* 2016; 134(suppl 200):19–23 CrossRef Medline
43. Ramalho J, Semelka RC, Ramalho M, et al. **Gadolinium-based contrast agent accumulation and toxicity: an update.** *AJNR Am J Neuroradiol* 2016;37:1192–98 CrossRef Medline
44. Marshall O, Lu H, Brisset JC, et al. **Impaired cerebrovascular reactivity in multiple sclerosis.** *JAMA Neurol* 2014;71:1275–81 CrossRef Medline
45. Field AS, Laurienti PJ, Yen YF, et al. **Dietary caffeine consumption and withdrawal: confounding variables in quantitative cerebral perfusion studies?** *Radiology* 2003;227:129–35 CrossRef Medline
46. Trangmar SJ, Chiesa ST, Llodio I, et al. **Dehydration accelerates reductions in cerebral blood flow during prolonged exercise in the heat without compromising brain metabolism.** *Am J Physiol Heart Circ Physiol* 2015;309:598–607 CrossRef Medline
47. Mathew RJ, Wilson WH. **Substance abuse and cerebral blood flow.** *Am J Psychiatry* 1991;148:292–305 CrossRef Medline
48. Calamante F. **Arterial input function in perfusion MRI: a comprehensive review.** *Prog Nucl Magn Reson Spectrosc* 2013;74:1–32 CrossRef Medline
49. De Keyser J, Steen C, Mostert JP, et al. **Hypoperfusion of the cerebral white matter in multiple sclerosis: possible mechanisms and pathophysiological significance.** *J Cereb Blood Flow Metab* 2008;28: 1645–51 CrossRef Medline
50. Hernández-Torres E, Kassner N, Forkert ND, et al. **Anisotropic cerebral vascular architecture causes orientation dependency in cerebral blood flow and volume measured with dynamic susceptibility contrast magnetic resonance imaging.** *J Cereb Blood Flow Metab* 2017;37:1108–19 CrossRef Medline
51. Doucette J, Wei L, Kames C, et al. **Anisotropic cerebral vascular architecture causes orientation dependency in cerebral blood flow and volume measured with spin echo dynamic susceptibility contrast magnetic resonance imaging.** In: *Proceedings of the Annual Meeting of the International Society for Magnetic Resonance in Medicine,* Honolulu, Hawaii. April 22–27, 2017
52. Deichmann R, Gottfried J, Hutton C, et al. **Optimized EPI for fMRI studies of the orbitofrontal cortex.** *Neuroimage* 2003;19(2 Pt 1): 430–41 CrossRef Medline
53. D'haeseleer M, Cambron M, Vanopdenbosch L, et al. **Vascular aspects of multiple sclerosis.** *Lancet Neurol* 2011;10:657–66 CrossRef Medline
54. Christiansen CF, Christensen S, Farkas DK, et al. **Risk of arterial cardiovascular diseases in patients with multiple sclerosis: a population-based cohort study.** *Neuroepidemiology* 2010;35:267–74 CrossRef Medline
55. Aboul-Enein F, Rauschka H, Kornek B, et al. **Preferential loss of myelin-associated glycoprotein reflects hypoxia-like white matter damage in stroke and inflammatory brain diseases.** *J Neuropathol Exp Neurol* 2003;62:25–33 CrossRef Medline
56. D'haeseleer M, Beelen R, Fierens Y, et al. **Cerebral hypoperfusion in multiple sclerosis is reversible and mediated by endothelin-1.** *Proc Natl Acad Sci U S A* 2013;110:5654–58 CrossRef Medline
57. Saindane AM, Law M, Ge Y, et al. **Correlation of diffusion tensor and dynamic perfusion MR imaging metrics in normal-appearing corpus callosum: support for primary hypoperfusion in multiple sclerosis.** *AJNR Am J Neuroradiol* 2007;28:767–72 Medline
58. Holland CM, Charil A, Csapo I, et al. **The relationship between normal cerebral perfusion patterns and white matter lesion distribution in 1,249 patients with multiple sclerosis.** *J Neuroimaging* 2012; 22:129–36 CrossRef Medline
59. Haider L, Zrzavy T, Hametner S, et al. **The topograpy of demyelination and neurodegeneration in the multiple sclerosis brain.** *Brain* 2016;139(Pt 3):807–15 CrossRef Medline
60. Mahad DH, Trapp BD, Lassmann H. **Pathological mechanisms in progressive multiple sclerosis.** *Lancet Neurol* 2015;14:183–93 CrossRef Medline
61. Wise RG, Harris AD, Stone AJ, et al. **Measurement of OEF and absolute CMRO2: MRI-based methods using interleaved and combined hypercapnia and hyperoxia.** *Neuroimage* 2013;83:135–47 CrossRef Medline

Who's Contributing Most to American Neuroscience Journals: American or Foreign Authors?

P. Charkhchi, M. Mirbolouk, R. Jalilian, and D.M. Yousem

ABSTRACT

BACKGROUND AND PURPOSE: With globalization, the contributions of authors from abroad to the American published literature has increased. We sought to determine the changes with time in the proportional contributions of American and non-American authors in the American neurosciences literature. We hypothesized the following: 1) During the past 21 years, manuscript contributions of American institutions have proportionally decreased in neuroradiology, more than in neurosurgery or neurology; 2) contributions of Asian institutions have affected neuroradiology more than neurosurgery and neurology; and 3) American articles garner more citations.

MATERIALS AND METHODS: We reviewed the May issues of 2 of the highest impact American-based neurology, neurosurgery, and neuroradiology journals published from 1997 to 2017. We counted the number of articles published by nation based on the institution of origin. We looked at trends across time and compared neurology, neurosurgery, and neuroradiology journals. We also gathered data on the number of citations of each article by nationality.

RESULTS: We reviewed 3025 articles. There was a significantly lower ratio of American to non-American authorship in neuroradiology versus neurology/neurosurgery journals (odds ratio = 0.70; 95% confidence interval, 0.60–0.82). There was a significantly decreasing trend in American authorship across the 21 years in neuroradiology. Of the countries outside the United States, Japan contributed most for neuroradiology and neurosurgery journals, and the UK, for neurology. American-authored articles were cited, on average, 1.25 times more frequently than non-American-authored articles.

CONCLUSIONS: Non-American contributions have impacted neuroradiology more than other clinical neuroscience fields with Asian authorship showing the greatest impact. That impact is growing, and the causes are manifold. Nonetheless American-authored articles are cited more.

The number of neuroscience articles and journals has grown during the past decade.[1]

The authorship trend in neuroscience is changing.[1] Although the United States along with European countries like Germany and the UK had been the dominant contributors to the neuroscience literature as a whole, countries in the Far East are contributing more and more to the academic world on the basis of trend lines from 2006 to 2015.[1] This ever-changing landscape of authorship emphasizes the importance of examining this trend and any biases it may yield. Although Peccora et al[2] reported that the number of publications in anesthesiology by American authors has declined during the past decades, the authorship characteristics of clinical publications in neurology, neurosurgery, and neuroradiology have not been investigated.

This study aimed to assess changes in the contribution rates and impact of different nations (based on the first author's institution) on publications in the top American-published neurology, neurosurgery, and neuroradiology journals during a 21-year period.

We hypothesized the following: 1) Between 1997 and 2017, contributions from institutions outside the United States have increased significantly across the specialties, but most in neuroradiology; 2) the contributions from Asian institutions have affected neuroradiology more than neurosurgery and neurology; and 3) despite a growing number of international contributions to clinical neurosciences journals, American articles garner more citations per article published, possibly reflecting an implicit bias.

MATERIALS AND METHODS

We targeted 3 different clinical neurosciences fields: neurology, neurosurgery, and neuroradiology. We chose the 2 most cited journals published in the United States in these 3 fields: the *Annals*

Received January 7, 2018; accepted after revision February 10.

From the Department of Radiology and Radiological Science, Division of Neuroradiology, Johns Hopkins Medical Institutions, Baltimore, Maryland.

Please address correspondence to David M. Yousem, MD, MBA, Department of Radiology and Radiological Science, Division of Neuroradiology, Johns Hopkins Medical Institutions, 600 N Wolfe St, Baltimore, MD 21287; e-mail: dyousem1@jhu.edu

Indicates article with supplemental on-line tables.

http://dx.doi.org/10.3174/ajnr.A5624

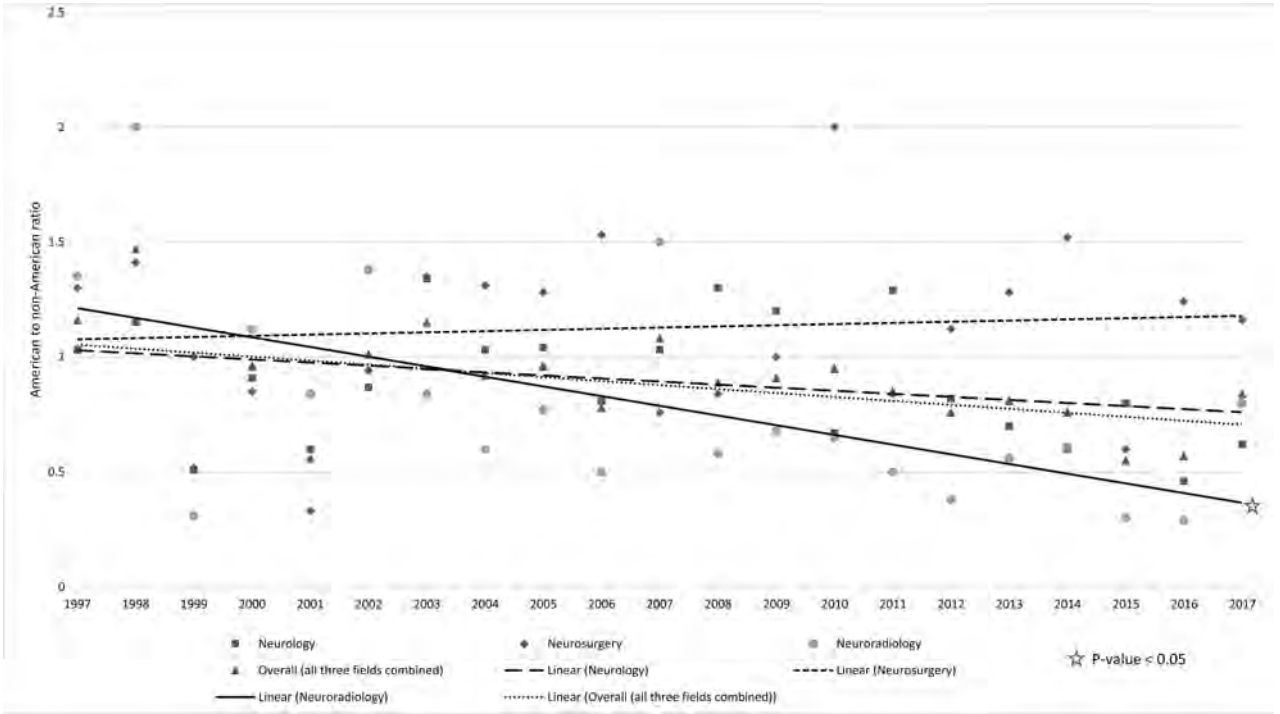

FIG 1. The ratio of American to non-American authorship falls significantly ($P < .05$) during the 21 years for neuroradiology only.

of Neurology and *Neurology* in the field of neurology,[3] the *Journal of Neurosurgery* and *Journal of Neurotrauma* in the field of neurosurgery,[4] and the *American Journal of Neuroradiology* and *Human Brain Mapping* in neuroradiology.[5]

We collected information about the institution of origin of the first author of all articles in the May issue (a randomly selected month) of these 6 journals between the 1997 and 2017 as a proxy to track the trends during the past 21 years.

The country of the first author's institution was extracted for each article in the May issue of the 6 journals. We then used Google Scholar to track the number of citations of each article. We collected the cumulative number of citations of all articles from May 1997 to May 2017 by querying Google Scholar between September 18, 2017, and November 27, 2017. The articles and Google Scholar were accessed remotely using the electronic portal of our medical library through the Internet.[6]

Our study is a retrospective bibliometric analysis. All statistical analyses were performed using STATA, Version 11 (StataCorp, College Station, Texas). First, we used descriptive statistics to calculate the ratio of American to non-American institutions and the most frequent non-American countries publishing in American journals from 1997 to 2017. Continuous data were summarized using means and SDs; categoric data were summarized using weighted percentages. Then we performed logistic regression analysis to examine the difference in authors' nationalities (American to non-American ratio) and Asian contributions across the 3 neuroscience fields. To assess whether the ratio difference changed during the 21 years, we included the interaction term between the year of publication and each field into the logistic models. To assess the difference in the number of citations between articles originating in the United States and outside the United States among the 3 fields, we counted the citation numbers per article and then compared the average number of citations between American and non-American institutions in each year, from 1997 to 2017. In addition, we used Poisson regression analysis to assess the influence of nationality on the number of citations overall and in each field. Because articles published earlier may have garnered more citations, we also analyzed the citations in two 10-year periods (1997–2006 and 2007–2017).

When we assessed Asian countries for their contributions, we included Japan, South Korea, China, Taiwan, Singapore, and Thailand. We also looked at trends based on the continent of origin.[7]

RESULTS

Data were collected from 3025 articles: 1120 in neurology, 860 in neurosurgery, and 1045 in neuroradiology. In total, 1393 (46.0%) articles were from American institutions and 1632 (54.0%) were from non-American institutions.

Across the years studied, neuroradiology journals (compared with neurology and neurosurgery journals) showed the lowest American authorship rate in 2016, 2015, 2013, 2012, 2011, 2010, 2009, 2008, 2006, 2005, 2004, 2003, and 1999, representing 13/21 years studied (Fig 1). Neurology had the lowest American authorship rate in 5/21 years (2017, 2014, 2002, 1998, and 1997), with 3/21 years (2000, 2001, 2007) represented by neurosurgery (Online Table 1). There was a significantly lower ratio of American authorship to non-American in neuroradiology journals (OR = 0.70; 95% CI, 0.60–0.82). Compared with neuroradiology journals, neurology and neurosurgery journals had a higher ratio of American to non-American authorship (OR = 1.29; 95% CI, 1.09–1.53 and OR = 1.59; 95% CI, 1.33–1.91, respectively). There was a decreasing trend in the American authorship ratio across the 21 years in neuroradiology because there was a significant nega-

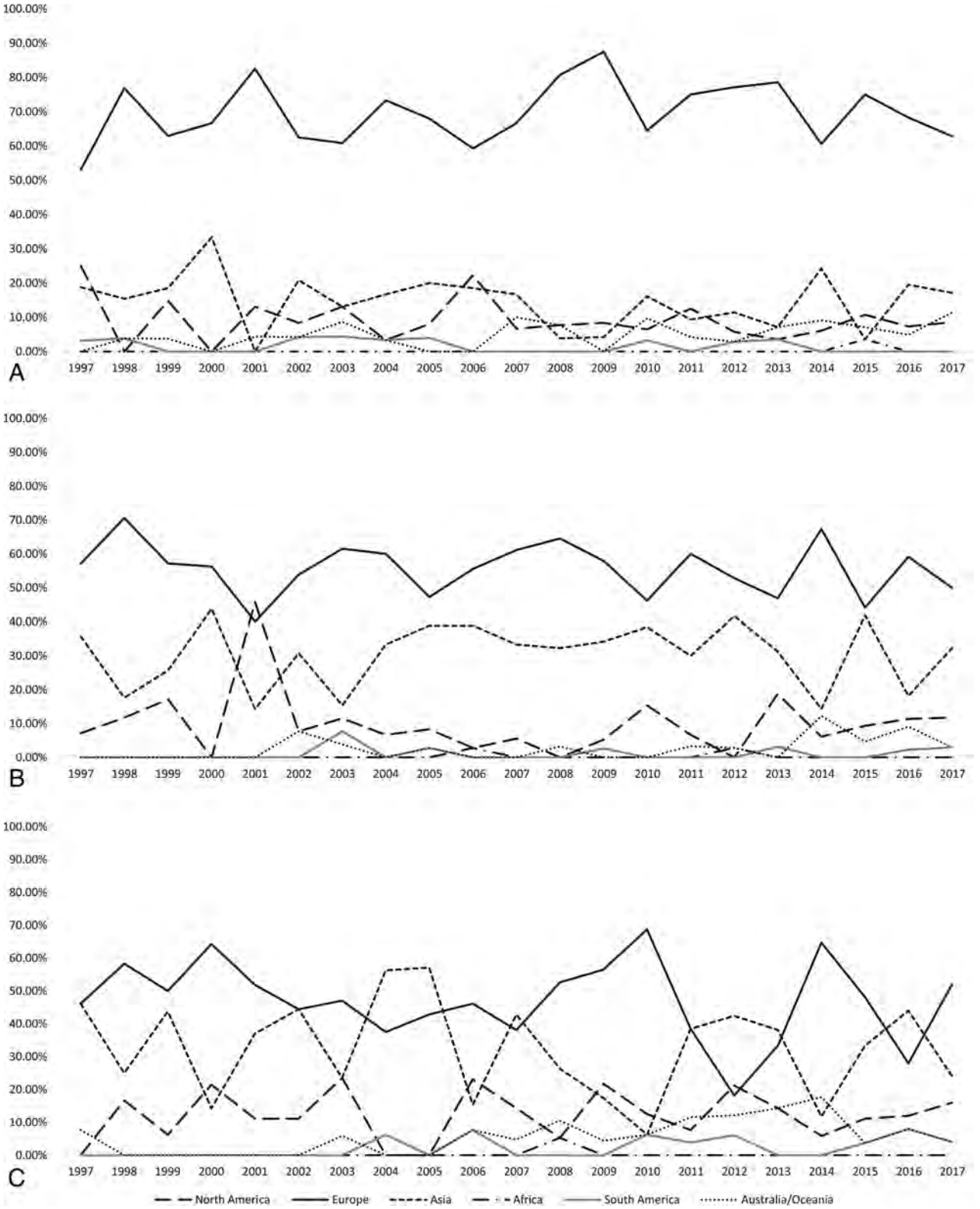

FIG 2. Participation of different continents (%) in American neurology (*A*), neuroradiology (*B*), and neurosurgery (*C*) journals, excluding the United States. The trend of publications by continent is demonstrated over time by field showing the dominance of European contributors for neurology only.

tive interaction between the year of publication and the neuroradiology field (interaction term = 0.95; 95% CI, 0.93–0.97).

After excluding the United States, we observed that countries from Europe showed a higher percentage of participation in the 2 neurology journals reviewed for all 21 years followed by countries from Asia and North America (mainly Canada) for most years (Fig 2). We observed the same trend in neuroradiology for most years—that is, that Europe, as a continent, had more articles. In

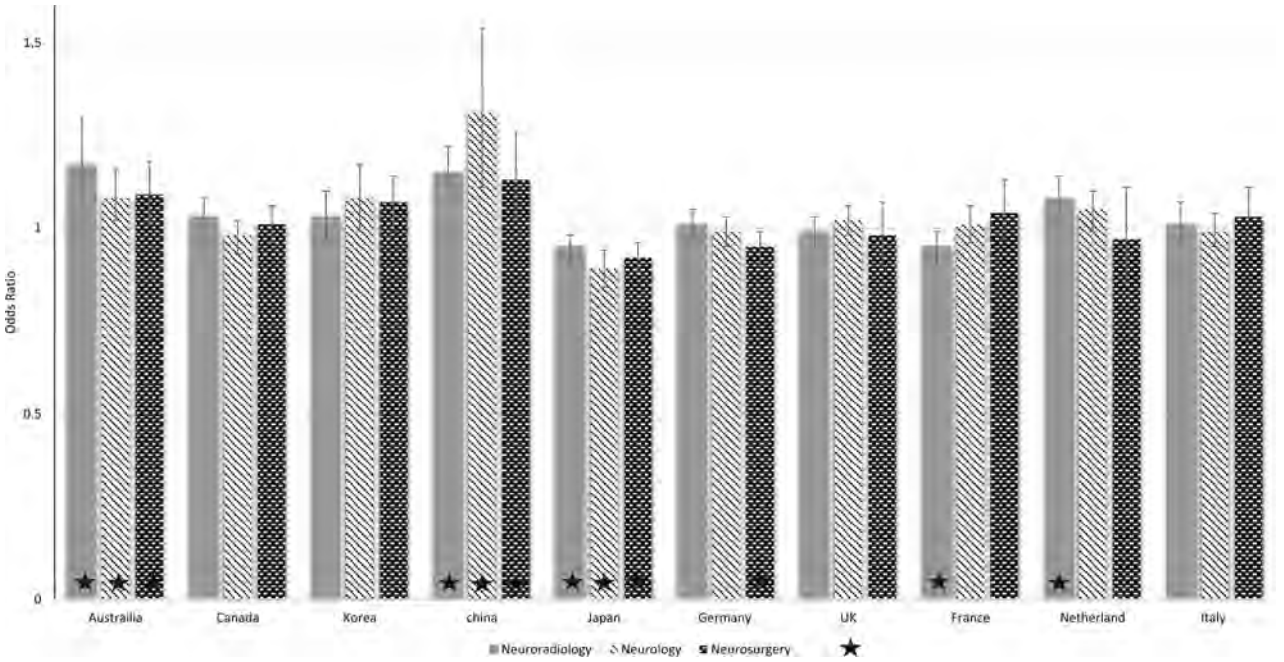

FIG 3. The contributions of China and Australia across all fields have significantly increased, while Japanese articles have shown a decline. ★ indicates a statistically significant difference at $P < .05$.

neurosurgery, the gap between the continents of Europe and Asia was less; we even observed higher participation of countries from Asia than Europe in 2004, 2005, 2007, 2012, 2013, and 2016 (Fig 3). Among countries with the highest rate of participation in the past 21 years in all 3 fields, Australia showed a significant, increasing trend of contributions in all 3 fields (neurology: OR = 1.08; 95% CI, 1.01–1.15; neuroradiology: OR = 1.17, 95% CI, 1.06–1.29; neurosurgery: OR = 1.09; 95% CI, 1.01–1.18). There was an increasing trend only in neuroradiology for the Netherlands (OR = 1.08; 95% CI, 1.02–1.40). There was a decreasing trend for France in neuroradiology (OR = 0.94; 95% CI, 0.90–0.99), and a decreasing trend for Germany in neurosurgery (OR = 0.94; 95% CI, 0.91–0.99) (Fig 3). Of the non-American neuroscience articles, Japanese institutions contributed 197/1632 (12.1%) articles, the highest of any non-American country. The country that contributed most per year in neurology was the UK in 9/21 years (2016, 2015, 2013, 2012, 2010, 2009, 2003, 2002, 1999); in neurosurgery, it was Japan in 12/21 years (2015, 2013, 2011, 2007, 2005, 2004, 2003, 2002, 2001, 1999, 1998, 1997); and in neuroradiology, it was also Japan in 11/21 years (2010, 2009, 2007, 2006, 2005, 2004, 2002, 2001, 2000, 1999, 1997). Of 1632 neuroscience articles from non-American institutions, 376 (23.04%) originated in Asian countries. Of the Far East Asian countries, Japan (52.39%) had the highest article number followed by South Korea (20.74%), China (19.41%), Taiwan (5.59%), Singapore (1.33%), and Thailand (0.53%). Compared with neurology, there was a greater contribution by Asian authors in neuroradiology and neurosurgery (OR = 2.90; 95% CI, 2.17–3.87 and OR = 2.48; 95% CI, 1.83–3.36, respectively). Although Japan had a large rate of contributions overall, there was a decreasing trend for Japan in the past 21 years in all 3 fields (neurology: OR = 0.89; 95% CI, 0.84–0.94; neuroradiology: OR = 0.94; 95% CI, 0.91–0.98; and neurosurgery: OR = 0.92; 95% CI, 0.88–0.95). At the same time, the contribution of China has significantly increased in all 3 fields (neurology: OR = 1.31; 95% CI, 1.11–1.53; neuroradiology: OR = 1.14; 95% CI, 1.07–1.22; and neurosurgery: OR = 1.13; 95% CI, 1.02–1.25) across the years.

Overall, American-authored articles were cited, on average (mean = 81.9), 1.25 times more frequently than non-American-authored articles (mean = 65.2) (Fig 4). When we compared the total number of citations per number of articles between articles originating in the United States and outside the United States, neurosurgery articles from US institutions had a higher impact than those from non-US institutions in 11 of 21 years. In the neurology (14/21) and neuroradiology (16/21) fields, for most years, articles from American institutions had a higher impact than those from non-American institutions (On-line Table 2).

When we ran Poisson models, overall, there was a positive effect (coefficient = 0.22; 95% CI, 0.10–0.35) between American institutions and the number of citations. This effect remained significant in the neurology (coefficient = 0.28; 95% CI, 0.11–0.45) and neurosurgery (coefficient = 0.21; 95% CI, 0.03–0.40) fields, but there was no significant association between the number of citations and American institutions in neuroradiology (coefficient = 0.19; 95% Cl, −0.07–0.45). When we divided the study into two 10-year periods to assess citation numbers, overall (all 3 fields combined) there was a positive effect between American institutions and the number of citations in both the first 10-year (coefficient = 0.18; 95% CI, 0.17–0.35) and the second 10-year block (coefficient = 0.20; 95% CI, 0.06–0.34) periods. This effect remained significant in neurology in only the first 10-year period (coefficient = 0.29; 95% CI, 0.07–0.51) and in the second 10-year period for neurosurgery (coefficient = 0.21; 95% CI, 0.01–0.40), but there was no significant association between

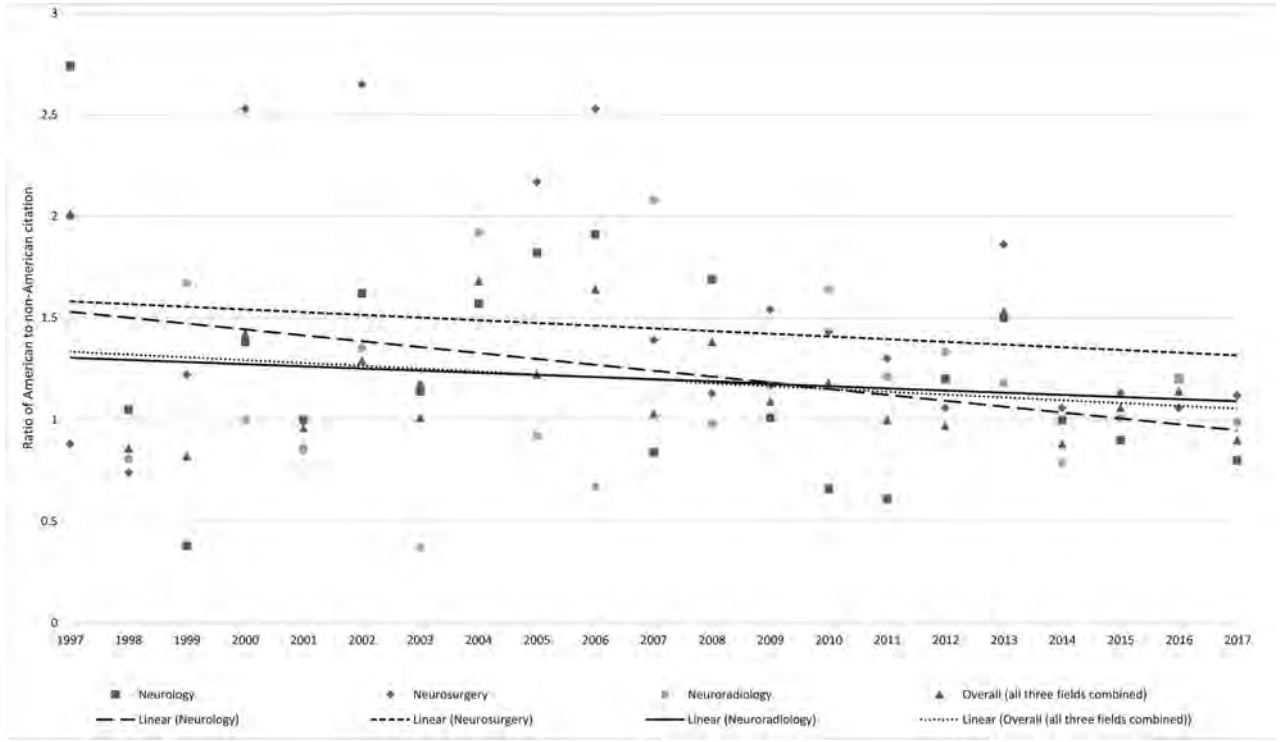

FIG 4. The citation trends of American versus non-American articles show a downward trend for all journals but remain in favor of American authors, except most recently in neurology, in which the trend crosses below the even mark.

the number of citations and American institutions in neuroradiology in either 10-year period.

DISCUSSION

We demonstrated the rates of American and non-American authorship in American-published clinical neuroscience journals across neuroradiology, neurology, and neurosurgery specialties during 21 years. As we hypothesized, we found a larger contribution of authors from non-American institutions in neuroradiology compared with neurology and neurosurgery. There was a significantly decreasing trend in American authorship ratios across the 21 years in neuroradiology, but we did not find any such significant trend in neurology and neurosurgery. In addition, Japan was the most frequent non-American country supplying publications in American neuroradiology and neurosurgery journals, while the UK was the leading non-American country in neurology. Nevertheless, the influence of Japan has been decreasing with time in all 3 fields, even as the contributions of China show a significant uptick in publications. Overall, we found that the contributions from Asian institutions have affected neuroradiology and neurosurgery more than neurology. We also found that American articles received more citations per article; this effect was more pronounced in neurology and neurosurgery and was not significant in neuroradiology.

We found that in 15 of 21 years, American neuroradiology journals published more articles with first authors from non-American institutions than American institutions in the May edition. Although this effect can be seen in some years before 2007, it is more pronounced in the past 10 years in the neuroradiology field (Fig 1). Similarly, there was a tendency to publish articles with first authors from non-American institutions in neurology journals (12/21 years), especially in the last 7 years (Fig 1). On the other hand, American neurosurgery journals, for most years, published more articles from American institutions (14/21 years). When we compared the 3 fields, neurology and neurosurgery journals had a higher ratio of America-to-non-American authorship compared with neuroradiology. In addition, we found a decreasing trend in American authorship ratios across the 21 years in neuroradiology. This trend could be due to several factors, including more familiarity with the English language through the universality of the Internet with English the preferred language of communication in the science world.[8] This facilitates writing articles and the submission process for international authors. The narrowing of what previously was a technology gap between the United States and other countries could be another facilitating factor. Growth in global collaboration would be another reason for the observed result; when we looked at the first author's institution, however, there were articles with authors collaborating from different countries, especially in more recent years. Across the years, changes in research funding in the budget of the National Institutes of Health and in the budgets of foreign countries may affect research participation and publishing trends.[9] The decline in Medicare reimbursement recently has also led to more emphasis on relative value unit production, even in American academic medical centers, and that may impact academic activities.[10] We also question whether the American millennial generation is less inclined to spend hours outside the traditional work week performing research the way previous generations may have.

The increased contribution of foreign countries can be beneficial to American journals; for example, China has studies with

larger sample sizes owing to its massive population. The US literature is benefiting from outstanding researchers who do not live in United States; some studies, because of the regulations placed on American researchers, simply cannot be conducted in the United States. On the other hand, the decreasing trend may be a concern for US academic medical centers. We posit that both the clinical workload and lack of financial support for research could explain decreased American institution contributions in high-impact American journals. The clinical workload as measured by the relative value unit continues to increase[11] in radiology, which may mean less time for research unless funded by grant support. Devoting more internal and extramural funds to the neurosciences and radiology has been recommended in the past.[12] It is estimated, however, that National Institutes of Health support for diagnostic radiology will decrease in 2018.[13] Inadequate funding would eventually lead to less education on clinical research for students, residents, fellows, and young faculty, setting the stage for a negative impact in the years ahead.[10] Publishing in high-impact journals can be a bonus to attract younger, talented radiologists to academic settings as they decide between private and academic jobs. Increasing the funding resources and not relying on only government support are crucial to expanding the research activity. We also suggest that incorporating more training in research methodology in residency and fellowship programs may help overcome some hurdles that may prevent academic contributions by trainees. At a local level, more recognition by department chairs for manuscript publication/grant procurement rather than clinical activity could be accomplished by shifting monetary incentives, awards, public commendation, and advancement in rank in favor of academic output, not relative value unit production. Universities can educate the younger generation on the benefits of high-impact research and the occasional need for effort beyond the standard work week to accomplish those goals. Adding funded research years to residencies and offering these tracks as a separate Accreditation Council for Graduate Medical Education–approved program have been successful in such programs initiated at the University of Pennsylvania and Johns Hopkins.

Few studies have addressed the authorship trends based on nationality in the neuroscience fields. Lim et al[14] assessed the first author nationality of 2 radiology journals, *Radiology* and the *American Journal of Roentgenology*, for a 10-year period. They found that the Japanese are the leading authors after Americans in these 2 general radiology journals. Our study also had this finding in neuroradiology. Lim et al also showed that authors from other Asian countries including Korea increased significantly in this period.[14] In our study, we showed that of Asian countries, China is on the rise while Japan had a decreasing contribution trend in American literature.

The national origin of the institution may impact the publication and citation rates if the authors are from nondeveloped and non-English-speaking countries because there are barriers to access to advanced technology and language proficiency.[15-17] We found that from non-American countries, European followed by Asian institutions had the most articles in the American neurology and neuroradiology literature. In American neurosurgery journals, articles from Asia had an equal or greater number of contributions compared with European institutions. Most interesting, we observed an increasing contribution trend from Australia in all 3 fields of neuroscience.

We found that from 1997 to 2017, articles originating in the United States had higher average numbers of citations than articles originating in other countries for most years in all 3 fields and significantly in neurosurgery and neurology. Our results are in line with those of previous studies showing that the most cited articles usually originated in the United States.[18-20]

As other studies indicated, several factors are associated with a higher number of citations for articles originating in the United States, including the following: 1) the large size of the scientific and especially radiology community in the United States, 2) massive financial resources in the United States, and 3) American authors' tendencies to cite articles that originate in the United States rather than abroad,[18,21,22] which may represent unconscious or implicit bias. This bias is defined as attitudes that affect understanding, actions, and decisions in an unconscious manner, favoring American publications. Journal editors confront implicit bias in peer review; though a large proportion of submissions to American journals come from China and other countries in Asia, these countries remain underrepresented in terms of manuscripts accepted.[23]

Several limitations are noteworthy. First, we collected data from only 2 journals in each of the 3 fields and only 1 month (May issue) in each year. The 2 journals were selected on the basis of the Internet references provided for American journals that had the highest Impact Factor. The bias is that these are journals published in America. This might limit our generalizability, though we believe we collected many articles compared with other similar bibliometric studies. Second, regarding the number of citations in an article, we recognize that there is a direct relationship between publication year and the number of citations accumulated. The number of citations expected by 2017 for an article published in 2015 is likely much less than one that has 10–15 years to accumulate citations. Nonetheless, this factor holds true for all articles and all 3 journals and would not be biased between American and non-American authors.

CONCLUSIONS

We have found that the proportion of non-American contributions to the 2 American neuroradiology journals that have the highest Impact Factor is higher than that for American neurology and neurosurgery journals. That international influence is increasing with time. Articles from Japanese institutions predominate in neuroradiology and neurosurgery, but articles from the UK have a greater impact on neurology; however, the impact from Japan is decreasing even as the contributions from China have risen. Whether from European or Asian countries, articles authored from these nations receive fewer citations in the literature than American-authored articles across all 3 clinical neurosciences, less so however in neuroradiology.

ACKNOWLEDGMENTS

We recognize Marco Carone (University of Washington) for his advice on the statistical tests to use for these analyses.

Disclosures: David M. Yousem—*UNRELATED*: *Consultancy*: medicolegal expert witness; *Expert Testimony*: medicolegal; *Payment for Lectures Including Service on Speakers Bureaus*: American College of Radiology Education Center*; *Royalties*: Elsevier for 5 books. *Money paid to the institution.

REFERENCES

1. Yeung AW, Goto TK, Leung WK. **The changing landscape of neuroscience research, 2006–2015: a bibliometric study.** *Front Neurosci* 2017;11:120 CrossRef Medline
2. Peccora C, Hsu R, Yazdi CA, et al. **Publishing trends in two American journals in anesthesiology: results of an 80-year geographical survey**. *J Anesth Hist* 2016;2:6–12 CrossRef Medline
3. Scimago Journal & Country Rank. http://www.scimagojr.com/journalrank.php?category=2728. Accessed September 15, 2017
4. NEUROSURGIC.com. http://neurosurgic.com/index.php?option=com_content&view=category&layout=blog&id=101&Itemid=465. Accessed September 15, 2017
5. Scimago Journal & Country Rank. http://www.scimagojr.com/journalrank.php?category=2741. Accessed September 15, 2017
6. Welch Medical Library. http://welch.jhmi.edu/welchone/. Accessed September 15, 2017
7. COUNTRIES-of the-WORLD.COM. 7 continents of the world. https://www.countries-ofthe-world.com/continents-of-the-world.html. Accessed February 4, 2018
8. Drubin DG, Kellogg DR. **English as the universal language of science: opportunities and challenges.** *Mol Biol Cell* 2012;23:1399 CrossRef Medline
9. Press WH. **Presidential address: what's so special about science (and how much should we spend on it?).** *Science* 2013;342:817–22 CrossRef Medline
10. Meador KJ. **Decline of clinical research in academic medical centers.** *Neurology* 2015;85:1171–76 CrossRef Medline
11. Lu Y, Zhao S, Chu PW, et al. **An update survey of academic radiologists' clinical productivity.** *J Am Coll Radiol* 2008;5:817–26 CrossRef Medline
12. Alderson PO, Bresolin LB, Becker GJ, et al. **Enhancing research in academic radiology departments: recommendations of the 2003 Consensus Conference.** *Radiology* 2004;232:405–08 CrossRef Medline
13. National Institutes of Health. Research Portfolio Online Reporting Tools. Estimates of Funding for Various Research, Condition, and Disease Categories (RCDC). https://report.nih.gov/categorical_spending.aspx. Accessed January 30, 2018
14. Lim KJ, Yoon DY, Yun EJ, et al. **Characteristics and trends of radiology research: a survey of original articles published in AJR and Radiology between 2001 and 2010.** *Radiology* 2012;264:796–802 CrossRef Medline
15. Paiva CE, Araujo RL, Paiva BS, et al. **What are the personal and professional characteristics that distinguish the researchers who publish in high- and low-impact journals? A multi-national web-based survey.** *Ecancermedicalscience* 2017;11:718 CrossRef Medline
16. Dubey D, Sawhney A, Atluru A, et al. **Trends in authorship based on gender and nationality in published neuroscience literature.** *Neurol India* 2016;64:97–100 CrossRef Medline
17. Shekhani HN, Shariff S, Bhulani N, et al. **Bibliometric analysis of manuscript characteristics that influence citations: a comparison of six major radiology journals.** *AJR Am J Roentgenol* 2017;209:1191–96 CrossRef Medline
18. Yoon DY, Yun EJ, Ku YJ, et al. **Citation classics in radiology journals: the 100 top-cited articles, 1945–2012.** *AJR Am J Roentgenol* 2013;201:471–81 CrossRef Medline
19. Brinjikji W, Klunder A, Kallmes DF. **The 100 most-cited articles in the imaging literature.** *Radiology* 2013;269:272–76 CrossRef Medline
20. Pagni M, Khan NR, Cohen HL, et al. **Highly cited works in radiology: the top 100 cited articles in radiologic journals.** *Acad Radiol* 2014;21:1056–66 CrossRef Medline
21. Campbell FM. **National bias: a comparison of citation practices by health professionals.** *Bull Med Libr Assoc* 1990;78:376–82 Medline
22. Hong SJ, Lim KJ, Hwang HJ, et al. **The 100 top-cited articles in pulmonary imaging: a bibliometric analysis.** *J Thorac Imaging* 2017;32:198–202 CrossRef Medline
23. American Association for the Advancement of Science. Journals and Funders Confront Implicit Bias in Peer Review. https://www.aaas.org/news/journals-and-funders-confront-implicit-bias-peer-review. Accessed December 22, 2017

Multisite Concordance of DSC-MRI Analysis for Brain Tumors: Results of a National Cancer Institute Quantitative Imaging Network Collaborative Project

K.M. Schmainda, M.A. Prah, S.D. Rand, Y. Liu, B. Logan, M. Muzi, S.D. Rane, X. Da, Y.-F. Yen, J. Kalpathy-Cramer, T.L. Chenevert, B. Hoff, B. Ross, Y. Cao, M.P. Aryal, B. Erickson, P. Korfiatis, T. Dondlinger, L. Bell, L. Hu, P.E. Kinahan, and C.C. Quarles

ABSTRACT

BACKGROUND AND PURPOSE: Standard assessment criteria for brain tumors that only include anatomic imaging continue to be insufficient. While numerous studies have demonstrated the value of DSC-MR imaging perfusion metrics for this purpose, they have not been incorporated due to a lack of confidence in the consistency of DSC-MR imaging metrics across sites and platforms. This study addresses this limitation with a comparison of multisite/multiplatform analyses of shared DSC-MR imaging datasets of patients with brain tumors.

MATERIALS AND METHODS: DSC-MR imaging data were collected after a preload and during a bolus injection of gadolinium contrast agent using a gradient recalled-echo–EPI sequence (TE/TR = 30/1200 ms; flip angle = 72°). Forty-nine low-grade (n = 13) and high-grade (n = 36) glioma datasets were uploaded to The Cancer Imaging Archive. Datasets included a predetermined arterial input function, enhancing tumor ROIs, and ROIs necessary to create normalized relative CBV and CBF maps. Seven sites computed 20 different perfusion metrics. Pair-wise agreement among sites was assessed with the Lin concordance correlation coefficient. Distinction of low- from high-grade tumors was evaluated with the Wilcoxon rank sum test followed by receiver operating characteristic analysis to identify the optimal thresholds based on sensitivity and specificity.

RESULTS: For normalized relative CBV and normalized CBF, 93% and 94% of entries showed good or excellent cross-site agreement ($0.8 \leq$ Lin concordance correlation coefficient ≤ 1.0). All metrics could distinguish low- from high-grade tumors. Optimum thresholds were determined for pooled data (normalized relative CBV = 1.4, sensitivity/specificity = 90%:77%; normalized CBF = 1.58, sensitivity/specificity = 86%:77%).

CONCLUSIONS: By means of DSC-MR imaging data obtained after a preload of contrast agent, substantial consistency resulted across sites for brain tumor perfusion metrics with a common threshold discoverable for distinguishing low- from high-grade tumors.

ABBREVIATIONS: AIF = arterial input function; HGG = high-grade glioma; LCCC = Lin concordance correlation coefficient; LGG = low-grade glioma; NAWM = normal-appearing white matter; nCBF = normalized cerebral blood flow; nRCBV = normalized relative cerebral blood volume; rCBV = relative cerebral blood volume; SN = sensitivity (in the context of receiver operating characteristic analysis); SP = specificity (in the context of receiver operating characteristic analysis); T1+C = postcontrast T1WI

Current Response Assessment in Neuro-Oncology criteria,[1] which include anatomic imaging only, are often insufficient for determining tumor response and progression after therapy. Frequently, imaging changes on postcontrast MR imaging or FLAIR are not the result of increased tumor activity but rather a consequence of the treatment itself. These changes, which can include edema, inflammation, or increased vascular or blood-brain barrier permeability, make it difficult to distinguish true

Received November 1, 2017; accepted after revision February 7, 2018.

From the Department of Radiology (K.M.S., M.A.P., S.D.R.) and Division of Biostatistics (Y.L., B.L.), Institute for Health and Society, Medical College of Wisconsin, Milwaukee, Wisconsin; Department of Radiology (M.M., S.D.R., P.E.K.), University of Washington, Seattle, Washington; Department of Radiology (X.D.), Harvard Medical School, Brigham and Women's Hospital, Boston, Massachusetts; Athinoula A. Martinos Center for Biomedical Imaging (Y.-F.Y., J.K.-C.), Department of Radiology, Harvard Medical School/Massachusetts General Hospital, Charlestown, Massachusetts; Department of Radiology (T.L.C., B.H., B.R.) and Departments of Radiation Oncology, Radiology, and Biomedical Engineering (Y.C., M.P.A.), University of Michigan, Ann Arbor, Michigan; Department of Radiology (B.E., P.K.), Mayo Clinic, Rochester, Minnesota; Imaging Biometrics LLC (T.D.), Elm Grove, Wisconsin; Division of Imaging Research (L.B., C.C.Q.), Barrow Neurological Institute, Phoenix, Arizona; and Department of Radiology (L.H.), Mayo Clinic, Scottsdale, Arizona.

This work was supported by the National Institutes of Health/National Cancer Institute: U01 CA176110 (K.M.S., M.A.P., S.D.R., T.D.), U01 CA148131 (M.M., P.E.K.), U01 CA166104 (T.L.C., B.H.), U01 CA154601 (X.D., Y.-F.Y., J.K.-C.), U01 CA160045 (B.E., P.K.), U01 CA 183848 (Y.C., M.P.A.), R01 CA158079 (L.B., C.C.Q.), R01 CA082500 (K.M.S., M.A.P., S.D.R.), R50 CA211270 (M.M.), and P01 CA085878, U24CA180927, U24CA180918 (J.K.-C.).

Paper previously presented, in part, at: Annual Meeting and Exhibition of the International Society of Magnetic Resonance in Medicine, April 22–27, 2017; Honolulu, Hawaii.

Please address correspondence to Kathleen M. Schmainda, PhD, Medical College of Wisconsin, Department of Radiology, 8701 W Watertown Plank Rd, Milwaukee, WI 53226; e-mail: kathleen@mcw.edu

Indicates open access to non-subscribers at www.ajnr.org

http://dx.doi.org/10.3174/ajnr.A5675

tumor progression from treatment response.[2-6] Because of these difficulties, patients are often precluded from switching to potentially more effective therapies within treatment windows of 3–5 months.[1] Clearly, better indications of tumor response that are not confounded by these treatment adverse effects are needed.

Perfusion MR imaging methods, which have repeatedly demonstrated the ability to provide biologically relevant information for treatment management, have the potential to overcome these limitations. For brain perfusion, the DSC-MR imaging methods have been most commonly used. With DSC-MR imaging, T2- or T2*-weighted images are acquired with high temporal resolution during a bolus administration of a gadolinium contrast agent.[7] The derived relative CBV (rCBV) maps have demonstrated the ability to predict tumor grade[8,9] and survival,[10] distinguish treatment effects from recurrent tumor,[11,12] and predict response to antiangiogenic therapy more reliably than standard MR imaging.[13-15]

Despite this promise, the translation of DSC-MR imaging for routine clinical use has been hindered by a lack of consistency in the methods used and the rCBV values reported to make the noted distinctions. However, often a threshold determined for one purpose, such as distinguishing low- from high-grade tumor,[16] is used for another purpose such as predicting outcomes.[17] Consequently, the present confusion may be due to the lack of well-defined studies performed under carefully controlled conditions that test a specific outcome. This study addresses these limitations by providing carefully curated DSC-MR imaging datasets of low-grade glioma (LGG) and high-grade glioma (HGG) to multiple sites that participate in the National Cancer Institute Quantitative Imaging Network. With this approach, variations in image acquisition and preprocessing are eliminated and postprocessing methods can be directly compared in their ability to distinguish LGGs from HGGs. In addition, the threshold for this distinction can be identified both for each individual site and as a consensus recommendation.

MATERIALS AND METHODS

Patients

All subjects recruited from a single site provided informed written consent according to institutional review board policy. Subjects with histologically confirmed, newly diagnosed, and treatment-naïve glial tumors who had preoperative DSC-MR imaging were included in this study. Subjects with purely oligodendroglial lesions were not included due to demonstrated differences in rCBV compared with astrocytic tumors.[18] Due to the disparity in the number of subjects histologically diagnosed with low- and high-grade tumors, consecutive subjects with low-grade tumors between 2008 and 2014 and high-grade tumors from 2010 to 2014 were identified. Subjects were excluded if anatomic images were not available for lesion delineation or when DSC-MR imaging data were of poor quality.

Imaging

Studies were performed on 1.5T or 3T MR imaging systems. Standard precontrast MRIs were acquired including FLAIR (TE/TR/NEX/matrix = 126/9000 ms/2200–2500 ms/2/252 × 215) and T1WI spin-echo (TE/TR/NEX/matrix = 11 ms/650 ms/2/256), after which gadolinium contrast agent was administered. Either 0.05 mmol/kg of gadobenate dimeglumine (MultiHance; Bracco Diagnostics, Princeton, New Jersey) ($n = 48$) or 0.1 mmol/kg of gadodiamide (Omniscan; GE Healthcare, Piscataway, New Jersey) ($n = 1$) was administered before obtaining the postcontrast T1-weighted images. This initial gadolinium administration serves as a preload for the subsequent DSC-MR imaging acquisition. A preload results in more accurate rCBV because it reduces the T1 leakage effects that can confound the DSC-MR imaging data analysis.[9,19-21] After collecting the postcontrast T1WI (T1+C), using parameters equivalent to the precontrast settings, we acquired DSC-MR imaging data (gradient recalled-echo–EPI: TR = 1100–1250 ms, TE = 30 ms, flip angle = 70°–80°, 12–17 slices, slice thickness = 4–5 mm, interslice gap = 0–1.5 mm, matrix = 96 × 96/128 × 128, FOV = 165–240 × 165–240 mm^2). The gradient recalled-echo–EPI data were collected for 120 seconds with 0.1 mmol/kg of gadolinium injected at 60 seconds. For ease of coregistration of the DSC-MR images to anatomic images, a spin-echo "reference" scan (TE/TR/NEX/matrix = 14 ms/500 ms/1/256 × 192) was obtained using a slice prescription matching the more limited slice prescription of the DSC-MR imaging examination.

Central Preprocessing

The preprocessing workflow is schematized in Fig 1. All preprocessing was performed in OsiriX Imaging Software (http://www.osirix-viewer.com) using the IB Delta Suite (Imaging Biometrics, Elm Grove, Wisconsin). Six datasets provided for each case included the following: 1) T1+C images; 2) DSC-MR imaging time-series co-registered to the T1+C images; 3) an arterial input function (AIF), which included 3 AIF locations in each file; 4) a whole-brain mask and ROIs of 5) normal-appearing white matter (NAWM) and 6) tumor. The NAWM was used to compute normalized rCBV (nRCBV) and normalized CBF (nCBF) maps.

The DSC-MR imaging volume was co-registered to the T1+C images via the reference scan obtained with the same slice prescription as the DSC-MR imaging. The AIF locations were determined semiautomatically using IB Neuro (Imaging Biometrics) with manual adjustments when necessary. An average signal generated from 3 pixels constituted the AIF. The whole-brain mask was made available to prevent disparity in values that could result from threshold variations that each software platform might use. Using the IB Delta Suite, we determined tumor ROIs from deltaT1 maps, which are standardized difference maps[22] that enable clear visualization of enhancing lesions free of bright signal from blood products or proteinaceous material. Nonenhancing lesions, apparent as areas of dark signal on T1WIs, were delineated by a neuroradiologist with >20 years of experience. Each ROI was created as a 16-bit binary DICOM file that included only whole voxels rather than contoured points. This approach prevents differences in the applied ROIs because each software platform applies different rules regarding whether a voxel is considered inside or outside an ROI. Anonymized datasets were uploaded to The Cancer Imaging Archive,[23,24] where they were further vetted to ensure the compatibility of complete datasets for the analysis platform of each site. All sites were blinded to tumor grade.

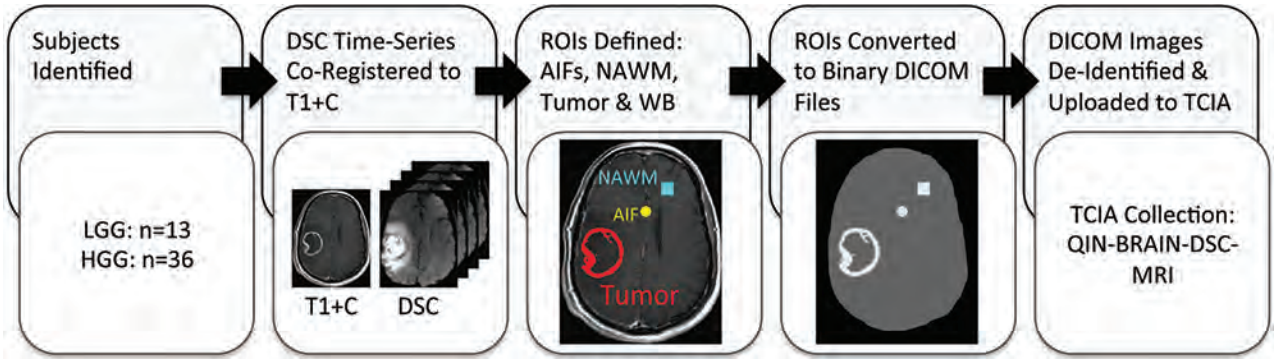

FIG 1. Preprocessing workflow. Forty-nine subjects were identified, 13 of whom had a diagnosis of low-grade glioma and 36 with a diagnosis of high-grade glioma. The DSC-MR image volume was co-registered to the T1+C images via the reference scan obtained with the same slice prescription as the DSC-MR imaging. Six datasets were provided for each case including the following: 1) T1+C images; 2) DSC-MR imaging time-series registered to the T1+C images; 3) an AIF, which included 3 AIF locations in each file; 4) a whole brain (WB) mask and ROIs of 5) normal-appearing white matter (NAWM), and 6) tumor. Each ROI was created as a 16-bit binary DICOM file that included only whole voxels rather than contoured points. Anonymized datasets were uploaded to The Cancer Imaging Archive. QIN indicates Quantitative Imaging Network.

Table 1: Teams and rCBV analysis methods

Team/Entry No.	Software	Scaling	Leakage Correction	Description
A1	IB Neuro	NAWM	Yes	Modified BSW[21]
B1	IB Neuro	NAWM	Yes	Modified BSW[21]
C1	IB Neuro	NAWM	Yes	Modified BSW[21]
B2	Matlab[a]	NAWM	Yes	120-point TI (BSW[21])
B3	Matlab	AIF	Yes	120-point TI (BSW[21])
D1	nordicICE	NAWM	Yes	120-point TI (BSW[21])
D2	nordicICE	Population AIF	Yes	120-point TI (BSW[21])
E1	PGUI (LC)[b]	NAWM	Yes	120-point TI (BSW[21])
E2	PGUI (C)	NAWM	Yes	AUC of C(t) ratio for ROI/AIF
E3	PGUI (PM LC)	NAWM	Yes	Bayesian parametric FT[44]
D3	Slicer[c]	NAWM	Yes	120-point TI (BSW[21])
F1	FIAT[d]	NAWM	Yes	Modified Weisskoff[45,46]
G1	MCcbv[e]	NA	Yes	Modified Weisskoff[45,46]
A2	IB Neuro	NA (standardized)[47]	Yes	Modified BSW[21] 2006
A3	IB Neuro	NAWM	No	Leakage correction not used
B4	IB Neuro	NAWM	No	Leakage correction not used
E4	PGUI	NAWM	No	Leakage correction not used
E5	PGUI	NAWM	No	Deconvolution of residue function (sSVD)
E6	PGUI	NAWM	No	Deconvolution of residue function (oSVD)
A4	IB Neuro	N/A (standardized)[47]	No	Leakage correction not used

Note:—TI indicates trapezoidal integration; BSW, Boxerman-Schmainda-Weisskoff; NA, not applicable; FT, Fourier Transform; sSVD, standard singular value decomposition; oSVD, block circulant singular value decomposition; C(t) ratio, concentration time course.

[a] MathWorks, Natick, Massachusetts.

[b] Perfusion Graphical User Interface; MINDlab, Center of Functionally Integrative Neuroscience, Aarhus University Hospital Norrebrogade, Denmark.[44]

[c] http://www.slicer.org.

[d] Functional Image Analysis Tool (University of Michigan).

[e] Mayo Clinic cerebral blood volume (Mayo Clinic, Rochester, Minnesota).[37]

Image and Statistical Analyses

Seven sites (1–7) using 7 different software platforms provided 20 different rCBV measurements (Table 1) and 12 different CBF measurements (Table 2). Details for each software platform are listed in the tables. Several sites used >1 platform or analysis method. When applicable, the analysis for measurements of standardized rCBV was grouped separately from nRCBV due to image-scale differences. Agreement between each pair of values was assessed by computing the Lin concordance correlation coefficient (LCCC). An LCCC > 0.8 indicates good agreement, and LCCC > 0.9 indicates excellent agreement.

The ability of each metric to distinguish LGG from HGG was determined using the Wilcoxon rank sum test, with $P < .05$ indicating significance. A receiver operating characteristic analysis was performed to identify the threshold that provides the optimal sensitivity (SN) and specificity (SP) to distinguish LGG from HGG. The DeLong test for comparing ≥2 receiver operating characteristic curves was used to determine whether there were differences in the ability of each measurement to classify tumors.

To determine "consensus" cutoff points, we created boxplots of the sum of SN and SP. Optimal thresholds were identified as those with maximum SN + SP mean, according to the Youden selection criteria with small variance. The random effects model was used to assess the reliability of measurements across sites and platforms. The reliability is quantified by the following:

Table 2: Teams and nCBF analysis methods

Team/Entry No.	Software	Scaling	Description
A5	IB Neuro	NAWM	SVD: deconvolution of ΔR2* with AIF
B5	IB Neuro	NAWM	SVD: deconvolution of ΔR2* with AIF
C2	IB Neuro	NAWM	SVD: circular deconvolution of ΔR2* with AIF
B6	Matlab	NAWM	SVD applied to leakage-corrected tissue ΔR2* and AIF ΔR2* curves
D4	nordicICE	NAWM	No AIF
D5	nordicICE	Population AIF	Population AIF
E7	PGUI	NAWM	nCBF
E8	PGUI	NAWM	sSVD
E9	PGUI	NAWM	oSVD
E10	PGUI	NAWM	Bayesian FT deconvolution[44]
D6	Slicer	NAWM	No AIF
F2	FIAT	NAWM	nCBF

Note:—SVD indicates singular value decomposition; sSVD, standard singular value decomposition; oSVD, block circulant singular value decomposition; FT, Fourier Transform..

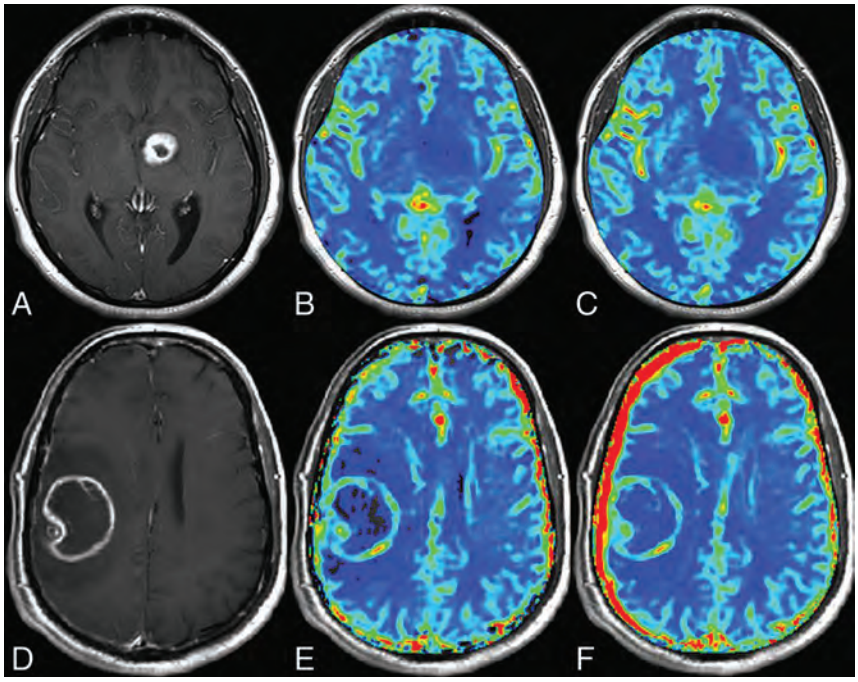

FIG 2. Sample parameter maps. Shown are postcontrast T1-weighted images (*A* and *D*) and corresponding rCBV (*B* and *E*) and CBF (*C* and *F*) maps for one patient with a low-grade glioma (*A–C*) and another patient with a high-grade glioma (*D–F*).

$$Reliability = \frac{\sigma^2_{\text{within}}}{\sigma^2_{\text{within}} + \sigma^2_{\text{between}}},$$

where σ is the SD within or between software platforms.

Finally, to assess the clinical relevance of the study observations, we determined the false-positive rate from T1+C images in comparison with each of the perfusion parameters (nRCBV, standardized rCBV, nCBF). The false-positive rate is defined as the proportion of low-grade tumors thought to be aggressive and/or high-grade, as indicated by the decision for tumor resection, relative to all tumors resected. The false-negative rate was not determined because data from all patients, including those who did not undergo an operation, were not available. By means of the T1+C images, the false-positive rate was defined as the proportion of tumors that are low-grade and had contrast agent–enhancing lesions. For the perfusion parameters, a false-positive rate is defined as a low-grade tumor with a value above the threshold determined for distinguishing low- from high-grade tumors.

RESULTS

Sixty-three subjects met inclusion criteria for this study, with 14 excluded for the following reasons: The contrast agent bolus was delayed during DSC acquisition, preventing capture of the postbolus steady-state signal ($n = 4$); the contrast agent bolus was injected too slowly and in an irregular pattern ($n = 4$); the contrast agent bolus was not present during acquisition of images ($n = 2$); there were severe ghosting and motion artifacts of DSC images ($n = 2$); or anatomic images were not available for lesion delineation ($n = 2$). Forty-nine coregistered LGG ($n = 13$) and HGG ($n = 36$) DSC-MR imaging datasets were preprocessed, anonymized, and uploaded to The Cancer Imaging Archive (Fig 1). Tumor grade was confirmed with histopathology a median of 3 days (range, 0–4 days) following MR imaging. Examples of postprocessed datasets are shown in Fig 2. LCCC results are displayed in a matrix listing each nRCBV (Fig 3) or nCBF (Fig 4) entry on both the x- and y-axes. For tumor nRCBV, 75% of the entries showed excellent agreement with LCCC $\geq$ 0.9 and 19% with good agreement ($0.80 \leq$ LCCC < 0.90), leaving only 6% with poor concordance (LCCC < 0.80). The concordance was best for nRCBV values determined with leakage correction. For nCBF, only 59% had $0.90 \leq$ LCCC ≤ 1.0 and 34% had $0.80 \leq$ LCCC ≤ 0.89.

For all software platforms, both nRCBV and nCBF showed statistically significant differences between LGG and HGG (Tables 3 and 4), with a mean nRCBV = 1.4 ± 0.13 and mean nCBF = 1.57 ± 0.24. The SN/SP for nRCBV ranged from 81%–97%/77%–85% and was slightly worse for nCBF with SN/SP = 64%–97%/69%–85%. By means of the DeLong test, no significant differences were found among the 18 nRCBV ($P = .72$) metrics to distinguish LGG from HGG. While differences among the nCBF metrics were borderline significant ($P = .05$), if the entry with the lowest area under the curve (0.658) was excluded, there was no significant difference between the remaining measures ($P = .49$). The DeLong test for the standardized rCBV showed no significant distinction between the 2 submissions for this measure ($P = .23$).

Alternatively, the data can be pooled, as shown by the boxplots of SN + SP (Fig 5), for which median and quartile values are indicated. The maximum sums were the following: nRCBV = 1.4

TEAM/ENTRY		A1	B1	C1	B2	B3	D1	D2	E1	E2	E3	D3	F1	G1	A3	B4	E4	E5	E6
	LEAKAGE	Yes	Yes	Yes	Yes	Yes	Yes	Yes	Yes	Yes	Yes	Yes	Yes	Yes	No	No	No	No	No
A1	Yes	1.00	1.00	1.00	0.99	0.99	0.99	0.99	0.97	0.88	0.93	0.96	0.91	0.98	0.96	0.96	0.92	0.79	0.88
B1	Yes		1.00	1.00	0.99	0.99	0.99	0.99	0.97	0.88	0.93	0.96	0.91	0.98	0.96	0.96	0.92	0.79	0.88
C1	Yes			1.00	0.99	0.99	0.99	0.99	0.97	0.88	0.93	0.96	0.91	0.98	0.94	0.96	0.92	0.79	0.88
B2	Yes				1.00	1.00	1.00	1.00	0.98	0.90	0.94	0.98	0.88	0.99	0.98	0.98	0.94	0.81	0.90
B3	Yes					1.00	0.99	0.99	0.98	0.89	0.94	0.98	0.88	0.99	0.98	0.98	0.94	0.81	0.89
D1	Yes						1.00	1.00	0.98	0.88	0.94	0.97	0.91	0.98	0.97	0.97	0.92	0.79	0.88
D2	Yes							1.00	0.98	0.88	0.94	0.97	0.91	0.98	0.97	0.97	0.92	0.79	0.88
E1	Yes								1.00	0.92	0.92	0.98	0.83	0.98	1.00	0.99	0.98	0.84	0.92
E2	Yes									1.00	0.92	0.92	0.77	0.92	0.93	0.93	0.95	0.93	1.00
E3	Yes										1.00	0.94	0.87	0.93	0.92	0.92	0.89	0.86	0.92
D3	Yes											1.00	0.84	0.98	0.99	0.99	0.96	0.85	0.92
F1	Yes												1.00	0.85	0.82	0.82	0.76	0.68	0.77
G1	Yes													1.00	0.98	0.98	0.96	0.83	0.92
A3	No														1.00	1.00	0.98	0.86	0.93
B4	No															1.00	0.98	0.86	0.93
E4	No																1.00	0.91	0.95
E5	No																	1.00	0.97
E6	No																		1.00

LCCC ≥ 0.90
0.80 ≤ LCCC < 0.90
LCCC < 0.80

FIG 3. Lin concordance results for nRCBV. Listed are the Lin concordance correlation coefficients for the nRCBV values for each pair of sites. Whether leakage correction was applied is indicated by *green labels*, with *red labels* indicating no leakage correction. Pairs with excellent concordance (LCCC > 0.90) are highlighted with *blue-filled squares*; very good concordance (0.80 < LCCC < 0.90), with *green squares*; and weaker concordance (LCCC < 0.80), with *white squares*.

TEAM/ ENTRY	A5	B5	C2	B6	D4	D5	E7	E8	E9	E10	D6	F2
A5	1.00	1.00	0.96	0.88	0.93	0.98	0.96	0.96	0.92	0.85	0.96	0.89
B5		1.00	0.97	0.87	0.94	0.98	0.96	0.97	0.93	0.84	0.96	0.89
C2			1.00	0.84	0.96	0.96	0.96	0.94	0.91	0.79	0.97	0.85
B6				1.00	0.73	0.88	0.90	0.80	0.80	0.84	0.88	0.97
D4					1.00	0.91	0.88	0.95	0.91	0.76	0.91	0.74
D5						1.00	0.97	0.94	0.93	0.84	0.94	0.90
E7							1.00	0.92	0.94	0.86	0.94	0.93
E8								1.00	0.96	0.87	0.92	0.81
E9									1.00	0.90	0.89	0.83
E10										1.00	0.81	0.83
D6											1.00	0.88
F2												1.00

LCCC ≥ 0.90
0.80 ≤ LCCC < 0.90
LCCC < 0.80

FIG 4. Lin concordance results for nCBF. Listed are the Lin concordance correlation coefficients for the normalized CBF values for each pair of sites. Pairs with excellent concordance (LCCC > 0.90) are highlighted with *blue-filled squares*; very good concordance (0.80 < LCCC <0.90), with *green squares*; and weaker concordance (LCCC < 0.80), with *white squares*.

(SN/SP = 90%/77%) and nCBF = 1.58 (SN/SP = 86%/77%). For these consensus thresholds, the minimum individual SN/SP was 83%/77% for nRCBV and 80%/70% for nCBF.

For the 18 nRCBV measurements, the reliability was determined to be 0.93, indicating that 93% of the variation can be attributed to differences in tumors, and 7%, to differences in analysis methods. The reliability was 95% for nRCBV determined with leakage correction and 93% for the group without leakage correction. For the nRCBV computed with one of the most common leakage-correction algorithms (Boxerman-Schmainda-Weisskoff[21]), the reliability improved to 98%. The reliability of standardized rCBV was 96%. For the 12 nCBF measurements, the reliability was 61%.

Finally, the false-positive rate using T1+C was found to be 31%. In comparison, the false-positive rate across all software platforms was 15%–23% for nRCBV, 15%–31% for nCBF, and 8%–15% for standardized rCBV.

DISCUSSION

By means of carefully curated DSC-MR imaging datasets, obtained with a single acquisition approach, all nRCBV and nCBF metrics, processed by 7 different sites, could distinguish LGG from HGG. The optimal nRCBV and nCBF thresholds varied by only 9% and 15%, respectively. Unique to this study, consensus thresholds of nRCBV = 1.4 and nCBF = 1.58 were determined, indicating good accuracy overall and for each individual site. These results should bolster confidence in the ability of DSC-MR imaging to provide reliable and consistent cross-platform perfusion metrics for the evaluation of brain tumors and, specifically, for distinguishing low- from high-grade gliomas.

The range of nRCBV threshold values determined in this study is much tighter than the 0.7–3.0 range previously reported for distinguishing tumor grade,[25,26] predicting differences in survival,[10,17,27-29] and distinguishing true progression from pseudoprogression[30] and tumor from treatment effect.[11,12,31] While this large range of threshold values has been attributed to different acquisition and postprocessing schemes,[20] differences in patient populations and the clinical questions addressed also contribute to the variabilities. While it is unlikely that a single threshold can be universally applied for all clinical questions, these studies suggest that with well-defined studies to address a specific outcome under carefully controlled conditions, it is possible to reach consensus.

The present study also demonstrates a greater cross-platform concordance than that previously reported. For example, in one study,[32] 2 commercial software packages (nordicICE; NordicNeuroLab, Bergen, Norway and Brain-STAT; GE Healthcare) were compared. Like the present study, 1 dataset of 24 patients with de novo glioblastoma was used and ROIs of tumor and reference brain were predetermined. However, unlike the present study, vastly different mathematic algorithms were applied, resulting in very disparate definitions for nRCBV and CBF; thus, a wide range of values was reported. In the present study, most algorithms involved the integration of the concentration-time course and the application of Boxerman-Schmainda-Weisskoff leakage correction,[21] which, in a subanalysis, also showed better reliability. In the previous study, 5 of 10 algorithms relied on the determination of the AIF.[32] Using AIF to compute nRCBV resulted in coefficients of variation of 15%, but only 2% when AIF was not used. The challenges of reliably determining the AIF are well-known and may largely explain the poor repeatability.[33,34] Most software platforms in this study did not incorporate AIF for nRCBV calculation and may therefore also explain the excellent concordance across sites. Yet, the computa-

Table 3: nRCBV low- vs high-grade thresholds and ROC analysis results

Team/ Entry No.	Software Platform	Leakage Correction Used	LG vs HG (*P* Value)	Threshold	SN	SP	AUC
A1	IB Neuro	Yes	5.34E-06	1.605	0.861	0.846	0.889
B1	IB Neuro	Yes	5.36E-06	1.605	0.861	0.846	0.889
C1	IB Neuro	Yes	5.39E-06	1.605	0.861	0.846	0.889
B2	Matlab	Yes	2.02E-06	1.315	0.972	0.769	0.892
B3	Matlab	Yes	1.75E-06	1.330	0.972	0.769	0.896
D1	nordicICE	Yes	3.30E-06	1.305	0.972	0.769	0.895
D2	nordicICE	Yes	3.30E-06	1.305	0.972	0.769	0.895
E1	PGUI (LC)	Yes	7.32E-06	1.615	0.861	0.846	0.892
E2	PGUI (C)	Yes	1.14E-05	1.400	0.861	0.769	0.871
E3	PGUI (PM LC)	Yes	1.18E-05	1.400	0.889	0.769	0.856
D3	Slicer	Yes	1.08E-06	1.415	0.944	0.769	0.891
F1	FIAT	Yes	2.50E-05	1.235	0.944	0.769	0.853
G1	McCBV	Yes	1.26E-06	1.425	0.944	0.769	0.891
A3	IB Neuro	No	1.55E-06	1.330	0.917	0.769	0.895
B4	IB Neuro	No	1.56E-06	1.330	0.917	0.769	0.895
E4	PGUI	No	6.94E-06	1.450	0.861	0.769	0.887
E5	PGUI	No	5.67E-05	1.585	0.806	0.846	0.872
E6	PGUI	No	1.19E-05	1.395	0.861	0.769	0.873

Note:—AUC indicates area under the curve; LG, low-grade; HG, high-grade.

Table 4: nCBF low- vs high-grade thresholds and ROC analysis results

Team/Entry No.	Software	LG vs HG (*P* Value)	Threshold	SN	SP	AUC
A5	IB Neuro	2.90E-05	1.815	0.806	0.846	0.861
B5	IB Neuro	2.38E-05	1.555	0.917	0.769	0.864
C2	IB Neuro	3.82E-06	1.415	0.944	0.769	0.880
B6	Matlab	2.61E-04	2.045	0.722	0.846	0.814
D4	nordicICE	9.81E-06	1.255	0.972	0.769	0.868
D5	nordicICE	3.03E-05	1.580	0.861	0.846	0.866
E7	PGUI	1.30E-04	1.575	0.806	0.846	0.846
E8	PGUI	3.85E-05	1.375	0.917	0.692	0.845
E9	PGUI	1.67E-04	1.460	0.833	0.769	0.812
E10	PGUI	7.86E-03	1.920	0.639	0.692	0.658
D6	Slicer	1.04E-06	1.405	0.944	0.769	0.887
F2	FIAT	2.65E-04	1.460	0.861	0.769	0.816

Note:—AUC indicates area under the curve; LG, low-grade; HG, high-grade.

tion of CBF requires the determination of AIF and is likely a primary reason for the greater variance in comparison with nRCBV (Figs 3 and 4). Also, the individual nCBF thresholds calculated using IB Neuro varied across sites because some sites chose to use circular deconvolution of the AIF for processing while others did not.

Five of 10 analysis methods in the previous software comparison study often used γ-variate fitting.[32] Several studies reported a lower SNR[35] as well as greater inaccuracy when γ-variate fitting was used for brain tumor DSC-MR imaging data, especially in the presence of contrast agent leakage.[19,20] Although γ-variate fitting suppresses the postbolus baseline, making it appear that leakage has been corrected, there is no physiologic basis for this correction and it does not appropriately consider leakage that can occur during the bolus.[36] Gamma-variate fitting was not used by any of the software platforms evaluated in the present study.

In another study,[37] nRCBV values were generated from 3 FDA-approved software packages including IB Neuro 1.1, FuncTool software 4.5.3 (GE Healthcare) and nordicICE 2.3.13 and 1 in-house software platform. While effort was made to use the tools in a similar way, more user interaction was required of some (FuncTool, nordicICE), and FuncTool did not have the option for leakage correction. The largest differences between the in-house and commercial software occurred with the tool that required the most user interaction (nordicICE), further motivating the development of more automated workflows with less need for user interaction. Yet another study comparing these same 3 packages also found significant differences, with the outlying package depending heavily on the type of rCBV metric used.[38] This finding again suggests that it is imperative that the same output metric be used when making such comparisons.

Of relevance to the current study, rCBV maps generated with IB Neuro showed superior leakage correction and stronger correlation with image-guided microvessel quantification as well as higher accuracy in distinguishing tumor recurrence from pseudoprogression/radiation necrosis compared with other software platforms.[39] These results are relevant, given the number of sites in the present study that chose to use IB Neuro for their processing.

A limitation of the current study is the use of a DSC-MR imaging dataset that was obtained at a single center using a single approach. Use of a range of acquisition methods would likely result in greater variation in the DSC-MR imaging perfusion results. A previous study confirmed this by comparing a range of acquisition and analysis methods, which also influenced the ability to distinguish high-grade tumor from reference brain.[20] However, a consensus regarding best practices for DSC-MR imaging data acquisition is being reached, as described in a recent review,[40] and includes the approach used for this study. Specifically, use of a preload of contrast agent and a flip angle $<90°$ is proving to be one of the most accurate approaches, further confirmed by 2 recent studies,[19,41] both incorporating sophisticated simulations of DSC-MR imaging data representative of brain tumor. Use of a preload might also be an important reason for greater consistency across postprocessing methods in this study compared with previous studies (eg, Orsingher et al[32]). Collecting DSC-MR imaging data after preload was shown to decrease the dependence of tumor rCBV on the chosen method of analysis.[20]

An additional limitation of this study is the use of laboratory or proprietary commercial packages for which many of the details of the algorithmic implementation are not available and thus cannot be further evaluated as potential sources of differences. Also, the software platforms used for this study were dictated entirely by platforms being used at each participating site. Consequently, this is not a comprehensive comparison of

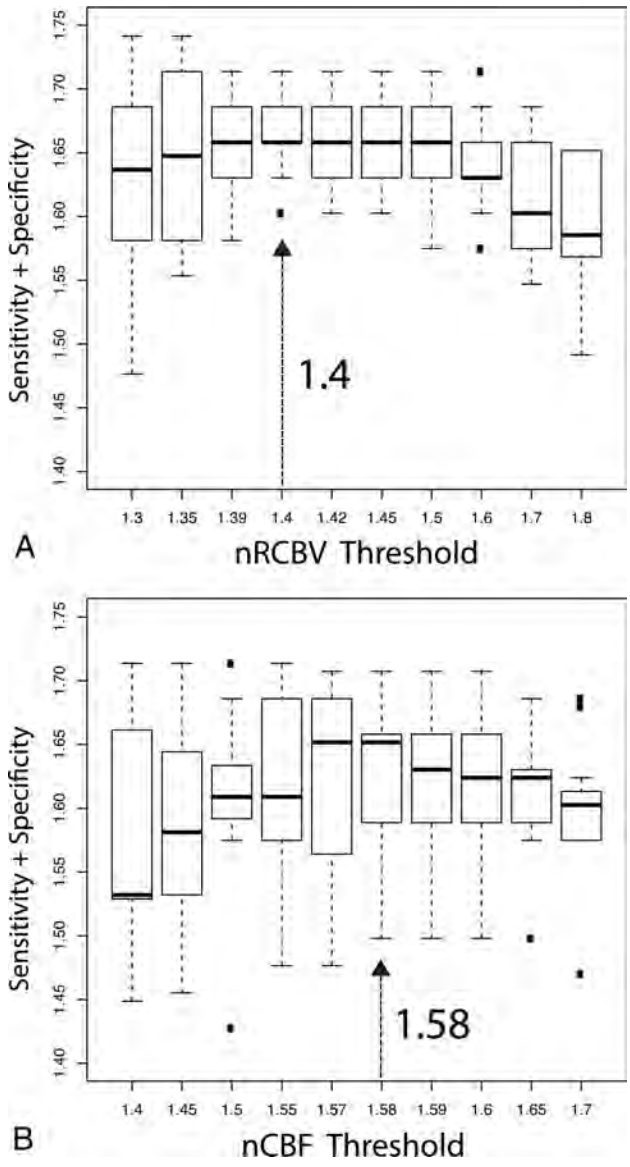

FIG 5. Boxplots showing the sum of sensitivity and specificity values for nRCBV (*A*) and nCBF (*B*) for all sites and metrics. From these data, values that gave a maximum sum of specificity plus sensitivity and minimal variance were chosen as the consensus threshold values.

all available software platforms with DSC-MR imaging postprocessing capabilities.

The general application of the results of this study is somewhat limited because the preprocessing steps were carefully controlled so that consistent input data were provided to all sites and software platforms. In practice, subjective manipulation of the preprocessing steps is common; therefore, consistency is less likely, as the discussion of the previous studies reveals. Yet the identification of preprocessing as a key confound should not inhibit use of DSC-MR imaging but rather motivate improving automation of the preprocessing steps. In fact, several efforts to automate tumor segmentation are well underway,[42,43] which remove this source of discrepancy entirely.

CONCLUSIONS

This study demonstrates that nRCBV and nCBF can be used to distinguish LGG from HGG in a consistent fashion and using a single consensus threshold. This result should increase confidence in using nRCBV primarily, but also nCBF, on a routine basis, potentially motivating its incorporation into the updated Response Assessment in Neuro-Oncology criteria. Finally, these results provide strong motivation for the development of more automated preprocessing workflows that are less dependent on subjective user interaction.

Disclosures: Kathleen M. Schmainda—*RELATED*: *Grant*: National Institutes of Health/National Cancer Institute, *Comments*: U01 176110, R01 CA082500*; *UNRELATED*: *Grants/Grants Pending*: National Institutes of Health, *Comments*: National Institutes of Health grants submitted on various topics*; *Other*: Imaging Biometrics, *Comments*: ownership interest. Ying Liu—*UNRELATED*: *Employment*: Medical College of Wisconsin*; *Grants/Grants Pending*: National Institutes of Health.* Jayashree Kalpathy-Cramer—*RELATED*: *Grant*: National Institutes of Health, *Comments*: National Institutes of Health/National Cancer Institute grants U24CA180927, U24CA180918, U01CA154601*; *UNRELATED*: *Consultancy*: INFOTECHsoft; *Grants/Grants Pending*: National Institutes of Health/National Science Foundation, *Comments*: R01EY019474-05 National Science Foundation.* Thomas L. Chenevert—*RELATED*: *Grant*: National Institutes of Health*; *UNRELATED*: *Grants/Grants Pending*: National Institutes of Health*; *Patents (Planned, Pending or Issued)*: University of Michigan*; *Royalties*: University of Michigan.* Benjamin Hoff—*RELATED*: *Grant*: National Institutes of Health, *Comments*: U01 CA085878.* Brian Ross—*RELATED*: *Grant*: National Institutes of Health, *Comments*: This was part of an National Institutes of Health grant to the University of Michigan.* Yue Cao—*RELATED*: *Grant*: National Institutes of Health.* Panagiotis Korfiatis—*RELATED*: *Grant*: National Cancer Institute, *Comments*: CA160045.* Bradley Erickson—*RELATED*: *Grant*: National Cancer Institute, *Comments*: CA160045.* C.C. Quarles—*RELATED*: *Grant*: National Cancer Institute.* Laura Bell—*RELATED*: *Grant*: National Institutes of Health/National Cancer Institute R01 CA158079.* Timothy Dondlinger—*RELATED*: *Grant*: National Institutes of Health*; *UNRELATED*: *Employment*: Imaging Biometrics LLC. P.E. Kinahan—*RELATED*: *Grant*: GE Healthcare, *Comments*: research grant*; *Other*: cofounder of PET/X LLX.* *Money paid to the Institution.

REFERENCES

1. Wen PY, Macdonald DR, Reardon DA, et al. **Updated response assessment criteria for high-grade gliomas: Response Assessment in Neuro-Oncology working group.** *J Clin Oncol* 2010;28:1963–72 CrossRef Medline
2. Brandsma D, van den Bent MJ. **Pseudoprogression and pseudoresponse in the treatment of gliomas.** *Curr Opin Neurol* 2009;22:633–38 CrossRef Medline
3. Wen PY, Norden AD, Drappatz J, et al. **Response assessment challenges in clinical trials of gliomas.** *Curr Oncol Rep* 2010;12:68–75 CrossRef Medline
4. Macdonald DR, Cascino TL, Schold SC Jr, et al. **Response criteria for phase II studies of supratentorial malignant glioma.** *J Clin Oncol* 1990;8:1277–80 CrossRef Medline
5. Vymazal J, Wong EY. **Response patterns of recurrent glioblastomas treated with tumor-treating fields.** *Semin Oncol* 2014;41(Suppl 6):S14–24 CrossRef Medline
6. Aquino D, Gioppo A, Finocchiaro G, et al., **MRI in glioma immunotherapy: evidence, pitfalls, and perspectives.** *J Immunol Res* 2017;2017:5813951 CrossRef Medline
7. Rosen BR, Belliveau JW, Vevea JM, et al. **Perfusion imaging with NMR contrast agents.** *Magn Reson Med* 1990;14:249–65 CrossRef Medline
8. Lee SJ, Kim JH, Kim YM, et al. **Perfusion MR imaging in gliomas: comparison with histologic tumor grade.** *Korean J Radiol* 2001;2:1–7 CrossRef Medline
9. Schmainda KM, Rand SD, Joseph AM, et al. **Characterization of a first-pass gradient-echo spin-echo method to predict brain tumor grade and angiogenesis.** *AJNR Am J Neuroradiol* 2004;25:1524–32 Medline
10. Law M, Oh S, Babb JS, et al. **Low-grade gliomas: dynamic susceptibility-weighted contrast-enhanced perfusion MR imaging: prediction of patient clinical response.** *Radiology* 2006;238:658–67 CrossRef Medline
11. Hu LS, Eschbacher JM, Heiserman JE, et al. **Reevaluating the imag-**

ing definition of tumor progression: perfusion MRI quantifies recurrent glioblastoma tumor fraction, pseudoprogression, and radiation necrosis to predict survival. *Neuro Oncol* 2012;14:919–30 CrossRef Medline
12. Prah MA, Al-Gizawiy MM, Mueller WM, et al. **Spatial discrimination of glioblastoma and treatment effect with histologically-validated perfusion and diffusion magnetic resonance imaging metrics.** *J Neurooncol* 2018;136:13–21 CrossRef Medline
13. Schmainda KM, Prah M, Connelly J, et al. **Dynamic-susceptibility contrast agent MRI measures of relative cerebral blood volume predict response to bevacizumab in recurrent high-grade glioma.** *Neuro Oncol* 2014;16:880–88 CrossRef Medline
14. Kickingereder P, Wiestler B, Burth S, et al. **Relative cerebral blood volume is a potential predictive imaging biomarker of bevacizumab efficacy in recurrent glioblastoma.** *Neuro Oncol* 2015;17:1139–47 CrossRef Medline
15. Harris RJ, Cloughesy TF, Hardy AJ, et al. **MRI perfusion measurements calculated using advanced deconvolution techniques predict survival in recurrent glioblastoma treated with bevacizumab.** *J Neurooncol* 2015;122:497–505 CrossRef Medline
16. Law M, Yang S, Wang H, et al. **Glioma grading: sensitivity, specificity and predictive values of perfusion MR imaging and proton MR spectroscopic imaging compared to conventional imaging.** *AJNR Am J Neuroradiol* 2003;24:1989–98 Medline
17. Law M, Young RJ, Babb JS, et al. **Gliomas: predicting time to progression or survival with cerebral blood volume measurements at dynamic susceptibility-weighted contrast-enhanced perfusion MR imaging.** *Radiology* 2008;247:490–98 CrossRef Medline
18. Saito T, Yamasaki F, Kajiwara Y, et al. **Role of perfusion-weighted imaging at 3T in the histopathological differentiation between astrocytic and oligodendroglial tumors.** *Eur J Radiol* 2012;81:1863–69 CrossRef Medline
19. Semmineh NB, Stokes AM, Bell LC, et al. **A population-based Digital Reference Object (DRO) for optimizing dynamic susceptibility contrast (DSC)-MRI methods for clinical trials.** *Tomography* 2017; 3:41–49 CrossRef Medline
20. Paulson ES, Schmainda KM**. Comparison of dynamic susceptibility-weighted contrast-enhanced MR methods: recommendations for measuring relative cerebral blood volume in brain tumors.** *Radiology* 2008;249:601–13 CrossRef Medline
21. Boxerman JL, Schmainda KM, Weisskoff RM. **Relative cerebral blood volume maps corrected for contrast agent extravasation significantly correlate with glioma tumor grade, whereas uncorrected maps do not.** *AJNR Am J Neuroradiol* 2006;27:859–67 Medline
22. Bedekar D, Jensen T, Rand S, et al. **Delta T1 method: an automatic post-contrast ROI selection technique for brain tumors**. In: *Proceedings of the Annual Meeting and Exhibition of the International Society for Magnetic Resonance in Medicine*, Stockholm, Sweden. May 1–7, 2010
23. Clark K, Vendt B, Smith K, et al. **The Cancer Imaging Archive (TCIA): maintaining and operating a public information repository.** *J Digit Imaging* 2013;26:1045–57 CrossRef Medline
24. Schmainda KM, Prah MA, Connelly JM, et al. **Glioma DSC-MRI perfusion data with standard imaging and ROIs.** The Cancer Imaging Archive. http://doi.org/10.7937/K9/TCIA.2016.5DI84Js8. Accessed July 27, 2016
25. Sugahara T, Korogi Y, Tomiguchi S, et al. **Posttherapeutic intraaxial brain tumor: the value of perfusion-sensitive contrast-enhanced MR imaging for differentiating tumor recurrence from nonneoplastic contrast-enhancing tissue.** *AJNR Am J Neuroradiol* 2000;21: 901–09 Medline
26. Lev MH, Ozsunar Y, Henson JW, et al. **Glial tumor grading and outcome prediction using dynamic spin-echo MR susceptibility mapping compared with conventional contrast-enhanced MR: confounding effect of elevated rCBV of oligodendrogliomas [corrected].** *AJNR Am J Neuroradiol* 2004;25:214–21 Medline
27. Hirai T, Murakami R, Nakamura H, et al. **Prognostic value of perfusion MR imaging of high-grade astrocytomas: long-term follow-up study.** *AJNR Am J Neuroradiol* 2008;29:1505–10 CrossRef Medline
28. Jiang Z, Le Bas JF, Grand S, et al. **Prognostic value of perfusion MR imaging in patients with oligodendroglioma: a survival study.** *J Neuroradiol* 2011;38:53–61 CrossRef Medline
29. Saraswathy S, Crawford FW, Lamborn KR, et al. **Evaluation of MR markers that predict survival in patients with newly diagnosed GBM prior to adjuvant therapy.** *J Neurooncol* 2009;91:69–81 CrossRef Medline
30. Kong DS, Kim ST, Kim EH, et al. **Diagnostic dilemma of pseudoprogression in the treatment of newly diagnosed glioblastomas: the role of assessing relative cerebral blood flow volume and oxygen-6-methylguanine-DNA methyltransferase promoter methylation status.** *AJNR Am J Neuroradiol* 2011;32:382–87 CrossRef Medline
31. Hu LS, Baxter LC, Smith KA, et al. **Relative cerebral blood volume values to differentiate high-grade glioma recurrence from posttreatment radiation effect: direct correlation between image-guided tissue histopathology and localized dynamic susceptibility-weighted contrast-enhanced perfusion MR imaging measurements.** *AJNR Am J Neuroradiol* 2009;30:552–58 CrossRef Medline
32. Orsingher L, Piccinini S, Crisi G. **Differences in dynamic susceptibility contrast MR perfusion maps generated by different methods implemented in commercial software.** *J Comput Assist Tomogr* 2014; 38:647–54 CrossRef Medline
33. Knutsson L, Larsson EM, Thilmann O, et al. **Calculation of cerebral perfusion parameters using regional arterial input functions identified by factor analysis.** *J Magn Reson Imaging* 2006;23:444–53 CrossRef Medline
34. Jafari-Khouzani K, Emblem KE, Kalpathy-Cramer J, et al. **Repeatability of cerebral perfusion using dynamic susceptibility contrast MRI in glioblastoma patients.** *Transl Oncol* 2015;8:137–46 CrossRef Medline
35. Perkio J, Aronen HJ, Kangasmäki A, et al. **Evaluation of four post-processing methods for determination of cerebral blood volume and mean transit time by dynamic susceptibility contrast imaging.** *Magn Reson Med* 2002;47:973–81 CrossRef Medline
36. Paulson ES, Prah DE, Schmainda KM. **Spiral Perfusion Imaging With Consecutive Echoes (SPICE) for the simultaneous mapping of DSC- and DCE-MRI parameters in brain tumor patients: theory and initial feasibility.** *Tomography* 2016;2:295–307 CrossRef Medline
37. Korfiatis P, Kline TL, Kelm ZS, et al. **Dynamic susceptibility contrast-MRI quantification software tool: development and evaluation.** *Tomography* 2016;2:448–56 CrossRef Medline
38. Kelm ZS, Korfiatis PD, Lingineni RK, et al. **Variability and accuracy of different software packages for dynamic susceptibility contrast magnetic resonance imaging for distinguishing glioblastoma progression from pseudoprogression.** *J Med Imaging (Bellingham)* 2015;2:026001 CrossRef Medline
39. Hu LS, Kelm Z, Korfiatis P, Dueck, et al. **Impact of software modeling on the accuracy of perfusion MRI in glioma.** *AJNR Am J Neuroradiol* 2015;36:2242–49 CrossRef Medline
40. Boxerman JL, Shiroishi MS, Ellingson BM, et al. **Dynamic susceptibility contrast MR imaging in glioma: review of current clinical practice.** *Magn Reson Imaging Clin N Am* 2016;24:649–70 CrossRef Medline
41. Leu K, Boxerman JL, Ellingson BM. **Effects of MRI protocol parameters, preload injection dose, fractionation strategies, and leakage correction algorithms on the fidelity of dynamic-susceptibility contrast MRI estimates of relative cerebral blood volume in gliomas.** *AJNR Am J Neuroradiol* 2017;38:478–84 CrossRef Medline
42. Havaei M, Davy A, Warde-Farley D, et al. **Brain tumor segmentation with deep neural networks.** *Med Image Anal* 2017;35:18–31 CrossRef Medline
43. Menze BH, Jakab A, Bauer S, et al. **The Multimodal Brain Tumor Image Segmentation Benchmark (BRATS).** *IEEE Trans Med Imaging* 2015;34:1993–2024 CrossRef Medline
44. Bjornerud A, Sorensen AG, Mouridsen K, et al. **T1- and T2*-dominant**

extravasation correction in DSC-MRI, Part I, theoretical considerations and implications for assessment of tumor hemodynamic properties. *J Cereb Blood Flow Metab* 2011;31:2041–53 CrossRef Medline

45. Weisskoff RM, Zuo CS, Boxerman JL, et al. **Simultaneous blood volume and permeability mapping using a single Gd-based contrast injection.** In: *Proceedings of the Annual Meeting and Exhibition of the Society of Magnetic Resonance in Medicine*, San Francisco, California. August 6–12, 1994
46. Liu HL, Wu YY, Yang WS, et al. **Is Weisskoff model valid for the correction of contrast agent extravasation with combined T1 and T2* effects in dynamic susceptibility contrast MRI?** *Med Phys* 2011; 38:802–09 CrossRef Medline
47. Bedekar D, Jensen T, Schmainda KM. **Standardization of relative cerebral blood volume (rCBV) image maps for ease of both inter- and intrapatient comparisons.** *Magn Reson Med* 2010;64:907–13 CrossRef Medline

Edge Contrast of the FLAIR Hyperintense Region Predicts Survival in Patients with High-Grade Gliomas following Treatment with Bevacizumab

N. Bahrami, D. Piccioni, R. Karunamuni, Y.-H. Chang, N. White, R. Delfanti, T.M. Seibert, J.A. Hattangadi-Gluth, A. Dale, N. Farid, and C.R. McDonald

ABSTRACT

BACKGROUND AND PURPOSE: Treatment with bevacizumab is standard of care for recurrent high-grade gliomas; however, monitoring response to treatment following bevacizumab remains a challenge. The purpose of this study was to determine whether quantifying the sharpness of the fluid-attenuated inversion recovery hyperintense border using a measure derived from texture analysis—edge contrast—improves the evaluation of response to bevacizumab in patients with high-grade gliomas.

MATERIALS AND METHODS: MRIs were evaluated in 33 patients with high-grade gliomas before and after the initiation of bevacizumab. Volumes of interest within the FLAIR hyperintense region were segmented. Edge contrast magnitude for each VOI was extracted using gradients of the 3D FLAIR images. Cox proportional hazards models were generated to determine the relationship between edge contrast and progression-free survival/overall survival using age and the extent of surgical resection as covariates.

RESULTS: After bevacizumab, lower edge contrast of the FLAIR hyperintense region was associated with poorer progression-free survival ($P = .009$) and overall survival ($P = .022$) among patients with high-grade gliomas. Kaplan-Meier curves revealed that edge contrast cutoff significantly stratified patients for both progression-free survival (log-rank $\chi^2 = 8.3$, $P = .003$) and overall survival (log-rank $\chi^2 = 5.5$, $P = .019$).

CONCLUSIONS: Texture analysis using edge contrast of the FLAIR hyperintense region may be an important predictive indicator in patients with high-grade gliomas following treatment with bevacizumab. Specifically, low FLAIR edge contrast may partially reflect areas of early tumor infiltration. This study adds to a growing body of literature proposing that quantifying features may be important for determining outcomes in patients with high-grade gliomas.

ABBREVIATIONS: EC = edge contrast; GBM = glioblastoma; GTR = gross total resection; HGG = high-grade glioma; MSRS = Maximally Selected Rank Statistics; OS = overall survival; PFS = progression-free survival; RANO = Response Assessment in Neuro-Oncology; STR = subtotal resection; VOL = volume

High-grade glioma (HGG) is among the most common primary brain tumors in adults and is associated with a poor prognosis.[1] Moreover, monitoring the efficacy of different therapeutic agents in patients with HGG remains a challenge. The Response Assessment in Neuro-Oncology (RANO) and the Macdonald criteria are the current standards for response assessment to therapy in patients with HGG and have been shown to correlate with overall survival (OS).[2-4] However, determining tumor response becomes particularly challenging following treatment with antiangiogenic agents such as bevacizumab, due to the tendency of these agents to decrease contrast enhancement and T2 fluid-attenuated inversion recovery hyperintensity in the absence of a true tumor response.[2,5-11] Recent data have demonstrated that the RANO criteria may lead to earlier detection of tumor progression following treatment with bevacizumab because they take into account nonenhancing tumor progression.[12-14] In a recent study, the RANO criteria were shown to be more sensitive to tumor progression than the Macdonald criteria with the detection of at least 35% of patients in an HGG cohort who had nonenhancing tumor

Received October 17, 2017; accepted after revision February 7, 2018.

From the Center for Multimodal Imaging and Genetics (N.B., N.W., C.R.M.), Department of Psychiatry (N.B., Y.-H.C., C.R.M.), Department of Radiology (N.B., N.W., R.D., A.D., N.F., C.R.M.), Multimodal Imaging Laboratory (N.B., N.W., A.D., C.R.M.), Department of Neurosciences (D.P., A.D., N.F.), and Department of Radiation Medicine (R.K., T.M.S., J.A.H.-G.), University of California, San Diego, La Jolla, California.

We acknowledge funding from National Institutes of Health grants R01NS065838 (C.R.M.), UL1TR000100 (J.A.H.-G.), and KL2TR00144 (J.A.H.-G.); American Cancer Society Award ACS-IRG 70-002 (J.A.H.-G.); and American Cancer Society RSG-15-229-01-CCE (C.R.M).

Please address correspondence to Naeim Bahrami, PhD, Center for Multimodal Imaging and Genetics, University of California, San Diego, 9452 Medical Center Dr, La Jolla, CA 92037: e-mail: nabahrami@ucsd.edu, naeim.bahrami@gmail.com; @Naeimbah

Indicates open access to non-subscribers at www.ajnr.org
Indicates article with supplemental on-line table.
Indicates article with supplemental on-line photos.
http://dx.doi.org/10.3174/ajnr.A5620

progression in T2 FLAIR regions.[14] Thus, the evaluation of T2 FLAIR changes may be critical to the detection of early tumor progression following treatment with antiangiogenic agents.

Despite a growing appreciation of the importance of abnormal findings on T2 FLAIR for evaluating tumor response and progression, these features are typically evaluated qualitatively.[14-16] This type of assessment relies on considerable reader expertise because T2 FLAIR changes can also reflect tumor growth or other processes that result in T2 prolongation, including radiation effects, edema, ischemic injury, infection, seizures, and postoperative gliosis. Given that subjectively differentiating such entities may be difficult or vary across experts, a quantitative assessment of T2 FLAIR abnormalities could aid in distinguishing early nonenhancing tumor progression from treatment-related changes.

Recent studies have shown that specific features of the FLAIR signal, including increased nodularity, blurring of tumor borders, and mass effect may improve the detection of tumor progression.[17-19] These studies and others have demonstrated that specific FLAIR phenotypes alone or in combination with other imaging features (eg, contrast enhancement, perfusion) are predictive of survival following treatment with bevacizumab.[12,20-22]

Nowosielski et al in 2014[20] found that "T2-circumscribed" tumors, characterized by a bulky appearance and sharp FLAIR borders, are associated with poorer survival, whereas Norden et al in 2008[10] suggested that a more infiltrative T2 FLAIR pattern may represent a more aggressive tumor. These studies suggest that sharpness of T2 FLAIR borders could have prognostic value following treatment with bevacizumab and provide a valuable biomarker of tumor progression. However, there appears to be discrepancy in the literature as to whether a "well-defined" versus "vague, ill-defined" FLAIR border indicates a poorer prognosis. Given the variability in terminology used in these qualitative studies and the ambiguous criteria for defining FLAIR borders, quantitative imaging metrics that are standardized across studies and independent of interrater and intrarater bias are needed to systematically address this question.

In this study, we used texture analysis to examine whether quantifying the sharpness of the FLAIR hyperintense border (ie, edge contrast [EC]) improves the evaluation of response to bevacizumab in patients with HGG. EC is a type of texture analysis that has been shown in previous studies to distinguish well-defined versus vague borders in grade II and III gliomas and has been validated against neuroradiologic reads.[23] On the basis of our previous work demonstrating that "ill-defined" FLAIR borders are associated with poorer survival in patients with grade II and III gliomas,[24] we hypothesized that patients with low EC (ie, vague borders) of the FLAIR hyperintense region will have poorer progression-free survival (PFS) and OS compared with patients with high EC (ie, sharp borders). We also hypothesized that EC will be a stronger predictor of PFS and OS than the volume of the FLAIR or contrast-enhancement region following treatment with bevacizumab.

MATERIALS AND METHODS

Patients

This retrospective study was approved by the institutional review board. From 2011 to 2015, sixty patients with HGGs were identified at our institution who had both pre- and postbevacizumab MRIs, including T1 pre- and postcontrast and 3D-FLAIR. Patients were excluded if they received bevacizumab for any other reason than recurrent tumor (eg, radiation necrosis), the baseline scan was >60 days before initiating bevacizumab therapy or the follow-up scan was >60 days after initiation of treatment, there were significant artifacts on imaging, or the imaging sequence was not available at 1 of the 2 time points (pre- and postbevacizumab). Thirty-three patients with HGGs met the inclusion criteria to form the final study cohort (On-line Table). Twenty-nine patients had glioblastomas (GBMs), 2 patients had anaplastic astrocytomas, and 2 patients had anaplastic oligodendrogliomas. The final cohort included 23 men and 10 women; the average age was 55 years with a range of 31–74 years. All patients had at least 1 operation before treatment with bevacizumab, with the most recent operation before the initiation of bevacizumab being a subtotal resection (STR, $n = 20$) or a gross total resection (GTR, $n = 13$). All patients received chemoradiation with temozolomide (alone or in combination with other agents) as the initial treatment. On recurrence, 15 patients received bevacizumab monotherapy, whereas 18 received bevacizumab in combination with other agents (carboplatin, irinotecan, lomustine [CCNU], temozolomide). No MRIs obtained within the first 60 days following the operation were included, to avoid immediate postsurgical effects such as hemorrhage. The patients included in this study represented a subset (33 of 40) of the patients reported in a previous publication that examined the utility of advanced diffusion imaging (ie, restriction spectrum imaging) for the evaluation of the response to bevacizumab.[25]

MR Imaging and Preprocessing

All the MR imaging scans were acquired on a 3T Signa Excite HDx scanner (GE Healthcare, Milwaukee, Wisconsin) using an 8-channel head coil. The imaging protocol included pre- and postgadolinium 3D volumetric T1-weighted inversion recovery echo-spoiled gradient-echo imaging with TE/TR = 2.8/6.5 ms, TI = 450 ms, flip angle = 8 °, FOV = 24 cm, voxel size = 0.93 × 0.93 × 1.2 mm; and a 3D T2-weighted FLAIR sequence with TE/TR = 126/6000 ms, TI = 863, FOV = 24 cm, voxel size = 0.93 × 0.93 × 1.2 mm.

Before analysis, raw data were corrected for bias field and distortion.[26] Then, correction for patient motion was performed using in-house software. The pre- and postcontrast 3D inversion recovery echo-spoiled gradient-echo and FLAIR images were registered to each other using rigid body registration at each of the 2 time points.

Volumes of Interest

Contrast-enhanced volumes (CE_{VOL}) and FLAIR hyperintense volumes ($FLAIR_{VOL}$) were segmented semiautomatically (Amira software package; Visage Imaging, San Diego, California) on the coregistered FLAIR and postcontrast 3D inversion recovery echo-spoiled gradient-echo images acquired both pre- and posttreatment, while regions of necrosis and the resection cavity were excluded. The final $FLAIR_{VOL}$ also excluded the CE_{VOL} to obtain an estimate of the nonenhancing lesion. All volumes of interest were drawn by 2 trained image analysts

(R.D. and N.F.) and approved by a board-certified neuroradiologist with expertise in neuro-oncology.[2]

Edge Contrast Calculation

The following postprocessing and image-enhancement steps were applied to the $FLAIR_{VOL}$ to extract the lesion surfaces and calculate the EC (On-line Figs 1 and 2, which present the flowchart for the EC extraction). We applied 3D analysis to the lesions to enhance the local precision and decrease the partial volume effect.[27-30]

Step 1) Morphologic operations of erosion and dilation were applied to the $FLAIR_{VOL}$ binary mask using the spheric 3D mask ($r = 3$) to remove the holes and small islands (On-line Fig 1*A*, -*B*).

Step 2) The contour of the $FLAIR_{VOL}$ binary mask was extracted in 3D, indexing the surface of the $FLAIR_{VOL}$ lesion.

Step 3) The gradients of the FLAIR image were calculated in 3D using the first derivative of the FLAIR image (On-line Fig 1*C*).

Step 4) The gradients of the $FLAIR_{VOL}$ from step 3 were overlaid on the surface of the 3D binary mask from step 2 to create the hyperintense surface with the initial EC (On-line Fig 1*D*). EC is defined as the gradient magnitude of the lesion edges.

Step 5) The initial EC was modified by removing the pixels with the highest 10% intensity to minimize the effect of edge magnitude arising from the CSF and skull (On-line Fig 1*E*, -*F*).

Step 6) Four EC parameters were calculated for each edge magnitude layer; $EC_{100\%}$ = average magnitude of all points on the edge, $EC_{75\%}$ = average magnitude of the lowest 75% of points, $EC_{50\%}$ = average magnitude of the lowest half of points, and $EC_{25\%}$ = average magnitude of the lowest 25% of points. This approach was selected to determine whether EC of the whole FLAIR border versus a subset of the FLAIR border with lower EC (ie, areas that could represent local tumor infiltration) predicts PFS/OS postbevacizumab. These 4 parameters were calculated on each scan (pre- and postbevacizumab) for each patient. The change in EC was defined as the change in EC parameters between the pre- and postbevacizumab scan.

Table 1: Summary of the imaging parameters pre- and postbevacizumab

Parameter	Prebevacizumab Mean (SD) × 10^3	Postbevacizumab Mean (SD) × 10^3	*P* Value (*T* Value)
$EC_{100\%}$	2.52 (0.57)	2.43 (0.57)	.256 (1.15)
$EC_{75\%}$	1.91 (0.53)	1.77 (0.47)	.281 (1.08)
$EC_{50\%}$	1.51 (0.48)	1.38 (0.40)	.277 (1.11)
$EC_{25\%}$	1.06 (0.38)	0.98 (0.30)	.184 (1.35)
$FLAIR_{VOL}$[a]	121.88 (70.68)	77.317 (38.55)	.002 (4.28)
CE_{VOL}[a]	24.90 (15.26)	9.16 (9.17)	<.001 (6.34)

[a] $P < .05$.

Progression-Free Survival and Overall Survival

PFS and OS were calculated for all patients from the date of initiation of bevacizumab to tumor progression or death, respectively. Tumor progression was verified by direct pathologic confirmation when available or evidence of progression based on MR imaging and neurologic status jointly determined by a board-certified neuroradiologist (N.F.) and board-certified neuro-oncologist (D.P.) using the RANO criteria.

Statistics

Paired *t* tests were conducted to compare EC, $FLAIR_{VOL}$, and CE_{VOL} parameters pre- and postbevacizumab. Multivariate Cox proportional hazards models that included age and the extent of the resection (ie, subtotal resection versus gross total resection) as covariates were used to determine the relationship between each EC measure, $FLAIR_{VOL}$, and CE_{VOL} postbevacizumab and the pre- and postchange in each of these measures with PFS/OS. Maximally Selected Rank Statistics (MSRS) were used to identify optimal cutoff points for EC that stratified patients according to PFS/OS. Kaplan-Meier survival analyses were conducted on the basis of the subgroups obtained from the MSRS split and compared using a log-rank test. In the case of no progression or death, the event time was censored at the date of last follow-up. In all cases, 2-tailed $P < .05$ was considered statistically significant.

RESULTS

Pre- to Postbevacizumab Changes in EC, $FLAIR_{VOL}$, and CE_{VOL}

At the group level, there were no significant differences between pre- and postbevacizumab EC parameters. However, inspection of individual subject data revealed that 37% of patients had a ≥10% decrease in $EC_{100\%}$ postbevacizumab, whereas 46% of patients had a ≥10% decrease in $EC_{75\%}$, $EC_{50\%}$, and $EC_{25\%}$. There was a significant decrease in both CE_{VOL} [$t(32) = 6.34$, $P < .001$] and $FLAIR_{VOL}$ [$t(32) = 4.28$, $P < .001$] at the group level (Table 1).

Table 2: Summary of the multivariate CPH models with age and surgical extent (subtotal, gross total resection) as covariates

Edge	Time	PFS *P* Value	PFS HR	PFS 95% CI	OS *P* Value	OS HR	OS 95% CI
$EC_{100\%}$	Postbevacizumab	.009[a]	0.37	0.18–0.78	.046[b]	0.42	0.18–0.98
$EC_{75\%}$	Postbevacizumab	.013[b]	0.33	0.13–0.79	.041[b]	0.34	0.12–0.96
$EC_{50\%}$	Postbevacizumab	.015[b]	0.29	0.10–0.78	.026[b]	0.25	0.07–0.85
$EC_{25\%}$	Postbevacizumab	.018[b]	0.21	0.05–0.77	.022[b]	0.16	0.03–0.77
$FLAIR_{VOL}$	Postbevacizumab	.872	1.000	1.000–1.000	.204	1.000	1.000–1.000
CE_{VOL}	Postbevacizumab	.758	1.000	1.000–1.000	.258	1.000	1.000–1.000
$\Delta EC_{100\%}$	Pre- and postbevacizumab	.018[b]	2.81	1.92–6.65	.033[b]	2.98	1.09–8.16
$\Delta EC_{75\%}$	Pre- and postbevacizumab	.039[b]	2.75	1.05–7.19	.050	3.06	0.99–9.39
$\Delta EC_{50\%}$	Pre- and postbevacizumab	.058	2.91	0.96–8.08	.054	3.54	0.97–12.88
$\Delta EC_{25\%}$	Pre- and postbevacizumab	.067	3.74	0.090–15.42	.056	4.76	0.95–23.64
$\Delta FLAIR_{VOL}$	Pre- and postbevacizumab	.360	1.000	1.000–1.000	.487	1.000	1.000–1.000
ΔCE_{VOL}	Pre- and postbevacizumab	.951	1.000	1.000–1.000	.926	1.000	1.000–1.000

Note:—CPH indicates Cox proportional hazards; HR, hazard ratio.

[a] $P < .01$.

[b] $P < .05$.

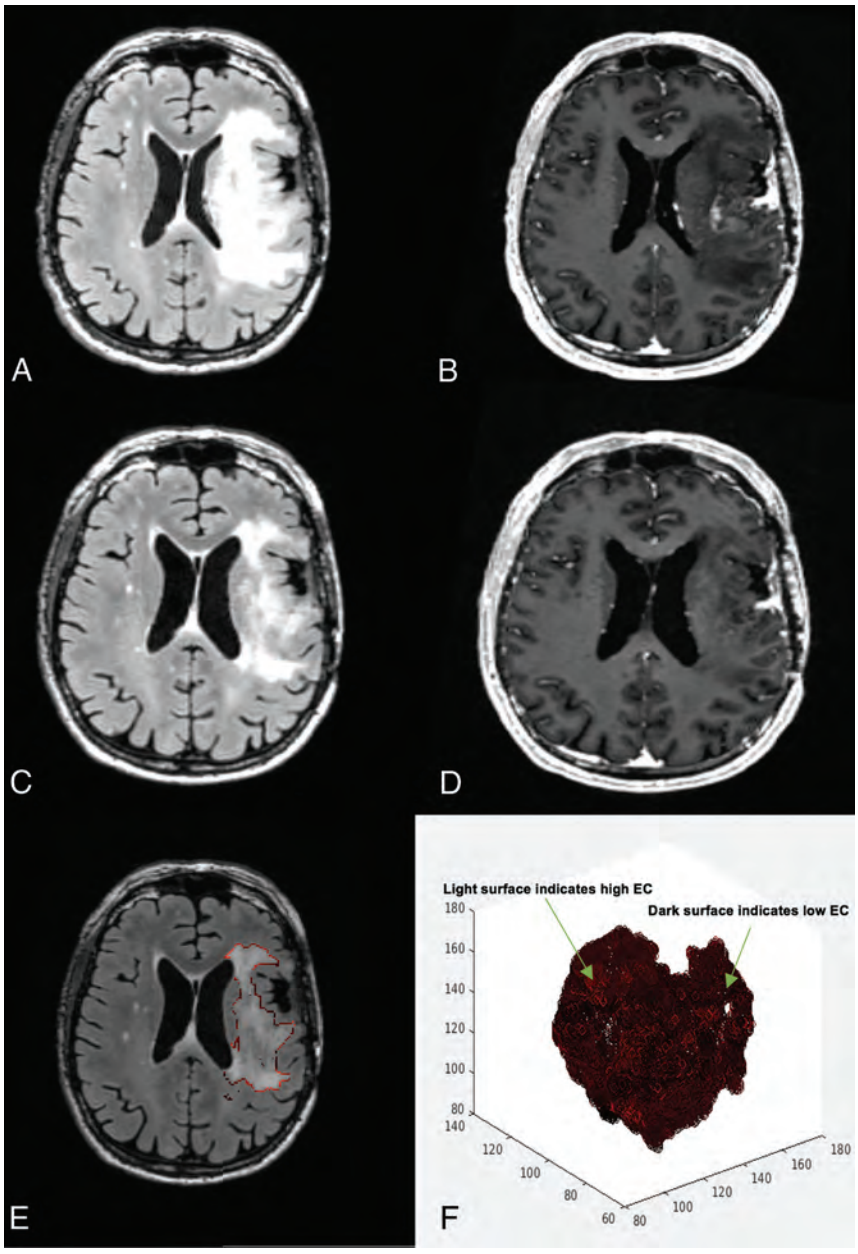

FIG 1. A 58-year-old man's MR imaging post-subtotal resection with low edge contrast. The patient had a poor survival estimation, with a PFS of 1.8 months and OS of 7.3 months. *A*, FLAIR prebevacizumab. *B*, T1 postcontrast prebevacizumab. *C*, FLAIR postbevacizumab. *D*, T1 postcontrast postbevacizumab. *E*, Overlay of the EC contour over the postbevacizumab FLAIR image. *F*, 3D presentation of the surface of the hyperintense region. Darker areas on the surface indicate lower EC/more indistinct border, whereas the lighter areas toward red show higher EC/more distinct border.

Seventy-six percent of patients showed a ≥50% decrease in CE_{VOL}, whereas an additional 6% of patients showed a decrease of 25%–50%. Thirty percent of the patients showed a corresponding decrease of ≥50% in $FLAIR_{VOL}$ surrounding the contrast-enhancement region, whereas an additional 18% showed a decrease of 25%–50% in $FLAIR_{VOL}$ following bevacizumab.

There were no significant associations between change in any of the EC parameters and change in $FLAIR_{VOL}$ or CE_{VOL} (all P values > .05). However, post hoc analysis revealed that 53% of patients with high postbevacizumab $EC_{100\%}$ ($EC_{100\%}$ > $median_{EC100\%}$ = 2117.62) had large decreases in CE_{VOL} (ΔCE_{VOL} > 71.2%) and 59% had large decreases in $FLAIR_{VOL}$ ($\Delta FLAIR_{VOL}$ > 32.3%). In addition, 38% and 50% of patients with low postbevacizumab $EC_{100\%}$ had large decreases in CE_{VOL} and $FLAIR_{VOL}$, respectively.

Survival Analysis

Median PFS following initiation of bevacizumab was 3.94 months (with 31 patients meeting the PFS end point), whereas the median OS following initiation of bevacizumab was 6.80 months (with 25 patients meeting the OS end point). Multivariate Cox proportional hazards models indicated that all EC thresholds postbevacizumab and $\Delta EC_{100\%}$ and $\Delta EC_{75\%}$ pre- to postbevacizumab were associated with poorer PFS, whereas all EC thresholds were associated with OS (Table 2). Post-$EC_{100\%}$ showed the highest association with PFS, whereas $\Delta EC_{75\%}$ showed the highest association with OS. However, the overlap in confidence intervals among the EC parameters suggests that they did not significantly differ from one another in their associations with PFS or OS. In both cases, lower EC values were associated with poorer survival. Pre- and postbevacizumab thresholds showed similar associations with PFS/OS in which $\Delta EC_{100\%}$ showed the highest association with PFS and $\Delta EC_{75\%}$ showed the highest association with OS. There were no associations between $FLAIR_{VOL}$ and CE_{VOL} with PFS/OS postbevacizumab or pre- and postbevacizumab. Figure 1 shows an example of a patient with low EC and poor PFS/OS, whereas Fig 2 shows an example of a patient with high EC and good PFS/OS.

MSRS was used to identify optimal cutoff points for post-EC values that stratified the patients according to PFS/OS. A post-$EC_{100\%}$ value of 2750.9 was determined to best stratify patients for PFS and OS. Kaplan-Meier survival curves revealed that the post-$EC_{100\%}$ cutoff significantly separated the groups for PFS [log-rank χ^2 (1) = 8.3, P = .003] (Fig 3*A*). Similarly, the post-$EC_{100\%}$ cutoff significantly stratified the groups for OS [log-rank χ^2 (1) = 5.5, P = .019]. Both analyses categorized 8 patients with better PFS/OS and 25 patients with poorer PFS/OS (Fig 3*B*). Given the small number of patients with better OS and PFS, a median split was also used to divide patients into more balanced groups. Similarly, the post-$EC_{100\%}$ cutoff significantly stratified groups for PFS and OS.

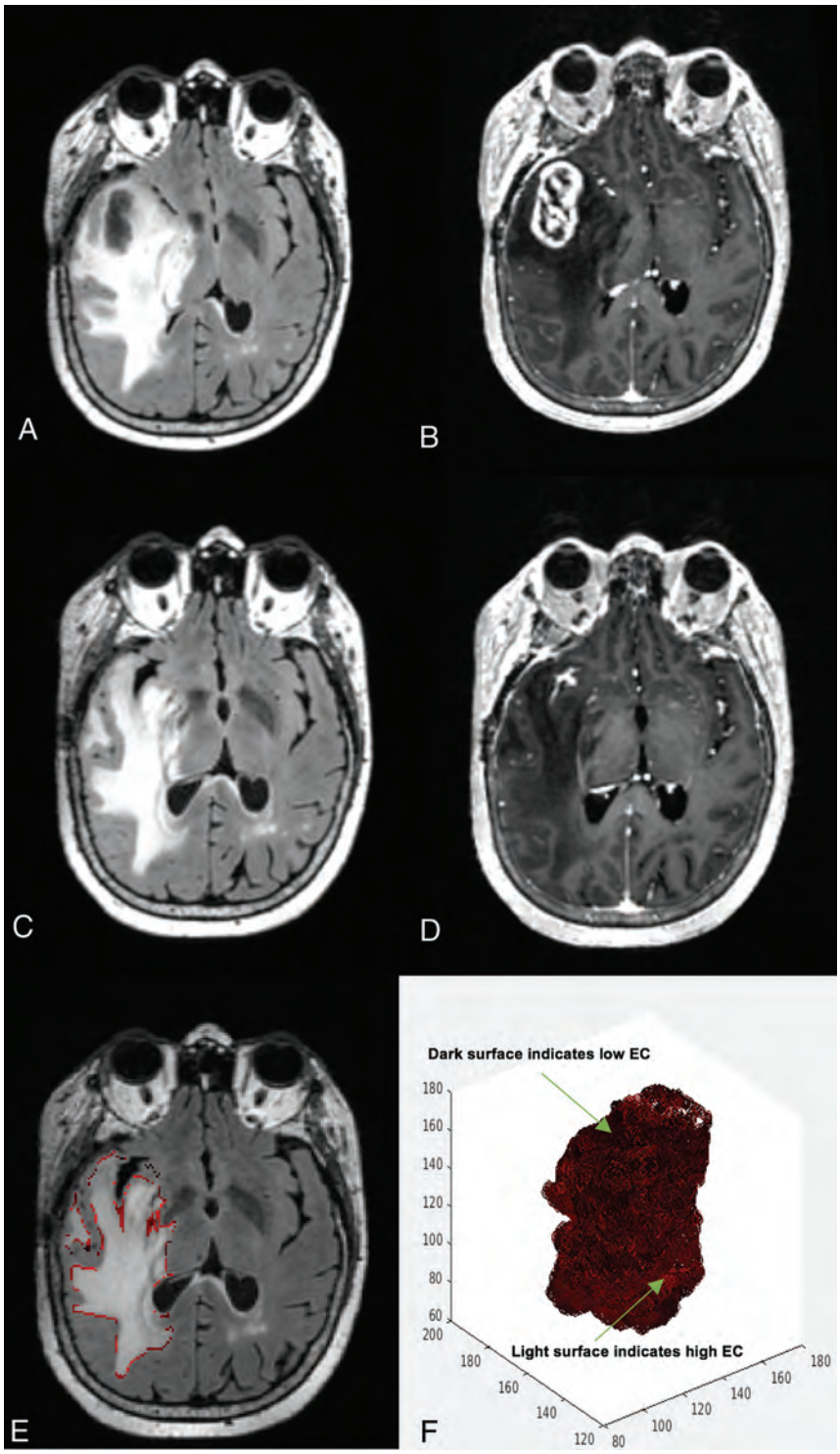

FIG 2. A 60-year-old woman's MR imaging post-subtotal resection with high edge contrast. The patient had a high survival estimation with PFS of 11.5 months and OS of 13.6 months. *A*, FLAIR prebevacizumab. *B*, T1 postcontrast prebevacizumab. *C*, FLAIR postbevacizumab. *D*, T1 postcontrast postbevacizumab. *E*, Overlay of the EC contour over the postbevacizumab FLAIR image. *F*, 3D presentation of the surface of the hyperintense region. Darker areas on the surface indicate lower EC and more indistinct border, whereas the lighter areas toward red show higher EC and more distinct border.

DISCUSSION

In this study, we introduce a new, quantitative imaging technique for characterizing the FLAIR border in patients with HGG and highlight a clinical scenario in which it may have prognostic value. We demonstrate that patients with vague, ill-defined FLAIR borders (low EC) have poorer PFS and OS compared with patients with sharper FLAIR borders (high EC). We also demonstrate that most patients with sharper EC postbevacizumab had a greater decrease in the volume of the contrast enhancement and FLAIR regions despite the lack of a direct association among these measures. However, EC was the only imaging measure associated with PFS/OS, and this association was robust to the EC threshold used. These findings are in line with previous research suggesting that neither FLAIR nor contrast-enhancement volumes are significant predictors of PFS/OS following bevacizumab.[25,31] Rather, quantitative estimates of FLAIR border patterns may have the potential to serve as a reliable biomarker for nonenhancing tumor progression in patients with HGG following treatment with bevacizumab.

In the current study, EC is a measure of the sharpness of the FLAIR hyperintense border and provides a quantitative measure that is not biased by inter- and intrarater variability. Although it is not clear what various EC levels of the FLAIR sharpness represent biologically, tumor infiltration following treatment with bevacizumab is one possible mechanism that reduces EC. Previous studies have shown that antiangiogenic therapy leads to the use of pre-existing cerebral blood vessels by tumor cells—a process known as vascular cooption—and consequently results in increased infiltrative growth. As a result, nonenhancing regions of FLAIR hyperintensity in patients with HGGs undergo a shift to an infiltrative pattern defined, in part, by a more ill-defined or vague FLAIR border.[10,32,33] The association between an "invasive" FLAIR border and infiltrative tumor growth[34] has been validated in histologic specimens of patients treated with bevacizumab.[32] However, the sharpness of the FLAIR border may also be partially unmasked by decreases in edema, despite the lack of an association between changes in EC and FLAIR volumes. Thus, it is possible that changes in both edema and tumor infiltration influenced our postbevacizumab EC measures. Nevertheless, we provide initial evidence that this FLAIR border pattern can be quantified on 3D imaging

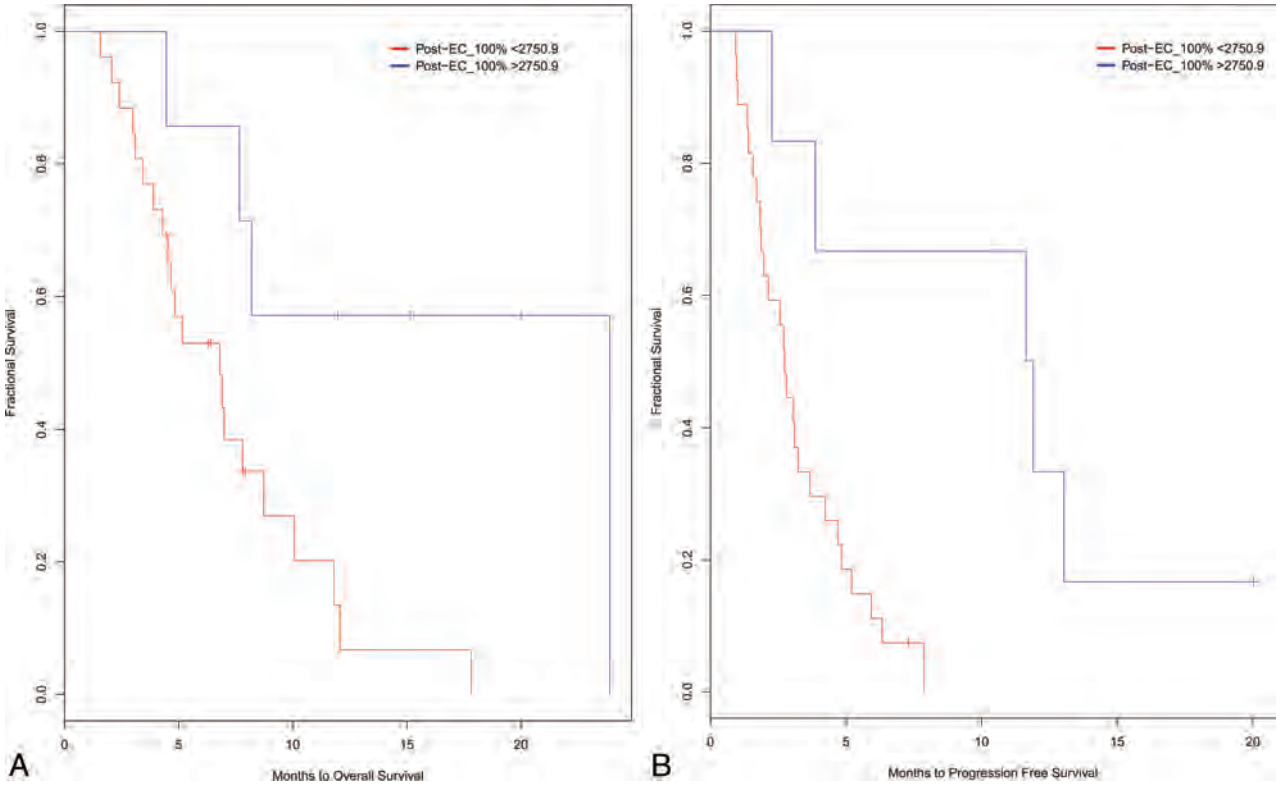

FIG 3. Stratification of patients based on MSRS analysis for splits in post-$EC_{100\%}$. Kaplan-Meier curves for high and low change groups for PFS (*A*) and OS (*B*).

and may serve as a valuable biomarker of early tumor progression, which may, in part, reflect infiltration in patients with HGGs.

In this study, we also demonstrate that the prognostic value of EC appears highly robust to the EC threshold used. Although different thresholds for EC showed slightly different associations with PFS and OS, the overlap in confidence intervals indicates that the differences among the thresholds are small and may not be clinically meaningful. EC robustness indicates that a global measure of FLAIR border sharpness may be just as sensitive as one that focuses on the "vaguest" regions of the border following treatment with bevacizumab. This is in line with previous studies that have shown that patterns of nonenhancing tumor progression are diffuse rather than focal following treatment with bevacizumab.[9] EC consistency pattern may not be present in other clinical scenarios or following treatment with other chemotherapeutic agents in which more focal regions of tumor growth have been identified and different EC levels may have different prognostic values.

This study is the first to use a 3D texture analysis technique to quantify the sharpness of the FLAIR hyperintense border and demonstrate an association with PFS and OS in patients with HGG treated with bevacizumab. This method of 3D edge extraction may increase the level of precision and the reliability of FLAIR border pattern assessment relative to visual ratings used in previous studies. Such a measure may be particularly useful in large-scale clinical trials of antiangiogenic treatments in which standardized, high-throughput image analysis methods are critical and expert readings may introduce systematic bias and be too labor-intensive. This measure may eventually serve as an adjunct to standard qualitative MR imaging interpretation, especially in settings in which neuro-oncology volume and expertise in nuanced neuroradiology interpretation may be lower.

There are some limitations to this study. First, our sample size was relatively small, and all patients were recruited from the same institution. Second, we included a heterogeneous group of patients with HGG (ie, grade III and GBM). Given recent evidence that molecular information (eg, *IDH* status) may be as important or more important for predicting OS than histopathologic diagnosis,[24] we included both groups. Unfortunately, we did not have molecular information on many patients (On-line Table). Although *IDH* status was available for 17 of our patients, only 3 patients had *IDH*-mutant status, precluding any meaningful analysis of these data. As a result, we were not able to determine how EC patterns relate to different molecular subtypes or how our imaging variables could be used in combination with molecular status to predict survival in patients with HGGs. These latter investigations are currently underway at our institution. Finally, the current resolution of MR imaging may be too low to adequately capture microscopic tumor infiltration in the brain. Although we propose that tumor infiltration is a likely reason for decreases in EC postbevacizumab, higher resolution MR imaging will help to increase the value of quantitative MR imaging metrics such as ours.

CONCLUSIONS

Our study introduces a quantitative measurement of FLAIR border patterns that may serve as a biomarker for detecting early nonenhancing tumor progression following treatment with bev-

acizumab in HGG. However, whether this measure has clinical utility following treatment with bevacizumab or other antiangiogenic agents will need to be established in further investigation with larger patient cohorts that are stratified according to molecular subtype and other important biologic and treatment-related variables.

ACKNOWLEDGMENTS

We thank the patients at the University of California, San Diego Moores Cancer Center Neuro-Oncology Program for their generous participation.

Disclosures: Naeim Bahrami—*RELATED*: *Grant*: American Cancer Society, *Comments*: RSG-15–229-01-CCE.* Tyler M. Seibert—*UNRELATED*: *Grants/Grants Pending*: Varian Medical Systems, *Comments*: coinvestigator on a grant to study MRI distortion effects on radiation treatment planning*; *Payment for Development of Educational Presentations*: WebMD, *Comments*: I received honoraria for educational materials for physicians, no sponsored promotions. Jona A. Hattangadi-Gluth—*UNRELATED*: *Grants/Grants Pending*: Varian Medical Systems, *Comments*: I have a research grant from Varian Medical Systems outside the scope and unrelated to the current work.* Anders Dale—*UNRELATED*: *Board Membership*: Human Longevity, CorTechs Labs, *Comments*: I serve as a member of Scientific Advisory Boards of Human Longevity and the CorTechs Labs. The terms of these arrangements have been reviewed by and approved by the University of California, San Diego, in accordance with its conflict of interest policies; *Employment*: Oslo University Hospital, *Comments*: appointed as Professor II (equal to an adjunct appointment within the University of California system). Annual compensation is NOK 131,963 Kr (approximately $16,595 annually at the current exchange rate). The terms of these arrangements have been reviewed by and approved by University of California, San Diego, in accordance with its conflict of interest policies; *Grants/Grants Pending*: GE Healthcare, *Comments*: I receive funding through research grants with GE Healthcare. The terms of these arrangements have been reviewed by and approved by University of California, San Diego, in accordance with its conflict of interest policies*; *Stock/Stock Options*: CorTechs Labs, *Comments*: I am a founder of and hold equity in CorTechs Labs. The terms of these arrangements have been reviewed by and approved by University of California, San Diego, in accordance with its conflict of interest policies. Carrie R. McDonald—*RELATED*: *Grant*: American Cancer Society, *Comments*: RSG-15–229-01-CCE.* *Money paid to the institution.

REFERENCES

1. Wen PY, Kesari S. **Malignant gliomas in adults.** *N Engl J Med* 2008; 359:492–507 CrossRef Medline
2. Wen PY, Macdonald DR, Reardon DA, et al. **Updated response assessment criteria for high-grade gliomas: Response Assessment in Neuro-Oncology working group.** *J Clin Oncol* 2010;28:1963–72 CrossRef Medline
3. Chinot OL, Macdonald DR, Abrey LE, et al. **Response assessment criteria for glioblastoma: practical adaptation and implementation in clinical trials of antiangiogenic therapy.** *Curr Neurol Neurosci Rep* 2013;13:347 CrossRef Medline
4. Macdonald DR, Cascino TL, Schold SC, et al. **Response criteria for phase II studies of supratentorial malignant glioma.** *J Clin Oncol* 1990;8:1277–80 CrossRef Medline
5. Galldiks N, Rapp M, Stoffels G, et al. **Response assessment of bevacizumab in patients with recurrent malignant glioma using [18F]fluoroethyl-L-tyrosine PET in comparison to MRI.** *Eur J Nucl Med Mol Imaging* 2013;40:22–33 CrossRef Medline
6. Kothari PD, White NS, Farid N, et al. **Longitudinal restriction spectrum imaging is resistant to pseudoresponse in patients with high-grade gliomas treated with bevacizumab.** *AJNR Am J Neuroradiol* 2013;34:1752–57 CrossRef Medline
7. Jeyaretna DS, Curry WT Jr, Batchelor TT, et al. **Exacerbation of cerebral radiation necrosis by bevacizumab.** *J Clin Oncol* 2011;29: e159–62 CrossRef Medline
8. Pope WB, Lai A, Nghiemphu P, et al. **MRI in patients with high-grade gliomas treated with bevacizumab and chemotherapy.** *Neurology* 2006;66:1258–60 CrossRef Medline
9. Pope WB, Xia Q, Paton VE, et al. **Patterns of progression in patients with recurrent glioblastoma treated with bevacizumab.** *Neurology* 2011;76:432–37 CrossRef Medline
10. Norden AD, Young GS, Setayesh K, et al. **Bevacizumab for recurrent malignant gliomas: efficacy, toxicity, and patterns of recurrence.** *Neurology* 2008;70:779–87 CrossRef Medline
11. Gonzalez J, Kumar AJ, Conrad CA, et al. **Effect of bevacizumab on radiation necrosis of the brain.** *Int J Radiat Oncol Biol Phys* 2007;67: 323–26 CrossRef Medline
12. Hattingen E, Jurcoane A, Daneshvar K, et al. **Quantitative T2 mapping of recurrent glioblastoma under bevacizumab improves monitoring for non-enhancing tumor progression and predicts overall survival.** *Neuro Oncol* 2013;15:1395–404 CrossRef Medline
13. Pope WB, Qiao XJ, Kim HJ, et al. **Apparent diffusion coefficient histogram analysis stratifies progression-free and overall survival in patients with recurrent GBM treated with bevacizumab: a multicenter study.** *J Neurooncol* 2012;108:491–98 CrossRef Medline
14. Huang RY, Rahman R, Ballman KV, et al. **The impact of T2 FLAIR evaluation per RANO criteria on response assessment of recurrent glioblastoma patients treated with bevacizumab.** *Clin Cancer Res* 2016;22:575–81 CrossRef Medline
15. Sathornsumetee S, Desjardins A, Vredenburgh JJ, et al. **Phase II trial of bevacizumab and erlotinib in patients with recurrent malignant glioma.** *Neuro Oncol* 2010;12:1300–10 CrossRef Medline
16. Quant EC, Norden AD, Drappatz J, et al. **Role of a second chemotherapy in recurrent malignant glioma patients who progress on bevacizumab.** *Neuro Oncol* 2009;11:550–55 CrossRef Medline
17. Drabycz S, Roldán G, de Robles P, et al. **An analysis of image texture, tumor location, and MGMT promoter methylation in glioblastoma using magnetic resonance imaging.** *Neuroimage* 2010;49:1398–405 CrossRef Medline
18. Carpentier A, McNichols RJ, Stafford RJ, et al. **Laser thermal therapy: real-time MRI-guided and computer-controlled procedures for metastatic brain tumors.** *Lasers Surg Med* 2011;43:943–50 CrossRef Medline
19. Kim JW, Park CK, Park SH, et al. **Relationship between radiological characteristics and combined 1p and 19q deletion in World Health Organization grade III oligodendroglial tumours.** *J Neurol Neurosurg Psychiatry* 2011;82:224–27 CrossRef Medline
20. Nowosielski M, Wiestler B, Goebel G, et al. **Progression types after antiangiogenic therapy are related to outcome in recurrent glioblastoma.** *Neurology* 2014;82:1684–92 CrossRef Medline
21. Taillibert S, Vincent LA, Granger B, et al. **Bevacizumab and irinotecan for recurrent oligodendroglial tumors.** *Neurology* 2009;72:1601–06 CrossRef Medline
22. Artzi M, Bokstein F, Blumenthal DT, et al. **Differentiation between vasogenic-edema versus tumor-infiltrative area in patients with glioblastoma during bevacizumab therapy: a longitudinal MRI study.** *Eur J Radiol* 2014;83:1250–56 CrossRef Medline
23. Kinoshita M, Sakai M, Arita H, et al. **Introduction of high throughput magnetic resonance T2-weighted image texture analysis for WHO grade 2 and 3 gliomas.** *PLoS One* 2016;11:e0164268 CrossRef Medline
24. Delfanti RL, Piccioni DE, Handwerker J, et al. **Imaging correlates for the 2016 update on WHO classification of grade II/III gliomas: implications for IDH, 1p/19q and ATRX status.** *J Neurooncol* 2017;135: 601–09 CrossRef Medline
25. McDonald CR, Delfanti RL, Krishnan AP, et al. **Restriction spectrum imaging predicts response to bevacizumab in patients with high-grade glioma.** *Neuro Oncol* 2016;18:1579–90 CrossRef Medline
26. Jovicich J, Czanner S, Greve D, et al. **Reliability in multi-site structural MRI studies: effects of gradient non-linearity correction on phantom and human data.** *Neuroimage* 2006;30:436–43 CrossRef Medline
27. Nachimuthu DS, Baladhandapani A. **Multidimensional texture characterization: on analysis for brain tumor tissues using MRS and MRI.** *J Digit Imaging* 2014;27:496–506 CrossRef Medline
28. Li X, Xia H, Zhou Z, et al. **3D texture analysis of hippocampus based on MR images in patients with Alzheimer disease and mild cogni-**

tive impairment. In: *Proceedings of the 3rd International Conference on Biomedical Engineering and Informatics,* Yantai, China. October 16–18, 2010;1:1–4
29. Suoranta S, Holli-Helenius K, Koskenkorva P, et al. **3D texture analysis reveals imperceptible MRI textural alterations in the thalamus and putamen in progressive myoclonic epilepsy type 1, EPM1.** *PLoS One* 2013;8:e69905 CrossRef Medline
30. Zhang J, Yu C, Jiang G, et al. **3D texture analysis on MRI images of Alzheimer's disease.** *Brain Imaging Behav* 2012;6:61–69 CrossRef Medline
31. Ellingson BM, Cloughesy TF, Lai A, et al. **Quantitative volumetric analysis of conventional MRI response in recurrent glioblastoma treated with bevacizumab.** *Neuro Oncol* 2011;13:401–09 CrossRef Medline
32. de Groot JF, Fuller G, Kumar AJ, et al. **Tumor invasion after treatment of glioblastoma with bevacizumab: radiographic and pathologic correlation in humans and mice.** *Neuro Oncol* 2010;12:233–42 CrossRef Medline
33. Narayana A, Kelly P, Golfinos J, et al. **Antiangiogenic therapy using bevacizumab in recurrent high-grade glioma: impact on local control and patient survival.** *J Neurosurg* 2009;110:173–80 CrossRef Medline
34. Claes A, Idema AJ, Wesseling P. **Diffuse glioma growth: a guerilla war.** *Acta Neuropathol* 2007;114:443–58 CrossRef Medline

Postcontrast T1 Mapping for Differential Diagnosis of Recurrence and Radionecrosis after Gamma Knife Radiosurgery for Brain Metastasis

B. Wang, Y. Zhang, B. Zhao, P. Zhao, M. Ge, M. Gao, F. Ding, S. Xu, and Y. Liu

ABSTRACT

BACKGROUND AND PURPOSE: The differential diagnosis of radionecrosis and tumor recurrence in brain metastases is challenging. We investigated the diagnostic efficiency of postcontrast T1 mapping in solving this problem.

MATERIALS AND METHODS: Between March 2016 and June 2017, fifty-six patients with brain metastases who underwent contrast-enhanced cerebral T1 mapping were recruited for this prospective study. The findings revealed new enhancement after gamma knife radiosurgery. The subjects were assigned to radionecrosis and recurrence groups based on follow-up (median, 11.5 months) and histopathologic results. T1 values of lesions 5 ($T1_{5min}$) and 60 ($T1_{60min}$) minutes after administration of contrast agent and their difference ($T1_{differ}$) were compared between the 2 groups with the 2-tailed Mann-Whitney *U* test. Receiver operating characteristic curves were used to determine the optimum cutoff values for differential diagnosis.

RESULTS: There were significant differences between the 2 groups in $T1_{5min}$, $T1_{60min}$, and $T1_{differ}$ values ($P = .012$, $P = .004$, and $P < .001$, respectively). Relative to $T1_{5min}$ and $T1_{60min}$, $T1_{differ}$ exhibited greater sensitivity and specificity ($P < .001$, respectively) in identifying radionecrosis. The optimum $T1_{differ}$ value for differential diagnosis was 71.1 ms (area under the curve = 0.97; 95% CI, 0.93–1.00), with sensitivity and specificity of 81.5% and 96.5%, respectively.

CONCLUSIONS: Postcontrast T1 mapping is optimal for the differential diagnosis of radionecrosis and tumor recurrence. Among T1 parameters, $T1_{differ}$ is the most powerful parameter for differential diagnosis. Advantages in terms of quantitative analysis and high resolution portend the wide use of postcontrast T1 mapping in the future.

ABBREVIATIONS: AUC = area under the curve; BM = brain metastases; GKR = gamma knife radiosurgery; rCBV = relative cerebral blood volume; $T1_{5min}$ = T1 values at 5 minutes after contrast administration; $T1_{60min}$ = T1 values at 60 minutes after contrast administration; $T1_{differ}$ = the difference between $T1_{60min} - T1_{5min}$

Brain metastases (BM) are the most common tumors of the central nervous system. The presence of metastatic disease in the CNS portends a poor prognosis and is a leading cause of morbidity and mortality.[1] Gamma knife radiosurgery (GKR) has become a popular treatment option for BM because it has good performance in local tumor control and results in improved quality of life and prolonged survival.[2,3] Despite these benefits, GKR is associated with a risk of deleterious effects on surrounding healthy tissue, which results in the so-called radiation damage.[4] Radionecrosis results from late-delayed radiation damage, which occurs 6 weeks to months after radiation treatment for BM.[5] MR imaging is considered a standard method of follow-up examination after GKR. However, conventional MR imaging findings pose a challenge for distinguishing radionecrosis and tumor recurrence.[6] Because management strategies for radionecrosis and tumor recurrence are completely different, it is crucial to improve the diagnostic accuracy of MR imaging to ensure further optimal treatment.[7]

Advanced MRI techniques are regarded as powerful tools for improving the diagnostic accuracy of radionecrosis and tumor recurrence.[8,9] Dynamic susceptibility-weighted contrast-enhanced perfusion MR imaging is the most common method of advanced

Received November 9, 2017; accepted after revision March 3, 2018.

From the School of Medicine (B.W.), and Shandong Medical Imaging Research Institute (Y.Z., B.Z.), Shandong University, Jinan, P.R. China; and Department of Neurosurgery (P.Z., M.Ge, M.Gao, F.D., S.X., Y.L.), Provincial Hospital Affiliated with Shandong University, Jinan, P.R. China.

We gratefully acknowledge the financial support of the National Natural Science Foundation of China (81641176), the Natural Science Foundation of Shandong Province (ZR2014HM069 and ZR2014ITM002), the Science and Technology Planning Project of Shandong Province (2015GSF118161, 2017CXGC1209, 2014GSF118046, and 2016GSF201092), The National Key Research and Development Program (2016YFC0106105). and the Taishan Scholars Program (No. tsqn20161070).

Please address correspondence to Yingchao Liu, MD, or Shangchen Xu, MD, Department of Neurosurgery, Provincial Hospital Affiliated with Shandong University, Jingwu Rd 324, Jinan, 250021 P.R. China; e-mail: Yingchao Liu, 13805311573@126.com, and Shangchen Xu, Shangchenxu@sina.com

Indicates open access to non-subscribers at www.ajnr.org

Indicates article with supplemental on-line tables.

http://dx.doi.org/10.3174/ajnr.A5643

imaging. However, previous studies have found that it was difficult to make a differential diagnosis between radionecrosis and tumor recurrence when the values of relative CBV (rCBV) are in the range of 1.4–2.1[10,11] and the range of uncertainty is even greater in practice, especially when one takes into account multiple institutions and variable analyses. In addition, DSC perfusion MR imaging is highly susceptible to hemosiderin deposition adjacent to vessels or fissures.[8,11] Dynamic contrast-enhanced perfusion imaging has become increasingly popular for this differential diagnosis.[12,13] It measures the changes in T1 relaxation associated with the disrupted blood-brain barrier following contrast administration. However, some degree of overlap between the 2 disease entities has been observed in most studies.[14] Moreover, dynamic contrast-enhanced perfusion also has the disadvantages of low imaging resolution and high sensitivity to susceptibility artifacts in comparison with routine MR images. Findings on the efficiency of apparent diffusion coefficient maps and fractional anisotropy values derived from diffusion tensor imaging are controversial[15,16] because of their low sensitivity and specificity in assessing the treatment response after GKR. MR spectroscopy has also been used in many studies; however, because of its low spatial resolution, signal-to-noise ratio, and reproducibility, this method is not considered a feasible tool for assessing the treatment response.[17,18] In addition, none of the abovementioned approaches simultaneously provide high resolution and quantitative assessment. It is therefore necessary to develop a quantitative method for improving the accuracy of the differential diagnosis after GKR.

Late gadolinium enhancement is a useful technique for detection of myocardial scarring.[19] Zach et al[20]reported that delayed-contrast MR imaging for calculating high-resolution treatment-response assessment maps could clearly differentiate tumor/nontumor tissue in patients with brain tumor. They suggested that the delayed enhancement was a result of damaged vessel lumens that are unable to provide efficient clearance of contrast from the tissues, resulting in delayed contrast accumulation.[21] Recent pathologic findings have also demonstrated the presence of gliosis and scarring in radionecrotic lesions.[22,23] Tumor recurrence is characterized by neovascularization and cell proliferation. The difference in vascularity and the extravascular, extracellular space in the 2 entities may result in the different contrast enhancement kinetics. Although profound, their work was based on a qualitative method, which may fare poorly in comparisons across patients and institutions. Therefore, we wanted to validate a quantitative method to differentiate radionecrosis from tumor recurrence on the basis of pathologic differences. The concentration of the contrast agent can influence T1 relaxation times of tissues. Fortunately, the T1 mapping—a MR imaging technique that enables quantitative evaluation of T1 relaxation times of tissues—would help reflect the pathologic differences in lesions. In this study, we explored the possibility and efficiency of postcontrast T1 mapping as a treatment response indicator after GKR for BM in primary clinical applications.

MATERIALS AND METHODS

Study Population

Written informed consent was obtained from all volunteers before commencement of the study and after receiving approval from the ethics committee of the Shandong Provincial Hospital. All experiments were performed in compliance with the Declaration of Helsinki.

Between March 2016 and June 2017, a total of 78 patients recruited from our hospital were evaluated by postcontrast T1 mapping. The inclusion criteria were as follows: 1) histopathologic diagnosis of primary cancer; 2) solitary brain metastases that met the criterion of Response Assessment in Neuro-Oncology–Brain Metastases on primary MR images; 3) treatment by only GKR; 4) newly enhanced lesions (lost enhancement and gained it back, or with enlarging enhancement) revealed inside the irradiated nidus after injection of contrast agent during follow-up MR imaging examination; and 5) a postirradiation period of >5 months. We excluded 22 patients for imaging quality (artifacts, low signal-to-noise ratio) and MR imaging contraindications. Finally, 56 patients (30 women; 26 men; median age, 59 years; age range, 31–80 years) were included in this study.

MR Imaging

All patients were imaged in the supine position with a 3T MR imaging machine (Magnetom Skyra; Siemens, Erlangen, Germany) using a transmit-receive quadrature 16-channel head-and-neck coil. The imaging protocol was the same for all patients. Dynamic susceptibility-weighted contrast-enhanced perfusion images were acquired after administration of 0.1 mmol per kg of body weight of Gd-DTPA, followed by a 20-mL saline flush with an injection velocity of 4.0 mL/s; these images were acquired during 50 scan phases. T1-mapping images were acquired 5 minutes after Gd-DTPA administration for a total scan time of 1 minute. Routine T1WI was performed after the first T1 mapping. Finally, with the same T1-mapping sequence as before, images were acquired 60 minutes after Gd-DTPA administration. A gamma knife rigid head frame, which was matched with the head coil, was fixed on the patient's head. The Brain Dot Engine technique (Siemens) was used for the registration. These measures could guarantee identical slice position and angulation when the patient was repositioned between the 5- and 60-minute time points. Slice positions for all imaging sequences were identical during the entire scan.

T1-Mapping Sequence

This volumetric multisection quantitative MR imaging pulse sequence, which combined the principles of T1-weighting and MR imaging, was used for a single acquisition. This sequence had 2 flip angles and thus generated 2 self-registered images per section, each with different levels of T1-weighting. These 2 acquired images were processed to generate quantitative MR imaging maps that portray T1 distribution. The technique was described previously.[24] To guarantee the accuracy of T1 values, we used actual flip angle imaging, which is a steady-state 3D echo-spoiled gradient echo B_1 mapping method based on a dual-repetition time (TR) acquisition ($TR_2 = N \times TR_1$, where N is typically an integer on the order of 5) for the bias correction in T1 mapping.[25] In addition, a water phantom scan was performed for the correction of the magnetic field and radiofrequency field before the MR imaging examination. Last, 2 ROIs, which were completely symmetric, were separately placed on both sides of normal-appearing white matter. If the T1 difference between these ROIs was <50

Table 1: Clinical characteristics of the study population[a]

Variables	Radionecrosis	Recurrence	Summary
Age (IQR) (yr)	58 (52.5–66)	59 (53–67)	58.5 (53–65.8)
Sex (M/F)	13:16	13:14	26:30
Primary tumor history			
Lung (No.) (%)	18 (62.0)	16 (59.3)	34 (60.7)
Digestive tract (No.) (%)	2 (6.9)	4 (14.8)	6 (10.6)
Breast (No.) (%)	4 (13.8)	4 (14.8)	8 (14.3)
Kidney (No.) (%)	2 (6.9)	2 (7.4)	4 (7.1)
Skin (No.) (%)	3 (10.3)	1 (3.7)	4 (7.1)
Location			
Occipital (No.) (%)	7 (24.1)	4 (14.8)	11 (19.6)
Parietal (No.) (%)	5 (17.2)	7 (25.9)	12 (21.4)
Frontal (No.) (%)	7 (24.1)	5 (18.5)	12 (21.4)
Temporal (No.) (%)	3 (10.3)	2 (7.4)	5 (18.5)
Cerebellum (No.) (%)	4 (13.8)	6 (22.2)	10 (37.0)
Brain stem (No.) (%)	1 (3.4)	1 (3.7)	2 (7.4)
Basal ganglia (No.) (%)	2 (6.9)	2 (7.4)	4 (14.8)
MD (median) (IQR) (cm)	2.2 (1.6–2.5)	2.5 (1.7–3.4)	2.3 (1.6–2.8)
Dose (median) (IQR) (Gy)	18 (18–21)	18 (18–21)	18 (18–21)
KPS (median) (IQR)	70 (70–90)	70 (60–90)	70 (70–90)

Note:—KPS indicates Karnofsky Performance Status Scale; MD, maximum diameters; IQR, interquartile range.
[a] Data are presented as descriptive statistics (median or count). Numbers in parentheses represent the range of data.

Table 2: Radiographic characteristics of the study population

Parameters	Radionecrosis	Tumor Recurrence	*P* Value
$T1_{5min}$ (median) (IQR) (ms)	914 (824–1055)	817 (567–924)	.012
$T1_{60min}$ (median) (IQR) (ms)	798 (682–920)	981 (774–1160)	.004
$T1_{differ}$ (median) (IQR) (ms)	−126 (−276 to −79)	214 (109–269)	<.001
rCBV (median) (IQR)	1.12 (0.86–1.35)	2.57 (2.15–3.13)	<.001

ms, we considered it qualified. Parameters for T1 mapping in the present study were as follows: FOV, 236 × 236 mm; slice thickness, 2.0 mm; 80 axial slices; TE, 2.46 ms; TR, 5.93 ms; voxel size, 0.6 × 0.6 × 2.0 mm; T1 estimate, 1000 ms; the first flip angle, 2°; the second flip angle, 14°; bandwidth, 814 Hz/px; and generalized autocalibrating partially parallel acquisition reconstruction, 1.

DSC Perfusion Sequence

The imaging parameters of DSC perfusion were as following: TR/TE, 1600/30 ms; bandwidth, 1748 Hz/pixel; 21 axial slices; FOV, 220 × 220 mm; voxel size, 1.8 × 1.8 × 4 mm^3; slice thickness, 4.0 mm; and flip angle, 90°.

Lesion Diagnosis

Although histopathologic confirmation is the criterion standard for differentiating radionecrosis and tumor recurrence of BM after GKR, it could be obtained in only a small group of patients with BM in our study. Radiographic and clinical assessments were the most common methods to identify them in our center. Patients' conditions and lesions were thereafter regularly evaluated by clinical manifestations and routine MR imaging every 3 months. We made a final diagnosis of radiation necrosis when a target lesion showed complete response, partial response, or stable disease, depending on the Response Assessment in Neuro-Oncology–Brain Metastases method, on subsequent follow-up MR images for a minimum of 6 months. If the lesion presented with progression on serial MR imaging and the patient's neurologic condition deteriorated progressively, we diagnosed tumor recurrence. Clinical assessments were performed by a neurosurgeon (15 years of experience), and radiographic assessments were performed by a neuroradiologist (20 years of experience). Divergence between clinical and radiographic assessment was resolved by stereotactic biopsy.

Data Processing and Quantitative Analysis

All imaging data were analyzed using commercial software for MR imaging data (syngo.via; Siemens). An ROI was drawn to cover only the area of enhancement inside the lesions on postcontrast T1-weighted images (in which the target lesions have the largest extent of enhancement). Then, these ROIs were separately copied into T1-mapping images acquired at 5 and 60 minutes after contrast administration. Thus, T1 values at 5 minutes ($T1_{5min}$) and 60 minutes ($T1_{60min}$) after contrast administration were acquired. Measurements of ROIs were performed 2 times for each patient's T1-mapping images, with an interval of 2 months between measurements. The average T1 value of each measurement was considered to represent the T1 value of the lesion. Then, the difference ($T1_{differ}$) between these 2 values ($T1_{60min} - T1_{5min}$) was calculated. To visually reflect the different components of mixed lesions, we created a $T1_{differ}$ map ($T1_{60min} - T1_{5min}$). ROIs were also copied into the CBV map. The average value represents the value of enhancement of the lesion (CBV_{lesion}). Another ROI with a similar area was drawn on contralateral normal-appearing white matter. The average value represents the value of normal-appearing white matter (CBV_{NAWM}): Mean rCBV = CBV_{lesion} / CBV_{NAWM}.

Statistical Analysis

Descriptive statistics (median and other measures) were determined for each parameter. Intergroup differences were tested for significance using the 2-tailed Mann-Whitney *U* test. The Wilcoxon paired test was used to determine the significance of differences between $T1_{5min}$ and $T1_{60min}$ in both groups. For statistical analysis of T1-value trends, a trend map was calculated to demonstrate the trends across time for the 2 different processes. Correlation between $T1_{differ}$ and rCBV was tested by the Spearman correlation analysis. Sensitivity was defined as the ratio of accurately diagnosed recurrent metastases to the total number of recurrent metastatic lesions, and specificity was defined as the ratio of accurately diagnosed radionecrosis to the total number of radionecrotic lesions. Receiver operating characteristic curve analysis was used to determine the optimum cutoff values for differential diagnosis of recurrence and radionecrosis. $P < .05$ was considered statistically significant. All calculations were performed using SPSS (Version 20; IBM, Armonk, New York).

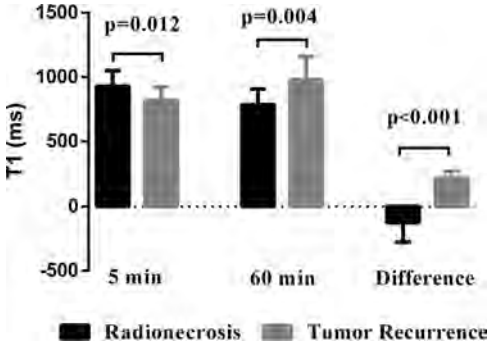

FIG 1. Comparison of TI_{5min}, TI_{60min}, and TI_{differ} between the radionecrosis and tumor recurrence groups. There were significant differences in each of the 3 parameters ($P = .012$, $P = .004$, and $P < .001$, respectively) between the 2 groups.

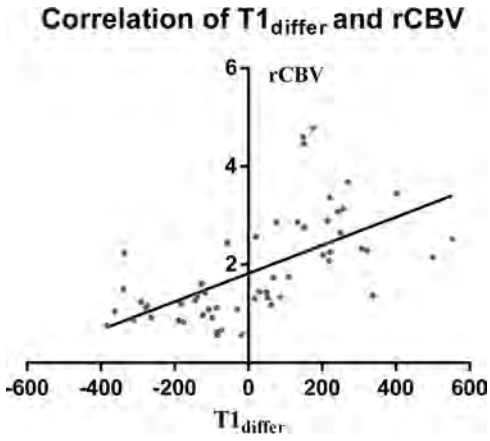

FIG 2. Correlation between TI_{differ} and rCBV. TI_{differ} significantly correlated with rCBV ($r = 0.70$; 95% CI, 0.53–0.82; $P < .001$).

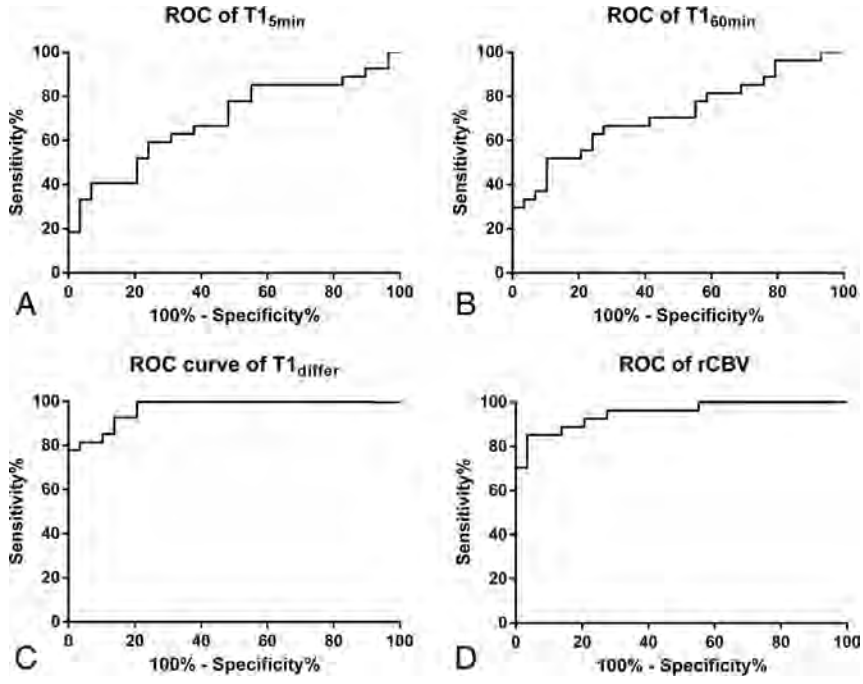

FIG 3. Receiver operating characteristic curves of TI_{5min} (*A*), TI_{60min} (*B*), TI_{differ} (*C*), and rCBV (*D*) for radionecrosis after stereotactic radiosurgery reveals that TI_{differ} has a similar diagnostic performance compared with rCBV (AUC = 0.97; 95% CI, 0.93–1.00 versus AUC = 0.95; 95% CI, 0.90–1.00).

RESULTS

Diagnostic Outcomes

The clinical characteristics of the study population are given in Table 1. None of the parameters were significantly different between the 2 groups. Eight (14.3%) patients were diagnosed with tumor recurrence, and 5 patients (8.9%) were diagnosed with radionecrosis based on histopathologic findings. Among the remaining lesions, 19 (33.9%) and 24 (42.9%), respectively, met the diagnostic criteria for tumor recurrence and radionecrosis. In total, 27 (48.2%) and 29 (51.8%) lesions were assigned to the tumor recurrence and radionecrosis groups, respectively.

Quantitative Assessment

Descriptive statistics for $T1_{5min}$, $T1_{60min}$, $T1_{differ}$, and rCBV of both groups are summarized in Table 2. All the parameters differed significantly between the 2 groups ($P = .012$, $P = .004$, $P < .001$, and $P < .001$, respectively; Fig 1). Significant differences were observed between $T1_{60min}$ and $T1_{5min}$ in both groups ($P < .001$, respectively). The radionecrosis group generally showed a decreasing trend in T1 values with time, while the recurrence group generally showed an increasing trend. $T1_{differ}$ significantly correlated with the rCBV value ($r = 0.70$; 95% CI, 0.53–0.82; $P < .001$, Fig 2).The detailed information of each patient is shown in On-line Tables 1 and 2.

Diagnostic Performance

All parameters of the T1 map had a potential to distinguish radionecrosis from tumor recurrence. The receiver operating characteristic curve analysis indicated that $T1_{differ}$ (area under the curve [AUC] = 0.97; 95% CI, 0.93–1.00) had a higher diagnostic performance for discriminating radionecrosis and tumor recurrence than $T1_{5min}$ (AUC = 0.69; 95% CI, 0.55–0.83) and $T1_{60min}$ (AUC = 0.72; 95% CI, 0.58–0.86; $P < .001$, respectively). However, $T1_{differ}$ did not perform significantly better than rCBV (AUC = 0.95; 95% CI, 0.90–1.00; $P = .274$, Fig 3). The optimum $T1_{differ}$ for the differential diagnosis was 71.1 ms, yielding an accuracy profile of the best sensitivity and specificity of 81.5% and 96.5%, respectively (likelihood ratio = 23.6). The optimum rCBV for the differential diagnosis was 1.74, yielding an accuracy profile of the best sensitivity and specificity of 85.1% and 96.5%, respectively (likelihood ratio = 24.7). The optimum $T1_{5min}$ and $T1_{60min}$ for differential diagnosis were 673.6 and1086.0 ms, respectively.

DISCUSSION

A high proportion of patients with BM have undergone GKR in the past 2 decades.[26] Assessment of enhanced lesions after GKR, which constitutes a diagnostic dilemma, is an urgent requirement in

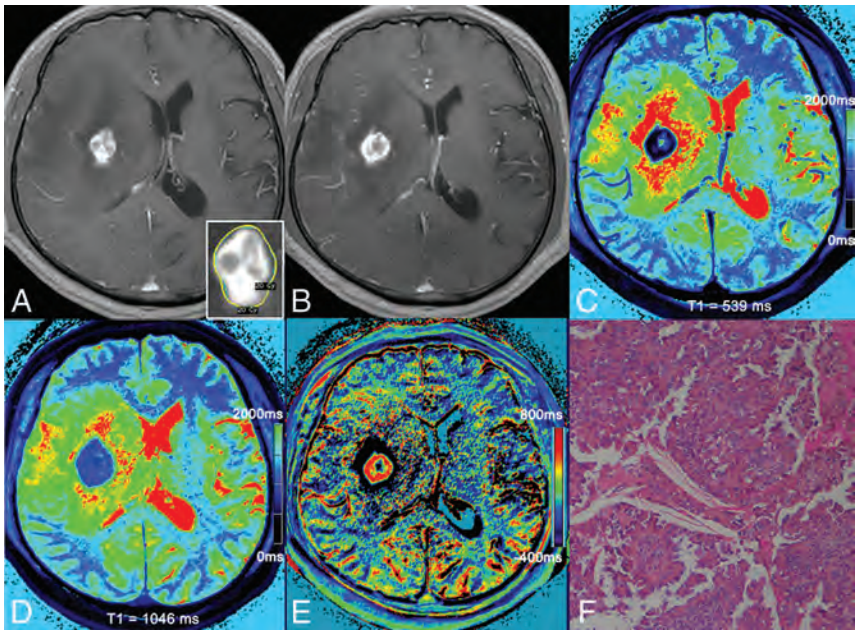

FIG 4. A 48-year-old male patient with cerebral metastasis from the lungs was treated with GKR (*A*). Follow-up MR imaging shows that enhancement returned at 5 months after GKR (*B*), while T1 mapping 5 minutes (*C*) and 60 minutes (*D*) after contrast administration reveals $T1_{5min}$ and $T1_{60min}$ values of 539 ms and 1064 ms, respectively, in the area of enhancement. The $T1_{differ}$ map revealed a positive area in the lesion (*E*). Histopathologic finings reveal lung cancer cells in the lesion (*F*).

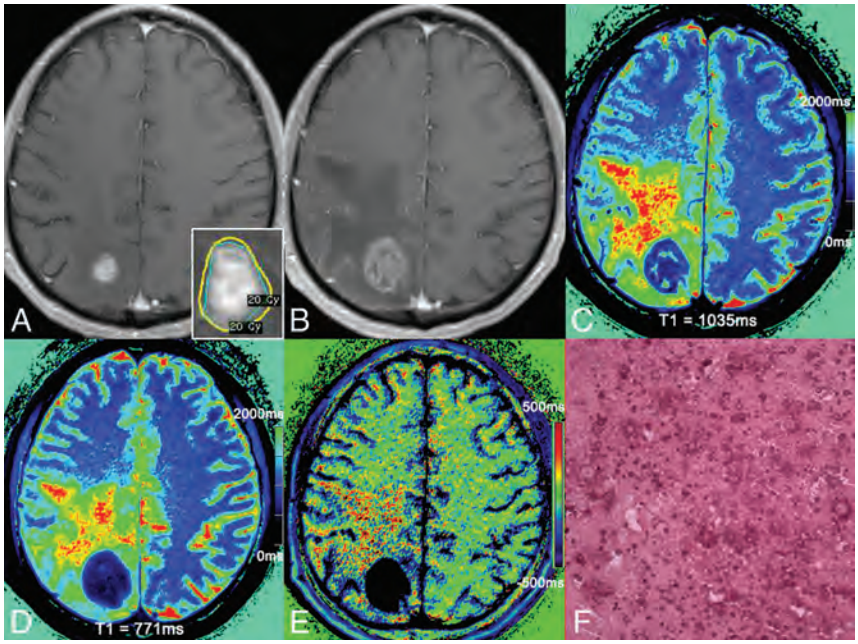

FIG 5. A 62-year-old female patient with brain metastasis from the breast was treated by GKR (*A*). Follow-up MR imaging shows a 210% increment in maximal diameter at 6 months after GKR (*B*). The results of T1 mapping at 5 minutes (*C*) and 60 minutes (*D*) after contrast administration reveal $T1_{5min}$ and $T1_{60min}$ values of 1035 and 771 ms, respectively, in the area of enhancement. The $T1_{differ}$ map reveals negative areas in the lesion (*E*). Histopathologic findings confirmed them as radionecrosis (*F*).

the management of BM.[4-6,27] In this study, with the help of a postcontrast T1 mapping technique, we present a new, high-resolution, quantitative method for resolving this issue.

Hemodynamic alteration in tumor recurrence is a consequence of a combination of intra- and extravascular aspects, including neoangiogenesis, vascular dilation, and the high permeability of morbid vessels inside tumors.[28,29] The common feature of vessel morphology in the tumor area is undamaged vessel lumens.[21] These combined pathophysiologic changes provide a basis for rapid contrast agent accumulation in the early period of contrast enhancement, resulting in an obvious decrease in T1 values. On the other hand, the compact structure of tumors prevents continuous accumulation of contrast agent, and more important, the undamaged vessel lumens contribute to the fast clearance of contrast agent in the late period,[30,31] resulting in an increase in T1 values compared with those in the early period. Therefore, the positive part within the irradiated area in the $T1_{differ}$ map represents the tumor recurrence. Figure 4 shows an example of T1 mapping of tumor recurrence.

Although enhancement of radionecroses also results from increased vascular permeability, there is an obvious difference in the hemodynamic alteration between radionecrosis and tumor recurrence. In contrast to the rapid contrast agent accumulation in tumor recurrence, transport of contrast agent in radionecrosis is a consequence of slow permeability.[32,33] In radionecrosis, vessels present with significantly damaged lumens.[21] In addition, large extravascular and extracellular spaces can be found within the entity.[22,23] These changes contribute to the continuous-but-slow accumulation of contrast agent.[19,22] In addition, the damaged vessel lumens and lack of neovascularization prevent rapid clearance of the contrast agent in the late period, resulting in a decrease in T1 values relative to those in the early period. Therefore, the negative part within the irradiated area in the $T1_{differ}$ map represents radionecrosis. Figure 5 shows an example of T1 mapping in radionecrosis.

Previous studies have focused on measuring changes in signal intensity using contrast-enhanced T1WI sequences.[27,34,35] Recently, Wagner et al[27] found that subtraction of signal intensity is efficient in the differential diagnosis between radionecrosis and tumor recurrence. In comparison with signal intensity, T1 mapping has the following advantages: First, the T1 value is a quantitative metric, which enables the intra- and interpatient comparison across different institutions. Second, quantitative $T1_{differ}$ mapping could better reflect the heterogeneity of enhanc-

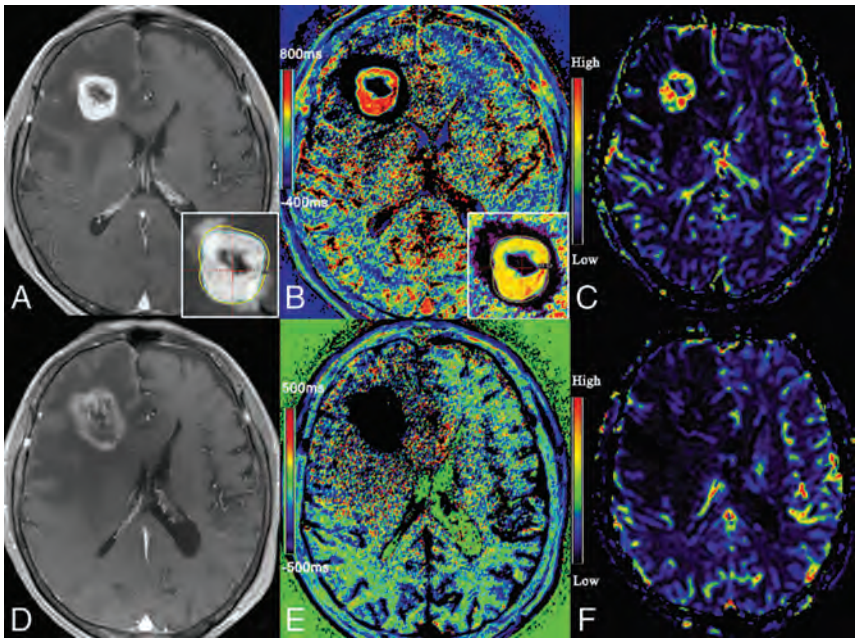

FIG 6. MR image of a 54-year-old female patient with cerebral metastasis from the digestive tract. Contrast-enhanced TI-weighted image shows enhancement in the previously irradiated lesion 6 months later, after the first GKR (*A*). The TI_{differ} map demonstrates it as a mixed lesion and detects the parts of tumor recurrence to guide the treatment plan (*B*). The recurrent part is confirmed by a cerebral blood volume map (*C*). Follow-up MR imaging (6 months after re-irradiation) shows a 90% increment in maximal diameter (*D*). The TI_{differ} map demonstrates it as radionecrosis (*E*). The radionecrosis is confirmed by a CBV map (*F*).

ing lesions (subvolume of lesions) in an objective approach. These advantages suggest that T1 mapping may be more practical in clinical diagnosis and treatment. However, whether subtraction of T1 mapping has a higher resolution than signal intensity remains uncertain. Furthermore, we made progress in the methodology, in which we used a gamma knife rigid head frame and Brain Dot Engine technique to guarantee identical slice position and angulation. Thus, the subtraction of T1 mapping could be precisely done at the voxel-to-voxel level.

Although the present results showed that $T1_{5min}$, $T1_{60min}$, and $T1_{differ}$ could help distinguish radionecrosis and tumor recurrence, we regard $T1_{differ}$ as a better parameter for the differential diagnosis. Theoretically, $T1_{differ}$ should be negative in radionecrosis and positive in recurrence. In the present study, 5 patients with radionecrosis and 2 with recurrence showed opposite tendencies. Nevertheless, the $T1_{differ}$ values were all within a reliable interval. The presence of an admixture of components in lesions might be responsible for this discrepancy. Thus, we conclude that the ratio of tumor recurrence to radionecrosis is the key point underlying this bias because these 2 opposite hemodynamic compartments may counteract each other to some extent. This is also an inherent pitfall accompanying other techniques for identifying tumor recurrence and radionecrosis.

Our results demonstrate that $T1_{differ}$ correlated with rCBV, and they had similar diagnostic performances. Even so, in comparison with DSC perfusion, T1 mapping has many advantages: First, T1 mapping is a quantitative imaging method. Second, quantitative $T1_{differ}$ mapping could better reflect the heterogeneity in enhancing lesions. Third, T1 mapping is less sensitive to susceptibility artifacts. Fourth, bolus injection with a high velocity is not necessary for T1 mapping. Thus, patients who are taking chemotherapeutic drugs may benefit because their vessels are too fragile to accept this velocity. Last, T1 mapping has a better coregistration with anatomic images, a great advantage in that $T1_{differ}$ could be used for the re-irradiation of recurrent BM in the gamma knife planning system. Figure 6 shows an example of a $T1_{differ}$ map guiding the precise treatment of recurrent tumor using a radiation-treatment-planning system. On the basis of these advantages, we strongly recommend T1 mapping being performed in the patients who could benefit from this technique.

Some limitations of this study should be addressed here. First, only 13 patients were diagnosed by histopathologic examination after GKR. For patients with a high probability of radionecrosis, this is an inherent dilemma in clinical treatment because the risk of possible complications of biopsy might outweigh the benefits of the histopathologic diagnosis. In addition, the long observation period justifies the diagnosis of the remaining lesions based on MR imaging data. Second, a limited number of patients were recruited in this study. However, the present study group was nearly homogeneous, and all data were acquired through a consistent MR imaging protocol.

CONCLUSIONS

Taking advantage of the postcontrast T1 mapping technique, we set up a new method for assessing the treatment response after GKR for BM. Our results show that radionecrosis and tumor recurrence exhibit different trends for T1 values after Gd-DTPA administration. Although $T1_{5min}$, $T1_{60min}$, and $T1_{differ}$ differ significantly between the 2 groups in the present study, $T1_{differ}$ is a better differential marker for radionecrosis and tumor recurrence. Despite some limitations of this study, we believe that the benefits of T1 mapping will promote its wide application and provide more concrete evidence for treatment of BM in the future.

Disclosures: Yingchao Liu—*RELATED*: *Grant*: National Natural Science Foundation of China (81641176), Natural Science Foundation of Shandong Province (ZR2014TM002), Science and Technology Planning Project of Shandong Province (2014GSF118046, 2015GSF118161, 2016GSF201092, and 2017CXGC1209), and Taishan Scholars Program (No. tsqn20161070). Shangchen Xu—*RELATED*: *Grant*: Natural Science Foundation of Shandong Province (ZR2014HM069).

REFERENCES

1. Patel TR, Knisely JP, Chiang VL. **Management of brain metastases: surgery, radiation, or both?** *Hematol Oncol Clin North Am* 2012;26:933–47 CrossRef Medline
2. Pinkham MB, Whitfield GA, Brada M. **New developments in intra-**

cranial stereotactic radiotherapy for metastases. *Clin Oncol (R Coll Radiol)* 2015;27:316–23 CrossRef Medline
3. Mahajan A, Ahmed S, McAleer MF, et al. **Post-operative stereotactic radiosurgery versus observation for completely resected brain metastases: a single-centre, randomised, controlled, phase 3 trial.** *Lancet Oncol* 2017;18:1040–48 CrossRef Medline
4. Curnes JT, Laster DW, Ball MR, et al. **MRI of radiation injury to the brain.** *AJR Am J Roentgenol* 1986;147:119–24 CrossRef Medline
5. Lyubimova N, Hopewell JW. **Experimental evidence to support the hypothesis that damage to vascular endothelium plays the primary role in the development of late radiation-induced CNS injury.** *Br J Radiol* 2004;77:488–92 CrossRef Medline
6. Stockham AL, Tievsky AL, Koyfman SA, et al. **Conventional MRI does not reliably distinguish radiation necrosis from tumor recurrence after stereotactic radiosurgery.** *J Neurooncol* 2012;109:149–58 CrossRef Medline
7. Brandsma D, Stalpers L, Taal W, et al. **Clinical features, mechanisms, and management of pseudoprogression in malignant gliomas.** *Lancet Oncol* 2008;9:453–61 CrossRef Medline
8. Verma N, Cowperthwaite MC, Burnett MG, et al. **Differentiating tumor recurrence from treatment necrosis: a review of neuro-oncologic imaging strategies.** *Neuro Oncol* 2013;15:515–34 CrossRef Medline
9. Dhermain FG, Hau P, Lanfermann H, et al. **Advanced MRI and PET imaging for assessment of treatment response in patients with gliomas.** *Lancet Neurol* 2010;9:906–20 CrossRef Medline
10. Barajas RF, Chang JS, Sneed PK, et al. **Distinguishing recurrent intra-axial metastatic tumor from radiation necrosis following gamma knife radiosurgery using dynamic susceptibility-weighted contrast-enhanced perfusion MR imaging.** *AJNR Am J Neuroradiol* 2009;30:367–72 Medline
11. Mitsuya K, Nakasu Y, Horiguchi S, et al. **Perfusion weighted magnetic resonance imaging to distinguish the recurrence of metastatic brain tumors from radiation necrosis after stereotactic radiosurgery.** *J Neurooncol* 2010;99:81–88 CrossRef Medline
12. Mills SJ, Soh C, O'Connor JP, et al. **Enhancing fraction in glioma and its relationship to the tumoral vascular microenvironment: a dynamic contrast-enhanced MR imaging study.** *AJNR Am J Neuroradiol* 2010;31:726–31 CrossRef Medline
13. Larsen VA, Simonsen HJ, Law I, et al. **Evaluation of dynamic contrast-enhanced T1-weighted perfusion MRI in the differentiation of tumor recurrence from radiation necrosis.** *Neuroradiology* 2013;55:361–69 CrossRef Medline
14. Koh MJ, Kim HS, Choi CG, et al. **Which is the best advanced MR imaging protocol for predicting recurrent metastatic brain tumor following gamma-knife radiosurgery: focused on perfusion method.** *Neuroradiology* 2015;57:367–76 CrossRef Medline
15. Fugo KR, Lawson MA, Lee BJ. **Ibotenic acid lesions reduce noradrenergic activation in ventromedial hypothalamus during hypoglycemia.** *Brain Res* 2006;1111:105–10 CrossRef Medline
16. Biousse V, Newman NJ, Hunter SB, et al. **Diffusion weighted imaging in radiation necrosis.** *J Neurol Neurosurg Psychiatry* 2003;74:382–84 CrossRef Medline
17. Weybright P, Sundgren PC, Maly P, et al. **Differentiation between brain tumor recurrence and radiation injury using MR spectroscopy.** *AJR Am J Roentgenol* 2005;185:1471–76 CrossRef Medline
18. Smith EA, Carlos RC, Junck LR, et al. **Developing a clinical decision model: MR spectroscopy to differentiate between recurrent tumor and radiation change in patients with new contrast-enhancing lesions.** *AJR Am J Roentgenol* 2009;192:W45–52 CrossRef Medline
19. Mahrholdt H. **Delayed enhancement cardiovascular magnetic resonance assessment of non-ischaemic cardiomyopathies.** *Eur Heart J* 2005;26:1461–74 CrossRef Medline
20. Zach L, Guez D, Last D, et al. **Delayed contrast extravasation MRI: a new paradigm in neuro-oncology.** *Neuro Oncol* 2015;17:457–65 CrossRef Medline
21. Zach L, Guez D, Last D, et al. **Delayed contrast extravasation MRI for depicting tumor and non-tumoral tissues in primary and metastatic brain tumors.** *PLoS One* 2012;7:e52008 CrossRef Medline
22. Wong CS, Van der Kogel AJ. **Mechanisms of radiation injury to the central nervous system: implications for neuroprotection.** *Mol Interv* 2004;4:273–84 CrossRef Medline
23. Chamberlain MC, Glantz MJ, Chalmers L, et al. **Early necrosis following concurrent Temodar and radiotherapy in patients with glioblastoma.** *J Neurooncol* 2007;82:81–83 CrossRef Medline
24. Wang HZ, Riederer SJ, Lee JN. **Optimizing the precision in T1 relaxation estimation using limited flip angles.** *Magn Reson Med* 1987;5:399–416 CrossRef Medline
25. Yarnykh VL. **Actual flip-angle imaging in the pulsed steady state: a method for rapid three-dimensional mapping of the transmitted radiofrequency field.** *Magn Reson Med* 2007;57:192–200 CrossRef Medline
26. Andrews DW, Scott CB, Sperduto PW, et al. **Whole brain radiation therapy with or without stereotactic radiosurgery boost for patients with one to three brain metastases: phase III results of the RTOG 9508 randomised trial.** *Lancet* 2004;363:1665–72 CrossRef Medline
27. Wagner S, Gufler H, Eichner G, et al. **Characterisation of lesions after stereotactic radiosurgery for brain metastases: impact of delayed contrast magnetic resonance imaging.** *Clin Oncol (R Coll Radiol)* 2017;29:143–50 CrossRef Medline
28. Aronen HJ, Gazit IE, Louis DN, et al. **Cerebral blood volume maps of gliomas: comparison with tumor grade and histologic findings.** *Radiology* 1994;191:41–51 CrossRef Medline
29. Cha S, Johnson G, Wadghiri YZ, et al. **Dynamic, contrast-enhanced perfusion MRI in mouse gliomas: correlation with histopathology.** *Magn Reson Med* 2003;49:848–55 CrossRef Medline
30. Hompland T, Gulliksrud K, Ellingsen C, et al. **Assessment of the interstitial fluid pressure of tumors by dynamic contrast-enhanced magnetic resonance imaging with contrast agents of different molecular weights.** *Acta Oncol* 2013;52:627–35 CrossRef Medline
31. Watling CJ, Lee DH, Macdonald DR, et al. **Corticosteroid-induced magnetic resonance imaging changes in patients with recurrent malignant glioma.** *J Clin Oncol* 1994;12:1886–89 CrossRef Medline
32. Lüdeman L, Grieger W, Wurm R, et al. **Glioma assessment using quantitative blood volume maps generated by T1-weighted dynamic contrast-enhanced magnetic resonance imaging: a receiver operating characteristic study.** *Acta Radiol* 2006;47:303–10 CrossRef Medline
33. Lüdeman L, Grieger W, Wurm R, et al. **Quantitative measurement of leakage volume and permeability in gliomas, meningiomas and brain metastases with dynamic contrast-enhanced MRI.** *Magn Reson Imaging* 2005;23:833–41 CrossRef Medline
34. Mathews VP, Caldemeyer KS, Ulmer JL, et al. **Effects of contrast dose, delayed imaging, and magnetization transfer saturation on gadolinium-enhanced MR imaging of brain lesions.** *J Magn Reson Imaging* 1997;7:14–22 CrossRef Medline
35. Schörner W, Laniado M, Niendorf HP, et al. **Time-dependent changes in image contrast in brain tumors after gadolinium-DTPA.** *AJNR Am J Neuroradiol* 1986;7:1013–20 Medline

Comparative Analysis of Diffusional Kurtosis Imaging, Diffusion Tensor Imaging, and Diffusion-Weighted Imaging in Grading and Assessing Cellular Proliferation of Meningiomas

L. Lin, R. Bhawana, Y. Xue, Q. Duan, R. Jiang, H. Chen, X. Chen, B. Sun, and H. Lin

ABSTRACT

BACKGROUND AND PURPOSE: An accurate evaluation of the World Health Organization grade and cellular proliferation is particularly important in meningiomas. Our aim was to prospectively evaluate and compare diffusional kurtosis imaging, DTI, and DWI metrics in determining the grade and cellular proliferation of meningiomas.

MATERIALS AND METHODS: Ninety-six consecutive patients with histopathologically confirmed meningiomas were included in this study. Mean kurtosis, radial kurtosis, axial kurtosis, fractional anisotropy, mean diffusivity, and ADC were semiautomatically obtained in the solid components of tumors. Each normalized diffusion value was compared between high-grade meningiomas and low-grade meningiomas using the Mann-Whitney *U* test. Receiver operating characteristic, multiple logistic regression, and Pearson correlation analysis were used for statistical evaluations.

RESULTS: Diffusional kurtosis imaging metrics (mean kurtosis, radial kurtosis, and axial kurtosis) were significantly higher in high-grade meningiomas than in low-grade meningiomas ($P \leq .001$). Mean diffusivity and ADC were significantly lower in high-grade meningiomas than in low-grade meningiomas ($P = .003$ and .002). Mean kurtosis had significantly greater area the under curve values than mean diffusivity and fractional anisotropy in differentiating high-grade meningiomas from low-grade meningiomas ($P = .038$ and .002). Mean kurtosis was the only variable that could be used to independently differentiate high-grade meningiomas and low-grade meningiomas ($P < .001$). Significant correlations were found between the Ki-67 labeling index and kurtosis metrics ($P < .001$), as well as for mean diffusivity and ADC ($P = .004$, and .007).

CONCLUSIONS: Compared with other diffusion metrics, mean kurtosis may serve as an optimal parameter for evaluating and predicting the meningioma grade. Moreover, diffusion metrics may potentially reflect cellular proliferation.

ABBREVIATIONS: AK = axial kurtosis; DKI = diffusional kurtosis imaging; FA = fractional anisotropy; FSPGR = fast-spoiled gradient recalled; HGM = high-grade meningioma; LGM = low-grade meningioma; MD = mean diffusivity; MK = mean kurtosis; PPV = positive predictive value; RK = radial kurtosis

Meningiomas are the most common type of intracranial brain tumors, accounting for approximately 30% of all primary brain neoplasms.[1] Pathologically, meningiomas are classified into 3 grades according to the World Health Organization.[2] The grading of meningiomas has a high clinical relevance for determining treatment strategy and evaluating prognosis. However, the patient's prognosis can not only be determined by the tumor grade but also depends on the proliferative activity of tumors.[3] Previous studies have documented that Ki-67 expression is an important biomarker of cellular proliferation.[4] Therefore, an evaluation of Ki-67 expression is also required in clinical practice for meningiomas.

At present, the presurgical diagnosis of meningiomas mainly relies on their radiologic features. However, it is difficult to distinguish low-grade (World Health Organization grade I) from high-grade (World Health Organization grade II or III) meningiomas. Heterogeneous enhancement, unclear tumor-brain interface, marked perilesional edema, and parenchymal or bone invasion may be indicative of high-grade meningiomas (HGMs).[5] However, no specific or reliable features of conventional MR imaging have been found to differentiate HGMs from low-grade meningiomas (LGMs).

Received November 15, 2017; accepted after revision February 24, 2018.

From the Departments of Radiology (L.L., R.B., Y.X., Q.D., R.J., B.S., H.L.) and Pathology (H.C.), Fujian Medical University Union Hospital, Fuzhou, Fujian, China; and Department of Radiology (X.C.), Fujian Cancer Hospital and Fujian Medical University Cancer Hospital, Fuzhou, Fujian, China.

This work was supported by grants from the Youth Scientific Research Project of Fujian Provincial Health and the Family Planning Commission, China (No.2017-2-24) and the Natural Science Foundation of Fujian Province, China (No.2015J01396).

Please address correspondence to Yunjing Xue, MD, Department of Radiology, Fujian Medical University Union Hospital, No. 29 Xinquan Rd, Fuzhou, Fujian 350001, P.R. China; e-mail: xueyunjing@126.com

Indicates open access to non-subscribers at www.ajnr.org
Indicates article with supplemental on-line tables.
Indicates article with supplemental on-line photo.

http://dx.doi.org/10.3174/ajnr.A5662

Diffusion MR imaging is a technique that can measure the degree of mobility of water molecules within biologic tissue. Conventional DWI and DTI can provide conventional diffusion metrics, such as ADC, fractional anisotropy (FA), and mean diffusivity (MD), but they are not sufficiently accurate in evaluating the meningioma grade and Ki-67 expression[3,6-10] because conventional DWI and DTI assume that water diffusion follows a Gaussian distribution. However, the complexity of normal and pathologic tissue leads to hindered diffusion of water molecules and, therefore, should follow a non-Gaussian distribution.[11,12] Diffusional kurtosis imaging (DKI) is an advanced non-Gaussian diffusion imaging technique that can more accurately characterize the complicated water diffusion in pathologic tissues and provide additional information about tumor heterogeneity by measuring the kurtosis metrics, including mean kurtosis (MK), axial kurtosis (AK), and radial kurtosis (RK).[13] In recent years, several studies have been conducted using DKI in the diagnosis and differential diagnosis of intracranial neoplasms, including glioma, metastasis, and lymphoma.[11,14-16] However, to our knowledge, the use of DKI in evaluating meningiomas was still lacking, and no comparison of DKI with DTI and DWI was reported. Because DKI, DTI, and DWI may reflect microstructural features of tumors, it should be valuable to explore and compare their roles in the grading of meningiomas. Thus, the aim of this study was to evaluate and compare the utility of diffusion metrics obtained from DKI (MK, AK, RK), DTI (FA, MD), and DWI (ADC) in grading meningiomas and to assess the correlations between diffusion metrics and the Ki-67 labeling index.

MATERIALS AND METHODS

Patients

Studies were performed abiding by the rules and guidelines of the Fujian Medical University Union Hospital committee on clinical investigations. Informed consent from all the patients was obtained following the protocol set by the local ethics committee of the hospital. From our institution, 102 patients with suspected meningioma on conventional MR imaging between August 2014 and October 2016 were consecutively enrolled in the study. Preoperative imaging, including DWI and DKI, was performed, and image data were prospectively analyzed. The inclusion criteria were as follows: 1) histopathologically confirmed as meningiomas, and 2) surgical resection performed within 10 days after the MR imaging examination. We applied the following exclusion criteria: patients with any previous relevant treatment history (including radiation therapy, chemotherapy, or an operation) and MR imaging data with motion artifacts. Histologic diagnoses and tumor grading were based on the 2016 World Health Organization Classification of Tumors of the Central Nervous System.[2] Three patients were excluded because of substantial motion artifacts, and 3 patients were excluded because their lesions were confirmed to be nonmeningiomas. Finally, 96 patients were included.

Data Acquisition

A 3T MR imaging scanner (Discovery 750 system; GE Healthcare, Milwaukee, Wisconsin) and an 8-channel receiver head coil were used to examine all the patients before the operation. Imaging data were acquired by 2 blinded neuroradiologists independently (with 6 and 17 years' experience).

All patients underwent conventional and contrast-enhanced MR imaging. MR imaging was performed using the following routine sequences: axial T1-weighted FLAIR images (TR/TE = 1750/23 ms, TI = 780 ms, NEX = 1, matrix = 320 × 320, FOV = 24 cm, slice thickness = 5 mm, spacing = 1.5 mm); axial T2-weighted FSE images (TR/TE = 6488/94 ms, NEX = 1.5, matrix = 512 × 512, FOV = 24 cm, slice thickness = 5 mm, spacing = 1.5 mm); axial T2-weighted FLAIR images (TR/TE = 8500/143 ms, TI = 2100 ms, flip angle = 111°, NEX = 1, matrix = 288 × 224, FOV = 24 cm, slice thickness = 5 mm, spacing = 1.5 mm); contrast-enhanced 3D axial T1-weighted fast-spoiled gradient recalled (FSPGR) images (TR/TE = 8.2/3.2ms, matrix = 256 × 256, slice thickness = 1 mm, FOV = 24 cm, TI = 450 ms, flip angle = 12°, 144 contiguous partitions). Postcontrast images were obtained after an intravenous contrast injection of 0.1 mmol/kg of gadopentetate dimeglumine (Magnevist; Bayer HealthCare Pharmaceuticals, Wayne, New Jersey).

DKI used a spin-echo EPI diffusion sequence for image acquisition (TR/TE = 6000/94 ms, NEX = 1, matrix = 128 × 128, number of sections = 48, sections thickness = 3 mm, spacing = 0 mm, FOV = 24 cm, B_0 = 3, *b* values = 1000 and 2000 s/mm, number of directions = 30 for each, acquisition time = 6 minutes 24 seconds).

A spin-echo EPI DWI sequence was also used. Parameters were as follows: TR/TE = 3000/70 ms, NEX = 4, matrix = 160 × 160, number of sections = 20, sections thickness = 5 mm, spacing = 1.5 mm, FOV = 24 cm, b=0 and 1000 s/mm^2, and acquisition time = 42 seconds.

All MR imaging was performed on the same slices paralleling the line combining the anterior/posterior commissure with the same range to cover the entire brain.

Image Processing

The DKI dataset was first corrected for eddy current distortion and simple head motion using the FMRIB Software Library (FSL; http://www.fmrib.ox.ac.uk/fsl) in reference to the B_0 images. All data were used to calculate the diffusion kurtosis (b=0, 1000, and 2000 s/mm^2) and diffusion tensor (b=0 and 1000 s/mm^2) simultaneously. The DKI and DTI data were processed by using the Diffusional Kurtosis Estimator (Version 2.5.1; Medical University of South Carolina, Charleston, South Carolina). DWI was acquired in 3 orthogonal directions and combined into a trace image, and ADC maps were generated automatically by the MR imaging system software. The diffusion metric maps were processed using ImageJ software (Version 1.50i; National Institutes of Health, Bethesda, Maryland).

Before we delineated the ROI, the image resolution and number of slices of enhanced T1 FSPGR, T2 FSE, and ADC maps were changed to match the DKI metric maps. Although the scan matrix, slice thickness, and spacing were different in enhanced T1 FSPGR, T2 FSE, DWI, and DKI, the image resolutions finally generated by the scanner were 256 × 256, 512 × 512, 256 × 256, and 256 × 256, respectively, due to interpolation. Thus, the image resolution of T2 FSE was first resized to 256 × 256, and the number slices of enhanced T1 FSPGR, T2 FSE, and ADC was changed to 48 without interpolation. All these protocols were finished in ImageJ, as shown in On-line Figure.

We performed a semiautomatic ROI-setting method, in line with our previous study.[17] Two neuroradiologists (with 7 and 10 years'

experience) blinded to the cases and unaware of the histopathologic diagnosis randomly reviewed and analyzed image data, and the average values of the 2 readers were collected as the final results. According to conventional MR images, especially contrast-enhanced T1-weighted images, ROIs over the solid tumor and contralateral normal-appearing white matter were semiautomatically delineated using the Wand Tool in ImageJ. Cystic components, necrosis, hemorrhage, and calcification were avoided while estimating the solid region of the tumor. Contralateral normal-appearing white matter was defined in the centrum semiovale in the hemisphere contralateral to the lesion in accordance with former studies.[7,10] If a tumor was located on the midline, the ROI for comparison was chosen in the centrum semiovale of both hemispheres, and the mean value was used. Afterward, the same ROIs were obtained from anatomic MR images for all parametric maps. Furthermore, the diffusion values in the solid components of tumors were normalized to the corresponding values in the contralateral normal-appearing white matter to reduce intersubject variation.

Pathology and Immunohistochemistry

The pathologic and immunohistochemical diagnoses of the meningiomas were determined by a neuropathologist (with 7 years' experience). In each case, the tumor proliferation index was estimated as the percentage of tumor cell nuclei labeled with the Ki-67 monoclonal antibody in formalin-fixed paraffin tissue sections. All cells with nuclear staining of any intensity were considered positive for Ki-67; areas with the highest density of positive tumor nuclei were selected for counting.

Statistical Analysis

Statistical analyses were performed with SPSS software (Version 19.0. IBM, Armonk, New York) and MedCalc for Windows (Version 11.4.2.0; MedCalc Software, Mariakerke, Belgium). The demographic data, radiologic features, and normalized diffusion metrics were compared between HGM and LGM with the χ^2 test for categoric variables, independent-sample *t* tests for normally distributed continuous variables, or the Mann-Whitney *U* test for other continuous variables. The receiver operating characteristic curve analyses were performed to determine the diagnostic efficiency of normalized diffusion parameters. The *Z*-test was applied to compare the differences in areas under the curve among all diffusion metrics. A stepwise multiple logistic regression analysis of all normalized diffusion metrics was also performed to find the most valuable metric for grading meningiomas. The associations between Ki-67 values and normalized diffusion metrics were calculated with the Pearson correlation analyses. The interobserver variability of measurements was assessed using an intraclass correlation coefficient. *P* values $< .05$ were considered significant for all the tests.

RESULTS

Patient Characteristics and Tumor Features on Conventional MR Imaging

Among all the patients, 84 (87.5%) had LGMs and 12 (12.5%) had HGMs, including atypical meningiomas ($n = 10$) and anaplastic meningiomas ($n = 2$). The subtypes of low-grade meningiomas included meningothelial meningiomas ($n = 18$), fibrous meningiomas ($n = 24$), transitional meningiomas ($n = 32$), psammomatous meningiomas ($n = 3$), angiomatous meningiomas ($n = 5$), microcystic meningiomas ($n = 2$), atypical meningiomas ($n = 10$), and anaplastic meningiomas ($n = 2$). Thirteen of 84 patients with LGMs (15.5%) and 2 of 12 patients with HGMs (16.6%) were men. Five HGMs (41.7%) and 13 LGMs (15.5%) demonstrated heterogeneous enhancement. Four HGMs (33.3%) and 7 LGMs (8.3%) showed unclear tumor-brain interface. Nine HGMs (75.0%) and 44 LGMs (52.4%) were observed with peritumoral edema. Three HGMs (25.0%) and 9 LGMs (10.7%) had bone invasion. No significant differences in sex, enhancement pattern, peritumoral edema, and bone invasion were found between HGMs and LGMs ($P = 1.0$, .075, .245, and .351, respectively). However, there were significant differences in the tumor-brain interface between the 2 groups ($P = .040$), and the ages of patients with HGMs (60.25 ± 14.88 years) were slightly older than those of patients with LGMs (52.37 ± 10.36 years) ($P = .022$). In addition, the median of maximum tumor size was 7.76 cm^2 in LGMs (range, 3.64∼15.33 cm^2) and 8.98 cm^2 in HGMs (range, 7.53∼14.55 cm^2). The median of maximum peritumoral edema area was 9.22 cm^2 in LGMs (range, 3.42∼19.6 cm^2) and 17.70 cm^2 in HGMs (range, 5.82∼ 22.23 cm^2). There were no statistically significant differences in maximum tumor size and peritumoral edema area between the 2 groups ($P = .306$ and .200, respectively).

Comparisons of the Normalized Diffusion Metrics between HGMs and LGMs

Figure 1 shows the manifestations of high-grade and low-grade meningiomas on conventional images and diffusion maps. Table 1, On-line Table 1, and Fig 2 show the quantitative comparison of differences in normalized diffusion parameters between the 2 meningioma groups. As shown in On-line Table 2, the intraclass correlation coefficients of diffusion metric values were between 0.801 and 0.993. DKI values, including MK, AK, and RK, were significantly higher in HGMs than in LGMs ($P \leq .001$ for all). Additionally, MD and ADC were significantly lower in HGMs than in LGMs ($P = .003$ and .002, respectively). However, FA did not show a significant difference between the 2 groups ($P = .938$).

Comparisons of the Diagnostic Efficiency of the Normalized Diffusion Metrics in Differentiating Tumor Grades

The normalized diffusion metrics were further used for the receiver operating characteristic curve analyses in differentiating meningioma grades (Table 2 and Fig 3). MK exhibited the maximal area under the curve for differentiating HGMs from LGMs. RK and AK had lower ones, followed by ADC and MD. The optimal cutoff value of MK was 0.99 with a sensitivity of 95.24%, a specificity of 66.67%, a negative predictive value of 95.2%, a positive predictive value of 66.7%, and a Youden index of 0.619 in the diagnosis. Moreover, the area under the curve of MK was significantly higher than that of MD and FA in differentiating LGMs and HGMs ($P < .038$ and $P = .002$, respectively). However, no significant difference between MK and ADC was found in terms of area under the curve ($P = .135$), and these results are shown in On-line Tables 3–5.

The multivariable stepwise logistic regression analysis showed that MK was the only variable that could be used to independently

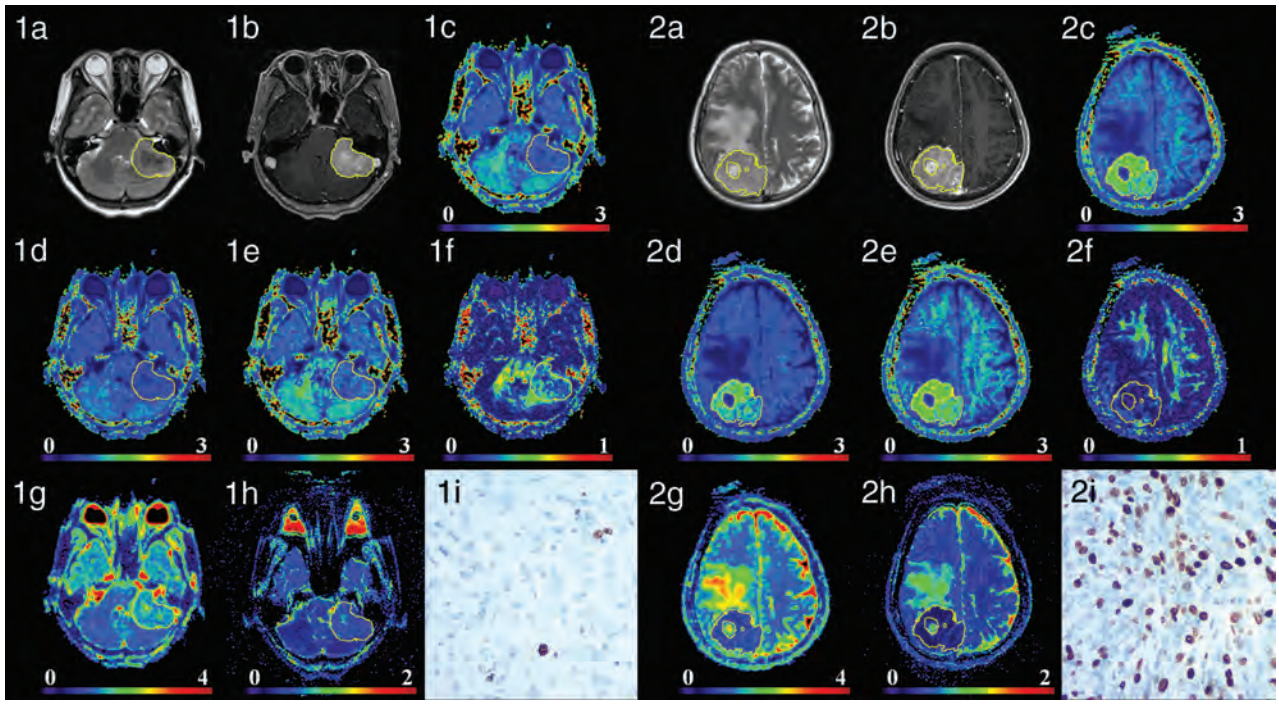

FIG 1. Two patients with low-grade transitional meningiomas in the anterior cranial fossa (*1a–1h*) and high-grade anaplastic meningiomas in the right cerebral convexity (*2a–2h*). Images *a–i* are T2WI, contrast-enhanced T1 FLAIR, MK, AK, RK, FA, MD, ADC, and Ki-67 (100×) images, respectively. For low-grade meningiomas, the intensity was low on MK, AK, and RK maps and high on MD and ADC maps. For high-grade meningiomas, the intensity was high on MK, AK, and RK maps and low on MD and ADC maps. MK, AK, and RK increased, while MD and ADC decreased as the tumor grade increased, whereas FA showed no obvious trend. The Ki-67 values of the 2 patients were 1% and 30%.

Table 1: Kurtosis and conventional diffusion metric values in the solid region of the tumor normalized by contralateral NAWM[a]

Lesion	MK	AK	RK	FA	MD	ADC
LGMs	0.85 (0.80∼0.92)	0.93 (0.84∼0.99)	0.82 (0.72∼0.90)	0.54 (0.41∼0.83)	1.18 (1.10∼1.30)	1.18 (1.08∼1.30)
HGMs	1.02 (0.91∼1.08)	1.08 (0.97∼1.16)	0.99 (0.87∼1.05)	0.59 (0.41∼0.74)	1.09 (0.97∼1.18)	1.03 (0.98∼1.15)
P value	<.001	.001	<.001	.938	.003	.002

Note:—NAWM indicates normal-appearing white matter.

[a] Data are medians, with interquartile ranges in parentheses.

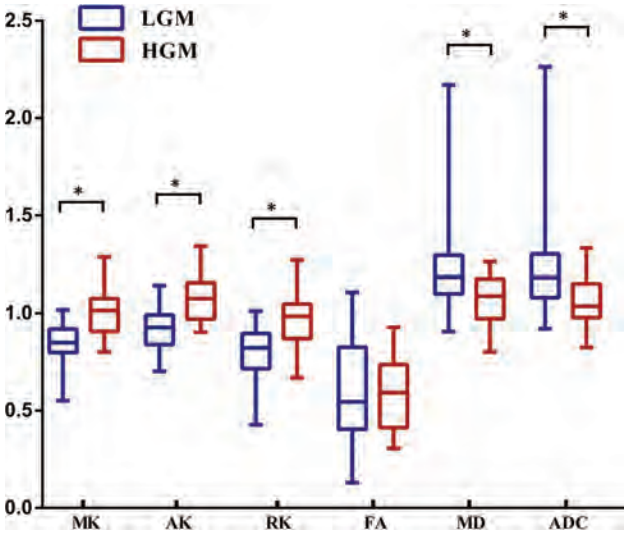

FIG 2. Comparisons of the normalized diffusion metrics between high- and low-grade meningiomas. Lower and upper hinges of boxes denote the 25th and 75th percentiles, respectively. Median (50th percentile) of each distribution is indicated by the line. Whiskers on either side extend to the most extreme data point. *Asterisk* indicates $P < .01$.

differentiate HGMs and LGMs (when MK increases every 0.1, odds ratio = 5.614; 95% confidence interval, 2.150–14.659; $P < .001$).

Correlation between Ki-67 and the Normalized Diffusion Metrics

The level of the proliferation index Ki-67 was available for 59 patients. The difference in Ki-67 between HGMs and LGMs was significant (12.27% ± 8.10% versus 2.61% ± 1.69%, $P < .001$). Significant correlations were found between Ki-67 and the kurtosis metrics (MK: $r = 0.639$, $P < .001$; AK: $r = 0.617$, $P < .001$; RK: $r = 0.597$, $P < .001$), as well as for MD ($r = -0.369$, $P = .004$) and ADC ($r = -0.365$, $P = .007$). Corresponding scatter diagrams are shown in Fig 4. The correlation coefficient was maximal for MK and AK, and RK had a lower one, followed by MD and ADC.

DISCUSSION

An accurate evaluation of the World Health Organization grade and cellular proliferation is particularly important in meningiomas. In this research, our results demonstrated that DKI, DTI, and DWI enabled the differentiation of low-grade from high-grade meningiomas. However, MK obtained from DKI had a

Table 2: ROC results of all normalized diffusion metrics for differentiating low- from high-grade meningiomas

Metrics	AUC	Cutoff	Sensitivity	Specificity	Youden	PPV	NPV
MK	0.842	0.99	95.24	66.67	61.91	95.2	66.7
AK	0.830	0.965	66.67	83.33	50.00	96.6	26.3
RK	0.817	0.981	97.62	58.33	55.95	94.3	77.8
FA	0.493	0.743	33.33	83.33	16.66	93.3	15.2
MD	0.769	1.114	71.43	75.00	46.43	95.2	27.3
ADC	0.781	1.045	89.29	58.33	47.62	93.7	43.8

Note:—AUC indicates area under the curve; Cutoff, cutoff value; Youden, Youden index; ROC, receiver operating characteristic; PPV, positive predictive value; NPV, negative predictive value.

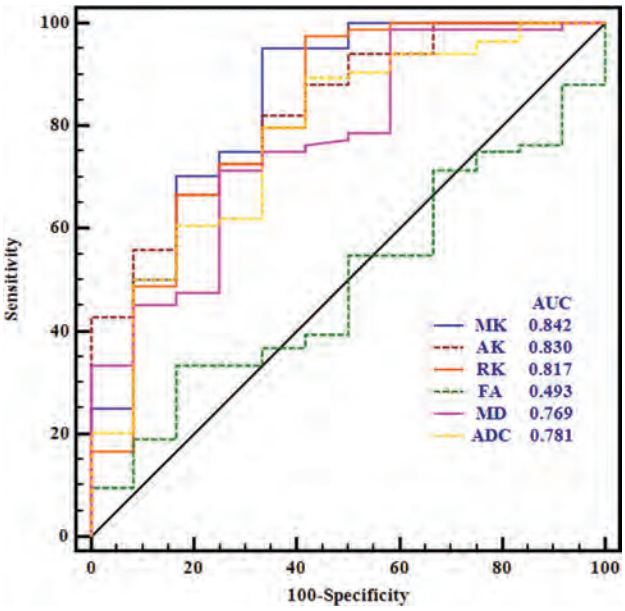

FIG 3. Receiver operating characteristic curves for all normalized diffusion metrics in distinguishing high- from low-grade meningiomas.

greater diagnostic value than DTI metrics in grading meningiomas. MK was the strongest independent predictor associated with the grade of meningioma. In addition, significant correlations were revealed between Ki-67 and the kurtosis metrics, MD and ADC.

There were controversial reports about the value of conventional diffusion imaging in grading meningiomas. Although some studies reported that DTI and DWI can help differentiate malignant from benign meningiomas,[12,18-20] others suggested that conventional diffusion imaging was not indicative of malignancy grade.[8,21] In this research, MD and ADC metrics were found effective in the differentiation of HGMs from LGMs, while no significant difference in FA was observed, in line with some previous studies.[18,22,23] The discrepancies between these studies and our own may be due to the differences in case sizes and inclusion subtypes. In addition, conventional measures of anisotropy using diffusion imaging ignored the interaction between orientation coherence and voxel size, which may cause a strong bias. Recent research indicated that the grade of meningiomas may be better assessed with microscopic anisotropy and microscopic FA.[24] However, the controversial reports of DTI and DWI may also infer that the reliability of conventional diffusion imaging for grading meningiomas should be explored in a further study. On the contrary, the results of our current study showed that DKI metrics were significantly higher in HGMs than in LGMs; these findings were consistent with those of a previous study.[25] Pathologically, HGMs were characterized by increased mitotic activity, necrosis, nuclear atypia, and small cells with increased intracellular complex protein molecules and nucleus-to-cytoplasm ratio.[8,26] As an advanced diffusion imaging sequence, DKI can provide additional kurtosis information, which might characterize the heterogeneity of the microenvironment.[16] The increase of kurtosis in HGMs probably reflects a higher degree of microstructural complexity within the tumor.

By performing receiver operating characteristic curve analyses, we found that MK obtained from DKI had a significantly better diagnostic performance than MD and FA derived from DTI. Furthermore, multiple logistic regression analyses revealed that MK was the most significant parameter for grading meningiomas. This is because the diffusion of water molecules in vivo always follows a non-Gaussian distribution. DKI can characterize non-Gaussian water diffusion, while conventional diffusion imaging techniques only assume a Gaussian distribution. Thus, DTI might not be accurate enough to characterize the heterogeneity of tumors. On the contrary, kurtosis is more accurate and sensitive for the detection of microstructural changes,[23] and MK can indicate microstructural complexity in tumor tissue.[11] Hence, MK may serve as a more appropriate diffusion metric for assessing and predicting the grade of meningiomas.

In the current study, we further assessed the correlations between diffusion metrics and cellular proliferation of meningiomas. We chose Ki-67 as a biomarker for reflecting tumor cellular proliferation because it is widely used in clinical practice. An elevated Ki-67 proliferation index has been associated with an increased risk of recurrence and poor prognosis in meningiomas.[27] According to the results, significant positive correlations were revealed between Ki-67 and all kurtosis metrics, while Ki-67 was negatively correlated with MD and ADC. In malignant tumors, the complexity and heterogeneity of the microenvironment increase and water molecule movement shows restriction both inside and outside of cells. Kurtosis is believed to be generally proportional to the complexity of the microstructure.[16,28,29] Thus, kurtosis metrics are likely to increase in malignant tumors, while diffusion values are likely to decrease. Meanwhile, the presence of an elevated Ki-67 expression in HGMs indicated an increased mitotic index and cell proliferation. Consequently, cellular proliferation of meningiomas can be noninvasively quantified by diffusion kurtosis metrics. Similar to our observation, a prior study reported the positive correlation between Ki-67 and kurtosis metrics.[25]

The application of diffusion kurtosis metrics in meningiomas is limited.[25] To our best knowledge, this is the first study to compare DKI with DTI and DWI in grading meningiomas. Our results

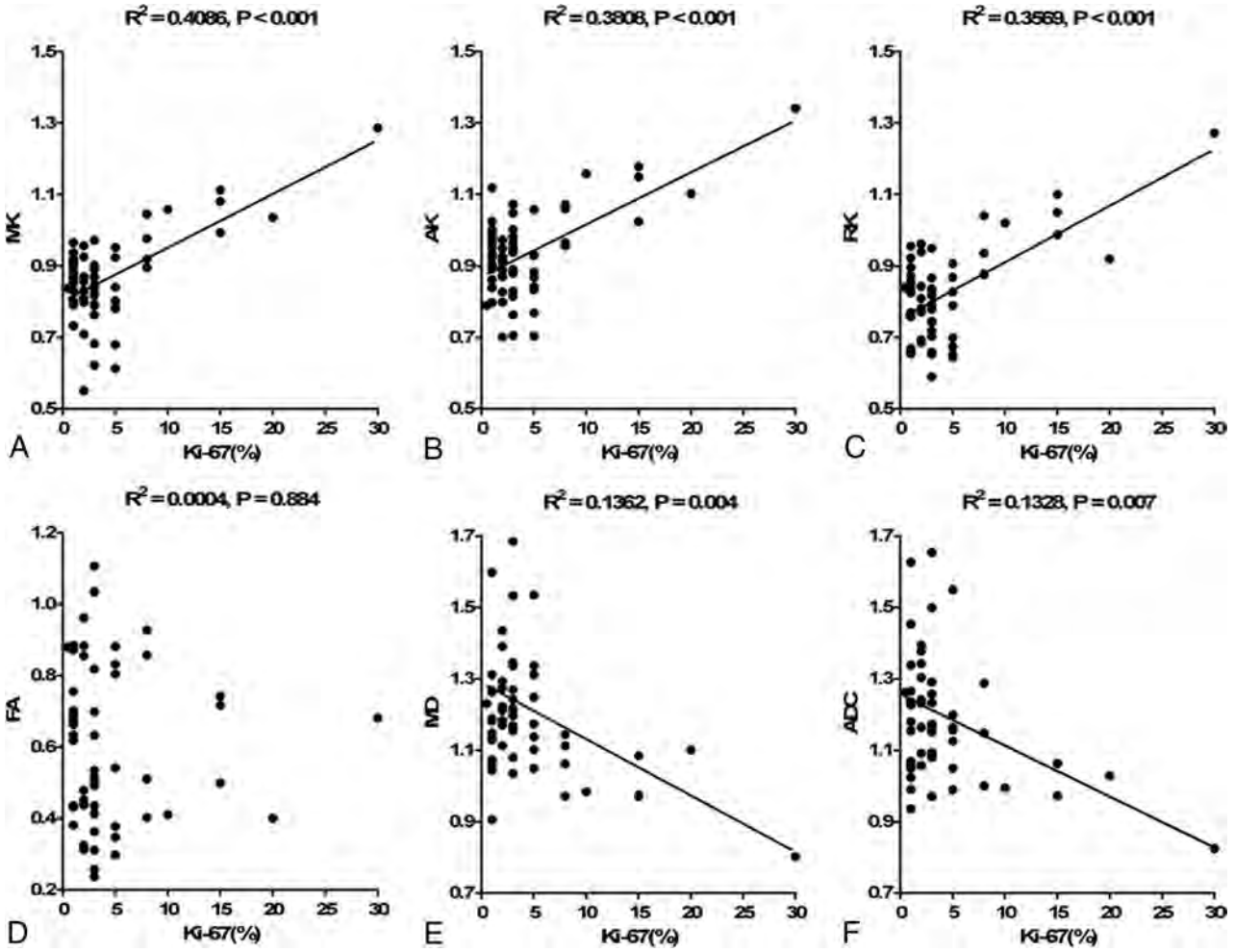

FIG 4. Correlations between Ki-67 and each normalized diffusion metric. Scatter diagrams demonstrate the correlations between the Ki-67 labeling index and MK (*A*), AK (*B*), RK (*C*), FA (*D*), MD (*E*), and ADC (*F*).

show that DKI had significantly greater diagnostic properties than DTI in grading meningiomas. In the future, external validation should be performed on a new population to confirm our findings. In addition, a larger, multicenter study population should be explored to obtain meaningful positive and negative predictive values and the real proportions of low- and high-grade meningiomas. We believe that DKI across time may provide clinical practice with robust results and it can consolidate the confidence of clinicians in the grading of meningiomas. Moreover, the promising results found in our study can be partially attributed to the use of a semiautomated method based on threshold segmentation. To date, this is the first study using the semiautomatic method for the measurement of meningiomas. The intraclass correlation analyses showed that the reproducibility of this method was excellent. In addition, it is more reliable, more accurate, and more objective than other methods and has been proposed in our previous studies on gliomas.[17]

This study has several limitations. First, the number of HGMs was relatively limited. A larger sample size may include more cases with HGMs to further verify our results. Second, detailed histologic characteristics such as cell density and nucleoplasmic ratio were not estimated in this study, so the correlation analyses between histologic heterogeneity and diffusion parameters were unavailable. Third, the discordance of some parameters between the DWI and DKI sequences may affect our results. Future studies with consistent parameter settings would help to confirm the findings of the current study. Fourth, the ROI placement of diffusion parameters was not correlated with fragmental histologic specimens, and an MR imaging–guided biopsy may be needed to confirm the correlations between diffusion metrics and Ki-67. Fifth, conventional DKI needs relatively long acquisition times, and it may be incompatible with daily clinical practice. A rapid DKI sequence may be beneficial to the clinical use of meningioma grading in further research.

CONCLUSIONS

Diffusion techniques, including DKI, DTI, and DWI, were useful in grading meningiomas. Moreover, MK demonstrated a better diagnostic efficiency than DTI metrics and was most closely associated with the grade of meningioma. In addition, diffusion metrics showed great potential in reflecting the cellular proliferation of meningiomas.

ACKNOWLEDGMENTS

The authors thank Zebin Xiao and Zhongping Zhang for their advice on manuscript writing and Ganggang Xu for his assistance with the statistical analyses.

REFERENCES

1. Riemenschneider MJ, Perry A, Reifenberger G. **Histological classification and molecular genetics of meningiomas.** *Lancet Neurol* 2006; 5:1045–54 CrossRef Medline
2. Louis DN, Perry A, Reifenberger G, et al. **The 2016 World Health Organization Classification of Tumors of the Central Nervous System: a summary.** *Acta Neuropathol* 2016;131:803–20 CrossRef Medline
3. Tang Y, Dundamadappa SK, Thangasamy S, et al. **Correlation of apparent diffusion coefficient with Ki-67 proliferation index in grading meningioma.** *AJR Am J Roentgenol* 2014;202:1303–08 CrossRef Medline
4. Abry E, Thomassen IØ, Salvesen ØO, et al. **The significance of Ki-67/MIB-1 labeling index in human meningiomas: a literature study.** *Pathol Res Pract* 2010;206:810–15 CrossRef Medline
5. Lin BJ, Chou KN, Kao HW, et al. **Correlation between magnetic resonance imaging grading and pathological grading in meningioma.** *J Neurosurg* 2014;121:1201–08 CrossRef Medline
6. Watanabe Y, Yamasaki F, Kajiwara Y, et al. **Preoperative histological grading of meningiomas using apparent diffusion coefficient at 3T MRI.** *Eur J Radiol* 2013;82:658–63 CrossRef Medline
7. Yiping L, Kawai S, Jianbo W, et al. **Evaluation parameters between intra-voxel incoherent motion and diffusion-weighted imaging in grading and differentiating histological subtypes of meningioma: a prospective pilot study.** *J Neurol Sci* 2017;15 372:60–69 CrossRef Medline
8. Sanverdi SE, Ozgen B, Oguz KK, et al. **Is diffusion-weighted imaging useful in grading and differentiating histopathological subtypes of meningiomas?** *Eur J Radiol* 2012;81:2389–95 CrossRef Medline
9. Yamasaki F, Kurisu K, Satoh K, et al. **Apparent diffusion coefficient of human brain tumors at MR imaging.** *Radiology* 2005;235:985–91 CrossRef Medline
10. Baskan O, Silav G, Bolukbasi FH, et al. **Relation of apparent diffusion coefficient with Ki-67 proliferation index in meningiomas.** *Br J Radiol* 2016;89:20140842 CrossRef Medline
11. Van Cauter S, Veraart J, Sijbers J, et al. **Gliomas: diffusion kurtosis MR imaging in grading.** *Radiology* 2012;263:492–501 CrossRef Medline
12. Surov A, Gottschling S, Mawrin C, et al. **Diffusion-weighted imaging in meningioma: prediction of tumor grade and association with histopathological parameters.** *Transl Oncol* 2015;8:517–23 CrossRef Medline
13. Poot DH, den Dekker AJ, Achten E, et al. **Optimal experimental design for diffusion kurtosis imaging.** *IEEE Trans Med Imaging* 2010;29:819–29 CrossRef Medline
14. Tan Y, Wang XC, Zhang H, et al. **Differentiation of high-grade-astrocytomas from solitary-brain-metastases: comparing diffusion kurtosis imaging and diffusion tensor imaging.** *Eur J Radiol* 2015; 84:2618–24 CrossRef Medline
15. Pang H, Ren Y, Dang X, et al. **Diffusional kurtosis imaging for differentiating between high-grade glioma and primary central nervous system lymphoma.** *J Magn Reson Imaging* 2016;44:30–40 CrossRef Medline
16. Tietze A, Hansen MB, Østergaard L, et al. **Mean diffusional kurtosis in patients with glioma: initial results with a fast imaging method in a clinical setting.** *AJNR Am J Neuroradiol* 2015;36:1472–78 CrossRef Medline
17. Jiang R, Jiang J, Zhao L, et al. **Diffusion kurtosis imaging can efficiently assess the glioma grade and cellular proliferation.** *Oncotarget* 2015;6:42380–93 CrossRef Medline
18. Wang S, Kim S, Zhang Y, et al. **Determination of grade and subtype of meningiomas by using histogram analysis of diffusion-tensor imaging metrics.** *Radiology* 2012;262:584–92 CrossRef Medline
19. Toh CH, Castillo M, Wong AM, et al. **Differentiation between classic and atypical meningiomas with use of diffusion tensor imaging.** *AJNR Am J Neuroradiol* 2008;29:1630–35 CrossRef Medline
20. Zikou A, Alexiou GA, Goussia A, et al. **The role of diffusion tensor imaging and dynamic susceptibility perfusion MRI in the evaluation of meningioma grade and subtype.** *Clin Neurol Neurosurg* 2016; 146:109–15 CrossRef Medline
21. Santelli L, Ramondo G, Della Puppa A, et al. **Diffusion-weighted imaging does not predict histological grading in meningiomas.** *Acta Neurochir (Wien)* 2010;152:1315–19; discussion 1319 CrossRef Medline
22. Jolapara M, Kesavadas C, Radhakrishnan VV, et al. **Role of diffusion tensor imaging in differentiating subtypes of meningiomas.** *J Neuroradiol* 2010;37:277–83 CrossRef Medline
23. Lu H, Jensen JH, Ramani A, et al. **Three-dimensional characterization of non-Gaussian water diffusion in humans using diffusion kurtosis imaging.** *NMR Biomed* 2006;19:236–47 CrossRef Medline
24. Szczepankiewicz F, van Westen D, Englund E, et al. **The link between diffusion MRI and tumor heterogeneity: mapping cell eccentricity and density by diffusional variance decomposition (DIVIDE).** *Neuroimage* 2016;142:522–32 CrossRef Medline
25. Xing F, Tu N, Koh TS, et al. **MR diffusion kurtosis imaging predicts malignant potential and the histological type of meningioma.** *Eur J Radiol* 2017;95:286–92 CrossRef Medline
26. Nagar VA, Ye JR, Ng WH, et al. **Diffusion-weighted MR imaging: diagnosing atypical or malignant meningiomas and detecting tumor dedifferentiation.** *AJNR Am J Neuroradiol* 2008;29:1147–52 CrossRef Medline
27. Modha A, Gutin PH. **Diagnosis and treatment of atypical and anaplastic meningiomas: a review.** *Neurosurgery* 2005;57:538–50; discussion 538–50 CrossRef Medline
28. Zhuo J, Xu S, Proctor JL, et al. **Diffusion kurtosis as an in vivo imaging marker for reactive astrogliosis in traumatic brain injury.** *Neuroimage* 2012;59:467–77 CrossRef Medline
29. Steven AJ, Zhuo J, Melhem ER. **Diffusion kurtosis imaging: an emerging technique for evaluating the microstructural environment of the brain.** *AJR Am J Roentgenol* 2014;202:W26–33 CrossRef Medline

Sequential Apparent Diffusion Coefficient for Assessment of Tumor Progression in Patients with Low-Grade Glioma

I.E. Chen, N. Swinburne, N.M. Tsankova, M.M. Hefti, A. Aggarwal, A.H. Doshi, A. Hormigo, B.N. Delman, and K. Nael

ABSTRACT

BACKGROUND AND PURPOSE: Early and accurate identification of tumor progression in patients with low-grade gliomas is challenging. We aimed to assess the role of quantitative ADC analysis in the sequential follow-up of patients with low-grade gliomas as a potential imaging marker of tumor stability or progression.

MATERIALS AND METHODS: In this retrospective study, patients with a diagnosis of low-grade glioma with at least 12 months of imaging follow-up were retrospectively reviewed. Two neuroradiologists independently reviewed sequential MR imaging in each patient to determine tumor progression using the Response Assessment in Neuro-Oncology criteria. Normalized mean ADC (ADC_{mean}) and 10th percentile ADC (ADC_{10}) values from FLAIR hyperintense tumor volume were calculated for each MR image and compared between patients with stable disease versus tumor progression using univariate analysis. The interval change of ADC values between sequential scans was used to differentiate stable disease from progression using the Fisher exact test.

RESULTS: Twenty-eight of 69 patients who were evaluated met our inclusion criteria. Fifteen patients were classified as stable versus 13 patients as having progression based on consensus reads of MRIs and the Response Assessment in Neuro-Oncology criteria. The interval change of ADC values showed greater concordance with ultimate lesion disposition than quantitative ADC values at a single time point. The interval change in ADC_{10} matched the expected pattern in 12/13 patients with tumor progression (overall diagnostic accuracy of 86%, $P < .001$). On average, the ADC_{10} interval change predicted progression 8 months before conventional MR imaging.

CONCLUSIONS: The interval change of ADC_{10} values can be used to identify progression versus stability of low-grade gliomas with a diagnostic accuracy of 86% and before apparent radiologic progression on conventional MR imaging.

ABBREVIATIONS: LGG = low-grade glioma; ROC = receiver operating characteristic

Diffuse gliomas are the most common type of low-grade gliomas (LGGs), defined by the World Health Organization as grade II diffuse astrocytomas or oligodendrogliomas, most of which have now been found to carry a gain-of-function mutation in the *isocitrate dehydrogenase* gene. *Isocitrate dehydrogenase*–mutant diffuse astrocytomas and oligodendrogliomas are relatively slow-growing tumors but inevitably undergo anaplastic transformation into high-grade tumors.[1] This transformation can manifest differently in the amount of time to progression for each patient.[2] Distinguishing LGGs from high-grade gliomas is important for prognosis and guiding treatment.[3]

The Response Assessment in Neuro-Oncology criteria have been established for assessment of progression in patients with LGGs using both clinical (ie, neurologic) and radiologic terms.[4] In clinically stable patients, progression is likely to be determined radiologically. Imaging surveillance of patients with LGGs is routinely conducted by sequential MR imaging. LGGs are most commonly (>90%) nonenhancing tumors that are therefore best depicted on FLAIR imaging. Radiologic progression of LGGs is often inferred from an increase in tumor size on FLAIR images or development of enhancement on T1-weighted postcontrast MR imaging.[5-8] In the absence of new or progressive enhancement, determination of radiologic progression in LGGs might be challenging because slow progression is manifested by small, incremental, and asymptomatic increases in size on FLAIR hyperintense lesion.[7] Therefore, despite using standardized criteria such as the Response Assessment in Neuro-

Received August 30, 2017; accepted after revision February 24, 2018.

From the Departments of Radiology (I.E.C., N.S., A.A., A.H.D., B.N.D., K.N.), Pathology (N.M.T., M.M.H.), and Neurology (A.H.), Icahn School of Medicine at Mount Sinai, New York, New York.

Please address correspondence to Kambiz Nael, MD, Department of Radiology, Icahn School of Medicine at Mount Sinai, Box 1234, One Gustave L. Levy Place, New York, NY 10029; e-mail: Kambiznael@gmail.com; @kambiznael

Indicates open access to non-subscribers at www.ajnr.org

http://dx.doi.org/10.3174/ajnr.A5639

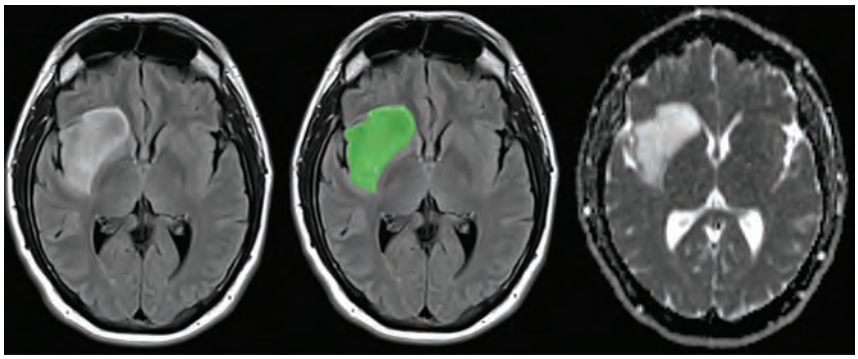

FIG 1. A VOI was generated using a voxel-based signal intensity threshold method subsuming the entire region of FLAIR hyperintensity. Using coregistered images, we transferred the VOI to ADC for quantitative ADC analysis.

Oncology, final tumor assignments as stable versus progression may vary greatly among neuroradiologists, associated with intraobserver variability and potential missed diagnoses.[9]

ADC derived from DWI has been shown to reflect tumor cellularity[10,11] and can have clinical implications for characterizing gliomas. While ADC has been extensively studied to evaluate tumor grade[12-15] or response to treatment,[16,17] the literature on the role of ADC in the assessment of tumor progression in patients with LGGs remains sparse, with mixed results.[18]

More research is necessary to further evaluate the contribution of ADC in predicting tumor progression in LGGs so that any change in treatment and management may be determined earlier than is possible with conventional sequences. The purpose of this study was to assess the role of quantitative ADC analysis in the sequential follow-up of patients with LGGs as a potential imaging marker of tumor stability or progression.

MATERIALS AND METHODS

Patients

This retrospective study was performed under institutional review board approval with a waiver of informed consent. Digital charts of patients with histologically proved LGGs between 2010 and 2015 were retrospectively reviewed. Inclusion criteria were as follows: 1) a histopathologic diagnosis of grade II diffuse astrocytoma, grade II oligodendroglioma, or grade II glioma with mixed oligodendroglial and astrocytic morphology; 2) no prior interventions except for biopsy or anticonvulsant medications; 3) at least 12 months of clinical and imaging follow-up from the date of the operation or biopsy; and 4) availability of diagnostic MR imaging with inclusion of DWI. Study end points were clinical and imaging evidence of progression using the Response Assessment in Neuro-Oncology criteria[4] or a second surgical resection.

Demographic data including age, sex, initial tumor size, tumor type, extent of the initial surgical resection, duration of follow-up, and number of MRIs were noted for each patient.

Image Acquisition

MR imaging was performed using 8 MR imaging scanners: 2 Skyra 3T (Siemens, Erlangen, Germany), 2 Aera 1.5T (Siemens), and 4 Signa 1.5T (GE Healthcare, Milwaukee, Wisconsin) within our radiology department. The imaging protocol included transverse T1-weighted imaging (TR/TE/flip angle, 600–1800/9–19 ms/180°), T2WI (TR/TE/flip angle, 3100–7000/86–105 ms/180°), FLAIR (TR/TE/TI, 8000–12,000/98–130/2400–2700 ms), DWI, and postcontrast T1-weighted imaging.

DWI was acquired using a single-shot spin-echo EPI sequence (TR/TE, 4900/98 ms [1.5T] or 4100/95 ms [3T]; FOV, 220 × 220 mm; matrix, 128 × 128 mm; slices, 30 × 5 mm). Diffusion gradients were applied along 3 orthogonal directions with b=0 and 1000 s/mm^2. A total volume of 0.1 mmol/kg of gadobenate dimeglumine was injected intravenously for postcontrast T1-weighted imaging.

Qualitative Image Analysis

Image analysis was performed in separate reading sessions, independently, by 2 board-certified neuroradiologists who were blinded to the patient outcome. MR imaging studies of each patient were interpreted sequentially by each reader and designated as stable or progressed in comparison with prior MR imaging using the Response Assessment in Neuro-Oncology criteria.[4] Progression was defined as development of new lesions, increase in enhancement, or increase in the size of a FLAIR hyperintense region by 25%. Discrepancies were resolved by a consensus read. Clinically, progression was defined by definite clinical deterioration related to the tumor or failure to return for follow-up because of death or a deteriorating condition as assessed by the treating neuro-oncologist. Each patient was assigned a final assessment score of "stable" (score = 0) for patients who remained stable throughout the entire follow-up time and "progressed" (score = 1) for patients who showed progression.

Quantitative ADC Analysis

Quantitative ADC analysis was performed using a Food and Drug Administration–approved commercial software package (Olea Sphere; Olea Medical, La Ciotat, France). ADC and FLAIR were coregistered on each examination using a 6-*df* transformation and a mutual information cost function. Subsequently, a VOI was generated using a voxel-based signal intensity threshold method subsuming the entire region of FLAIR hyperintensity (Fig 1). From each VOI, a histogram was generated on the basis of voxel-based ADC values. These values were normalized to an ROI placed in the normal-appearing white matter in the contralateral centrum semiovale. Normalized mean ADC (ADC_{mean}) and 10th percentile ADC (ADC_{10}) values and normalized ratios were exported for statistical analysis. In addition, ADC_{mean} and ADC_{10} ratios were compared between sequential scans in each patient and scored to assess the fit with the expected pattern. An interval decrease of ADC values of ≥20% was an unfavorable pattern, suggestive of progression. Any other pattern, including an increase or a decrease by <20%, was considered a favorable pattern and suggestive of relative stability.

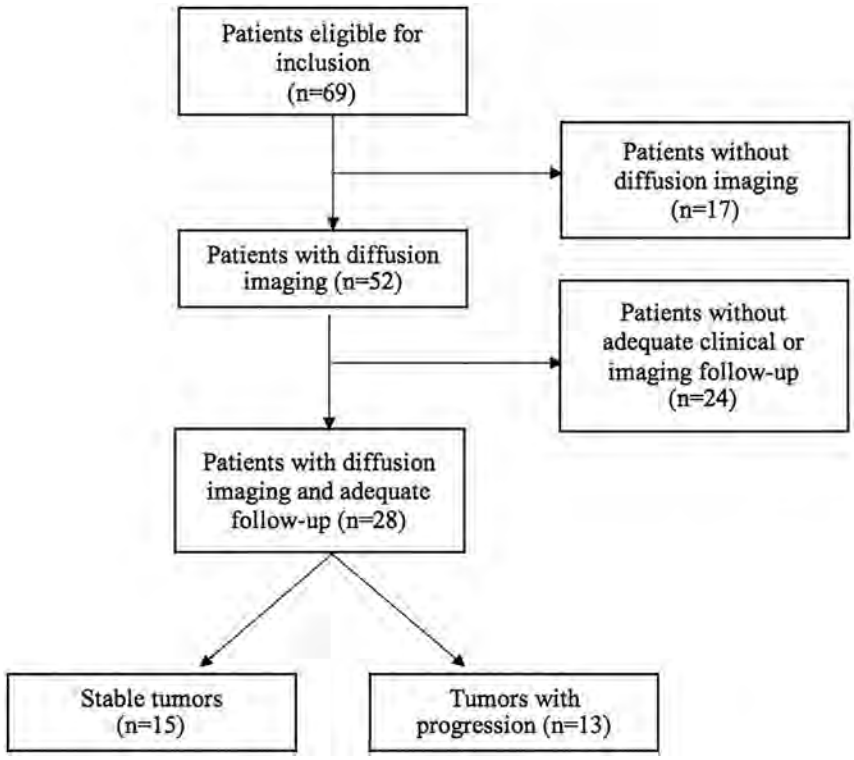

FIG 2. Study flow diagram.

Table 1: Baseline and clinical data in patients with and without progression—univariate analysis

Patient Characteristics	Total (*n* = 28)	Progressed (*n* = 13)	Stable (*n* = 15)	*P* Value
Age (mean) (SD) (yr)	50.4 (16.6)	49.1 (19.0)	51.6 (14.8)	.70
Sex, male/female	14:14	7:6	7:8	.56
Initial tumor size (mean) (SD) (mL)	30.7 (33.8)	32.3 (26.3)	29.4 (40.1)	.82
Tumor type, oligo/astro	19/9	9/4	10/5	.80
Follow-up time (mean) (range) (mo)	40.9 (12–109)	42.8 (12–89)	39.3 (12–109)	.75
No. of MRIs/patient (mean) (SD)	8.8 (4.3)	9.8 (5.0)	7.9 (3.6)	.26
Extent of initial tumor resection (No.) (>50% of initial volume)	15 (53.5%)	8 (61.5%)	7 (46.6%)	.68

Note:—oligo indicates oligodendroglioma; astro, astrocytoma.

Surgical Resection

All patients had initial surgical resection to confirm the diagnosis of LGG. The extent of the initial surgical resection was assessed in comparison with the preoperative MR image using the FLAIR volume and dichotomized as follows: 1) core biopsy or limited (<50% resection of initial tumor volume), or 2) >50% resection of the initial tumor volume. In addition, 13 of 28 patients had a subsequent resection, which was considered an end point in our study. The results of that second surgical pathology were compared with our neuroimaging variables.

Statistical Analysis

Statistical analysis was performed using MedCalc for Windows (Version 12.2.1; MedCalc Software, Mariakerke, Belgium). Clinical characteristics and neuroimaging variables were compared between subjects with progression and stable disease using univariate analysis with the Fisher exact test for categoric variables and the unpaired 2-tailed Student *t* test for continuous variables. Interobserver agreement was tested using a linear weighted κ test. Receiver operating characteristic (ROC) analysis was performed to determine the optimal parameters in distinguishing progression from stable disease. Optimal thresholds were calculated for each ROC curve to maximize both sensitivity and specificity using the Youden J statistic.

All lesions were scored into their respective groups without any indeterminate classifications. The patterns of interval changes of ADC_{mean} and ADC_{10} were assessed for diagnostic correlation using the Fisher exact test among patients with progression and stable disease. An interval change of ADC ratios of >20% between 2 consecutive studies was considered significant. For each subject, a regression line was generated across multiple MRIs, and a final score of stable versus progression was assigned on the basis of the slope of this line. This was calculated using the average value of 1 SD of the ADC values, which was approximately 0.2. Accuracy statistics including sensitivity, specificity, and overall diagnostic accuracy were reported. $P < .05$ was used to indicate statistical significance.

RESULTS

Of 69 patients who were evaluated, 41 patients were excluded due to lack of DWI ($n = 17$) or inadequate clinical or imaging follow-up ($n = 24$) (Fig 2). As a result, 28 patients (14 men and 14 women; mean age, 50.4 ± 16.6 years) were included in our analysis. Nineteen patients had oligodendrogliomas (grade II, currently diagnosed as *isocitrate dehydrogenase*-mutant and 1p/19q-codeleted), and 9 patients had diffuse astrocytomas (grade II, currently diagnosed as *isocitrate dehydrogenase*-mutant). Fourteen tumors were in the frontal lobe, 6 were in the parietal lobe, 5 were in the temporal lobe, and 3 were in both the frontal and temporal lobes.

A total of 247 MR imaging scans at different time points were evaluated (mean, 8.8 ± 4.3 scans per patient). The mean follow-up time was 40.9 months (range, 12–109) months. The final designation obtained from the consensus read of the 2 neuroradiologists showed tumor progression in 13 patients and stable disease in 15 patients.

The patients' age, sex, initial tumor size, tumor type, extent of initial tumor resection, duration of follow-up, and number of MRIs are summarized in Table 1.

Lesion Analysis

For subjective assessment of disease progression when evaluating conventional imaging (FLAIR and T1-postcontrast), observers 1

and 2 correctly identified 8/13 (sensitivity, 61.5%) and 7/13 (sensitivity, 53.8%), respectively, as tumor progression compared with final assignment. Stable disease was identified in 216/228 (94.7%) and 222/228 (97.4%) scans by observers 1 and 2, respectively. The interobserver agreement was $\kappa = 0.61$ (95% CI, 0.4–0.77).

Table 2: Diagnostic accuracy of ADC interval change—Fisher exact test

ADC	Interval Change	Stable Tumors (n = 15)	Progressed (n = 13)	P Value	Overall Diagnostic Accuracy
Mean	Decrease	7/15	6/13	.8	50%
	Plateau/increase	8/15	7/13		
10th percentile	Decrease	3/15	12/13	<.001	86%
	Plateau/increase	12/15	1/13		

Quantitative Assessment

The overall ADC_{mean} values were lower in patients who were ultimately shown to have tumor progression compared with patients with stable tumors (1.68 ± 0.23 versus 2.04 ± 0.78), though the difference was not statistically significant ($P = .13$). The average of ADC_{10} values

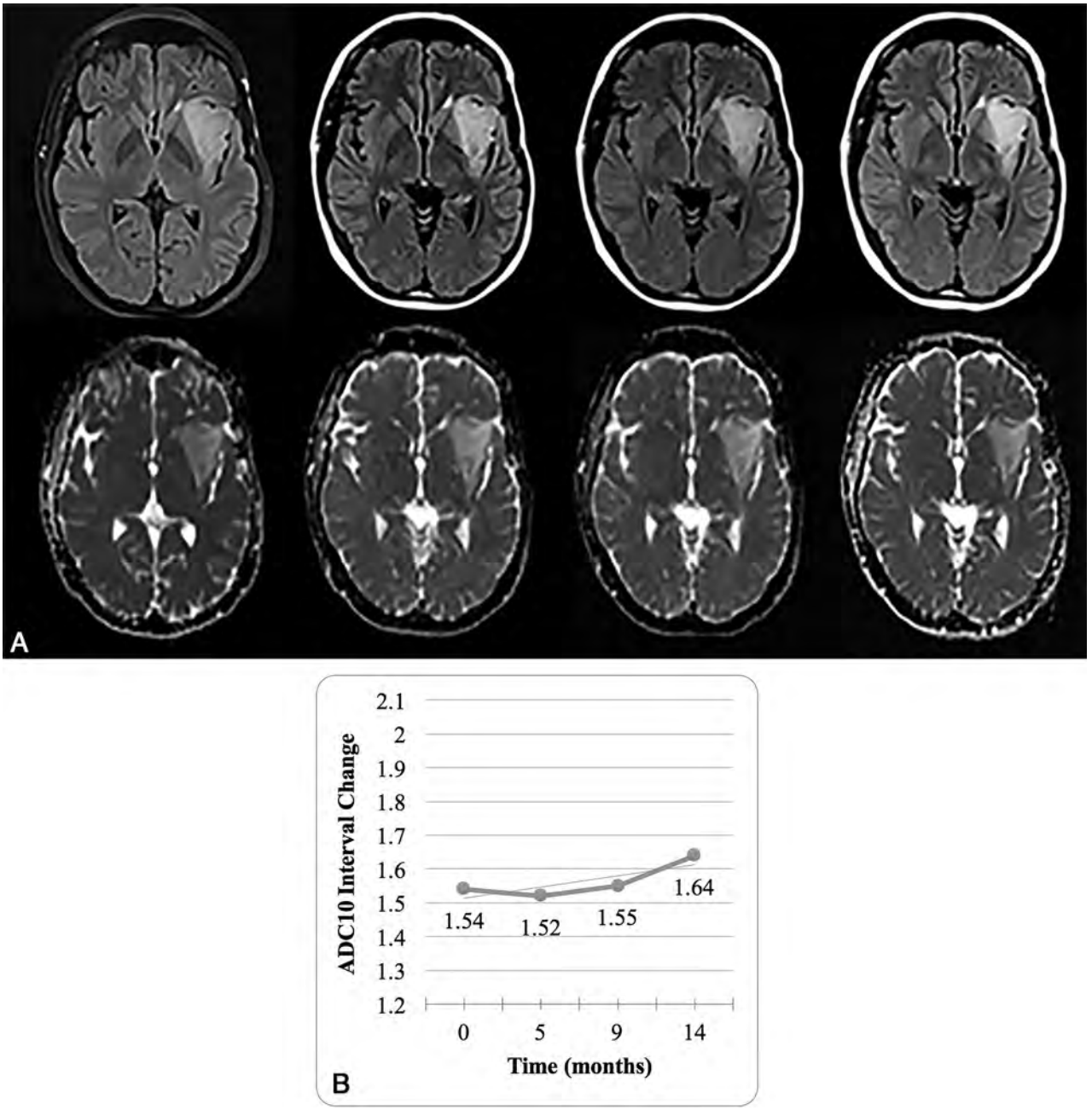

FIG 3. A 34-year-old woman diagnosed with grade II oligodendroglioma. *A*, Axial FLAIR/ADC images from 4 sequential MR images are shown (upper row: FLAIR; lower row: ADC; from left to right: first scan after initial diagnosis and at 5, 9, and 14 months). Review of FLAIR images shows stable extent of tumor during the entire follow-up. *B*, Plotting the normalized ADC_{10} values demonstrates no significant decrease in ADC_{10} values, concordant with stability of the tumor.

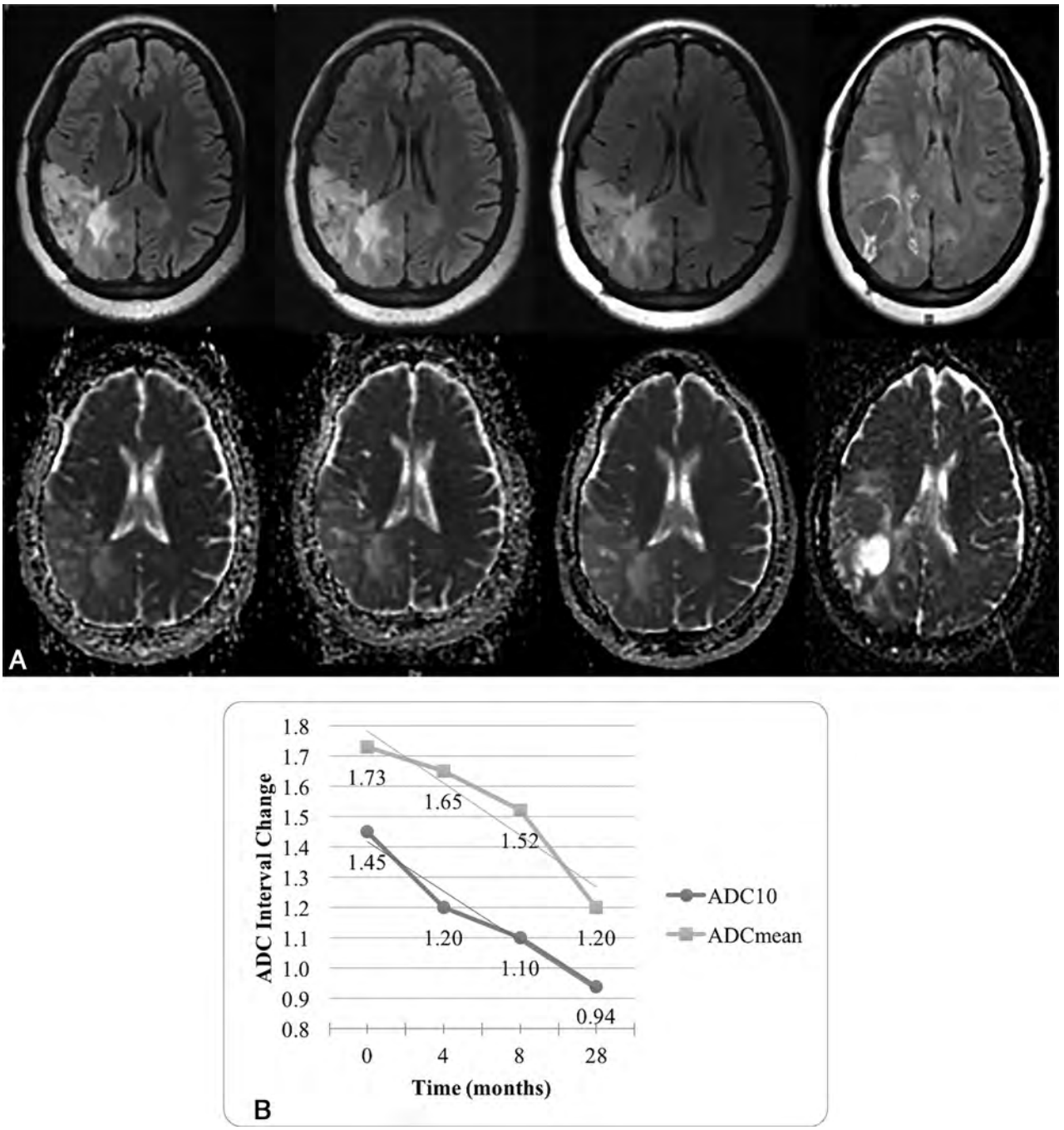

FIG 4. A 73-year-old woman diagnosed with a grade II oligodendroglioma. *A*, Axial FLAIR/ADC images from 4 sequential scans are shown (upper row: FLAIR; lower row: ADC; from left to right: first scan after initial diagnosis and at 4, 8, and 28 months). Disease progression was diagnosed at 28 months on conventional imaging and confirmed by surgical pathology. *B*, Both normalized ADC_{10} and ADC_{mean} ratios are plotted, demonstrating an interval decrease of ADC_{10} as early as 4 months following baseline examination, indicating eventual tumor progression. *C*, Histograms of quantitative normalized ratios of ADC_{10} and ADC_{mean} for each MR imaging examination.

was significantly ($P = .03$) lower in patients with ultimate tumor progression compared with patients with stable tumors (1.21 ± 0.24 versus 1.49 ± 0.37, $P = .03$). ROC analysis showed sensitivity/specificity and overall diagnostic accuracy of 84.6%/40%/62.3% (95% CI, 0.42–0.80) for ADC_{mean} at a threshold of 1.8 and 46.2%/93.3%/69.7% (95% CI, 0.55–0.89) for ADC_{10} at a threshold of 1.1.

If one applied the Fisher exact test for analysis of disease progression using the sequential ADC interval change score, the interval change in ADC_{mean} matched the expected pattern in 6/13 patients with tumor progression and 8/15 patients with stable disease (sensitivity, 53.3%; specificity, 46.2%; overall diagnostic accuracy, 49.7%). The interval change in the ADC_{10} score matched the expected pattern in 12/13 patients with tumor progression and 12/15 patients with stable disease (sensitivity, 92.3%; specificity, 80%; overall diagnostic accuracy, 86.2%). The ORs for identifying tumor progression were 1 ($P = .90$) for ADC_{mean} and 48 ($P = .001$) for ADC_{10}, respectively. Table 2 summarizes the

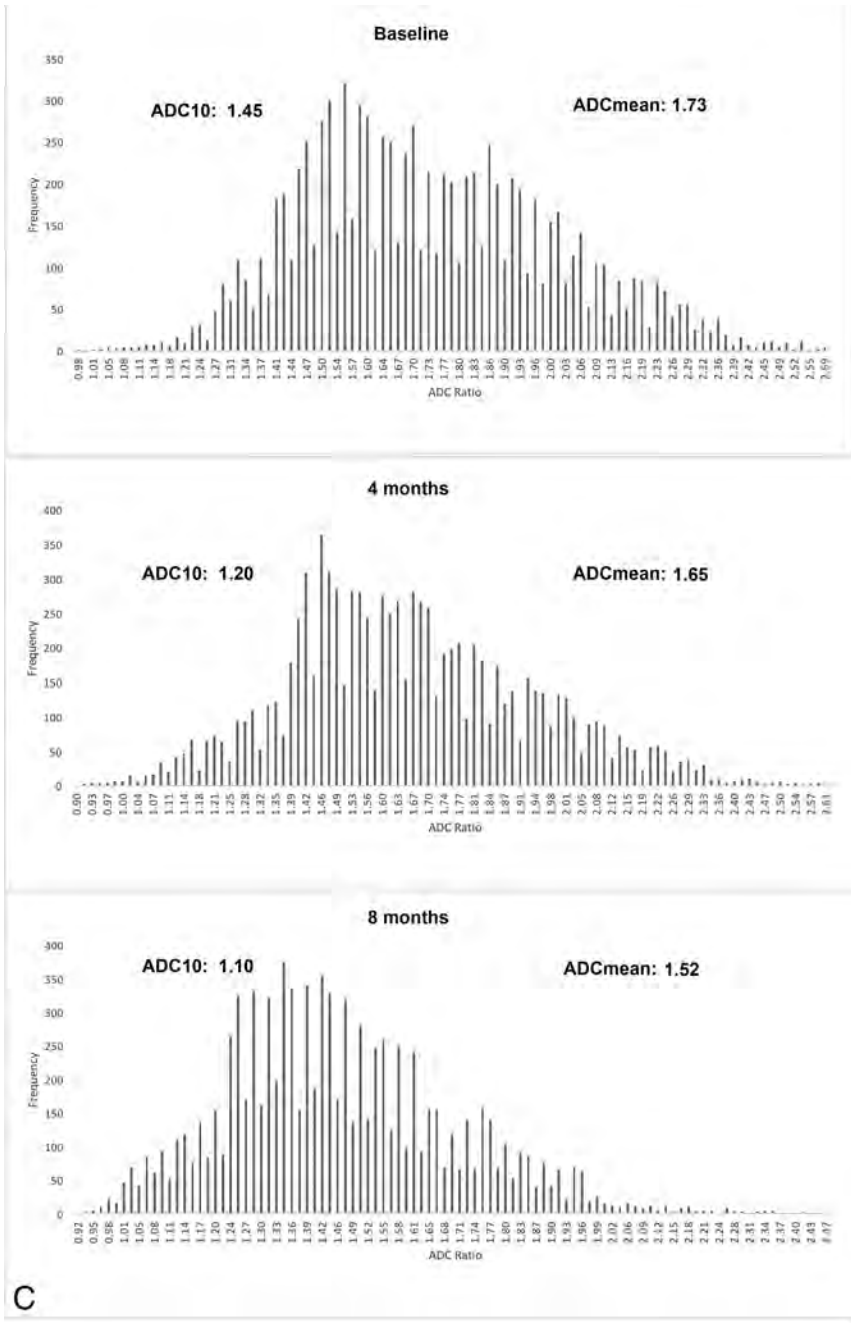

FIG 4. Continued.

results and diagnostic accuracy of the ADC interval change in identifying progression-versus-stable tumor.

Figure 3 shows an example of a stable pattern of ADC_{10} interval change in a patient who remained stable through the follow-up.

In 12/13 patients with radiologic progression, the ADC_{10} interval change correctly predicted progression, on average, 8 months (range, 4.1–15.1 months) before the lesions progressed on conventional imaging on consensus interpretation. In 3 patients who were determined to have stable disease, an interval change in ADC_{10} incorrectly pointed to progression approximately 4.8 months (range, 3–6 months) earlier than conventional sequences. Figure 4 shows an example of how the interval decrease in ADC_{10} can identify tumor progression earlier than conventional imaging.

All our patients who demonstrated radiologic progression ($n = 13$) underwent a second surgical resection and/or biopsy. Higher grade transformation (grades III and IV) was found in 8 patients, while 5 patients maintained their initial grade despite a progressive increase in size and extent of the tumor.

The overall ADC_{mean} values were 1.70 ± 0.22 and 1.63 ± 0.25 in patients with stable grades compared with patients with higher grade transformation, respectively ($P = .64$). ROC analysis was not significant ($P = .62$) in differentiating stable-versus-higher grade transformation (area under the curve, 0.62; sensitivity, 50%; specificity, 83.3%; 95% CI, 0.33–0.86). The average of ADC_{10} values was 1.36 ± 0.18 and 1.16 ± 0.22 in patients with stable grades compared with patients with higher grade transformation, respectively ($P = .09$). ROC analysis did not reach statistical significance ($P = .07$) in differentiating stable-versus-higher grade transformations (area under the curve, 0.75; sensitivity, 87.5%; specificity, 66.7%; 95% CI, 0.46–0.94).

DISCUSSION

ADC values of glioma tumors inversely correlate with tumor cellular density.[10,11] This correlation has been studied as a possible means of identifying and grading LGGs,[12-15] as well as monitoring the response to treatment.[16,17] In this study, we demonstrated that a progressive downward trend of ADC_{10} interval change can predict tumor progression in patients with LGGs and before apparent radiologic progression on conventional MR imaging.

Our results show that the interval change of ADC_{10} is superior in the early detection of LGG progression in comparison with single-time-point quantitative ADC values. We demonstrated that the interval change in the ADC_{10} score matched the expected pattern in 12/13 patients with tumor progression and 12/15 patients with stable disease, yielding an overall diagnostic accuracy of 86%. Using ADC_{10} interval change, we detected progression, on average, approximately 8 months before it was apparent on conventional imaging. Using single-time-point ADC values and traditional threshold methodology resulted in only a modest diagnostic performance, with an overall diagnostic accuracy of 62.3% at a threshold of 1.8 for ADC_{mean} and 69.7% at a threshold of 1.1 for ADC_{10}.

The superiority of evaluating interval ADC changes instead of

set threshold ADC values may be explained, in part, by the heterogeneous nature of LGG tumors. Specifically, tumor heterogeneity with existing variable and mixed tissue patterns due to the spatial variation in their cellular density, microenvironmental factors, and water content may result in varying quantitative ADC values across these tumors. By evaluating the interval change in ADC values in a particular lesion, the heterogeneity inherent in the individual tumor type can be internally controlled, resulting in an "individualized correction" that helps minimize confounding pathophysiologic factors.

Another reason for the modest performance of threshold methodology is the heterogeneity of scanners used in our study, which is an inherent limitation for any clinical research performed in a large institution using multiple MR imaging scanners. Despite the use of standardized imaging protocol and parameters, variability related to different MR imaging gradient systems and calibrations, software packages, and image scaling remains a major source of errors in quantitative image analysis such as ours.[19]

We also showed that ADC_{10} was predictive of LGG progression, whereas ADC_{mean} was not. In contrast to mean values that can be diluted by tissue and microenviromental heterogeneity, the lowest 10th percentile value was chosen to represent regions of tumor with the highest cellular density and proliferation. This is consistent with prior reports showing that the lowest representation of ADC using fifth percentile[20] or 10th percentile ADC values[21,22] has a higher correlation with tumor grade and cellular density in comparison with ADC_{mean} values.

One limitation of this study was the small sample size, and a larger cohort would be needed to further validate our results. For example, in our patients with higher grade transformation, we found lower values of ADC_{10} in comparison with patients with stable tumor; however, this difference did not reach statistical significance ($P = .09$), despite prior promising results.[12,13] Failure to demonstrate a significant difference may be a consequence of our sample size. The retrospective nature of our study could also introduce unknown errors including, but not limited to, selection and recall bias. Like many other studies, for quantitative analysis, we relied on the segmentation of tumor, which can introduce errors due to varying expertise and subjectivity of the observer. ADC values derived from regional ROIs can underestimate the heterogeneity of tumoral density[23] and are prone to operator-dependent sampling bias.[24] To minimize this variability, we used a semiautomated segmentation to create VOIs based on FLAIR hyperintense tumor. This VOI methodology has been shown to be more reproducible compared with other segmentation methods such as ROI-based analysis.[25] Quantitative analysis of ADC values may vary among different institutions depending on the variety of imaging parameters, type of scanner hardware and software, and image postprocessing. Therefore, the results should be interpreted within this context. We tried to minimize these errors using a standardized imaging protocol and parameters and also normalizing the ADC values to the contralateral side for the MR imaging study. We also performed a weekly calibration of our scanners using a diffusion phantom. Nevertheless, these confounding factors are inevitable for longitudinal clinical studies such as ours in which several MR imaging scanners were used.

CONCLUSIONS

The interval change of ADC_{10} values can be used to identify progression of LGGs with a diagnostic accuracy of 86% and before apparent radiologic progression on conventional MR imaging. Further investigation with larger patient populations is required to confirm these findings. If its value is established in a larger prospective clinical study, ADC_{10} has the potential to be used for prediction of LGG progression earlier in the disease course when radiologic progression is not apparent on FLAIR or T1 postcontrast imaging.

Disclosures: Bradley N. Delman—*UNRELATED*: *Consultancy*: Bayer HealthCare Pharmaceuticals, *Comments*: money paid to the institution; *Payment for Lectures Including Service on Speakers Bureaus*: Bayer HealthCare Pharmaceuticals; *Travel/Accommodations/Meeting Expenses Unrelated to Activities Listed*: Bayer HealthCare Pharmaceuticals. Kambiz Nael—*UNRELATED*: *Board Membership*: Olea Medical, *Comments*: Medical Advisory Board.

REFERENCES

1. Delgado-López PD, Corrales-García EM, Martino J, et al. **Diffuse low-grade glioma: a review on the new molecular classification, natural history and current management strategies.** *Clin Transl Oncol* 2017;19:931–44 CrossRef Medline
2. Larsen J, Wharton SB, McKevitt F, et al. **'Low grade glioma': an update for radiologists.** *Br J Radiol* 2017;90:20160600 CrossRef Medline
3. Nahed BV, Redjal N, Brat DJ, et al. **Management of patients with recurrence of diffuse low grade glioma: a systematic review and evidence-based clinical practice guideline.** *J Neurooncol* 2015;125:609–30 CrossRef Medline
4. van den Bent MJ, Wefel JS, Schiff D, et al. **Response assessment in neuro-oncology (a report of the RANO group): assessment of outcome in trials of diffuse low-grade gliomas.** *Lancet Oncol* 2011;12:583–93 CrossRef Medline
5. Fouke SJ, Benzinger T, Gibson D, et al. **The role of imaging in the management of adults with diffuse low grade glioma: a systematic review and evidence-based clinical practice guideline.** *J Neurooncol* 2015;125:457–79 CrossRef Medline
6. Asari S, Makabe T, Katayama S, et al. **Assessment of the pathological grade of astrocytic gliomas using an MRI score.** *Neuroradiology* 1994;36:308–10 CrossRef Medline
7. Kim MM, Lawrence TS, Cao Y. **Advances in magnetic resonance and positron emission tomography imaging: assessing response in the treatment of low-grade glioma.** *Semin Radiat Oncol* 2015;25:172–80 CrossRef Medline
8. Pallud J, Capelle L, Taillandier L, et al. **Prognostic significance of imaging contrast enhancement for WHO grade II gliomas.** *Neuro Oncol* 2009;11:176–82 CrossRef Medline
9. Vos MJ, Uitdehaag BM, Barkhof F, et al. **Interobserver variability in the radiological assessment of response to chemotherapy in glioma.** *Neurology* 2003;60:826–30 CrossRef Medline
10. Hayashida Y, Hirai T, Morishita S, et al. **Diffusion-weighted imaging of metastatic brain tumors: comparison with histologic type and tumor cellularity.** *AJNR Am J Neuroradiol* 2006;27:1419–25 Medline
11. Chenevert TL, Stegman LD, Taylor JM, et al. **Diffusion magnetic resonance imaging: an early surrogate marker of therapeutic efficacy in brain tumors.** *J Natl Cancer Inst* 2000;92:2029–36 CrossRef Medline
12. Cui Y, Ma L, Chen X, et al. **Lower apparent diffusion coefficients indicate distinct prognosis in low-grade and high-grade glioma.** *J Neurooncol* 2014;119:377–85 CrossRef Medline
13. Hathout L, Ellingson BM, Cloughesy TF, et al. **Patient-specific characterization of the invasiveness and proliferation of low-grade gliomas using serial MR imaging and a mathematical model of tumor growth.** *Oncol Rep* 2015;33:2883–88 CrossRef Medline
14. Kitis O, Altay H, Calli C, et al. **Minimum apparent diffusion coeffi-**

cients in the evaluation of brain tumors. *Eur J Radiol* 2005;55:393–400 CrossRef Medline
15. Murakami R, Hirai T, Sugahara T, et al. **Grading astrocytic tumors by using apparent diffusion coefficient parameters: superiority of a one- versus two-parameter pilot method.** *Radiology* 2009;251:838–45 CrossRef Medline
16. Hein PA, Eskey CJ, Dunn JF, et al. **Diffusion-weighted imaging in the follow-up of treated high-grade gliomas: tumor recurrence versus radiation injury.** *AJNR Am J Neuroradiol* 2004;25:201–09 Medline
17. Higano S, Yun X, Kumabe T, et al. **Malignant astrocytic tumors: clinical importance of apparent diffusion coefficient in prediction of grade and prognosis.** *Radiology* 2006;241:839–46 CrossRef Medline
18. Brasil Caseiras G, Ciccarelli O, Altmann DR, et al. **Low-grade gliomas: six-month tumor growth predicts patient outcome better than admission tumor volume, relative cerebral blood volume, and apparent diffusion coefficient.** *Radiology* 2009;253:505–12 CrossRef Medline
19. Chenevert TL, Malyarenko DI, Newitt D, et al. **Errors in quantitative image analysis due to platform-dependent image scaling.** *Transl Oncol* 2014;7:65–71 CrossRef Medline
20. Kang Y, Choi SH, Kim YJ, et al. **Gliomas: histogram analysis of apparent diffusion coefficient maps with standard- or high-b-value diffusion-weighted MR imaging–correlation with tumor grade.** *Radiology* 2011;261:882–90 CrossRef Medline
21. Wen Q, Jalilian L, Lupo JM, et al. **Comparison of ADC metrics and their association with outcome for patients with newly diagnosed glioblastoma being treated with radiation therapy, temozolomide, erlotinib and bevacizumab.** *J Neurooncol* 2015;121:331–39 CrossRef Medline
22. McDonald CR, Delfanti RL, Krishnan AP, et al. **Restriction spectrum imaging predicts response to bevacizumab in patients with high-grade glioma.** *Neuro Oncol* 2016;18:1579–90 CrossRef Medline
23. Cha S. **Update on brain tumor imaging: from anatomy to physiology.** *AJNR Am J Neuroradiol* 2006;27:475–87 Medline
24. Tozer DJ, Jäger HR, Danchaivijitr N, et al. **Apparent diffusion coefficient histograms may predict low-grade glioma subtype.** *NMR Biomed* 2007;20:49–57 CrossRef Medline
25. Jung SC, Choi SH, Yeom JA, et al. **Cerebral blood volume analysis in glioblastomas using dynamic susceptibility contrast-enhanced perfusion MRI: a comparison of manual and semiautomatic segmentation methods.** *PLoS One* 2013;8:e69323 CrossRef Medline

MRI Planimetry and Magnetic Resonance Parkinsonism Index in the Differential Diagnosis of Patients with Parkinsonism

V.C. Constantinides, G.P. Paraskevas, G. Velonakis, P. Toulas, E. Stamboulis, and E. Kapaki

ABSTRACT

BACKGROUND AND PURPOSE: Differential diagnosis of multiple system atrophy, progressive supranuclear palsy, and corticobasal degeneration from Parkinson disease on clinical grounds is often difficult. MR imaging biomarkers could assist in a more accurate diagnosis. We examined the utility of MR imaging surface measurements (MR imaging planimetry) in the differential diagnosis of patients with parkinsonism.

MATERIALS AND METHODS: Fifty-two patients with Parkinson-plus (progressive supranuclear palsy, $n = 24$; corticobasal degeneration, $n = 9$; multiple system atrophy, $n = 19$), 18 patients with Parkinson disease, and 15 healthy controls were included. Corpus callosum, midbrain, and pons surfaces; relevant indices; and the Magnetic Resonance Parkinsonism Index were calculated. Corpus callosum subsection analysis was performed, and the corpus callosum posteroanterior gradient was introduced.

RESULTS: A Magnetic Resonance Parkinsonism Index value of >12.6 discriminated progressive supranuclear palsy from other causes of parkinsonism with a 91% sensitivity and 95% specificity. No planimetry measurement could accurately discriminate those with multiple system atrophy with parkinsonism from patients with Parkinson disease. A corpus callosum posteroanterior gradient value of ≤191 was highly specific (97%) and moderately sensitive (75%) for the diagnosis of corticobasal degeneration versus all other groups. A midbrain-to-corpus callosum posteroanterior gradient ratio of ≤0.45 was highly indicative of progressive supranuclear palsy over corticobasal degeneration (sensitivity 86%, specificity 88%).

CONCLUSIONS: MR imaging planimetry measurements are potent imaging markers of progressive supranuclear palsy and promising markers of corticobasal degeneration but do not seem to assist in the diagnosis of multiple system atrophy with parkinsonism.

ABBREVIATIONS: CBD = corticobasal degeneration; CC = corpus callosum; $CC_{P\text{-}A\ grad}$ = corpus callosum posteroanterior gradient; MRPI = Magnetic Resonance Parkinsonism Index; MSA = multiple system atrophy; MSA-C = multiple system atrophy cerebellar type; MSA-P = multiple system atrophy with parkinsonism; PD = Parkinson disease; PSP = progressive supranuclear palsy

Multiple system atrophy (MSA), progressive supranuclear palsy (PSP), and corticobasal degeneration (CBD) are neurodegenerative parkinsonian disorders that compose the Parkinson-plus syndromes. Despite the presence of distinct clinical features, differential diagnosis is often difficult.[1] Diagnostic criteria for PSP and MSA lack sensitivity, particularly in atypical cases and at the early stages of the diseases.[2,3] Recently established criteria of CBD, on the other hand, are considered to lack specificity, and misdiagnosis may reach up to 50%.[4] Thus, objective diagnostic markers are needed to improve diagnostic accuracy in parkinsonian disorders.

PSP is characterized by relatively selective midbrain and superior cerebellar peduncle atrophy,[5] as well as anterior corpus callosum thinning.[6] Pons and middle cerebellar peduncle atrophy is pronounced in MSA.[7] Patients with CBD present with asymmetric frontoparietal cortical atrophy as well as middle and posterior corpus callosum (CC) thinning.[8,9] By means of MR imaging planimetry, the midbrain-to-pons surface ratio and the Magnetic Resonance Parkinsonism Index (MRPI), calculated by multiplying the pontine-to-midbrain area ratio by the middle cerebellar peduncle-to-superior cerebellar peduncle width ratio, have been suggested to assist in a more accurate and earlier diagnosis of PSP and, to a lesser extent, of MSA.[10] To the best of our knowledge, no MR imaging planimetry study has incorporated midbrain, pons, and CC surface measurements in all 3 Parkinson-plus syndromes.

The aim of the present study was to examine the utility of

Received November 9, 2017; accepted after revision February 7, 2018.

From the 1st Department of Neurology (V.C.C., G.P.P., E.S., E.K.), National and Kapodistrian University of Athens, Medical School, Eginition Hospital, Athens, Greece; and Research Unit of Radiology (G.V., P.T.), 2nd Department of Radiology, National and Kapodistrian University of Athens, Medical School, Athens, Greece.

Please address correspondence to Vasilios C. Constantinides, MD, 1st Department of Neurology, National and Kapodistrian University of Athens, Medical School, Eginition Hospital, 72-74 Vas. Sofias Ave, Athens, Greece, P.C. 11528; e-mail: vassilis.kon@hotmail.com, vconstan@med.uoa.gr

Indicates article with supplemental on-line table.

Indicates article with supplemental on-line photos.

http://dx.doi.org/10.3174/ajnr.A5618

Table 1: Demographic and clinical characteristics[a]

	Controls *n* = 15	PSP *n* = 24	CBD *n* = 9	MSA *n* = 19	PD *n* = 18	*P* Value
Demographic data						
Sex (M/F)	8:7	13:11	4:5	14:5	10:8	.454[b]
Age (yr)	62.6 (9.0)	63.2 (6.8)	67.9 (5.6)	64.2 (7.1)	64.4 (9.3)	.433[c]
Disease duration (yr)	NA	3.3 (1.8)	3.3 (1.8)	3.1 (2.1)	10.6 (6.1)	<.001[c]
Clinical data						
UPDRS III	NA	21.3 (9.8)	25.2 (7.1)	19.6 (19.1)	32.3 (11.5)	.875[c]
$UPDRS_{brad}$	NA	6.1 (4.7)	12.5 (3.6)	7.7 (9.3)	14.5 (8.4)	.134[c]
$UPDRS_{rig}$	NA	4.1 (3.0)	7.2 (4.4)	3.9 (5.6)	9.2 (6.5)	.266[c]
White matter lesion burden assessment						
Fazekas PVH score	0.38 (0.65)	0.71 (0.75)	0.70 (0.48)	0.37 (0.50)	0.47 (0.62)	.321[c]
Fazekas DWMH score	0.77 (0.73)	0.54 (0.66)	0.40 (0.52)	0.53 (061)	0.53 (0.51)	.684[c]

Note:—DWMH indicates deep white matter hyperintensity; UPDRS, Unified Parkinson Disease Rating Scale; $UPDRS_{brad}$, bradykinesia subscore of UPDRS; $UPDRS_{rig}$, rigidity subscore of UPDRS; PVH, periventricular; NA, not applicable.

[a] Data are presented as mean (SD).

[b] χ^2 test.

[c] ANOVA.

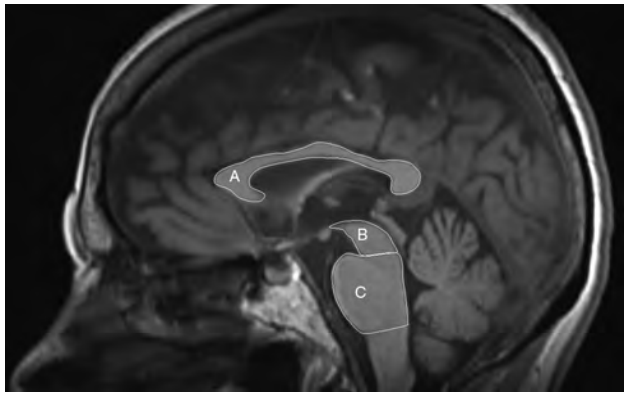

FIG 1. MR imaging planimetry measurements. Midsagittal T1-weighted image depicts corpus callosum (*A*), midbrain tegmentum (*B*), and pons (*C*) surfaces.

already-suggested MR imaging brain stem surfaces and ratios in the differential diagnosis of patients with parkinsonism, including CBD, and to assess novel ones (incorporating the CC surface and CC subsections) in a well-characterized, prospectively diagnosed cohort.

MATERIALS AND METHODS

Patients

Patients were consecutively and prospectively recruited (between 2011 and 2014) as part of the Parkinson-Plus Registry of the 1st Department of Neurology, National and Kapodistrian University of Athens. Detailed neurologic history was obtained, and a comprehensive neurologic examination was performed in all patients, with a follow-up of at least 2 years. Standard laboratory tests to exclude secondary causes of parkinsonism were performed in all patients, as appropriate.

All patients fulfilled the established the diagnostic criteria for probable PSP with a Richardson syndrome phenotype,[11] probable corticobasal degeneration with a probable corticobasal syndrome phenotype,[4] or multiple system atrophy.[12] None of the included patients had a history of stroke or other focal lesions, in accordance with the exclusion criteria of the established diagnostic criteria.

The Unified Parkinson's Disease Rating Scale III was applied in all patients to measure the severity of parkinsonism. The bradykinesia and rigidity subscores were also included.

CSF β amyloid ($A\beta_{42}$), τ protein (τ_T), and phosphorylated τ protein at threonine-181 ($\tau_{P\text{-}181}$) were measured in all patients, as described elsewhere.[13] Patients with a typical Alzheimer disease CSF biochemical profile were excluded (ie, decreased $A\beta_{42}$, elevated τ_T and $\tau_{P\text{-}181}$ according to cutoff values of our laboratory).[13] Thus 5 patients fulfilling the criteria for probable CBD were excluded.

Finally, 52 patients with Parkinson-plus were included (PSP, $n = 24$; CBD, $n = 9$; MSA, $n = 19$). For comparison, a group of 18 patients with Parkinson disease (PD) diagnosed according to the UK Parkinson's Disease Society Brain Bank clinical diagnostic criteria were used.[14] Furthermore, 15 otherwise healthy individuals, with no history of neurologic, psychiatric, or other major diseases and no signs of parkinsonism or cognitive dysfunction who were admitted to our department for nonrelevant issues (headache, dizziness, and so forth) served as a control group. Demographic data of our cohort are presented in Table 1.

Ethical Issues

All patients (or the next of kin caretaker in cases of compromised mental capacity) gave written informed consent for participation in the study, which was performed according to the ethics guidelines of the 1964 Declaration of Helsinki and had the approval of the Scientific and Ethics Committee of Eginition Hospital.

MR Imaging Acquisition

MR imaging was performed on a variety of high-field (1.5T to 3T) MR imaging units. The sequences included T1-weighted axial, sagittal, and coronal images or 3D T1-weighted turbo field echo sequences. MR imaging specifications were as follows: TR range, 500–650 ms; TE range, 10–15 ms; FOV range, 24–25 cm; matrix range, 192 × 256 to 320 × 320; section thickness, 1–5 mm; intersection spacing, 1 mm.

Midbrain, pons, and CC surfaces were measured at the midsagittal plane. Lines parallel to the mammillary–posterior commissural plane at the rostral and caudal pontine border were used to determine the midbrain and pons surfaces (Fig 1), according to the method of Kato et al.[15] Middle cerebellar peduncle width was measured parasagittally, and superior cerebellar peduncle width was measured coronally (On-line Fig 1), according to the method of Longoni et al.[16] The validity of the method has already been

Table 2: ROC curve analysis of the discriminative power of morphometric measurements in patients with PSP, MSA, and CBD compared with all other groups

	AUC (SD)	*P* Value	Cutoff Value	Sensitivity (%)	Specificity (%)	Likelihood Ratio
PSP vs all groups						
Midbrain	0.94 (0.03)	<.001	≤107	79	97	24.54
Midbrain/pons	0.93 (0.03)	<.001	≤0.22	88	84	5.42
Midbrain/CC	0.92 (0.04)	<.001	≤0.21	92	80	4.58
MRPI	0.98 (0.01)	<.001	>12.6	91	95	18.48
MSA (total) vs all groups						
Pons	0.74 (0.08)	.001	≤475	63	85	4.23
Midbrain/pons	0.86 (0.05)	<.001	≥0.29	74	90	7.05
MRPI	0.91 (0.04)	<.001	≤7.32	74	94	11.78
CBD vs all groups						
Corpus callosum	0.79 (0.09)	.004	≤470	67	95	12.33
$CC_{P\text{-}A\ grad}$	0.83 (0.10)	.002	≤191	75	97	25.12
Pons/$CC_{P\text{-}A\ grad}$	0.81 (0.08)	.003	≥2.22	89	71	2.98

Note:—AUC indicates area under the curve.

established as excellent, with low intra- and interrater variability of the measurements.[16-18] All surfaces were manually traced by G.V. with the DICOM viewer R3.0-Sp3 (Philips Healthcare, Best, the Netherlands).

CC subsections were determined according to the classification of Hofer and Frahm.[19] According to this classification, the CC can be subdivided into 5 sections (CC_1 to CC_5), which represent, from anterior to posterior, the following brain regions: 1) prefrontal cortex, 2) premotor and supplementary motor cortex, 3) primary motor cortex, 4) primary sensory cortex, and 5) parietal, occipital, and temporal cortices (On-line Fig 2). To optimize diagnostic accuracy, we calculated and compared various indices based on CC subsections. Of these indices, the CC posteroanterior gradient ($CC_{P\text{-}A\ grad}$) provided the greatest discriminative power and was therefore used. The $CC_{P\text{-}A\ grad}$ was calculated by subtracting the CC_1 subsection from the remaining CC subsections ($CC_{P\text{-}A\ grad} = CC_2 + CC_3 + CC_4 + CC_5 – CC_1$). The rationale behind the implementation of the $CC_{P\text{-}A\ grad}$ was the relatively selective (CC_2 to CC_4) atrophy in CBD, with a preserved CC_1 surface (On-line Fig 3).

The Fazekas periventricular and deep white matter hyperintensity score was used to measure while matter lesion burden.[20]

Statistical Analysis

Numeric variables were checked for normality and homogeneity of variances by the Shapiro-Wilk and Levene tests, respectively. Analysis of covariance, using the diagnosis, sex, and magnetic field strength (1.5T versus 3T) as co-factors and age as a covariate, followed by post hoc Bonferroni correction for multiple comparisons or the Kruskal-Wallis test (followed by the Dunn post hoc test), was used as appropriate. Receiver operating characteristic curve analysis was applied for determination of the diagnostic value of each biomarker.

Two sets of analyses were performed. Initially, each diagnostic group (PSP, MSA, and CBD) was compared with all other groups, to examine the utility of planimetry MR imaging markers in the clinical scenario of a patient with parkinsonism of unknown etiology. The second analysis included pair-wise comparison of diagnoses that can be difficult to differentiate in clinical practice (ie, PSP versus multiple system atrophy with parkinsonism [MSA-P] versus CBD versus PD).

Analyses were performed by SPSS Statistics, Version 22.0.0.0 (IBM, Armonk, New York; 2013) and GraphPad Prism, Version 5.03 (GraphPad Software, San Diego, California; 2009).

RESULTS

Clinical and Demographic Data

Groups did not differ among each other with respect to age and sex (Table 1). As expected, disease duration was significantly greater in those with PD compared with patients with Parkinson-plus. ANCOVA revealed significant effects by diagnostic group, but none of the cofactors and covariates affected the models significantly.

Planimetry Measurements

Patients with PSP exhibited significantly smaller midbrain surfaces compared with all other groups, resulting in smaller midbrain/CC and midbrain/pons ratios, as well as greater MRPI values (On-line Table). Furthermore, they presented with mild pons atrophy (numerically greater than MSA-P but lower than multiple system atrophy cerebellar type [MSA-C]).

Patients with MSA had smaller pons surfaces and pons-derived surface ratios as well as MRPI values. This difference came from patients with MSA-C because patients with MSA-P exhibited pons surfaces comparable with those of controls. Likewise, their midbrain and CC surfaces were like those of controls.

Patients with CBD had smaller CC surfaces compared with the other groups and numerically decreased midbrain surfaces (On-line Fig 4).

Comparison of Each Group versus All Other Groups

The MRPI provided excellent discriminative power for PSP versus all other groups, with a value of ≥12.6 providing 91% sensitivity and 95% specificity (Table 2 and On-line Fig 5). The MRPI was better compared with other indices for the differential diagnosis of MSA versus all other groups, with moderate sensitivity (74%) and excellent specificity (94%) for a cutoff point of ≤7.32.

The $CC_{P\text{-}A\ grad}$ with a cutoff point of ≤191 mm^2 provided 97% specificity and 75% sensitivity for the diagnosis of CBD. A CC surface of ≤470 mm^2 provided moderate sensitivity (67%) and excellent specificity (95%) for the diagnosis of CBD.

Pair-Wise Group Comparisons

The MRPI achieved very good discrimination between PSP and MSA-P with 100% specificity and sensitivity (Table 3). Likewise, the MRPI discriminated patients with PSP from those with PD with a sensitivity of 86% and a specificity of 100%. The midbrain/$CC_{P\text{-}A\ grad}$ ratio provided 86% sensitivity and 88% specificity in the differential diagnosis of PSP from CBD. No MR imaging measurement was clinically useful in differentiating patients with PD from those with MSA-P. The $CC_{P\text{-}A\ grad}$ provided moderate sensitivity and excellent specificity in the differential diagnosis of patients with CBD from those with PD (75% and 100%, respectively). Midbrain surface discriminated between patients with MSA-P and CBD with a sensitivity and specificity of 89%.

Table 3: Pair-wise analysis of the discriminative power of morphometric measurements with ROC curve analysis

	MRPI	Midbrain (mm^2)	Pons (mm^2)	CC (mm^2)	$CC_{P\text{-}A\ grad}$ (mm^2)	Midbrain/Pons	Midbrain/CC	Midbrain/$CC_{P\text{-}A\ grad}$	Pons/CC
PSP vs MSA-P									
Cutoff	≥11.0	≤129	NS	NS	NS	≤0.22	≤0.19	≤0.45	NS
Sens (%)	100	96				88	75	86	
Spec (%)	100	89				89	100	100	
PSP vs PD									
Cutoff	≥12.7	≤109	≤523	NS	NS	≤0.21	≤0.19	≤0.40	NS
Sens (%)	86	79	75			71	75	77	
Spec (%)	100	94	78			100	100	94	
PSP vs CBD									
Cutoff	≥13.7	≤100	NS	≥470	≥192	≤0.19	≤0.18	≤0.45	≥0.87
Sens (%)	73	71		92	91	67	71	86	46
Spec(%)	100	100		67	75	89	100	88	100
MSA-P vs PD									
Cutoff	≤8.0	NS	NS	NS	NS	NS	NS	NS	NS
Sens (%)	56								
Spec (%)	89								
CBD vs PD									
Cutoff	NS	≤146	≤563	≤479	≤193	NS	NS	NS	NS
Sens (%)		100	100	67	75				
Spec (%)		67	56	94	100				
MSA-P vs CBD									
Cutoff	≤11.0	≥129	NS	≥478	≥199	NS	NS	NS	NS
Sens (%)	100	89		89	100				
Spec (%)	63	89		67	75				

Note:—NS indicates not significant; Sens, sensitivity; Spec, specificity; ROC, receiver operating characteristic.

DISCUSSION

The present study aimed at examining the utility of MR imaging planimetry measurements as surrogate markers of midbrain, pons, and CC atrophy, in the differential diagnosis of patients with Parkinson-plus syndrome.

Patients with PSP in our cohort were characterized by severe midbrain and, to a lesser extent, pons atrophy. Of the patients with MSA, only those with MSA-C presented with pons atrophy. On the contrary, patients with MSA-P were not characterized by pons atrophy. Patients with CBD had predominantly CC atrophy and mild midbrain atrophy. Patients with PD did not differ from control subjects.

Most studies support midbrain and superior cerebellar peduncle atrophy as predominant features in patients with PSP.[21,22] This translates into a significantly higher MRPI and lower midbrain-to-pons surface ratio values in patients with PSP.[10,23,24] The MRPI was indeed the most potent imaging marker for the differential diagnosis of PSP from all other groups in our cohort. This also applied to the differential diagnosis of PSP from MSA-P or PD. It has been reported that these imaging findings are present early in the disease course of patients with PSP, often before the complete clinical phenotype of Richardson syndrome is evident.[21,22,25] This finding renders the MRPI and midbrain-to-pons surface ratio useful in the early differentiation of patients with PSP from those with MSA-P and PD.

Low MRPI values have been suggested to further aid in the differential diagnosis of MSA from other causes of parkinsonism.[17,26-28] In our cohort, low MRPI values were moderately sensitive (74%) and highly specific (94%) in the differentiation of patients with MSA from all other groups. This however was due to the inclusion of patients with MSA-C in the MSA group. These patients have particularly low MRPI values, due to pronounced pons and middle cerebellar peduncle atrophy. After we excluded patients with MSA-C, the MRPI was not clinically useful in the differential diagnosis of patients with MSA-P from those with PD or CBD. Thus, we could not establish the utility of the MRPI in the discrimination of patients with MSA-P from other patients with parkinsonism, except for PSP. Considering that patients with MSA-C are rarely confused with other patients with Parkinson-plus, due to their predominant cerebellar symptoms, low MRPI values may not provide clinically relevant assistance in most cases.

Patients with CBD in our cohort had decreased CC surfaces compared with other groups. A low (<470 mm^2) corpus callosum surface was highly specific (95%) for CBD but lacked sensitivity (67%). This finding is in agreement with a single planimetry study that demonstrated CC atrophy in patients with CBD compared with PSP, with substantial between-group overlap however.[29] CC subsection analysis indicated a posteroanterior CC atrophy gradient in CBD, with relative preservation of the CC1 segment (prefrontal cortex). PSP, on the other hand, had more pronounced anterior CC atrophy. This generated the $CC_{P\text{-}A\ grad}$, which provided improved sensitivity (75%) and specificity (97%) in the diagnosis of CBD versus all other groups. The $CC_{P\text{-}A\ grad}$ was superior to all other indices in the differentiation of CBD from PD, with excellent specificity (100%) and moderate sensitivity (75%). Furthermore, the midbrain/$CC_{P\text{-}A\ grad}$ ratio was superior to the MRPI in the differential diagnosis of PSP from CBD (sensitivity 86%, specificity 88%).

Most planimetry studies of Parkinson-plus syndromes in the field lack pathologic confirmation, as is the case with our study. To compensate for the problem, we exclusively included prospectively diagnosed patients who fulfilled the "probable" diagnostic criteria. To keep the possibility of misdiagnosis as low as possible, all patients were followed up for at least 2 years. None of the patients presented with any atypical clinical features during this

period. Furthermore, we used CSF biochemical profile analysis to exclude patients with an underlying Alzheimer disease pathology.

The sample size of our cohort is moderate, as is expected for diseases as rare as Parkinson-plus syndromes, but comparable with most studies on the subject. Intra- and interrater agreement of MR imaging surface measurements was not tested in the present study because it has already been proved excellent in previous studies.[17,22,25,28]

Further studies of larger cohorts of patients with Parkinson-plus syndrome, incorporating clinical, imaging, and pathologic data, would assist in further elucidating the complex interaction among underlying pathology, atrophy profile, and clinical phenotype. These studies could examine the utility of more focused planimetry markers, which take into account the topographic selectivity of atrophy (such as the $CC_{P\text{-}A\ grad}$).

CONCLUSIONS

MR imaging planimetry can facilitate the differential diagnosis of patients with parkinsonism. Midbrain surface and relevant indices (such as the MRPI) are already established markers of PSP. Likewise, corpus callosum surface indices are promising markers of CBD. MR imaging planimetry, however, does not assist in the differential diagnosis of MSA-P from PD.

REFERENCES

1. Rolland Y, Vérin M, Payan C, et al; NNIPPS Study Group. **A new MRI rating scale for progressive supranuclear palsy and multiple system atrophy: validity and reliability.** *J Neurol Neurosurg Psychiatry* 2011; 82:1025–32 CrossRef Medline
2. Respondek G, Roeber S, Kretzschmar H, et al. **Accuracy of the National Institute for Neurological Disorders and Stroke/Society for Progressive Supranuclear Palsy and neuroprotection and natural history in Parkinson plus syndromes criteria for the diagnosis of progressive supranuclear palsy.** *Mov Disord* 2013;28:504–09 CrossRef Medline
3. Osaki Y, Ben-Shlomo Y, Lees AJ, et al. **A validation exercise on the new consensus criteria for multiple system atrophy.** *Mov Disord* 2009;24:2272–76 CrossRef Medline
4. Armstrong MJ, Litvan I, Lang AE, et al. **Criteria for the diagnosis of corticobasal degeneration.** *Neurology* 2013;80:496–503 CrossRef Medline
5. Hauw JJ, Daniel SE, Dickson D, et al. **Preliminary NINDS neuropathologic criteria for Steele-Richardson-Olszewski syndrome (progressive supranuclear palsy).** *Neurology* 1994;44:2015–19 CrossRef Medline
6. Yamauchi H, Fukuyama H, Nagahama Y, et al. **Atrophy of the corpus callosum, cognitive impairment, and cortical hypometabolism in progressive supranuclear palsy.** *Ann Neurol* 1997;41:606–14 CrossRef Medline
7. Wenning GK, Tison F, Ben Shlomo Y, et al. **Multiple system atrophy: a review of 203 pathologically proven cases.** *Mov Disord* 1997;12: 133–47 CrossRef Medline
8. Dickson DW, Bergeron C, Chin SS, et al; Office of Rare Diseases of the National Institutes of Health. **Office of Rare Diseases neuropathologic criteria for corticobasal degeneration.** *J Neuropathol Exp Neurol* 2002;61:935–46 CrossRef Medline
9. Yamauchi H, Fukuyama H, Nagahama Y, et al. **Atrophy of the corpus callosum, cortical hypometabolism, and cognitive impairment in corticobasal degeneration.** *Arch Neurol* 1998;55:609–14 CrossRef Medline
10. Quattrone A, Nicoletti G, Messina D, et al. **MR imaging index for differentiation of progressive supranuclear palsy from Parkinson disease and the Parkinson variant of multiple system atrophy.** *Radiology* 2008;246:214–21 CrossRef Medline
11. Litvan I, Agid Y, Calne D, et al. **Clinical research criteria for the diagnosis of progressive supranuclear palsy (Steele-Richardson-Olszewski syndrome): report of the NINDS-SPSP international workshop.** *Neurology* 1996;47:1–9 CrossRef Medline
12. Gilman S, Wenning GK, Low PA, et al. **Second consensus statement on the diagnosis of multiple system atrophy.** *Neurology* 2008;71: 670–76 CrossRef Medline
13. Paraskevas GP, Kasselimis D, Kourtidou E, et al. **Cerebrospinal fluid biomarkers as a diagnostic tool of the underlying pathology of primary progressive aphasia.** *J Alzheimers Dis* 2017;55:1453–61 CrossRef Medline
14. Hughes AJ, Daniel SE, Kilford L, et al. **Accuracy of clinical diagnosis of idiopathic Parkinson's disease: a clinico-pathological study of 100 cases.** *J Neurol Neurosurg Psychiatry* 1992;55:181–84 CrossRef Medline
15. Kato N, Arai K, Hattori T. **Study of the rostral midbrain atrophy in progressive supranuclear palsy.** *J Neurol Sci* 2003;210:57–60 CrossRef Medline
16. Longoni G, Agosta F, Kostić VS, et al. **MRI measurements of brainstem structures in patients with Richardson's syndrome, progressive supranuclear palsy-parkinsonism, and Parkinson's disease.** *Mov Disord* 2011;26:247–55 CrossRef Medline
17. Cosottini M, Ceravolo R, Faggioni L, et al. **Assessment of midbrain atrophy in patients with progressive supranuclear palsy with routine magnetic resonance imaging.** *Acta Neurol Scand* 2007;116: 37–42 CrossRef Medline
18. Morelli M, Arabia G, Salsone M, et al. **Accuracy of magnetic resonance parkinsonism index for differentiation of progressive supranuclear palsy from probable or possible Parkinson disease.** *Mov Disord* 2011;26:527–33 CrossRef Medline
19. Hofer S, Frahm J. **Topography of the human corpus callosum revisited; comprehensive fiber tractography using diffusion tensor magnetic resonance imaging.** *Neuroimage* 2006;32:989–94 CrossRef Medline
20. Fazekas F, Chawluk JB, Alavi A. **MR signal abnormalities at 1.5 T in Alzheimer's dementia and normal aging.** *AJR Am J Roentgenol* 1987; 8:421–26 CrossRef Medline
21. Aiba I, Hashizume Y, Yoshida M, et al. **Relationship between brainstem MRI and pathological findings in progressive supranuclear palsy: study in autopsy cases.** *J Neurol Sci* 1997;152:210–17 CrossRef Medline
22. Slowinski J, Imamura A, Uitti RJ, et al. **MR imaging of brainstem atrophy in progressive supranuclear palsy.** *J Neurol* 2008;255:37–44 CrossRef Medline
23. Hussl A, Mahlknecht P, Scherfler C. **Diagnostic accuracy of the magnetic resonance Parkinsonism index and the midbrain-to-pontine area ratio to differentiate progressive supranuclear palsy from Parkinson's disease and the Parkinson variant of multiple system atrophy.** *Mov Disord* 2010;25:2444–49 CrossRef Medline
24. Kim YH, Ma HI, Kim YJ. **Utility of the midbrain tegmentum diameter in the differential diagnosis of progressive supranuclear palsy from idiopathic Parkinson's disease.** *J Clin Neurol* 2015;11:268–74 CrossRef Medline
25. Morelli M, Arabia G, Novellino F, et al. **MRI measurements predict PSP in unclassifiable parkinsonisms: a cohort study.** *Neurology* 2011;77:1042–47 CrossRef Medline
26. Massey LA, Jäger HR, Paviour DC, et al. **The midbrain to pons ratio: a simple and specific MRI sign of progressive supranuclear palsy.** *Neurology* 2013;80:1856–61 CrossRef Medline
27. Kaasinen V, Kangassalo N, Gardberg M, et al. **Midbrain-to-pons ratio in autopsy-confirmed progressive supranuclear palsy: replication in an independent cohort.** *Neurol Sci* 2015;36:1251–53 CrossRef Medline
28. Oba H, Yagishita A, Terada H, et al. **New and reliable MRI diagnosis for progressive supranuclear palsy.** *Neurology* 2005;64:2050–55 CrossRef Medline
29. Gröschel K, Hauser T-K, Luft A, et al. **Magnetic resonance imaging-based volumetry differentiates progressive supranuclear palsy from corticobasal degeneration.** *Neuroimage* 2004;21:714–24 CrossRef Medline

Dark Rims: Novel Sequence Enhances Diagnostic Specificity in Multiple Sclerosis

J.-M. Tillema, S.D. Weigand, M. Dayan, Y. Shu, O.H. Kantarci, C.F. Lucchinetti, and J.D. Port

ABSTRACT

BACKGROUND AND PURPOSE: The 2010 McDonald criteria are designed to sensitively detect MS; however, the low specificity of these criteria can occasionally lead to the misdiagnosis of MS. The purpose of this study was to determine whether a novel double inversion recovery MR imaging technique has the potential to increase the specificity of diagnostic criteria distinguishing MS from non-MS white matter lesions.

MATERIALS AND METHODS: This was a cross-sectional observational study. MR imaging data were acquired between 2011 and 2016. A novel double inversion recovery sequence that suppresses CSF and GM signal was used (GM-double inversion recovery). We compared WM lesions in a group of patients with multiple sclerosis and in a second group of positive controls with white matter lesions who did not have a diagnosis of MS. The presence of a rim on the GM-double inversion recovery MR imaging sequence was combined with the 2001 and 2010 McDonald disseminated-in-space criteria. Multiple MR imaging markers, including lesion location, size, and the presence of a rim, were compared between groups as well as a quantitative measure of lesion T1 hypointensity.

RESULTS: MR images from 107 patients with relapsing-remitting MS (median age, 32 years) and 36 positive control (median age, 39 years) subjects were analyzed. No significant differences were found in age and sex. In patients with MS, 1120/3211 lesions (35%) had a rim on GM-double inversion recovery; the positive control group had only 9/893 rim lesions (1%). Rims were associated with a decrease in the lesion T1 ratio. Using the 2010 MR imaging criteria plus the presence of rims on GM-double inversion recovery, we achieved 78% and 97% specificity in subjects with ≥1 and ≥2 rim lesions, respectively.

CONCLUSIONS: The addition of a novel GM-double inversion recovery technique enhanced specificity for diagnosing MS compared with established MR imaging criteria.

ABBREVIATIONS: DIR = double inversion recovery; DIS = dissemination in space; EDSS = Expanded Disability Status Scale; IQR = interquartile range; PC = positive control

MR imaging has had a central role in the early diagnosis of multiple sclerosis. When applied in the appropriate clinical context, the McDonald criteria[1] are able to sensitively detect MS, especially compared with the prior diagnostic criteria.[2] The 2010 revisions to the McDonald criteria were intended to capture MS earlier, because studies revealed that early conversion from clinically isolated syndrome to MS could be predicted by simplification and additional weighting of the MR imaging criteria.[3]

Despite these well-validated diagnostic criteria, their specificity remains suboptimal, especially when the pretest probability is low: for example, when the clinical presentation is atypical, when radiologic criteria are inappropriately applied to scenarios in which the clinical presentation is inconsistent with clinically isolated syndrome, or in cases of radiologically isolated syndrome. This low specificity can lead to the potential misdiagnosis of MS, which has been identified as a significant clinical problem.[4] A survey reported that misdiagnosis and subsequent treatment of MS had been seen in at least 1 case in the previous year by >90% of partici-

Received October 27, 2017; accepted after revision February 10, 2018.

From the Departments of Neurology (J.-M.T., M.D., O.H.K., C.F.L.), Health Sciences Research (S.D.W.), and Radiology (Y.S., J.D.P.), Mayo Clinic, Rochester, Minnesota.

Mayo Clinic has filed a patent on behalf of J.-M.T., Y.S., C.F.L., and J.D.P. that is broadly relevant to this work. Specifically, the GM-DIR sequence described in the patent was used for this study.

This publication was supported by grant No. KL2 TR000136 (National Center for Advancing Translational Sciences) and W81XWH-13–1-0098 (Department of Defense).

The views herein are solely the responsibility of the authors and do not necessarily represent the official views of the National Institutes of Health.

Please address correspondence to Jan-Mendelt Tillema, MD, Department of Neurology, Mayo Clinic, 200 First St SW, Rochester, MN 55901; e-mail: tillema.janmendelt@mayo.edu

Indicates open access to non-subscribers at www.ajnr.org

Indicates article with supplemental on-line tables.

Indicates article with supplemental on-line photo.

http://dx.doi.org/10.3174/ajnr.A5636

pating neurologists.[4] Another recent study reviewed the spectrum of 110 possible cases of misdiagnosed MS.[5]

These studies found that a significant contributing factor to the misdiagnoses was overreliance on the interpretation of abnormal findings on MR imaging. MR imaging–based studies in patients presenting with abnormal findings on MRIs revealed that when 2001 and/or 2010 MR imaging dissemination-in-space (DIS) criteria were (perhaps inappropriately) applied, the specificity of these criteria was not as robust as the sensitivity.[6,7] Therefore, while the diagnostic MR imaging criteria are helpful and sensitive, they were not designed to facilitate the differentiation of MS from other conditions, and specificity remains a significant concern in the clinic.

To address this problem, prior studies have added MR imaging sequences to conventional MR imaging protocols,[8] including SWI, T2* imaging,[9] and 7T field strength,[10,11] yielding interesting sequences for future studies. Recently proposed revisions to the existing MRI criteria[12] may further enhance diagnostic accuracy, still to be confirmed in larger studies. Despite these revisions, the clinical need for a reliable imaging marker specific for MS remains unmet.

In the current study, we applied a novel inversion recovery sequence (gray matter double inversion recovery [GM-DIR]) designed to suppress MR signal from both gray matter and CSF. This was used in conjunction with a clinical routine DIR, which suppresses white matter and CSF signal. We observed that white matter lesions in subjects with MS have dark rims on the GM-DIR. We specifically addressed the question of whether the presence of a "rim lesion" on GM-DIR can differentiate patients with MS from those without MS who have white matter lesions of other etiologies.

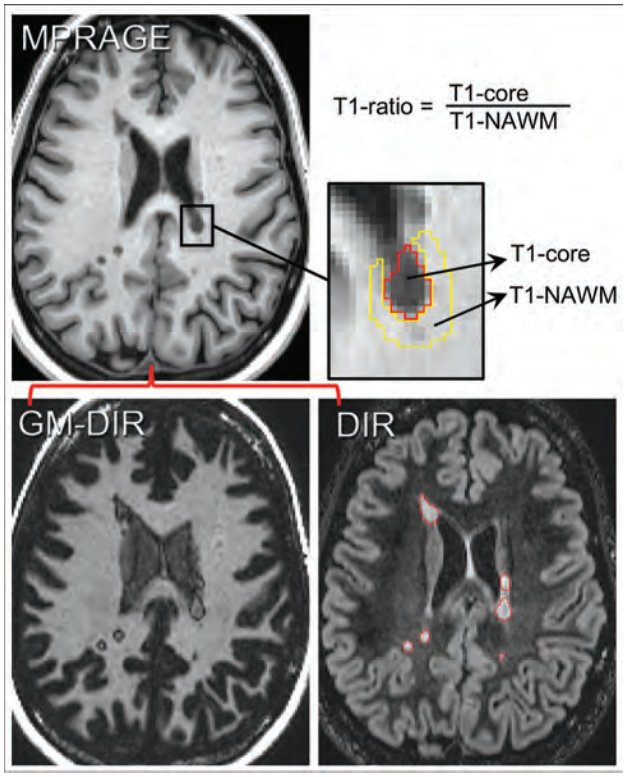

FIG 1. Method for determining the T1 ratio. First GM-DIR and DIR images are coregistered to the MPRAGE images. Next, lesions are manually segmented on DIR images (*red lines* surround individual lesions). The signal intensity within the lesion (T1 core) and outside of the lesion (T1 normal-appearing WM) is measured, and the T1 ratio is computed from those intensity values as shown.

MATERIALS AND METHODS

Subjects

After institutional review board approval, subjects seen at our MS center (Mayo Clinic, Rochester, Minnesota) were enrolled. All subjects provided written informed consent. The inclusion criteria for the MS subject cohort were patients of any age with relapsing-remitting MS, applying the 2010 McDonald criteria. Effort was made to recruit those with early MS, but disease duration was not used as an exclusion criterion. The inclusion criteria for the positive control (PC) subject cohort were the presence of T2 hyperintensities noted on an available routine clinical MR imaging scan and no clinical diagnosis of MS. To better match subjects with MS, we restricted positive controls with small-vessel disease to younger than 65 years of age. The exclusion criterion for both cohorts was the inability to obtain a nonsedated MR image.

Clinical Information

Patient characteristics at MR imaging were obtained by performing a comprehensive review of the medical record. PC subjects were identified via automated review of radiology reports and neurology clinics. Abstracted clinical information included the reason for performing the MR imaging, differential diagnostic considerations, and final diagnosis. In some cases, demyelinating disease remained in the differential diagnosis, but subjects did not meet the clinical criteria for MS. Therefore, we split the 2 positive control groups: 1) "definite" PCs, in which demyelinating disease was ruled out, and 2) "indeterminate" PCs, in which clinical, laboratory, or imaging findings suggested possible demyelinating disease, not fitting the MS criteria. After enrollment, 3 indeterminate subjects had converted to MS. However, for the analysis, they remained in the PC-indeterminate category (as opposed to reclassifying them as having MS).

MR Imaging Acquisition

Dedicated MR imaging research scans were prospectively acquired on either a 3T Discovery MR750 (8-channel head coil) (GE Healthcare, Milwaukee, Wisconsin) or a 3T Skyra scanner (32-channel head coil) (Siemens, Erlangen, Germany). Volumetric 1.0-mm isotropic-resolution sequences included GM-DIR, MPRAGE, and standard DIR (representative images are shown in Fig 1). Detailed sequence parameters are listed in On-line Table 1.

MR Imaging Processing

All steps were completed using FreeSurfer (Version 5.3.0; http://surfer.nmr.mgh.harvard.edu),[13,14] FSL (Version 5.0.8; http://www.fmrib.ox.ac.uk/fsl),[15,16] and in-house-created lesion-scoring software. Processing steps included the following: 1) registration of standard DIR and GM-DIR images to MPRAGE (boundary-based registration),[16] 2) detecting and outlining white matter lesions on the T2-weighted standard DIR imaging, 3) obtaining quantitative lesion metrics from both DIR and T1-weighted MPRAGE imaging (vol-

ume, T1-signal change), and 4) scoring lesion characteristics (location and GM-DIR rim).

All lesions were detected and measured on standard DIR images using a seed-growing semiautomated approach in MRIcron (http://www.nitrc.org/projects/mricron/),[17] saving binary masks for each lesion. Next, for each individual lesion, volume and T1 hypointense signal change were abstracted from the T1-weighted MPRAGE images, and a T1 ratio was calculated (methods detailed in Fig 1). Briefly, the mean T1 signal intensity within the lesion (T1 core) was measured by eroding 1 voxel. If eroding left no core volume (eg, very small lesions), the lesion was omitted from correlation analysis between the T1 measure and rim presence but was incorporated in the final lesion counts. The T1 normal-appearing WM measure was from surrounding white matter by 2 cycles of dilating the outer border of the lesion, restricted to white matter only. T1 ratios were calculated by dividing the T1 core by T1 normal-appearing WM values, reflecting the amount of lesion T1 hypointensity.

Lesion-Characteristic Scoring

Each lesion was reviewed and independently scored by 2 raters blinded to the diagnosis (J.-M.T., J.D.P.), using in-house-created lesion-scoring software. We recorded lesion location (juxtacortical, deep white matter, periventricular, infratentorial) and the presence/absence of GM-DIR rims. "Lesion rim" was defined as having a thin hypointense rim around the lesion that was complete and visible in all 3 planes; incomplete rims were tabulated as "no rim." Consensus was met on all lesions in a joint reviewing session.

Table 1: Demographic and clinical features

Characteristic	MS (n = 107)	PC (n = 36)	P
Sex (No.) (%)			.78
Female	74 (69%)	24 (67%)	
Male	33 (31%)	12 (33%)	
Age (yr)			.36
Median (IQR)	32 (17–43)	39 (15–54)	
Range	9–60	8–74	
Age group (No.) (%)			.42
Pediatric	31 (29%)	13 (36%)	
Adult	76 (71%)	23 (64%)	
Clinical course (No.) (%)			–
RRMS	107 (100%)	0	
Possible PC	0	10 (28%)	
Definite PC	0	26 (72%)	
Disease duration (yr)			
Median (IQR)	4 (1–8)	–	
Range	0–33	–	
EDSS score			–
Median (IQR)	1.5 (1.0–2.0)	–	
Range	0.0–6.0	–	

Note:—RRMS indicates relapsing-remitting MS.

Table 2: Diagnosis distribution for positive control subjects

PC Diagnosis	PC Definite (No.) (%)	PC Indeterminate (No.) (%)	PC Total (No.) (%)
Nonspecific (vascular, migraine)	20 (77)	9 (90)	29 (81)
Ischemic/cerebrovascular	1 (4)	0	1 (3)
Tumor	2 (8)	2 (20)	4 (11)
Leukoencephalopathy/diffuse WM disease	2 (8)	0	2 (6)
Possible demyelinating	0	10 (100)	10 (28)
Other inflammatory	8 (31)	1 (10)	9 (25)

Statistical Analysis

Descriptive statistics were used to summarize patient demographics and MR imaging measures. We analyzed MR imaging characteristics by calculating patient-level summary statistics: the total number and volume of lesions, median lesion volume, and number and fraction of rim lesions. Sensitivity, specificity, and predictive values were obtained using the 2001 and 2010 McDonald MR imaging criteria,[1,2] both without and with the addition of the presence of rims. In subjects in whom the DIS criteria were not met, clinically obtained spinal cord imaging (available in all) was reviewed to assure that no additional lesions would make those subjects fulfill the DIS criteria. Similarly, each case meeting the 2001 MRI criteria was reviewed for additional strict radiologically isolated syndrome criteria by an experienced reviewer (O.H.K.).[18]

In patients with MS, rank correlations were calculated between the Expanded Disability Status Scale (EDSS) and the number of rim lesions per patient. A penalized logistic regression model with clinical group as the outcome (MS versus PC) was used to obtain overall and region-specific estimates of the relative odds of MS for those with-versus-without rims. Models were adjusted for age, sex, total number of lesions, and median lesion size. We used penalization to stabilize odds ratio estimates and to reduce potential sparse-data bias.[19]

RESULTS

Subjects

One hundred eight patients with relapsing-remitting MS and 38 positive controls were enrolled. One of the subjects with MS was excluded because the clinical course fit that of primary-progressive disease. Excessive motion was present in 2 PC subjects, leaving 107 relapsing-remitting MS and 36 PC subjects.

Demographic and clinical information is summarized in Tables 1 and 2. The PC group had a slightly higher median age (39 versus 32 years), but no significant differences were found in age and sex. A comparable number of pediatric patients (defined as 18 years of age or younger) were in both the MS and PC groups (29% versus 36%, $P = .42$), and age distribution was not significantly different. Of the PCs, 26 were classified as definite and 10 as indeterminate. The most likely diagnostic consideration was reported (multiple diagnoses possible), most commonly including "nonspecific" leukoaraiosis or possible migraine-related changes. Of the possible demyelinating cases, 3 had solitary lesions. These were either periventricular or juxtacortical with imaging characteristics suggestive of demyelinating disease. None of the PCs fulfilled the strictly applied more extensive radiologically isolated syndrome criteria.[18]

We reviewed 4104 lesions: 3211 lesions in 107 subjects with MS subjects and 893 lesions in the PC group ($n = 36$). In the MS group, 1120/3211 lesions (35%) had a rim, but only 9/893 lesions (1%) in the PC group had a rim. Figures 2 and 3 show representative rim lesion images.

The On-line Figure shows lesion volumes and T1 ratios in both groups. Rim lesions were larger than non-rim lesions: median lesion volume, 130 mm^3 (interquartile range [IQR], 73–285 mm^3)

for rim lesions versus 40 mm^3 (IQR, 23–76 mm^3) for non-rim lesions ($P < .001$). The median T1 ratio in MS lesions without a rim was 0.85 (IQR, 0.80–0.89) versus 0.72 (IQR, 0.67–0.78) in MS lesions with a rim ($P < .001$). PC rim lesions, though only 9 in total, had a median T1 ratio of 0.77 (IQR, 0.73–0.79) compared with 0.86 (IQR, 0.82–0.90) without a rim. Rims were more likely in larger lesions and cases with a higher lesion load (rank correlation, 0.77 and 0.78, respectively; both, $P < .001$).

Subject-level lesion distribution is summarized in On-line Table 2. No significant differences were seen in lesion count (20 lesions for both groups; $P = .22$) or lesion volume per subject (2.6 cm^3 for MS versus 2.1 cm^3 for PC, $P = .79$). Median lesion size in MS was larger, also not significant (62 versus 48 mm^3, $P = .08$). Subjects with MS had a median of 5 lesions (IQR, 2–13 lesions) with rims per subject versus 0 (IQR, 0–0) in PCs ($P < .001$). None of the definite PC subjects had a rim lesion. In the indeterminate group, 7/10 subjects had a single rim lesion and 1 subject had 2 rim lesions. The median fraction of lesions that were rim lesions per patient was 33% in MS, but <1% in PC subjects. At least 1 rim lesion was found in 104/107 (97%) subjects with MS and only 8/36 (22%) PC subjects.

On-line Table 3 shows the regional distribution of lesions. In positive controls, rim lesions were found only in the juxtacortical and periventricular white matter, and none in deep white matter, the most common (48%) site of PC lesions. Having ≥1 rim lesion was associated with a >10-fold increase in the odds of MS after accounting for age, sex, total number of lesions, and the subject's median lesion size. These greatly elevated odds ratios were calculated using penalized logistic regression, a method that was chosen to provide more reliable estimates by reducing bias and artifactual associations.

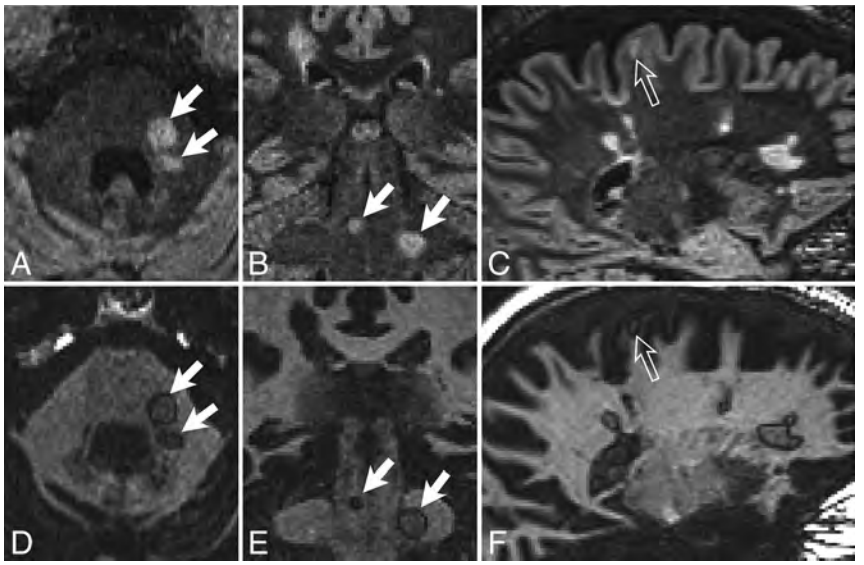

FIG 2. Examples of typical white matter lesions in subjects with MS. DIR images (*A–C*) and GM-DIR images (*D–F*) are shown for 2 different subjects with MS (*A*, *B*, *D*, *E*; *C* and *F*). Note the thin, single-pixel-wide dark rim surrounding most lesions on the GM-DIR images. Rims appear the same regardless of location (infratentorial, *white arrows*; juxtacortical, *open arrows;* periventricular, unlabeled).

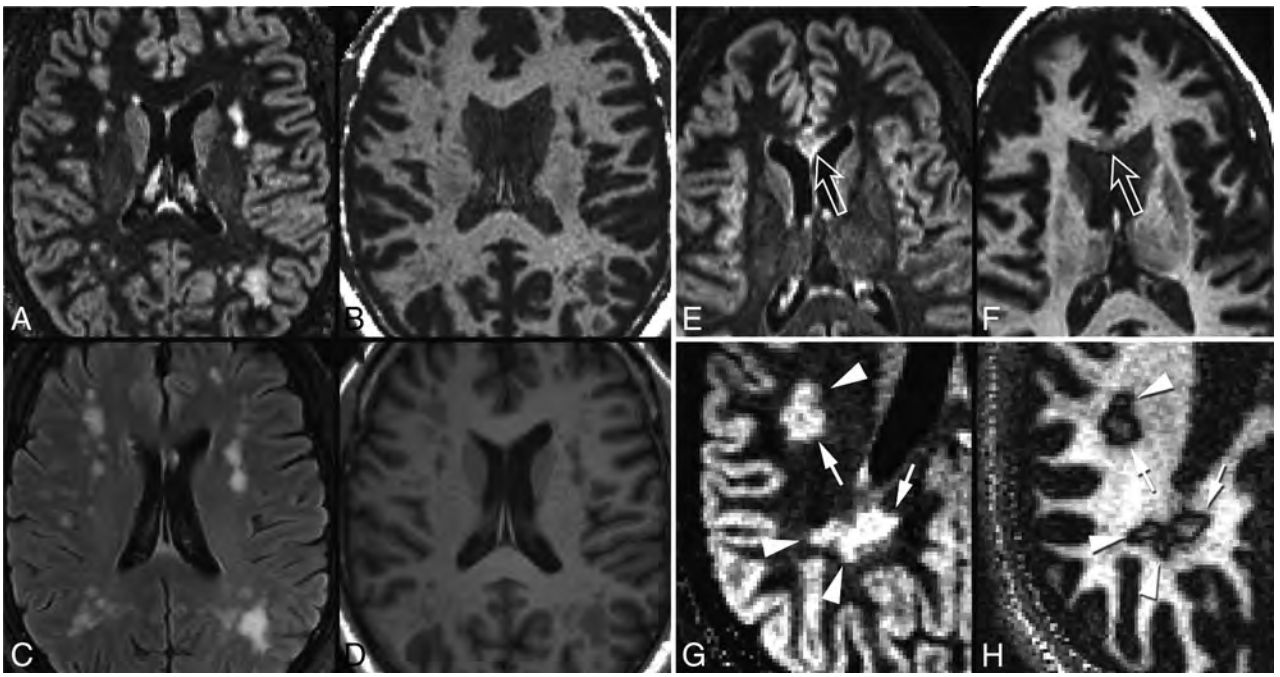

FIG 3. Examples of PC subjects without rim lesions, and "daughter lesions." One PC subject with small-vessel disease (*A*, DIR; *B*, GM-DIR; *C*, T2 FLAIR; *D*, T1) shows typical juxtacortical and deep white matter lesions. Note the lack of rims around these lesions on GM-DIR. Another PC subject (*E*, DIR; *F*, GM-DIR) with neuromyelitis optica has a demyelinating corpus callosum lesion (*open arrows*) that also lacks a rim. One subject with MS (*G*, DIR; *H*, GM-DIR) shows typical conglomerate lesions on DIR imaging. GM-DIR imaging better demonstrates the separation and outline of smaller lesions (*arrowheads*) from larger lesions (*arrows*).

Table 3: Sensitivity and specificity for various MRI criteria with or without rim lesions

Criteria	% Subjects with MS	% Total PC Subjects	% Indeterminate PC Subjects	% Definite PC Subjects	Sensitivity[a]	Specificity[a]
Rim lesions alone						
1+ rim	97% (104/107)	22% (8/36)	80% (8/10)	0% (0/26)	97%	78%
2+ rims	88% (94/107)	3% (1/36)	10% (1/10)	0% (0/26)	88%	97%
Involving DIS 2001[1]						
MRI-DIS only	77% (82/107)	44% (16/36)	20% (2/10)	54% (14/26)	77%	56%
MRI-DIS + 1+ rim	76% (81/107)	6% (2/36)	20% (2/10)	0% (0/26)	76%	94%
MRI-DIS + 2+ rims	71% (76/107)	0% (0/36)	0% (0/10)	0% (0/26)	71%	100%
MRI-DIS + 3+ rims	65% (70/107)	0% (0/36)	0% (0/10)	0% (0/26)	65%	100%
Involving DIS 2010[2]						
MRI-DIS only	100% (107/107)	83% (30/36)	60% (6/10)	92% (24/26)	100%	17%
MRI-DIS + 1+ rim	97% (104/107)	17% (6/36)	60% (6/10)	0% (0/26)	97%	83%
MRI-DIS + 2+ rims	88% (94/107)	3% (1/36)	10% (1/10)	0% (0/26)	88%	97%
MRI-DIS + 3+ rims	73% (78/107)	0% (0/36)	0% (0/10)	0% (0/26)	73%	100%

[a] Based on the total PC group.

Table 3 summarizes the potential diagnostic use of rim lesions by comparing them with the sensitivity of the standard diagnostic DIS criteria. The presence of ≥1 rim lesion had a sensitivity of 97% and specificity of 78%; the presence of ≥2 rim lesions decreased the sensitivity to 88%, while specificity increased to 97%. In contrast, applying standard MR imaging criteria alone had a low specificity (56% for the 2001 criteria, 17% for the 2010 criteria). Adding the requirement of ≥1 rim to the 2001 criteria improved the specificity to 94%, while adding this to the 2010 criteria kept the high sensitivity (97%) and increased the specificity to 83%. Most important, the positive and negative predictive values were greatly increased when rim information was added to the MR imaging DIS criteria: The positive predictive value increased from 75% to 94% with the 2010 criteria plus ≥1 rim lesion, and negative predictive value increased from 35% to 91% with this addition.

During the study, 3 of the indeterminate PC subjects eventually developed a diagnosis of MS. One developed a progressive course, and the other 2 patients developed new lesions on follow-up MR imaging. The only subject in the PC group with 2 rim lesions had an imaging pattern that was thought atypical for MS, with predominantly deep white matter lesions. Despite having 30 lesions, this subject did not meet the 2001 radiologically isolated syndrome criteria and had no other CSF/spinal cord abnormalities.

Not all lesions in patients with MS had a rim. We performed correlations between the EDSS score and rim presence, despite relatively early disease (median disease duration, 3 years) and disability (median EDSS score, 1.5). The rank correlation was only weakly positive at 0.20 for the EDSS score and the number of rim lesions ($P = .04$). Disease duration had no significant effect on the presence of rim lesions.

DISCUSSION

Our findings strongly suggest that the rim lesions detected using our novel GM-DIR MR imaging sequence could improve the specificity of an MS diagnosis. Specifically, the presence of a hypointense rim around demyelinating lesions was highly sensitive and specific for MS. Only 3/107 patients with MS lacked lesions with a typical rim, but all had typical attacks and lesions. In contrast, the PC cohort included only a single case with 2 rim lesions; no subject had more. Overall, the addition of this MR imaging marker increased the specificity from 17% to 78% when ≥1 rim lesion was present and to 97% when ≥2 lesions were present.

This MR imaging marker could be very helpful in clinical scenarios in which differentiation of MS from other conditions is not straightforward. The current MR imaging criteria for dissemination in space and time are highly sensitive for detecting MS and reliably diagnosing patients who present with an initial demyelinating event (clinically isolated syndrome). However, in less clear-cut clinical presentations, the question often arises as to whether the presentation fits that of demyelinating disease. The misdiagnosis of MS is not entirely uncommon, and overreliance on MR imaging measures is often a culprit.[4,5] Better and more reliable MR imaging markers therefore could not only prevent unnecessary treatment but could also potentially limit subsequent MR imaging studies and unnecessary anxiety.[6,20]

GM-DIR rims have a characteristic "pencil thin" appearance at the junction of the lesion and adjacent normal-appearing white matter (Figs 2 and 3). We hypothesized that rims arise from a well-known artifact of inversion recovery sequences, the opposed-magnetization (or bounce point) artifact.[21,22] This phenomenon creates a 1-pixel-wide dark band at the boundaries of tissues with significantly different T1 relaxation times. This idea is supported by the fact that the T1 ratios in our subjects were lower in lesions with rims (On-line Figure), indicating a significant difference in T1 relaxation times between the core of the lesion and the surrounding normal-appearing WM. Detecting these rim "artifacts" on GM-DIR images is straightforward and would be quite practical in a busy clinical setting.

Others have detected rims around MS lesions using various MR imaging techniques (eg, susceptibility-weighted imaging, 7T MR imaging),[10,23,24] albeit not at the numbers and magnitude we report. These previous studies have postulated that iron or other metals accumulate within microglia and macrophages on the edge of slowly expanding (or smoldering) lesions.[23] This phenomenon could very well be another explanation of the rims seen in our study, but most of our data are from the early MS course when smoldering lesions are typically not expected.[25] Unfortunately, we did not have SWI available in all cases. Prior studies have shown that 10%–15% of MS lesions have iron accumulation at the edge,[23,26] which is lower than the frequency of our rim detection. Additional studies are needed to determine whether detected rims

are the consequence of opposed magnetization effects due to iron deposition or explained by other mechanisms. We noted heterogeneity of the signal change within lesions on GM-DIR but no presence of a central vein sign that has been described in SWI and T2* techniques.[9,11,27-30] If the rim we observed was suspected to be due to the opposed magnetization effect, in the future, one could optimize the GM-DIR parameters to further enhance this phenomenon.

There are several limitations to our study. We did not have longitudinal follow-up on all patients to confirm the diagnostic accuracy. The diagnostic criterion standard used for this study was the clinical impression. When consideration of demyelinating disease persisted but the clinical criteria for MS could not be met, we placed patients in the indeterminate PC group. Thus, the indeterminate group could have included some patients with preclinical disease despite not fulfilling the radiologically isolated syndrome criteria. In fact, 3 of the 10 cases of indeterminate PC were diagnosed with MS at follow-up. Two of these 3 had clear rim lesions on GM-DIR, and in a post hoc analysis, the specificity was increased further when taking into account their conversion status.

Another limitation is the lack of longitudinal imaging to accurately assess marker reliability across time as well as different MR imaging scanner vendors. Furthermore, we do not have other measures such as SWI, T2*, or 7T MR imaging to see whether these measures would similarly distinguish cases. Because contrast-enhanced images were not obtained as part of our study, it is unknown whether rims on GM-DIR are associated with lesion stage. It would be unlikely in our study setting that 35% of all MS lesions were enhancing.

Finally, most of our study cohort consisted of patients with early MS; therefore, whether our findings can be extrapolated to progressive or long-standing MS remains to be determined. Given that rim lesions were present in both early and longer disease duration in our cohort, it is more likely that rims are a lesion-specific phenomenon rather than a disease stage phenomenon. T1 hypointense lesions are commonly encountered very early in the demyelinating process when significant edematous change is present. The persistence of the T1 hypointense lesion is subsequently correlated with a more destructive "black hole" lesion, as has been shown in prior studies. The strong correlation of the rim marker with T1 signal will need to be explored in longitudinal studies. The persistence of T1 hypointensities (black holes) has been associated with poor recovery and more pronounced tissue damage in MS.[31-34] If the rim marker is a result of opposed magnetization artifacts arising from the differences in T1 signal change across a lesion, the rim lesions could serve as an additional important marker in quantitative studies on WM lesion damage severity and repair.

CONCLUSIONS

The addition of a novel GM-DIR technique to routine clinical imaging significantly enhanced specificity for diagnosing MS compared with the established criteria. As always, the use of these criteria should be in the context of the clinical presentation. However, the addition of the GM-DIR sequence provides a potentially important MR imaging marker to enhance the clinical diagnostic approach to MS, especially in patients in whom the disease course is not entirely clear.

ACKNOWLEDGMENTS

The authors recognize and acknowledge the major contribution of our colleague Dr Istvan Pirko, who died during this study. Dr Pirko was instrumental in the entire study. He initiated the groundwork for the development of this sequence in late 2011, made the powerful initial observations of the rim pattern on white matter lesions, and obtained grant funding to initiate this study.

The authors wish to also acknowledge Mandie Maroney-Smith for her assistance managing the imaging protocol and scheduling research subjects, Dan Rettmann and Peter Kollasch for their guidance in helping to configure the sequences on our MR imaging scanners, and Josh Trzasko for his insight in the bounce point artifact.

Disclosures: Jan-Mendelt Tillema—*RELATED*: *Grant*: KL2 TR000136 (National Center for Advancing Translational Sciences).* Stephen D. Weigand—*RELATED*: *Grant*: Department of Defense.* Claudia F. Lucchinetti—*UNRELATED*: *Grant*: Novartis, Biogen, National MS Society, Mallinckrodt. John D. Port—*RELATED*: *Grant*: Department of Defense.* Orhun H. Kantarci—*UNRELATED*: *Grants/Grants Pending*: Biogen, *Comments*: funding for CHAMPS and CHAMPIONS data reanalyses*; *Payment for Lectures Including Service on Speakers Bureaus*: Biogen, *Comments*: invited professorship to Biogen, Boston; *Travel/Accommodations/Meeting Expenses Unrelated to Activities Listed*: Novartis, *Comments*: Istanbul MS Days meeting travel and accommodation, 2017. *Money paid to the institution.

REFERENCES

1. Polman CH, Reingold SC, Banwell B, et al. **Diagnostic criteria for multiple sclerosis: 2010 revisions to the McDonald criteria.** *Ann Neurol* 2011;69:292–302 CrossRef Medline
2. McDonald WI, Compston A, Edan G, et al. **Recommended diagnostic criteria for multiple sclerosis: guidelines from the International Panel on the Diagnosis of Multiple Sclerosis.** *Ann Neurol* 2001;50:121–27 CrossRef Medline
3. Montalban X, Tintoré M, Swanton J, et al. **MRI criteria for MS in patients with clinically isolated syndromes.** *Neurology* 2010;74:427–34 CrossRef Medline
4. Solomon AJ, Klein EP, Bourdette D. "**Undiagnosing" multiple sclerosis: the challenge of misdiagnosis in MS.** *Neurology* 2012;78:1986–91 CrossRef Medline
5. Solomon AJ, Bourdette DN, Cross AH, et al. **The contemporary spectrum of multiple sclerosis misdiagnosis: a multicenter study.** *Neurology* 2016;87:1393–99 CrossRef Medline
6. Lebrun C, Cohen M, Chaussenot A, et al. **A prospective study of patients with brain MRI showing incidental T2 hyperintensities addressed as multiple sclerosis: a lot of work to do before treating.** *Neurol Ther* 2014;3:123–32 CrossRef Medline
7. Liu S, Kullnat J, Bourdette D, et al. **Prevalence of brain magnetic resonance imaging meeting Barkhof and McDonald criteria for dissemination in space among headache patients.** *Mult Scler* 2013;19:1101–05 CrossRef Medline
8. Traboulsee A, Simon JH, Stone L, et al. **Revised Recommendations of the Consortium of MS Centers Task Force for a Standardized MRI Protocol and Clinical Guidelines for the Diagnosis and Follow-Up of Multiple Sclerosis.** *AJNR Am J Neuroradiol* 2016;37:394–401 CrossRef Medline
9. Solomon AJ, Schindler MK, Howard DB, et al. **"Central vessel sign" on 3T FLAIR* MRI for the differentiation of multiple sclerosis from migraine.** *Ann Clin Transl Neurol* 2016;3:82–87 CrossRef Medline
10. Absinta M, Sati P, Schindler M, et al. **Persistent 7-Tesla phase rim predicts poor outcome in new multiple sclerosis patient lesions.** *J Clin Invest* 2016;126:2597–609 CrossRef Medline
11. Kilsdonk ID, Wattjes MP, Lopez-Soriano A, et al. **Improved differ-**

entiation between MS and vascular brain lesions using FLAIR* at 7 Tesla. *Eur Radiol* 2014;24:841–49 CrossRef Medline
12. Filippi M, Rocca MA, Ciccarelli O, et al; MAGNIMS Study Group. **MRI criteria for the diagnosis of multiple sclerosis: MAGNIMS consensus guidelines.** *Lancet Neurol* 2016;15:292–303 CrossRef Medline
13. Dale AM, Fischl B, Sereno MI. **Cortical surface-based analysis, I: segmentation and surface reconstruction.** *Neuroimage* 1999;9:179–94 CrossRef Medline
14. Fischl B, Sereno MI, Dale AM. **Cortical surface-based analysis, II: inflation, flattening, and a surface-based coordinate system.** *Neuroimage* 1999;9:195–207 CrossRef Medline
15. Woolrich MW, Jbabdi S, Patenaude B, et al. **Bayesian analysis of neuroimaging data in FSL.** *Neuroimage* 2009;45(1 Suppl):S173–86 CrossRef Medline
16. Jenkinson M, Bannister P, Brady M, et al. **Improved optimization for the robust and accurate linear registration and motion correction of brain images.** *Neuroimage* 2002;17:825–41 CrossRef Medline
17. Rorden C, Brett M. **Stereotaxic display of brain lesions.** *Behav Neurol* 2000;12:191–200 CrossRef Medline
18. Okuda DT, Siva A, Kantarci O, et al; Radiologically Isolated Syndrome Consortium (RISC), Club Francophone de la Sclérose en Plaques (CFSEP). **Radiologically isolated syndrome: 5-year risk for an initial clinical event.** *PLoS One* 2014;9:e90509 CrossRef Medline
19. Gelman A, Jakulin A, Pittau MG, et al. **A weakly informative default prior distribution for logistic and other regression models.** *Ann Appl Stat* 2008;2:1360–83 CrossRef
20. Rudick RA, Miller AE. **Multiple sclerosis or multiple possibilities: the continuing problem of misdiagnosis.** *Neurology* 2012;78:1904–06 CrossRef Medline
21. Hearshen DO, Ellis JH, Carson PL, et al. **Boundary effects from opposed magnetization artifact in IR images.** *Radiology* 1986;160: 543–47 CrossRef Medline
22. Pusey E, Lufkin RB, Brown RK, et al. **Magnetic resonance imaging artifacts: mechanism and clinical significance.** *Radiographics* 1986; 6:891–911 CrossRef Medline
23. Dal-Bianco A, Grabner G, Kronnerwetter C, et al. **Slow expansion of multiple sclerosis iron rim lesions: pathology and 7 T magnetic resonance imaging.** *Acta Neuropathol* 2017;133:25–42 CrossRef Medline
24. Haacke EM, Makki M, Ge Y, et al. **Characterizing iron deposition in multiple sclerosis lesions using susceptibility weighted imaging.** *J Magn Reson Imaging* 2009;29:537–44 CrossRef Medline
25. Frischer JM, Weigand SD, Guo Y, et al. **Clinical and pathological insights into the dynamic nature of the white matter multiple sclerosis plaque.** *Ann Neurol* 2015;78:710–21 CrossRef Medline
26. Chawla S, Kister I, Wuerfel J, et al. **Iron and non-iron-related characteristics of multiple sclerosis and neuromyelitis optica lesions at 7T MRI.** *AJNR Am J Neuroradiol* 2016;37:1223–30 CrossRef Medline
27. Kilsdonk ID, Lopez-Soriano A, Kuijer JP, et al. **Morphological features of MS lesions on FLAIR* at 7 T and their relation to patient characteristics.** *J Neurol* 2014;261:1356–64 CrossRef Medline
28. Mistry N, Abdel-Fahim R, Samaraweera A, et al. **Imaging central veins in brain lesions with 3-T T2*-weighted magnetic resonance imaging differentiates multiple sclerosis from microangiopathic brain lesions.** *Mult Scler* 2016;22:1289–96 CrossRef Medline
29. Mistry N, Dixon J, Tallantyre E, et al. **Central veins in brain lesions visualized with high-field magnetic resonance imaging: a pathologically specific diagnostic biomarker for inflammatory demyelination in the brain.** *JAMA Neurol* 2013;70:623–28 CrossRef Medline
30. Lummel N, Boeckh-Behrens T, Schoepf V, et al. **Presence of a central vein within white matter lesions on susceptibility weighted imaging: a specific finding for multiple sclerosis?** *Neuroradiology* 2011;53:311–17 CrossRef Medline
31. van Walderveen MA, Kamphorst W, Scheltens P, et al. **Histopathologic correlate of hypointense lesions on T1-weighted spin-echo MRI in multiple sclerosis.** *Neurology* 1998;50:1282–88 CrossRef Medline
32. Bitsch A, Kuhlmann T, Stadelmann C, et al. **A longitudinal MRI study of histopathologically defined hypointense multiple sclerosis lesions.** *Ann Neurol* 2001;49:793–96 CrossRef Medline
33. Barkhof F, Bruck W, De Groot CJ, et al. **Remyelinated lesions in multiple sclerosis: magnetic resonance image appearance.** *Arch Neurol* 2003;60:1073–81 CrossRef Medline
34. Brück W, Bitsch A, Kolenda H, et al. **Inflammatory central nervous system demyelination: correlation of magnetic resonance imaging findings with lesion pathology.** *Ann Neurol* 1997;42:783–93 CrossRef Medline

Association of Quantified Location-Specific Blood Volumes with Delayed Cerebral Ischemia after Aneurysmal Subarachnoid Hemorrhage

W.E. van der Steen, I.A. Zijlstra, D. Verbaan, A.M.M. Boers, C.S. Gathier, R. van den Berg, G.J.E. Rinkel, B.A. Coert, Y.B.W.E.M. Roos, C.B.L.M. Majoie, and H.A. Marquering

ABSTRACT

BACKGROUND AND PURPOSE: Delayed cerebral ischemia is a severe complication of aneurysmal SAH and is associated with a high case morbidity and fatality. The total blood volume and the presence of intraventricular blood on CT after aneurysmal SAH are associated with delayed cerebral ischemia. Whether quantified location-specific (cisternal, intraventricular, parenchymal, and subdural) blood volumes are associated with delayed cerebral ischemia has been infrequently researched. This study aimed to associate quantified location-specific blood volumes with delayed cerebral ischemia.

MATERIALS AND METHODS: Clinical and radiologic data were collected retrospectively from consecutive patients with aneurysmal SAH with available CT scans within 24 hours after ictus admitted to 2 academic centers between January 2009 and December 2011. Total blood volume was quantified using an automatic hemorrhage-segmentation algorithm. Segmented blood was manually classified as cisternal, intraventricular, intraparenchymal, or subdural. Adjusted ORs with 95% confidence intervals for delayed cerebral ischemia per milliliter of location-specific blood were calculated using multivariable logistic regression analysis.

RESULTS: We included 282 patients. Per milliliter increase in blood volume, the adjusted OR for delayed cerebral ischemia was 1.02 (95% CI, 1.01–1.04) for cisternal, 1.02 (95% CI, 1.00–1.04) for intraventricular, 0.99 (95% CI, 0.97–1.02) for intraparenchymal, and 0.96 (95% CI, 0.86–1.07) for subdural blood.

CONCLUSIONS: Our findings suggest that in patients with aneurysmal subarachnoid hemorrhage, the cisternal blood volume has a stronger relation with delayed cerebral ischemia than the blood volumes at other locations in the brain.

ABBREVIATIONS: aOR = adjusted odds ratio; aSAH = aneurysmal subarachnoid hemorrhage; DCI = delayed cerebral ischemia; IPH = intraparenchymal hemorrhage; IVH = intraventricular hemorrhage; SDH = subdural hemorrhage; WFNS = World Federation of Neurosurgical Societies

Although case fatality rates have been declining during the past years, aneurysmal subarachnoid hemorrhage (aSAH) is still a devastating disease with a case fatality of approximately 30%.[1] Delayed cerebral ischemia (DCI) is a severe complication that occurs in approximately 20%–30% of patients and is associated with high morbidity and mortality.[2] One of the strongest predictors of DCI is the amount of blood on the admission CT scan.[3-6]

Apart from the amount of extravasated blood, the breakthrough of blood from the subarachnoid cisterns into the ventricle system is also associated with the occurrence of DCI. Various studies have shown that the presence of an intraventricular hemorrhage (IVH) in patients with aSAH is an independent risk factor for DCI.[5,7-11] However, conflicting results regarding the association between the presence of intraparenchymal hemorrhage (IPH) and DCI in patients with SAH are found.[9,11-14] The occurrence of subdural hemorrhage (SDH) is relatively rare after SAH, and its association with DCI is currently unknown.[15]

Although various studies determined the association between

Received June 7, 2017; accepted after revision February 12, 2018.

From the Department of Biomedical Engineering and Physics (W.E.v.d.S., A.M.M.B., H.A.M.), Department of Radiology (W.E.v.d.S., I.A.Z., A.M.M.B., R.v.d.B., C.B.L.M.M., H.A.M), Neurosurgical Center Amsterdam (W.E.v.d.S., D.V., B.A.C.), and Department of Neurology (W.E.v.d.S., Y.B.W.E.M.R.), Academic Medical Center, Amsterdam, the Netherlands; Department of Robotics and Mechatronics (A.M.M.B.), University of Twente, Enschede, the Netherlands; and Department of Neurology and Neurosurgery (C.S.G., G.J.E.R.), Brain Center Rudolf Magnus, University Medical Center, Utrecht, the Netherlands.

Wessel E. van der Steen and IJsbrand A. Zijlstra contributed equally to this work.

Henk A. Marquering received a research grant from Fonds NutsOhra (1403-023) to study the prognostic value of quantified blood in patients with aneurysmal subarachnoid hemorrhage.

Paper previously presented as an abstract at: European Stroke Organisation Conference, May 16–18 2017; Prague, Czech Republic.

Please address correspondence to Wessel E. van der Steen, MD, Department of Radiology, Room L0-104, Academic Medical Center, Meibergdreef 9, 1105AZ, Amsterdam, the Netherlands; e-mail: w.e.vandersteen@amc.uva.nl

Indicates article with supplemental on-line photo.

http://dx.doi.org/10.3174/ajnr.A5626

the presence of IVH or IPH and DCI, only a few studies associated estimates of these volumes with DCI. One study found an association between IVH volume and DCI.[6] However, a more recent study did not confirm this finding.[16] The only study that determined IPH volume in patients with aSAH found no association with DCI.[5] These studies used radiologic scales such as the Hijdra sum score to estimate the cisternal blood volume, the IVH score for IVH volume, and the ABC/2 score for IPH volume.[6,17,18] These radiologic scales are not very accurate and are shown to have poor-to-moderate interobserver agreement, limiting their discriminative power.[16,19] Moreover, the ABC/2 score has been shown to overestimate the IPH volume.[20]

Quantitative measures have the promise of more precisely assessing blood volumes. Previous studies have found a strong relation between the quantified amount of total blood volume and DCI.[9,21] However, in these studies, the volumes of blood in the separate compartments of the brain were not analyzed separately. It is therefore currently unknown whether taking the blood volumes at these locations into account improves the prediction of DCI. In this study, we took the first step in addressing this issue by quantifying the cisternal, intraventricular, intraparenchymal, and subdural blood volumes separately and determining their independent associations with DCI.

MATERIALS AND METHODS

Population

We included patients from a retrospectively collected cohort consisting of all patients with aSAH admitted to the Academic Medical Center Amsterdam and University Medical Center Utrecht, the Netherlands, between January 2009 and December 2011.[9] Inclusion criteria were the following: 1) SAH proved on noncontrast CT; 2) aneurysm proved on either CTA, MRA, or DSA; and 3) NCCT performed within 24 hours after ictus and available for review. Patients who did not survive the first 3 days after SAH onset were excluded. Furthermore, patients with NCCTs whom we could not use for hemorrhage quantification, for instance due to movement and/or metal artifacts from previous treatment, were excluded.[22]

Clinical Data

Collected demographic and clinical variables were the following: age, sex, history of hypertension, neurologic condition on admission (according to the World Federation of Neurosurgical Societies [WFNS] scale),[23] time between ictus and admission, location of the aneurysm (anterior or posterior circulation) and treatment technique (no aneurysm treatment, clipping, or coiling), rebleeding, and the occurrence of clinical DCI during admission. Aneurysms of the posterior communicating artery were allocated to the posterior circulation.

Delayed Cerebral Ischemia

DCI was defined as the occurrence of new focal neurologic impairment or a decrease on the Glasgow Coma Scale score that could not be explained by any other cause. A CT scan of the brain was performed to rule out hydrocephalus, and blood was sampled to exclude a metabolic encephalopathy, such as infection or electrolyte disturbances, to exclude other causes of neurologic deterioration. An electroencephalogram was obtained in case of suspicion of seizures.[24] DCI was diagnosed by the treating physician who could be either a neurologist, neurosurgeon, or intensivist. A new cerebral infarct on follow-up CT, which could not be attributed to surgical clipping, endovascular treatment, or drain placement, was supportive but not required for the diagnosis of DCI (On-line Figure). The standard care to prevent DCI was similar in both participating centers. All patients received nimodipine (6 times daily, 60 mg orally) and intravenous fluids aiming at normovolemia. The mean arterial pressure was kept above 65 mm Hg. Furthermore, if the patient used antihypertensive medication, it was stopped at admission.

Image Analysis

The first scan after ictus was used for the analysis. However, if rebleeding occurred within 24 hours, the scan after rebleeding was used. All scans were reviewed for the presence of cisternal blood, IVH, IPH, and SDH by 2 observers (I.A.Z. and W.E.v.d.S.). The hemorrhage was segmented on admission NCCT using an automatic hemorrhage-segmentation algorithm.[22] All segmentations were checked and, if needed, manually corrected using ITK-SNAP, Version 3.4.0 (www.itksnap.org) by a trained observer (W.E.v.d.S.) who was blinded to outcome.[25] From this segmentation, the total blood volume was calculated in milliliters. Subsequently, segmented blood was classified as cisternal, intraparenchymal, intraventricular, or subdural by manually outlining the ventricular, intraparenchymal, and/or subdural part of the segmented total hemorrhage by a trained observer (W.E.v.d.S.) (Fig 1). If part of the SAH was in proximity of the Sylvian fissure and not clearly located inside of the fissure on NCCT, the CTA was evaluated to differentiate the cisternal and intraparenchymal part of the hematoma.[26] If contrast-enhanced vessels were present in the hematoma on CTA, this part was classified as cisternal. If no vessels were detected, it was classified as IPH. The classifications were checked by a second observer, an experienced radiologist (I.A.Z.). After we classified the blood as cisternal, intraparenchymal, intraventricular, or subdural, the location-dependent volumes could be calculated by multiplying the number of classified voxels by its voxel size.

Statistical Analysis

Baseline variables were compared between patients with and without DCI using the Fisher exact test for dichotomous and categoric variables, the independent samples *t* test for normally distributed continuous variables, and the Mann-Whitney *U* test for non-normally distributed continuous variables. Variables were checked for normality using the Shapiro-Wilk test ($W > 0.9$ was considered normally distributed).

Correlations between the cisternal blood volume and IVH, IPH, and SDH volume were calculated using the Spearman rank correlation coefficient.

Univariable logistic regression analysis of the total blood; cisternal blood; and IVH, IPH, and SDH volume with DCI was performed to determine ORs with 95% confidence intervals for DCI per milliliter of blood.

Associative models for the cisternal, IVH, IPH, SDH, and total blood volume were created by calculating adjusted odds ratios (aORs) by separately adding potential confounders to the univari-

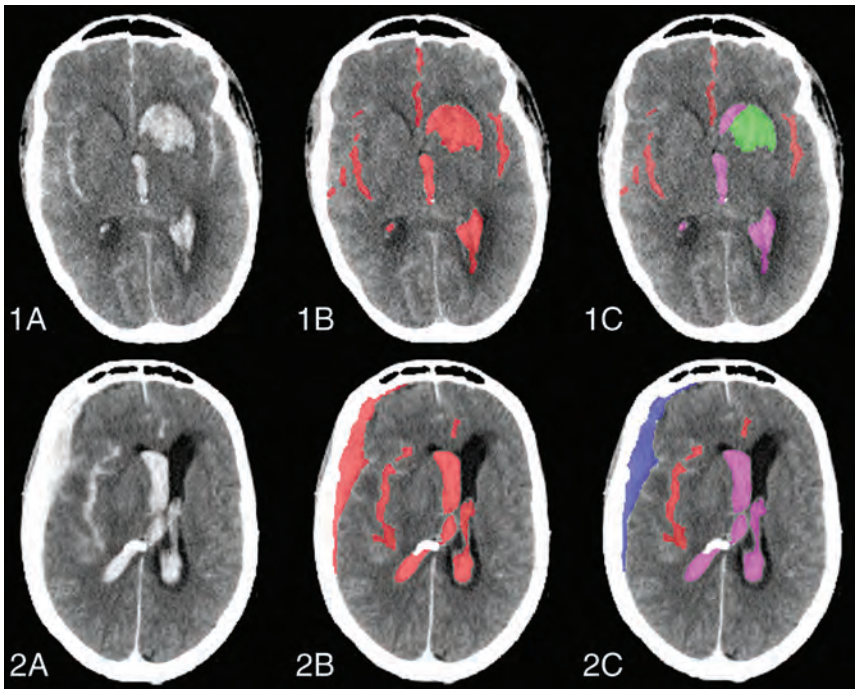

FIG 1. Classification of the total blood volume as cisternal, intraventricular, intraparenchymal, and subdural. *1A*, Axial slice of a noncontrast CT of a patient with aSAH with concomitant IVH and IPH. *1B*, Quantified total blood volume. *1C*, Classified cisternal (*red*), intraventricular (*magenta*), and intraparenchymal (*green*) blood. *2A*, Axial slice of a noncontrast CT scan of a patient with aSAH with concomitant IVH and SDH. *2B*. Quantified total blood volume. *2C*, Classified cisternal (*red*), intraventricular (*magenta*), and subdural (*blue*) blood.

able model. Variables that changed the OR of the univariable model by ≥10% were considered confounders and were included in the final associative model. Potential confounders were age, sex, neurologic condition on admission (WFNS grade), treatment technique (no treatment, clipping, or coiling), rebleeding, and hypertension in accordance with previous literature.[9,27] For the 4 associative models of cisternal, IVH, IPH, and SDH volume, the remaining 3 volumes were also included in the confounding analysis. In the associative model of the total volume, the location-dependent volumes were not added as confounders because the total volume consisted of these volumes.

A P value $< .05$ was considered statistically significant. Statistical analyses were performed using SPSS, Version 23.0.0.2 (IBM, Armonk, New York).

RESULTS

Of the 458 patients who were evaluated for study inclusion, 176 patients were excluded because of the following reasons: NCCT not available ($n = 33$); NCCT not suitable for assessment because of movement and/or metal artifacts ($n = 13$) or other technical reasons ($n = 16$); the first NCCT not performed within 24 hours ($n = 38$); no aneurysm found on CTA, MRA or DSA ($n = 29$); and death within 3 days after SAH onset ($n = 47$).[9]

Characteristics of the 282 included patients are shown in Table 1 for the total study population and stratified by DCI group. The mean age was 55.8 ± 12.0 years, and 73% were female. In this cohort, 61 (22%) patients developed DCI. Patients with DCI had larger total ($P = .01$) and cisternal ($P < .001$) blood volumes (Fig 2), more frequently had an IVH ($P = .003$), and had a larger IVH volume ($P = .01$).

There was a weak positive correlation between cisternal and IVH blood volumes (Spearman $\rho = 0.15$, $P = .01$), a weak negative correlation between cisternal and IPH blood volumes (Spearman $\rho = -0.16$, $P = .01$), and no correlation between cisternal and SDH blood volumes.

In the univariable analysis, both the total blood volume (OR = 1.02; 95% CI, 1.01–1.03) per milliliter increase in volume and the cisternal blood volume (OR = 1.02; 95% CI, 1.01–1.04) were significantly associated with DCI. After correction for confounders, the total (aOR = 1.02; 95% CI, 1.01–1.03) and cisternal (aOR = 1.02; 95% CI, 1.01–1.04) blood volumes remained significantly associated with DCI. In both the univariable and multivariable analysis, no statistically significant associations were found among the IVH volume (aOR = 1.02; 95% CI, 1.00–1.04), IPH volume (aOR = 0.99; 95% CI, 0.97–1.02), SDH volume (aOR = 0.96; 95% CI, 0.86–1.07), and DCI (Table 2).

DISCUSSION

In this study, we associated location-specific blood volumes with the occurrence of DCI. In our population, increasing cisternal blood volume was associated with a higher risk of DCI. This relation was not found with intraventricular, intraparenchymal, and subdural blood volume.

Our results confirm that larger amounts of blood in the subarachnoid space are associated with a higher chance of DCI.[3,5,9,21,28] The IVH volume was not significantly associated with DCI, though the point estimate of the aOR was like that of the cisternal volume, which may indicate a lack of power to show a statistically significant effect. The only other study that quantified IVH volume showed a higher median IVH volume in patients with DCI compared with patients without DCI.[28] In our study, patients with DCI also had a higher median IVH volume. Two other studies that used qualitative scores to assess IVH volume in patients with SAH found that a higher ventricular clot volume was independently associated with a higher risk of DCI.[5,6] Another study that included only patients with aSAH with concomitant IVH showed no association between IVH volume and DCI.[16] Our findings neither support nor reject the hypothesis that IVH volume is related to the occurrence of DCI.

We found no association between IPH volume and DCI, similar to findings of the only other study that assessed IPH volume.[5] Recently, 2 studies found an association between the presence of an IPH and DCI.[12,13] However, in both studies, a new ischemic lesion was used as the end point instead of clinical DCI. Not all patients with clinical DCI will develop a cerebral infarct, making the results of these studies difficult to compare with those of our study.[29]

Table 1: Patient characteristics

Parameter	All (*n* = 282)	No DCI (*n* = 221)	DCI (*n* = 61)	*P* Value
Age (mean) (±SD)	55.8 (12.0)	55.9 (11.8)	55.4 (13.0)	.80
Female sex (No.)	205 (73%)	163 (74%)	42 (69%)	.52
History of hypertension (No.)	79 (28%)	58 (26%)	21 (34%)	.26
Aneurysm location (No.)				.62
Anterior	212 (75%)	168 (76%)	44 (72%)	
Posterior	70 (25%)	53 (24%)	17 (28%)	
WFNS grade (No.)				.08
I	79 (28%)	68 (31%)	11 (18%)	
II	67 (24%)	50 (23%)	17 (28%)	
III	8 (3%)	6 (3%)	2 (3%)	
IV	68 (24%)	56 (25%)	12 (20%)	
V	59 (21%)	40 (18%)	19 (31%)	
Treatment modality (No.)				.23
No treatment	14 (5%)	13 (6%)	1 (2%)	
Clipping	138 (49%)	111 (50%)	27 (44%)	
Coiling	130 (46%)	97 (44%)	33 (54%)	
Rebleeding (No.)	34 (12%)	26 (12%)	8 (13%)	.83
Total blood volume (median) (IQR)	41.2 (23.6–62.5)	37.7 (21.8–57.9)	52.1 (34.5–78.1)	.01
Cisternal blood volume (median) (IQR)	29.8 (14.0–47.0)	25.2 (12.4–44.1)	39.7 (24.2–60.1)	<.001
IVH presence (No.)	187 (66%)	137 (62%)	50 (82%)	.003
IVH volume (median) (IQR)	0.7 (0.0–2.8)	0.5 (0.0–2.2)	1.2 (0.3–5.0)	.01
IPH presence (No.)	85 (30%)	70 (32%)	15 (25%)	.35
IPH volume (median) (IQR)	0.0 (0.0–3.3)	0.0 (0.0–3.6)	0.0 (0.0–0.8)	.29
SDH presence (No.)	16 (6%)	12 (5%)	4 (7%)	.76
SDH volume (median) (IQR)	0.0 (0.0–0.0)	0.0 (0.0–0.0)	0.0 (0.0–0.0)	.74

Note:—IQR indicates interquartile range.

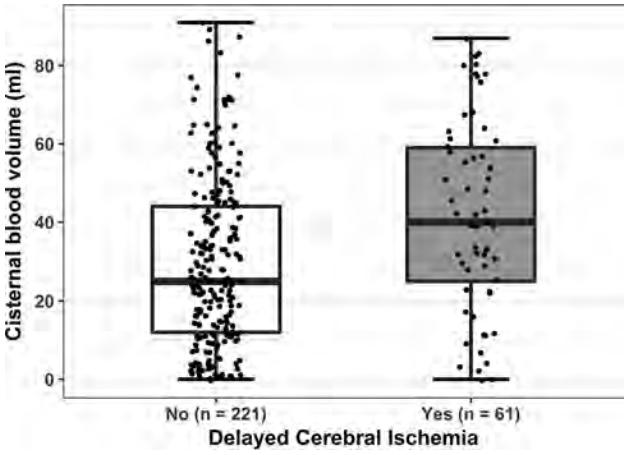

FIG 2. Dot boxplot of quantified cisternal blood volume in patients with and without DCI.

Table 2: Association of blood volumes and DCI per milliliter increase in volume

Variable	OR (95% CI)	aOR (95% CI)
Total blood volume	1.02 (1.01–1.03)[a]	1.02 (1.01–1.03)[a,b]
Cisternal blood volume	1.02 (1.01–1.04)[a]	1.02 (1.01–1.04)[a,c]
IVH volume	1.02 (1.00–1.04)	1.02 (1.00–1.04)[d]
IPH volume	0.99 (0.97–1.01)	0.99 (0.97–1.02)[e]
SDH volume	0.96 (0.85–1.08)	0.96 (0.86–1.07)[f]

[a] Statistically significant.
[b] Confounders: none.
[c] Confounders: none.
[d] Confounders: WFNS, cisternal blood volume.
[e] Confounders: WFNS, cisternal blood volume, and IVH volume.
[f] Confounders: WFNS, treatment, cisternal blood volume, IVH volume, and IPH volume.

Moreover, the presence rather than the volume of IPH was considered in these studies. The SDH volume has not been previously associated with the occurrence of DCI, to our knowledge.

Our results show a difference between cisternal and IVH volumes on the one hand and IPH and SDH volumes on the other in relation to DCI. A possible explanation might be that the ventricles are an overflow compartment of the cisterns. A larger volume of blood in the ventricles may actually result from a larger cisternal blood volume that has either been directly released into the ventricles or has been redistributed via the foramina of Luschka and possibly via the interpeduncular cistern.[30] However, in our data, only a weak correlation between the cisternal blood volume and the IVH volume was found. Intraparenchymal and subdural hematomas, on the other hand, are a more direct extension of blood from the aneurysm without an interstitial subarachnoid compartment. The underlying mechanism causing DCI (cerebral vasospasm, microthrombosis, microvascular spasm, inflammation, and/or cortical spreading ischemia) has been thought to be related to both rupture of an intracranial aneurysm and to blood being released into the subarachnoid space containing CSF.[31] The latter may not apply to the intraparenchymal compartment. This possibility may explain the absence of a relation between the IPH and SDH volumes and the occurrence of DCI. Furthermore, a complicating factor in the assessment of clinical DCI is caused by the presence of IPH because such a hematoma can already cause a focal neurologic deficit itself. Moreover, in general, it is difficult to score DCI when the condition of a patient deteriorates shortly after the aneurysm treatment, while the new hypodensity surrounding the initial hematoma on a CT scan can also be caused by edema or infarction due to the hematoma itself or the aneurysm treatment. This combination of factors could lead to underscoring of DCI in this time period.

An important strength of this study is the computer-assisted quantification of the volume of blood in all different compartments of the brain. With computer-assisted quantification, even a

very small layering of blood could be delineated, adding to the total volume of intracranial blood. This delineation allowed a calculation of risk per milliliter of blood and a more quantitative means to assess the association with DCI as opposed to the very coarse qualitative grading scales. A remaining limitation of the computer-assisted technique up to this moment is that even though the total blood volume could be segmented automatically, the ventricular, intraparenchymal, and subdural outlines were manually drawn. This feature may lead to some observer-dependent variation. We tried to limit this by inspection of the segmentations by an experienced radiologist; however, it has been proved difficult to accurately differentiate IPH and cisternal hematoma, especially in patients with ruptured middle cerebral artery aneurysms. We tried to overcome this problem by combining the NCCT with the CTA to allow differentiation between these 2 compartments and to assess the IPH volumes.[26] Nevertheless, even with the use of CTA, some misclassification of IPH may have occurred.

A weakness of this study is its retrospective design, which may have resulted in suboptimal analysis of the clinical data. However, by including all consecutive patients in a limited time span, we have tried to minimize this bias because all patient data were analyzed in the same way.

Our results suggest that patients with high cisternal blood volume have a high risk of DCI. Thus, these patients could be a target for intensive monitoring and new prophylactic treatment strategies.[32] However, even though our study shows associations between location-specific blood volumes and DCI, the question remains as to whether these volumes improve the existing prediction models, including, for instance, the modified Fisher score.[10] If this is the case, these volumes may be of clinical value. This will have to be confirmed by the development and validation of prediction models for DCI, including the location-specific volumes. Furthermore, in this study, patients were not routinely followed up after the admission period. Thus, the correlation between the location-specific volumes and clinical outcome could not be reliably determined. Future prospective studies are warranted to answer this important remaining question. Manual selection of the IVH, IPH, or SDH region is too cumbersome to use in daily practice. Automatic region-detection techniques should be developed before this can be used as a clinical tool.

CONCLUSIONS

In our population, increasing cisternal blood volume was associated with a higher risk of DCI. This relation was not found with intraventricular, intraparenchymal, and subdural blood volume. Our findings suggest that in patients with an aSAH, the cisternal blood volume has a stronger relation to DCI than the blood volumes at other locations in the brain.

Disclosures: René van den Berg—*UNRELATED*: *Consultancy*: Codman Neuro-DePuy Synthes Neurovascular. Charles B.L.M. Majoie—*UNRELATED*: *Consultancy*: Stryker, *Comments*: Consultations*; *Grants/Grants Pending*: TWIN Foundation, Dutch Heart Foundation.* Henk A. Marquering—*OTHER RELATIONSHIPS*: founder and shareholder of Nico-lab. *Money paid to the institution.

REFERENCES

1. Vergouwen MD, Jong-Tjien-Fa AV, Algra A, et al. **Time trends in causes of death after aneurysmal subarachnoid hemorrhage: a hospital-based study.** *Neurology* 2016;86:59–63 CrossRef Medline
2. Hijdra A, Braakman R, van Gijn J, et al. **Aneurysmal subarachnoid hemorrhage: complications and outcome in a hospital population.** *Stroke* 1987;18:1061–67 CrossRef Medline
3. Fisher CM, Kistler JP, Davis JM. **Relation of cerebral vasospasm to subarachnoid hemorrhage visualized by computerized tomographic scanning.** *Neurosurgery* 1980;6:1–9 CrossRef Medline
4. Frontera JA, Claassen J, Schmidt JM, et al. **Prediction of symptomatic vasospasm after subarachnoid hemorrhage: the modified Fisher scale.** *Neurosurgery* 2006;59:21–27; discussion 21–27 CrossRef Medline
5. Claassen J, Bernardini GL, Kreiter K, et al. **Effect of cisternal and ventricular blood on risk of delayed cerebral ischemia after subarachnoid hemorrhage: the Fisher scale revisited.** *Stroke* 2001;32:2012–20 CrossRef Medline
6. Hijdra A, van Gijn J, Nagelkerke NJ, et al. **Prediction of delayed cerebral ischemia, rebleeding, and outcome after aneurysmal subarachnoid hemorrhage.** *Stroke* 1988;19:1250–56 CrossRef Medline
7. Rosen DS, Macdonald RL, Huo D, et al. **Intraventricular hemorrhage from ruptured aneurysm: clinical characteristics, complications, and outcomes in a large, prospective, multicenter study population.** *J Neurosurg* 2007;107:261–65 CrossRef Medline
8. De Rooij NK, Greving JP, Rinkel GJ, et al. **Early prediction of delayed cerebral ischemia after subarachnoid hemorrhage: development and validation of a practical risk chart.** *Stroke* 2013;44:1288–94 CrossRef Medline
9. Zijlstra IA, Gathier CS, Boers AM, et al. **Association of automatically quantified blood volume after aneurysmal subarachnoid hemorrhage with delayed cerebral ischemia.** *AJNR Am J Neuroradiol* 2016;37:1588–93 CrossRef Medline
10. De Oliveira Manoel AL, Jaja BN, Germans MR, et al. **The VASOGRADE: a simple grading scale for prediction of delayed cerebral ischemia after subarachnoid hemorrhage.** *Stroke* 2015;46:1826–31 CrossRef Medline
11. Macdonald RL, Rosengart A, Huo D, et al. **Factors associated with the development of vasospasm after planned surgical treatment of aneurysmal subarachnoid hemorrhage.** *J Neurosurg* 2003;99:644–52 CrossRef Medline
12. Wan A, Jaja BN, Schweizer TA, et al. **Clinical characteristics and outcome of aneurysmal subarachnoid hemorrhage with intracerebral hematoma.** *J Neurosurg* 2016;125:1344–51 CrossRef Medline
13. Platz J, Güresir E, Wagner M, et al. **Increased risk of delayed cerebral ischemia in subarachnoid hemorrhage patients with additional intracerebral hematoma.** *J Neurosurg* 2017;126:504–10 CrossRef Medline
14. Crobeddu E, Mittal MK, Dupont S, et al. **Predicting the lack of development of delayed cerebral ischemia after aneurysmal subarachnoid hemorrhage.** *Stroke* 2012;43:697–701 CrossRef Medline
15. Schuss P, Konczalla J, Platz J, et al. **Aneurysm-related subarachnoid hemorrhage and acute subdural hematoma: single-center series and systematic review.** *J Neurosurg* 2013;118:984–90 CrossRef Medline
16. Kramer AH, Mikolaenko I, Deis N, et al. **Intraventricular hemorrhage volume predicts poor outcomes but not delayed ischemic neurological deficits among patients with ruptured cerebral aneurysms.** *Neurosurgery* 2010;67:1044–52; discussion 1052–53 CrossRef Medline
17. Hallevi H, Dar NS, Barreto AD, et al. **The IVH score: a novel tool for estimating intraventricular hemorrhage volume: clinical and research implications.** *Crit Care Med* 2009;37:969–74, e1 CrossRef Medline
18. Broderick JP, Brott TG, Duldner JE, et al. **Volume of intracerebral hemorrhage: a powerful and easy-to-use predictor of 30-day mortality.** *Stroke* 1993;24:987–93 CrossRef Medline
19. van der Jagt M, Hasan D, Bijvoet HW, et al. **Interobserver variability**

of cisternal blood on CT after aneurysmal subarachnoid hemorrhage. *Neurology* 2000;54:2156–58 CrossRef Medline
20. Scherer M, Cordes J, Younsi A, et al. **Development and validation of an automatic segmentation algorithm for quantification of intracerebral hemorrhage.** *Stroke* 2016;47:2776–82 CrossRef Medline
21. Friedman JA, Goerss SJ, Meyer FB, et al. **Volumetric quantification of Fisher grade 3 aneurysmal subarachnoid hemorrhage: a novel method to predict symptomatic vasospasm on admission computerized tomography scans.** *J Neurosurg* 2002;97:401–07 CrossRef Medline
22. Boers AM, Zijlstra IA, Gathier CS, et al. **Automatic quantification after subarachnoid hemorrhage on noncontrast CT.** *AJNR Am J Neuroradiol* 2014;35:2279–86 CrossRef Medline
23. Teasdale GM, Drake CG, Hunt W, et al. **A universal subarachnoid hemorrhage scale: report of a committee of the World Federation of Neurosurgical Societies.** *J Neurol Neurosurg Psychiatry* 1988;51:1457 Medline
24. Vergouwen MD, Vermeulen M, van Gijn J, et al. **Definition of delayed cerebral ischemia after aneurysmal subarachnoid hemorrhage as an outcome event in clinical trials and observational studies: proposal of a multidisciplinary research group.** *Stroke* 2010; 41:2391–95 CrossRef Medline
25. Yushkevich PA, Piven J, Hazlett HC, et al. **User-guided 3D active contour segmentation of anatomical structures: significantly improved efficiency and reliability.** *Neuroimage* 2006;31:1116–28 CrossRef Medline
26. van der Zande JJ, Hendrikse J, Rinkel GJ. **CT angiography for differentiation between intracerebral and intra-sylvian hematoma in patients with ruptured middle cerebral artery aneurysms.** *AJNR Am J Neuroradiol* 2011;32:271–75 CrossRef Medline
27. de Rooij NK, Rinkel GJ, Dankbaar JW, et al. **Delayed cerebral ischemia after subarachnoid hemorrhage: a systematic review of clinical, laboratory, and radiological predictors.** *Stroke* 2013;44:43–54 CrossRef Medline
28. Ko SB, Choi HA, Carpenter AM, et al. **Quantitative analysis of hemorrhage volume for predicting delayed cerebral ischemia after subarachnoid hemorrhage.** *Stroke* 2011;42:669–74 CrossRef Medline
29. Rabinstein AA, Friedman JA, Weigand SD, et al. **Predictors of cerebral infarction in aneurysmal subarachnoid hemorrhage.** *Stroke* 2004;35:1862–66 CrossRef Medline
30. Bedussi B, van der Wel NN, de Vos J, et al. **Paravascular channels, cisterns, and the subarachnoid space in the rat brain: a single compartment with preferential pathways.** *J Cereb Blood Flow Metab* 2017;37:1374–85 CrossRef Medline
31. Vergouwen MD, Vermeulen M, Coert BA, et al. **Microthrombosis after aneurysmal subarachnoid hemorrhage: an additional explanation for delayed cerebral ischemia.** *J Cereb Blood Flow Metab* 2008; 28:1761–70 CrossRef Medline
32. Macdonald RL. **Delayed neurological deterioration after subarachnoid haemorrhage.** *Nat Rev Neurol* 2014;10:44–58 CrossRef Medline

Blood Flow Mimicking Aneurysmal Wall Enhancement: A Diagnostic Pitfall of Vessel Wall MRI Using the Postcontrast 3D Turbo Spin-Echo MR Imaging Sequence

E. Kalsoum, A. Chabernaud Negrier, T. Tuilier, A. Benaïssa, R. Blanc, S. Gallas, J.-P. Lefaucheur, A. Gaston, R. Lopes, P. Brugières, and J. Hodel

ABSTRACT

SUMMARY: Our aim was to compare the detectability of aneurysmal wall enhancement in unruptured intracranial aneurysms between conventional and motion-sensitized driven equilibrium–prepared postcontrast 3D T1-weighted TSE sequences (sampling perfection with applicationoptimized contrasts by using different flip angle evolution, SPACE). Twenty-two patients with 30 unruptured intracranial aneurysms were scanned at 3T. Aneurysmal wall enhancement was more significantly detected using conventional compared with motion-sensitized driven equilibrium–prepared SPACE sequences (10/30 versus 2/30, $P < .0001$). Contrast-to-noise ratio measurements did not differ between conventional and motion-sensitized driven equilibrium–prepared sequences ($P = .51$). Flowing blood can mimic aneurysmal wall enhancement using conventional SPACE sequences with potential implications for patient care.

ABBREVIATIONS: AWE = aneurysmal wall enhancement; CNR = contrast-to-noise ratio; MSDE = motion-sensitized driven equilibrium; SPACE = sampling perfection with application-optimized contrasts by using different flip angle evolution; UIA = unruptured intracranial aneurysm

Vessel wall MR imaging is being increasingly used in patients with intracranial aneurysms,[1] with aneurysmal wall enhancement (AWE) considered suggestive of instability/rupture.[2-8] The most commonly used sequence for vessel wall MR imaging is 3D TSE, including a black-blood effect[9]; however flowing blood can still lead to lumen enhancement.[1,8]

Motion-sensitized driven equilibrium (MSDE) uses flow-sensitive dephasing gradients to suppress residual blood flow.[10] For the evaluation of AWE, only 1 recent study used MSDE,[6] while all the other studies[2-4,7,11-14] used a postcontrast sequence without any additional blood-suppression technique (conventional sequence).

The influence of blood-suppression techniques on the detectability of AWE has not yet been evaluated, to our knowledge. We aimed to compare the detectability of AWE in consecutive patients with unruptured intracranial aneurysms (UIAs) using conventional and an MSDE-prepared postcontrast 3D TSE sequence (sampling perfection with application-optimized contrasts by using different flip angle evolution, SPACE).

Received January 29, 2018; accepted February 5.

From the Departments of Neuroradiology (E.K., A.C.N., T.T., A.B., S.G., A.G., P.B., J.H.) and Neurophysiology (J.-P.L.), Centre Hospitalier Universitaire Henri Mondor, Créteil, France; Department of Interventional Neuroradiology (R.B.), Rothschild Foundation Hospital, Paris, France; and Neuroradiology Department (R.L.), Univ. Lille, INSERM, CHU Lille, U1171 - Degenerative and Vascular Cognitive Disorders, Lille, France.

Please address correspondence to Jérôme Hodel, MD, PhD, Department of Neuroradiology, CHU Henri Mondor, Créteil, France; e-mail: jerome.hodel@gmail.com

http://dx.doi.org/10.3174/ajnr.A5616

MATERIALS AND METHODS

Patients and Brain Imaging

This study was approved by the institutional review board of the Rothschild Foundation Hospital, Paris, France. From September 2016 to February 2017, twenty-two consecutive patients (17 women; 58.1 years of age; range, 25–85 years) with 30 asymptomatic UIAs were included. All patients underwent both DSA and 3T MR imaging within 1 week. Aneurysms were considered nonruptured on the basis of clinical (absence of recent or past acute headaches, no history of subarachnoid hemorrhage) and imaging (absence of recent or past SAH on FLAIR and SWI) data.

MR imaging was performed at 3T (Magnetom Skyra; Siemens, Erlangen, Germany) including DWI, FLAIR, SWI, TOF-MRA, contrast-enhanced MRA, and pre- and postcontrast 3D T1-weighted SPACE acquired with and without MSDE (4 acquisitions per patient). The order of the postcontrast SPACE sequence was randomized. SPACE parameters were similar to those in previous studies[2,4,11,12]: sagittal plane: TR/TE, 700/11 ms; slice thickness, 0.9 mm; FOV, 230 × 230 mm; matrix, 256 × 256 (interpolated to 512 × 512); voxel size, 0.45 mm; acquisition time, 4 minutes 33 seconds. MSDE preparation consisted of a first-order gradient moment of 500 mT × ms^2/m and a b-value of 1.75 s/mm^2, according to a previous study.[10]

Image Analysis

UIAs were defined in consensus using DSA images by 2 neuroradiologists (R.B. and E.K.). SPACE images were blindly and independently assessed in multiplanar mode (with image anal-

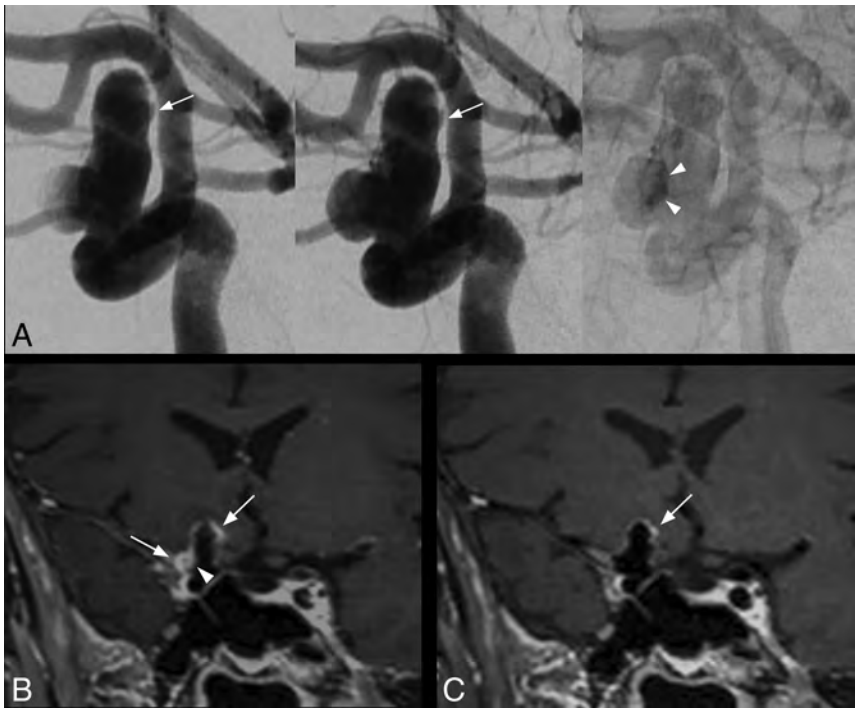

FIG 1. Saccular intracranial aneurysm in a 63-year-old patient. DSA angiogram (*A*, from left to right: early arterial phase, arterial phase, and venous phase) shows a 14-mm right internal carotid artery aneurysm with intrasaccular slow flowing/stagnant blood (*arrowheads*) and irregular shape (*arrow*). With conventional SPACE imaging (*B*), extensive AWE is visible, more prominent at the apex and at the lateral portion of the aneurysm (*B*, *arrows*). Note the enhancement within the aneurysm lumen visible only using conventional SPACE imaging (*B*, *arrowhead*), matching the stagnant blood on DSA (*A*, *arrowheads*). With MSDE SPACE imaging, AWE is only visible at the apex (*C*, *arrow*).

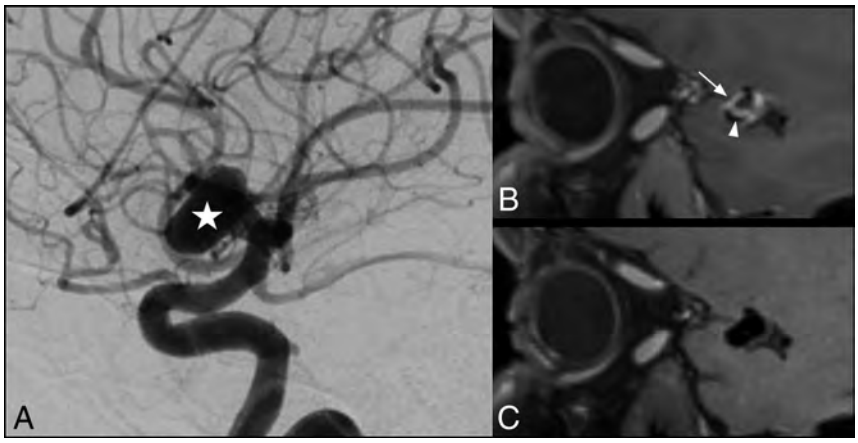

FIG 2. Saccular intracranial aneurysm in a 42-year-old patient. DSA angiogram shows an 11-mm aneurysm (*A*, *star*) arising from the M1 segment of the right middle cerebral artery. AWE is visible on the conventional SPACE image (*B*, *arrow*), while there is no enhancement visible on the corresponding MSDE SPACE image (*C*). Enhancement within the aneurysm lumen was also visible using a conventional SPACE image (*B*, *arrowhead*).

ysis in arbitrary planes) by 3 neuroradiologists: J.H., T.T., and A.C. Readers were blinded to clinical data and other sequences (except TOF-MRA) but were aware of patient aneurysm location.

Two independent blinded-reading sessions took place 2 weeks apart to avoid recall bias. Each UIA was analyzed only once per session, with pre- and postcontrast either conventional or MSDE-prepared SPACE sequences. For each of the 2 sets of SPACE acquisitions, the readers evaluated each UIA for AWE defined as a thick (>2 mm) area of aneurysmal wall with increased signal intensity between pre- and postcontrast images. Discrepancies were resolved by consensus.

Contrast-to-noise ratio (CNR) measurements were performed to ensure that the differences observed between SPACE sequences were not artifactual. Standardized ROIs (same size and location) were drawn within the following: 1) aneurysm lumen, 2) brain parenchyma, 3) anterior pituitary gland (ie, T1-enhancing tissue), and 4) background noise. CNR was measured in comparison with the parenchyma [$CNR = (SI_1 - SI_2)/SD_{noise}$] for aneurysm lumen and pituitary gland, with *SI* indicating signal intensity.

Statistical Analysis

Interobserver agreement was evaluated (Fleiss κ). Occurrence of AWE in the whole cohort and CNR values were compared between conventional and MSDE-prepared SPACE images (Fisher exact and paired *t* test, respectively).

RESULTS

Thirty UIAs (mean long axis, 6.5 mm; range, 2.5–16 mm; mean short axis, 4.6 mm; range, 2–13 mm) were visible in the 22 patients (1.4 per patient; maximum, 4), affecting the basilar ($n = 1$), anterior cerebral ($n = 1$), middle cerebral ($n = 10$), anterior communicating ($n = 8$), or internal carotid artery ($n = 10$), including ophthalmic ($n = 4$) and intracavernous ($n = 2$) carotid segments.

Interrater agreement was almost perfect ($\kappa = 0.87$; 95% CI, 0.72–1.00; and $\kappa = 0.81$; 95% CI, 0.63–0.98) with conventional and MSDE-prepared SPACE images, respectively.

AWE was more frequently detected using a conventional (10/30 UIAs, 33.3%) than the MSDE-prepared (2/30, 6.7%) SPACE sequence ($P < .0001$). AWE was found using both sequences in 2 UIAs (Fig 1) and only with conventional SPACE in 8 with a circumferential appearance (Fig 2).

CNR did not differ between the 2 SPACE sequences for the pituitary gland (ie, T1-enhancing tissue) (321.9 ± 103.7 versus 304.8 ± 60.4 for conventional and MSDE-SPACE, respectively, $P = .51$) and was higher for the aneurysm lumen with MSDE-prepared SPACE sequences (102.4 ± 83.1 versus 180.2 ± 36.4, $P = .008$).

DISCUSSION

MSDE preparation reduced the occurrence of AWE, suggesting flowing blood mimicking AWE on conventional images. Such pitfalls may have biased previous studies evaluating AWE and could also have implications for patient care.

Double inversion recovery, MSDE,[10] or delay alternating with nutation for tailored excitation (DANTE) can be used for vessel wall MR imaging. We performed MSDE, considering its excellent blood suppression and adaptability to 3D imaging readout (while double inversion recovery is time-consuming and not easily adaptable for large-FOV 3D imaging). Low first-order gradient moment/b-values and composite pulses were used to avoid signal loss and eddy current effects, respectively.

With conventional SPACE sequences, our results (AWE in 33.3% of UIAs) were similar to those previously published.[2] The rate of AWE was lower (6.7%) using MSDE, similar to that of Nagahata et al[6] also using this technique (4.8% of UIAs). AWE detected using MSDE-prepared SPACE sequences can be related to wall inflammation and/or alternatively to an incomplete suppression of flowing blood not yet degraded by gradients. Such slow inflows may also be associated with degenerative remodeling and thus aneurysm growth.[15]

There is conflicting evidence on the relationship between AWE and aneurysm size. Some studies found no relationship between wall enhancement and aneurysm size,[2,4] with others demonstrating a positive correlation.[12] Considering our results, such discrepancy could be due to the relationship between intrasaccular flowing blood and aneurysm size.[2,12]

Limitations include a small number of patients and lack of histopathologic analysis (reference standard for AWE) because patients did not undergo an operation. However, our purpose was not to assess accuracy for the diagnosis of wall inflammation because we aimed to evaluate the influence of MSDE on AWE detectability. We focused only on UIA; further studies including patients with ruptured aneurysms with histologic analysis available may demonstrate the advantages of MSDE preparation.

ACKNOWLEDGMENTS

We thank Aurélien Monnet and Wadie Ben Hassen from Siemens Healthineers for their support.

REFERENCES

1. Mandell DM, Mossa-Basha M, Qiao Y, et al; Vessel Wall Imaging Study Group of the American Society of Neuroradiology. **Intracranial vessel wall MRI: Principles and Expert Consensus Recommendations of the American Society of Neuroradiology.** *AJNR Am J Neuroradiol* 2017;38:218–29 CrossRef Medline
2. Edjlali M, Gentric JC, Régent-Rodriguez C, et al. **Does aneurysmal wall enhancement on vessel wall MRI help to distinguish stable from unstable intracranial aneurysms?** *Stroke* 2014;45:3704–06 CrossRef Medline
3. Endo H, Niizuma K, Fujimura M, et al. **Ruptured cerebral microaneurysm diagnosed by 3-dimensional fast spin-echo T1 imaging with variable flip angles.** *J Stroke Cerebrovasc Dis* 2015;24:e231–35 CrossRef Medline
4. Hu P, Yang Q, Wang DD, et al. **Wall enhancement on high-resolution magnetic resonance imaging may predict an unsteady state of an intracranial saccular aneurysm.** *Neuroradiology* 2016;58:979–85 CrossRef Medline
5. Matouk CC, Mandell DM, Gunel M, et al. **Vessel wall magnetic resonance imaging identifies the site of rupture in patients with multiple intracranial aneurysms: proof of principle.** *Neurosurgery* 2013; 72:492–96 CrossRef Medline
6. Nagahata S, Nagahata M, Obara M, et al. **Wall enhancement of the intracranial aneurysms revealed by magnetic resonance vessel wall imaging using three-dimensional turbo spin-echo sequence with motion-sensitized driven-equilibrium: a sign of ruptured aneurysm?** *Clin Neuroradiol* 2016;26:277–83 CrossRef Medline
7. Omodaka S, Endo H, Niizuma K, et al. **Circumferential wall enhancement on magnetic resonance imaging is useful to identify rupture site in patients with multiple cerebral aneurysms.** *Neurosurgery* 2017 Jun 6. [Epub ahead of print] CrossRef Medline
8. Omodaka S, Endo H, Niizuma K, et al. **Quantitative assessment of circumferential enhancement along the wall of cerebral aneurysms using MR imaging.** *AJNR Am J Neuroradiol* 2016;37:1262–66 CrossRef Medline
9. Busse RF, Hariharan H, Vu A, et al. **Fast spin echo sequences with very long echo trains: design of variable refocusing flip angle schedules and generation of clinical T2 contrast.** *Magn Reson Med* 2006; 55:1030–37 CrossRef Medline
10. Wang J, Yarnykh VL, Hatsukami T, et al. **Improved suppression of plaque-mimicking artifacts in black-blood carotid atherosclerosis imaging using a multislice motion-sensitized driven-equilibrium (MSDE) turbo spin-echo (TSE) sequence.** *Magn Reson Med* 2007;58: 973–81 CrossRef Medline
11. Fu Q, Guan S, Liu C, et al. **Clinical significance of circumferential aneurysmal wall enhancement in symptomatic patients with unruptured intracranial aneurysms: a high-resolution MRI study.** *Clin Neuroradiol* 2017 Jun 27. [Epub ahead of print] CrossRef Medline
12. Liu P, Qi H, Liu A, et al. **Relationship between aneurysm wall enhancement and conventional risk factors in patients with unruptured intracranial aneurysms: a black-blood MRI study.** *Interv Neuroradiol* 2016;22:501–05 CrossRef Medline
13. Qiao Y, Steinman DA, Qin Q, et al. **Intracranial arterial wall imaging using three-dimensional high isotropic resolution black blood MRI at 3.0 Tesla.** *J Magn Reson Imaging* 2011;34:22–30 CrossRef Medline
14. Zhang L, Zhang N, Wu J, et al. **High resolution three dimensional intracranial arterial wall imaging at 3 T using T1 weighted SPACE.** *Magn Reson Imaging* 2015;33:1026–34 CrossRef Medline
15. Cebral J, Ollikainen E, Chung BJ, et al. **Flow conditions in the intracranial aneurysm lumen are associated with inflammation and degenerative changes of the aneurysm wall.** *AJNR Am J Neuroradiol* 2017;38:119–26 CrossRef Medline

Use of Diffusional Kurtosis Imaging and Dynamic Contrast-Enhanced MR Imaging to Predict Posttraumatic Epilepsy in Rabbits

W. Li, X. Wang, X. Wei, and M. Wang

ABSTRACT

BACKGROUND AND PURPOSE: Finding a reliable biomarker to thoroughly assess the brain structure changes in posttraumatic epilepsy is of great importance. Our aim was to explore the value of diffusional kurtosis imaging combined with dynamic contrast-enhanced MR imaging in the evaluation of posttraumatic epilepsy.

MATERIALS AND METHODS: A modified weight-drop device was used to induce traumatic brain injury. Rabbits were exposed to traumatic brain injury or sham injury. Diffusional kurtosis imaging and dynamic contrast-enhanced MR imaging were performed 1 day after injury. Posttraumatic epilepsy was investigated 3 months after injury. The traumatic brain injury group was further divided into 2 groups: the posttraumatic epilepsy and the non-posttraumatic epilepsy groups. Mean kurtosis and volume transfer coefficient values in the cortex, hippocampus, and thalamus were analyzed. After follow-up, the experimental animals were sacrificed for Nissl staining.

RESULTS: The posttraumatic epilepsy group comprised 8 rabbits. In the ipsilateral cortex, the volume transfer coefficient in the traumatic brain injury group was higher than that in the sham group; the volume transfer coefficient in the posttraumatic epilepsy group was higher than that in the non-posttraumatic epilepsy group. In the ipsilateral hippocampus, the volume transfer coefficient in the posttraumatic epilepsy group was higher than that in the non-posttraumatic epilepsy and sham groups. No difference was observed between the non-posttraumatic epilepsy and sham groups. In the ipsilateral cortex, mean kurtosis in the traumatic brain injury group was lower than that in the sham group, and mean kurtosis in the posttraumatic epilepsy group was lower than that in the non-posttraumatic epilepsy group. In the ipsilateral thalamus and hippocampus, mean kurtosis in the traumatic brain injury group was lower than that in the sham group, and mean kurtosis in the posttraumatic epilepsy group was lower than that in the non-posttraumatic epilepsy group. In the contralateral thalamus, mean kurtosis in the traumatic brain injury group was lower than that in the sham group; however, no difference was observed between the posttraumatic epilepsy and non-posttraumatic epilepsy groups.

CONCLUSIONS: Diffusional kurtosis imaging and dynamic contrast-enhanced MR imaging could be used to predict the occurrence of posttraumatic epilepsy in rabbits exposed to experimental traumatic brain injury.

ABBREVIATIONS: DCE = dynamic contrast-enhanced; DKI = diffusional kurtosis imaging; K^{trans} = volume transfer coefficient; MK = mean kurtosis; PTE = posttraumatic epilepsy; TBI = traumatic brain injury; THRIVE = T1 high-resolution isotropic volume excitation

During the past 30 years, given the continuous development of medical technology, the mortality rate from traumatic brain injury (TBI) has decreased from 50% to 25%.[1] Additionally, with the development of brain injury rehabilitation, most patients with limb function impairment exhibit a certain degree of recovery of function.[2] However, a fraction of patients in the rehabilitation process and chronic injury period exhibit neurologic abnormalities with great impact on quality of life.[3] The occurrence of neu-

Received December 27, 2017; accepted after revision March 3, 2018.

From the Department of Radiology (W.L., X. Wang, X. Wei, M.W.), Shanghai Jiao Tong University Affiliated Sixth People's Hospital, Shanghai, China; and Imaging Center (W.L.), Kashgar Prefecture Second People's Hospital, Kashgar, Xinjiang, China.

Wenbin Li and Xuan Wang are co-first authors.

This work was supported by the National Natural Science Foundation of China (grant No. 81271540), the Natural Science Foundation of Xinjiang Province (grant No. 2016D01C083), and the Shanghai Key Discipline of Medical Imaging (grant No. 2017ZZ02005).

Research involving animal participants had ethics approval. All applicable international, national, and/or institutional guidelines for the care and use of animals were followed. All procedures performed in studies involving animals were in accordance with the ethical standards of the institution or practice at which the studies were conducted.

Please address correspondence to Xuan Wang, MD, and Wen-Bin Li, MD, Department of Radiology, Shanghai Jiao Tong University Affiliated Sixth People's Hospital, 600 Yishan Rd, Shanghai, China, 200233; e-mail: 1072884137@qq.com, liwenbin@sjtu.edu.cn

Indicates open access to non-subscribers at www.ajnr.org

http://dx.doi.org/10.3174/ajnr.A5656

rologic abnormalities after TBI is still not well-understood; this issue makes treatment difficult.[4]

Posttraumatic epilepsy (PTE) is a common neurologic abnormality after TBI, which can not only increase patient disability and severely affect quality of life[5] but also cause damage to neurons and increase the degree of brain tissue damage, leading to disease progression and increased mortality.[6] Posttraumatic seizures are divided into 3 types: those occurring 24 hours after trauma, those occurring within the first week after trauma, and those occurring later than 1 week after trauma. In multivariate analysis, risk factors for later seizures were brain contusion with subdural hematoma, skull fracture, loss of consciousness or amnesia for >1 day, and age 65 years or older. Only patients with advanced seizures developed PTE.[7] The incidence of PTE ranges from 5% to 30% after TBI.[8,9] Therefore, it is important to identify a difference between PTE and posttraumatic seizures in the early stages. Age, penetrating brain injury, intracranial hemorrhage, midline shift of >5 mm, coma time of >24 hours, loss of consciousness, delayed memory time, or multiple bilateral parietal brain contusion and frontal temporal lobe lesions are risk factors for PTE.[10] Additionally, the cumulative incidence of PTE is approximately 2.1%, 4.2%, or 16.7% after 30 years in mild, moderate, or severe traumatic brain injury, respectively.[7,11] Therefore, the degree of injury is an important factor that influences the occurrence of PTE.

The above-mentioned risk factors for PTE align with factors that can be regularly used in the medical history and physical examination. However, determining the extent of damage after TBI requires a more objective method. In clinical work, the Glasgow Coma Scale score is used to evaluate the degree of injury in TBI.[12] Although the Glasgow Coma Scale score can be a more objective evaluation of a patient's function after injury, it does not adequately predict the development of PTE. An electroencephalogram can detect electrical activity of the brain in normal and abnormal conditions, especially in patients with epilepsy, and can find abnormal discharge of brain neurons to locate the lesion and evaluate its extent. However, a fraction of patients with epilepsy have electroencephalogram analysis that is negative for abnormal electrical discharge.[13] Moreover, Jennett and Van De Sande[13] found that 20% of patients with PTE had normal electroencephalogram results 3 months after brain injury. Therefore, the clinical evaluation of TBI in the prediction of PTE is limited.[14]

An important pathophysiologic event after TBI is the disruption of the blood-brain barrier, allowing movement of restricted components into the brain extracellular space, causing a series of secondary pathophysiologic changes, including PTE.[15] Imaging studies of traumatic brain injury are of great importance in the discovery of minor trauma and identification of biomarkers that facilitate diagnosis, prognosis, and treatment evaluation. Several previous studies using multimodal MR imaging technology, including T2 mapping,[16] T1ρ,[17] and diffusion-weighted imaging,[18] to quantitatively assess brain tissue changes after TBI showed that some of these parameters could predict the occurrence of PTE.[19]

Several studies have shown that dynamic contrast-enhanced (DCE) MR imaging and the associated volume transfer coefficient (K^{trans}) values could be used to quantitatively determine the permeability of the BBB.[20] Therefore, DCE MR imaging and K^{trans} values may have predictive value for PTE. As a new technique, diffusional kurtosis imaging (DKI) primarily focuses on the intracellular and extracellular components of the nervous system, and its structural characteristics are reflected by the degree of tissue diffusion, such as gray matter and white matter diffusion. In the case of random motion, the diffusion motion of water molecules satisfies the Gaussian distribution. For real biologic tissue, the diffusion of water molecules occurs between the intercellular spaces and cells. This movement is not necessarily free movement; therefore, the true movement of the water molecules is non-Gaussian in distribution. The greater the degree of water molecule diffusion in the surrounding environment is, the more complex the constituent elements in the body are and the more obvious the non-Gaussian dispersion is. The initial goal of the DKI model was to quantify the extent of dispersion from the Gaussian distribution. The DKI model of organization of diffusion components was created without the assumption of benefits of model variables and stability calculations; therefore, it reflects various microstructural changes. DKI provides a new perspective and thereby enhances clinical applications. DKI has been used in the assessment of TBI.[21] In this study, we aimed to investigate the value of DCE MR imaging and DKI technology in detecting brain microstructural changes and the prediction of PTE.

MATERIALS AND METHODS

Experimental Animals and Treatment

We obtained 38 clean-grade New Zealand white rabbits (2.5–3 kg; age, 2–4 months; 19 males and 19 females) from Shanghai Jiao Tong University Affiliated Sixth People's Hospital Experimental Animal Center. Animals were housed at 22°C ± 1°C with humidity controlled at 50%–60%, lights on from 18:00–06:00, and free access to food and water. After 2 weeks of environmental adaptation, the animals fasted for 6 hours before the TBI operation. The experimental study was approved by Shanghai Jiao Tong University Affiliated Sixth People's Hospital.

The TBI group was further divided into PTE and non-PTE groups according to the final outcome. MR imaging was performed at 1 day after trauma, and the scan sequences included T2-weighted, T1-weighted, DCE MR imaging, and DKI.

TBI Model

The TBI model we used is an adaptation of a previously published model.[13,20] The rabbits were subjected to auricular vein puncture, insertion of a venous indwelling needle, and injection of 2.5% pentobarbital sodium at 1 mL/kg, to achieve deep anesthesia (disappearance of conjunctival reflex) before being heparinized (25 U/mL) and fixed in a prone position on the experiment table. The bilateral parietal and frontal bones were exposed with blunt forceps, and a round bone window of approximately 8 mm to 1 cm in diameter was created with a dental drill at the right parietal bone. The integrity of the dura should not be breached. TBI group rabbits were later subjected to brain injury by dropping a 60-g weight onto the dura from a height of 20 cm, as previously described.[14] We used 1200-g × cm intensity in our model, which causes a degree of damage similar to that caused by middle and heavy brain trauma. Sham group animals were subjected to craniotomy, but no impact.

The bone window was sealed with solid paraffin, and the fascia and scalp were sutured. The operation was performed under sterile conditions. We followed standard aseptic practices, such as washing hands, wearing surgical clothes, wearing gloves, disinfection of skin at the operation site, and performing a single operation throughout the procedure. Animals were later allowed to recover from anesthesia.

Follow-Up and PTE Evaluation

The rabbits were randomly divided into 2 groups: the sham-operated group (sham group, $n = 8$) and the injured group (TBI group, $n = 30$). During the follow-up, all rabbits from the injured group were observed for 6 hours a day for 1 week; then, for 1 week every 4 weeks; and then, for a total of 3 times for 3 months. During the follow-up period of 3 months, 2 rabbits died on the third and fifth days after injury in the injured group of 30 rabbits, and the exact cause of death is unknown. Finally, 28 rabbits in the injured group were used for follow-up for 3 months. According to the improved method of Racine,[22] animals were assessed for seizure behavior for 1 week to 3 months following the trauma. Seizure behavior was scored as follows: 0, no seizure behavior; 1, staring; 2, nodding or wet dog shakes, with or without facial tics; 3, limb jitters; 4, standing, jitters, and persistent double forelimb nods; 5, bilateral limb fibrillation, loss of balance and falling, and tonic-clonic seizures; and 6, fatal seizure. The experimental rabbits that scored ≥3 points were defined as having epilepsy. In the experimental group, there was at least 1 seizure in the 8 animals that were assigned to the PTE group. Therefore, the final grouping was as follows: a PTE group of 8, a non-PTE group of 20, and sham group of 8.

MR Imaging

MR imaging was performed at 24 hours after TBI on a 3T MR imaging scanner (Intera Achieva SMI-2.1; Philips Healthcare, Best, the Netherlands) with a special, small animal 8-channel head coil. The MR imaging sequence included T1, DKI, T2, and DCE MR imaging. The middle of the rabbit bilateral inner canthus connection was used as a positioning mark. The scanning parameters were as follows: T1: TR/TE = 500/20 ms, number of signal averages = 6, layer thickness = 2 mm, FOV = 100 × 100 mm, matrix = 224 × 270; T2: TR/TE = 1600/100 ms, number of signal averages = 6, layer thickness = 2 mm, FOV = 100 × 100 mm, matrix = 200 × 192; DKI: 6 b-values (b=0, 500, 1000, 1500, 2000, 2500 s/mm^2), FOV = 100 × 100 mm, TR/TE = 1128/75 ms, layer thickness = 2 mm, number of signal averages = 4. Then, 3D T1 high-resolution isotropic volume excitation (THRIVE) was used to complete the DCE MR imaging. First, a basic THRIVE sequence was performed at flip angles of 4° and 8°, respectively. Next, animals were injected with Gd-DTPA (0.1 mmol/kg) with the specific method, and parameters were as follows: TR/TE = 6.8/3.2 ms, flip angle = 8°, spatial resolution = 3 × 3 × 3 mm, and continuous scanning of thirty 3D-THRIVE sequences to obtain T1 maps. Normal saline was injected 2 minutes after injection of the contrast agent. The total scan time for thirty 3D-THRIVE sequences was 7.5 minutes. Total scan time for all MR imaging was approximately 22 minutes.

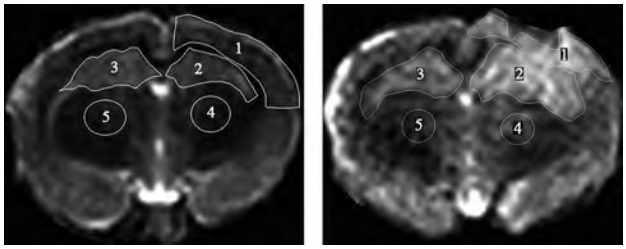

FIG 1. T2-weighted MR imaging displaying the manually outlined ROI. *Left*, Sham group ROIs: all ROIs correspond to ROIs as identified in the TBI group. *Right*, TBI group ROIs: ROI 1, ipsilateral cortex; ROI 2, ipsilateral hippocampus; ROI 3, contralateral hippocampus; ROI 4, ipsilateral thalamus; and ROI 5, contralateral thalamus.

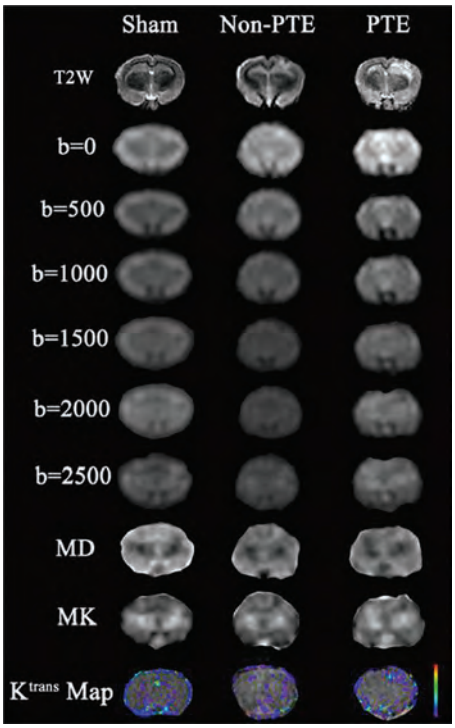

FIG 2. MR imaging from a representative animal in the PTE, non-PTE, and sham groups. The K^{trans} values of the PTE and non-PTE groups were higher than those of the sham operation group. In addition, the K^{trans} values of the corresponding ROI in the PTE group were higher than those in the non-PTE group.

Data Processing

DKI scans were analyzed according to a previous fitting method,[23] and the corresponding mean kurtosis (MK) map and MK values were obtained. All DCE MR imaging was transmitted to image-analysis software (CINE tool; GE Healthcare, Milwaukee, Wisconsin) to obtain quantitative K^{trans} values for DCE MR imaging, with the middle cerebral artery used as the input artery. According to previous methods,[20,24] the K^{trans} value was calculated by the 2-chamber model.[25] The ROI, including the ipsilateral cortex, the ipsilateral thalamus, the contralateral thalamus, the ipsilateral hippocampus, and the contralateral hippocampus, was defined on the basis of the T2-weighted image (Fig 1). The high signal area of the image was identified as the lesion, and the MK and K^{trans} values of the different regions were calculated (Fig 2). The procedure was performed by 2 radiologists in consensus.

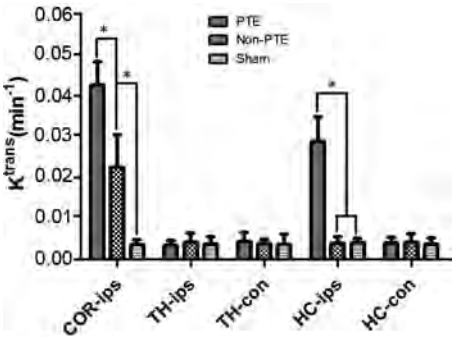

FIG 3. Comparison of K^{trans} in all ROIs among all study groups. The *asterisk* indicates comparison between the 2 groups, $P < .01$; COR-ips, ipsilateral cortex; TH-ips, ipsilateral thalamus; TH-con, contralateral thalamus; HC-ips, ipsilateral hippocampus; HC-con, contralateral hippocampus.

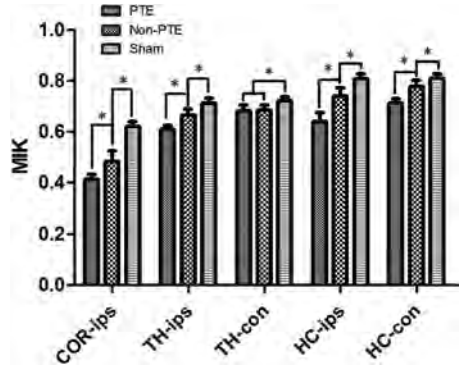

FIG 4. Comparison of MK in all ROIs among all study groups. The *asterisk* indicates comparison between the 2 groups, $P < .01$; COR-ips, ipsilateral cortex; TH-ips, ipsilateral thalamus; TH-con, contralateral thalamus; HC-ips, ipsilateral hippocampus; HC-con, contralateral hippocampus.

Nissl Staining

At the end of the experimental period, all rabbits were euthanized and perfused with 500 mL of 10% formaldehyde at first fast and then slow, lasting 1 hour. Brains were removed and postfixed in 4% formaldehyde and stored in the refrigerator at 4°C for 3–4 days. After dehydration and paraffin embedding, 4-μm sections were cut and subjected to Nissl staining, as previously described.[26] The differences in the neuron number in the contralateral hippocampus in PTE, non-PTE, and sham groups were analyzed.

Statistical Analysis

By means of SPSS 16 for statistical analysis (IBM, Armonk, New York), all values were expressed as the mean ± SD. Using the 1-way ANOVA, we analyzed the differences in K^{trans} and MK values among the 3 groups. Post hoc least significant difference tests were performed when the ANOVA group effects were significant. $P < .05$ was considered significant.

RESULTS

Comparison of K^{trans} Values among the Groups

We compared K^{trans} values among the 3 groups (Fig 3). In the ipsilateral cortex, there were significant differences in the K^{trans} values among the 3 groups ($P < .001$); the PTE and non-PTE groups had higher K^{trans} values than the sham group ($P < .001$). The K^{trans} value in the PTE group was significantly higher than in the non-PTE group ($P < .001$). In the ipsilateral hippocampus, the K^{trans} value of the PTE group was greater than that in the non-PTE and sham groups ($P < .001$). There were no significant differences in K^{trans} among the 3 groups in the ipsilateral thalamus, contralateral hippocampus, and contralateral thalamus (all $P > .05$).

Changes in MK Values following Injury

We also compared MK values among the 3 groups (Fig 4). In the injured cortex, the MK value of the PTE group was significantly lower than that in the non-PTE and sham groups ($P < .001$); the MK value of the non-PTE group was also significantly lower than that in the sham group ($P < .001$). In the ipsilateral thalamus and the ipsilateral and contralateral hippocampi, there were similar significant differences among the 3 groups, with a lower MK in the PTE group than in the non-PTE and sham groups and in the non-PTE group than in the sham group ($P < .001$). In the contralateral thalamus, the MK values in the TBI groups were lower than those in the sham group ($P < .001$), but there was no significant difference between the PTE and non-PTE groups.

Assessment of Neuronal Damage

We used Nissl staining to compare the number of cell bodies present in the contralateral hippocampus. Compared with the sham group, the PTE and non-PTE groups had reduced numbers of cell bodies in the contralateral hippocampus (Fig 5). We used a visual method under light microscope magnification of 100 to begin multiple counting of the total Nissl bodies in each field, which is only an approximate count of human judgment. Quantitative Nissl-positive cell numbers are very subjective; therefore, there are no accurate quantitative data given in this article. To prevent Nissl body staining from being obscured by other stains, such as hematoxylin-eosin, only Nissl staining was performed.

DISCUSSION

In this study, DCE MR imaging and DKI were used to detect brain microstructural changes in different ROIs 1 day after TBI and to predict the development of PTE 3 months after TBI. Our results showed the following: 1) the incidence of PTE in rabbits was 28.6% after TBI; 2) MK values of the PTE group were lower than those of the non-PTE group in the damaged side of the cortex, ipsilateral hippocampus, ipsilateral thalamus, and contralateral hippocampus, indicating that the structural complexity of the PTE group was lower than that in the non-PTE group.

The incidence of PTE in different studies varied, with a range of 5%–30% in the clinical research,[8] while in studies that used fluid percussion to create severe TBI models, the incidence ranged from 30% to 52%.[27] This study adopted the drop-device model of traumatic brain injury in rabbits. We used 1200-g × cm intensity in our model, which causes a degree of damage similar to that caused by moderate and severe brain trauma.[27] Similarly, we found that the incidence of PTE at 3 months was 28.6%.

After trauma, damage from TBI disrupts the BBB, which can cause a series of complications.[1] Previous studies have indicated that disruption of the BBB in the injured cortex is closely related to the development of PTE.[15] In the process of BBB disruption,

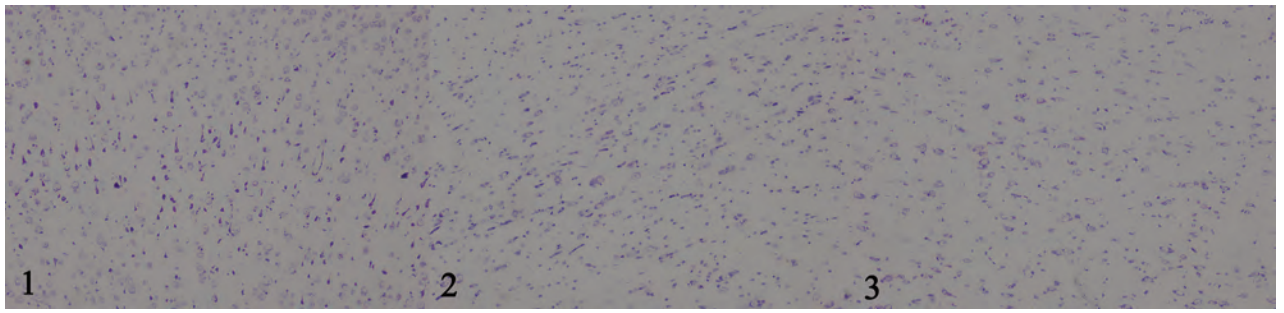

FIG 5. Comparison of the number of cell bodies in the contralateral hippocampus: 1) sham group (100×). 2) Non-PTE group (100×). 3) PTE group (100×). The number of cell bodies in the contralateral hippocampus in the PTE group was lower than that in the non-PTE and sham groups. The number of cell bodies in the non-PTE group was also lower than that in the sham group.

there is increased permeability from the blood vessels to the extracellular space, which can cause a series of pathologic changes.[28] This effect could contribute to the accumulation of extracellular potassium, resulting in the increase of *N*-methyl-D-aspartate receptor–mediated nerve activity and ultimately leading to epileptic discharge. In addition to damage to the injury cortex, the ipsilateral hippocampus could also be involved in the occurrence of PTE. A previous study showed that the diffusion tensor of the ipsilateral hippocampus predicted the occurrence of PTE.[19,29] The ipsilateral hippocampus injury could lead to increased chronic inflammation, neurodegeneration,[15] and hippocampal mossy fiber sprouting.[27] These changes, especially the occurrence and extent of mossy fiber sprouting in the hippocampus, are closely related to epilepsy.[27]

Immonen et al[30] used MR imaging technology to study brain injury in experimental rats for 11 months. These researchers' results showed changes in the focal cortical lesion and adjacent areas, including the perifocal and contralateral cortices and the ipsilateral and contralateral hippocampi.[30] We obtained similar results in this study. The MK values of the PTE group were significantly lower than those of the non-PTE and sham groups in the ipsilateral cortex, thalamus, and ipsilateral hippocampus, indicating that the damage occurred not only in the impact cortex but also in the ipsilateral thalamus and hippocampus. The underlying pathologic changes might be that the structural complexity of these regions was reduced. After TBI, local brain cell degeneration, disintegration, and apoptosis can reduce the organizational complexity of restricted areas, decreasing the MK value. In addition, comparable with previous findings,[19,29] this pathologic change may be related to the occurrence of PTE.

Damage to the cortex and ipsilateral thalamus may do harm to the thalamic cortical pathway. This pathway damage can promote the formation of epileptic networks. Furthermore, the onset of epilepsy is closely related to hippocampal mossy fiber sprouting.[31] Kharatishvili et al[27] found that the traumatic ipsilateral hippocampus average diffusion coefficient value mapped from DTI can predict mossy fiber sprouting. Additionally, they also found that the ipsilateral hippocampus had a series of pathologic changes, such as degeneration and mossy fiber sprouting, after TBI in the follow-up period. These pathologic changes can cause significant reduction in the degree of tissue complexity, thereby reducing MK.

The results of this study should be considered in the context of its limitations. First, we did not obtain an electroencephalogram for the experimental animals because several studies have indicated that the electroencephalogram is negative for PTE.[13,32] Thus, we only used the modified Racine method to evaluate the occurrence of PTE. Second, experimental animals are better to divide with the same sex distribution in each group, but we did not pay attention to the effect of animal sex on the study results, which may influence our results. Third, the injury of brain tissue will have a continuous dynamic pathologic process after TBI, such as the proliferation of glia at a later time, which will alter the MK value.[33] Thus, we examined only the MK changes at 1 day after TBI. Fourth, the follow-up time was relatively short, being only 3 months.

CONCLUSIONS

DKI and DCE MR imaging could be used to predict the occurrence of PTE in rabbits exposed to experimental traumatic brain injury.

Disclosures: Wenbin Li—*RELATED*: *Grant*: This study was funded by the National Natural Science Foundation of China (grant No. 81271540), the Natural Science Foundation of Xinjiang Province (grant No. 2016D01C083), and the Shanghai Key Discipline of Medical Imaging (grant No. 2017ZZ02005)*; *UNRELATED*: *Employment*: Shanghai Jiao Tong University Affiliated Sixth People's Hospital. *Money paid to the institution.

REFERENCES

1. Lu J, Marmarou A, Choi S, et al. **Mortality from traumatic brain injury.** *Acta Neurochir Suppl* 2005;95:281–85 CrossRef Medline
2. Rigon J, Burro R, Guariglia C, et al. **Self-awareness rehabilitation after traumatic brain injury: a pilot study to compare two group therapies.** *Restor Neurol Neurosci* 2017;35:115–27 CrossRef Medline
3. Verellen RM, Cavazos JE. **Post-traumatic epilepsy: an overview.** *Therapy* 2010;7:527–31 Medline
4. Pitkänen A, Immonen R. **Epilepsy related to traumatic brain injury.** *Neurotherapeutics* 2014;11:286–96 CrossRef Medline
5. Gupta PK, Sayed N, Ding K, et al. **Subtypes of post-traumatic epilepsy: clinical, electrophysiological, and imaging features.** *J Neurotrauma* 2014;31:1439–43 CrossRef Medline
6. Temkin NR, Dikmen SS, Anderson GD, et al. **Valproate therapy for prevention of posttraumatic seizures: a randomized trial.** *J Neurosurg* 1999;91:593–600 CrossRef Medline
7. Annegers JF, Hauser WA, Coan SP, et al. **A population-based study of seizures after traumatic brain injuries.** *N Engl J Med* 1998;338:20–24 CrossRef Medline
8. Frey LC. **Epidemiology of posttraumatic epilepsy: a critical review.** *Epilepsia* 2003;44(Suppl 10):11–17 Medline

9. Lucke-Wold BP, Nguyen L, Turner RC, et al. **Traumatic brain injury and epilepsy: underlying mechanisms leading to seizure.** *Seizure* 2015;33:13–23 CrossRef Medline
10. Messori A, Polonara G, Carle F, et al. **Predicting posttraumatic epilepsy with MRI: prospective longitudinal morphologic study in adults.** *Epilepsia* 2005;46:1472–81 CrossRef Medline
11. Annegers JF, Grabow JD, Groover RV, et al. **Seizures after head trauma: a population study.** *Neurology* 1980;30:683–89 CrossRef Medline
12. McNett M. **A review of the predictive ability of Glasgow Coma Scale scores in head-injured patients.** *J Neurosci Nurs* 2007;39:68–75 CrossRef Medline
13. Jennett B, Van De Sande J. **EEG prediction of post-traumatic epilepsy.** *Epilepsia* 1975;16:251–56 CrossRef Medline
14. Lu HY, Li TC, Tu YK, et al. **Predicting long-term outcome after traumatic brain injury using repeated measurements of Glasgow Coma Scale and data mining methods.** *J Med Syst* 2015;39:14 CrossRef Medline
15. Tomkins O, Feintuch A, Benifla M, et al. **Blood-brain barrier breakdown following traumatic brain injury: a possible role in posttraumatic epilepsy.** *Cardiovasc Psychiatry Neurol* 2011;2011:765923 CrossRef Medline
16. Kharatishvili I, Sierra A, Immonen RJ, et al. **Quantitative T2 mapping as a potential marker for the initial assessment of the severity of damage after traumatic brain injury in rat.** *Ex Neurol* 2009;217:154–64 CrossRef Medline
17. Sepponen RE, Pohjonen JA, Sipponen JT, et al. **A method for T1 rho imaging.** *J Comput Assist Tomogr* 1985;9:1007–11 CrossRef Medline
18. Shakir A, Aksoy D, Mlynash M, et al. **Prognostic value of quantitative diffusion-weighted MRI in patients with traumatic brain injury.** *J Neuroimaging* 2016;26:103–08 CrossRef Medline
19. Kharatishvili I, Immonen R, Gröhn O, et al. **Quantitative diffusion MRI of hippocampus as a surrogate marker for post-traumatic epileptogenesis.** *Brain* 2007;130(Pt 12):3155–68 CrossRef Medline
20. Wei XE, Wang D, Li MH, et al. **A useful tool for the initial assessment of blood-brain barrier permeability after traumatic brain injury in rabbits: dynamic contrast-enhanced magnetic resonance imaging.** *J Trauma* 2011;71:1645–50; discussion 1650–51 CrossRef Medline
21. Zhuo J, Xu S, Proctor JL, et al. **Diffusion kurtosis as an in vivo imaging marker for reactive astrogliosis in traumatic brain injury.** *Neuroimage* 2012;59:467–77 CrossRef Medline
22. Phelan KD, Shwe UT, Williams DK, et al. **Pilocarpine-induced status epilepticus in mice: a comparison of spectral analysis of electroencephalogram and behavioral grading using the Racine scale.** *Epilepsy Res* 2015;117:90–96 CrossRef Medline
23. Wang D, Guo ZH, Liu XH, et al. **Examination of hippocampal differences between Alzheimer disease, amnestic mild cognitive impairment and normal aging: diffusion kurtosis.** *Curr Alzheimer Res* 2015;12:80–87 CrossRef Medline
24. Wei XE, Zhang YZ, Li YH, et al. **Dynamics of rabbit brain edema in focal lesion and perilesion area after traumatic brain injury: a MRI study.** *J Neurotrauma* 2012;29:2413–20 CrossRef Medline
25. Tofts PS, Brix G, Buckley DL, et al. **Estimating kinetic parameters from dynamic contrast-enhanced T(1)-weighted MRI of a diffusable tracer: standardized quantities and symbols.** *J Magn Reson Imaging* 1999;10:223–32 Medline
26. Tong J, Liu W, Wang X, et al. **Inhibition of Nogo-66 receptor 1 enhances recovery of cognitive function after traumatic brain injury in mice.** *J Neurotrauma* 2013;30:247–58 CrossRef Medline
27. Kharatishvili I, Nissinen JP, McIntosh TK, et al. **A model of posttraumatic epilepsy induced by lateral fluid-percussion brain injury in rats.** *Neuroscience* 2006;140:685–97 CrossRef Medline
28. Tomkins O, Friedman O, Ivens S, et al. **Blood-brain barrier disruption results in delayed functional and structural alterations in the rat neocortex.** *Neurobiol Dis* 2007;25:367–77 CrossRef Medline
29. Immonen R, Kharatishvili I, Gröhn O, et al. **MRI biomarkers for post-traumatic epileptogenesis.** *J Neurotrauma* 2013;30:1305–09 CrossRef Medline
30. Immonen RJ, Kharatishvili I, Niskanen JP, et al. **Distinct MRI pattern in lesional and perilesional area after traumatic brain injury in rat: 11 months follow-up.** *Exp Neurol* 2009;215:29–40 CrossRef Medline
31. Gröhn O, Sierra A, Immonen R, et al. **Multimodal MRI assessment of damage and plasticity caused by status epilepticus in the rat brain.** *Epilepsia* 2011;52(Suppl 8):57–60 CrossRef Medline
32. Appleton RE, Demellweek C. **Post-traumatic epilepsy in children requiring inpatient rehabilitation following head injury.** *J Neurol Neurosurg Psychiatry* 2002;72:669–72 CrossRef Medline
33. Filibian M, Frasca A, Maggioni D, et al. **In vivo imaging of glia activation using 1H-magnetic resonance spectroscopy to detect putative biomarkers of tissue epileptogenicity.** *Epilepsia* 2012;53:1907–16 CrossRef Medline

Value of Quantitative Collateral Scoring on CT Angiography in Patients with Acute Ischemic Stroke

A.M.M. Boers, R. Sales Barros, I.G.H. Jansen, O.A. Berkhemer, L.F.M. Beenen, B.K. Menon, D.W.J. Dippel, A. van der Lugt, W.H. van Zwam, Y.B.W.E.M. Roos, R.J. van Oostenbrugge, C.H. Slump, C.B.L.M. Majoie, and H.A. Marquering, on behalf of the MR CLEAN investigators

ABSTRACT

BACKGROUND AND PURPOSE: Many studies have emphasized the relevance of collateral flow in patients presenting with acute ischemic stroke. Our aim was to evaluate the relationship of the quantitative collateral score on baseline CTA with the outcome of patients with acute ischemic stroke and test whether the timing of the CTA acquisition influences this relationship.

MATERIALS AND METHODS: From the Multicenter Randomized Clinical Trial of Endovascular Treatment of Acute Ischemic Stroke in the Netherlands (MR CLEAN) data base, all baseline thin-slice CTA images of patients with acute ischemic stroke with intracranial large-vessel occlusion were retrospectively collected. The quantitative collateral score was calculated as the ratio of the vascular appearance of both hemispheres and was compared with the visual collateral score. Primary outcomes were 90-day mRS score and follow-up infarct volume. The relation with outcome and the association with treatment effect were estimated. The influence of the CTA acquisition phase on the relation of collateral scores with outcome was determined.

RESULTS: A total of 442 patients were included. The quantitative collateral score strongly correlated with the visual collateral score (ρ = 0.75) and was an independent predictor of mRS (adjusted odds ratio = 0.81; 95% CI, .77–.86) and follow-up infarct volume (exponent β = 0.88; $P < .001$) per 10% increase. The quantitative collateral score showed areas under the curve of 0.71 and 0.69 for predicting functional independence (mRS 0–2) and follow-up infarct volume of >90 mL, respectively. We found significant interaction of the quantitative collateral score with the endovascular therapy effect in unadjusted analysis on the full ordinal mRS scale (P = .048) and on functional independence (P = .049). Modification of the quantitative collateral score by acquisition phase on outcome was significant (mRS: P = .004; follow-up infarct volume: $P < .001$) in adjusted analysis.

CONCLUSIONS: Automated quantitative collateral scoring in patients with acute ischemic stroke is a reliable and user-independent measure of the collateral capacity on baseline CTA and has the potential to augment the triage of patients with acute stroke for endovascular therapy.

ABBREVIATIONS: EVT = endovascular therapy; FIV = follow-up infarct volume; ICA-T = ICA carotid bifurcation; IQR = interquartile range; MR CLEAN = Multicenter Randomized Clinical Trial of Endovascular Treatment of Acute Ischemic Stroke in the Netherlands; qCS = quantitative collateral score; vCS = visual collateral score

Several large, randomized, controlled trials have proved the benefit of endovascular therapy (EVT) in patients with acute ischemic stroke with intracranial large-vessel occlusion.[1-6] Nevertheless, most patients remain functionally disabled despite successful recanalization. Many studies have emphasized the relevance of the assessment of collateral flow on baseline imaging to identify patients who would potentially benefit from EVT.[7-10] Until now, a patient's collateral status at baseline is the only proved treatment-effect modifier.[9] Accordingly, a recent randomized EVT trial even used the collateral capacity as an inclusion criterion, with the assumption that patients with poor collaterals will not benefit from treatment.[4] For assessment of collateral flow in the acute setting, single-phase CTA is the most widely used imag-

Received December 1, 2017; accepted after revision February 9, 2018.

From the Departments of Biomedical Engineering and Physics (A.M.M.B., R.S.B., I.G.H.J., H.A.M.), Radiology and Nuclear Medicine (A.M.M.B., I.G.H.J., O.A.B., L.F.M.B., C.B.L.M.M., H.A.M.), and Neurology (Y.B.W.E.M.R.), Academic Medical Center, Amsterdam, the Netherlands; Department of Robotics and Mechatronics (A.M.M.B., C.H.S.) and MIRA Institute for Biomedical Engineering and Technical Medicine (C.H.S.), University of Twente, Enschede, the Netherlands; Department of Clinical Neurosciences (B.K.M.), Hotchkiss Brain Institute, Cumming School of Medicine, University of Calgary, Foothills Hospital, Calgary, Alberta, Canada; Departments of Neurology (D.W.J.D.) and Radiology (A.v.d.L.), Erasmus MC, Rotterdam, the Netherlands; Department of Radiology (W.H.v.Z.), Maastricht UMC, Maastricht, the Netherlands; and Department of Neurology (R.J.v.O.), Maastricht UMC and Cardiovascular Research Institute Maastricht, Maastricht, the Netherlands.

This study was supported by a grant from the Stichting Toegepast Wetenschappelijk Instituut voor Neuromodulatie (TWIN). The MR CLEAN trial was funded by the Dutch Heart Foundation and through unrestricted grants from Angiocare BV, Covidien/ev3, MEDAC GmbH/Lamepro, and Penumbra.

Please address correspondence to Anna M.M. Boers, MSc, Department of Biomedical Engineering & Physics, Academic Medical Center, Meibergdreef 9, 1100 DD Amsterdam, the Netherlands; e-mail: amm.boers@gmail.com

http://dx.doi.org/10.3174/ajnr.A5623

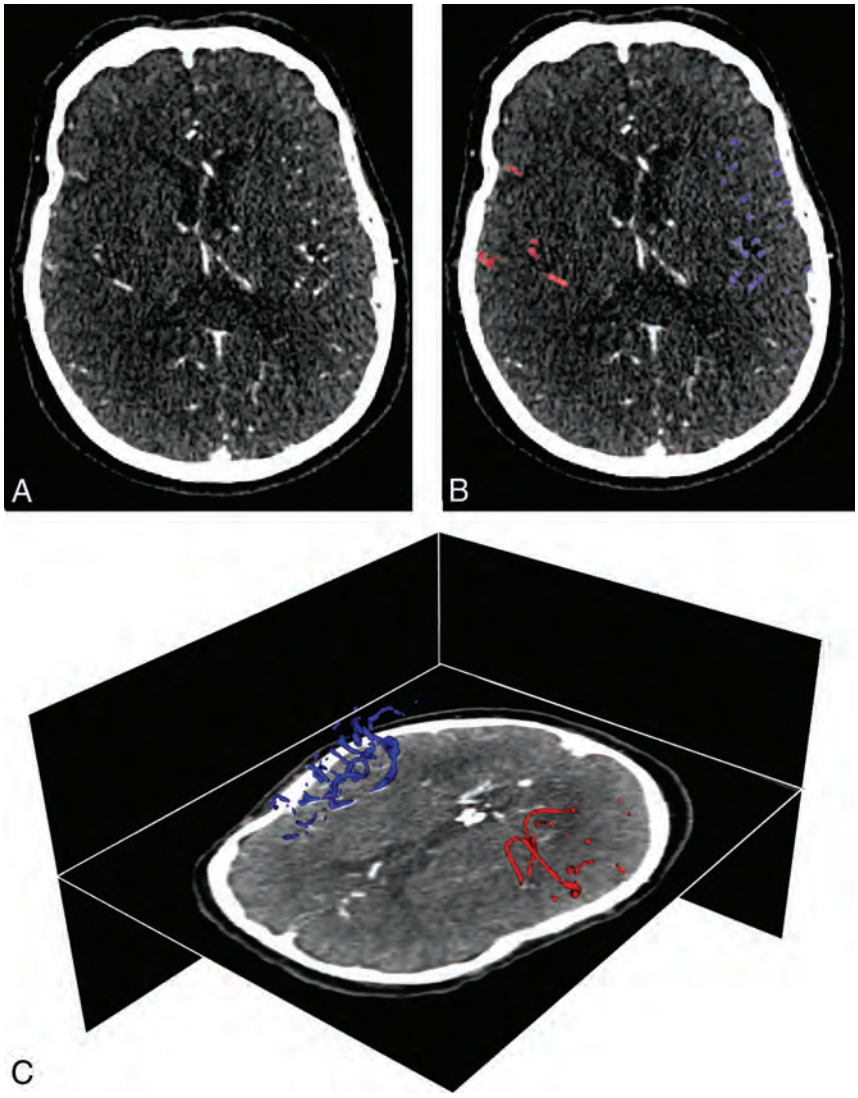

FIG 1. An example of quantitative collateral capacity scoring. *A*, An axial plane of a baseline CTA image acquired in the peak venous phase with a right-sided M1 segment occlusion of the MCA territory. *B*, Segmentation results of automated quantitative collateral assessment of the ipsilateral (*red*) and contralateral (*blue*) hemispheres. The quantitative collateral score was 46%. *C*, 3D representation of the segmented vasculature.

ing technique. Unfortunately, research regarding the value of the collateral capacity and its clinical applicability on CTA is limited by scoring methods that use coarse subjective scales susceptible to relatively poor interobserver agreement.[11] Hence, standardization is needed.[12]

An issue with single-phase CTA is that collateral assessment using this technique is heavily influenced by the timing of the CTA snapshot. Acquiring CTA too early after contrast bolus administration runs the risk of underestimating collateral capacity, while a delayed venous phase scan may hamper detection of the primary occlusion.

Recently, we introduced a technique to automatically quantify a patient's collateral capacity on single-phase CTA.[13] The aim of this study was to assess whether this quantitative measure has the potential to accurately assess collateral capacity on CTA. We also investigated its relation with radiologic and clinical outcomes in the study population of the Multicenter Randomized Clinical Trial of Endovascular Treatment of Acute Ischemic Stroke in the Netherlands (MR CLEAN).[1] Furthermore, we aimed to examine whether the timing of this CTA acquisition influences this relationship.

MATERIALS AND METHODS

Study Participants

We used data from MR CLEAN[1] for this post hoc analysis. MR CLEAN (ran between December 2010 and March 2014) was a randomized clinical trial of EVT plus standard care (intervention group) versus standard care alone (control group) in patients with a proximal arterial anterior circulation occlusion demonstrated on CTA and treatable within 6 hours after symptom onset. Patient eligibility has been described previously.[14] The MR CLEAN trial protocol was approved by the Medical and Ethical Review Committee (Medisch Ethische Toetsings Commissie of the Erasmus MC, Rotterdam, the Netherlands) and the research board of each participating center. All patient data were anonymized before analysis, and all patients or their legal representatives provided written informed consent.

For the present study, we selected patients who received thin-slice CTA imaging with a maximum of 2.5-mm slice thickness who had a proved occlusion of the internal carotid artery, carotid bifurcation (ICA-T), or M1 or M2 segment of the MCA. Patients with extreme artifacts or insufficient scan quality were excluded.

Outcomes

The primary clinical outcome was the degree of disability scored at 90 days on the mRS, a 7-point scale ranging from 0 (no symptoms) to 6 (death).[15] Secondary clinical outcome was functional independence at 90 days, defined as mRS 0–2.

Primary radiologic outcome was follow-up infarct volume (FIV) assessed on noncontrast CT at 1 week (range, 3–9 days). If follow-up noncontrast CT was not available at 1 week due to death or discharge, noncontrast CT at 24 hours (range, 12–48 hours) was used to assess FIV. Secondary radiologic outcome was FIV dichotomized into small and large infarcts, with a cutoff value of 90 mL.

Quantitative Assessment of Collateral Capacity

We used a previously presented method to quantify the collateral capacity in an automated fashion.[13] Briefly, this method consisted of estimation of the potential tissue-at-risk, segmentation of the

Table 1: Baseline characteristics

Characteristic	All (*N* = 442)
Age in years, median [IQR]	66 [54–76]
Female sex, % (*n*)	41.4 (183)
Left hemisphere infarct, % (*n*)	52.9 (234)
NIHSS score at baseline, median [IQR]	18 [14–22]
Alteplase (tPA) delivered, % (*n*)	88.9 (392)
Allocated to endovascular therapy, % (*n*)	46.8 (207)
Atrial fibrillation, % (*n*)	26.7 (118)
Myocardial infarction, % (*n*)	14.9 (66)
Peripheral arterial disease, % (*n*)	5.2 (23)
Diabetes mellitus, % (*n*)	13.6 (60)
Hypertension, % (*n*)	45.4 (200)
History of ischemic stroke, % (*n*)	10.6 (47)
Tobacco use, % (*n*)	26.3 (116)
Use of statins, % (*n*)	79.4 (350)
Onset to randomization in minutes, median [IQR]	201 [150–256]
Prestroke modified Rankin Scale score, % (*n*)	
0	79.9 (353)
1	10.4 (46)
≥2	5.7 (25)
ASPECTS at baseline, % (*n*)	
0–4	2.2 (10)
5–7	11.2 (49)
8–10	86.6 (381)
Occlusion location, % (*n*)	
ICA	0.7 (3)
ICA-T	27.4 (121)
M1	63.3 (280)
M2	8.6 (38)

arterial vasculature, and comparison of the hemispheres. First, a probability map[16] was used to estimate the extent of the potential tissue-at-risk on the basis of the level of occlusions in our dataset (ICA, ICA-T, M1, and M2). In this process, coregistration of the probability map with each patient's CTA was performed using Elastix (v.4.8; http://elastix.isi.uu.nl) to correct shape, orientation, and size. The potential tissue-at-risk was estimated by the region that had >5% chance of being infarcted at follow-up, given the level of occlusion. This region was mirrored to the contralateral hemisphere to serve as a reference. Second, the vasculature within these regions was segmented using a multiscale approach that enforces segmentation of solely the smaller arterial vasculature (eg, exclusion of the circle of Willis). Thus, mean vessel diameters (ranging from 0.9 to 3.1 mm) served as the target range. These diameters were based on a detailed statistical cerebroarterial atlas derived from 700 MR angiography images.[17] The sum of the multiplication of the segmented vasculature volume with its voxel-based density values represented the vascular appearance in each hemisphere. The quantitative collateral score (qCS) was calculated as the ratio of vascular appearance between hemispheres, via the following equation:

$$qCS = 100 \times \frac{VA_{\text{ipsilateral}}}{VA_{\text{contralateral}}};\ 0 \le qCS \le 100$$

where $VA_{\text{ipsilateral}}$ and $VA_{\text{contralateral}}$ are the vascular appearance of the affected and contralateral sides, respectively. qCS is expressed in percentages.

Visual Assessment of Collateral Capacity

The imaging committee of MR CLEAN assessed the visual collateral score (vCS) using the method of Tan et al.[18] All observers had >10 years of experience and were blinded to all clinical findings except the symptom side. Two neuroradiologists independently graded all CTA images. A third reader resolved any discrepancies. In the 4-point vCS scale, a score of zero indicated absent collaterals (0% filling of the occluded territory), 1 indicated poor collaterals (>0% and ≤50% filling of the occluded territory), 2 indicated moderate collaterals (>50% and <100% filling of the occluded territory), and 3 indicated good collaterals (100% filling of the occluded territory).[18] A mixture of the CTA source images and maximum-intensity-projections was used for visual assessment. If different slices expressed different filling, an average collateral score over all available slices was determined. Agreement beyond chance with a κ of 0.60 has previously been reported in MR CLEAN.[9] An example of qCS scoring is shown in Fig 1.

Follow-Up Infarct Volume

Follow-up infarct volume was assessed on follow-up noncontrast CT. In case of hemicraniectomy, the last scan before the operation was selected. Ischemic lesions were segmented using validated software, resulting in a binary mask of the FIV.[19] Adjacent hyperdense areas suspicious for hemorrhagic transformation were considered part of the FIV. All FIVs were inspected and adjusted if necessary by a trained observer (A.M.M.B.) with >4 years of experience and at least 1 neuroradiologist (W.H.v.Z., L.F.M.B., or C.B.L.M.M.) with >15 years of experience. A consensus reading with 2 neuroradiologists was performed to resolve any discrepancies. The FIV was calculated in milliliters by multiplying the number of voxels of the segmented ischemic lesion by its voxel size.

Assessment of CTA Image-Acquisition Phase

The scoring method introduced by Rodriguez-Luna et al[20] was used to assess phases of the CTA image acquisition. A trained observer (A.M.M.B.) measured the contrast density in Hounsfield units in the unaffected hemisphere of the M1 segment of the MCA territory (arterial structure) and the confluence of sinuses (venous structure). On the basis of these contrast measurements, all CTA studies were classified into 1 of the 5 acquisition phases: "early arterial," "peak arterial," "equilibrium," "peak venous," or "late venous." Phases were further dichotomized into "early arterial" and "arteriovenous" (peak arterial through late venous phase).

Statistical Analysis

Dichotomous variables were presented as a proportion of the population. Continuous variables were presented as mean and SD if normally distributed or as median and interquartile range (IQR) otherwise.

Relationship of the Quantitative Collateral Score with the Reference Score

The vCS was used as a reference standard to evaluate the quantitative scoring method qCS. One-way ANOVA was performed to test for differences in qCS values among vCS groups. The Spearman rank correlation coefficient was calculated to determine the relationship of qCS with vCS.

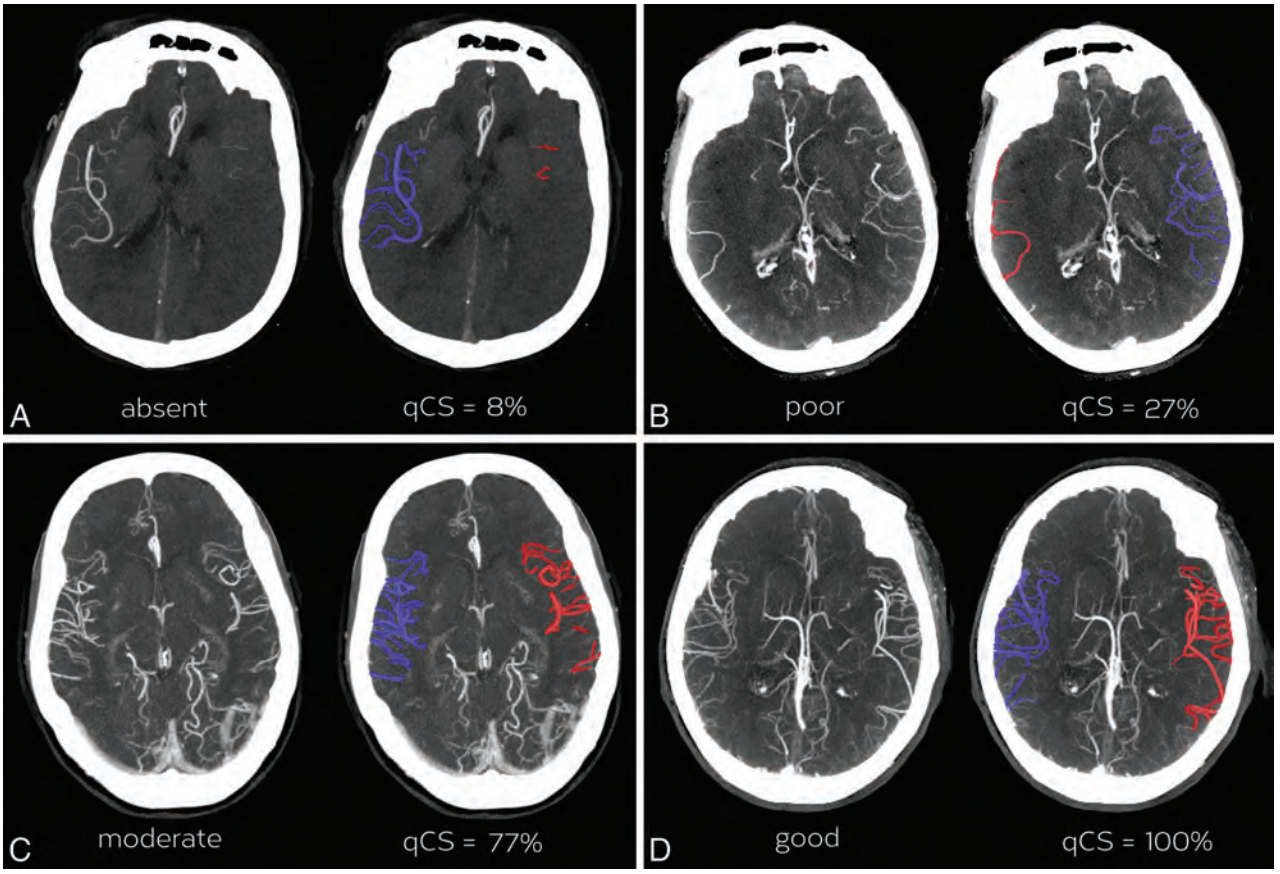

FIG 2. Case examples of 4 patients with different visually scored collateral grades and corresponding quantitative collateral scores. Each panel shows a maximum-intensity-projection of the CTA image (*left*) and the segmented vasculature for qCS calculation (*right*). The automated segmentation on the ipsilateral side is shown in blue and the segmentation on the contralateral side is shown in red. *A*, Absent collaterals (visual collateral score = 0). CTA of an 83-year-old man with a left-sided M2 occlusion acquired in the early arterial phase. Follow-up infarct volume was 205 mL, and the mRS score was 6. *B*, Poor collaterals (vCS = 1). CTA of a 79-year-old man with a right-sided M1 occlusion acquired in the equilibrium phase. FIV was 245 mL, and the mRS score was 6. *C*, Moderate collaterals (vCS = 2). CTA of a 45-year-old woman with a left-sided M1 occlusion acquired in the peak arterial phase. FIV was 24 mL, and the mRS score was 2. *D*, Good collaterals (vCS = 3). CTA of a 76-year-old woman with a left-sided ICA-T occlusion acquired in the late venous phase. FIV was 48 mL, and the mRS score was 3.

Relationship of Collateral Capacity Scores with Outcome

Spearman rank correlation coefficients with 95% CIs were calculated for both scoring methods to determine the relation with clinical and radiologic outcome measures. The effect of the collateral scores on outcome was estimated with univariate and multivariable modeling. The effect on the primary clinical outcome (mRS) was calculated using ordinal logistic regression and reported as adjusted and unadjusted ORs with 95% CIs. The effect of collateral scores on FIV was analyzed with linear regression and reported as adjusted and unadjusted βs with 95% CIs. FIV was log-transformed to best satisfy the linear model (normal distribution of residuals and homoscedasticity). The exponent of β determines the relative difference in FIV per 1-point increase in the collateral score. Receiver operating characteristic analysis was performed to assess the association with dichotomized outcomes. Areas under the curve were tested for differences using the approach of DeLong et al.[21] Multivariable modeling included prespecified prognostic variables: EVT allocated; age; stroke severity measured on the NIHSS score at baseline; time of stroke symptom onset to randomization; the presence of previous stroke, atrial fibrillation, or diabetes mellitus; and occlusion site (ICA-T versus not).

Treatment Effect Modification by Collateral Capacity Scores

We used multiplicative interaction terms to test for modification of treatment effect on clinical and imaging outcomes by collateral capacity, as measured with qCS and vCS.

Influence of Phase of CTA Image Acquisition

To study the influence of CTA acquisition phase, we used modeling with multiplicative interaction terms to test for modification of the effect of collateral capacity on outcomes by acquisition phase. The relation of the collateral measures to outcome was determined via the Spearman correlation for each individual acquisition phase, as well as for the dichotomized phases.

A 2-sided P value $<.05$ was considered significant for all tests. All statistical analyses were performed in SPSS, Version 24.0 (IBM, Armonk, New York).

RESULTS

From the 500 patients in MR CLEAN, 58 subjects were excluded from the present study for the following reasons: Thirty-two did not have available thin-slice CTA images, 14 had incomplete head

scans, 8 scans showed insufficient quality (extreme noise, $n = 5$; extreme motion artifacts, $n = 3$), 3 had an occlusion in the anterior cerebral artery, and 1 patient was excluded because of a coregistration error. Thus, 442 patients met the study-specific inclusion criteria. Baseline characteristics are shown in Table 1.

The mean age was 64.8 ± 13.8 years, 207 (46.8%) were allocated to EVT, the median FIV was 87 mL (IQR, 32–190), and the median mRS at 90 days was 4 (IQR, 2–5), with 111 (25.1%) achieving functional independence (mRS 0–2).

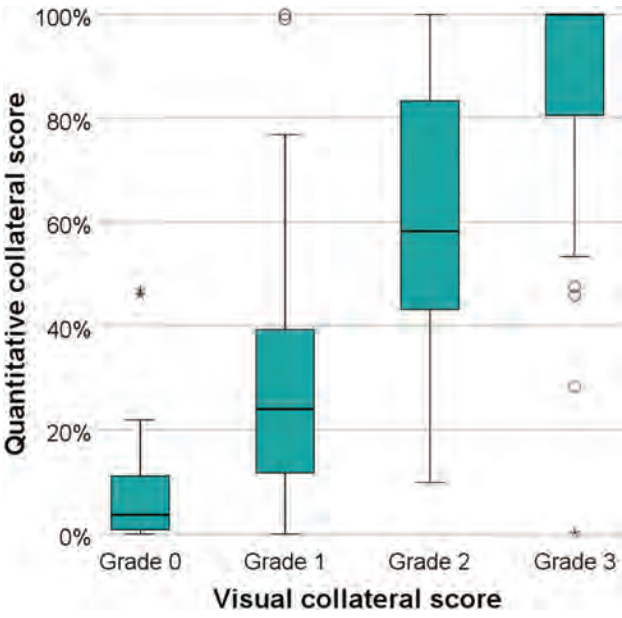

FIG 3. Distribution of quantitative collateral scores per visual collateral score, ranging from absent collaterals (0% filling of the occluded territory) to good collaterals (100% filling of the occluded territory). The quantitative collateral score was significantly different among all visual collateral score groups, except for absent collaterals (grade 0) versus poor collaterals (grade 1).

Relation with Reference Score

Figure 2 illustrates 4 case examples of CTA images with corresponding vCSs and qCSs. The distribution of the qCS per vCS is shown in Fig 3. The qCS was significantly different among all vCS groups ($P < .05$), except for absent collaterals versus poor collaterals ($P = .46$). The correlation between qCS and vCS was strong and statistically significant with a Spearman ρ of 0.75 ($P < .001$).

Relation with Outcome

Both vCS and qCS showed significant correlations with mRS (both $P < .001$) and FIV (both $P < .001$) (Table 2). The relation of vCS with mRS and FIV was weaker (mRS: $\rho = -.31$; FIV: $\rho = -.44$) compared with qCS (mRS: $\rho = -.40$; FIV: $\rho = -.46$), but this difference was not statistically significant. Adjusted for the prespecified prognostic variables, the OR for an increase in mRS was 0.81 (95% CI, 0.77–0.86; $P < .001$) per 10% increase in qCS. Linear regression analysis showed that an increase of 10% in qCS led to a relative decrease in FIV of 13% (exponent of $\beta = 0.87$, $P < .001$) in the adjusted analysis. Results of the all regression analyses for the effect of collateral scores on outcome are shown in Tables 3 and 4.

Receiver operating characteristic analysis showed areas under the curve of, respectively, 0.68 and 0.65 for qCS and vCS for discrimination between favorable and unfavorable functional outcomes (Fig 4*A*). This difference was not significant ($P = .21$). When we assessed the power to distinguish small from large infarcts, qCS showed an area under the curve of 0.71, compared with an area under the curve of 0.69 for the vCS measure ($P = .23$) (Fig 4*B*).

Table 2: Spearman rank ρ (95% CI) of collateral measures with outcomes for all studies and per CTA acquisition phase

	All Studies (*N* = 442)	Early Arterial (*n* = 91)	Peak Arterial (*n* = 56)	Equilibrium (*n* = 123)	Peak Venous (*n* = 114)	Late Venous (*n* = 58)
Follow-up infarct volume						
Visual collateral score	−.44 (−.53 to −.36)[a]	−.35 (−.55 to −.13)[a]	−.46 (−.65 to −.21[a]	−.51 (−.64 to −.35)[a]	−.49 (−.64 to −.29[a]	−.47 (−.66 to −.24)[a]
Quantitative collateral score	−.46 (−.54 to −.37)[a]	−.45 (−.62 to −.24)[a]	−.46 (−.66 to −.19)[a]	−.51 (−.65 to −.34)[a]	−.41 (−.56 to −.20)[a]	−.52 (−.70 to −.29)[a]
mRS at 90 days						
Visual collateral score	−.31 (−.39 to −.22)[a]	−.19 (−.38 to .03)	−.22 (−.49 to −.04)	−.28 (−.49 to −.15)[a]	−.29 (−.45 to −.09)[a]	−.41 (−.63 to −.19)[a]
Quantitative collateral score	−.40 (−.48 to −.32)[a]	−.35 (−.53 to −.13)[a]	−.34 (−.55 to −.10)[a]	−.38 (−.58 to −.25)[a]	−.30 (−.42 to −.08)[a]	−.37 (−.59 to −.12)[a]

[a] Significant correlation at $P < .01$.

Table 3: Results of adjusted and unadjusted regression analyses for the effect of collateral capacity on follow-up infarct volume

	Adjusted			Unadjusted		
	β Log-Transformed (95% CI)[a]	Exp. (β)[b]	*P* Value	β Log-Transformed (95% CI)[a]	Exp. (β)[b]	*P* Value
Visual collateral score per 1 point	−0.49 (−0.61 to −0.37)	0.60	<.001	−0.59 (−0.71 to −0.47)	0.54	<.001
Quantitative collateral score per 10%	−0.13 (−0.16 to −0.099)	0.88	<.001	−0.14 (−0.18 to −0.11)	0.87	<.001

Note:—Exp. (β) indicates exponent of β.

[a] Due to the non-normal distribution of follow-up infarct volume, a log +1 transformation was performed to best fit the assumptions associated with the linear regression model.

[b] Exponent of β was calculated to determine the relative difference of follow-up infarct volume with an increase in collateral scores.

Table 4: Results of adjusted and unadjusted regression analyses for the effect of collateral capacity on modified Rankin Scale

	Adjusted		Unadjusted	
	Odds Ratio (95% CI)	*P* Value	Odds Ratio (95% CI)	*P* Value
Visual collateral score per 1 point	0.61 (0.50–0.75)	<.001	0.51 (0.42–0.62)	<.001
Quantitative collateral score per 10%	0.81 (0.77–0.86)	<.001	0.85 (0.81–0.90)	<.001

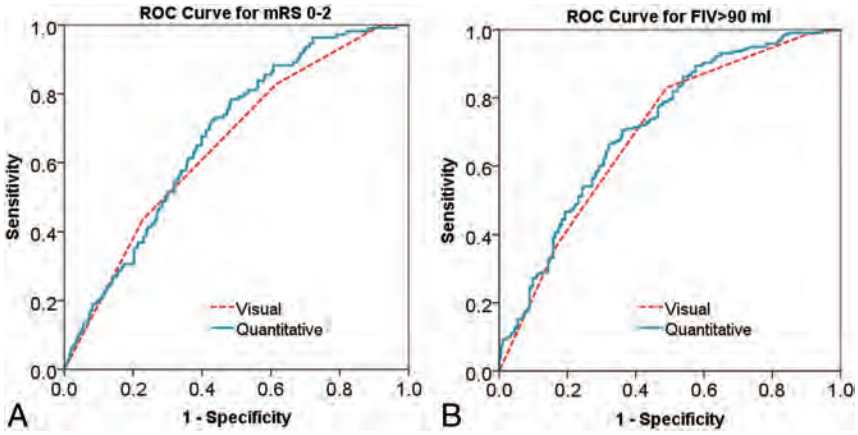

FIG 4. Receiver operating characteristic curve analysis of visual and quantitative collateral scores for discriminating favorable outcome (mRS 0–2) with areas under the curve of, respectively, 0.65 and 0.68 (*A*) and large infarct (FIV of >90 mL) with areas under the curve of, respectively, 0.69 and 0.71 (*B*).

Table 5: *P* values of interaction analysis for primary and secondary outcome measures

	FIV (Continuous)	FIV ≤90 mL vs FIV >90 mL	mRS (Ordinal)	mRS 0–2 vs 3–6
vCS-unadjusted analysis	.40	.43	.23	.11
vCS-adjusted analysis	.60	.54	.10	.075
qCS-unadjusted analysis	.15	.75	.048[a]	.049[a]
qCS-adjusted analysis	.33	.48	.081	.18

[a] $P < .05$, 2-sided.

Association with Treatment Effect

Results of the interaction analysis for the qCS and vCS measures are shown in Table 5. A significant interaction of qCS and the EVT effect was found in the unadjusted analysis on the full ordinal mRS scale ($P = .048$) and on favorable outcome (mRS 0–2) with a P value of .049. This effect was absent after adjustment for predefined baseline variables. No significant modification of treatment effect by vCS was found in this substudy of MR CLEAN.

Influence of Phase on CTA Image Acquisition

Baseline CTA was acquired in the early arterial phase in 20.6% ($n = 91$), peak arterial phase in 12.7% ($n = 56$), equilibrium phase in 27.8% ($n = 123$), early venous phase in 25.8% ($n = 114$), and late venous phase in 13.1% ($n = 58$). Bar graphs (Fig 5) depict the distribution of qCS within the early arterial and arteriovenous phases and the number of patients reaching functional independence.

A significant modification of the effect of qCS on clinical and imaging outcomes (mRS at day 90 and FIV) by acquisition phase was found in unadjusted (both $P < .001$) and adjusted analysis (mRS: $P = .004$; FIV: $P < .001$). The strength of the relationship between collateral capacity and outcome was greater in the arteriovenous phase. This effect modification was absent with vCS as a determinant of mRS (unadjusted $P = .50$, adjusted $P = .89$) and FIV (unadjusted $P = .19$, adjusted $P = .32$), respectively.

Spearman correlation coefficients for collateral measures with imaging and clinical outcomes per CTA image acquisition phase are shown in Table 2. A significant correlation of qCS with both mRS and FIV was observed among all phases, as well as for vCS with FIV. Correlation of vCS with mRS measured in the early arterial and peak arterial phases did not reach statistical significance (respectively $P = .052$ and $P = .11$). Overall, correlations of both qCS and vCS with outcome were weaker in the early arterial phase ($n = 91$, 20.6%) than in the arteriovenous phase ($n = 331$, 79.4%).

DISCUSSION

In this post hoc analysis of MR CLEAN, we found that collateral capacity estimated on baseline CTA quantitatively correlates well with current visual assessment. We provide evidence that quantitative assessment of collateral capacity is a strong independent predictor of outcome. Overall, patients with a low qCS are associated with larger FIVs on follow-up imaging and worse functional outcomes. We showed that acquiring an image in an early stage after contrast bolus was common in MR CLEAN. We demonstrated that the timing of the CTA acquisition modifies the effect of quantitative collateral assessment on outcome in such a way that early arterial acquisitions are inferior to arteriovenous acquisitions.

Despite the growing body of research on collateral circulation and the evidence that it could guide treatment decisions, only a few studies have addressed the use of automated quantitative analysis to assess the collateral capacity. The promise of extracting quantitative imaging parameters enables producing observer-independent and consistent results and may aid physicians in discriminating those who may do poorly with EVT. This could be especially helpful for physicians in local hospitals who seldom deal with patients with acute stroke and therefore lack experience in grading collateral capacity. Moreover, a reliable quantitative measure augments the ability of clinical research to fully explore the role of collateral circulation in evaluating and understanding stroke pathophysiology.

Our study is not the first to use quantitative analysis for estimation of collateral capacity. Ernst et al[22] proposed an atlas-based method for automated quantification of the collateral abundance on time-of-flight and contrast-enhanced MRA imaging and found, in concordance with our study, that poorly visible collaterals identify patients with poor outcome. However, we found no other study that examined the clinical value of quantitatively assessed collateral capacity on CTA. Even though CTA (single-phase in particular) is limited in its ability to evaluate the cerebral circulation, it is the most widely used imaging technique in acute stroke. Thus, our study shows the benefit of quantitating collaterals in the current acute workflow that involves rapid triage of patients with stroke.

We observed a substantial effect of the collateral capacity assessed on CTA on a patient's functional outcome, in line with previous studies. For example, a qCS of 30% would increase the odds of a better functional outcome (ie, decreasing 1 point on the mRS scale) with 57%, compared with a qCS of 0%. Also, that we

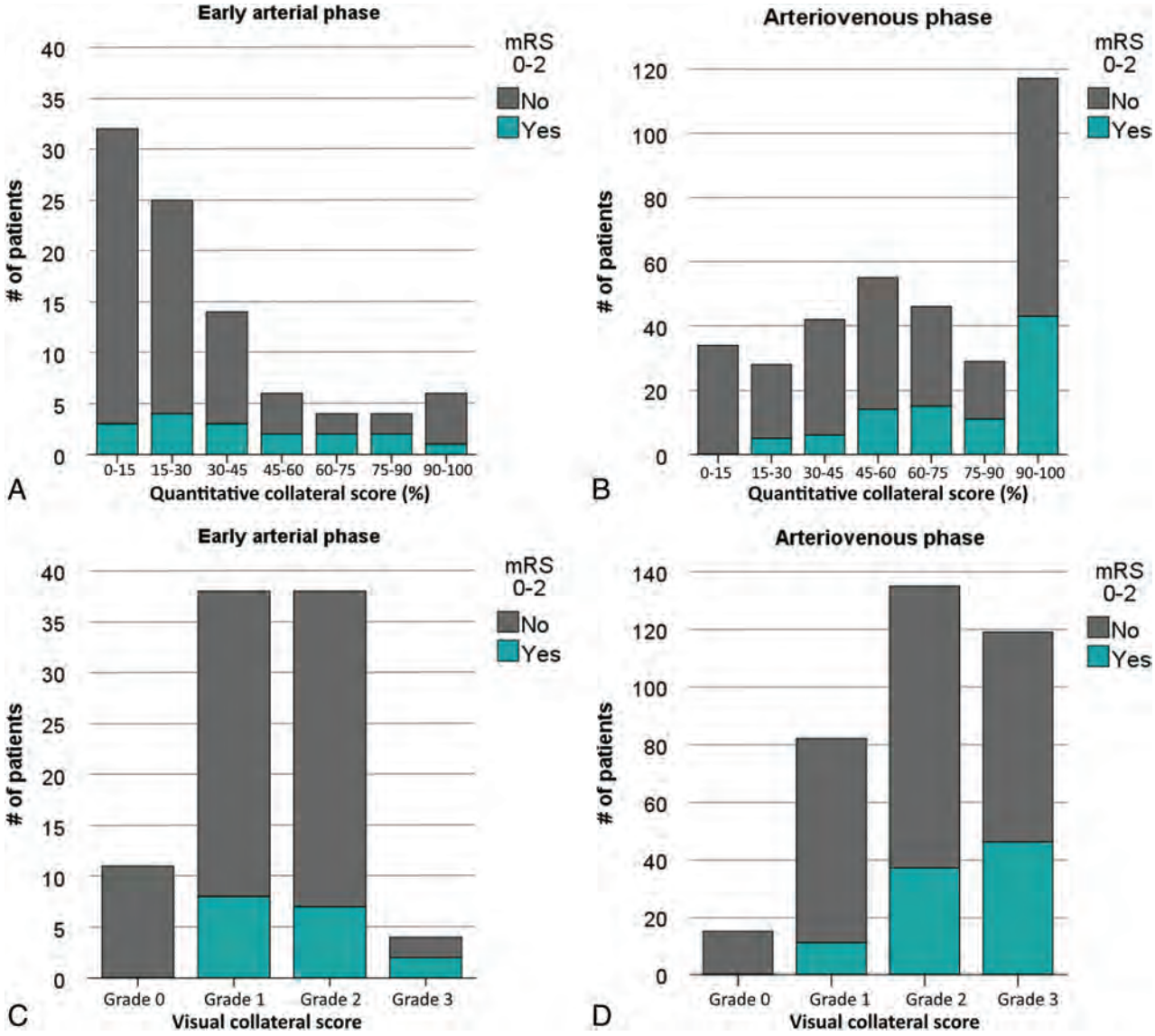

FIG 5. Bar graphs depict the proportion of functional independence (mRS 0–2) by quantitative collateral score strata for CTA image acquisition in the early arterial phase (*A*) and arteriovenous phase (*B*), and by visual collateral scores in the early arterial phase (*C*) and arteriovenous phase (*D*).

found a significant modification of treatment effect by collaterals highlights the importance of collateral grading on baseline imaging, confirming the statement of the Acute Stroke Imaging Research Roadmap III on the role of imaging selection on outcomes in acute stroke reperfusion clinical trials.[12]

A modification of the EVT effect by visually scored collaterals was absent in this substudy, which contrasts with the findings in a previous study of the entire MR CLEAN population.[9] This discrepancy is most likely due to the difference in study populations.

We found that with early acquisitions after contrast administration, patients with poor collaterals did unexpectedly well, whereas not a single patient with a qCS of <15% reached functional independence in the arteriovenous phase. This finding illustrates the downside of conventional single-phase CTA, in which the risk of underestimation is considerable because of the lack of temporal information.[23-25] Our data confirm that the strength of the relation between collateral capacity and outcome increases with the acquisition phase. We did not find an effect modification of visually graded collaterals by CTA acquisition phase. This can possibly be explained by the low number of patients in the lower grades. A substantial number of patients in our study having untimely CTA acquisitions raises concern, especially when using collateral capacity as a selection tool for EVT. Our study emphasizes that one should be aware of the limitations of single-phase CTA in evaluating a patient's collateral capacity. In future work, our method could benefit from an automated CTA acquisition phase measurement to easily gain knowledge on optimal or suboptimal timing as a measure of reliability. This could be realized by expanding the cerebroarterial atlas with venous structures and ROIs as proposed by Rodriguez-Luna et al.[20]

We can only speculate that due to newer CT scanners and the increasing awareness of physicians of the role of collaterals in

acute stroke, the timing of image acquisition in general may improve. Upcoming techniques such as multiphase CTA and dynamic CTA overcome this problem by sequential imaging at the same level in the brain. Multiphase or dynamic CTA is better at prognostication of clinical outcomes than single-phase CTA.[26-28] Moreover, dynamic CTA has proved superior in predicting the FIV.[27] Our method of quantitatively scoring the collateral capacity can easily be extended to these imaging techniques. This transition could be achieved by applying our method to each individual sequence after correcting for head movement via coregistration. Subsequently, the values within each voxel could be condensed to a single value such as the average or maximum. Also, measuring the time-to-peak within the voxels would allow showing the speed of contrast filling within the arteries (contrary to the contralateral side), which might aid the physician in recognizing the tissue-at-risk. Additional research is warranted to further elucidate the role of quantitative collateral scoring within these techniques.

Our study has some limitations. We excluded some patients with thick-slice CTAs compared with thin slices; the former results in suboptimal vessel segmentation, a key requirement in quantitative collateral scoring. In addition, we did not exclude patients who had a proximal stenosis. Such patients could have had delayed filling due to the flow-limiting stenosis. In MR CLEAN, 57 patients were scored as having cervical internal carotid artery stenosis.[29] This might have affected the interpretation of the collateral capacity. Furthermore, we did not evaluate the relation of qCS with collateral scores as assessed on multivessel DSA, the criterion standard for collateral assessment, on the grounds that sample sizes were too small to consider DSA a reference standard: Of all patients in MR CLEAN having both CTA and DSA of sufficient quality to evaluate complete collateral circulation, imaging data of a mere 45 patients could be used for evaluation.[30] Moreover, Jansen et al[30] have shown that the agreement between CTA- and DSA-based visual collateral assessment is low. The relation of qCS with DSA-based collateral scores is therefore also expected to be weak.

With the recent pooling of multiple randomized controlled trials,[31] larger datasets may become available to investigate how qCS fared against DSA. Moreover, the computation time required for image postprocessing of 6–10 minutes on a modern PC is rather high. Future work must focus on reducing this computation time before this approach could be applied in clinical practice where speed is of the essence. In addition, the quantitative method makes use of a cerebroarterial atlas derived from healthy subjects. Even though data of 700 subjects was used to create this atlas, it is possible that the vascular anatomy of a patient with acute stroke deviates from that in these healthy subjects, leading to over- and underestimation of the presence of arteries distal to the clot. Adding a component that identifies clot location (manually or automated) will likely increase the accuracy.

CONCLUSIONS

We provide evidence that quantitative collateral scoring is a reliable measure of the collateral capacity on baseline CTA in patients with acute stroke. Our results show that qCS could help clinicians make EVT treatment decisions and predict clinical and imaging outcomes. Furthermore, qCS can be standardized relatively easily compared with current subjective measures of collateral assessment in patients presenting with acute ischemic stroke.

Disclosures: Anna M.M. Boers—*UNRELATED*: *Stock/Stock Options*: Nico-lab BV. O.A. Berkhemer—*UNRELATED*: *Consultancy*: Stryker*. Bijoy K. Menon—*OTHER RELATIONSHIPS*: patent pending for systems of triage in acute stroke. Diederik W.J. Dippel—*UNRELATED*: *Grants/Grants Pending*: Dutch Heart Foundation, Dutch Brain Foundation, Angiocare BV, Medtronic/Covidien/ev3, MEDAC GmbH/Lamepro, Penumbra, Stryker, Topic Medical/Concentric*. Aad van der Lugt—*UNRELATED*: *Consultancy*: Stryker*; *Grants/Grants Pending*: Dutch Heart Foundation, Dutch Brain Foundation, Stryker, Penumbra*. Wim H. van Zwam—*UNRELATED*: *Payment for Lectures Including Service on Speakers Bureaus*: Cerenovus, Stryker*. Charles B.L.M. Majoie—*UNRELATED*: *Grants/Grants Pending*: Dutch Heart Foundation, European Commission, TWIN Foundation, Stryker*. Henk A. Marquering—*OTHER RELATIONSHIPS*: cofounder and shareholder of Nico-lab BV. *Money paid to the institution.

REFERENCES

1. Berkhemer OA, Fransen PS, Beumer D, et al. **A randomized trial of intraarterial treatment for acute ischemic stroke.** *N Engl J Med* 2015; 372:11–20 CrossRef Medline
2. Campbell BC, Mitchell PJ, Kleinig TJ, et al; EXTEND-IA Investigators. **Endovascular therapy for ischemic stroke with perfusion-imaging selection.** *N Engl J Med* 2015;372:1009–18 CrossRef Medline
3. Saver JL, Goyal M, Bonafe A, et al; SWIFT PRIME Investigators. **Stent-retriever thrombectomy after intravenous t-PA vs. t-PA alone in stroke.** *N Engl J Med* 2015;372:2285–95 CrossRef Medline
4. Goyal M, Demchuk AM, Menon BK, et al; ESCAPE Trial Investigators. **Randomized assessment of rapid endovascular treatment of ischemic stroke.** *N Engl J Med* 2015;372:1019–30 CrossRef Medline
5. Jovin TG, Chamorro A, Cobo E, et al; REVASCAT Trial Investigators. **Thrombectomy within 8 hours after symptom onset in ischemic stroke.** *N Engl J Med* 2015;372:2296–306 CrossRef Medline
6. Nogueira RG, Jadhav AP, Haussen DC, et al; DAWN Trial Investigators. **Thrombectomy 6 to 24 hours after stroke with a mismatch between deficit and infarct.** *N Engl J Med* 2018;378:11–21 CrossRef Medline
7. Christoforidis GA, Mohammad Y, Kehagias D, et al. **Angiographic assessment of pial collaterals as a prognostic indicator following intra-arterial thrombolysis for acute ischemic stroke.** *AJNR Am J Neuroradiol* 2005;26:1789–97 Medline
8. Menon BK, Smith EE, Modi J, et al. **Regional leptomeningeal score on CT angiography predicts clinical and imaging outcomes in patients with acute anterior circulation occlusions.** *AJNR Am J Neuroradiol* 2011;32:1640–45 CrossRef Medline
9. Berkhemer OA, Jansen IG, Beumer D, et al; MR CLEAN Investigators. **Collateral status on baseline computed tomographic angiography and intra-arterial treatment effect in patients with proximal anterior circulation stroke.** *Stroke* 2016;47:768–76 CrossRef Medline
10. Liebeskind DS, Tomsick TA, Foster LD, et al; IMS III Investigators. **Collaterals at angiography and outcomes in the Interventional Management of Stroke (IMS) III trial.** *Stroke* 2014;45:759–64 CrossRef Medline
11. McVerry F, Liebeskind DS, Muir KW. **Systematic review of methods for assessing leptomeningeal collateral flow.** *AJNR Am J Neuroradiol* 2012;33:576–82 CrossRef Medline
12. Warach SJ, Luby M, Albers GW, et al; Stroke Imaging Research (STIR) and VISTA-Imaging Investigators. **Acute stroke imaging research roadmap III imaging selection and outcomes in acute stroke reperfusion clinical trials: consensus recommendations and further research priorities.** *Stroke* 2016;47:1389–98 CrossRef Medline
13. Boers AM, Sales Barros R, Jansen IG, et al. **Quantitative collateral grading on CT angiography in patients with acute ischemic stroke.** In: Cardoso MJ, Arbel T, Gao F, et al, eds. *Molecular Imaging, Reconstruction and Analysis of Moving Body Organs, and Stroke Imaging and Treatment. Proceedings of the Fifth International Workshop, CMMI 2017, Second International Workshop, RAMBO 2017, and First International Workshop, SWITCH 2017, Held in Conjunction with MICCAI*

2017, Québec City, Quebec, Canada. September 14, 2017. New York: Springer-Verlag International Publishing; 2017:176–84
14. Fransen PS, Beumer D, Berkhemer OA, et al; MR CLEAN Investigators. **MR CLEAN, a Multicenter Randomized Clinical Trial of Endovascular Treatment for Acute Ischemic Stroke in the Netherlands: study protocol for a randomized controlled trial.** *Trials* 2014;15:343 CrossRef Medline
15. Saver JL. **Novel end point analytic techniques and interpreting shifts across the entire range of outcome scales in acute stroke trials.** *Stroke* 2007;38:3055–62 CrossRef Medline
16. Boers AM, Berkhemer OA, Slump CH, et al; MR CLEAN trial investigators. **Topographic distribution of cerebral infarct probability in patients with acute ischemic stroke: mapping of intra-arterial treatment effect.** *J Neurointerv Surg* 2017;9:431–36 CrossRef Medline
17. Forkert ND, Fiehler J, Suniaga S, et al. **A statistical cerebroarterial atlas derived from 700 MRA datasets.** *Methods Inf Med* 2013;52:467–74 CrossRef Medline
18. Tan IY, Demchuk AM, Hopyan J, et al. **CT angiography clot burden score and collateral score: correlation with clinical and radiologic outcomes in acute middle cerebral artery infarct.** *AJNR Am J Neuroradiol* 2009;30:525–31 CrossRef Medline
19. Boers AM, Marquering HA, Jochem JJ, et al; MR CLEAN investigators. **Automated cerebral infarct volume measurement in follow-up noncontrast CT scans of patients with acute ischemic stroke.** *AJNR Am J Neuroradiol* 2013;34:1522–27 CrossRef Medline
20. Rodriguez-Luna D, Dowlatshahi D, Aviv RI, et al; PREDICT/Sunnybrook ICH CTA Study Group. **Venous phase of computed tomography angiography increases spot sign detection, but intracerebral hemorrhage expansion is greater in spot signs detected in arterial phase.** *Stroke* 2014;45:734–39 CrossRef Medline
21. DeLong ER, DeLong DM, Clarke-Pearson DL. **Comparing the areas under two or more correlated receiver operating characteristic curves: a nonparametric approach.** *Biometrics* 1988;44:837–45 CrossRef Medline
22. Ernst M, Forkert ND, Brehmer L, et al. **Prediction of infarction and reperfusion in stroke by flow- and volume-weighted collateral signal in MR angiography.** *AJNR Am J Neuroradiol* 2015;36:275–82 CrossRef Medline
23. Nambiar V, Sohn SI, Almekhlafi MA, et al. **CTA collateral status and response to recanalization in patients with acute ischemic stroke.** *AJNR Am J Neuroradiol* 2014;35:884–90 CrossRef Medline
24. Casault C, Al Sultan AS, Trivedi A, et al. **Collateral scoring on CT angiogram must evaluate phase and regional pattern.** *Can J Neurol Sci* 2017;44:503–07 CrossRef Medline
25. Frölich AM, Wolff SL, Psychogios MN, et al. **Time-resolved assessment of collateral flow using 4D CT angiography in large-vessel occlusion stroke.** *Eur Radiol* 2014;24:390–96 CrossRef Medline
26. Menon BK, d'Esterre CD, Qazi EM, et al. **Multiphase CT angiography: a new tool for the imaging triage of patients with acute ischemic stroke.** *Radiology* 2015;275:510–20 CrossRef Medline
27. Beyer SE, Thierfelder KM, von Baumgarten L, et al. **Strategies of collateral blood flow assessment in ischemic stroke: prediction of the follow-up infarct volume in conventional and dynamic CTA.** *AJNR Am J Neuroradiol* 2015;36:488–94 CrossRef Medline
28. van den Wijngaard IR, Holswilder G, Wermer MJH, et al. **Assessment of collateral status by dynamic CT angiography in acute MCA stroke: timing of acquisition and relationship with final infarct volume.** *AJNR Am J Neuroradiol* 2016;37:1231–36 CrossRef Medline
29. Berkhemer OA, Borst J, Kappelhof M, et al; MR CLEAN Investigators. **Extracranial carotid disease and effect of intra-arterial treatment in patients with proximal anterior circulation stroke in MR CLEAN.** *Ann Intern Med* 2017;166:867–75 CrossRef Medline
30. Jansen IG, Berkhemer OA, Yoo AJ, et al. **Comparison of CTA- and DSA-based collateral flow assessment in patients with anterior circulation stroke.** *AJNR Am J Neuroradiol* 2016;37:2037–42 CrossRef Medline
31. Goyal M, Menon BK, van Zwam WH, et al; HERMES collaborators. **Endovascular thrombectomy after large-vessel ischaemic stroke: a meta-analysis of individual patient data from five randomised trials.** *Lancet* 2016;387:1723–31 CrossRef Medline

Clinical Outcomes of Endovascular Treatment within 24 Hours in Patients with Mild Ischemic Stroke and Perfusion Imaging Selection

X. Shang, M. Lin, S. Zhang, S. Li, Y. Guo, W. Wang, M. Zhang, Y. Wan, Z. Zhou, W. Zi, and X. Liu

ABSTRACT

BACKGROUND AND PURPOSE: Endovascular thrombectomy has been accepted as the standard of care for patients with acute ischemic stroke. Our aim was to investigate the clinical outcomes of patients with mild ischemic stroke with acute proximal large-vessel occlusion after endovascular treatment within 24 hours of symptom onset.

MATERIALS AND METHODS: Between January 2014 and August 2017, ninety-three Chinese patients with mild ischemic stroke (NIHSS scores, 0–8) and large-vessel occlusion with endovascular treatment were retrospectively enrolled from 7 comprehensive stroke centers. They were divided into 2 groups: ≤6 hours and 6–24 hours from symptom onset to groin puncture. We analyzed their modified Rankin Scale scores at 90 days, symptomatic intracranial hemorrhage at 48 hours, and mortality during 90 days. Multivariable linear regression analysis was used to identify predictors for NIHSS shift after discharge.

RESULTS: Twenty-nine patients received endovascular treatment within 6–24 hours after symptom onset and had an imaging mismatch based on perfusion CT or diffusion-weighted MR imaging. There were no substantial differences between the 2 groups in 90-day functional independence ($P = .54$) and the risks of the combination of symptomatic intracranial hemorrhage and death ($P = .72$). Two significant indicators of NIHSS shift were 48-hour symptomatic intracranial hemorrhage (unstandardized $\beta = 7.28$; 95% CI, 3.48–11.1; $P < .001$) and baseline systolic blood pressure (unstandardized $\beta = 0.08$; 95% CI, 0.03–0.14; $P = .005$).

CONCLUSIONS: Patients with mild ischemic stroke and large-vessel occlusion in the anterior circulation, an imaging mismatch, and endovascular treatment within 6–24 hours of initial symptoms showed no heterogeneity in the efficacy and safety outcome compared with those treated ≤6 hours from symptom onset.

ABBREVIATIONS: LVO = large-vessel occlusion; MIS = mild ischemic stroke; sICH = symptomatic intracranial hemorrhage

Endovascular thrombectomy has been accepted as the standard of care for patients with acute anterior large-vessel occlusion (LVO) since the publication of 5 randomized clinical trials in 2015.[1-5] Now, screening eligible patients and allowing the treatment to benefit more patients, including those with mild and progressive stroke, wake-up stroke, and unknown onset of ischemic events, are of great interest.

Patients with mild ischemic stroke (MIS) account for >15% of patients with acute ischemic stroke.[6] MIS presents with slight clinical deficit, rapidly improving symptoms, and an uncertain aggressive therapy risk-benefit ratio, which often confuses the clinician's decision.[7] Due to the fragile collateral circulation in patients with MIS and LVO, their clinical symptoms could worsen gradually in the short term, and they may finally have severe dis-

Received January 4, 2018; accepted after revision February 26.

From the Department of Neurology (X.S., S.Z., Y.G., X.L.), Jinling Clinical College of Nanjing Medical University, Nanjing, Jiangsu, China; Department of Neurology (X.S., Z.Z.), Yijishan Hospital of Wannan Medical College, Wuhu, Anhui, China; Department of Neurology (M.L.), Fuzhou General Hospital of Nanjing Military Region, Fuzhou, Fujian, China; Department of Neurology (S.Z.), Affiliated Hospital of Yangzhou University, Yangzhou University, Yangzhou, Jiangsu, China; Department of Neurology (S.L., W.Z., X.L.), Jinling Hospital, Southern Medical University, Nanjing, Jiangsu, China; Department of Neurology (Y.G.), Huai'an First People's Hospital, Nanjing Medical University, Huai'an, Jiangsu, China; Department of Radiology (W.W.), First People's Hospital of Yangzhou, Yangzhou University, Yangzhou, Jiangsu, China; Department of Neurology (M.Z.), Research Institute of Surgery, Daping Hospital, Third Military Medical University, Chongqing, China; and Department of Neurology (Y.W.), Hubei Zhongshan Hospital, Wuhan, Hubei, China.

This study was partly supported by the National Natural Science Foundation of China (No. 81530038, 81400993 and 81671172), the National Key Research and Development Program (No.2017YFC1307901), the Chinese Postdoctoral Science Fund (No. 2015M572815), and the scientific research fund of Wannan Medical College in Anhui Province, China to X. Shang (WK2016F32, Wuhu).

Xianjin Shang and Min Lin contributed equally to this work.

Please address correspondence to Xinfeng Liu, MD, PhD, Department of Neurology, Jinling Hospital, Jinling Clinical College of Nanjing Medical University, Nanjing 210002, Jiangsu, China; e-mail: xfliu2@vip.163.com, and Wenjie Zi, MD, PhD, Department of Neurology, Jinling Hospital, Jinling Clinical College of Nanjing Medical University, Nanjing 210002, Jiangsu, China; e-mail: ziwenjie1981@163.com

Indicates open access to non-subscribers at www.ajnr.org

Indicates article with supplemental on-line table.

http://dx.doi.org/10.3174/ajnr.A5644

ability, so timely endovascular recanalization remains critical.[8-11] However, further studies of high quality are needed to confirm the efficacy and safety of thrombectomy for these patients.

Recently, the DWI or CTP Assessment with Clinical Mismatch in the Triage of Wake Up and Late Presenting Strokes Undergoing Neurointervention with Trevo (DAWN) study confirmed that patients with acute ischemic stroke (NIHSS scores, ≥10) with a mismatch between the severity of the clinical deficit and the infarct volume and undergoing thrombectomy within 6–24 hours have similar efficacy and safety profiles compared with those treated within 6 hours of symptom onset.[12] However, whether this finding applies to patients with MIS (NIHSS scores, ≤8) treated >6 hours after the onset of symptoms is unknown. The purpose of this study was to retrospectively evaluate the efficacy and safety of endovascular treatment performed in patients with acute stroke with NIHSS scores of 0–8 within 24 hours of symptom onset.

MATERIALS AND METHODS

Patients

We retrospectively enrolled consecutive patients with ischemic stroke in China who were admitted to 7 comprehensive stroke centers (Jinling Hospital, Yijishan Hospital, Fuzhou General Hospital of Nanjing Military Region, Affiliated Hospital of Yangzhou University, Daping Hospital, Hubei Zhongshan Hospital, and No.123 Hospital of the People's Liberation Army) between January 2014 and August 2017 within 24 hours of symptom onset and who had LVO in the anterior circulation (MCA M1/M2, ICA, anterior cerebral artery) but not arterial aneurysms and arteriovenous malformations by CTA/MRA.

All eligible patients met the following inclusion criteria: 1) 18 years of age or older; 2) presenting with mild neurologic deficits with an admission NIHSS score of ≤8; and 3) emergency endovascular treatment within 24 hours, including primary treatment and rescue treatment. Patients without prior functional independence (mRS score of >2) and those with intra-arterial thrombolysis alone were excluded.

Most patients received endovascular treatment with ≤6 hours from symptom onset (group A). Patients who received endovascular recanalization therapy >6 hours after symptom onset, whose clinical presentations were disproportionately severe relative to the occlusive artery verified by CTA/MRA, and who had an imaging mismatch by perfusion CT or diffusion-weighted MR imaging were assigned to group B.

This study was approved by the ethics committee of each participating center, but written consent was waived due to its retrospective nature.

Data

We retrieved the demographic, clinical, and neuroimaging data from each center. We included various data: age, sex, vascular risk factors (hypertension, hyperlipidemia, diabetes, smoking, and drinking habits), medical history (coronary heart disease, atrial fibrillation, history of stroke or TIA), baseline blood glucose level, systolic blood pressure and total cholesterol level, intravenous thrombolysis, occlusion sites, stroke etiology, time from onset to treatment, time from puncture to reperfusion, NIHSS scores (baseline, 24 hours, and discharge), ASPECTS, collateral flow scores, modified TICI score, symptomatic intracranial hemorrhage (sICH) at 48 hours, mortality, and mRS scores during 90 days.

All radiologic data and clinical medical records of subjects were sent to the core laboratory in our hospital (Jinling Hospital) and were reviewed in a blinded fashion by 2 physicians or interventionists (Y.G. and S.Z.) with advice of a third experienced physician/interventionist (W.Z.) when there was disagreement.

Definition

The etiology of stroke was divided into 3 categories (large atherosclerosis, cardioembolism, and others/undetermined) based on the Trial of ORG 10172 in Acute Stroke Treatment classification.[13] Neurologic deterioration at 24 hours was defined as a ≥4-point increase from the baseline NIHSS score. NIHSS shift represented the discharge NIHSS score minus the baseline NIHSS score.

The occlusion site of the vessel was divided into ICA, MCA M1, MCA M2, anterior cerebral artery, and tandem occlusion corresponding to the artery occlusion occurring in >2 different parts of continuous vessels. The collateral flow grading system was used to evaluate collateral flow, ranging from grade 0 to 4, with zero representing no collateral flow, and 4, rapid and complete collateral flow.[14] The reperfusion status after the procedure was regarded as the modified TICI scale: 0–2a and 2b–3, which were divided by reperfusion of 50% of the affected vascular territory.[15] sICH at 48 hours after admission was any hemorrhage combined with an increase of ≥4 points in the total NIHSS score or ≥2 points in 1 NIHSS category according to the Heidelberg classification scheme.[16]

Clinical and Safety Outcomes

The primary outcome included functional outcome at 90 days, neurologic deterioration at 24 hours, and NIHSS shift at discharge. The functional outcomes were evaluated with the mRS scale at 90 days after symptom onset, assigned a score of 0–1, 0–2, and 3–6, respectively, representing excellent outcome, functional independence, and poor outcome. Patients' mRS scores at 3 months were retrieved from the stroke registry data base of each center, available either by telephone follow-up or outpatient visit. If patients were lost to follow-up, the 90-day mRS was replaced by the discharge mRS.[17] Secondary safety outcomes included the incidence of sICH at 48 hours and mortality during 90 days.

Statistical Analysis

Quantitative variables are shown as mean ± SD or median (interquartile range) as appropriate. Qualitative variables are presented as number and percentage. Comparisons between the 2 groups for quantitative/ordinal variables were made with the Student *t* test, Mann-Whitney *U* test, or analysis of variance, as appropriate. Qualitative variables were compared by the Pearson χ^2 or Fisher exact test, as appropriate. Significance was set at $P < .05$, and *P* values were 2-sided. Multivariable linear regression analysis for predictors of NIHSS shift was performed for variables at the .01 level of significance on univariate analysis (enter selection method). Statistical analysis was performed using SPSS Statistics 24.0 (IBM, Armonk, New York).

Outcome data of the studied groups[a]

Outcomes	Endovascular Treatment				Mechanical Thrombectomy			
	All	Group A (*n* = 64)	Group B (*n* = 29)	*P* (A vs B)	All	Group A (*n* = 56)	Group B (*n* = 23)	*P* (A vs B)
NIHSS score								
Deterioration at 24 hr	13 (14.0)	7 (10.9)	6 (20.7)	.22	12 (15.2)	6 (10.7)	6 (26.1)	.09
NIHSS shift at discharge[b]	−0.6	−0.6	−0.5	.94	−0.4	−0.6	0.1	.73
mRS at 90 days								
mRS 0–1	55 (59.1)	41 (64.1)	14 (48.2)	.15	46 (58.2)	35 (62.5)	11 (47.8)	.23
mRS 0–2	68 (73.1)	48 (75.0)	20 (69.0)	.54	56 (70.9)	42 (75.0)	14 (60.9)	.20
Safety outcome								
sICH at 48 hr	8 (8.6)	6 (9.4)	2 (6.9)	1.00	8 (10.1)	6 (10.7)	2 (8.7)	1.00
90-Day mortality	5 (5.4)	4 (6.3)	1 (3.4)	1.00	4 (5.1)	3 (5.4)	1 (4.3)	1.00
Composite outcome	10 (10.8)	8 (12.5)	2 (6.9)	.72	9 (11.4)	7 (12.5)	2 (8.7)	1.00

[a] Results are shown as number (%) unless stated otherwise.
[b] Excluding death.

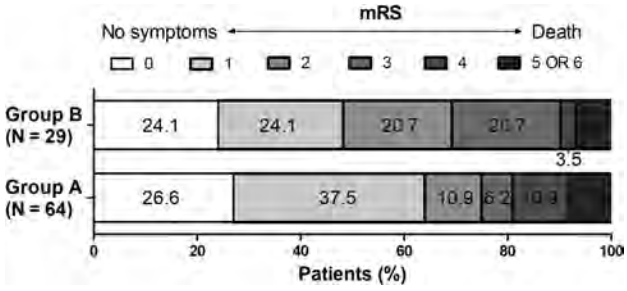

FIGURE. Distribution of mRS at 90 days between group A (onset to treatment ≤6 hours) and group B (onset to treatment >6 hours).

RESULTS

Patients

A total of 93 patients met the inclusion criteria during the study period. The mean age of eligible patients was 61.6 ± 13.8 years, and 68.8% (64/93) of patients were men (On-line Table). The ASPECTS median was 9 (interquartile range, 8–10; except for the missing data); 30.1% (28/93) of patients had poor collateral status before the procedure; the overall proportion of intravenous thrombolysis was 28%; and after endovascular treatment, >90% (84/93) of patients had restored distal reperfusion (modified TICI 2b–3).

There were 64 (68.8%) patients who received endovascular treatment within 6 hours after onset (group A), more than the 29 (31.2%) patients who received treatment >6 hours after symptom onset (group B). The proportion of intravenous thrombolysis between the 2 groups was similar (28.1% versus 27.6%, $P = .96$), and the times from onset to intravenous thrombolysis were similar (130.0 ± 72.7 minutes versus 141.6 ± 107.7 minutes; $P = .76$). Other baseline characteristics were comparable across the 2 groups, though there were slight differences in stroke etiology composition and hypertension (both $P < .05$).

Clinical Outcomes

As shown in the Table and the Figure, the excellent outcome (mRS 0–1) in patients with endovascular treatment was higher in group A compared with group B (64.1% versus 48.2%, $P = .15$), and the percentages of functional independence (mRS 0–2) were similar (75% versus 69%, $P = .54$). Of the 79 patients in the subgroup undergoing thrombectomy, the overall functional independence and excellent outcome were 70.9% and 58.2%, respectively, and good outcomes at 90 days were more common in the group treated within 6 hours, but these patients did not show any substantial differences compared with those in the group treated beyond 6 hours (Table).

The shift in NIHSS scores indicated that both groups had slight improvement in symptoms at discharge (−0.6 versus −0.5, $P = .94$). Multivariable linear regression of screening predictors for a shift in NIHSS scores indicated that sICH at 48 hours (unstandardized $\beta = 7.28$; 95% CI, 3.48–11.1; $P < .001$) and baseline systolic blood pressure (unstandardized $\beta = 0.08$; 95% CI, 0.03–0.14; $P = .005$) were associated with a harmful (positive) NIHSS shift. Intravenous thrombolysis, stroke etiology and occlusion site, reperfusion status, and other medical histories did not reach statistical significance in the multivariable analysis.

Safety Outcomes

sICH at 48 hours was not substantially different between the 2 endovascular groups (group A, 6 [9.4%]; group B, 2 [6.9%]). There were 4 (6.3%) deaths within 3 months in group A, 1 after discharge and 3 during hospitalization: One case of postprocedural symptomatic hemorrhage was associated with death from a severe cerebral hernia, 1 case of a surgical complication resulted in rupture of a blood vessel, and the remaining patient died of revascularization failure. The only fatal case (3.4%) in group B involved intracranial hemorrhage due to a procedural complication, and emergency removal of the hematoma was unable to save the patient.

DISCUSSION

Our study shows that in patients with acute ischemic stroke with LVO in the anterior circulation presenting with mild neurologic deficits inconsistent with occlusion site and imaging mismatch, the clinical and safety outcomes of endovascular therapy ≤6 hours and 6–24 hours after symptom onset are not substantially different. Baseline systolic blood pressure and 48-hour sICH were the main factors influencing the neurologic recovery at discharge.

Previous studies have shown that patients with mild stroke with LVO tend to have poor outcomes if not treated.[7,8] Mokin et al[18] studied 204 patients with mild acute stroke (NIHSS scores, 0–7) with LVO who were excluded from intravenous thrombolysis and endovascular treatment and found that 37% could not walk independently at discharge. Additionally, they found that

the higher the admission score, the worse the clinical outcome was.[18] In this study, we found that the overall functional independence of patients with endovascular therapy was 73.1% at 3 months, with 75% for group A and 69% for group B, respectively. Among the mechanical thrombectomy subgroup, the 90-day functional independence rate (70.9%) was comparable with the findings of Dargazanli et al[19] (78.3%) in patients with NIHSS scores in the range of 0–7; the findings of Pfaff et al[20] (63.6%) in patients with NIHSS scores of ≤8; and the findings of Dargazanli et al[21] and the ETIS Registry investigators in patients with NIHSS scores of <8 (81.2%). Of note, in our patients with 6–24 hours from symptom onset to treatment, salvageable brain tissue was confirmed by perfusion CT or MR imaging mismatch and mismatched neurologic deficits inconsistent with the occlusion vessels. These patients undergoing mechanical thrombectomy still presented with favorable clinical outcomes, having comparable functional independence even within a prolonged time window (60.9%), compared with patients treated within 6 hours from the present study (75%) and above studies.[19,21]

The safety outcomes in our study were acceptable, with the 48-hour sICH and 90-day mortality being 8.6% and 5.4%, respectively. These outcomes compare with 19.6% (any ICH) and 5.1% reported by Dargazanli et al,[19] the 6.1% and 9.1% reported by Pfaff et al,[20] and the 16.5% (any ICH) and 4.7% in Dargazanli et al and the ETIS Registry investigators' study.[21] Although there are differences between the above studies, such as patient eligibility and variable criteria, leading to different results, the overall tendency favors endovascular therapy in patients with MIS and LVO.

Moreover, we found no statistical difference in safety between the 2 groups. However, the sICH rate of the group treated in ≤6 hours was higher than that of the group treated in >6 hours. Traditionally, extended time from onset to vascular recanalization is associated with higher intracranial hemorrhagic risk.[22,23] The higher proportion of hypertension history and large vessel occlusion of determined etiology in the group treated in ≤6 hours might contribute to this difference. Another explanation might be that ASPECTSs in the group treated after >6 hours were better than those in the group treated in ≤6 hours. These findings indicate that smaller infarct volumes may be favorable. However, further analysis with more samples is needed.

To date, there are still no randomized clinical trials analyzing the effect of endovascular treatment for MIS. Goyal et al[24] and the HERMES collaborators conducted a meta-analysis of 5 major mechanical thrombectomy clinical trials. Only 177 patients with MIS were available for analysis, but they concluded that the direction of effect favored endovascular treatment for patients with MIS. The recent DAWN study also showed that patients with stroke treated 6–24 hours from the onset of symptoms also benefited from thrombectomy when they had salvageable brain tissue.[12] The main finding of our study is that endovascular treatment for patients with MIS 6–24 hours from symptom onset should be determined on the basis of clinical and imaging mismatch assessments.

This was a multicenter study in the Chinese population, but the relatively small sample size and retrospective design limited its power. Further prospective, randomized, controlled trials are warranted.

CONCLUSIONS

We found that the efficacy and safety of endovascular treatment were not heterogeneous ≤6 and 6–24 hours from symptom onset to groin puncture in patients with anterior circulation MIS and LVO and imaging mismatch based on perfusion CT or diffusion-weighted MR imaging.

ACKNOWLEDGMENTS

The authors sincerely thank all hospitals and participants for their help and thank Shiquan Yang (Department of Neurology, No.123 Hospital of the People's Liberation Army, Bengbu, Anhui, China) for providing cases. We also thank the reviewers for their helpful comments.

Disclosures: Xianjin Shang—*RELATED*: *Grant*: This study was partly supported by National Natural Science Foundation of China (No. 81530038, 81400993 and 81671172), National Key Research and Development Program (No.2017YFC1307901), Chinese Postdoctoral Science Fund (No. 2015M572815), and the scientific research fund of Wannan Medical College*. Min Lin—*RELATED*: *Grant*: This study was partly supported by National Natural Science Foundation of China (No. 81530038, 81400993 and 81671172), National Key Research and Development Program (No.2017YFC1307901), Chinese Postdoctoral Science Fund (No. 2015M572815), and the scientific research fund of Wannan Medical College.* Shun Li—*RELATED*: *Grant*: This study was partly supported by National Natural Science Foundation of China (No. 81530038, 81400993 and 81671172), National Key Research and Development Program (No.2017YFC1307901), Chinese Postdoctoral Science Fund (No. 2015M572815), and the scientific research fund of Wannan Medical College.* Wenjie Zi—*RELATED*: *Grant*: National Natural Science Foundation of China (No. 81530038, 81400993 and 81671172), *Comments*: This study was partly supported by National Key Research and Development Program (No.2017YFC1307901), Chinese Postdoctoral Science Fund (No. 2015M572815), and the scientific research fund of Wannan Medical College.* *Money paid to the institution.

REFERENCES

1. Jovin TG, Chamorro A, Cobo E, et al; REVASCAT Trial Investigators. **Thrombectomy within 8 hours after symptom onset in ischemic stroke.** *N Engl J Med* 2015;372:2296–306 CrossRef Medline
2. Campbell BC, Mitchell PJ, Kleinig TJ, et al; EXTEND-IA Investigators. **Endovascular therapy for ischemic stroke with perfusion-imaging selection.** *N Engl J Med* 2015;372:1009–18 CrossRef Medline
3. Saver JL, Goyal M, Bonafe A, et al; SWIFT PRIME Investigators. **Stent-retriever thrombectomy after intravenous t-PA vs. t-PA alone in stroke.** *N Engl J Med* 2015;372:2285–95 CrossRef Medline
4. Goyal M, Demchuk AM, Menon BK, et al; ESCAPE Trial Investigators. **Randomized assessment of rapid endovascular treatment of ischemic stroke.** *N Engl J Med* 2015;372:1019–30 CrossRef Medline
5. Berkhemer OA, Fransen PS, Beumer D, et al. **A randomized trial of intraarterial treatment for acute ischemic stroke.** *N Engl J Med* 2015; 372:11–20 CrossRef Medline
6. Heldner MR, Zubler C, Mattle HP, et al. **National Institutes of Health stroke scale score and vessel occlusion in 2152 patients with acute ischemic stroke.** *Stroke* 2013;44:1153–57 CrossRef Medline
7. Nedeltchev K, Schwegler B, Haefeli T, et al. **Outcome of stroke with mild or rapidly improving symptoms.** *Stroke* 2007;38:2531–35 CrossRef Medline
8. Rajajee V, Kidwell C, Starkman S, et al. **Early MRI and outcomes of untreated patients with mild or improving ischemic stroke.** *Neurology* 2006;67:980–84 CrossRef Medline
9. Smith EE, Abdullah AR, Petkovska I, et al. **Poor outcomes in patients who do not receive intravenous tissue plasminogen activator because of mild or improving ischemic stroke.** *Stroke* 2005;36:2497–99 CrossRef Medline
10. Heldner MR, Jung S, Zubler C, et al. **Outcome of patients with occlusions of the internal carotid artery or the main stem of the middle cerebral artery with NIHSS score of less than 5: comparison between thrombolysed and non-thrombolysed patients.** *J Neurol Neurosurg Psychiatry* 2015;86:755–60 CrossRef Medline
11. Smith EE, Fonarow GC, Reeves MJ, et al. **Outcomes in mild or rap-**

idly improving stroke not treated with intravenous recombinant tissue-type plasminogen activator: findings from Get With The Guidelines-Stroke. *Stroke* 2011;42:3110–15 CrossRef Medline

12. Nogueira RG, Jadhav AP, Haussen DC, et al; DAWN Trial Investigators. **Thrombectomy 6 to 24 hours after stroke with a mismatch between deficit and infarct.** *N Engl J Med* 2018;378:11–21 CrossRef Medline
13. Adams HP Jr, Bendixen BH, Kappelle LJ, et al. **Classification of subtype of acute ischemic stroke: definitions for use in a multicenter clinical trial—TOAST. Trial of Org 10172 in Acute Stroke Treatment.** *Stroke* 1993;24:35–41 Medline
14. Higashida RT, Furlan AJ, Roberts H, et al; Technology Assessment Committee of the American Society of Interventional and Therapeutic Neuroradiology, Technology Assessment Committee of the Society of Interventional Radiology. **Trial design and reporting standards for intra-arterial cerebral thrombolysis for acute ischemic stroke.** *Stroke* 2003;34:e109–37 CrossRef Medline
15. Tomsick T, Broderick J, Carrozella J, et a; Interventional Management of Stroke II Investigators. **Revascularization results in the Interventional Management of Stroke II trial.** *AJNR Am J Neuroradiol* 2008;29:582–87 CrossRef Medline
16. von Kummer R, Broderick JP, Campbell BC, et al. **The Heidelberg Bleeding Classification: classification of bleeding events after ischemic stroke and reperfusion therapy.** *Stroke* 2015;46:2981–86 CrossRef Medline
17. Minnerup J, Wersching H, Teuber A, et al; REVASK Investigators. **Outcome after thrombectomy and intravenous thrombolysis in patients with acute ischemic stroke: a prospective observational study.** *Stroke* 2016;47:1584–92 CrossRef Medline
18. Mokin M, Masud MW, Dumont TM, et al. **Outcomes in patients with acute ischemic stroke from proximal intracranial vessel occlusion and NIHSS score below 8.** *J Neurointerv Surg* 2014;6:413–17 CrossRef Medline
19. Dargazanli C, Consoli A, Gory B, et al; ETIS investigators. **Is reperfusion useful in ischaemic stroke patients presenting with a low National Institutes of Health Stroke Scale and a proximal large vessel occlusion of the anterior circulation?** *Cerebrovasc Dis* 2017;43:305–12 CrossRef Medline
20. Pfaff J, Herweh C, Pham M, et al. **Mechanical thrombectomy in patients with acute ischemic stroke and lower NIHSS scores: recanalization rates, periprocedural complications, and clinical outcome.** *AJNR Am J Neuroradiol* 2016;37:2066–71 CrossRef Medline
21. Dargazanli C, Arquizan C, Gory B, et al; ETIS REGISTRY Investigators. **Mechanical thrombectomy for minor and mild stroke patients harboring large vessel occlusion in the anterior circulation: a multicenter cohort study.** *Stroke* 2017;48:3274–81 CrossRef Medline
22. Khatri P, Wechsler LR, Broderick JP. **Intracranial hemorrhage associated with revascularization therapies.** *Stroke* 2007;38:431–40 CrossRef Medline
23. Hao Y, Yang D, Wang H, et al; ACTUAL Investigators (Endovascular Treatment for Acute Anterior Circulation Ischemic Stroke Registry). **Predictors for symptomatic intracranial hemorrhage after endovascular treatment of acute ischemic stroke.** *Stroke* 2017;48:1203–09 CrossRef Medline
24. Goyal M, Menon BK, van Zwam WH, et al; HERMES collaborators. **Endovascular thrombectomy after large-vessel ischaemic stroke: a meta-analysis of individual patient data from five randomised trials.** *Lancet* 2016;387:1723–31 CrossRef Medline

Slow Collateral Flow Is Associated with Thrombus Extension in Patients with Acute Large-Artery Occlusion

R. Zhang, Y. Zhou, S. Yan, S. Zhang, X. Ding, and M. Lou

ABSTRACT

BACKGROUND AND PURPOSE: It is still poorly understood about the dynamic changes of the thrombus after intravenous thrombolysis and how the remaining thrombus affects clinical outcome in human stroke. Collateral flow was assumed to help to deliver endo/exogenous tissue-type plasminogen activator to the clot. We aimed to analyze the impact of collateral flow on the dynamic changes of the thrombus in patients with acute large-artery occlusion who received intravenous thrombolysis.

MATERIALS AND METHODS: We reviewed consecutive patients with acute ischemic stroke with M1 segment or distal internal carotid artery occlusion who underwent multimodal MR imaging or CT perfusion before and 24 hours after intravenous thrombolysis without recanalization. Patients were divided into 3 groups (thrombus extension, shortening, and no change) according to thrombus-length change between baseline and 24 hours. Collateral flow was measured with arrival time delay and the collateral scoring system. Poor outcome was defined as a 3-month modified Rankin Scale score of ≥3.

RESULTS: Among 51 patients, 18 (35.3%) had thrombus extension, 14 (27%) had thrombus shortening, and 19 (37.3%) had thrombus without change. Arrival time delay was independently associated with thrombus extension (OR = 1.499; 95% CI, 1.053–2.135; $P = .025$). Similarly, the collateral score on the peak artery phase was independently associated with thrombus extension (OR = 0.456; 95% CI, 0.211–0.984; $P = .045$), whereas baseline National Institutes of Health Stroke Scale score (OR = 0.768; 95% CI, 0.614–0.961; $P = .021$) and baseline thrombus length (OR = 1.193; 95% CI, 1.021–1.394; $P = .026$) were associated with thrombus shortening. All patients with thrombus extension had poor outcomes.

CONCLUSIONS: Slow collateral flow was related to thrombus extension in patients with large-artery occlusion without recanalization after intravenous thrombolysis.

ABBREVIATIONS: ATD = arrival time delay; dGE-T1 = delayed gadolinium-enhanced T1; IVT = intravenous thrombolysis; LAO = large-artery occlusion; tMIP = temporally fused MIP

Previous studies have demonstrated that characteristics of thrombus, especially thrombus length, were closely related to the rate of recanalization, clinical outcome after intravenous thrombolysis (IVT),[1] and even stroke etiology in patients with acute ischemic stroke with large-artery occlusion (LAO).[2,3] However, the dynamic changes of the thrombus after IVT and how the remaining thrombus affects clinical outcome in human stroke are still poorly understood.

Collateral flow was assumed to help deliver endo-/exogenous tissue-type plasminogen activator to the clot. Indeed, evidence has shown that good collaterals were often related to short baseline thrombus.[4] Our previous study also demonstrated that rapid collaterals accomplished high recanalization rates after IVT.[5] We thus hypothesized that collateral velocity might have an impact on dynamic changes of the thrombus.

With rapid development of in vivo thrombus imaging techniques, baseline characteristics of thrombus have been widely studied. Delayed gadolinium-enhanced T1 (dGE-T1), which can delineate the distal end of the thrombus and avoid blooming artifacts of the susceptibility vessel sign, was proved a useful tool for accurate measurement of thrombus length when combined with time-of-flight MR angiography.[1] Similarly, 4D CT angiography, derived from CT perfusion, can not only outline intracranial thrombi better than conventional single-phase CTA[6] but also evaluate collateral flow with increased sensitivity.[7]

Therefore, we designed this study with the following objec-

Received November 27, 2017; accepted after revision February 6, 2018.

From the Departments of Neurology (R.Z., Y.Z., S.Y., S.Z., M.L.) and Radiology (X.D.), Second Affiliated Hospital of Zhejiang University, School of Medicine, Hangzhou, China; and Zhejiang University Brain Research Institute (M.L.), Hangzhou, China.

This work was support by the National Natural Science Foundation of China (81471170 and 81622017), the National Key Research and Development Program of China (2016YFC1301500), and the National Natural Science Foundation of China (81400946).

Please address correspondence to Min Lou, MD, PhD, Department of Neurology, Second Affiliated Hospital of Zhejiang University, School of Medicine, 88 Jiefang Rd, Hangzhou, 310009, China; e-mail: loumingxc@vip.sina.com, lm99@zju.edu.cn

Indicates open access to non-subscribers at www.ajnr.org

http://dx.doi.org/10.3174/ajnr.A5614

tives: 1) to assess the change of thrombus length in patients with LAO without recanalization at 24 hours after IVT detected on dGE-T1 and 4D-CTA derived from CTP, 2) to evaluate the relationship between the changing of thrombus length and collaterals, and 3) to find the influencing factors of different changing patterns of thrombus length.

MATERIALS AND METHODS

Ethics Statement

The protocol of MR imaging/CT-guided intravenous thrombolysis was approved by our local human ethics committee. All clinical investigations were conducted according to the principles expressed in the Declaration of Helsinki. Informed consent was obtained for all patients.

Patient Selection

We retrospectively reviewed our prospectively collected data base for consecutive patients with acute ischemic stroke who received IVT alone between June 2009 and March 2017. We enrolled patients using the following criteria: 1) They had a diagnosis of acute ischemic stroke confirmed by diffusion-weighted imaging or CTP, 2) received IVT within 6 hours from symptom onset, 3) had occlusion of middle cerebral artery M1 segment or distal internal carotid artery on baseline TOF-MRA or CTA, and 4) underwent follow-up CTP or multimodal MR imaging at 24 hours with no confirmed recanalization, which was defined as 0 or 1 of the Arterial Occlusive Lesion scale (details in the "Evaluation of Outcome" section). Patients with poor image quality because of motion artifacts were excluded.

Imaging Protocols

Subjects underwent MR imaging on a 3T system (Signa Excite HD; GE Healthcare, Milwaukee, Wisconsin) equipped with an 8-channel phased array head coil. The DWI sequence was used to measure the infarct volume (TR = 4000 ms, TE = 69.3 ms, b-value = 1000 s/mm^2, slice thickness = 5.0 mm, and interslice gap = 1.0 mm). TOF-MRA consisted of 3 slabs with TR = 20 ms, TE = 3.2 ms, flip angle = 15°, and slice thickness = 1.4 mm. Fluid-attenuated inversion recovery parameters were TR = 9000 ms, TE = 150 ms, TI = 2250 ms, and slice thickness = 5.0 mm. PWI was performed using the standard bolus passage of contrast method by injecting gadolinium (0.1 mmol/kg dose via a power injector). PWI parameters were the following: TR = 1500 ms, TE = 30 ms, and slice thickness = 5.0 mm. Conventional T1 parameters were TR = 1900 ms, TE = 25 ms, and slice thickness = 5.0 mm.

CTP was performed on a dual-source 64-slice CT scanner (Somatom Definition Flash; Siemens, Erlangen, Germany), including a nonenhanced head CT scan (120 kV, 320 mA, contiguous 5-mm axial slices), and volume perfusion CT (100 mm in the z-axis, 4-second delay after start of contrast medium injection, 74.5-second total imaging duration, 80 kV, 120 mA, effective dose = 3.68 mSv, slice thickness = 10 mm, collimation = 32 × 1.2 mm). Volume perfusion CT consisted of 26 consecutive spiral acquisitions of the brain. A 60-mL bolus of contrast medium (iopamidol, Imeron; Bracco, Milan, Italy) was used at a flow rate of 6 mL/s, followed by a 20-mL saline chaser at 6 mL/s.

Imaging Analysis

Two neurologists (R.Z. and Y.Z.), blinded to patients' clinical information, independently assessed the thrombus length on dGE-T1 and CTA, respectively, as described in our previous study.[1] For multimodal MR imaging, we coregistered the source images of TOF-MRA and dGE-T1 with MRIcron NIfTI viewer (http://www.mccauslandcenter.sc.edu/crnl/) because the distal vessels beyond the clot were clearly visible on dGE-T1. We then manually measured the distance between the proximal and distal ends of the occlusion, orienting along the central axis of the artery, as thrombus length. Similarly, we reconstructed 4D-CTA from CTP with commercially available software (MIStar; Apollo Medical Imaging Technology, Melbourne, Victoria, Australia); and temporally fused MIP (tMIP) datasets were created for the identification of the proximal and distal ends of clots. Thrombus length was measured along the central axis of the artery. For patients who underwent different imaging at baseline and 24 hours, we coregisterred the CTA images to the dGE-T1 images on MIStar software and calculated the thrombus length on the coregisterred CTA images. Thrombus extension was defined as (24-Hour Thrombus Length − Baseline Thrombus Length) / Baseline Thrombus Length >30%. Thrombus shortening was defined as (Baseline Thrombus Length − 24-Hour Thrombus Length) / Baseline Thrombus Length >30%. The others [−30% ≤ (Baseline Thrombus Length − 24-Hour Thrombus Length) ≤ 30%] were classified as thrombus without change.

Measurement of collateral flow velocity was quantified on PWI- or CTP-derived subtraction images, also described in our previous study.[5] Briefly, the artery that crossed the Sylvian fissure and was located at the end of the MCA M1 segment of each hemisphere was used to generate the arterial input function curve for the ischemic and contralateral hemispheres, respectively. The first time point when contrast reached the selected artery was then identified on the arterial input function curve for the ischemic and contralateral hemispheres, respectively. The arrival time delay (ATD) was defined as the time difference between these 2 time points.

The status of the leptomeningeal collateral circulation was evaluated by the scoring system of Tan et al.[8] In short, the collateral score was determined according to the following rules: 0, absent collaterals; 1, collateral filling ≤50% of the occluded territory; 2, collateral filling ≥50% but ≤100% of the occluded territory; and 3, collateral filling 100% of the occluded territory. Collaterals were evaluated on PWI- or CTP-derived subtraction images. Peak artery phase and tMIP reconstructions from PWI or CTP images that fuse contrast opacification across the duration were obtained. The collateral scores on peak artery phase images were recorded as peak scores of collaterals, which reflect both the velocity and extent of collaterals. Moreover, the collateral scores on tMIP were recorded as the tMIP scores of collaterals, which reflect the extent of the collaterals.

Evaluation of Outcome

We used the Arterial Occlusive Lesion scale (grade 0, complete occlusion of the target artery; grade 1, incomplete occlusion or partial local recanalization at the target artery with no distal flow; grade 2, incomplete occlusion or partial local recanalization at the

Table 1: Characteristics of patients with different changing patterns of thrombus length

	Thrombus Shortening (n = 14)	Thrombus without Change (n = 19)	Thrombus Extension (n = 18)	P Value
Age (yr) (mean)	62.79 ± 14.74	67.53 ± 13.47	70.44 ± 11.63	.275
Women (No.) (%)	4 (28.6)	7 (36.8)	9 (50)	.480
Comorbid conditions				
Atrial fibrillation (No.) (%)	7 (50)	9 (47.4)	10 (55.6)	.938
Hypertension (No.) (%)	10 (71.4)	15 (78.9)	16 (88.9)	.502
Diabetes (No.) (%)	1 (7.1)	2 (10.5)	5 (27.8)	.245
Hyperlipidemia (No.) (%)	10 (71.4)	10 (52.6)	8 (44.4)	.316
Smoking (No.) (%)	7 (50)	10 (52.6)	6 (33.3)	.461
Clinical variables				
NIHSS score (range)	6.5 (4.5–11.75)	11 (7–16)	16 (13–18)	<.001
Onset to imaging (mean) (min)	201.43 ± 98.09	233.58 ± 139.42	175.28 ± 67.20	.263
Previous antiplatelet use (No.) (%)	2 (14.3)	4 (21.1)	1 (6.6)	.406
Platelets (10^9/L) (mean)	189.50 ± 84.43	200.89 ± 98.60	179.94 ± 42.89	.723
INR (mean)	1.07 ± 0.14	1.02 ± 0.07	1.01 ± 0.08	.229
Baseline thrombus length (range) (mm)	12.99 (6.93–18.74)	8.0 (3.3–11.10)	13.31 (6.35–17.59)	.116
Baseline ATD (range) (sec)	3.24 (1.71–5.42)	2.77 (0.90–4.48)	7.24 (3.52–9.18)	.001
Peak score of collaterals (range)	3 (1–3)	3 (1–3)	1 (0–2)	.001
tMIP score of collaterals (range)	3 (1–3)	3 (2–3)	2 (1–3)	.176
Poor outcome (No.) (%)	7 (50)	16 (84.2)	18 (100)	.001

Note:—INR indicates international normalized ratio.

Table 2: Logistic regression for prediction of thrombus extension and shortening, including ATD in the model

	OR	95% CI	P Value
For thrombus extension (set without change as reference)			
NIHSS score	1.195	0.978–1.460	.081
Baseline thrombus length (mm)	0.981	0.853–1.129	.790
Baseline ATD (sec)	1.499	1.053–2.135	.025
For thrombus shortening (set without change as reference)			
NIHSS score	0.768	0.614–0.961	.021
Baseline thrombus length (mm)	1.193	1.021–1.394	.026
Baseline ATD (sec)	0.955	0.647–1.410	.818

Table 3: Logistic regression for prediction of thrombus extension and shortening, including baseline peak score of collaterals in the model

	OR	95% CI	P Value
For thrombus extension (set without change as reference)			
NIHSS score	1.146	0.935–1.404	.189
Baseline thrombus length (mm)	1.042	0.915–1.186	.537
Baseline peak score of collaterals	0.456	0.211–0.984	.045
For thrombus shortening (set without change as reference)			
NIHSS score	0.742	0.580–0.950	.018
Baseline thrombus length (mm)	1.220	1.037–1.435	.016
Baseline peak score of collaterals	0.899	0.316–2.557	.841

target artery with any distal flow; and grade 3, complete recanalization and restoration of the target artery with any distal flow) to define recanalization or no recanalization based on the presence (grade 2 or 3) or absence (grade 0 or 1) of any downstream flow on 24-hour TOF-MRA or 4D-CTA. Clinical outcome at 3 months was assessed with the mRS and dichotomized into good outcome (0–2) and poor outcome (3–6).

Statistical Analysis

The patients were trichotomized according to the changing pattern of the thrombus length. A 1-way analysis of variance or Kruskal-Wallis test was used among multiple groups. Variables with a $P < .05$ in univariate regression analyses and baseline thrombus length were included in the multinomial logistic regression. We performed all analyses blinded to the participant identifying information. Statistical significance was set at a probability value of <.05. All statistical analyses were performed with an SPSS package (Version 14.0 for Windows; IBM, Armonk, New York).

RESULTS

Fifty-one patients were included in the final analysis. The median age was 67 years (mean, 67 ± 13 years; range, 40–94 years) and 20 (39.2%) were women. The median baseline NIHSS score was 13 (interquartile range, 7–17). The mean time from onset to imaging was 204 ± 108 minutes. The median thrombus length was 11.10 mm (interquartile range, 6.05–15.90 mm) at baseline and 8.74 mm (interquartile range, 3.65–20.30 mm) at 24 hours. The median ATD was 3.63 seconds (interquartile range, 1.90–7.05 seconds) at baseline and 3.52 seconds (interquartile range, 1.29–6.30 seconds) at 24 hours. Thirty-one (60.8%) patients underwent CTP, while 20 (39.2%) patients underwent MR imaging.

Follow-up scans at 24 hours revealed thrombus extension in 18 (35.3%) patients, thrombus shortening in 14 (27.5%) patients, and thrombus with no change in 19 (37.3%) patients. As Table 1 shows, patients with thrombus extension had longer ATDs (7.24 versus 3.24 versus 2.77 seconds, $P = .001$, $P < .001$) and a lower peak score of collaterals (1 versus 3 versus 3, $P = .002$, $P = .004$) compared with those with thrombus shortening and no change. The tMIP scores of collaterals were comparable among the 3 groups (2 versus 3 versus 3, $P = .283$, $P = .150$). Patients with thrombus shortening had lower NIHSS scores compared with those with thrombus extension and no change (6.5 versus 16 versus 11, $P < .001$, $P = .022$). Moreover, the rate of poor outcome was significantly higher in patients with thrombus extension than in those with thrombus shortening (100% versus 50%, $P = .001$).

As Table 2 shows, a multinomial logistic regression model, including baseline NIHSS score, baseline thrombus length, and ATD, revealed that ATD was independently associated with

thrombus extension. Also, the peak score of collaterals but not the tMIP score of collaterals was independently associated with thrombus extension after adjusting for baseline NIHSS score and baseline thrombus length (Tables 3 and 4). Baseline NIHSS score and baseline thrombus length were the independent factors associated with thrombus shortening. The Figure is an example showing correlation between thrombus extension and slow collaterals.

Receiver operating characteristic analysis revealed an acceptable value of ATD for predicting thrombus extension, as a reference of thrombus without change (area under the curve, 0.804; 95% confidence interval, 0.663–0.945; $P = .002$). The cutoff point of ATD was 4.61 seconds, and this yielded a sensitivity of 77.2% and a specificity of 78.9%.

Receiver operating characteristic analysis also showed that baseline thrombus length can predict thrombus shortening, as a reference of thrombus without change (area under the curve, 0.733; 95% confidence interval, 0.551–0.916; $P = .024$). The cutoff point of baseline thrombus length was 12.5 mm, and this yielded a sensitivity of 71.4% and a specificity of 84.2%.

We also performed subanalysis for patients who underwent different imaging techniques for evaluation of collateral flow. In patients who underwent CTP, those with thrombus extension tended to have longer ATDs (7.24 versus 3.68 versus 4.48 seconds, $P = .006$, $P = .109$) and a lower peak score of collaterals (1 versus 3 versus 2, $P = .002$, $P = .124$) compared with those with thrombus shortening and no change; these findings were in accordance with our main results. In patients who underwent MR perfusion, those with thrombus extension tended to have longer ATDs (5.87 versus 3.06 versus 1.39 seconds, $P = .352$, $P = .076$) and a lower peak score of collaterals (1 versus 2 versus 3, $P = .352$, $P = .054$) compared with those with thrombus shortening and no change. The MR perfusion subgroup analysis was not significant due to the small sample size.

Table 4: Logistic regression for prediction of thrombus extension and shortening, including baseline tMIP score of collaterals in the model

	OR	95% CI	*P* Value
For thrombus extension (set without change as reference)			
NIHSS score	1.162	0.965–1.399	.113
Baseline thrombus length (mm)	1.076	0.953–1.216	.238
Baseline tMIP score of collaterals	0.759	0.341–1.690	.499
For thrombus shortening (set without change as reference)			
NIHSS score	0.719	0.563–0.917	.008
Baseline thrombus length (mm)	1.210	1.039–1.409	.014
Baseline tMIP score of collaterals	0.571	0.212–1.536	.267

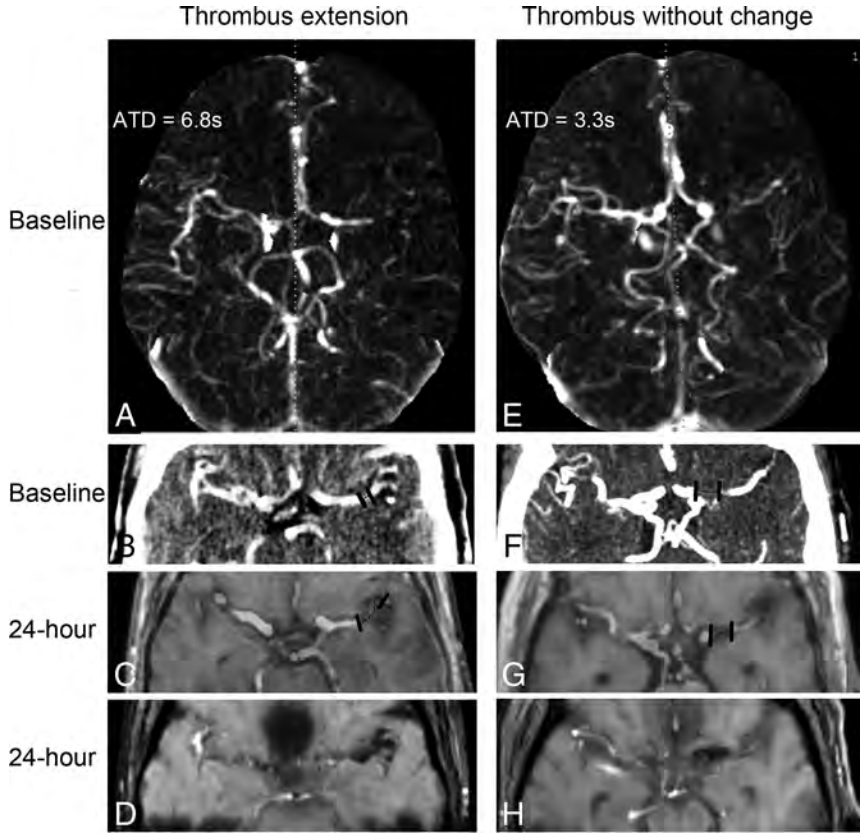

FIGURE. Representative examples of patients with different thrombus-changing patterns. *A–D*, Examples of thrombus extension. *A*, Arterial peak phase of 4D-CTA shows the collateral flow at baseline, with an arrival time delay of 6.8 seconds. Thrombus length was measured on tMIP of 4D-CTA (*B*) and a merged image of dGE-T1 and TOF-MRA (*C*), which was 4.0 mm at baseline and 18.8 mm at 24 hours. *D*, Magnitude image at 24 hours also shows the thrombus. *E–H*, Examples of thrombus without change. *E*, The arterial peak phase of 4D-CTA shows the collateral flow at baseline with an ATD of 3.3 seconds. Thrombus length was measured on tMIP of 4D-CTA (*F*) and the merged image of dGE-T1 and TOF-MRA (*G*), which was 11.2 mm at baseline and 10.9 mm at 24 hours. *H*, Magnitude image at 24 hours also shows the thrombus.

DISCUSSION

In this study, we illustrated the change pattern of thrombus in patients with LAO without recanalization at 24 hours after IVT and revealed that the rate of thrombus extension and shortening was 35.3% and 27%, respectively. Slow collateral filling was associated with thrombus extension, whereas a low NIHSS score and long thrombus length were related to thrombus shortening. Moreover, all patients with thrombus extension had poor outcome at 3 months.

Rapid collaterals had high rates of recanalization after IVT and endovascular therapy.[5,7] Our study further confirmed that slow collateral filling could be related to thrombus extension if recanalization was not achieved. Slow collateral flow represents the stasis of blood flow at the occlusion site, which may cause platelet aggregation, local accumulation of inflammatory mediators, leukocyte activation, and endothelial dysfunction.[9] Moreover, slower collateral flow can result in low shear stress to the thrombus because collateral flow velocity is a surrogate for the pressure drop across the collateral vessels and the occlusion site.[5] These hemodynamic changes thus create an environment conducive to the formation of a new clot and are therefore associated with the ex-

tension of the thrombus. Most interesting, collateral extent was not associated with thrombus extension. Extensive collaterals do not necessarily re-establish arterial blood flow but may serve as pathways for venous flow diversion known as cerebral venous steal, due to the increased inflow resistance and focal compression after infarction.[10] Therefore, the collateral flow may be diverted to veins; this diversion results in a decreased effect on the distal end of the clot. Overall, collateral status could interact with thrombus extension and reconstruct the local angioarchitecture.

It is interesting that we found that thrombus shortening was related to baseline long thrombus and a low NIHSS score. The mild symptoms in patients with relatively long thrombi may suggest good compensated perfusion of the affected brain tissue. Recent preclinical research has shown that better perfusion provided more tPA at the distal end of thrombus, which was helpful to the disruption of the thrombus during the initiation of IVT to 24 hours posttreatment.[11]

Approximately 6%–25% of patients with LAO still fail to achieve successful recanalization and have disabilities, though advances in the device technology of endovascular therapy have improved the speed and efficacy of recanalization in patients with LAO.[12,13] A previous study has demonstrated that unexplained early neurologic deterioration occurring after thrombolysis was independently associated with the susceptibility vessel sign extension in patients without recanalization.[14] In our study, no patients with thrombus extension had good outcomes at 3 months. Our findings indicate that collateral failure might act not only as a cause but possibly an inevitable secondary consequence of thrombus extension and expansion of infarction. Therefore, prevention of thrombus extension by early administration of antithrombotics and early improvement of collateral circulation is of equal importance for patients with LAO without recanalization.

Our study had several limitations. First, it had a retrospective design in a single stroke center (the Second Affiliated Hospital of Zhejiang University, School of Medicine) and a relatively small number of patients. This feature might have a potential risk of selection bias, though data were prospectively established using a stroke registry and standard CTP/MR imaging protocol. Second, thrombus length measured by dGE-T1 and 4D-CTA may be potentially different, though we used coregistration to minimize the discrepancy. Third, we included only patients with M1 segment or distal ICA occlusion to reduce the heterogeneity. It would be clinically important to investigate the thrombus-changing patterns at other sites regarding the various hemodynamics in different vessels. Fourth, our observation that thrombus extension is associated with slow collateral flow could not prove causality. Further studies with time-series data would be needed to demonstrate the causal relationship.

CONCLUSIONS

With in vivo thrombus imaging techniques, we first proved that slow collateral flow was related to thrombus extension in patients with LAO without recanalization after IVT. Meanwhile, no patients with thrombus extension had good outcomes at 3 months, which highlights the importance of prevention of thrombus extension and early improvement of collateral circulation in patients without recanalization.

Disclosures: Min Lou—*RELATED*: *Grant*: National Natural Science Foundation of China, National Key Research and Development Program of China, *Comments*: This work was support by the National Natural Science Foundation of China (81471170 and 81622017), the National Key Research and Development Program of China (2016YFC1301500), and the National Natural Science Foundation of China (81400946).* *Money paid to the institution.

REFERENCES

1. Yan S, Chen Q, Xu M, et al. **Thrombus length estimation on delayed gadolinium-enhanced T1.** *Stroke* 2016;47:756–61 CrossRef Medline
2. Kang DW, Jeong HG, Kim DY, et al. **Prediction of stroke subtype and recanalization using susceptibility vessel sign on susceptibility-weighted magnetic resonance imaging.** *Stroke* 2017;48:1554–59 CrossRef Medline
3. Zhang R, Zhou Y, Liu C, et al. **Overestimation of susceptibility vessel sign: a predictive marker of stroke cause.** *Stroke* 2017;48:1993–96 CrossRef Medline
4. Qazi EM, Sohn SI, Mishra S, et al. **Thrombus characteristics are related to collaterals and angioarchitecture in acute stroke.** *Can J Neurol Sci* 2015;42:381–88 CrossRef Medline
5. Zhang S, Zhang X, Yan S, et al. **The velocity of collateral filling predicts recanalization in acute ischemic stroke after intravenous thrombolysis.** *Sci Rep* 2016;6:27880 CrossRef Medline
6. Frölich AM, Schrader D, Klotz E, et al. **4D CT angiography more closely defines intracranial thrombus burden than single-phase CT angiography.** *AJNR Am J Neuroradiol* 2013;34:1908–13 CrossRef Medline
7. Zhang S, Chen W, Tang H, et al. **The prognostic value of a four-dimensional CT angiography-based collateral grading scale for reperfusion therapy in acute ischemic stroke patients.** *PLoS One* 2016;11:e0160502 CrossRef Medline
8. Tan JC, Dillon WP, Liu S, et al. **Systematic comparison of perfusion-CT and CT-angiography in acute stroke patients.** *Ann Neurol* 2007;61:533–43 CrossRef Medline
9. Diamond SL. **Systems analysis of thrombus formation.** *Circ Res* 2016;118:1348–62 CrossRef Medline
10. Pranevicius O, Pranevicius M, Pranevicius H, et al. **Transition to collateral flow after arterial occlusion predisposes to cerebral venous steal.** *Stroke* 2012;43:575–79 CrossRef Medline
11. Kim DE, Kim JY, Schellingerhout D, et al. **Quantitative imaging of cerebral thromboemboli in vivo: the effects of tissue-type plasminogen activator.** *Stroke* 2017;48:1376–85 CrossRef Medline
12. Campbell BC, Mitchell PJ, Kleinig TJ, et al; EXTEND-IA Investigators. **Endovascular therapy for ischemic stroke with perfusion-imaging selection.** *N Engl J Med* 2015;372:1009–18 CrossRef Medline
13. Berkhemer OA, Fransen PS, Beumer D, et al. **A randomized trial of intraarterial treatment for acute ischemic stroke.** *N Engl J Med* 2015;372:11–20 CrossRef Medline
14. Seners P, Hurford R, Tisserand M, et al. **Is unexplained early neurological deterioration after intravenous thrombolysis associated with thrombus extension?** *Stroke* 2017;48:348–52 CrossRef Medline

Multicentric Experience in Distal-to-Proximal Revascularization of Tandem Occlusion Stroke Related to Internal Carotid Artery Dissection

G. Marnat, M. Bühlmann, O.F. Eker, J. Gralla, P. Machi, U. Fischer, C. Riquelme, M. Arnold, A. Bonafé, S. Jung, V. Costalat, and P. Mordasini

ABSTRACT

BACKGROUND AND PURPOSE: Internal carotid dissection is a frequent cause of ischemic stroke in young adults. It may cause tandem occlusions in which cervical carotid obstruction is associated with intracranial proximal vessel occlusion. To date, no consensus has emerged concerning endovascular treatment strategy. Our aim was to evaluate our endovascular "distal-to-proximal" strategy in the treatment of this stroke subtype in the first large multicentric cohort.

MATERIALS AND METHODS: Prospectively managed stroke data bases from 2 separate centers were retrospectively studied between 2009 and 2014 for records of tandem occlusions related to internal carotid dissection. Atheromatous tandem occlusions were excluded. The first step in the revascularization procedure was intracranial thrombectomy. Then, cervical carotid stent placement was performed depending on the functionality of the circle of Willis and the persistence of residual cervical ICA occlusion, severe stenosis, or thrombus apposition. Efficiency, complications, and radiologic and clinical outcomes were recorded.

RESULTS: Thirty-four patients presenting with tandem occlusion stroke secondary to internal carotid dissection were treated during the study period. The mean age was 52.5 years, the mean initial NIHSS score was 17.29 ± 6.23, and the mean delay between onset and groin puncture was 3.58 ± 1.1 hours. Recanalization TICI 2b/3 was obtained in 21 cases (62%). Fifteen patients underwent cervical carotid stent placement. There was no recurrence of ipsilateral stroke in the nonstented subgroup. Twenty-one patients (67.65%) had a favorable clinical outcome after 3 months.

CONCLUSIONS: Endovascular treatment of internal carotid dissection–related tandem occlusion stroke using the distal-to-proximal recanalization strategy appears to be feasible, with low complication rates and considerable rates of successful recanalization.

ABBREVIATIONS: ICD = internal carotid dissection; sICH = symptomatic intracranial hemorrhage

Acute obstruction or occlusion of the extracranial ICA and additional intracranial ICA or MCA thrombus, so-called tandem occlusion, causes a severe form of ischemic stroke, which accounts for 10%–20% of major strokes and is associated with high rates of disability and death.[1,2] Most stenotic or occlusive lesions of the ICA are caused by atherosclerotic disease or acute dissection. These 2 pathologies constitute distinct stroke etiologies that affect 2 different patient populations, each with their own prognosis. Internal carotid dissection (ICD) is a frequent cause of ischemic stroke, especially in young adults.[3] In cervical carotid occlusive or near-occlusive disease, stroke is due to wall hematoma, accompanied by downstream intracranial embolus or hemodynamic impairment.[4]

Tandem occlusion stroke was known to have a very poor prognosis at the time when treatment consisted of intravenous thrombolysis alone.[2,5,6] Endovascular treatment is now increasingly performed following the results from recent randomized controlled trials (Multicenter Randomized Clinical Trial of Endovascular Treatment for Acute Ischemic Stroke in the Netherlands [MR CLEAN], Endovascular Treatment for Small Core and Proximal Occlusion Ischemic Stroke [ESCAPE], Extending the Time for Thrombolysis in Emergency Neurological Deficits-Intra-Arterial [EXTEND IA], Endovascular Revascularization With Soli-

Received December 7, 2017; accepted after revision February 7, 2018.

From the Interventional and Diagnostic Neuroradiology Department (G.M.), Bordeaux University Hospital, Bordeaux, France; University Institute of Diagnostic and Interventional Neuroradiology (J.G., P.M.) and Department of Neurology (M.B., U.F., M.A., S.J.), Bern University Hospital, Bern, Switzerland; and Interventional and Diagnostic Neuroradiology Department (O.F.E., P.M., C.R., A.B., V.C.), Montpellier University Hospital, Montpellier, France.

Gaultier Marnet, Vincent Costalat, and Pasquale Mordasini contributed equally to the study.

Please address correspondence to Gaultier Marnat, MD, Interventional and Diagnostic Neuroradiology Department, Bordeaux University Hospital, Place Amélie Raba-Léon, 33000 Bordeaux, France; e-mail: gaultier.marnat@chu-bordeaux.fr; gaultier_marnat@yahoo.fr

Indicates article with supplemental on-line table.

http://dx.doi.org/10.3174/ajnr.A5640

taire Device Versus Best Medical Therapy in Anterior Circulation Stroke Within 8 Hours [REVASCAT], Solitaire With the Intention For Thrombectomy as Primary Endovascular Treatment for Acute Ischemic Stroke [SWIFT PRIME], and DWI or CTP Assessment with Clinical Mismatch in the Triage of Wake Up and Late Presenting Strokes Undergoing Neurointervention with Trevo [DAWN]),[7-12] which demonstrated the superiority of combined endovascular strategies over stand-alone intravenous treatment in large-vessel occlusion stroke. Endovascular strategies, however, remain understudied in the specific setting of tandem occlusions and were even excluded from some thrombectomy clinical trials, such as ESCAPE and SWIFT PRIME.[7,8] Of several endovascular strategies that have been proposed during the past few years, the "proximal-to-distal" approach (the so-called antegrade approach) has been predominant.[13-21] It consists of stepwise treatment of the arterial occlusion, starting from the cervical internal carotid lesion and finishing with the intracranial occlusion. We propose a different approach, the "distal-to-proximal" approach, in which the intracranial occlusion is treated first to quickly restore cerebral blood flow. Then, treatment of the internal carotid cervical dissection is performed, depending on functionality of the circle of Willis and persistence of an occlusive dissection. This method had previously demonstrated promising results.[22]

The present study describes the technical and clinical results of the first multicenter study evaluating the distal-to-proximal endovascular approach in cases of tandem occlusion related to ICD.

MATERIALS AND METHODS

Sample

Records of all patients presenting with anterior circulation ischemic stroke treated with an endovascular approach in 2 separate institutions between August 2009 and April 2013 (Montpellier) and January 2010 and September 2014 (Bern) were retrospectively retrieved from prospectively maintained stroke data bases.

Patient Selection

Endovascular therapy was performed immediately after CT or MR imaging under the following conditions: 1) Diagnosis of ischemic stroke was established by CT/CTA/CT perfusion or MR/MRA/MR perfusion imaging; 2) the baseline NIHSS score was ≥4, or isolated aphasia or hemianopia was present; 3) hemorrhage had been excluded by cranial CT or MR imaging; 4) symptom duration was not longer than 24 hours; 5) no individual clinical or premorbid conditions or laboratory findings contraindicated treatment; and 6) tandem occlusion of the carotid-T or M1/M2 segment associated with cervical ICA obstruction or occlusion related to cervical ICA dissection was demonstrated by initial imaging and/or peri-interventional angiograms.

Decision-Making and Imaging

Initial NIHSS and Glasgow Coma Scale scores were assessed by a neurologist. CT and MR imaging were used, depending on the protocol of the center. The routine CT imaging protocol consisted of unenhanced CT and CT angiography and CT perfusion. The routine MR imaging protocol consisted of DWI, FLAIR, T2*/SWI, contrast-enhanced MR angiography including the supra-aortic trunks, and MR perfusion imaging. If tandem occlusion was suspected on initial imaging, it was confirmed with DSA based on the morphologic aspect of the cervical segment of the internal carotid artery (Fig 1) associated with a proximal intracranial vessel occlusion (carotid termination, M1, M1–M2 junction, and/or M2 segment of the middle cerebral artery). The ICD diagnosis was based on clinical, imaging, and angiographic data. We aimed to distinguish dissection from atheromatous cervical carotid artery lesions.

Intravenous Thrombolysis

Intravenous thrombolysis (0.9 mg/kg; 10% of the dose as a bolus and the remainder during 60 minutes) was administered to patients within a maximum of 4.5 hours after stroke onset. Conventional clinical and laboratory inclusion and exclusion criteria for intravenous thrombolysis were applied.

Endovascular Procedure

Endovascular treatment was performed with the patient under general anesthesia or conscious sedation. The decision on the type of sedation was made on an individual basis by the neurologist, neuroradiologist, and anesthesiologist on call. DSA was performed via a transfemoral approach using a biplane, high-resolution angiography system. In one center (Bern, Switzerland), a 4-vessel cerebral angiography was always performed before the intervention. In the other center (Montpellier, France), it was performed after intracranial recanalization through a second femoral approach to assess collateral circulation through the circle of Willis and leptomeningeal collaterals. An 8F guiding catheter or an 8F or 9F balloon-guiding catheter (Guider Softip XF, Boston Scientific, Fremont, California; Merci retriever, Concentric Medical, Mountain View, California) was introduced into the common carotid artery, and an angiographic run was performed to evaluate the occlusion. During this step, cervical internal carotid artery occlusion was demonstrated and eventually differentiated from carotid contrast agent stagnation related to isolated carotid termination thrombus. After we took into account both clinical data and angiographic morphology, ICD was distinguished from atheromatous occlusion.

In cases of obstruction related to cervical ICD, a 0.021-inch microcatheter (Headway microcatheter, MicroVention, Tustin, California; Prowler Select Plus microcatheter, Codman & Shurtleff, Raynham, Massachusetts) was navigated through the true lumen of the dissection over a 0.014-inch microwire (Transend 014, Stryker, Kalamazoo, Michigan; Traxcess, MicroVention; SilverSpeed-14, Covidien, Irvine, California). This maneuver was performed under flow arrest either through wedging of the guide catheter in the stenosis or inflation of the balloon-guide catheter to avoid thromboembolic events during crossing of the lesion. Once the microcatheter position in the true lumen had been confirmed distally by a careful contrast injection, an intermediate 5F guiding catheter (5MAX and 5MAX ACE Reperfusion Catheter, Penumbra, Alameda, California; Vasco +35ASPI, Balt Extrusion, Montmorency, France) was then advanced over the microcatheter into the distal internal carotid artery. After we crossed the thrombus over the microwire with the microcatheter, mechanical thrombectomy was performed with a Solitaire FR (Covidien) or Trevo stent (Stryker). The thrombectomy maneuver was also per-

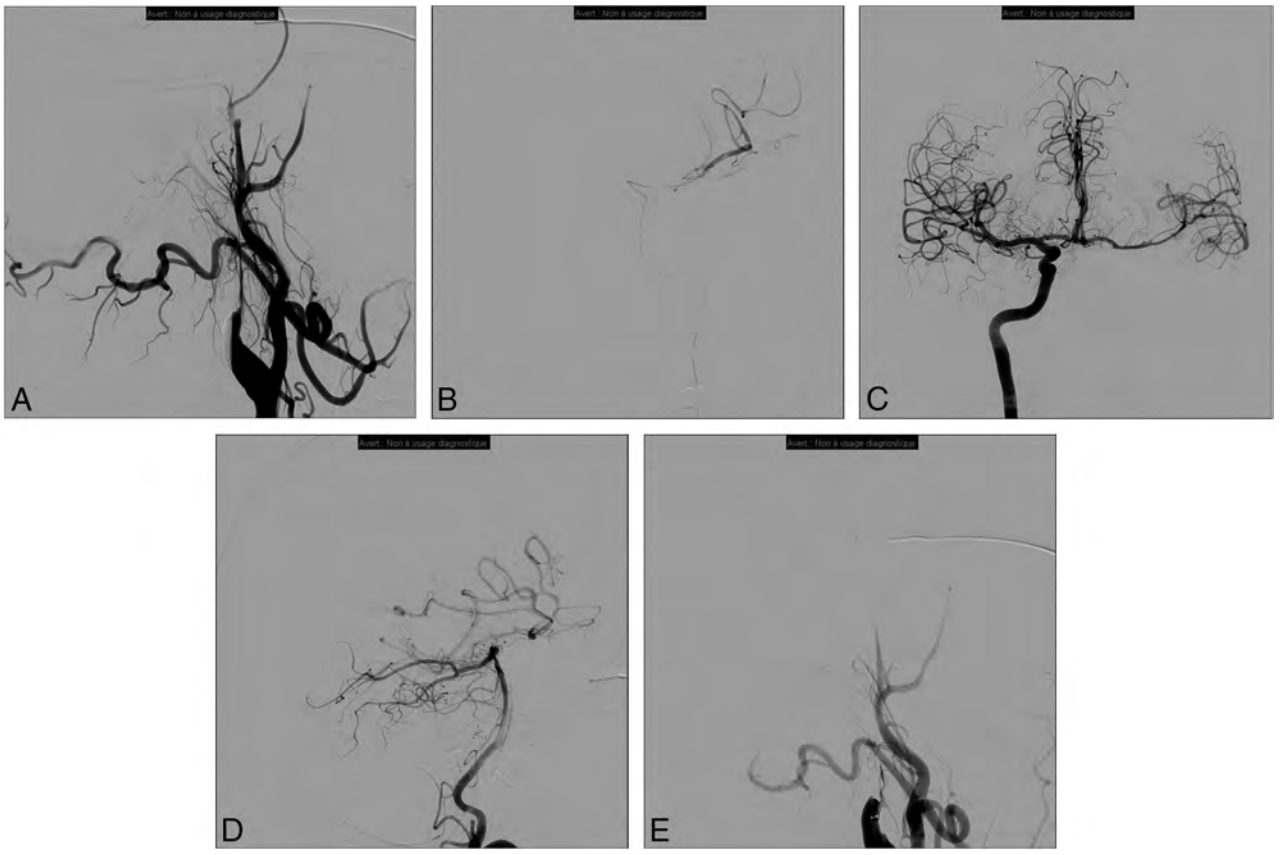

FIG 1. Patient presenting with right hemiplegia and aphasia (NIHSS score = 20). Initial MR imaging revealed a DWI-ASPECTS of 6 after 4.5 hours since symptom onset associated with left tandem ICA and middle cerebral artery occlusions. Initial angiogram (*A*) demonstrates left internal carotid occlusion related to cervical dissection. We then carefully navigate the microcatheter through the dissected ICA to the intracranial occlusion (*B*); then thrombectomy is performed. After contralateral femoral puncture, the right ICA run shows a functional circle of Willis and no residual left M1 occlusion (*C*). The posterior communicating artery is also permeable as seen on the left vertebral artery run (*D*). Consequently, we decided not to treat the cervical ICA dissection, and the artery is left in its initial condition (*E*).

formed under flow arrest and manual aspiration through the intermediate catheter to prevent clot fragmentation and distal embolism. As an alternative access technique, the stent retriever was deployed first through the microcatheter; then, the intermediate catheter was advanced over the pusher wire of the stent retriever using the stent retriever as an intracranial anchor (so-called anchoring technique) to gain intracranial access with the intermediate catheter, especially in cases with very tortuous anatomy.

The result of intracranial recanalization was evaluated using the TICI score. Successful recanalization was defined as TICI 2b or 3. If intracranial recanalization was achieved, treatment of the cervical carotid dissection was left to the discretion of the operator, taking into account the functionality of the circle of Willis, residual cervical occlusion/severe stenosis or thrombus apposition, and difficulty of the endovascular access.

The 0.014-inch microwire was introduced into the petrous segment of the carotid artery to preserve distal access to the true arterial lumen for cervical stent placement. In 1 center (Bern, Switzerland), a filter protection device (FilterWire EZ; Boston Scientific) was placed distal to the dissection when anatomically possible. Then, the guiding catheter and the intermediate catheter were retrieved into the common carotid artery. A 250- to 500-mg bolus of aspirin was administered intravenously before stent placement. Cervical carotid artery stent placement was performed using the carotid Wallstent (Boston Scientific), Precise (Cordis, Fremont, California), Cristallo Ideale (Medtronic, Roncadelle, Italy), or, in case of distal cervical carotid dissection, the LEO (Balt Extrusion), Enterprise (Codman & Shurtleff), or Wingspan (Stryker) stent. Appropriate positioning and opening of the stent were immediately assessed angiographically, and additional angioplasty was performed if necessary. Several stents were used if the dissection was extensive and occlusive in the upper cervical and pre-petrous segments.

Follow-Up

Follow-up CT or MR imaging was performed 24 hours after the acute therapy to assess infarction volume and hemorrhagic status. Symptomatic intracranial hemorrhage (sICH) was defined as a documented hemorrhage associated with a decline of $\geq$4 points in the NIHSS score. If no hemorrhage occurred, double antiplatelet therapy was initiated and continued for 3–6 months. Single antiplatelet treatment was then maintained for 1 year or life-long, depending on the protocol of the responsible center.

NIHSS was measured following recovery from the anesthetic and throughout hospitalization until discharge. Routine clinical follow-up was performed at 3 months by an independent neurologist to evaluate the patient's recovery using the mRS. Clinical

Table 1: Baseline characteristics of the population

Baseline Characteristics	Values
Age (mean) (range) (yr)	52.47 (30–73)
Sex (No.) (%)	
Female	12 (35.3%)
Male	22 (64.7%)
Initial NIHSS score (mean) (range)	17.29 (4–36)
High blood pressure (No.) (%)	14 (41.2%)
Associated IVT (No.) (%)	21 (61.8%)

Note:—IVT indicates intravenous thrombolysis.

outcome was quantified by 3-month mRS and mortality. Favorable outcome was defined as a mRS ≤ 2.

RESULTS

Patient Population

Between August 2009 and April 2013 (Montpellier) and January 2010 to September 2014 (Bern), 531 patients with anterior circulation ischemic stroke were treated in the 2 institutions. Tandem occlusion stroke related to ICD was identified in 34 of these patients (12 women and 22 men). The mean age was 52.47 ± 10.25 years (range, 30–73 years), and the mean NIHSS score was 17.29 ± 6.23 (range, 4–36). A history of high blood pressure was noted in 14 patients. Except for patients with unknown symptom onset, such as wake-up strokes, the average time from symptom onset to arterial puncture was 215.8 ± 66.07 minutes (range, 142–360 minutes). Intravenous thrombolysis was performed in 21 cases (61.8%). Baseline characteristics of the population are given in Table 1. Patients with presumed atheromatous tandem occlusions were excluded from the study.

Procedural Results and Early Evolution

Thirty-three (97%) patients were treated under general anesthesia, and 1 (3%) patient, under conscious sedation. Successful intracranial recanalization (TICI 2b or 3) was achieved in 23 patients (67.65%). The mean time from onset to revascularization was 329.71 ± 128.82 minutes (range, 180–855 minutes). The mean number of stent retriever passes was 2.03 (range, 1–4).

In our population of patients with ICD, 15 (44.12%) finally required cervical internal carotid stent deployment. Stent placement was technically feasible in all cases, and no distal thromboembolic events were associated with stent placement. Among the stented patient subgroup (n = 15), intracranial recanalization TICI 2b–3 was achieved in 8 patients (53.3%). In the nonstented subgroup, 15 patients (78.9%) benefited from revascularization, achieving TICI 2b–3. No periprocedural complications were observed in our multicenter cohort.

Representative endovascular strategies are illustrated in Figs 1 and 2.

Two patients (5.9%) were affected by sICH. In 1 patient who received a cervical internal carotid artery stent, sICH in the basal ganglia occurred early despite a TICI 3 recanalization. Nevertheless, the patient had a favorable outcome with an mRS of 2 after 3 months. In the second patient, severe intracranial hemorrhage occurred early on while the patient was in the intensive care unit after unsuccessful mechanical revascularization (TICI 1) without cervical carotid artery stent placement, resulting in a mRS of 4 at 3-month follow-up.

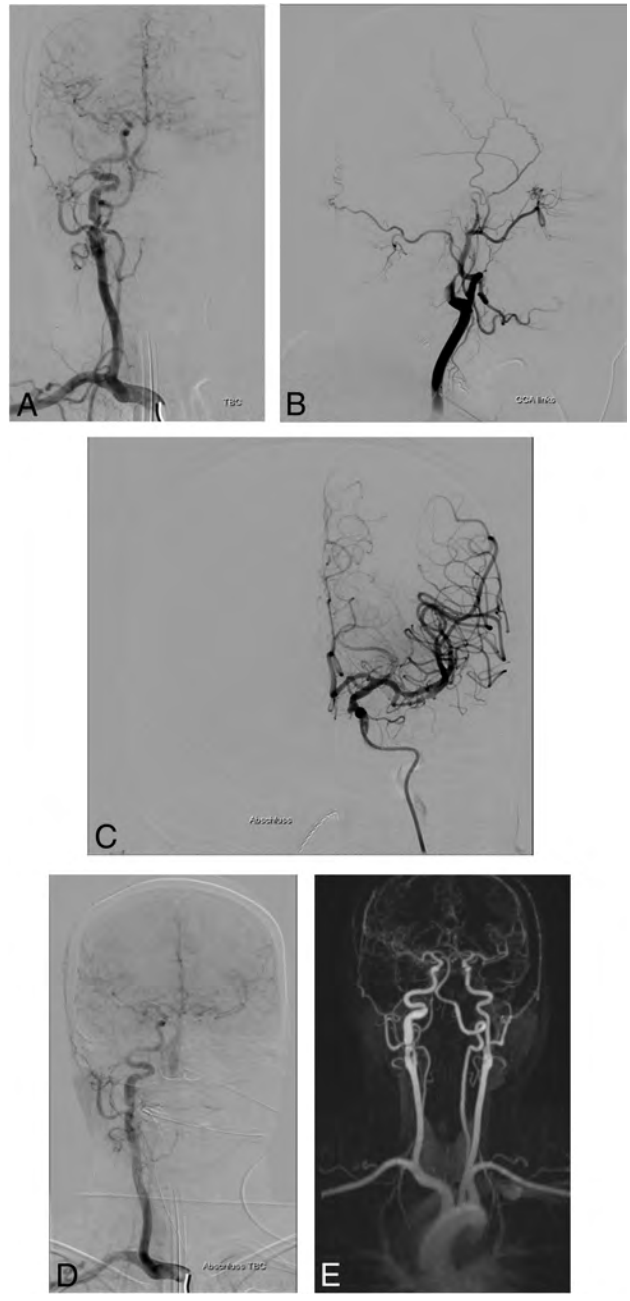

FIG 2. A 34-year-old woman presenting with right hemiplegia and aphasia (NIHSS score = 17). Initial contralateral angiogram depicting a left carotid-T occlusion with good leptomeningeal collaterals from the anterior cerebral artery (*A*). The left common carotid artery angiogram shows ICA occlusion related to cervical ICA dissection (*B*). After passing the dissection under proximal balloon occlusion with a microcatheter and an intermediate catheter, complete intracranial recanalization is achieved by mechanical thrombectomy using a Solitaire device (*C*). Control angiogram reveals extensive cervical ICA dissection with hemodynamic impairment (*D*). Contralateral injection shows functionality of the circle of Willis with good collateralization and patency of the left MCA (*E*). Therefore, the decision was made not to intervene on the left ICA. Control MRA after 3 months shows complete reconstitution of the left ICA under conservative management and without new neurologic events (mRS 1).

Clinical Assessment after 3 Months

After 3 months, 23 (67.65%) of the 34 patients treated for ICD tandem occlusion demonstrated a favorable outcome (7 patients with mRS = 0; seven with mRS = 1; nine with mRS = 2). The

Table 2: Clinical results

Procedural and Follow-Up Data	Values
Timing: onset-to-puncture (mean) (range) (min)	215.8 (142–360)
Intracranial occlusion topography (No.) (%)	
Internal carotid terminus	8 (23.5%)
M1	24 (70.6%)
M2	2 (5.9%)
No. of stent retriever passes (mean) (range)	2.03 (1–4)
Cervical ICA stenting (No.) (%)	15 (44.1%)
TICI 2b/3 (No.) (%)	23 (67.65%)
Timing: onset-to-revascularization (mean) (range) (min)	329.71 (180–855)
Favorable outcome (No.) (%)	23 (67.65%)
Mortality (No.) (%)	3 (8.8%)

Note:—Stentriever is trademarked technology of Stryker (Trevo).

mortality rate was 8.8% (3 patients). No patients were lost to clinical follow-up.

In the subgroup of patients who underwent ICA stent placement, 10 (66.7%) had mRS $\leq$ 2 at 3-month follow-up. In the unstented subgroup, 13 patients (68.4%) had a satisfactory clinical outcome. No stroke recurrence was observed in either of the subgroups.

The clinical results are summarized in Table 2 and the On-line Table.

DISCUSSION

Ischemic strokes due to a tandem occlusion caused by either atheromatous disease or a carotid dissection, if untreated, commonly have a poor prognosis and clinical outcome. Before the emergence of endovascular treatment, a very modest efficacy of intravenous thrombolysis was reported in the treatment of tandem occlusion.[2,23] Linfante et al[23] reported a very low rate of 31% recanalization on late 3-day imaging follow-up. Engelter et al[5] reported a 36% rate of good outcome after intravenous thrombolysis in patients with tandem occlusions due to ICD.

Endovascular treatment approaches for tandem occlusions remain insufficiently studied. In some of the recent multicenter randomized trials, tandem occlusion strokes have even been considered an exclusion criterion.[7,8] Most studies have analyzed tandem occlusion stroke by pooling atheromatous and ICD etiologies.[13,15,18-21,24-29] In our opinion, these 2 entities involve 2 different diseases, each with a specific pathophysiologic origin and patient population. ICD usually affects young patients with patent supra-aortic trunks and circle of Willis. Cervical atheromatous disease affects an older population with chronic arterial lesions of the cervical and intracranial arteries and a high stroke recurrence rate.[30] Thus, we consider these 2 etiologies completely different pathologies with different treatment strategies and prognoses.

The literature specifically addressing ICD tandem occlusion is scant.[14,17,31-35] Reported satisfactory intracranial recanalization rates vary between 50% and 100%, and associated rates of favorable outcome, between 50% and 80%. Our article reports the results of the first multicenter study of endovascular treatment of this specific lesion subtype.

Different approaches and strategies have been proposed for the treatment of tandem occlusions. Most of the published studies have reported the results of antegrade recanalization.[13,20] This consists of stepwise revascularization beginning from the cervical carotid artery lesion and ending by treating the intracranial occlusion. Despite overall satisfactory results, we believe that this approach can be improved. First, treating the cervical lesion with stent placement leads to significant prolongation of cerebral hypoperfusion. Cervical carotid stent placement may be difficult in a dissected vessel, and dissection can be extensive. Intracranial recanalization is performed as the second step, extending the duration of brain ischemia and potentially leading to larger infarct core volumes. The second disadvantage is that systematic cervical carotid stent placement necessitates antiplatelet medication, which may increase the risk of sICH.

Our approach is to focus first on intracranial revascularization.[22] This shortens the duration of cerebral ischemia. The first step consists of navigating through the cervical carotid lesion up to the distal segments of the ICA. Avoiding the false lumen of the dissected vessel represents the main challenge. In our experience, it has never been impossible to reach the intracranial ICA via the true lumen. We routinely use a triaxial approach. If one positions the intermediate catheter beyond the dissection, the cervical occlusion is only crossed once to perform intracranial thrombectomy. This limits the maneuvers at the level of the dissected portion of the ICA, reducing the duration of the procedure and complication risk.

Our endovascular strategy also avoids cervical ICA stent placement in a significant number of cases. In our study population, the decision about stent placement was made taking into account cervical ICA residual steno-occlusion, circle of Willis functionality, intracranial recanalization TICI grade, and pretherapeutic infarct volume based on imaging. In many cases, after we navigated inside the dissected ICA through the true lumen, this simple maneuver was sufficient to reopen the ICA lumen enough to obtain efficient blood flow. In these cases, no further stent placement procedure of the ICA was required. Then, depending on circle of Willis functionality, we did not systematically stented the cervical ICA. When there was a likelihood that stent placement would be technically difficult and/or a high risk of hemorrhage due to antiplatelet therapy because of large cerebral infarct volume, we specifically studied circle of Willis functionality. Using previously published angiographic features demonstrating the functionality of the circle of Willis,[36] we could decide not to stent the ICA if there was an efficient vascular supply from the contralateral ICA through the anterior or posterior communicating artery or leptomeningeal collaterals. Those 2 considerations leading to the decision not to stent the dissected ICA are supported by the low rate of delayed stroke recurrence after ICD.[4] In the present study, no patient in the nonstented subgroup had a recurrence. Therefore, treatment of ICD by stent placement in tandem occlusion in patients with acute stroke should be carefully weighed in the light of the potentially benign course of the disease under conservative management and taking into account clinical and angiographic information in decision-making.

The sICH rate of only 2 cases (5.9%) was low. In the first case, the patient benefited from complete intracranial recanalization and cervical ICA stent placement. He presented with a favorable neurologic outcome (mRS, 2 after 3 months). In the second patient, sICH was likely related to extended cerebral infarction after

failure of endovascular treatment (TICI score = 1), leading to a poor clinical outcome (mRS, 4 after 3 months).

Despite several limits of the present study, such as its retrospective nature, it is the largest study to date dealing with the endovascular treatment of acute stroke related to tandem occlusions due to ICD using the distal-to-proximal recanalization strategy. We also present the first reported multicenter experience with the recanalization treatment of this specific stroke subtype.

CONCLUSIONS

Endovascular treatment of ICD-related tandem occlusion stroke using the distal-to-proximal recanalization strategy appears feasible, with low complication rates and considerable rates of successful recanalization. This endovascular approach prioritizes the restoration of intracranial blood flow and focuses on making an informed decision about the need for stent placement of the cervical ICA. The decision should take into account clinical and angiographic information such as the degree of intracranial recanalization, dissection extent, infarct volume on initial imaging, and the functionality of the circle of Willis.

Disclosures: Omer Faruk Eker—*UNRELATED*: *Payment for Development of Educational Presentations*: Stryker, Medtronic*. Jan Gralla—*UNRELATED*: *Consulting Fee or Honorarium*: Medtronic, *Comments*: Global Principal Investigator of the STAR study and SWIFT DIRECT trial, consultant for Medtronic*; *Grants/Grants Pending*: SNF, *Comments*: research grant for MRI stroke imaging*. Urs Fischer—*UNRELATED*: *Consultancy*: Medtronic, Stryker, *Comments*: Advisory Board and consultancy*; *Grants/Grants Pending*: Medtronic, Swiss National Science Foundation, *Comments*: research grants for SWIFT DIRECT, ELAN, and SWITCH trials.* Marcel Arnold—*UNRELATED*: *Board Membership*: Amgen, Bayer, Bristol-Myers Squibb, Boehringer Ingelheim, Pfizer, Covidien, Daiichi Sankyo, *Comments*: honoraria for scientific advisory boards; *Grants/Grants Pending*: Swiss National Science Foundation, Swiss Heart Foundation*; *Payment for Lectures Including Service on Speakers Bureaus*: Bayer, Covidien, *Comments*: honoraria for lectures. Alain Bonafé—*UNRELATED*: *Consultancy*: Stryker, Medtronic, MicroVention. Vincent Costalat—*UNRELATED*: *Consultancy*: Stryker, Medtronic, Balt, Cerenovus; *Grants/Grants Pending*: Stryker, Medtronic*; *Payment for Development of Educational Presentations*: Stryker, Medtronic, Balt Extrusion. *Money paid to the institution.

REFERENCES

1. Grau AJ, Weimar C, Buggle F, et al. **Risk factors, outcome, and treatment in subtypes of ischemic stroke: the German stroke data bank.** *Stroke* 2001;32:2559–66 Medline
2. Rubiera M, Ribo M, Delgado-Mederos R, et al. **Tandem internal carotid artery/middle cerebral artery occlusion: an independent predictor of poor outcome after systemic thrombolysis.** *Stroke* 2006;37:2301–05 CrossRef Medline
3. Arauz A, Hoyos L, Espinoza C, et al. **Dissection of cervical arteries: long-term follow-up study of 130 consecutive cases.** *Cerebrovasc Dis* 2006;22:150–54 CrossRef Medline
4. Benninger DH, Georgiadis D, Kremer C, et al. **Mechanism of ischemic infarct in spontaneous carotid dissection.** *Stroke* 2004;35:482–85 CrossRef Medline
5. Engelter ST, Rutgers MP, Hatz F, et al. **Intravenous thrombolysis in stroke attributable to cervical artery dissection.** *Stroke* 2009;40:3772–76 CrossRef Medline
6. Engelter ST, Dallongeville J, Kloss M, et al; Cervical Artery Dissection and Ischaemic Stroke Patients-Study Group. **Thrombolysis in cervical artery dissection: data from the Cervical Artery Dissection and Ischaemic Stroke Patients (CADISP) database.** *Eur J Neurol* 2012;19:1199–206 CrossRef Medline
7. Saver JL, Goyal M, Bonafe A, et al; SWIFT PRIME Investigators. **Stent-retriever thrombectomy after intravenous t-PA vs. t-PA alone in stroke.** *N Engl J Med* 2015;372:2285–95 CrossRef Medline
8. Goyal M, Demchuk AM, Menon BK, et al; ESCAPE Trial Investigators. **Randomized assessment of rapid endovascular treatment of ischemic stroke.** *N Engl J Med* 2015;372:1019–30 CrossRef Medline
9. Jovin T, Chamorro A, Cobo E, et al; REVASCAT Trial Investigators. **Thrombectomy within 8 hours after symptom onset in ischemic stroke.** *N Engl J Med* 2015;372:2296–306 CrossRef Medline
10. Campbell BC, Mitchell PJ, Kleinig TJ, et al; EXTEND-IA Investigators. **Endovascular therapy for ischemic stroke with perfusion-imaging selection.** *N Engl J Med* 2015;372:1009–18 CrossRef Medline
11. Berkhemer O, Fransen P, Beumer D, et al. **A randomized trial of intraarterial treatment for acute ischemic stroke.** *N Engl J Med* 2015;372:11–20 CrossRef Medline
12. Nogueira RG, Jadhav AP, Haussen DC, et al; DAWN Trial Investigators. **Thrombectomy 6 to 24 hours after stroke with a mismatch between deficit and infarct.** *N Engl J Med* 2018;378:11–21 CrossRef Medline
13. Mpotsaris A, Bussmeyer M, Buchner H, et al. **Clinical outcome of neurointerventional emergency treatment of extra- or intracranial tandem occlusions in acute major stroke: antegrade approach with Wallstent and Solitaire stent retriever.** *Clin Neuroradiol* 2013;23:207–15 CrossRef Medline
14. Lavallée PC, Mazighi M, Saint-Maurice JP, et al. **Stent-assisted endovascular thrombolysis versus intravenous thrombolysis in internal carotid artery dissection with tandem internal carotid and middle cerebral artery occlusion.** *Stroke* 2007;38:2270–74 CrossRef Medline
15. Cohen JE, Gomori JM, Rajz G, et al. **Extracranial carotid artery stenting followed by intracranial stent-based thrombectomy for acute tandem occlusive disease.** *J Neurointerv Surg* 2015;7:412–17 CrossRef Medline
16. Dababneh H, Bashir A, Hussain M, et al. **Endovascular treatment of tandem internal carotid and middle cerebral artery occlusions.** *J Vasc Interv Neurol* 2014;14:26–31 Medline
17. Haussen DC, Jadhav A, Jovin T, et al. **Endovascular management vs intravenous thrombolysis for acute stroke secondary to carotid artery dissection: local experience and systematic review.** *Neurosurgery* 2016;78:709–16 CrossRef Medline
18. Malik AM, Vora NA, Lin R, et al. **Endovascular treatment of tandem extracranial/intracranial anterior circulation occlusions: preliminary single-center experience.** *Stroke* 2011;42:1653–57 CrossRef Medline
19. Papanagiotou P, Roth C, Walter S, et al. **Carotid artery stenting in acute stroke.** *J Am Coll Cardiol* 2011;58:2363–69 CrossRef Medline
20. Spiotta AM, Lena J, Vargas J, et al. **Proximal to distal approach in the treatment of tandem occlusions causing an acute stroke.** *J Neurointerv Surg* 2015;7:164–69 CrossRef Medline
21. Stampfl C, Ringleb P, Möhlenbruch M, et al. **Emergency cervical internal carotid artery stenting in combination with intracranial thrombectomy in acute stroke.** *AJNR Am J Neuroradiol* 2014;35:741–46 CrossRef Medline
22. Marnat G, Mourand I, Eker O, et al. **Endovascular management of tandem occlusion stroke related to internal carotid artery dissection using a distal to proximal approach: insight from the RECOST study.** *AJNR Am J Neuroradiol* 2016;37:1281–88 CrossRef Medline
23. Linfante I, Llinas RH, Selim M, et al. **Clinical and vascular outcome in internal carotid artery versus middle cerebral artery occlusions after intravenous tissue plasminogen activator.** *Stroke* 2002;33:2066–71 CrossRef Medline
24. Kappelhof M, Marquering HA, Berkhemer OA, et al. **Intra-arterial treatment of patients with acute ischemic stroke and internal carotid artery occlusion: a literature review.** *J Neurointerv Surg* 2015;7:8–15 CrossRef Medline
25. Fischer U, Mono M-L, Schroth G, et al. **Endovascular therapy in 201 patients with acute symptomatic occlusion of the internal carotid artery.** *Eur J Neurol* 2013;20:1017–24, e87 CrossRef Medline
26. Matsubara N, Miyachi S, Tsukamoto N, et al. **Endovascular intervention for acute cervical carotid artery occlusion.** *Acta Neurochir (Wien)* 2013;155:1115–23 CrossRef Medline
27. Maurer C, Joachimski F, Berlis A. **Two in one: endovascular treat-**

ment of acute tandem occlusions in the anterior circulation. *Clin Neuroradiol* 2015;25:397–402 CrossRef Medline
28. Suh DC, Kim JK, Choi CG, et al. **Prognostic factors for neurologic outcome after endovascular revascularization of acute symptomatic occlusion of the internal carotid artery.** *AJNR Am J Neuroradiol* 2007;28:1167–71 CrossRef Medline
29. Lescher S, Czeppan K, Porto L, et al. **Acute stroke and obstruction of the extracranial carotid artery combined with intracranial tandem occlusion: results of interventional revascularization.** *Cardiovasc Intervent Radiol* 2015;38:304–13 CrossRef Medline
30. Lovett JK, Coull AJ, Rothwell PM. **Early risk of recurrence by subtype of ischemic stroke in population-based incidence studies.** *Neurology* 2004;62:569–73 CrossRef Medline
31. Baumgartner RW, Georgiadis D, Nedeltchev K, et al. **Stent-assisted endovascular thrombolysis versus intravenous thrombolysis in internal carotid artery dissection with tandem internal carotid and middle cerebral artery occlusion.** *Stroke* 2008;39:e27–28 CrossRef Medline
32. Fields JD, Lutsep HL, Rymer MR, et al; Merci Registry Investigators. **Endovascular mechanical thrombectomy for the treatment of acute ischemic stroke due to arterial dissection.** *Interv Neuroradiol* 2012; 18:74–79 CrossRef Medline
33. Mourand I, Brunel H, Vendrell JF, et al. **Endovascular stent-assisted thrombolysis in acute occlusive carotid artery dissection.** *Neuroradiology* 2010;52:135–40 CrossRef Medline
34. Juszkat R, Liebert W, Stanisławska K, et al. **Extracranial internal carotid artery dissection treated with self-expandable stents: a single-centre experience.** *Cardiovasc Intervent Radiol* 2015;38:1451–57 CrossRef Medline
35. Pham M, Rahme RJ, Arnaout O, et al. **Endovascular stenting of extracranial carotid and vertebral artery dissections: a systematic review of the literature.** *Neurosurgery* 2011;68:856–66; discussion 866 CrossRef Medline
36. Abud DG, Spelle L, Piotin M, et al. **Venous phase timing during balloon test occlusion as a criterion for permanent internal carotid artery sacrifice.** *AJNR Am J Neuroradiol* 2005;26:2602–09 CrossRef Medline

Treatment of Distal Anterior Cerebral Artery Aneurysms with Flow-Diverter Stents: A Single-Center Experience

F. Cagnazzo, M. Cappucci, C. Dargazanli, P.-H. Lefevre, G. Gascou, C. Riquelme, A. Bonafe, and V. Costalat

ABSTRACT

BACKGROUND AND PURPOSE: Flow diversion for aneurysms beyond the circle of Willis is still debated. Our aim was to evaluate the safety and efficacy of flow diversion treatment of distal anterior cerebral artery aneurysms.

MATERIALS AND METHODS: Consecutive patients with distal anterior cerebral artery aneurysms treated from January 2014 to October 2017 were evaluated retrospectively with prospectively maintained data. Treatment was performed only for unruptured or recanalized aneurysms after coiling. Technical feasibility, procedural complications, aneurysm occlusion (O'Kelly-Marotta grading scale), and clinical outcome were evaluated.

RESULTS: Fifteen patients were included in the study, with 17 distal anterior cerebral artery saccular aneurysms treated with flow-diverter stents. Mean aneurysm size was 4.25 ± 3.9 mm; range, 2–9 mm. Flow diversion was used as retreatment among 6 previously coiled aneurysms (5 ruptured and coiled in the acute phase, and 1 unruptured and recanalized). Stent deployment was technically successful in all cases. During the perioperative period, 1 patient experienced a transient minor stroke (6%), whereas 2 patients reported acute in-stent thrombosis with disabling ischemic complications (13%). Fourteen patients and 16 aneurysms were available during a mean radiologic follow-up of 12 months (range, 3–24 months). Overall, 12 (75%) aneurysms were completely occluded (O'Kelly-Marotta grading scale score D), 1 aneurysm (6%) showed near-complete occlusion (O'Kelly-Marotta grading scale score C), and 3 aneurysms (19%) were incompletely occluded (O'Kelly-Marotta grading scale, score B). All 6 aneurysms previously coiled were completely occluded after flow diversion, whereas 70% of aneurysms treated with flow diverters alone showed complete/near-complete occlusion (O'Kelly-Marotta grading scale C–D). There were no cases of aneurysm rupture, in-stent occlusion, or retreatment during long-term follow-up.

CONCLUSIONS: Treatment of distal anterior cerebral artery aneurysms with flow-diverter stents is feasible and effective, with high rates of aneurysm occlusion. Flow diversion plus coiling, in the retreatment of lesions previously coiled, allowed higher rates of occlusion compared with flow diverters alone. However, the risk of ischemic complications is not negligible, and flow-diversion treatment should be evaluated only for aneurysms not amenable to simple coil embolization.

ABBREVIATIONS: ACA = anterior cerebral artery; OKM = O'Kelly-Marotta grading scale

Aneurysms arising from the anterior cerebral artery (ACA) distal to the anterior communicating artery complex account for 5%–10% of all intracranial aneurysms.[1,2] The distal access, the small caliber of the parent artery, and the frequency of wide-neck lesions are factors that contribute to the complexity of coiling, stent-assisted coiling, and remodeling techniques in distal ACA lesions.[3,4] In addition, due to the deep-seated location in the interhemispheric fissure, clip reconstruction or in situ bypass through an interhemispheric approach is technically challenging.[5] Based on their ability to reconstruct the parent artery, the off-label uses of flow-diverter stents are constantly extended, including aneurysms in distal locations and with unfavorable anatomy. Recently, the use of flow diversion in distal ACA aneurysms has been reported as an alternative treatment for lesions difficult to treat with conventional endovascular or surgical strategies. However, few publications have reported treatment-related outcomes of flow diversion in this location, and the efficacy and safety of this technique remain unclear.[6-15]

We present a retrospective series of 15 consecutive patients with 17 distal ACA aneurysms treated with flow-diverter stents at

Received November 28, 2017; accepted after revision February 6, 2018.

From the Neuroradiology Department, University Hospital Güi-de-Chauliac, Centre Hospitalier Universitaire de Montpellier, Montpellier, France.

Please address correspondence to Federico Cagnazzo, MD, Neuroradiology Department, CHU Gui De Chauliac, 80 Ave Augustin Fliche, 34000 Montpellier, France; e-mail: f.cagnazzo86@gmail.com

Indicates article with supplemental on-line tables.

http://dx.doi.org/10.3174/ajnr.A5615

our institution. In addition, we discuss the safety and efficacy of this treatment, comparing our experience with the results reported in the literature.

MATERIALS AND METHODS

Patient Selection

Our hospital institutional review board approved this retrospective study. The prospectively maintained data bases at our institution were retrospectively reviewed by 2 and, in case of inconsistency, by 3 investigators independently to identify patients with distal ACA aneurysms treated with flow-diverter stents between January 2014 and October 2017. Data collection included the following: demographics, aneurysm characteristics, diameter of the parent artery and ACA branches covered with the stent, details of the endovascular treatment, clinical presentation, follow-up imaging, and clinical outcome. Treatment strategy was made by multidisciplinary consensus (vascular neurosurgeons, interventional neuroradiologists). The decision to treat with flow-diverter stents was made on the basis of the following: 1) the presence of a wide neck, 2) a branching vessel coming from the aneurysm that could result in the coil falling out of the aneurysm into the branch, 3) recanalization of aneurysm incompletely occluded with previous coiling because of the unfavorable anatomy, and 4) unstable position of the microcatheter inside the aneurysm during coiling due to the distal location and tortuosity of the ICA.

Antiplatelet Therapy

The standard antiplatelet therapy included daily dual-antiplatelet medication with aspirin (Kardegic), 75 mg, and clopidogrel (Plavix), 75 mg, starting no less than 5 days before the treatment. In general, the therapy was maintained for a minimum of 6 months until the first clinical and radiologic follow-up. After 6 months, based on the clinical and radiologic evaluation, the patients were switched to 75 mg of aspirin for a minimum of 6 months or for life. Aspirin was continued after 1 year in case of flow reduction of the covered branch or in case of luminal narrowing related to the intimal hyperplasia; meanwhile, aspirin was stopped after the 1-year follow-up in case of incomplete aneurysm occlusion with the aim of improving the thrombosis of the aneurysm dome. VerifyNow P2Y12 assay (Accumetrics, San Diego, California) was used to test the platelet inhibition. In case of platelet inhibition of $<$40%, an additional loading dose of clopidogrel, 300 mg, or prasugrel, 10–20 mg, was administered before the procedure. Concurrent with the procedure, intravenous heparinization was performed (activated clotting time maintained above 250 seconds).

Description of Technique

All patients were treated under general anesthesia via a transfemoral approach. Access to the distal ACA was obtained in a triaxial fashion. Through a long femoral sheath, a 6F guiding catheter was advanced into the carotid artery. Vessel and aneurysm features were analyzed via biplane and 3D rotational angiography. Based on the aneurysm neck and parent artery diameter, a flow-diverter stent was chosen to allow enough wall apposition and coverage of the aneurysm neck. The stent was unsheathed under roadmap guidance through a 0.027-inch microcatheter navigated beyond the aneurysm neck. Immediately postdeployment, VasoCT (Philips Health care, Best, the Netherlands) with diluted iodinated contrast medium was used to assess stent apposition to the arterial wall.

Clinical and Imaging Assessment

Clinical evaluation was performed before, postprocedure, throughout the following days, and at discharge. The modified Rankin Scale was used for outcome assessment. Clinical follow-up evaluation was performed at 3, 6, 12, and 24 months. Usually, the degree of aneurysm occlusion was evaluated with MR angiography at 6 months and digital subtraction angiography at 12 and 24 months. Treatment outcomes were graded according to the O'Kelly-Marotta (OKM) grading scale,[16] based on the DSA images. The degree of filling (A = total, B = subtotal, C = entry remnant, D = no filling) and the degree of stasis (prolongation of stasis into 1 = arterial, 2 = capillary, 3 = venous phase) were rated before stent deployment, immediately after, and during follow-up.

Statistical Analysis

Statistical analysis was performed with GraphPad QuickCalcs software (GraphPad Software, San Diego, California). Summary statistics are presented for all data available using means ± SDs for continuous variables and frequency tabulations for categoric variables.

RESULTS

Baseline Population Characteristics

Population characteristics are summarized in On-line Table 1. In the 3-year period, 15 consecutive patients (10 women, 5 men; mean age, 60.9 ± 10.5 years; range, 40–77 years) with 17 distal ACA aneurysms were included in this study. Pretreatment mRS was 0 for 4 patients (26.6%), 1 for 6 patients (40%), and 2 for 5 patients (33%). Overall, 3 patients were hypertensive (20%), 3 patients were smokers (20%), 6 patients were hypertensive and smokers (40%), and only 1 patient presented with a family history of aneurysmal subarachnoid hemorrhage (6%).

Aneurysm Characteristics

All aneurysms were saccular with a mean size of 4.25 ± 3.9 mm; range, 2–9 mm. Five aneurysms (29%) were medium-sized (5.0–9.9 mm) (On-line Table 1). All reported aneurysms were localized in the distal portion of the ACA behind the anterior communicating artery. The aneurysms arose from the branching points of the cortical distal ACA branches. Accordingly, 3 aneurysms originated from the frontopolar division (17.5%); 10, from the callosomarginal division (59%); 2, from the anterior internal frontal artery division (12%); 1, from the middle internal frontal artery (6%); and 1, from the distal portion of the pericallosal artery (superior parietal artery) (6%). Eleven aneurysms were unruptured (65%), whereas 5 (29%) were previously ruptured and treated with coil embolization in the acute phase. One ruptured aneurysm was discovered 3 weeks after rupture (patient 4) and was treated with flow diversion in the subacute phase. Among the unruptured group, 1 aneurysm (6%) was previously coiled and treated with flow diversion because of recanalization (patient 3). Overall, 11 aneurysms had flow diverters as the first treatment (65%); and 6, as the retreatment (35%).

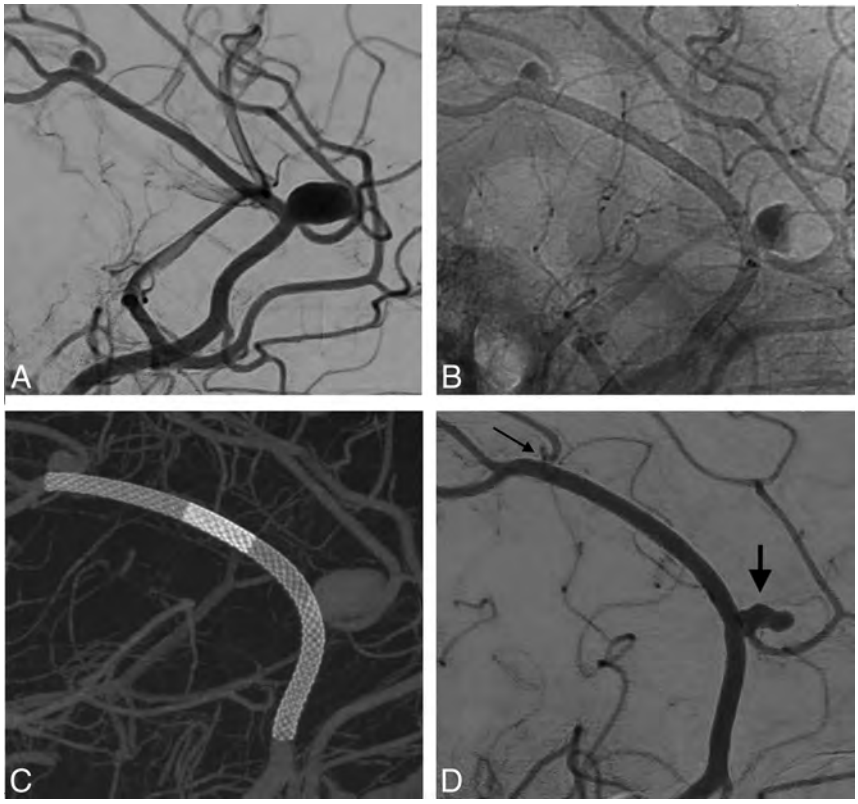

FIG 1. *A*, Left ICA angiography depicting 1 medium-sized aneurysm (7 × 9 mm) located at the callosomarginal artery and 1 small aneurysm (4 × 3 mm) located at the superior parietal artery bifurcation (patient 5). *B*, Flow stagnation immediately after the deployment of 2 telescopic PEDs (25 × 14 mm + 25 × 20 mm). *C*, Flat panel CT reconstruction shows successful stent implantation and correct vessel wall apposition. *D*, Eighteen-month DSA follow-up shows incomplete occlusion (*short arrow*) (OKM B2) and near-complete occlusion (*long arrow*) (OKM C2) of the aneurysms.

Treatment Characteristics and Technical Results

Overall, 12 aneurysms were treated with a Pipeline Embolization Device (PED; Covidien, Irvine, California); 3, with a Silk flow-diverter (Balt Extrusion, Montmorency, France); and 2, with a Flow-Redirection Endoluminal Device (FRED; MicroVention, Tustin, California). A single stent was used in all except 1 case (patient 5 with 2 aneurysms along the pericallosal artery was treated with 2 telescopic PEDs) (On-line Table 2). No multiple overlapping flow-diverter stents were used to cover the aneurysm neck.

In all cases, the stent was successfully navigated to the target area and deployed across the aneurysm neck. Correct stent apposition to the arterial wall was confirmed with VasoCT in all cases.

Clinical Outcome and Procedure-Related Complications

Treatment-related complications and clinical outcomes are summarized in On-line Table 2. Overall, 3 patients showed ischemic complications in the perioperative period. A minor transient stroke in the basal ganglia developed in the patient treated with 2 telescopic PEDs (patient 5) (Fig 1). This patient showed transient hemiparesis 24 hours after treatment. Immediate MR imaging demonstrated small embolic lesions in the basal ganglia. A dose adjustment of prasugrel from 10 to 20 mg was performed (the patient was resistant to clopidogrel), and the patient was discharged without neurologic deterioration. There were 2 major strokes related to stent thrombosis. One patient (patient 11) (Fig 2), after discontinuation of the dual-antiplatelet therapy due to low compliance with the medical treatment, developed severe hemiparesis 10 days after treatment with the Silk stent. MR imaging and DSA showed intrastent thrombosis and pericallosal territory infarct. Due to the absence of the penumbra ischemic area evaluated with MR imaging, DWI, FLAIR, and PWI (the patient arrived at the hospital 20 hours after the onset of symptoms), no additional acute endovascular or medical treatments were performed. The patient was discharged with severe hemiparesis (mRS 4) and normal dual-antiplatelet therapy. The second patient (patient 13), treated with aspirin and clopidogrel, developed moderate right hemiparesis and a confused state due to acute FRED stent thrombosis 12 hours after treatment. The stent was completely recanalized after systemic abciximab injection, and the patient was discharged with a mild right-leg weakness. All patients were available at the long-term clinical follow-up (the mean clinical follow-up was 14 months; range, 3–24 months). All except 1 (patient 11) presented with an mRS score of 0–2 (93%).

Angiographic Outcome of Aneurysms

The mean radiologic follow-up was 12.6 months (range, 3–24 months) (On-line Table 2). Fourteen patients and 16 aneurysms were available for the long-term angiographic follow-up. Overall, 12 (75%) aneurysms were completely occluded (OKM score D) (Fig 3), 1 aneurysm (6%) showed near-complete occlusion (OKM score C), and 3 aneurysms (19%) were incompletely occluded (OKM score B). The mean radiologic follow-up among the group of aneurysms with complete/near-complete occlusion (OKM C2–D) was higher compared with the group with incomplete occlusion (OKM B) (13.5 versus 7 months, $P = .014$). All 6 aneurysms previously coiled were completely occluded after flow diversion (OKM score D), whereas 7 of the 10 aneurysms treated with flow diverters alone showed complete/near-complete occlusion (OKM C–D) during follow-up ($P = .4$). The incidence of hypertension and smoking was 54% and 50% among the group of completely occluded and incompletely occluded aneurysms, respectively. There were no cases of aneurysm rupture, in-stent occlusion, or retreatment during long-term follow-up. Three cases of asymptomatic mild stent stenosis (<50%) were observed and were related to in-stent intimal hyperplasia. In case of mild stent stenosis, aspirin was continued after the 1-year follow-up.

Angiographic Outcome of Covered Branches

Angiographic outcomes of jailed branches are summarized in On-line Table 2. Immediately after stent deployment, there were no

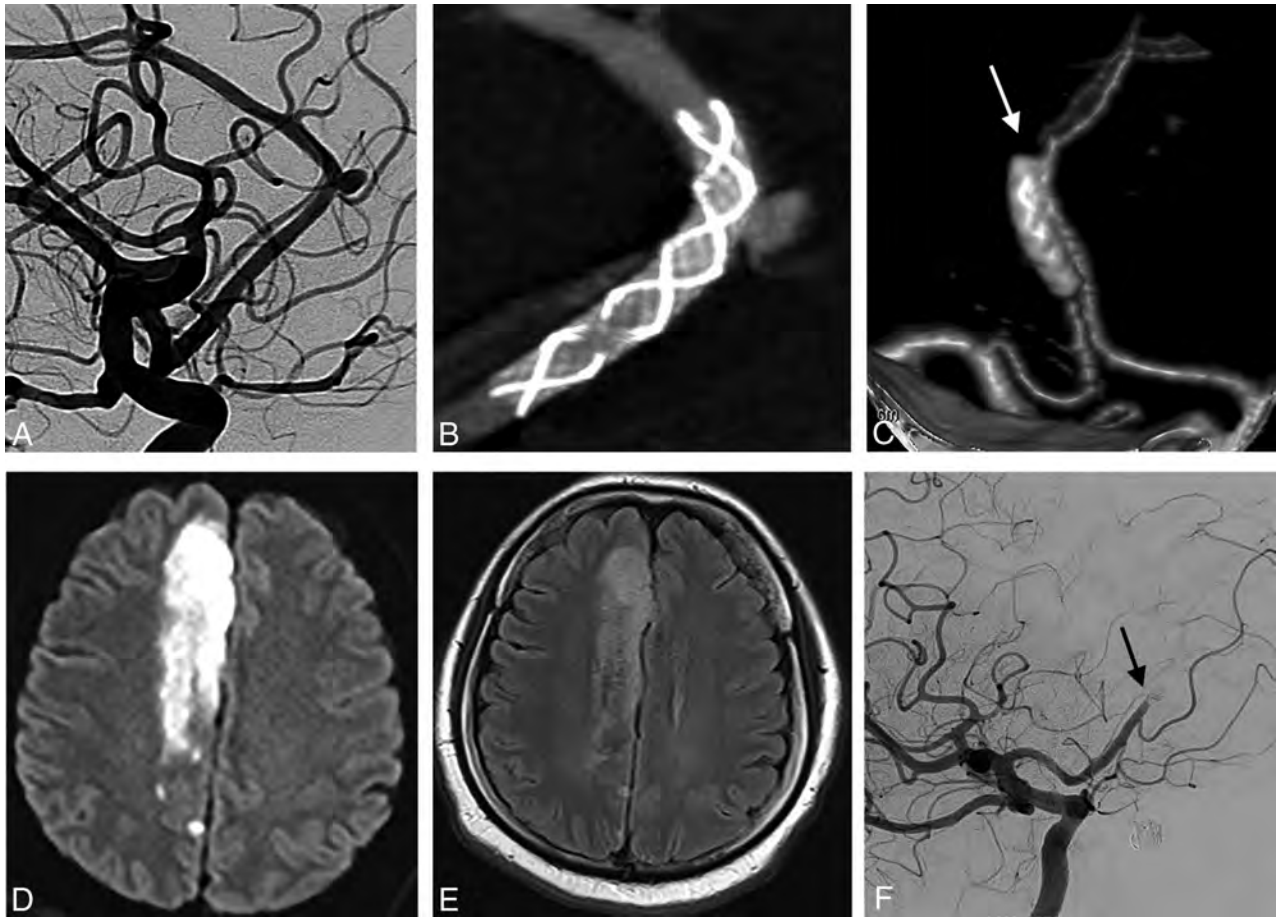

FIG 2. *A*, Patient 11 with a right 3 × 3 mm aneurysm originating from the callosomarginal bifurcation. *B*, Flat panel CT scan confirms correct vessel wall apposition of a single Silk (2 × 15 mm) stent. Ten days after treatment, due to inadvertent discontinuation of the dual-antiplatelet therapy, the patient was admitted to the emergency department with severe left hemiparesis (*C*). An urgent brain CT angiography shows occlusion of the right A2 distal to the stent (*white arrow*). *D*, Diffusion-weighted MR imaging detects an acute ischemic lesion on the territory of the right pericallosal artery. *E*, Because of the FLAIR positive for lesions (the patient arrived at the hospital 20 hours after the onset of the symptoms), no acute medical and endovascular treatments were performed. *F*, DSA was performed to confirm the complete stent occlusion (*black arrow*). The patient was discharged with severe left hemiparesis (mRS 4) and dual-antiplatelet therapy.

cases of arterial narrowing or flow changes of covered branches. Asymptomatic branch narrowing was observed in 3 patients during angiographic follow-up (20%). No cases of branch occlusion were diagnosed.

DISCUSSION

Our study demonstrates that flow-diversion treatment of small distal ACA aneurysms is effective with rates of complete and near-complete occlusion close to 81%. Flow diversion plus coiling, in retreatment of lesions previously coiled, allowed higher rates of occlusion (100%) compared with flow diverters alone (70%). Aneurysms arising from the distal ACA often presented with a wide-neck configuration that may necessitate double microcatheterization for stent-assisted coiling or balloon remodeling. However, dual-microcatheter manipulation in small arteries is challenging and can predispose the patient to increased risk of complications.[8] In our experience, the procedure was successful in all cases and appears to be a straightforward treatment option for lesions difficult to treat with conventional endovascular strategy. However, patients should be carefully selected due to the not negligible rate of perioperative ischemic events, with 13% permanent neurologic complications.

Angiographic Outcome

To the best of our knowledge, our study is the largest to date that specifically focused on the flow-diversion treatment of distal ACA aneurysms. Regarding the occlusion rates, our results are in line with those reported in previous studies that focused on distal aneurysm location. De Macedo Rodrigues et al[8] reported 70% complete occlusion of pericallosal aneurysms treated with PED devices. Similarly, other series reported rates of distal ACA aneurysm occlusion between 60% and 100% after flow-diverter stent deployment (On-line Table 3).[6-15] The flow redirection that allows aneurysm thrombosis and neck endothelization is in relation to local stent porosity that is influenced by stent sizing. Undersized stents are associated with a shorter deployment, more condensed pores, and higher mesh density, resulting in an increased flow-diversion effect.[17,18] In our series, the mean diameters of the proximal and distal portions of the parent artery were approximately 1.8 and 1.6 mm, respectively. The diameter of the devices used ranged between 2 and 2.75 mm (On-line Table 2), resulting in stent oversizing, subsequent device elongation, and relative reduction of metal stent coverage. Despite the theoretic reduction of the flow diversion, the effect of the stent was enough to allow high rates of aneurysm occlusion. However, a subgroup of analysis

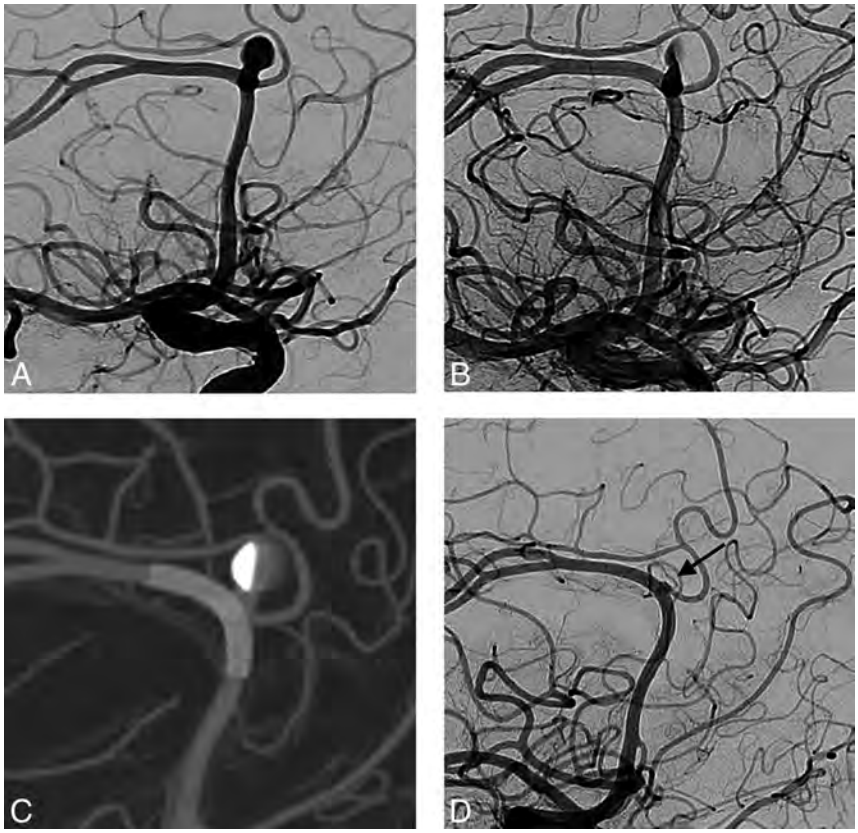

FIG 3. *A*, Patient 4 with a small left A2/A3 aneurysm located at the callosomarginal artery bifurcation. After an attempted coil embolization, due to the instability of the microcatheter inside the aneurysm (related to the tortuosity of the aortic arch and the cervical ICA), the aneurysm was treated with a flow-diverter stent. *B*, Flow stagnation immediately after deployment of a single PED (2.5 × 14 mm). *C*, Postintervention flat panel CT reconstruction shows adequate aneurysm neck coverage and proper vessel wall apposition. *D*, Twelve-month DSA follow-up shows complete occlusion of the aneurysm (*black arrow*).

showed that flow diversion plus coiling that was used for retreatment of lesions previously coiled allowed higher rates of occlusion (100%) compared with flow diverters alone (70%). This finding is in accordance with those of previous series comparing flow diverters alone versus flow diverter plus coiling.

Lin et al[19] reported higher rates of complete aneurysm occlusion among the group of aneurysms treated with PED plus coils, compared with those treated with flow diverters alone (93.1% versus 74.7%, $P = .03$). Accordingly, one of the shortcomings of this technique when the retreatment is required is the necessity of a second overlapped flow diverter with a higher risk of ischemic events, considering the small diameter of the parent artery. However, we found that the mean radiologic follow-up among the group of aneurysms showing adequate occlusion (OKM C2–D) was significantly higher compared with the group with incomplete occlusion (OKM B) (13.5 versus 7 months, $P = .014$) and showed that the length of follow-up can influence the aneurysm occlusion rate.

Although flow diversion allows a high rate of angiographic success, there are important concerns regarding possible occlusion of covered side branches. Theoretically, the pressure gradient across the jailed branch is reduced, and the artery can be occluded if the flow competition from the collateral circulation is well-represented.[20] Few studies focused on the flow remodeling of distal branches covered with flow-diverter stents. A recent meta-analysis of middle cerebral artery aneurysms treated with flow diversion showed 10% occlusion of covered MCA branches and 25% arterial narrowing or slow flow.[21] When we investigated the literature, the rate of flow modification of covered branches coming from the distal ACA ranges between 20% and 40%, with the absence of related symptoms.[6-15] Nossek et al[12] reported 1 asymptomatic (20%) A2 branch occlusion after treatment with 2 overlapping PEDs. Similarly, De Macedo Rodrigues et al[8] reported 40% asymptomatic narrowing of jailed callosomarginal arteries during follow-up (On-line Table 3). Our series confirmed the high rate of flow modification in jailed branches originating from the distal ACA. We found 20% asymptomatic arterial narrowing after treatment with a single flow-diverter stent (2 callosomarginal arteries and 1 frontopolar artery), whereas no cases of occlusion were detected.

Treatment-Related Complications

When we investigated the literature, the overall incidence of complications in series reporting distal aneurysms treated with flow-diverter stents ranged between 15% and 20%, with approximately 10% permanent neurologic deficits.[9,10,21,22] In a recent series of 42 patients treated with FRED devices deployed in small and distal vessels (2–3 mm), the overall rate of ischemic complications was close to 11% and the incidence of ischemic events among patients with distal ACA was nearly 10%.[11] However, in other recent studies of distal ACA aneurysms treated with the PED, the authors reported no complications related to the procedure.[6-10,12,13] In our experience, we had 6% (patient 5) transient complication, and 13% permanent complications (patients 11 and 13), and all were related to ischemic events in the perioperative period. One patient experienced ischemic events consequent to an insufficient platelet inhibition level (patient 5), and the other one, due to nonadherence with the antiplatelet therapy (patient 11). Accordingly, these findings underline the close relationship among ischemic injury, in-stent thrombosis, and antiplatelet function in the flow-diversion treatment of aneurysms located in small and distal vessels.

Complication rates for endovascular treatment of distal ACA aneurysms also remain a concern for the coiling, stent-assisted coiling, and balloon-remodeling techniques. Sturiale et al[23] reported 20% complications related to the treatment of 20 distal ACA aneurysms with coiling and stent-assisted coiling. In addition, when we reviewed the literature, the endovascular perioperative complications rate was close to 12%, with a procedure-re-

lated morbidity of 8%.[23] In a recent meta-analysis, neurologic morbidity and mortality rates were 15% and 9% after an operation, and 14% and 7% after endovascular treatment of distal ACA aneurysms.[24]

Recently, flow diversion with low-profile braided stents, as stent monotherapy, has been reported as an alternative option for the treatment of small and distally located intracranial aneurysms not amenable to conventional endovascular techniques. Aydin et al[25] described a series of 20 distal aneurysms treated with LEO Baby devices (LEO+Baby; Balt Extrusion) that were used as mini flow-diversion stents, reporting 73% total occlusion and 5% treatment-related complications.

Limitations of the Study

Our study has limitations intrinsic to single-center series, and it is not a population-based study. The number of patients was relatively small, though larger than other reported case series. The data, although prospectively collected, were analyzed retrospectively. In addition, the imaging outcome was assessed by operators and not independently. There was a lack of standardization of radiologic follow-up.

CONCLUSIONS

Treatment of distal anterior cerebral artery aneurysms with flow-diverter stents is effective, allowing high rates of aneurysm occlusion. Flow diversion plus coiling in the retreatment of lesions previously coiled allowed higher rates of occlusion, compared with flow diverters alone. In addition, the strategy appears straightforward and technically feasible. However, the risk of ischemic complications is not negligible, and flow-diversion treatment should be evaluated only for aneurysms not amenable to simple coil embolization.

ACKNOWLEDGMENTS

We thank Professor Beth De Felici for the English revision.

Disclosures: Federico Cagnazzo—*UNRELATED*: *Employment*: University of Florence.* Pierre-Henri Lefevre—*UNRELATED*: *Consultancy*: Medtronic, Stryker. Alain Bonafe—*UNRELATED*: *Consultancy*: Stryker, Medtronic, MicroVention. Vincent Costalat—*UNRELATED*: *Consultancy*: Stryker, Medtronic; *Grants/Grants Pending*: Stryker, Medtronic*; *Payment for Development of Educational Presentations:* Medtronic, Stryker, Balt Extrusion. *Money paid to the institution.

REFERENCES

1. Hernesniemi J, Tapaninaho A, Vapalahti M, et al. **Saccular aneurysms of the distal anterior cerebral artery and its branches.** *Neurosurgery* 1992;31:994–98; discussion 998–99 CrossRef Medline
2. Perlmutter D, Rhoton AL Jr. **Microsurgical anatomy of the distal anterior cerebral artery.** *J Neurosurg* 1978;49:204–28 CrossRef Medline
3. Waldenberger P, Petersen J, Chemelli A, et al. **Endovascular therapy of distal anterior cerebral artery aneurysms-an effective treatment option.** *Surg Neurol* 2008;70:368–77 CrossRef Medline
4. Cavalcanti DD, Abla AA, Martirosyan NL, et al. **Endovascular management of distal ACA aneurysms: single-institution clinical experience in 22 consecutive patients and literature review.** *AJNR Am J Neuroradiol* 2013;34:1593–99 CrossRef Medline
5. Hui FK, Schuette AJ, Moskowitz SI, et al. **Microsurgical and endovascular management of pericallosal aneurysms.** *J Neurointerv Surg* 2011;3:319–23 CrossRef Medline
6. Clarençon F, Di Maria F, Gabrieli J, et al. **Flow diverter stents for the treatment of anterior cerebral artery aneurysms: safety and effectiveness.** *Clin Neuroradiol* 2017;27:51–56 CrossRef Medline
7. Dabus G, Grossberg JA, Cawley CM, et al. **Treatment of complex anterior cerebral artery aneurysms with Pipeline flow diversion: mid-term results.** *J Neurointerv Surg* 2017;9:147–51 CrossRef Medline
8. De Macedo Rodrigues K, Kühn AL, Tamura T, et al. **Pipeline embolization device for pericallosal artery aneurysms: a retrospective single center safety and efficacy study.** *Oper Neurosurg (Hagerstown)* 2018;14:351–58 CrossRef Medline
9. Lin N, Lanzino G, Lopes DK, et al. **Treatment of distal anterior circulation aneurysms with the Pipeline embolization device: a US multicenter experience.** *Neurosurgery* 2016;79:14–22 CrossRef Medline
10. Martínez-Galdámez M, Romance A, Vega P, et al. **Pipeline endovascular device for the treatment of intracranial aneurysms at the level of the circle of Willis and beyond: multicenter experience.** *J Neurointerv Surg* 2015;7:816–23 CrossRef Medline
11. Möhlenbruch MA, Kizilkilic O, Killer-Oberpfalzer M, et al. **Multicenter experience with FRED Jr flow re-direction endoluminal device for intracranial aneurysms in small arteries.** *AJNR Am J Neuroradiol* 2017;38:1959–65 CrossRef Medline
12. Nossek E, Zumofen DW, Setton A, et al. **Treatment of distal anterior cerebral artery aneurysms with the Pipeline embolization device.** *J Clin Neurosci* 2017;35:133–38 CrossRef Medline
13. Pistocchi S, Blanc R, Bartolini B, et al. **Flow diverters at and beyond the level of the circle of Willis for the treatment of intracranial aneurysms.** *Stroke* 2012;43:1032–38 CrossRef Medline
14. Puri AS, Massari F, Asai T, et al. **Safety, efficacy, and short-term follow-up of the use of Pipeline embolization device in small (<2.5 mm) cerebral vessels for aneurysm treatment: single institution experience.** *Neuroradiology* 2016;58:267–75 CrossRef Medline
15. Vachhani JA, Nickele CM, Elijovich L, et al. **Flow diversion for treatment of growing A2 aneurysm in a child: case report and review of flow diversion for intracranial aneurysms in pediatric patients.** *World Neurosurg* 2016;96:607.e613–607.e617 CrossRef Medline
16. O'Kelly CJ, Krings T, Fiorella D, et al. **A novel grading scale for the angiographic assessment of intracranial aneurysms treated using flow diverting stents.** *Interv Neuroradiol* 2010;16:133–37 CrossRef Medline
17. Shapiro M, Raz E, Becske T, et al. **Variable porosity of the Pipeline embolization device in straight and curved vessels: a guide for optimal deployment strategy.** *AJNR Am J Neuroradiol* 2014;35:727–33 CrossRef Medline
18. Berg P, Iosif C, Ponsonnard S, et al. **Endothelialization of over- and undersized flow-diverter stents at covered vessel side branches: an in vivo and in silico study.** *J Biomech* 2016;49:4–12 CrossRef Medline
19. Lin N, Brouillard AM, Krishna C, et al. **Use of coils in conjunction with the Pipeline embolization device for treatment of intracranial aneurysms.** *Neurosurgery* 2015;76:142–49 CrossRef Medline
20. Saleme S, Iosif C, Ponomarjova S, et al. **Flow-diverting stents for intracranial bifurcation aneurysm treatment.** *Neurosurgery* 2014; 75:623–31; quiz 631 CrossRef Medline
21. Cagnazzo F, Mantilla D, Lefevre PH, et al. **Treatment of middle cerebral artery aneurysms with flow-diverter stents: a systematic review and meta-analysis.** *AJNR Am J Neuroradiol* 2017;38:2289–94 CrossRef Medline
22. Gawlitza M, Januel AC, Tall P, et al. **Flow diversion treatment of complex bifurcation aneurysms beyond the circle of Willis: a single-center series with special emphasis on covered cortical branches and perforating arteries.** *J Neurointerv Surg* 2016;8:481–87 CrossRef Medline

23. Sturiale CL, Brinjikji W, Murad MH, et al. **Endovascular treatment of distal anterior cerebral artery aneurysms: single-center experience and a systematic review.** *AJNR Am J Neuroradiol* 2013;34: 2317–20 CrossRef Medline
24. Petr O, Coufalová L, Bradáč O, et al. **Safety and efficacy of surgical and endovascular treatment for distal anterior cerebral artery aneurysms: a systematic review and meta-analysis.** *World Neurosurg* 2017;100:557–66 CrossRef Medline
25. Aydin K, Barburoglu M, Sencer S, et al. **Flow diversion with low-profile braided stents for the treatment of very small or uncoilable intracranial aneurysms at or distal to the Circle of Willis.** *AJNR Am J Neuroradiol* 2017;38:2131–37 CrossRef Medline

Surpass Streamline Flow-Diverter Embolization Device for Treatment of Iatrogenic and Traumatic Internal Carotid Artery Injuries

M. Ghorbani, H. Shojaei, K. Bavand, and M. Azar

ABSTRACT

SUMMARY: Iatrogenic and traumatic cerebral internal carotid artery injuries are uncommon but potentially lethal complications. Direct surgical repair of ICA injuries may be difficult in an acute setting. However, endovascular treatment with a flow-diverter embolization device is a feasible alternative technique that we experienced. In this clinical report, we describe demographic data, radiographic images, lesion characteristics, endovascular procedure notes, postprocedural hospital course, and follow-up digital subtraction angiography of 5 patients. At least 6-month follow-up was available in all patients without occurrence of rebleeding and other complications.

ABBREVIATIONS: FDD = flow-diverter embolization device; FESS = functional endoscopic sinus surgery

Iatrogenic and traumatic cerebral internal carotid artery injuries are uncommon but potentially lethal complications. Immediate diagnosis and management of these injuries may be lifesaving. The iatrogenic vascular injuries were categorized according to each diagnostic or therapeutic procedure responsible for the injury such as transsphenoidal surgery, functional endoscopic sinus surgery (FESS), skull base surgery, tumor surgery, central venous catheterization, and the others.[1] Traumatic vascular injuries can occur due to any penetrating or blunt trauma to the craniocervical region during gunshot, impulsion, and road traffic injuries.

Iatrogenic ICA injury during transsphenoidal surgery is a rare complication occurring in approximately in 0.20–1% of cases.[2] The presentation of this potentially fatal complication includes severe perioperative or postoperative bleeding, a false aneurysm of the ICA, or a carotid cavernous fistula.[3]

Traditionally, surgical ligation or endovascular occlusion of the ICA has been used to treat ICA injuries; however, surgical ligation is associated with a high incidence of major complications.[4] Lately, stent grafts have become a more usable option for the treatment of ICA injuries. Their complications are rare but include dissection, distal embolus, perforation, and occlusion. The low flexibility of stent-graft devices is another problem of deployment in vascular bends and curvature.

The Surpass Streamline flow-diverter device (FDD) (Stryker Neurovascular, Fremont, California) is part of a new generation of endoluminal devices for treating large or giant wide-neck aneurysms. The stent is a self-expanding tubular mesh made of cobalt-chromium with 30% metal coverage. In a series published by De Vries et al,[5] the investigators used Surpass to treat 37 patients, with an occlusion rate of 94% at nonbifurcation sites and 50% at bifurcation locations. One patient had a stroke following treatment, and no mortality was reported.

In this article, we present our experience with the management of iatrogenic and traumatic ICA injuries and their outcomes after endovascular treatment with Surpass Streamline FDD placement.

Case Series

A retrospective study was conducted, and all patients with an ICA injury related to iatrogenic or traumatic causes who underwent endovascular treatment with the Surpass Streamline FDD in our institution (Firoozgar Hospital) were included from 2015 to 2017. Patient demographic data, clinical charts, indications for treatment, radiographic images, lesion characteristics, operative notes, endovascular procedural notes, postprocedural hospital course, and follow-up DSAs were reviewed.

The etiologies of the ICA injuries were as follows: transsphenoidal surgery ($n = 2$), FESS ($n = 1$), car collision ($n = 1$), and gunshot ($n = 1$). Patient information, mechanism of injury, angiographic findings, treatment, and outcome are summarized in the Table.

Procedure Note. Informed consent was obtained from the pa-

Received October 25, 2017; accepted after revision January 31, 2018.

From the Division of Vascular and Endovascular Neurosurgery (M.G., H.S., K.B.), Firoozgar Hospital, Iran University of Medical Sciences, Tehran, Iran; and Department of Neurosurgery (M.A.), School of Medicine, Rasoul-e-Akram Hospital, Iran University of Medical Sciences, Tehran, Iran.

Please address correspondence to Hamidreza Shojaei, MD, Department of Neurosurgery, Firoozgar Hospital, Iran University of Medical Sciences, Hemmat Highway, Tehran, Iran; e-mail: shojaei.hamidreza@mail.com; @mohghorbany

http://dx.doi.org/10.3174/ajnr.A5607

Demographic data and clinical and angiographic findings of patients with ICA injury

Case No.	Sex	Age (yr)	Cause of Injury	Location	Treatment	GCS Score at Discharge	Outcome
1	Male	21	Gunshot	Paraclival ICA	Surpass FDD	15	Good
2	Female	40	TSS	Paraclival ICA	Surpass FDD	15	Good
3	Male	52	FESS	Cavernous ICA	Surpass FDD	15	Good
4	Male	20	Car collision	Cavernous ICA	Surpass FDD	15	Good
5	Female	39	TSS	Paraclival ICA	Surpass FDD	15	Good

Note:—GCS indicates Glasgow Coma Scale; TSS, transsphenoidal surgery.

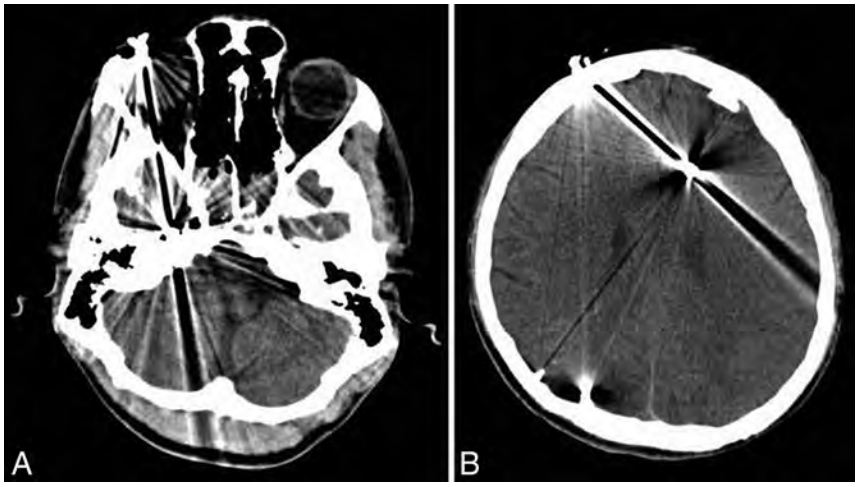

FIG 1. Axial spiral brain CT scans.

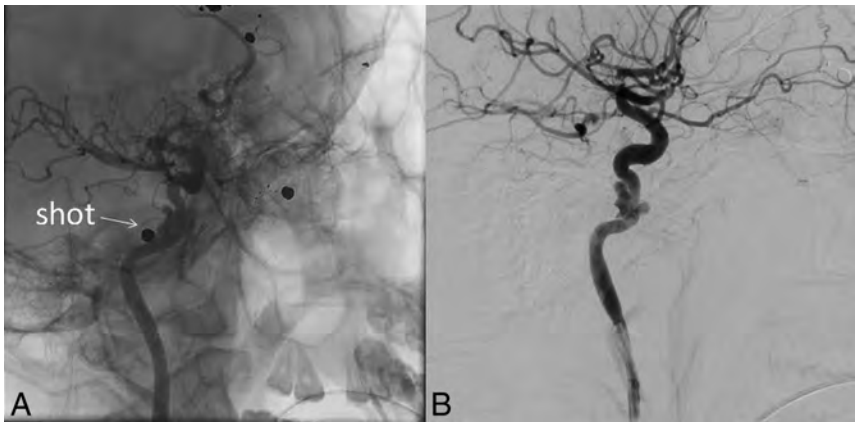

FIG 2. Lateral view of right ICA selective angiography.

tients or legal representative for the use of the Surpass Streamline FDD, including its off-label use. All procedures were performed with the patient under general anesthesia and in the angiographic suite. In iatrogenic ICA injuries, the operative site was packed before transfer to the angiographic suite to maintain homeostasis.

First, through a right-sided femoral access, selective DSA identified or confirmed the site of extravasations and ICA injuries. In 2 patients, the area of extravasation was the cavernous segment, and in 3 patients, it was the paraclival segment of the ICA.

For endovascular treatment, the existing sheath was exchanged for a 90-cm-long sheath with a 260-cm guiding wire, and then a 6F Envoy (Codman & Shurtleff, Raynham, Massachusetts) guiding catheter was introduced to the right or left ICA by a 0.035-inch hydrophilic guiding wire. The Surpass embolization device was passed over a 0.014-inch microwire and was placed across the extravasated area. Devices were deployed slowly and precisely without complications, and control DSA revealed good position of devices.

After FDD positioning and just before deployment, heparin was administered with an initial IV bolus of 60–70 IU/kg (maximum, 5000 U), followed by an IV infusion of 12–15 IU/kg/h (maximum, 1000 U/h). Then the FDD was deployed, and it covered the site of injury. After deployment, all patients received 650 mg (2 × 325 mg) of aspirin and 600 mg (4 × 75 mg) of clopidogrel as loading doses through an orogastric tube and continued with 75 mg of clopidogrel and 325 mg of aspirin daily. Systemic heparin infusion was maintained for 48 hours. Dual-antiplatelet therapy (aspirin, 325 mg, and clopidogrel, 75 mg daily) was continued for 6 months in all patients. At follow-up visits, neurologic examinations were performed, and follow-up DSA was performed for all patients after 6 months and confirmed the patency of the stents.

On the third day after discontinuation of heparin, the nasal tampon was removed in the operating room by an endoscope with the patient under general anesthesia.

Case 1. A 21-year-old man was shot and admitted to another hospital about 20 days prior. He underwent an operation to treat intracerebral hemorrhage and then was referred to our institution for more diagnostic and therapeutic interventions. His Glasgow Coma Scale score at this time was 15. His blood pressure and heart rate were stable. On neurologic examination, he had hemiparesis of the left-sided limbs. Noncontrast head CT revealed multiple shots in the cranial and cervical regions (Fig 1). Selective DSA revealed a vascular injury and dissecting aneurysm due to the gun injury in the paraclival segment of right ICA (Fig 2).

At this time, we decided to manage this injury with an endovascular technique. With the patient under general anesthesia, a Surpass Streamline FDD (4.0 × 20 mm) was deployed covering the site of injury, with heparin and dual-antiplatelet administration as mentioned before. Follow-up DSA was performed after

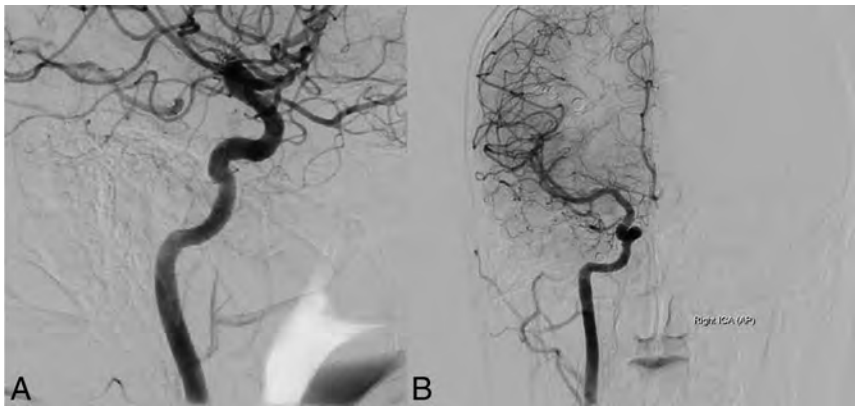

FIG 3. Posttreatment DSA. *A*, Lateral view of the right ICA, *B*, Anteroposterior view of the right ICA.

FIG 4. *A*, Anteroposterior view of left ICA selective angiography. *B*, Posttreatment anteroposterior view of left ICA angiography.

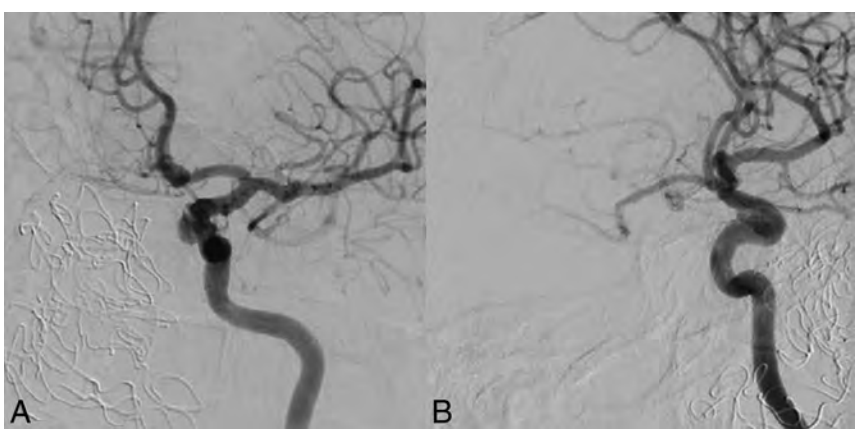

FIG 5. *A*, Lateral view of left ICA selective angiography. *B*, Oblique view of left ICA angiography.

6 months and confirmed the patency of the stent with complete recovery of the dissecting aneurysm (Fig 3).

Case 2. A 40-year-old female patient had massive arterial bleeding during an endoscopic transsphenoidal operation to treat clival chondrosarcoma. The site was packed and the patient was transferred to the angiographic suite under general anesthesia. Selective DSA via right femoral access showed a small iatrogenic injury at the medial wall of the paraclival segment of the left ICA with pseudoaneurysm formation (Fig 4*A*). A Surpass Streamline FDD (4.0 × 20 mm) was deployed covering the site of injury, with heparin and dual-antiplatelet administration as mentioned before. Follow-up DSA was performed after 6 months, confirming the patency of the stent with complete recovery of the injury (Fig 4*B*).

Case 3. A 52-year-old man underwent functional endoscopic sinus surgery for a nasal polyp at another hospital and then was referred to our institution with massive epistaxis occurring after 2 days. Selective DSA detected an iatrogenic left ICA laceration at the cavernous segment (Fig 5). A Surpass Streamline FDD (4.0 × 20 mm) was deployed covering the site of injury, with heparin and dual-antiplatelet administration as mentioned before. After 6 months, follow-up DSA was performed and revealed patency of the stent with complete recovery of the injury (Fig 6).

Case 4. A 20-year-old man with a history of a car collision about 1 month before was admitted to another hospital with intermittent epistaxis; an endoscopic nasal examination was performed in the operating room. Then, the patient was referred to our institution with suspicion of an ICA injury. Selective DSA revealed a traumatic pseudoaneurysm formation at the cavernous segment of the left ICA (Fig 7*A*). Treatment with a Surpass Streamline FDD (4.0 × 30 mm) deployment and heparin and dual-antiplatelet administration was performed successfully. After 6 months, follow-up DSA showed a good position of the device without any other complications (Fig 7*B*).

Case 5. A 39-year-old woman with a pituitary lesion suspicious for craniopharyngioma was admitted to our hospital for an operation. During endoscopic transsphenoidal surgery, massive arterial bleeding occurred and was packed, and the patient was transferred immediately to the angiographic suite under general anesthesia. Selective DSA showed a small iatrogenic injury at the paraclival segment of the left ICA with carotid cavernous fistula formation on the same side (Fig 8*A*). A Surpass Streamline FDD (4.0 × 20 mm) was deployed covering the site of injury, with heparin and dual-antiplatelet administration as mentioned before. After 6 months, follow-up DSA was performed and revealed patency of the stent with complete recovery of the injury (Fig 8*B*).

FIG 6. Posttreatment DSA. *A*, Lateral view of the left ICA. *B*, Anteroposterior view of the left ICA.

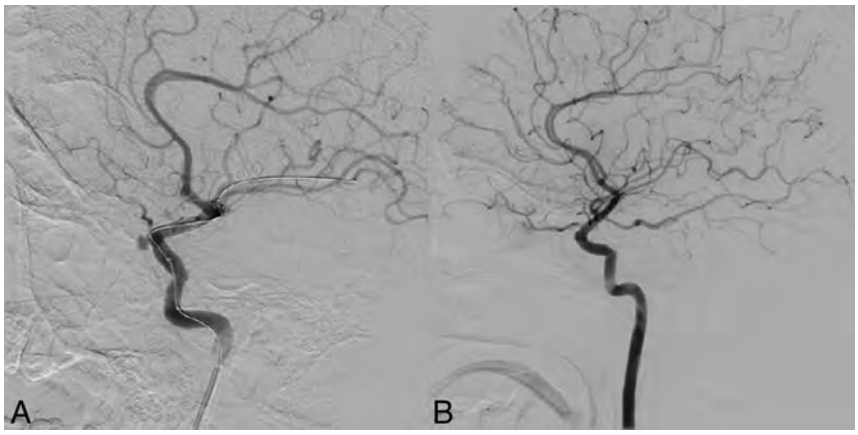

FIG 7. *A*, Lateral view of left ICA angiography during catheterization. *B*, Posttreatment DSA of the left ICA.

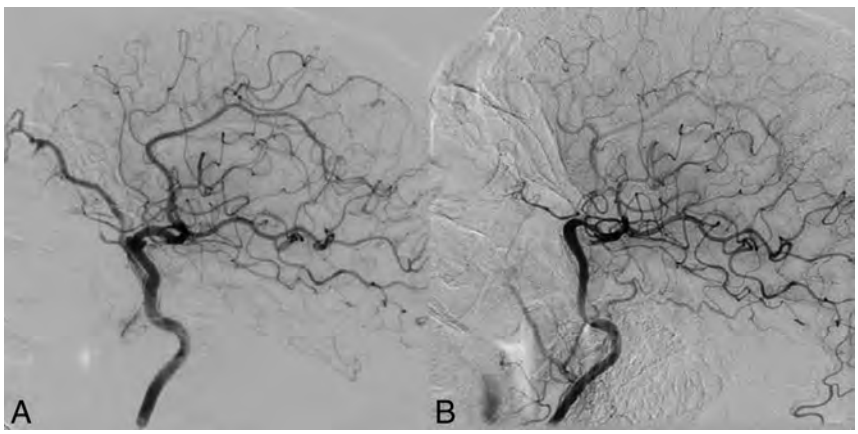

FIG 8. *A*, Lateral view of left ICA selective angiography. *B*, Posttreatment lateral view of left ICA angiography.

DISCUSSION

Iatrogenic and traumatic ICA injuries are rare complications but have high morbidity and mortality rates. ICA injuries during transsphenoidal surgery can have dire outcomes if they are not managed in a definitive and timely manner.[6] Carotid stenosis, occlusion, false aneurysms, and carotid cavernous fistulas have all been reported as angiographic manifestations of postsurgical vascular trauma.[7]

In 2018, Aydin et al[1] studied 21 patients who underwent endovascular embolization for iatrogenic vascular injury in the craniocervical region and concluded that endovascular management of such cases was a good option, with low mortality and morbidity rates. Endovascular management of these vascular injuries included parent artery occlusion ($n = 15$), aneurysm occlusion ($n = 3$), covered stent ($n = 1$), and conservative management ($n = 2$).[1] Kocer et al[8] revealed the possibility of using an endovascular stent graft for the treatment of iatrogenic ICA lacerations. In their cases, the use of stent grafts proved expedient, safe, and effective in the emergency treatment of a massive hemorrhage resulting from ICA injury that occurred during transsphenoidal surgery.

Endovascular treatment with covered stents has, for some time, been successfully used to treat subclavian and axillary arterial injuries.[9] Covered stent placement has also been reported as an option for iatrogenic ICA injuries during transsphenoidal surgery in patients who cannot tolerate ICA occlusion.[10] Morken et al[11] presented a patient with a meningioma who, during transsphenoidal resection, had a laceration of the ICA, which underwent endovascular treatment with a covered stent graft. However, in 1 case, iatrogenic vascular injury at the paraclival segment of the right ICA permitted deployment of a rigid stent graft at that straight segment, but in our opinion, stent graft deployment is not possible in curvilinear segments like the siphon of the ICA due to rigidity of this type of stent.

In 2015, Lancu et al[12] reported 1 case of iatrogenic ICA injury with a secondary carotid cavernous fistula after transsphenoidal surgery that was treated with a Silk flow-diverter stent (Balt Extrusion, Montmorency, France) placed within the injured internal carotid artery and coils placed within the cavernous sinus.

Wakhloo et al[13] and Colby et al[14] recently showed, in 2 case series, that Surpass is a new-generation flow diverter with unique device-specific and delivery-specific features, compared with clinically available endoluminal flow diverters, and has safety and efficacy in the treatment of intracranial aneurysms comparable with that of stent-assisted coil embolization.

Ogilvy et al[15] reported 3 patients with direct traumatic carotid

cavernous fistulas who were treated with either coils, coils and Onyx (Covidien, Irvine, California), or a detachable balloon followed by placement of a flow-diverting stent for endoluminal reconstruction, and all 3 patients recovered clinically. They concluded that a flow diverter may facilitate endothelialization of the injury to the internal carotid artery.

Our cases were 5 patients who had an iatrogenic or traumatic ICA injury, all treated with a Surpass Streamline FDD successfully and showing good outcome on follow-up without complications. All patients had small carotid defects, and 2 defects were in the cavernous segment of the ICA, including a curve in the artery. The FDD is made of a cobalt-chromium alloy with a low porosity (metal surface area coverage, 30%), a high mesh density (20–32 pores/mm^2), and a self-expanding, single-layer braided, tubular structure. The device comes in various diameters, ≤5.3 mm, and lengths, ≤50 mm. The 2-mm device has 48 wires; the 3- and 4-mm devices have 72 wires; and the 5-mm device has 96 wires, to provide a constant high mesh density over various diameters of the device, as supported by previous in vitro[16] and in vivo studies.[17]

All our patients had small carotid defects due to iatrogenic or traumatic injury. None of them could tolerate angiographically or clinically the balloon occlusion test, and patency of the ICA was important.

Multiple series of treatment of intracranial blister aneurysms by FDDs had high success and low complication rates in other centers.[18-20] We also had a successful experience with 18 patients with blister aneurysms treated by a different type of FDD. Small iatrogenic and traumatic defects of the wall of the ICA are comparable with blister aneurysms pathologically. Therefore, we considered the same strategy for our patients because there was no other proved safe treatment technique.

The Surpass Streamline FDD has been available since 2015 in our center and was chosen due to its higher mesh density, greater stability during deployment, and faster positioning in curved and nontortuous anatomy compared with other FDDs.

FDDs alone for the treatment of ICA iatrogenic and traumatic small injuries have not been reported before, to our knowledge. Due to the rarity of this complication, there is no other safe treatment, and the total number of patients studied is small, but all of them showed complete resolution of complications and good outcomes, which can be a basis for future studies.

REFERENCES

1. Aydin E, Gok M, Esenkaya A, et al. **Endovascular management of iatrogenic vascular injury in the craniocervical region.** *Turk Neurosurg* 2018;28:72–78 CrossRef Medline
2. Ciric I, Ragin A, Baumgartner C, et al. **Complications of transsphenoidal surgery: result of a national survey, review of the literature, and personal experience.** *Neurosurgery* 1997;40:225–36; discussion 236–37 CrossRef Medline
3. Raymond J, Hardy J, Czepko R, et al. **Arterial injuries in transsphenoidal surgery for pituitary adenoma; the role of angiography and endovascular treatment.** *AJNR Am J Neuroradiol* 1997;18:655–65 Medline
4. Chaloupka JC, Putman CM, Citardi MJ, et al. **Endovascular therapy for the carotid blowout syndrome in head and neck surgical patients: diagnostic and managerial considerations.** *AJNR Am J Neuroradiol* 1996;17:843–52 Medline
5. De Vries J, Boogaarts J, Van Norden A, et al. **New generation of flow diverter (Surpass) for unruptured intracranial aneurysms: a prospective single-center study in 37 patients.** *Stroke* 2013;44:1567–77 CrossRef Medline
6. Griauzde J, Gemmete JJ, Pandey AS, et al. **Emergency reconstructive endovascular management of intraoperative complications involving the internal carotid artery from trans-sphenoidal surgery.** *J Neurointervent Surg* 2015;7:67–71 CrossRef Medline
7. Pigott TJ, Holland IM, Punt JA. **Carotico-cavernous fistula after trans-sphenoidal hypophysectomy.** *Br J Neurosurg* 1989;3:613–16 CrossRef Medline
8. Kocer N, Kizilkilic O, Albayram S, et al. **Treatment of iatrogenic internal carotid artery laceration and carotid-cavernous fistula with endovascular stent graft placement.** *AJNR Am J Neuroradiol* 2002;23:442–46 Medline
9. White R, Krajcer Z, Johanson M, et al. **Results of a multicenter trial for the treatment of traumatic vascular injury with a covered stent.** *J Trauma* 2006;60:1189–95; discussion 1195–96 CrossRef Medline
10. Cockroft KM, Carew JF, Trost D, et al. **Delayed epistaxis resulting from external carotid artery injury requiring embolization: a rare complication of transsphenoidal surgery—case report.** *Neurosurgery* 2000;47:236–39 Medline
11. Morken MH, Cappelen J, Kvistad KA, et al. **Acute endovascular repair of iatrogenic right internal carotid arterial laceration.** *Acta Radiol Short Rep* 2013;2:2047981613496088 CrossRef Medline
12. Lancu D, Lum C, Ahmed ME, et al. **Flow diversion in the treatment of carotid injury and carotid-cavernous fistula after transsphenoidal surgery.** *Interv Neuroradiol* 2015;21:346–50 CrossRef Medline
13. Wakhloo AK, Lylyk P, de Vries J, et al; Surpass Study Group. **Surpass flow diverter in the treatment of intracranial aneurysms: a prospective multicenter study.** *AJNR Am J Neuroradiol* 2015;36:98–107 CrossRef Medline
14. Colby GP, Lin L, Caplan JM, et al. **Flow diversion of large internal carotid artery aneurysms with the Surpass device: impressions and technical nuance from the initial North American experience**. *J Neurointerv Surg* 2016;8:279–86 CrossRef Medline
15. Ogilvy CS, Motiei-Langroudi R, Ghorbani M, et al. **Flow diverter as useful adjunct to traditional endovascular techniques in treatment of direct carotid-cavernous fistulas.** *World Neurosurg* 2017;105:812–17 CrossRef Medline
16. Seong J, Wakhloo AK, Lieber BB. **In vitro evaluation of flow diverters in an elastase-induced saccular aneurysm model in rabbit.** *J Biomech Eng* 2007;129:863–72 CrossRef Medline
17. Sadasivan C, Cesar L, Seong J, et al. **An original flow diversion device for the treatment of intracranial aneurysms: evaluation in the rabbit elastase-induced model.** *Stroke* 2009;40:952–58 CrossRef Medline
18. Chalouhi N, Zanaty M, Tjoumakaris S, et al. **Treatment of blister-like aneurysms with the Pipeline Embolization Device.** *Neurosurgery* 2014;74:527–32 CrossRef Medline
19. Rouchaud A, Brinjikji W, Cloft HJ, et al. **Endovascular treatment of ruptured blister-like aneurysms: a systematic review and meta-analysis with focus on deconstructive versus reconstructive and flow-diverter treatments.** *AJNR Am J Neuroradiol* 2015;36:2331–39 CrossRef Medline
20. Peitz GW, Sy CA, Grandhi R. **Endovascular treatment of blister aneurysms.** *J Neurosurg Focus* 2017;42:E12 CrossRef Medline

Comparison of 3T Intracranial Vessel Wall MRI Sequences

A. Lindenholz, A.A. Harteveld, J.J.M. Zwanenburg, J.C.W. Siero, and J. Hendrikse

ABSTRACT

BACKGROUND AND PURPOSE: Intracranial vessel wall MR imaging plays an increasing role in diagnosing intracranial vascular diseases. For a complete assessment, pre- and postcontrast sequences are required, and including other sequences, these result in a long scan duration. Ideally, the scan time of the vessel wall sequence should be reduced. The purpose of this study was to evaluate different intracranial vessel wall sequence variants to reduce scan duration, provided an acceptable image quality can be maintained.

MATERIALS AND METHODS: Starting from the vessel wall sequence that we use clinically (6:42 minutes), 6 scan variants were tested (scan duration ranging between 4:39 and 8:24 minutes), creating various trade-offs among spatial resolution, SNR, and contrast-to-noise ratio. In total, 15 subjects were scanned on a 3T MR imaging scanner: In 5 subjects, all 7 variants were performed precontrast-only, and in 10 other subjects, the fastest variant (4:39 minutes) and our clinically used variant (6:42 minutes) were performed pre- and postcontrast.

RESULTS: The fastest variant (4:39 minutes) had higher or comparable SNRs/contrast-to-noise ratios of the intracranial vessel walls compared with the reference sequence (6:42 minutes). Qualitative assessment showed that the contrast-to-noise ratio was most suppressed in the fastest variant of 4:39 minutes and the variant of 6:42 minutes pre- and postcontrast. SNRs/contrast-to-noise ratios of the fastest variant were all, except one, higher compared with the variant of 6:42 minutes ($P < .008$). Furthermore, the fastest variant (4:39 minutes) detected all vessel wall lesions identified on the 6:42-minute variant.

CONCLUSIONS: A 30% faster vessel wall sequence was developed with high SNRs/contrast-to-noise ratios that resulted in good visibility of the intracranial vessel wall.

ABBREVIATIONS: CNR = contrast-to-noise ratio; DANTE = delay alternating with nutation for tailored excitation; PD = proton density; SENSE = sensitivity encoding; VIRTA = volumetric isotropically reconstructed turbo spin-echo acquisition; VISTA = volumetric isotropic turbo spin-echo acquisition

High-resolution intracranial vessel wall MR imaging plays an increasing role in diagnosing intracranial vascular diseases.[1,2] The main advantage of this imaging technique compared with lumen-based methods such as CT angiography and digital subtraction angiography is the visualization of the vessel wall itself, including the detection of vessel wall lesions that do not necessarily show (or only subtle) luminal narrowing.[3-7] Intracranial vessel wall imaging can be used for the detection and characterization of plaque burden in intracranial atherosclerotic disease, which is known to be one of the most important contributing factors to ischemic stroke and may be detected at an early stage.[8-10] It can also be helpful in the differentiation of other vascular diseases, such as vasculitis and reversible vasoconstriction syndrome, with, for instance, visualization of vessel wall enhancement.[11] Furthermore, intracranial vessel wall imaging may aid in the diagnosis of aneurysm rupture and intracranial dissection, though this is less supported in the literature.[12-14]

Intracranial vessel wall MR imaging requires high spatial resolution to visualize the thin vessel wall and potential accompanying vessel wall lesions. Currently, most 3D-acquired vessel wall sequences use a voxel size between 0.4 and 0.7 mm, though this is larger than the normal diameter of the intracranial vessel walls.[2,15] In addition, a high signal-to-noise ratio and contrast-to-noise-ratio (CNR) are required to delineate the vessel wall from surrounding tissue (ie, blood, CSF, and parenchyma).[1,2,16] At higher magnetic field strengths, a higher spatial resolution and/or SNR

Received March 7, 2017; accepted after revision February 17, 2018.

From the Department of Radiology (A.L., A.A.H., J.J.M.Z., J.C.W.S., J.H.) University Medical Center Utrecht, Utrecht, the Netherlands; and Spinoza Center for Neuroimaging (J.C.W.S.), Amsterdam, the Netherlands.

This work was supported by the European Research Council grant No. 637024 (J.H.).

Please address correspondence to A. Lindenholz, MD, Department of Radiology, University Medical Center Utrecht, Postbox 85500, 3508 GA Utrecht, the Netherlands; e-mail: A.Lindenholz@umcutrecht.nl

Indicates open access to non-subscribers at www.ajnr.org
Indicates article with supplemental on-line tables.
Indicates article with supplemental on-line photos.

http://dx.doi.org/10.3174/ajnr.A5629

Table 1: Scan parameters of the acquired scan variants

	TIWI VISTA[d] Variant 1	PD_W VISTA Variant 2[a]	TIWI VIRTA[d] Variant 3[b]	TIWI VIRTA Variant 4	TIWI VISTA Variant 5[c]	TIWI VISTA Variant 6	TIWI VIRTA Variant 7
Scan duration (min)	8:24	7:50	6:42	6:01	5:52	5:49	4:39
TR/TE (ms)	1500/38	2000/40	1500/37	1500/40	1500/40	1500/38	1500/40
FOV (mm^3)	200 × 166 × 45	200 × 166 × 45	200 × 166 × 45	200 × 166 × 45	200 × 166 × 45	200 × 166 × 45	200 × 166 × 45
Acquired voxel (mm^3)	0.5 × 0.5 × 0.5	0.5 × 0.5 × 0.5	0.6 × 0.6 × 1.0	0.5 × 0.5 × 1.0	0.5 × 0.5 × 0.5	0.6 × 0.6 × 0.6	0.5 × 0.5 × 1.0
Reconstructed voxel (mm^3)	0.5 × 0.5 × 0.5	0.5 × 0.5 × 0.5	0.5 × 0.5 × 0.5	0.5 × 0.5 × 0.5	0.5 × 0.5 × 0.5	0.6 × 0.6 × 0.6	0.5 × 0.5 × 0.5
Oversample factor	1.8	1.2	1.8	1.8	1.2	1.8	1.8
SENSE reduction factor	1.5	2	1.5	2	2	1.5	2
Overcontiguous slices	No (90)	No (90)	Yes (90)	Yes (90)	No (90)	No (75)	Yes (90)
TSE + startup echoes	56 + 3	60 + 5	56 + 5	56 + 5	60 + 5	56 + 4	56 + 5
Turbo direction	Radial	Radial	Y-axis	Radial	Radial	Radial	Radial
Refocusing control ($\alpha_{min}/\alpha_{max}$)	30/120	50/120	25/120	50/120	50/120	30/120	50/120
Readout bandwidth (Hz)	607.6	358.6	732.1	360.1	358.6	753	360.1
Reference tissue T1/T2 (ms)	1200/80	1200/100	1200/100	1200/100	1200/100	1200/80	1200/100
Anti-DRIVE	Yes	No	Yes	No	No	Yes	Yes
Elliptic *k*-space shutter	Yes	Yes	No	No	Yes	Yes	Yes

Note:—$\alpha_{min}/\alpha_{max}$ indicates α minimum and maximum; PD_W, proton density–weighted; Anti-DRIVE, anti-driven equilibrium.
[a] Adjusted from Qiao et al.[19]
[b] Currently used in our clinic.
[c] Adjusted from Qiao et al[19] with a shorter TR.
[d] Philips Healthcare.

can be achieved. Therefore, vessel wall MR imaging is currently performed at 3T and higher field strengths. However, with high spatial resolution, the SNR is still limited and the total scan duration is long. Recently published intracranial vessel wall MR imaging sequences have scan durations ranging from 5.0 to 10.2 minutes.[16-22] To assess vessel wall lesions, one needs pre- and postcontrast acquisitions to evaluate contrast enhancement of the vessel walls. For a complete examination, other sequences, such as time-of-flight MR angiography, diffusion-weighted imaging, and T2 fluid-attenuated inversion recovery images may also be needed, resulting in a long total scan duration. With longer scan durations, motion artifacts may increase, especially in neurologically impaired patients. Ideally, total scan duration of the pre- and postcontrast vessel wall sequence should be reduced without sacrificing image quality. In this study, SNR and CNR of 1 earlier reported intracranial vessel wall sequence[23,24] were compared with 6 variations, which include another previously reported sequence,[19] with different trade-offs among scan duration, resolution, and contrast. Subsequently, pre- and postcontrast images of the fastest vessel wall variant were compared with the current variant used in our daily clinical practice.[24]

MATERIALS AND METHODS

Participants

Fifteen subjects were included in this study. In 5 subjects (4 men; mean age, 37 years; range, 28–54 years), all 7 scan variants were performed (precontrast only). Additionally, precontrast and postcontrast comparisons were performed in 10 other subjects (9 men; mean age, 53 years; range, 24–68 years). Approval for this study was obtained from the institutional review board of University Medical Center Utrecht. The 10 volunteers who received contrast agent were part of the Posterior Intracranial Vessel Wall Imaging (PIVI) and Intracranial Vessel Wall Imaging (IVI) studies (NTR5688 and NTR2119, respectively, www.trialregister.nl). All subjects gave written informed consent.

Imaging Protocol

We used a 3T MR imaging system (Achieva; Philips Healthcare, Best, the Netherlands) with an 8-channel phased array sensitivity encoding (SENSE) head coil. All vessel wall sequences consisted of a 3D fast turbo spin-echo sequence and NEX of 1. Starting from our earlier described vessel wall sequence (variant 3 in Table 1),[23] 6 different variants were created, of which one is previously described (variant 2).[19] In the scan protocol of the precontrast-only acquisitions, the sequence acquisition order was equal in each subject (consecutively, variants 2, 5, 3, 4, 7, 1, and 6; Table 1). Variant 3 was used as a reference sequence for the 6 different precontrast-only acquisitions. Various trade-offs were created among contrast (TR, antidriven equilibrium), spatial resolution (voxel-size, elliptic *k*-space shutter), SNR (oversample factor in the phase-encoding direction, SENSE reduction factor, readout bandwidth, overcontiguous [overlapping] slices, TSE-train flip angle refocusing control), and scan duration (Table 1). All vessel wall scans were repeated with the radiofrequency and gradient turned off for sampling noise images from the receiver coil elements, including image-reconstruction effects such as elliptic *k*-space shutter and parallel (SENSE) reconstruction sensitivities. The noise images were accelerated by leaving out the delay after each TSE train to the next (turned off) excitation. The total scan session took 65 minutes and included the preparation phase, TOF-MRA (acquired voxel size, 0.4 × 0.7 × 1.0 mm^3; reconstructed voxel size, 0.36 × 0.36 × 0.5 mm^3; acquisition time, 5:12 minutes), and the 7 vessel wall scan variants, including their corresponding noise images. For the vessel wall sequences, the FOV was planned in a transverse/oblique orientation, which covered all large cerebral arteries of the circle of Willis.

In addition, in 10 other subjects, precontrast and postcontrast images were acquired of our earlier published and clinically used variant 3, which had good CSF suppression, and the fastest, variant 7 (consecutively, variants 3 and 7 in 8 subjects and consecutively, variants 7 and 3 in 2 subjects). We have chosen to compare the fastest variant, variant 7, with our clinically used variant for clinical and practical purposes. Before acquisition of the postcontrast sequences, a gadolinium-containing contrast agent (gadobutrol, Gadovist, 1.0 mmol/mL; Bayer Schering Pharma, Berlin, Germany) was administered intravenously. The total scan session took 45 minutes and included, consecutively, the preparation

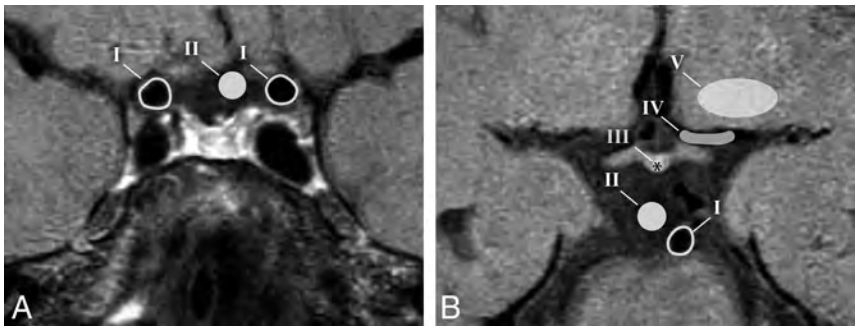

FIG 1. ROIs used in the magnitude images for calculating the signal-to-noise ratios. *A*, The circumferential of both carotid arteries (I) was used as a marker for the carotid vessel wall that runs through the suprasellar cistern, which was used as marker for CSF (II). *B*, The circumferential of the basilar artery (I) was used as marker for the basilar vessel wall that runs through the pontine cistern, which was used as second marker for CSF (II). For the pituitary stalk, a homogeneous hyperintense part of the center was used (III). In the lumen of the middle cerebral artery, an ROI was drawn as a marker for blood (IV), and in the left orbital gyrus, an ROI was drawn as marker for brain tissue (V). The ROIs are drawn for illustrative purposes, and the exact contours may differ in the real measurements, depending on patients' specific anatomies.

phase with the survey scans; TOF-MRA precontrast vessel wall sequences; postcontrast DWI; postcontrast vessel wall sequences (acquired ~20 minutes after the precontrast vessel wall sequence), including noise images; and finally, a postcontrast T2 FLAIR sequence.

Image Analysis

The mean signal and SD of the noise (SD_{Noise}) were obtained from the axial plane of the vessel wall images and noise images (magnitude), respectively. ROIs for the mean signal ($mean_{ROI}$) were manually drawn as follows: CSF was marked in the suprasellar and pontine cisterns for the intracranial internal carotid arteries and basilar artery, respectively; blood was marked in the lumen of the middle cerebral artery; brain tissue was marked in the left orbital gyrus; and the vessel wall was represented by the circumferential of the intracranial internal carotid arteries (left and right) and basilar artery (within the same slice number as the ROIs for CSF, Fig 1). In the 10 subjects who received contrast agent injection, a homogeneous hyperintense part of the center of the pituitary stalk was used as the ROI to compute the mean as a consistent marker for contrast enhancement (Fig 1). To compute the SD of the noise images, a larger circular ROI was drawn on the noise images, encompassing the ROIs used to compute the mean. The SNR was calculated as $SNR = Mean_{ROI} / SD_{Noise}$ for each subject and subsequently averaged for all subjects included in the comparison. The CNRs were calculated as $CNR_{x-y} = SNR_x - SNR_y$. As a measure of motion, vessel wall sequences were coregistered to the prior acquired sequence to calculate the registration parameters (ΔRotation and ΔTranslation), using the Elastix toolbox in MeVisLab (Version 2.7; MeVis Medical Solutions, Bremen, Germany).[25]

An expert neuroradiologist (J.H., with >15 years of experience), specialized in intracranial vessel wall imaging, assessed both pre- and postcontrast vessel wall images in multiple planes for image quality, which includes the visibility of the arterial vessel wall, the suppression of blood and CSF, and the existence of artifacts (slow-flow, motion, and free induction decay artifacts). The images of the 10 subjects who received contrast agent injection were also assessed for the presence of vessel wall lesions, including location and configuration (eccentric or concentric) and contrast enhancement, using methods previously described.[24,26] All scans were blinded and randomly ordered before assessment. When a lesion was found in only one of the variants, the location was re-examined in the other variant to check whether the lesion could be identified retrospectively. Furthermore, the vessel wall images were cross-correlated with the TOF-MRA images for a correct interpretation of the specific arteries, the potential vessel wall lesions, and the lumen of the artery. Included vessels were the anterior cerebral arteries (A1 and A2 segments), distal intracranial internal carotid arteries (clinoid or C5 and cavernous or C4 segments), middle cerebral arteries (M1, M2, and M3 segments), posterior cerebral arteries (P1 and P2 segments), the distal intracranial basilar artery, and distal intracranial vertebral arteries.

Statistical Analysis

All statistical comparisons were conducted using SPSS statistics (Version 21; IBM, Armonk, New York). Pairwise comparisons were performed between the clinically relevant SNRs and CNRs of the reference variant and the 6 other variants using generalized estimating equations to account for repeated measures on the same subjects. A Friedman test was performed for differences in SNR and CNR between both precontrast and postcontrast images of variants 3 and 7. A post hoc analysis with the Wilcoxon signed rank test was conducted with a Bonferroni correction applied to correct for multiple comparisons. A P value $< .008$ was considered significant.

RESULTS

All 15 subjects underwent the MR imaging successfully. The quality of all images was sufficient to be used for analysis. Image assessment was not hampered by motion artifacts in any of the scanned subjects.

Comparison of all 7 Scan Variants

Typical images of the 7 vessel wall scan variants are shown in Fig 2 (axial plane), Fig 3 (sagittal plane), and On-line Fig 1 (coronal plane). The images show clear differences among the variants in contrast and visibility of the vessel wall. Qualitative assessment of the images in the axial plane shows poor visibility of the vessel wall in variants 1 (8:24 minutes) and 6 (5:49 minutes), acquired with an isotropic voxel size. Variants 4 (6:01 minutes) and 7 (4:39 minutes), which were acquired with an anisotropic voxel size, had higher qualitative assessment scores compared with the other variants. Qualitative assessment of the axial, sagittal, and coronal images showed that CSF was most suppressed in variants 3 (6:42 minutes) and 7 (4:39 minutes). These 2 variants are compared before and after contrast administration in the next paragraph (Table 2). Variant 1 (8:24 minutes) also had an adequate CSF

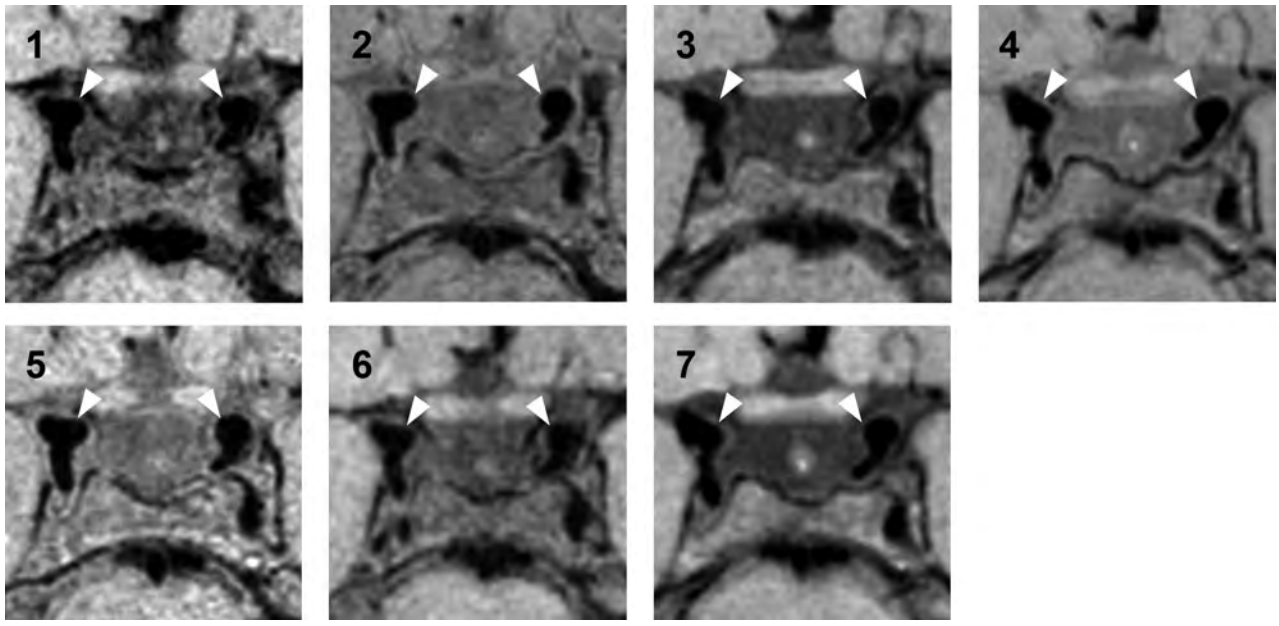

FIG 2. Sample images in the axial plane of the 7 different scan variants performed at 3T (precontrast, in order of decreasing scan duration). Both distal intracranial internal carotid arteries (*white arrowheads*) with the bifurcation of the posterior communicating artery are depicted, surrounded by CSF. *1*, T1WI VISTA variant 1 (8:24 minutes). *2*, Proton density–weighted VISTA variant 2 (7:50 minutes), adjusted from Qiao et al.[19] *3*, T1WI VIRTA variant 3 (6:42 minutes). *4*, T1WI VIRTA variant 4 (6:01 minutes). *5*, T1WI VISTA variant 5 (5:52 minutes), adjusted from Qiao et al[19] with a shorter TR. *6*, T1WI VISTA variant 6 (5:49 minutes). *7*, T1WI VIRTA variant 7 (4:39 minutes).

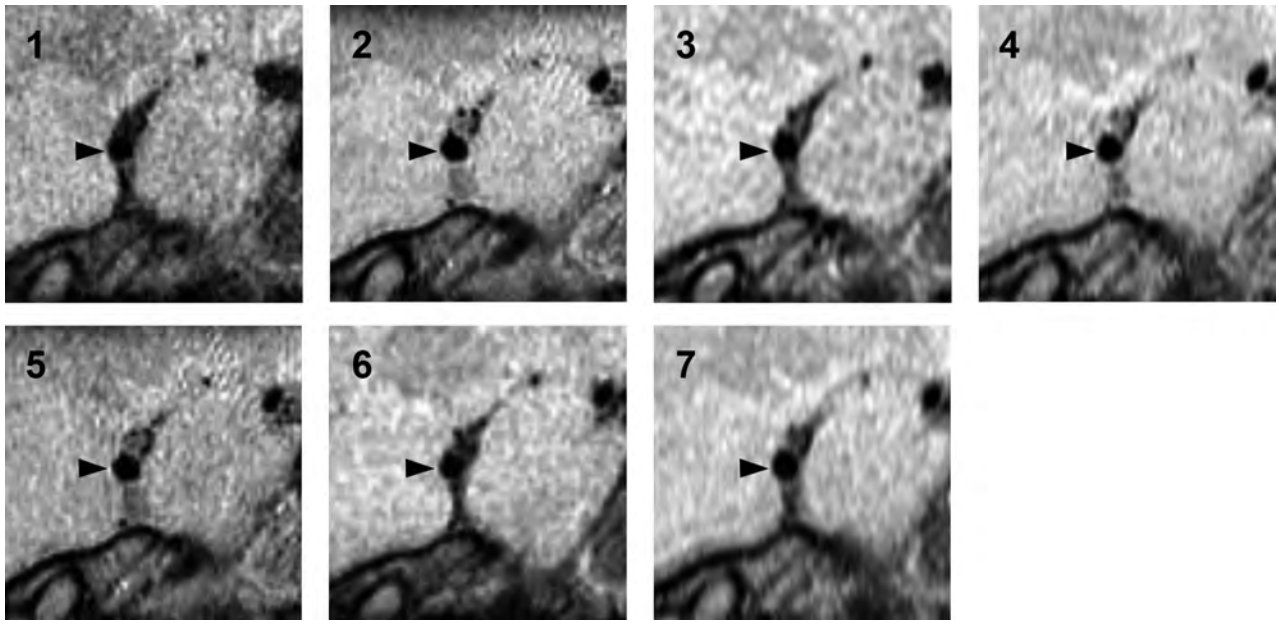

FIG 3. Sample images in the sagittal plane of the 7 different scan variants performed at 3T (precontrast, in the order of decreasing scan duration). The right MCA (*black arrowheads*) is depicted in all images, surrounded by CSF and brain parenchyma. *1*, T1WI VISTA variant 1 (8:24 minutes). *2*, Proton density–weighted VISTA variant 2 (7:50 minutes), adjusted from Qiao et al.[19] *3*, T1WI VIRTA variant 3 (6:42 minutes). *4*, T1WI VIRTA variant 4 (6:01 minutes). *5*, T1WI VISTA variant 5 (5:52 minutes), adjusted from Qiao et al[19] with a shorter TR. *6*, T1WI VISTA variant 6 (5:49 minutes). *7*, T1WI VIRTA variant 7 (4:39 minutes).

suppression, but the axial and sagittal images had an overall granular appearance, which made assessment and delineation of the vessel wall with the surrounding CSF challenging. This granular appearance was also seen to a lesser extent in variants 5 (5:52 minutes) and 6 (5:49 minutes), but with worse CSF suppression. In the axial plane, the vessel wall was best seen in variants 2 (7:50 minutes), 3 (6:42 minutes), 4 (6:01 minutes), and 7 (4:39 minutes). In both the sagittal and coronal planes, the vessel wall is of the highest quality in the isotropic variant 2 (7:50 minutes), though the contrast with the surrounding CSF is less, which makes delineation of the outer margins of the vessel wall more difficult. Due to the granular appearance, the perpendicular visibility (sagittal plane) of the middle cerebral artery was poor in variants 1 (8:24 minutes) and 6 (5:49 minutes). In the aniso-

Table 2: SNRs and CNRs of the precontrast and postcontrast scan variants 3 and 7[a]

	Precontrast			Postcontrast		
	T1WI VIRTA (Variant 3)[f]	T1WI VIRTA (Variant 7)	*P* Value	T1WI VIRTA (Variant 3)[f]	T1WI VIRTA (Variant 7)	*P* Value
SNR_{tissue}[b]	28.0 ± 1.8	40.5 ± 3.4	.005[g]	27.9 ± 1.3	42.4 ± 2.8	.005[g]
$SNR_{carotid\ vessel\ wall}$[c]	15.3 ± 1.4	20.8 ± 2.7	.005[g]	17.2 ± 0.9	26.4 ± 4.0	.005[g]
$SNR_{basilar\ vessel\ wall}$	13.0 ± 1.4	15.9 ± 1.7	.005[g]	13.4 ± 2.4	19.2 ± 1.8	.005[g]
$SNR_{suprasellar\ CSF}$	9.1 ± 2.0	11.9 ± 2.2	.007[g]	11.3 ± 0.7	14.1 ± 2.4	.013
$SNR_{pontine\ CSF}$	5.9 ± 2.1	8.0 ± 2.0	.007[g]	6.5 ± 1.8	11.2 ± 2.6	.007[g]
SNR_{blood}	3.6 ± 0.6	5.4 ± 1.2	.005[g]	3.8 ± 0.5	6.3 ± 1.4	.007[g]
$SNR_{pituitary\ gland}$	23.0 ± 3.4	33.4 ± 4.7	.005[g]	33.3 ± 3.5	49.5 ± 6.7	.005[g]
$CNR_{carotid\ vessel\ wall–CSF}$[d]	6.1 ± 1.6	9.0 ± 1.5	.005[g]	6.0 ± 0.7	12.3 ± 3.6	.007[g]
$CNR_{basilar\ vessel\ wall–CSF}$[e]	7.2 ± 1.4	7.9 ± 1.4	.059	7.0 ± 2.0	8.0 ± 1.9	.285
$CNR_{carotid\ vessel\ wall–blood}$[c]	11.6 ± 1.3	15.5 ± 2.9	.013	13.5 ± 1.0	20.1 ± 3.8	.007[g]

[a] Data are mean and SD calculated in 10 subjects. A Wilcoxon signed rank test was used to compare the differences between precontrast variants 3 and 7 and postcontrast variants 3 and 7 (additional statistical comparisons are shown in On-line Table 2).
[b] Tissue ROI is located at the left orbital gyri.
[c] The mean of the left and right distal intracranial internal carotid arteries.
[d] Suprasellar CSF is used as reference.
[e] Pontine CSF is used as reference.
[f] Currently used in our clinic.
[g] Statistically significant ($P < .008$).

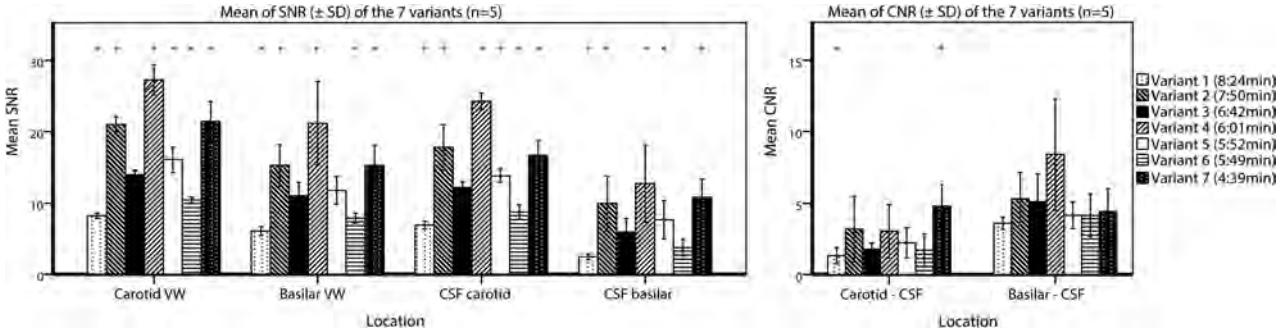

FIG 4. Barplots showing the mean and SD of the clinically relevant SNRs and CNRs of all 7 vessel wall imaging variants. The means and SDs are calculated for 5 subjects The mean of the left and right intracranial internal carotid arteries was used for the carotid vessel wall. The *asterisks* indicate a significant difference compared with reference variant 3 (corrected *P* value for multiple comparisons, $P < .008$) using generalized estimating equations to account for repeated measures on the same subjects. VW indicates vessel wall.

tropic variants 3 (6:42 minutes), 4 (6:01 minutes), and 7 (4.39 minutes), the vessel wall could be delineated in the sagittal plane, but the overall appearance was blurrier (Fig 3). All variants had sufficient blood suppression without flow artifacts, which could have limited assessment in the large intracranial arteries.

The mean SNRs and CNRs of the clinically most relevant regions (ie, the basilar and carotid vessel walls and the surrounding CSF) are shown in Fig 4, including the statistical comparisons with reference variant 3. The SNR and, more important, the calculated CNR results for all variants are shown in On-line Table 1. Relatively high SNRs of the vessel wall were measured for variants 2 (7:50 minutes), 4 (6:01 minutes), and 7 (4:39 minutes). In these 3 variants, the SNR of the intracranial internal carotid vessel wall was >21, and the SNR of the basilar vessel wall, >15. All 7 variants showed good blood signal suppression, which resulted in most variants having a relatively high CNR between blood and the intracranial internal carotid artery vessel wall (CNRs ranging from 5.7 to 23, On-line Table 1). All except 1 variant performed borderline in the CNRs of the carotid vessel wall and the surrounding CSF (ranging from 1.3 to 3.2). Variant 7 had the highest CNR between the carotid vessel wall and the surrounding CSF (4.8). All variants performed better in the CNRs between the basilar artery vessel wall and CSF, which were comparable in 6 of 7 variants (ranging from 3.6 to 5.3); only variant 4 (6:01 minutes) had a higher CNR (8.4) but also a large SD (3.9, Fig 4).

Comparison of Variant 3 (6:42 minutes) versus 7 (4:39 minutes)

The average SNRs and CNRs of both precontrast and postcontrast images of variants 3 and 7 are shown in Table 2. Comparing SNRs and CNRs of the precontrast and postcontrast scans (Table 2) for variants 3 and 7 showed that tissue, the basilar vessel wall, suprasellar CSF of only variant 7, pontine CSF, and blood SNR did not differ significantly (all *P* values > .008, On-line Table 2), while the SNR of the carotid vessel wall of variant 7 ($P = .005$) and the CNRs between the carotid vessel wall and CSF ($P = .005$ and .007 for variants 3 and 7, respectively) tended to be higher for the postcontrast images. Significant differences for the $SNR_{pituitary\ gland}$ were expected because of a strong enhancing pituitary gland on postcontrast images. For both precontrast and postcontrast vessel wall images, the SNRs and CNRs of variant 7 (4:39 minutes) were higher than those of variant 3 (6:42 minutes). These differences were all significant ($P < .008$), except for the

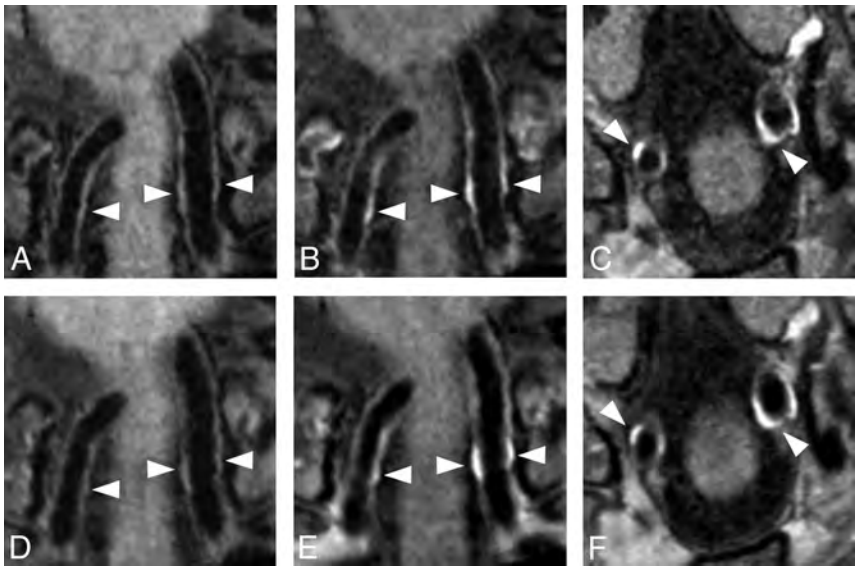

FIG 5. Matching vessel wall lesions of the distal vertebral arteries (*white arrowheads*) seen before and after contrast with variant 3 (6:42 minutes; *A–C*) and variant 7 (4:39 minutes; *D–F*) in a 59-year-old man with multiple cardiovascular risk factors. Subtle (concentric) wall thickening is seen in both the left and right vertebral arteries before contrast (*A* and *D*), with clear contrast enhancement on the postcontrast image (*B* and *E*). Variant 3 (6:42 minutes, *B* and *C*) was acquired approximately 2 minutes after contrast injection, and variant 7 (4:39 minutes, *E* and *F*), approximately 9 minutes after contrast injection. Some patient motion was seen in the postcontrast series of variant 7. Postcontrast transverse images of variants 3 (*C*) and 7 (*F*) show clear vessel wall enhancement in both vertebral arteries (*white arrowheads*).

$SNR_{suprasellar\ CSF}$ of variant 7, the $CNR_{basilar\ wall–CSF}$ of both variants ($P = .059$ and $P = .285$), and the $CNR_{carotid\ vessel\ wall–blood}$ of variant 3 ($P = .013$) (Table 2).

Qualitative assessment of both precontrast and postcontrast vessel wall images in multiple planes showed that in all subjects, the vessel wall could be delineated for both sequences (Fig 5). Overall, variant 7 (4:39 minutes) was slightly more affected by free induction decay artifacts in the outer regions of the FOV and slow-flow artifacts, but this finding did not affect the assessment of the large intracranial arteries. In 1 subject, variant 7 (4:39 minutes) showed small motion artifacts, but they did not have an influence on the assessment. Sixteen vessel wall lesions were identified in variant 3 (6:42 minutes), and 19, in variant 7 (4:39 minutes). In 4 of 10 subjects, no vessel wall lesions were detected. Vessel wall lesions (on the basis of the 19 detected vessel wall lesions) were found in the carotid arteries ($n = 3$), middle cerebral arteries ($n = 2$), vertebral arteries ($n = 10$), basilar artery ($n = 3$), and posterior cerebral artery ($n = 1$), of which 12 were enhancing (a full description of all lesions is found in On-line Table 3). All 16 lesions identified in vessel wall variant 3 (6:42 minutes) matched vessel wall lesions identified in variant 7 (4:39 minutes) (Fig 5). One vessel wall lesion was reported as eccentric in variant 3 and concentric in variant 7, and 1 lesion, as enhancing in variant 3 and nonenhancing in variant 7. Three lesions were missed with vessel wall variant 3: one lesion located at the bifurcation of the basilar artery P1, one at the left internal carotid artery, and 1 at the left vertebral artery.

DISCUSSION

The purpose of this study was to evaluate different variants of MR imaging sequences for intracranial vessel wall imaging to reduce scan duration, provided that an acceptable image quality could be maintained. In the precontrast comparison, the fastest one, variant 7 (4:39 minutes), had a significantly higher CNR between the vessel wall and blood, compared with variant 3, while it was about 30% faster. Also, the CNR between the vessel wall and CSF was better for variant 7 compared with variant 3. The favorable SNRs and CNRs of variant 7 also remained in the second comparison in which both precontrast and postcontrast images were acquired and were higher compared with our clinically used variant 3 (Table 2). Especially in the elderly population, the superior contrast between the vessel wall and CSF can be beneficial. In the aging brain, tissue atrophy increases and consequently the intracranial vessels are more richly surrounded by CSF.

The quality of an MR image is a balance of resolution, SNR/CNR, and scan duration. A gain in 1 aspect results in a sacrifice of another. The ideal balance is difficult to determine and depends on the specific application and the clinical question to be answered. Several pulse sequence optimizations have been developed to address these technical challenges.[17-19,21,26] For high CNR of the vessel wall, both blood and CSF need to be simultaneously suppressed.[1] 3D variable flip angle refocusing pulse sequences are used because of their high intrinsic black-blood properties and the ability to generate multiplanar reformatted images, but they have less effect on the slow-flowing CSF.[17,19-22,27] For better CSF suppression, proton density–weighted imaging with radial ordering modulation of the *k*-space (short TE),[19] anti-driven equilibrium,[18,23,28] or prepulses such as delay alternating with nutation for tailored excitation (DANTE)[17,21,29] and inversion recovery[30] have been proposed.

In 4 of 7 variants, the anti-driven equilibrium technique was used. This technique drives the magnetization back to the negative M_z-axis by further radiofrequency excitation and results in more adequate CSF suppression.[18,24,27] A second possibility to improve image contrast between the vessel wall and CSF is the use of a DANTE prepulse.[17,21,29] When one applies DANTE pulse trains, the longitudinal magnetization of static tissue largely remains but flowing spins are suppressed due to a spoiling effect.[29] This suppression is less for slow-flowing fluid, especially below 0.1 cm/s; therefore, DANTE will be less useful for CSF suppression around the distal cerebral arteries. The DANTE prepulse also improves the suppression of blood, notably for slow and turbulent flow. Slow flow is a well-known pitfall in the assessment of vessel wall imaging.[2] In the current study, the postcontrast vessel wall showed a higher SNR/CNR compared with the precontrast vessel wall, which may suggest slow-flow. Another explanation that may have led to higher SNRs of the postcontrast vessel walls is contrast

absorption into the vessel wall itself. The flow artifacts seen in variant 7 may be a potential problem, and a DANTE prepulse might be a viable addition for more effective blood suppression. A third option to improve the contrast between the vessel wall and surrounding tissue is using inversion recovery.[30] This technique is mainly applied in 2D acquisitions; however, reports have also been published with 3D acquisitions on a 7T MR imaging system.[31]

Generally, a lower minimum refocusing angle results in better flow suppression but also in a lower SNR. Because of the higher minimum refocusing angles in the TSE train of vessel wall variants 2, 4, 5, and 7, they may yield more SNRs but probably at the cost of blurring due to a worse point spread function.[16,32] This may also partly explain the "smoother" appearance in variants 4 and 7 (Fig 2). However, these sequences do show the vessel wall clearly, and in our opinion, radiologists often prefer blurring compared with images with a very narrow point spread function because this results in more noisy images, which are more difficult to assess, even though the true resolution is higher.

A disadvantage of variants 3, 4, and 7 might be the anisotropic resolution in the slice direction, which makes it less beneficial for multiplanar assessment (Figs 2 and 3).[1,19] In specific clinical situations, multiplanar reconstructions may be required, for example, when assessing lesions in the middle cerebral artery. However, in daily clinical practice, image interpretation can regularly be performed in the axial or oblique plane alone, and in these situations, a nearly isotropic voxel size may be adequate for interpretation of vessel wall images.[23,24,33] In addition, the scan variants with an anisotropic voxel size have a larger overall voxel size, which results in a higher SNR per voxel, but they also can offer a shorter effective scan time. On the other hand, using an anisotropic voxel size potentially increases partial volume effects compared with the isotropic-derived variants.[34] Consequently, vessel wall thickness might be overestimated or small lesions might be missed. To reduce the scan duration further, we applied an elliptic *k*-space shutter in 5 variants. Theoretically, this might also reduce the image quality because in enabling the elliptic *k*-space shutter, the outer part of the *k*-space is cut off, leading to a reduction in the effective resolution. However, in practice, the effect may be limited, particularly because the longer scan durations needed for a full acquisition make the images more prone to motion artifacts. Another way to reduce scan duration is the use of 2D methods as an alternative to 3D imaging methods. These 2D methods have anisotropic voxels because the slice thickness is normally much larger than the in-plane voxel size. When these slices are planned perpendicular to the vessels, this is not a problem. However, these 2D methods have the drawback of small coverage and the need to be focused on a limited vessel wall region. The optimal ROI may be difficult to determine beforehand.[26,35]

Besides several advanced pulse sequence optimization techniques, better hardware may also improve image quality. In the current study, a relatively low number of receiver channels (8 channels) was used. Currently, up to 32 channels are commonly used to investigate vessel wall sequences.[16,20,27] Also, when one uses a higher number of channels in the receiver coil, more possibilities such as parallel imaging might be available to reduce the scan duration without severely compromising image quality. Moreover, parallel imaging, like SENSE, also performs better at higher field strengths.[36] Another novel acceleration technique to reduce the scan duration even further may be compressed sensing.[37] This technique has already shown promising results for extracranial carotid vessel wall imaging.[38]

This study has some limitations. First, the true quality of an MR image is the result of a multidimensional trade-off among numerous parameters. Many of the parameters are also interrelated and may have a combined effect on resolution, SNR/CNR, or scan duration, and it is difficult to compare these parameters one-to-one for true image quality. Furthermore, in the comparison of all 7 variants, the same order of sequences was used, which may have led to more motion artifacts in the later scheduled sequences. However, the extent of movement, measured in ΔRotation and ΔTranslation between subsequent sequences, did not increase during the acquisition time (On-line Fig 2). Also, in the second comparison (variant 3 versus 7), contrast enhancement may have been stronger due to a longer absorption time in the latest scheduled variant (in our study mostly variant 7). However, statistical comparison (variants 3 and 7 versus variants 7 and 3) did not show any significant differences (data not shown). This study lacked a systematic comparison among the different parameters to investigate the effect on image quality. Vessel wall variants were created to reduce scan duration with the focus on the development of a clinically usable sequence that can be incorporated into existing scan protocols.

The second limitation is the manually drawn ROIs for measuring the SNR. Although we tried to be consistent in the location, it was not always possible to use the exact same slice number for all variants for the SNR measurement of the vessel wall and CSF, mainly due to intrasubject differences such as patient movement and intersubject differences in planning and anatomy. Furthermore, due to flow effects of CSF in the basal cisterns, a better delineation can be made of the proximal intracranial arteries compared with the more distal intracranial arteries, where the CSF flow is lower. In general, the SNR of the vessel wall may be underestimated because of partial volume effects and difficulties of manually drawing an ROI around the circumferential of the vessel wall. This effect is even more obvious in the thinner basilar artery vessel wall, where the measured SNRs are consistently lower compared with the intracranial internal carotid artery vessel wall with surrounding tissue/CSF. Also, the CSF was often more suppressed in the pontine cistern, most likely due to a faster CSF flow, which resulted in still comparable or even higher CNRs of the basilar artery and CSF compared with the intracranial internal carotid arteries and CSF (Table 2 and On-line Table 1). This partly subjective determination of the circumferential of the vessel walls and CSF is subject to measurement errors. However, the same approach was used in all 7 variants; therefore, it is unlikely that it influenced the relative differences in performance of the compared variants.

Third, no histology or in vivo reference standard for vessel wall imaging of the vessel wall lesions that were identified in this study was available. Therefore, no validation against the ground truth could be performed. Earlier reports already described relatively high numbers of vessel wall lesions or atherosclerotic plaques in asymptomatic subjects.[28,39,40] In the current study, mostly

healthy volunteers were used for assessment of the intracranial vessel wall. Larger patient groups, including symptomatic patients, are needed for a more thorough assessment of vessel wall lesion visibility and contrast enhancement and, subsequently, the true utility of the faster vessel wall variants in clinical practice.

CONCLUSIONS

In this study, a considerably faster clinically feasible vessel wall sequence (4:39-minute scan duration) with high SNRs and CNRs was developed, which resulted in a good visibility of the intracranial vessel wall in the axial plane. Qualitative assessment showed promising results in overall image quality and detecting vessel wall lesions. The faster scan duration allows pre- and postcontrast acquisition of vessel wall images with sufficient remaining scan duration for other imaging sequences in patient studies.

ACKNOWLEDGMENTS

The authors acknowledge Dr Hugo J. Kuijf from the Image Sciences Institute, University Medical Center Utrecht, for his technical support in coregistering the vessel wall sequences using MeVisLab and Chris van Kesteren from the Radiology Department of the University Medical Center Utrecht, for his support in figure layout.

Disclosures: Arjen Lindenholz—*RELATED*: *Grant*: European Research Council, *Comments*: grant No. 637024,* Anita A. Harteveld—*RELATED*: *Grant*: European Research Council under the European Union Horizon 2020 Programme (H2020)/European Research Council grant agreement No. 637024.* Jaco J.M. Zwanenburg—*UNRELATED*: *Grants/Grants Pending*: European Research Council starting grant, *Comments*: funding from the European Research Council under the European Union Seventh Framework Programme (FP7/2007–2013)/European Research Council grant agreement No. 337333. Title of the grant: "Towards Understanding Cerebral Small Vessel Disease: Innovative, MRI-Based, Functional Markers to Discover the Terra Incognita between Large Vessels and Macroscopic Brain Lesions."* *Money paid to the institution.

REFERENCES

1. Dieleman N, van der Kolk AG, Zwanenburg JJ, et al. **Imaging intracranial vessel wall pathology with magnetic resonance imaging: current prospects and future directions.** *Circulation* 2014;130:192–201 CrossRef Medline
2. Mandell DM, Mossa-Basha M, Qiao Y, et al. **Intracranial vessel wall MRI: principles and expert consensus recommendations of the American Society of Neuroradiology.** *AJNR Am J Neuroradiol* 2017;38:218–29 CrossRef Medline
3. Qiao Y, Anwar Z, Intrapiromkul J, et al. **Patterns and implications of intracranial arterial remodeling in stroke patients.** *Stroke* 2016;47:434–40 CrossRef Medline
4. Zou XD, Chung YC, Zhang L, et al. **Middle cerebral artery atherosclerotic plaques in recent small subcortical infarction: a three-dimensional high-resolution MR study.** *Biomed Res Int* 2015;2015:540217 CrossRef Medline
5. Yoon Y, Lee DH, Kang DW, et al. **Single subcortical infarction and atherosclerotic plaques in the middle cerebral artery: high-resolution magnetic resonance imaging findings.** *Stroke* 2013;44:2462–67 CrossRef Medline
6. Alexander MD, Yuan C, Rutman A, et al. **High-resolution intracranial vessel wall imaging: imaging beyond the lumen.** *J Neurol Neurosurg Psychiatry* 2016;87:589–97 CrossRef Medline
7. Bodle JD, Feldmann E, Swartz RH, et al. **High-resolution magnetic resonance imaging: an emerging tool for evaluating intracranial arterial disease.** *Stroke* 2013;44:287–92 CrossRef Medline
8. Ritz K, Denswil NP, Stam OC, et al. **Cause and mechanisms of intracranial atherosclerosis.** *Circulation* 2014;130:1407–14 CrossRef Medline
9. Holmstedt CA, Turan TN, Chimowitz MI. **Atherosclerotic intracranial arterial stenosis: risk factors, diagnosis, and treatment.** *Lancet Neurol* 2013;12:1106–14 CrossRef Medline
10. Qureshi AI, Caplan LR. **Intracranial atherosclerosis.** *Lancet* 2014;383:984–98 CrossRef Medline
11. Obusez EC, Hui F, Hajj-Ali RA, et al. **High-resolution MRI vessel wall imaging: spatial and temporal patterns of reversible cerebral vasoconstriction syndrome and central nervous system vasculitis.** *AJNR Am J Neuroradiol* 2014;35:1527–32 CrossRef Medline
12. Choi YJ, Jung SC, Lee DH. **Vessel wall imaging of the intracranial and cervical carotid arteries.** *J Stroke* 2015;17:238–55 CrossRef Medline
13. Edjlali M, Gentric JC, Régent-Rodriguez C, et al. **Does aneurysmal wall enhancement on vessel wall MRI help to distinguish stable from unstable intracranial aneurysms?** *Stroke* 2014;45:3704–06 CrossRef Medline
14. Nagahata S, Nagahata M, Obara M, et al. **Wall enhancement of the intracranial aneurysms revealed by magnetic resonance vessel wall imaging using three-dimensional turbo spin-echo sequence with motion-sensitized driven-equilibrium: a sign of ruptured aneurysm?** *Clin Neuroradiol* 2016;26:277–83 CrossRef Medline
15. Lindenholz A, van der Kolk AG, Zwanenburg JJM, et al. **The use and pitfalls of intracranial vessel wall imaging: how we do it.** *Radiology* 2018;286:12–28 CrossRef Medline
16. Zhu C, Haraldsson H, Tian B, et al. **High resolution imaging of the intracranial vessel wall at 3 and 7 T using 3D fast spin echo MRI.** *MAGMA* 2016;29:559–70 CrossRef Medline
17. Wang J, Helle M, Zhou Z, et al. **Joint blood and cerebrospinal fluid suppression for intracranial vessel wall MRI.** *Magn Reson Med* 2016;75:831–38 CrossRef Medline
18. Yang H, Zhang X, Qin Q, et al. **Improved cerebrospinal fluid suppression for intracranial vessel wall MRI.** *J Magn Reson Imaging* 2016;44:665–72 CrossRef Medline
19. Qiao Y, Steinman DA, Qin Q, et al. **Intracranial arterial wall imaging using three-dimensional high isotropic resolution black blood MRI at 3.0 Tesla.** *J Magn Reson Imaging* 2011;34:22–30 CrossRef Medline
20. Zhang L, Zhang N, Wu J, et al. **High resolution three dimensional intracranial arterial wall imaging at 3 T using T1 weighted SPACE.** *Magn Reson Imaging* 2015;33:1026–34 CrossRef Medline
21. Xie Y, Yang Q, Xie G, et al. **Improved black-blood imaging using DANTE-SPACE for simultaneous carotid and intracranial vessel wall evaluation.** *Magn Reson Med* 2016;75:2286–94 CrossRef Medline
22. Li ML, Xu YY, Hou B, et al. **High-resolution intracranial vessel wall imaging using 3D CUBE T1 weighted sequence.** *Eur J Radiol* 2016;85:803–07 CrossRef Medline
23. Dieleman N, Yang W, van der Kolk AG, et al. **Qualitative evaluation of a high-resolution 3D multi-sequence intracranial vessel wall protocol at 3 Tesla MRI.** *PLoS One* 2016;11:e0160781 CrossRef Medline
24. Dieleman N, Yang W, Abrigo JM, et al. **Magnetic resonance imaging of plaque morphology, burden, and distribution in patients with symptomatic middle cerebral artery stenosis.** *Stroke* 2016;47:1797–802 CrossRef Medline
25. Klein S, Staring M, Murphy K, et al. **Elastix: a toolbox for intensity-based medical image registration.** *IEEE Trans Med Imaging* 2010;29:196–205 CrossRef Medline
26. Swartz RH, Bhuta SS, Farb RI, et al. **Intracranial arterial wall imaging using high-resolution 3-Tesla contrast-enhanced MRI.** *Neurology* 2009;72:627–34 CrossRef Medline
27. Fan Z, Yang Q, Deng Z, et al. **Whole-brain intracranial vessel wall imaging at 3 Tesla using cerebrospinal fluid-attenuated T1-weighted 3D turbo spin echo.** *Magn Reson Med* 2017;77:1142–50 CrossRef Medline
28. Harteveld AA, van der Kolk AG, van der Worp HB, et al. **High-resolution intracranial vessel wall MRI in an elderly asymptomatic population: comparison of 3T and 7T.** *Eur Radiol* 2017;27:1585–95 CrossRef Medline

29. Li L, Miller KL, Jezzard P. **DANTE-prepared pulse trains: a novel approach to motion-sensitized and motion-suppressed quantitative magnetic resonance imaging.** *Magn Reson Med* 2012;68:1423–38 CrossRef Medline
30. Edelman RR, Chien D, Kim D. **Fast selective black blood MR imaging.** *Radiology* 1991;181:655–60 CrossRef Medline
31. van der Kolk AG, Hendrikse J, Brundel M, et al. **Multi-sequence whole-brain intracranial vessel wall imaging at 7.0 Tesla.** *Eur Radiol* 2013;23:2996–3004 CrossRef Medline
32. Mugler JP 3rd. **Optimized three-dimensional fast-spin-echo MRI.** *J Magn Reson Imaging* 2014;39:745–67 CrossRef Medline
33. Dieleman N, van der Kolk AG, van Veluw SJ, et al. **Patterns of intracranial vessel wall changes in relation to ischemic infarcts.** *Neurology* 2014;83:1316–20 CrossRef Medline
34. Antiga L, Wasserman BA, Steinman DA. **On the overestimation of early wall thickening at the carotid bulb by black blood MRI, with implications for coronary and vulnerable plaque imaging.** *Magn Reson Med* 2008;60:1020–28 CrossRef Medline
35. Xu WH, Li ML, Gao S, et al. **In vivo high-resolution MR imaging of symptomatic and asymptomatic middle cerebral artery atherosclerotic stenosis.** *Atherosclerosis* 2010;212:507–11 CrossRef Medline
36. Wiesinger F, Van de Moortele PF, Adriany G, et al. **Potential and feasibility of parallel MRI at high field.** *NMR Biomed* 2006;19:368–78 CrossRef Medline
37. Lustig M, Donoho D, Pauly JM. **Sparse MRI: The application of compressed sensing for rapid MR imaging.** *Magn Reson Med* 2007;58:1182–95 CrossRef Medline
38. Li B, Li H, Li J, et al. **Relaxation enhanced compressed sensing three-dimensional black-blood vessel wall MR imaging: preliminary studies.** *Magn Reson Imaging* 2015;33:932–38 CrossRef Medline
39. Bos D, van der Rijk MJ, Geeraedts TE, et al. **Intracranial carotid artery atherosclerosis: prevalence and risk factors in the general population.** *Stroke* 2012;43:1878–84 CrossRef Medline
40. Homburg PJ, Plas GJ, Rozie S, et al. **Prevalence and calcification of intracranial arterial stenotic lesions as assessed with multidetector computed tomography angiography.** *Stroke* 2011;42:1244–50 CrossRef Medline

Anatomic and Angiographic Analyses of Ophthalmic Artery Collaterals in Moyamoya Disease

T. Robert, G. Cicciò, P. Sylvestre, A. Chiappini, A.G. Weil, S. Smajda, C. Chaalala, R. Blanc, M. Reinert, M. Piotin, and M.W. Bojanowski

ABSTRACT

BACKGROUND AND PURPOSE: Moyamoya disease is a progressive neurovascular pathology defined by steno-occlusive disease of the distal internal carotid artery and associated with the development of compensatory vascular collaterals. The etiology and exact anatomy of vascular collaterals have not been extensively studied. The aim of this study was to describe the anatomy of collaterals developed between the ophthalmic artery and the anterior cerebral artery in a Moyamoya population.

MATERIALS AND METHODS: All patients treated for Moyamoya disease from 2004 to 2016 in 4 neurosurgical centers with available cerebral digital subtraction angiography were included. Sixty-three cases were evaluated, and only 38 met the inclusion criteria. Two patients had a unilateral cervical internal carotid occlusion that limited analysis of ophthalmic artery collaterals to one hemisphere. This study is consequently based on the analysis of 74 cerebral hemispheres.

RESULTS: Thirty-eight patients fulfilled the inclusion criteria. The most frequently encountered anastomosis between the ophthalmic artery and cerebral artery was a branch of the anterior ethmoidal artery (31.1%, 23 hemispheres). In case of proximal stenosis of the anterior cerebral artery, a collateral from the posterior ethmoidal artery could be visualized (16 hemispheres, 21.6%). One case (1.4%) of anastomosis between the lacrimal artery and the middle meningeal artery that permitted the vascularization of a middle cerebral artery territory was also noted.

CONCLUSIONS: Collaterals from the ophthalmic artery are frequent in Moyamoya disease. Their development depends on the perfusion needs of the anterior cerebral artery territories. Three other systems of compensation could be present (callosal circle, leptomeningeal anastomosis, and duro-pial anastomoses).

ABBREVIATIONS: ACA = anterior cerebral artery; OA = ophthalmic artery; STA = superficial temporal artery

Moyamoya disease is a neurovascular pathology characterized by the progressive stenosis of the supraclinoidal portion of the internal carotid artery and its 2 main branches: the anterior cerebral artery (ACA) and middle cerebral artery in their proximal segments.[1-3] During the evolution of the pathology, the development of collaterals maintains a minimal perfusion to the cerebral parenchyma and, in particular, the ACA territories.[3-5] In most cases, the ICA stenosis is distal to the ophthalmic artery (OA),[1] thus allowing this artery to develop the necessary collaterals.[3] A detailed analysis of the role of the OA in supplying the ACA and MCA territories is lacking in the literature. By analyzing angiographic images, we aimed to study how the OA participates in creating collaterals in Moyamoya disease.

MATERIALS AND METHODS

Patient Selection

On the basis of a prospective data base from 2004 to 2016 with demographics, 63 patients with the diagnosis of Moyamoya disease or syndrome have been evaluated in our institutions (Sainte Justine Hospital, Montreal; Notre-Dame Hospital, Montreal; Rothschild Foundation Hospital, Paris; and Regional Hospital, Lugano). In this study, the first digital subtraction angiography of these patients was available in only 38 cases. In 2 of these cases, unilateral cervical ICA stenosis limited our analysis of OA collaterals to only 1 hemisphere. Therefore, a retrospective analysis of OA collaterals was possible in 74 cerebral hemispheres. For each patient, additional data were collected retrospectively. We looked for the presence of an etiology, the duration of the symptoms, the

Received September 27, 2017; accepted after revision February 7, 2018.

From the Department of Interventional Neuroradiology (T.R., G.C., S.S., R.B., M.P.), Rothschild Foundation Hospital, Paris, France; University of Montreal (P.S.), Montreal, Quebec, Canada; Department of Neurosurgery (A.G.W., C.C., M.W.B.), Notre-Dame Hospital, Montreal, Quebec, Canada; and Department of Neurosurgery (T.R., A.C., M.R.), Neurocenter of Southern Switzerland, Lugano, Switzerland.

Please address correspondence to Thomas Robert, MD, Department of Neurosurgery, Neurocenter of the Southern Switzerland, Ospedale Civico di Lugano, Via Tesserete, 46, 6901 Lugano, Switzerland; e-mail: thomas.robert43@gmail.com

http://dx.doi.org/10.3174/ajnr.A5622

Table 1: Demographic data and clinical presentation

Variable	Patients (*n* = 38)
Age (median) (range) (yr)	39.8 (1–67)
Female	28 (73.7%)
Clinical presentation	
Ischemic stroke	23 (60.5%)
Hemorrhagic stroke	9 (23.7%)
Hemorrhagic stroke with intraventricular hemorrhage	2 (5.3%)
SAH secondary to aneurysm rupture	3 (7.9%)
Incidental discovery	1 (2.6%)
mRS at diagnosis	
1	12 (31.6%)
2	15 (39.5%)
3	4 (10.5%)
4	1 (2.6%)
5	6 (15.8%)

type of clinical sign (ischemic or hemorrhagic), and the evaluation by a modified Rankin Scale score.

Analysis of the Ophthalmic Artery Collateral Anatomy

A 6-vessel DSA with the patient under local anesthesia with 3D reconstruction was conducted on all patients of this study. The Suzuki grading system[6] was applied to each cerebral hemisphere; as suggested by Baltsavias et al,[7] different arterial collaterals were categorized into leptomeningeal, duro-pial, and periventricular collaterals. For each ophthalmic artery evaluated, careful attention was paid to the presence of a rete mirabile modification of the OA, to the presence of 1 or multiple anastomotic vascular networks between branches of the OA and branches of a cerebral artery, and to the cerebral territory supplied by branches of the OA.

Treatment and Clinical Evolution

Modalities of medical and surgical treatments were recorded. Follow-up started at the time of the first clinical sign and ended with the last visit. A neurologic examination with evaluation of the mRS was systematically performed for each visit.

RESULTS

Clinical Presentation

Between 2004 and 2016, thirty-eight patients fulfilled the inclusion criteria for this study. Patient baseline data and clinical signs are described in Table 1. The mean age was 40 years (range, 1–67 years) with a female preponderance (female/male ratio: 2.8:1). The most common clinical sign was an ischemic stroke in 23 patients (60.5%). Other patients presented with bleeding: intraparenchymal hematoma (9 patients, 23.7%), intraparenchymal bleeding with a ventricular component (2 patients, 5.3%), and a subarachnoid hemorrhage secondary to an associated aneurysm rupture in 3 patients (7.9%). In 1 patient, Moyamoya disease was discovered incidentally while investigating a frontal parasagittal meningioma. The initial mRS score was 1 in 12 patients (31.6%), 2 in 15 (39.5%), 3 in 4 (10.5%), 4 in 1 (2.6%), and 5 in 6 (15.8%).

Angiographic Analysis of Moyamoya Disease

We analyzed the ophthalmic arteries and their collaterals to the cerebral parenchyma for each cerebral hemisphere. It was not possible to assess the OA in 2 patients due to a unilateral cervical ICA occlusion. The results of our evaluation are summarized in Table 2. The Suzuki stage was 0 in 9 patients presenting with a unilateral Moyamoya syndrome (12.2%), I in 10 hemispheres (13.5%), II in 10 (13.5%), III in 14 sides (18.9%), IV in 15 (20.3%), V in 5 (6.8%), and VI in 11 hemispheres (14.9%). Leptomeningeal collaterals were the most frequently observed (51 hemispheres, 68.9%). Duro-pial collaterals from branches of the external carotid artery to the territory of the ACA were noted in 5 hemispheres (6.8%), and periventricular collaterals, in 47 sides (63.5%). The presence of collaterals from branches of the ophthalmic artery was noted in 35 cases (47.3%) and was most frequent in Suzuki grades III–V. A rete mirabile modification of the ophthalmic artery was present in 17 cases (23%).

Table 2: Angiographic Suzuki grade and presence of collaterals

Cerebral Hemispheres Studied	*n* = 74
Suzuki stage	
0	9 (12.2%)
I	10 (13.5%)
II	10 (13.5%)
III	14 (18.9%)
IV	15 (20.3%)
V	5 (6.8%)
VI	11 (14.9%)
OA–intracranial artery collaterals	35 (47.3%)
Rete mirabile of the OA	17 (23%)
Anterior ethmoidal artery–ACA branch direct collaterals	15 (20.3%)
Anterior ethmoidal artery–ACA branch collaterals via anterior falcine artery	23 (31.1%)
Posterior ethmoidal artery–orbitofrontal artery	16 (21.6%)
Recurrent meningeal artery–MMA–Sylvian branch	1 (1.4%)
Collaterals	
Leptomeningeal collaterals to ACA territory	51 (68.9%)
Duro-pial collaterals to ACA territory	5 (6.8%)
Posterior callosal artery collateral	22 (29.7%)
Periventricular collaterals	47 (63.5%)

Note:—MMA indicates middle meningeal artery.

Collaterals from the Anterior Ethmoidal Artery

The most frequently encountered anastomosis between the ophthalmic artery and a cerebral artery was a branch of the anterior ethmoidal artery. It was found in 31.1% (23 hemispheres). Figure 1 illustrates one of these cases. The anterior ethmoidal artery supplies the anterior falcine artery, which develops a duro-pial collateral with the callosomarginal, anteromedial frontal, or frontopolar artery. These collaterals could supply the territory of the anterior cerebral artery when there was poor development of collaterals from the posterior callosal artery.

Collaterals from the Posterior Ethmoidal Artery

In 16 hemispheres (21.6%) in our series, when there was a proximal stenosis of the anterior cerebral artery, a collateral from the posterior ethmoidal artery was seen. The posterior ethmoidal artery supplied the paramedian part of the planum sphenoidale, and by its proximity, it developed a collateral with the homolateral orbitofrontal artery. By retrograde flow, the orbitofrontal artery supplied the A2 segment of the ACA. Figure 2 shows an example of this collateral artery.

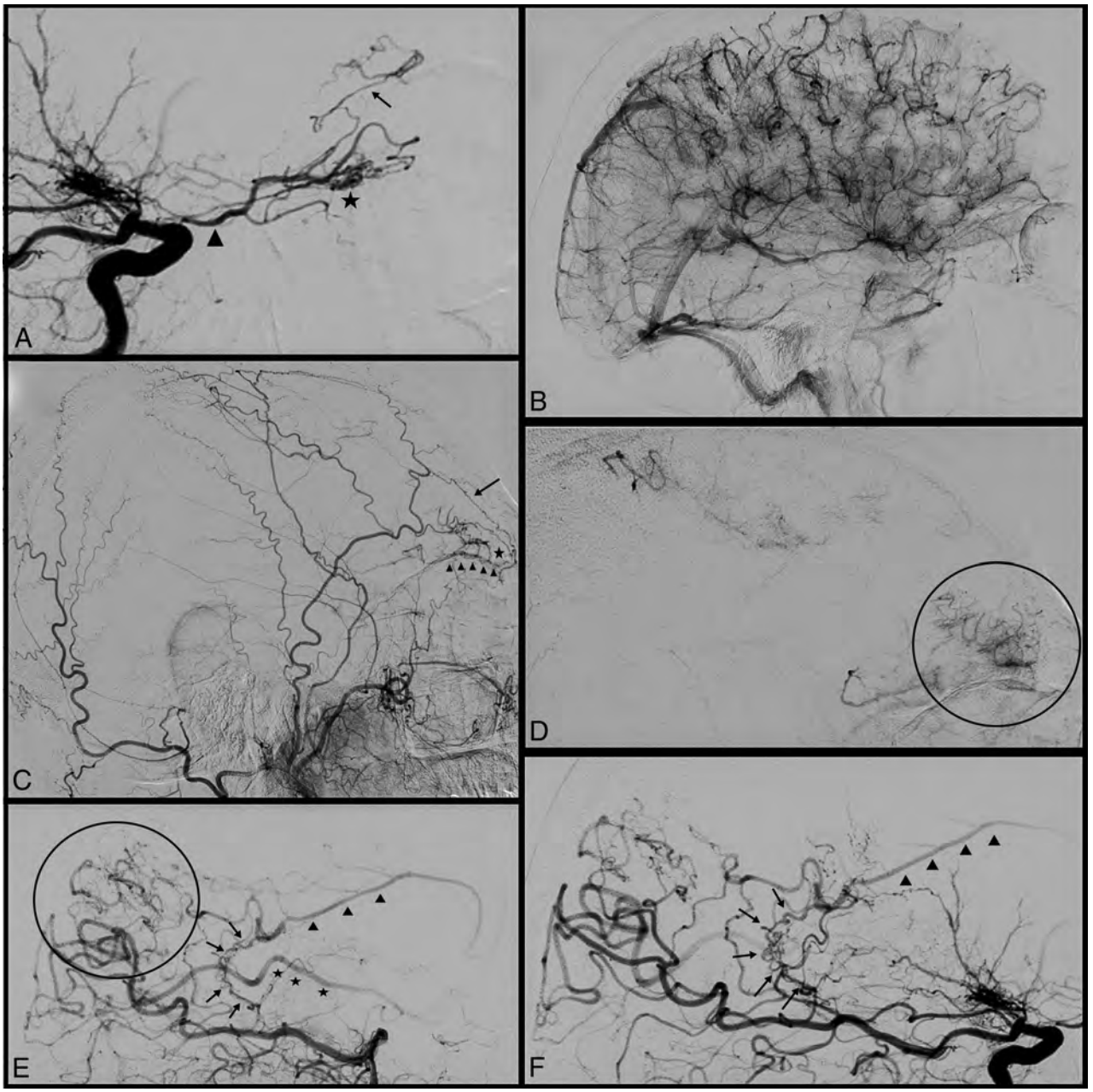

FIG 1. Illustrative case 1. *A*, Lateral ICA angiogram with the ophthalmic artery (*triangle*) with a rete mirabile modification of its third segment (*asterisk*) and an anterior ethmoidal artery anastomosis with retrograde perfusion of an anterior cerebral artery branch (*black arrow*). *B*, Parenchymal time of the angiogram in *A* shows the complete perfusion of the frontal lobe. *C*, Lateral external carotid artery angiogram of the same patient shows the presence of an anastomosis between the ophthalmic artery and the superficial temporal artery (*black arrow*) via the dorsal nasal artery. Note the presence of anterior ethmoidal artery anastomosis with pial branches of the anterior cerebral artery (*asterisk*). The *arrowheads* show anastomotic branches under the orbital roof. *D*, Parenchymal time of the angiogram in *C* that shows the perfusion of the frontopolar region by the anastomosis described earlier. *E*, An example of retrograde perfusion of the pericallosal artery (*arrowheads*) on the lateral vertebral artery angiogram by callosal circle (*arrows*) and cortical leptomeningeal anastomoses. Note also the presence of retrograde opacification of an MCA branch (*asterisks*). *F*, Another example of retrograde perfusion of the pericallosal artery (*arrowheads*) on a lateral vertebral artery angiogram by a well-developed callosal circle (*arrows*).

Collaterals from the Lacrimal Artery

In only 1 case in our series (1.4%) did the ophthalmic artery supply a part of the MCA territory through the recurrent meningeal artery. The anterior branch of the middle meningeal artery originated from the lacrimal artery and passed through the superior orbital fissure. This branch of the middle meningeal artery developed duro-pial collaterals with cortical branches of the MCA.

Treatment and Clinical Follow-Up

Among the 38 patients, 21 were treated with an antiplatelet therapy. Aspirin was always the first-line treatment. Three of them presented with a recurrent ischemic stroke and were placed under dual-antiplatelet therapy. No hemorrhagic stroke was noted under antiaggregation therapy. Six patients benefited from surgical treatment. Six patients had a bilateral superficial temporal artery (STA)–middle cerebral artery anastomosis, and 4 others had a

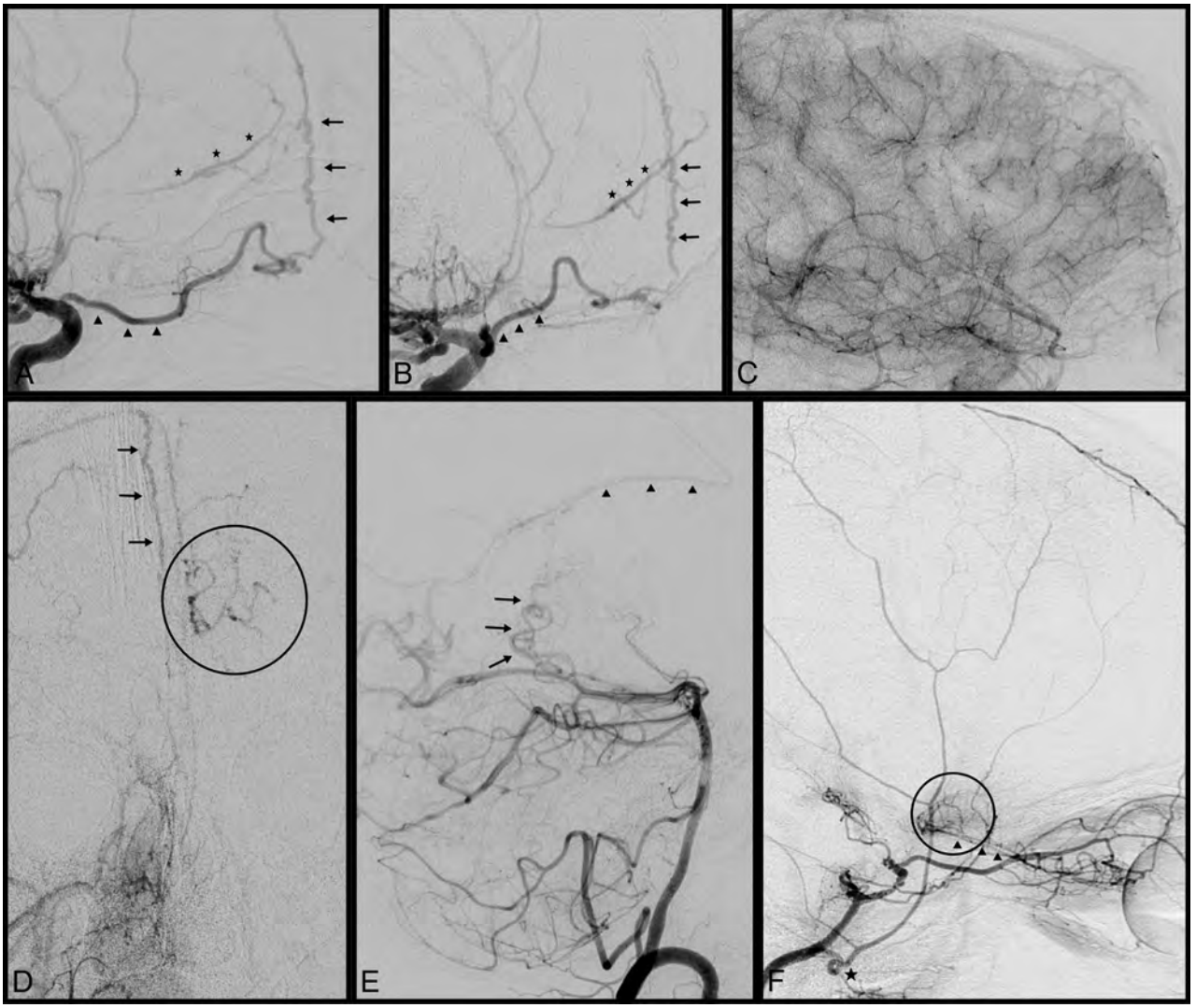

FIG 2. Illustrative case 2. *A*, Lateral ICA angiogram with the ophthalmic artery (*triangles*) having an anterior ethmoidal artery anastomosis by a falcine artery (*arrows*) with retrograde perfusion of an anterior cerebral artery branch (*asterisks*). The same angiogram as shown in *A* in an oblique view. *C*, Parenchymal time of the angiogram of *A* and *B* that shows the complete perfusion of the frontal lobe. *D*, An example of a duro-pial anastomosis from the right middle meningeal artery via the falcine arteries (*arrows*) to the left cingulate gyrus. *E*, The presence of retrograde perfusion of the pericallosal artery (*arrowheads*) on a lateral vertebral artery angiogram by a callosal circle (*arrows*). *F*, Lateral ICA angiogram with complete occlusion of the supraclinoidal segment of the ICA and posterior ethmoidal artery anastomosis (*arrowheads*). Note the presence of an ICA origin of the middle meningeal artery (*asterisk*).

STA-MCA anastomosis only at 1 side. For the last patient, the STA was too small to permit the anastomosis and a myosynangiosis was performed. As a complication of the operation, 1 patient had an ischemic stroke contralateral to the operated hemisphere that was imputed to a hypoperfusion during the induction. The mean follow-up was 50 months (range, 1–138 months). At the last visit, 8 patients (40%) had a poor clinical outcome (mRS $\geq$ 3) that was directly correlated to the clinical presentation of the patient before treatment.

DISCUSSION

Moyamoya disease is a progressive neurovascular pathology defined by stenosis of the distal internal carotid artery and middle and anterior cerebral arteries associated with the development of vascular collaterals. The scientific literature regarding this pathology is limited because of the rarity of Moyamoya disease.[4] Most articles described the surgical techniques and their outcome, but only a few authors provided detailed angiographic descriptions of the different types of collaterals that naturally develop. In particular, Baltsavias et al[7] described the collaterals that had developed in the anterior and posterior[8] circulations. They classified the different anastomosis into 4 types using superselective angiography. Although it is known that the OA may provide collaterals, a detailed analysis is not available in the literature, to our knowledge. A lot of questions remain concerning these collaterals: Are they frequent? Is there a pattern? Do certain collaterals develop more frequently than others? What are the other possibilities of maintaining blood flow to territories of the anterior cerebral arteries?

The most frequent collaterals found in our series came from branches of the anterior ethmoidal artery. Normally, this artery vascularizes the dura of the medial third of the anterior fossa and the anterior third of the falx cerebri, the latter via the anterior

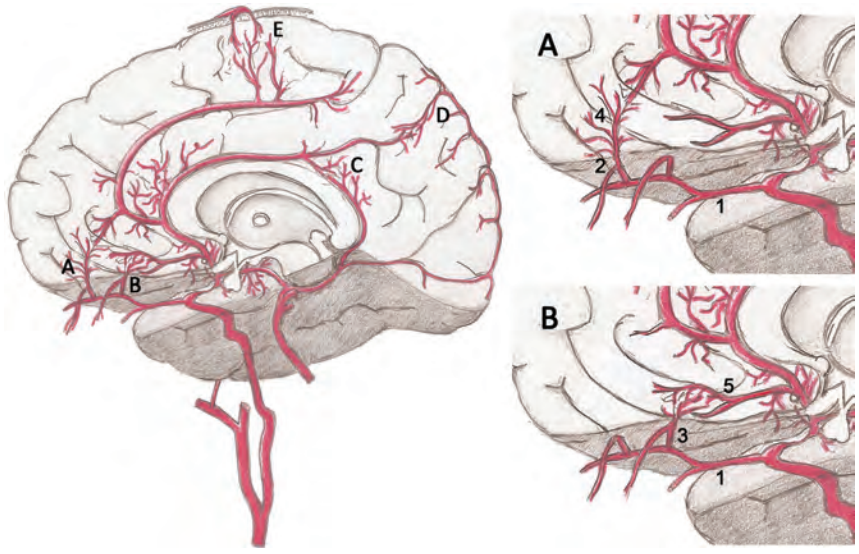

FIG 3. Illustration showing the 4 systems of arterial collaterals to supply the ACA territories. *A*, Anterior ethmoidal artery anastomosis (1: ophthalmic artery; 2: anterior ethmoidal artery; 4: anterior falcine artery). *B*, Posterior ethmoidal artery anastomosis (1: ophthalmic artery; 3: posterior ethmoidal artery; 5: orbitofrontal artery). *C*, Callosal circle. *D*, Leptomeningeal anastomosis (posterior cerebral artery–ACA). *E*, Duro-pial anastomosis from a branch of the middle meningeal artery.

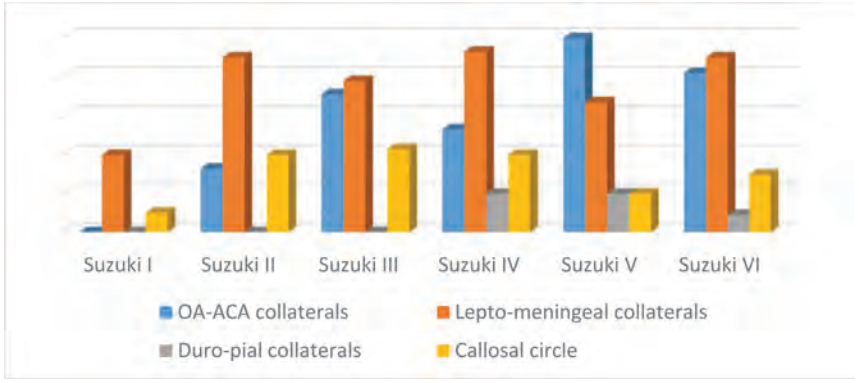

FIG 4. Evolution of the systems that permit the perfusion of the ACA territories as a function of the Suzuki grade.

falcine artery. Baltsavias et al[7] described duro-pial anastomoses between the middle meningeal artery and cortical branches. In their description of the duro-pial anastomoses, they gave an example of an anastomosis between an anterior ethmoidal artery and an orbitofrontal artery.[7] These small collaterals help in the perfusion of a callosomarginal artery from a well-developed anterior falcine artery.

Another type of collateral described in our series is a connection between the posterior ethmoidal artery and a proximal branch of the anterior cerebral artery. This less frequent anastomosis has a posteriorly oriented trajectory and may perfuse retrogradely an artery that originates near the anterior communicating complex. This anastomosis has already been described by Chung and Weon[9] in a case report in which the authors described the rete mirabile appearance of the ophthalmic artery. We have 2 hypotheses to explain the development of this anastomosis. First, we suggest that this anastomosis is a duro-pial anastomosis between a dural branch of the posterior ethmoidal artery and the orbitofrontal artery. This orbitofrontal artery is in the olfactory sulcus and takes its origin from the A2 near the A1–A2 junction. A retrograde flow from the posterior ethmoidal artery may supply the entire pericallosal artery. The second hypothesis takes into account the presence of the remnant of the primitive olfactory artery, an embryologic artery described by Padget.[10] She described the primitive olfactory artery as the anterior branch of the primitive internal carotid artery. Its maximal development is the sixth stage (20–24 mm) when it is an A1 branch that follows the olfactory tract to the posterior part of the cribriform plate. This artery then enters the ethmoidal cells and the orbit to anastomose with ophthalmic artery branches. After this stage, the medial part of the artery regresses, the distal part becomes the dural branches of the posterior ethmoidal branch, and the proximal part develops into a recurrent artery that enters the anterior perforated substance. After comparing their results with the works of Abbie[11] and Shellshear, Padget[10] considered the primitive olfactory artery as the embryologic precursor of the recurrent artery of Heubner. Lasjaunias et al[12] cited the interesting works of Padget and added phylogenic information. In horses and monkeys, the anterior cerebral artery is supplied by the ophthalmic artery through an artery that courses into the posterior part of the cribriform plate.

The last type of collateral observed in our series is the supply of the territory of the middle cerebral artery by the ophthalmic artery via the middle meningeal artery. This anastomosis is only possible with the persistence or the development of the recurrent meningeal artery. The recurrent meningeal artery is an anastomotic artery between the lacrimal artery and the middle meningeal artery that is the remnant of the orbital branch of the stapedial artery. Uchino et al[13] and Komiyama et al[14] have observed that the incidence of an embryonic remnant of an artery is most frequent in patients with Moyamoya disease and suggested a congenital origin of the pathology. With only 1 case of this anastomosis noted in our series, we have not reached any conclusions, but it remains an interesting observation.

In the present series, only a few cases of Moyamoya disease in the first stages present with vascular collaterals from the ophthalmic artery. We also noted that in Suzuki stage III, most cases have already developed OA-ACA collaterals. These collaterals seem to be functional earlier than the duro-pial collaterals developed from the middle meningeal artery. In advanced stages of the disease (Suzuki V and VI), the proportion of OA-ACA collaterals is high.

It is very difficult to understand which factors influence the

development of OA-ACA collaterals. Our impression is that there is a lack of blood supply, which stimulates the development of collaterals. We identified no more than 4 systems that allow maintaining the supply of the ACA territories. These 4 systems are illustrated in Fig 3. The first one is the callosal circle (Fig 3*A*), which is the anastomosis of the posterior and anterior callosal arteries. The second one is the leptomeningeal collaterals (Fig 3*B*) from cortical arteries of the MCA or posterior cerebral artery. The third one is duro-pial anastomosis (Fig 3*C*) from the middle meningeal artery, and the last one, OA-ACA anastomosis (Fig 3*D*). A balance among these 4 systems permitting maintenance of the cerebral perfusion seems to be the most important factor explaining the development of OA-ACA collaterals. The balance among these 4 systems found in our series is shown in Fig 4. Baltsavias et al[7] described another possible system that could supply the ACAs, the development of transcallosal anastomosis from the choroidal to the pericallosal arteries.

Few articles[2-4,7,8,12] elucidate the precise anatomy of collaterals developed in the Moyamoya disease. The sequence of the development is not known, and the only information we have is summarized in the Suzuki score.[6] We think that the understanding of the evolution of these collaterals is key to managing these patients. With enough information, it could be easier to select patients who need bypass surgery and determine the best time to perform it.

Limitations

Our study is a retrospective study based on conventional cerebral DSA without selective injection to evaluate the anastomosis between the OA and the cerebral arteries. The other important limitation is that most of our patients had only 1 conventional DSA and thereafter were followed by MRA. It is impossible to evaluate the development of these collaterals during the evolution of the Moyamoya disease.

CONCLUSIONS

Collaterals from the ophthalmic artery are frequent in Moyamoya disease, particularly at Suzuki stage III. Their development depends on the lack of blood supply to the ACA territories as well as on the ability of the 3 other systems (callosal circle, leptomeningeal anastomosis, and duro-pial anastomoses) to compensate. Selective injection of the OA at various stages of the disease may help to better understand the dynamics involved in the development of collaterals from the OA in Moyamoya disease.

REFERENCES

1. Scott RM, Smith ER. **Moyamoya disease and moyamoya syndrome.** *N Engl J Med* 2009;360:1226–37 CrossRef Medline
2. Bang OY, Fujimura M, Kim SK. **The pathophysiology of Moyamoya disease: an update.** *J Stroke* 2016;18:12–20 CrossRef Medline
3. Burke GM, Burke AM, Sherma AK, et al. **Moyamoya disease: a summary.** *Neurosurg Focus* 2009;26:E11 CrossRef Medline
4. Kim JS. **Moyamoya disease: epidemiology, clinical features, and diagnosis.** *J Stroke* 2016;18:2–11 CrossRef Medline
5. Kwag HJ, Jeong DW, Lee SH, et al. **Intracranial hemodynamic changes during adult moyamoya disease progression.** *J Clin Neurol* 2008;4:67–74 CrossRef Medline
6. Suzuki J, Takaku A. **Cerebrovascular "moyamoya" disease: disease showing abnormal net-like vessels in base of brain.** *Arch Neurol* 1969;20:288–99 CrossRef Medline
7. Baltsavias G, Khan N, Valavanis A. **The collateral circulation in pediatric moyamoya disease.** *Childs Nerv Syst* 2015;31:389–98 CrossRef Medline
8. Baltsavias G, Khan N, Filipce V, et al. **Selective and superselective angiography of pediatric moyamoya disease angioarchitecture in the posterior circulation.** *Interv Neuroradiol* 2014;20:403–12 CrossRef Medline
9. Chung JI, Weon YC. **Ophthalmic rete mirabile: the first angiographic documentation of embryonic ophthalmic collaterals in a patient with moyamoya disease: a case report.** *Interv Neuroradiol* 2008;14:293–96 CrossRef Medline
10. Padget DH. **The development of the cranial arteries in the human embryo.** *Contrib Embryol* 1948;32:205–62
11. Abbie AA. **The morphology of the fore-brain arteries, with especial reference to the evolution of the basal ganglia.** *J Anat* 1934;68:433–70 Medline
12. Lasjaunias P, Brugge KG, Berenstein A. *Surgical Neuroangiography*. New York: Springer-Verlag; 2006
13. Uchino A, Saito N, Takahashi M, et al. **Cerebral arterial variations associated with Moyamoya disease diagnosed by MR angiography.** *Neuroradiol J* 2014;27:697–701 CrossRef Medline
14. Komiyama M, Nakajima H, Nishikawa M, et al. **High incidence of persistent primitive arteries in moyamoya and quasi-moyamoya diseases.** *Neurol Med Chir (Tokyo)* 1999;39:416–20; discussion 420–22 CrossRef Medline

Segmentation of the Globus Pallidus Internus Using Probabilistic Diffusion Tractography for Deep Brain Stimulation Targeting in Parkinson Disease

E.H. Middlebrooks, I.S. Tuna, S.S. Grewal, L. Almeida, M.G. Heckman, E.R. Lesser, K.D. Foote, M.S. Okun, and V.M. Holanda

ABSTRACT

BACKGROUND AND PURPOSE: Although globus pallidus internus deep brain stimulation is a widely accepted treatment for Parkinson disease, there is persistent variability in outcomes that is not yet fully understood. In this pilot study, we aimed to investigate the potential role of globus pallidus internus segmentation using probabilistic tractography as a supplement to traditional targeting methods.

MATERIALS AND METHODS: Eleven patients undergoing globus pallidus internus deep brain stimulation were included in this retrospective analysis. Using multidirection diffusion-weighted MR imaging, we performed probabilistic tractography at all individual globus pallidus internus voxels. Each globus pallidus internus voxel was then assigned to the 1 ROI with the greatest number of propagated paths. On the basis of deep brain stimulation programming settings, the volume of tissue activated was generated for each patient using a finite element method solution. For each patient, the volume of tissue activated within each of the 10 segmented globus pallidus internus regions was calculated and examined for association with a change in the Unified Parkinson Disease Rating Scale, Part III score before and after treatment.

RESULTS: Increasing volume of tissue activated was most strongly correlated with a change in the Unified Parkinson Disease Rating Scale, Part III score for the primary motor region (Spearman $r = 0.74$, $P = .010$), followed by the supplementary motor area/premotor cortex (Spearman $r = 0.47$, $P = .15$).

CONCLUSIONS: In this pilot study, we assessed a novel method of segmentation of the globus pallidus internus based on probabilistic tractography as a supplement to traditional targeting methods. Our results suggest that our method may be an independent predictor of deep brain stimulation outcome, and evaluation of a larger cohort or prospective study is warranted to validate these findings.

ABBREVIATIONS: DBS = deep brain stimulation; FGATIR = fast gray matter acquisition T1 inversion recovery; GPe = globus pallidus externus; GPi = globus pallidus internus; M1 = primary motor cortex; MNI = Montreal Neurological Institute; PD = Parkinson disease; SMA/PMC = supplementary motor area/premotor cortex; SN = substantia nigra; STN = subthalamic nucleus; UPDRS III = Unified Parkinson Disease Rating Scale, Part III; VTA = volume of tissue activated

Globus pallidus internus (GPi) deep brain stimulation (DBS) is an established treatment for Parkinson disease (PD).[1] Successful motor symptom reduction has been validated in randomized clinical trials with DBS of the GPi.[2,3] Similar to other conditions and other targets, variability in outcomes remains, and the underpinning of such variability remains incompletely understood. While there are numerous potential mechanistic bases for these outcomes, 1 potential explanation lies in the limitations of preoperative functional targeting.

Traditional methods of indirect targeting, whereby DBS-lead targets are defined by a rigid coordinate-based stereotaxy using readily identifiable macrostructures (eg, coordinate-based localization relative to a line through the anterior/posterior commissure line), have become outdated as stand-alone targeting methods. The use of more sophisticated direct targeting has become a standard for GPi-DBS lead implantation, using MR imaging sequences such as fast gray matter acquisition T1 inversion recovery (FGATIR)[4] and diffusion tensor imaging tractography,[5,6] as well as software advancements in targeting (eg, high-quality deformable brain atlases).[4] Intraoperatively, the functional targeting is often supplemented by careful microelectrode recording and macrostimulation, fine-tuning the final position of the DBS electrode before the lead is secured in place. Nevertheless, preoperative targeting and subsequent DBS programming based on image-

Received December 17, 2017; accepted after revision February 24, 2018.

From the Departments of Radiology (E.H.M.) and Neurosurgery (S.S.G.) and Division of Biomedical Statistics and Informatics (M.G.H., E.R.L.), Mayo Clinic, Jacksonville, Florida; Departments of Radiology (I.S.T.), Neurology (L.A., M.S.O.), and Neurosurgery (K.D.F.), University of Florida, Gainesville, Florida; and Center of Neurology and Neurosurgery Associates (V.M.H.), BP-A Beneficência Portuguesa de São Paulo, São Paulo, Brazil.

Please address correspondence to Erik H. Middlebrooks, MD, 4500 San Pablo Rd, Jacksonville, FL 32224; e-mail: Middlebrooks.Erik@mayo.edu

Indicates article with supplemental on-line photo.

http://dx.doi.org/10.3174/ajnr.A5641

guided functional information are not routinely performed at many institutions worldwide and are being recognized by multiple groups as a potential strategy for surgical planning.[7,8]

With continued advances in diffusion-weighted MR imaging during the preceding decade, it has become possible to routinely obtain high-quality multidirection diffusion imaging in the clinical setting. Diffusion-based probabilistic tractography has previously been used in the segmentation of various deep nuclei based on structural-connectivity profiles, particularly within the thalamus.[9-12] A previous study examining such MR imaging probabilistic tractography to segment the globus pallidus internus in healthy controls found mixed results with multiple datasets and failed to demonstrate some known corticopallidal connections.[13]

In the current pilot study, we examined the role of segmentation of the globus pallidus internus based on probabilistic tractography in the setting of deep brain stimulation. To our knowledge, there are no prior studies evaluating globus pallidus segmentation on the basis of probabilistic tractography in patients with GPi-DBS. On the basis of our experience with DBS localization in the GPi, we believe that the optimal GPi target for control of movement symptoms lies within the posterior ventral GPi. Anatomic and physiologic studies in primates and humans have also shown that the sensorimotor territory of the GPi is ventral and posterior.[14,15] Thus, we hypothesized that clinical improvement will correlate with the volume of tissue activated (VTA) overlapping the GPi regions most connected to the primary and supplementary motor areas.

MATERIALS AND METHODS

The use of the study data was approved by the University of Florida institutional review board. The study design was a retrospective analysis of consecutive patients with the diagnosis of PD undergoing GPi-DBS who had undergone multidirection diffusion-weighted MR imaging as part of their preoperative targeting MR imaging. Seventeen such patients were identified. Six patients were excluded from further analysis (1 patient had bilateral DBS leads placed with no Unified Parkinson Disease Rating Scale, Part III [UPDRS III] score recorded between lead placements, 1 patient did not have the needed raw diffusion data archived, 2 patients had inadequate postoperative imaging for lead localization, and 2 patients had excessive head motion). Eleven patients underwent further analysis. Three of the 11 patients underwent bilateral lead placement at 2 separate time points. For these 3 patients, only the information obtained from the first lead placement was used in this study to satisfy the statistical assumption of independent measurements.

Chart Review

A retrospective chart review was conducted for the collection of relevant clinical and demographic data. Demographic and disease information collected included age at DBS, sex, disease duration, and handedness. Each patient's most effective stimulation settings were also recorded. Settings were initially determined to maximize symptom control and minimize stimulation-induced adverse effects. The most common adverse effects were pulling of the contralateral arm and/or leg due to stimulation of the posterior limb of the internal capsule when the deeper contacts were used in some patients. The UPDRS III score was measured at the preoperative visit and the 6-month follow-up; change in the UPDRS III score (preoperative minus 6-month follow-up) was calculated and was the primary outcome measure of the study. Tremor-suppressing medications were held stable at the preoperative optimized dose for the duration of the study.

Image Acquisition

All patients underwent preoperative MR imaging for DBS planning. As part of the imaging protocol, patients underwent a T1-weighted MPRAGE and multidirection diffusion-weighted imaging. All scans were obtained on a 3T Verio scanner (Siemens, Erlangen, Germany) using a 12-channel head coil.

The multidirection diffusion-weighted imaging was acquired at an isotropic resolution of $1.6 \times 1.6 \times 1.6$ mm with no gap for a total of 70 slices. A total of 64 diffusion directions were acquired at a b-value of 1000 s/mm^2. Total imaging time was 12 minutes 14 seconds (TR = 10,800 ms, TE = 100 ms, phase partial Fourier = 5/8, generalized autocalibrating partially parallel acquisition = 2, bandwidth = 1098 Hz/Px, and EPI factor = 130).

The MPRAGE imaging was acquired in the axial plane after the administration of gadolinium-based intravenous contrast (0.1 mm/kg). Imaging parameters included an in-plane resolution of 0.6×0.6 mm with a slice thickness of 1.0 mm, TR = 1720 ms, TE = 3.29 ms, TI = 865 ms, flip angle = 9°, and bandwidth = 170 Hz/Px. Image acceleration included a 7/8 phase partial Fourier imaging and generalized autocalibrating partially parallel acquisition = 2.

Additionally, a volumetric FGATIR sequence was obtained, as previously reported,[4] for targeting purposes.

All postoperative CT scans were obtained on an Aquilion scanner (Toshiba Medical Systems, Tokyo, Japan) using a 0.5×0.5 mm in-plane resolution with a slice thickness of 1 mm.

Surgical Procedure

GPi-DBS was planned contralateral to the patient's most symptomatic upper extremity. All surgical procedures were performed by the same surgeon (K.D.F.). For targeting, brain MR imaging was acquired before the initial procedure. On the day of the operation, a Cosman-Roberts-Wells head ring was placed, and stereotactic high-resolution CT was performed. In-house software was used to fuse the CT and MR imaging data. The postcontrast T1-weighted MPRAGE and FGATIR MRI sequences were paired with a deformable brain atlas in order to identify the corpus striatum, the globus pallidus, and the optic tract anatomy. Single microelectrode recording was sequentially performed to establish the border between the globus pallidus externus (GPe) and the GPi by the sound of the border cells. The inferior GPi border was established by the sound of the optic tract. Macrostimulation was performed to assure the best lead position.

ROI

In contrast to the prior study in healthy controls, we limited our connectivity targets to known predominant connections of the globus pallidus internus.[13] ROIs for probabilistic tractography were defined in Montreal Neurological Institute (MNI) template space and created using the FSLView "atlas" function (https://fsl.fmrib.ox.ac.uk/fsl/fslwiki/FslView). Masks were created for the

caudate, GPe, GPi, putamen, and subthalamic nucleus (STN) from the MNI Basal Ganglia Human Area Template.[16] The substantia nigra (SN) mask was generated using atlasing of the basal ganglia.[17] Cortical ROIs were concatenated for the primary motor cortex (M1) and supplementary motor area and premotor cortex (SMA/PMC) from the MNI Human Motor Area Template.[18] Masks for the prefrontal cortex and thalamus were generated from the Harvard-Oxford Cortical and Subcortical Atlases, respectively.[19-22] Last, the pedunculopontine nucleus was manually drawn in MNI space to approximate the location of this poorly visualized structure within the midbrain-pontine tegmentum inferior, posterior, and lateral to the red nucleus.

Imaging Preprocessing

Diffusion data underwent standard preprocessing consisting of re-alignment and eddy current correction using the FMRIB Software Library (FSL; http://www.fmrib.ox.ac.uk/fsl). The diffusion-weighted data were normalized to the MNI_ICBM_2009b_NLIN_ASYM atlas space (http://neuro.debian.net/pkgs/mni-icbm152-nlin-2009c.html).

Preoperative MPRAGE and postoperative CT were coregistered by a 2-stage linear registration consisting of a rigid and subsequent affine registration used in the Advanced Normalization Tools software package (http://stnava.github.io/ANTs/).[19] Next, these volumes were also normalized to the MNI_ICBM_2009b_NLIN_ASYM atlas space with the SyN registration approach in the Advanced Normalization Tools.[23,24]

Diffusion Data Processing

Voxelwise diffusion parameters were estimated from the preprocessed diffusion data using a Markov Chain Monte Carlo sampling in the FSL BEDPOSTX (https://fsl.fmrib.ox.ac.uk/fsl/fslwiki/FDT) function. Next, probabilistic tractography was performed with PROBTRACKX2 (https://fsl.fmrib.ox.ac.uk/fsl/fslwiki/FDT) in FSL to calculate a probability of connection of each voxel within the left and right GPi masks to each of the 10 previously defined target masks. Five thousand total fiber tracks were generated with a curvature threshold = 0.2, step length = 0.5 mm, and maximum steps = 2000. Last, all GPi voxels were classified by the 1 target mask with the greatest number of propagated paths by the FSL "find_the_biggest" function.

Volume of Tissue Activated Modeling

The DBS electrodes were localized on the normalized postoperative CT using the Lead-DBS software package (http://www.lead-dbs.org).[25] Manual corrections, when necessary, were performed to ensure the accuracy of the contact locations. Once contact locations were determined, the VTA was simulated using the patient's most effective programming settings, as implemented in Horn et al.[8] Briefly, a finite-element method solution was derived using a tissue-specific conductivity model. The volume of overlap between each patient's simulated VTA and each of the 10 segments within the patient-specific GPi segmentation was calculated.

Statistical Analysis

Continuous variables were summarized with the sample median and range. Categoric variables were summarized with the number and percentage of patients. The degree of association between the VTA in each of the 10 different brain regions and the change in the UPDRS III score from preoperative to 6-month follow-up visits were evaluated by estimating the Spearman correlation coefficient *r*. Although Spearman tests of correlation were also performed, due to the pilot nature of the study and the corresponding small sample size, results of these tests are primarily given for completeness, and emphasis should be placed on the Spearman correlation coefficient *r* values when interpreting results. For brain regions in which <3 patients had a value greater than zero regarding the VTA, the Spearman correlation was not assessed because these regions were essentially noninformative due to lack of variability in measures. Associations of age and disease duration with change in the UPDRS III score were examined in a similar manner. *P* values $\leq .05$ were considered statistically significant. All statistical tests were 2-sided. Statistical analyses were performed using SAS (Version 9.4; SAS Institute, Cary, North Carolina) and R Statistical and computing software (Version 3.2.3; http://www.r-project.org).

RESULTS

A summary of patient characteristics, DBS characteristics, and outcomes is shown in the Table. The median age at DBS was 62 years (range, 49–73 years), almost all patients were male ($n = 10$ [91%]), and the median disease duration was 9 years (range, 6–16 years). The median UPDRS III score was 42 (range, 27–55) before the operation and 21 (range, 13–40) at 6-month follow-up, corresponding to a median decrease of 15 (range, 12-point increase to a 31-point decrease).

Group averages for each of the 10 segmented regions are shown in Fig 1. Of the 10 GPi segments assessed, only 4 (GPe, M1, SMA/PMC, SN) had at least some VTA in >2 patients (Table and On-line Figure) and were therefore evaluated further for association with change in the UPDRS III score. For these 4 GPi segments, the VTA was most strongly correlated with change in the UPDRS III score for the segment most connected to the M1 region (Spearman $r = 0.74$, $P = .010$, Fig 2), followed by the SMA/PMC (Spearman $r = 0.47$, $P = .15$, Fig 2), GPe (Spearman $r = 0.16$, $P = .64$, Fig 2), and SN (Spearman $r = 0.15$, $P = .67$, Fig 2) regions. Of note, we did not observe a strong correlation with change in the UPDRS III score for either age at DBS (Spearman *r*, -0.23, $P = .49$) or disease duration (Spearman $r = -0.08$, $P = .81$), indicating that these 2 variables would have had minimal confounding influence on the correlations between the VTA and change in the UPDRS III score.

DISCUSSION

The GPi is considered the primary output structure of the basal ganglia and is known to have an increase in its neuronal activity before the onset of PD motor symptoms.[26] GPi-DBS has been successfully used to abolish dyskinesias in patients with treatment-resistant hyperkinetic movements, tremor, and dystonia in PD.[15,27] In this pilot study, we assessed a novel method of segmentation of the GPi based on probabilistic tractography. We found that a greater VTA in the somatosensory region of the GPi within our defined M1 segment and, to a lesser degree, the SMA/

Patient and deep brain stimulation characteristics and outcomes[a]

Variable	Summary (*N* = 11)
Patient characteristics	
Age at DBS (mean) (range) (yr)	62 (49–73)
Male sex (No.) (%)	10 (90.9%)
Disease duration (mean) (range) (yr)	9 (6–16)
Handedness (right) (No.) (%)	10 (90.9%)
Deep brain stimulation information	
Volume of tissue activated (mm^3)	
Caudate	
No. (%) of patients with values of >0	0 (0.0%)
Median (minimum, maximum)	0.0 (0.0, 0.0)
GPe	
No. (%) of patients with values of >0	11 (100.0%)
Median (minimum, maximum)	19.3 (0.8, 78.4)
M1	
No. (%) of patients with values of >0	8 (72.7%)
Median (minimum, maximum)	3.6 (0.0, 42.9)
PPN	
No. (%) of patients with values of >0	1 (9.1%)
Median (minimum, maximum)	0.0 (0.0, 7.9)
PFC	
No. (%) of patients with values of >0	2 (18.2%)
Median (minimum, maximum)	0.0 (0.0, 5.5)
Putamen	
No. (%) of patients with values of >0	2 (18.2%)
Median (minimum, maximum)	0.0 (0.0, 38.8)
SMA/PMC	
No. (%) of patients with values of >0	6 (54.6%)
Median (minimum, maximum)	4.8 (0.0, 46.5)
STN	
No. (%) of patients with values of >0	0 (0.0%)
Median (minimum, maximum)	0.0 (0.0, 0.0)
SN	
No. (%) of patients with values of >0	8 (72.7%)
Median (minimum, maximum)	5.8 (0.0, 36.3)
Thalamus	
No. (%) of patients with values of >0	1 (9.1%)
Median (minimum, maximum)	0.0 (0.0, 0.5)
Outcomes	
Preoperative UPDRS III score (range)	42 (27–55)
6-Month follow-up UPDRS III score (range)	21 (13–40)
Change in UPDRS III score (preoperative minus 6-month follow-up) (range)	15 (−12–31)

Note:—PFC indicates prefrontal cortex; PPN, pedunculopontine nucleus.
[a] The sample median (minimum, maximum) is given for continuous variables.

PMC segment, corresponded with greater improvement in the UPDRS III score.

The globus pallidus, with the putamen, forms the lentiform nucleus and primarily exhibits inhibitory control on movement.[28] The GPi has extensive connections to deep brain structures. A predominant output of the GPi consists of pallidothalamic connections comprising the ansa lenticularis and lenticular fasciculus (components of the thalamic fasciculus). The ansa lenticularis and lenticular fasciculus exit the GPi along the inferomedial and medial borders, respectively. These projections largely consist of efferent fibers to the thalamic ventralis oralis nucleus, mediodorsal nucleus, and centromedian parafascicular complex.[29-31] Additional fibers within the ansa lenticularis connect the GPi to the STN before formation of the thalamic fasciculus, which terminates in the thalamus.[32] These STN-GPi connections may drive increased excitation within the GPi in PD, secondary to diminished inhibition of the STN from the GPe.[32,33] Nearly 15% of GPi fibers connect to the SN, arising from the medial inferior border of the GPi.[34] Connections have also been illustrated between the GPi and pedunculopontine nucleus, exiting from the medial portion of the GPi.[35-38] Along the border between the GPi and GPe, inhibitory fibers exit the medial GPe and connect via the lateral border of the GPi.[33,34] Last, the posterolateral border of the GPi has been shown to connect to the adjacent putamen and may produce a decrease in GPi inhibition in PD secondary to decreased putaminal excitation.[13,39,40]

While many of these deep connections of the GPi have been well-described, there has historically been little attention to direct cortical connections from the GPi. Tracer studies in rats and monkeys, as well as human DTI studies, have demonstrated the presence of these corticopallidal fibers, particularly in relation to the prefrontal cortex, SMA, pre-SMA, primary motor, and primary sensory cortices.[41-45] Additional information regarding the connectivity of the GPi to the motor cortex (M1 region) has been elucidated from studies measuring local field potentials, where β oscillations in the range of 13–40 Hz have been recorded from the GPi in a movement-related manner, similar to recordings noted in the primary motor cortex.[46-48] Because the GPi is the main output structure of the basal ganglia, increased excitation of this structure produces some of the hypomotor symptoms seen in PD. However, the role of these corticopallidal connections in the pathophysiology and treatment of movement disorders has not been well-investigated to date. We hypothesized that the efficacy of DBS could be secondary to suppressing the connections arising from the M1 region.

In our study, we could elucidate direct connections between the GPi and cortex, specifically the prefrontal cortex, SMA, PMC, and M1 regions. As previously reported by Milardi et al[43] using constrained spheric deconvolution, these fiber pathways are distinct from the hyperdirect pathway passing through the internal capsule. The results of this pilot study suggest that a larger VTA in the segment corresponding to dominant connectivity to the M1 region in patients with PD may be correlated with a greater improvement in the UPDRS III score. Findings were similar, though weaker, for the SMA/PMC segment, whereas no notable correlation with change in the UPDRS III score was observed for the VTA in the globus pallidus externus and SN segments. The idea that structural and functional connectivity measures represent independent outcome predictors has been previously shown in other treatment targets.[8,49-51] For instance, Horn et al[8] have shown that connectivity measures within the STN are potentially independent outcome predictors in DBS of PD. Most interesting, they found a positive correlation with the clinical response within the STN and connectivity to the SMA, while a negative correlation with the clinical response was found with the primary motor cortex.[8] This anticorrelation between the DBS electrode and the primary motor cortex presenting in the STN, and not in GPi, may be explained by the development of motor adverse effects, such as verbal fluency problems,[52] when stimulating the M1 region in the smaller STN.

Remarkably, in contradistinction to the prior study by da Silva et al,[13] we found that the posterior ventral portion of the GPi corresponds to a corticopallidal area most connected to the primary motor cortex. The area most connected to the SMA/PMC

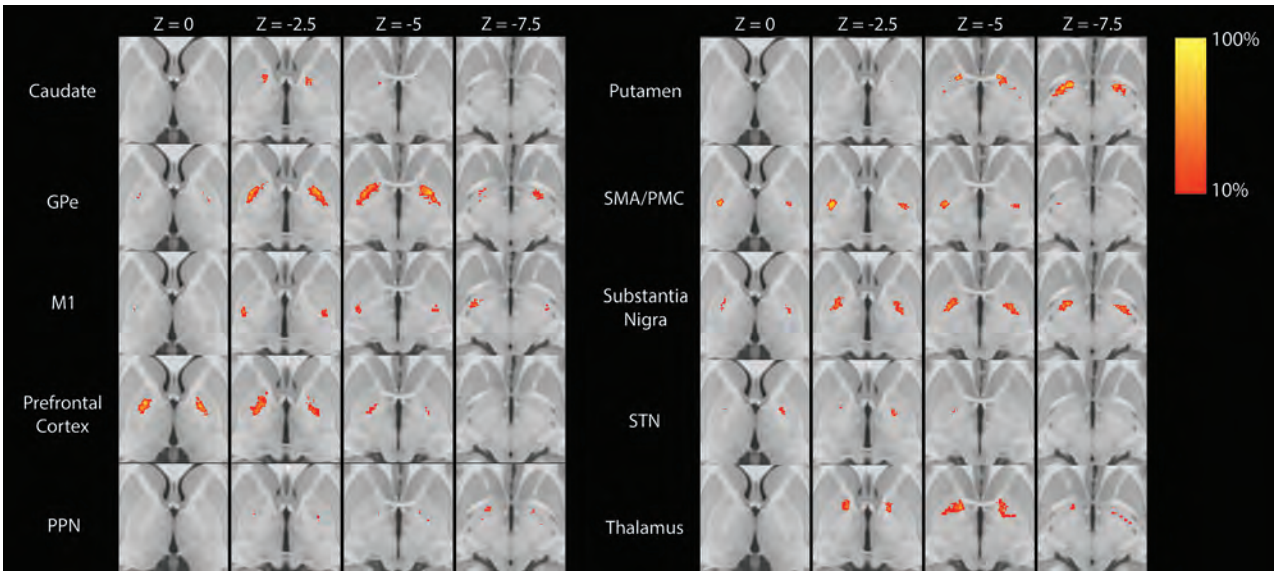

FIG 1. Statistical heat maps illustrating the group average location of each of the 10 GPi segments. Maps are thresholded at >10%. PPN indicates pedunculopontine nucleus.

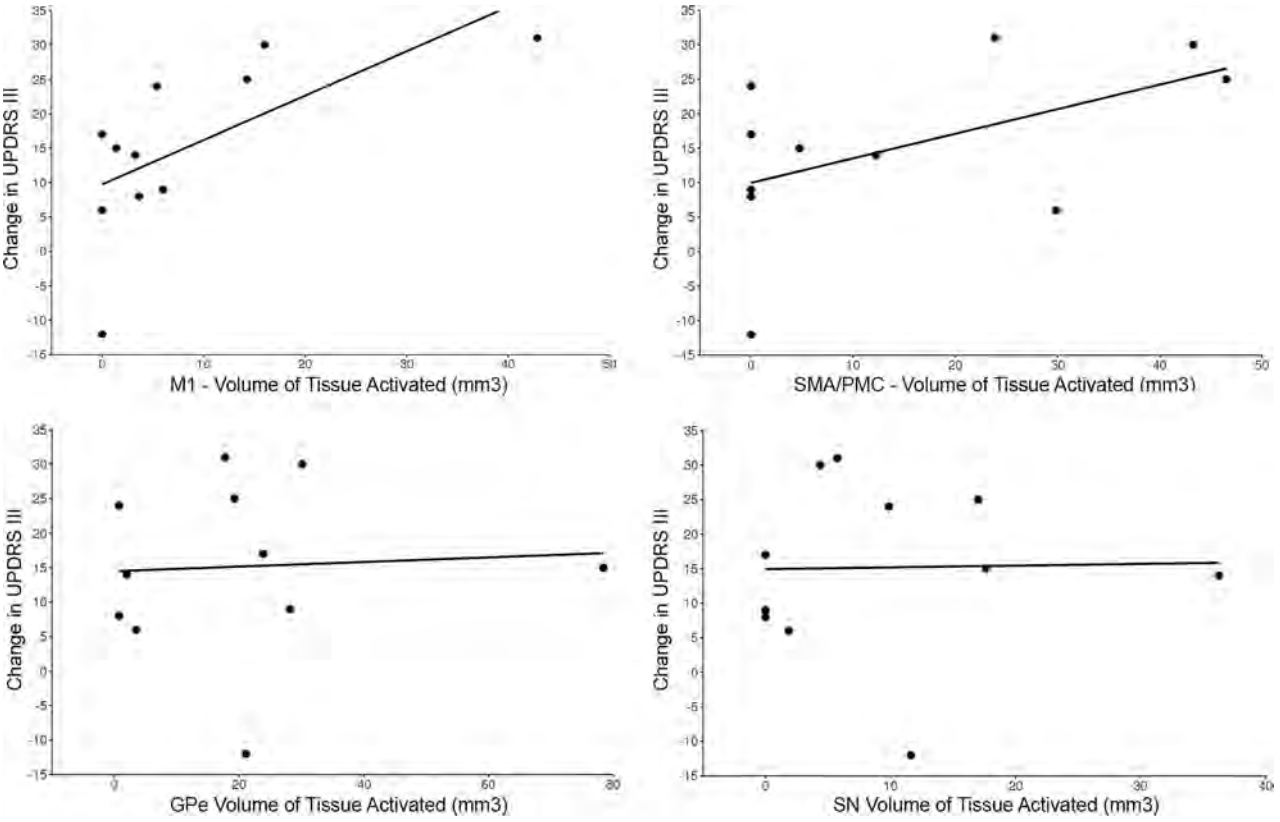

FIG 2. Scatterplots showing the change in the UPDRS score relative to volumes of tissue activated in the primary motor segment (upper left), supplementary motor area/premotor cortex segment (upper right), globus pallidus externus segment (lower left), and substantia nigra segment (bottom right).

was in proximity yet slightly more ventral in the posterior GPi (Fig 3). These findings are like those reported in prior animal tracer and DTI studies.[41-45] The basis for the discrepancy with the prior study is uncertain. One potential explanation is the reduction of voxel volume by greater than a factor of 3, potentially allowing better discrimination of these small areas of corticopallidal connectivity.[13] Also, differences in the number of diffusion directions could potentially alter angular resolution, though the number of diffusion directions obtained in the prior study was not published.[13]

Accuracy in structural and functional targeting is vital for successful deep brain stimulation. The GPi shows more variation in position relative to the midpoint of the line traversing the anterior/posterior commissure line compared with other deep nuclei. This

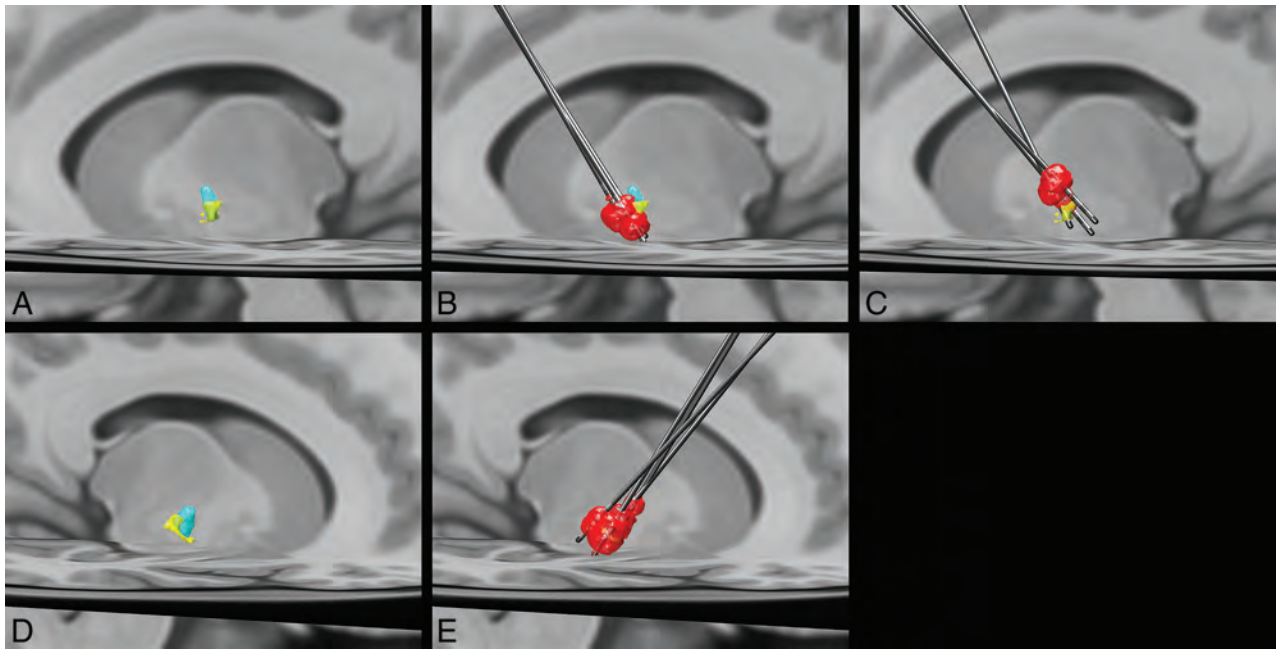

FIG 3. Left (*A*) and right (*D*) group average volumes for segments with maximal connectivity to the primary motor cortex (yellow) and supplementary motor area/premotor cortex (light blue). *B*, Left DBS leads and volumes of tissue activated (red) for the 3 patients with improvement in the UPDRS III of >10 (mean improvement in the score = 26.7) after DBS. A more ventral location and greater overlap with the primary motor cortex segment can be appreciated. *C*, Left DBS leads and volumes of tissue activated (red) in the 3 patients with the least improvement in the UPDRS III score (mean improvement in the score = 0.7) show a more dorsal location of the volume of tissue activated with less overlap with the primary motor cortex segment of the GPi. *E*, Right DBS leads and volumes of tissue activated. All patients had an improvement in the UPDRS III score of >10 (mean improvement in the score = 19).

variation may have partly contributed to the inconsistency in outcomes of early studies of GPi-DBS. Substantial improvement in targeting by direct structural targeting, such as FGATIR MR imaging,[4] and sophisticated targeting software using atlas overlays and a deformable brain atlas have contributed to improved anatomic targeting.[4] The supplementation of targeting in functional neurosurgery using connectivity measures, such as DTI, is also a promising technique.[5,6,8] Despite these advances, improvement in preoperative functional mapping within the deep nuclei is needed to maximize the benefits of direct-targeting methods.

While debate exists on the optimal target nucleus, 1 advantage of GPi stimulation versus STN is the size of the GPi, meaning a lower probability of off-target stimulation and unintended adverse effects. However, the need for a larger VTA to achieve a desired therapeutic effect in the GPi means increased energy usage and decreased battery life. Improvement in preoperative targeting by incorporating measures of connectivity may allow the maximization of the therapeutic effect within the GPi and help overcome some of these drawbacks by providing a more specific and focused treatment target. Given the lower rate of adverse stimulation effects, the GPi could become an even more attractive target.

Our study has several notable limitations. The greatest limitation is the small sample size, which results in a lack of precision of estimated correlations. Although we did identify 1 statistically significant association despite the small sample size, larger studies are needed to better elucidate the role of our methods in supplementing preoperative GPi targeting. However, the small sample size is appropriate for the pilot nature of the study. Second, the retrospective nature only allows modeling of VTAs from data that were historically recorded, limiting comparison of different stimulation parameters in each patient. Third, the role of corticopallidal connections in PD pathophysiology warrants further exploration, given the paucity of existing knowledge. Because these connections in humans have largely been described by noninvasive MR tractography, further confirmation of their existence in anatomic specimens is needed. Last, the methods used in this study inherently oversimplify the connectivity profiles of the VTA because each voxel is assigned to only the target of the most propagated paths. While this feature potentially limits the methods in understanding the pathophysiology behind GPi-DBS, the goal of this investigation was the establishment of a reliable and reproducible subject-specific functional preoperative target for GPi-DBS placement.

CONCLUSIONS

Despite advances in preoperative targeting for DBS, reproducible methods for defining subject-specific connectivity targets with the GPi are lacking. Our preliminary study has shown an independent predictive value of connectivity-based segmentation of the GPi on patient outcomes. Our clinically feasible technique may be of benefit in supplementing direct structural targeting, as well as in DBS programming, to maximize therapeutic outcomes. Larger studies will be needed to further corroborate these findings.

Disclosures: Erik H. Middlebrooks—*UNRELATED*: *Grant*: Varian Medical Systems; *Consultancy:* Varian Medical Systems. Kelly D. Foote—*UNRELATED*: *Consultancy*: Medtronic; *Grants/Grants Pending*: Medtronic, Boston Scientific, St. Jude.* Michael S. Okun—*UNRELATED*: *Grant*: National Institutes of Health, *Comments*: DBS re-

search is supported by R01 NR014852 and R01NS096008.* *Money paid to the institution.

REFERENCES

1. Obeso JA, Olanow CW, Rodriguez-Oroz MC, et al; Deep-Brain Stimulation for Parkinson's Disease Study Group. **Deep-brain stimulation of the subthalamic nucleus or the pars interna of the globus pallidus in Parkinson's disease.** *N Engl J Med* 2001;345:956–63 CrossRef Medline
2. Okun MS, Fernandez HH, Wu SS, et al. **Cognition and mood in Parkinson's disease in subthalamic nucleus versus globus pallidus interna deep brain stimulation: the COMPARE trial.** *Ann Neurol* 2009;65:586–95 CrossRef Medline
3. Odekerken VJ, van Laar T, Staal MJ, et al. **Subthalamic nucleus versus globus pallidus bilateral deep brain stimulation for advanced Parkinson's disease (NSTAPS study): a randomised controlled trial.** *Lancet Neurol* 2013;12:37–44 CrossRef Medline
4. Sudhyadhom A, Haq IU, Foote KD, et al. **A high resolution and high contrast MRI for differentiation of subcortical structures for DBS targeting: the Fast Gray Matter Acquisition T1 Inversion Recovery (FGATIR).** *Neuroimage* 2009;47(Suppl 2):T44–52 CrossRef Medline
5. Alho AT, Hamani C, Alho EJ, et al. **Magnetic resonance diffusion tensor imaging for the pedunculopontine nucleus: proof of concept and histological correlation.** *Brain Struct Funct* 2017;222:2547–58 CrossRef Medline
6. Sajonz BE, Amtage F, Reinacher PC, et al. **Deep Brain Stimulation for Tremor Tractographic Versus Traditional (DISTINCT): study protocol of a randomized controlled feasibility trial.** *JMIR Res Protoc* 2016;5:e244 CrossRef Medline
7. Pouratian N, Zheng Z, Bari AA, et al. **Multi-institutional evaluation of deep brain stimulation targeting using probabilistic connectivity-based thalamic segmentation.** *J Neurosurg* 2011;115:995–1004 CrossRef Medline
8. Horn A, Reich M, Vorwerk J, et al. **Connectivity predicts deep brain stimulation outcome in Parkinson disease.** *Ann Neurol* 2017;82:67–78 CrossRef Medline
9. Behrens TE, Berg HJ, Jbabdi S, et al. **Probabilistic diffusion tractography with multiple fibre orientations: what can we gain?** *Neuroimage* 2007;34:144–55 CrossRef Medline
10. Behrens TE, Johansen-Berg H, Woolrich MW, et al. **Non-invasive mapping of connections between human thalamus and cortex using diffusion imaging.** *Nat Neurosci* 2003;6:750–57 CrossRef Medline
11. Traynor C, Heckemann RA, Hammers A, et al. **Reproducibility of thalamic segmentation based on probabilistic tractography.** *Neuroimage* 2010;52:69–85 CrossRef Medline
12. Elias WJ, Zheng ZA, Domer P, et al. **Validation of connectivity-based thalamic segmentation with direct electrophysiologic recordings from human sensory thalamus.** *Neuroimage* 2012;59:2025–34 CrossRef Medline
13. da Silva NM, Ahmadi SA, Tafula SN, et al. **A diffusion-based connectivity map of the GPi for optimised stereotactic targeting in DBS.** *Neuroimage* 2017;144:83–91 CrossRef Medline
14. Parent A, Hazrati LN. **Functional anatomy of the basal ganglia, I: the cortico-basal ganglia-thalamo-cortical loop.** *Brain Res Brain Res Rev* 1995;20:91–127 CrossRef Medline
15. Tisch S, Zrinzo L, Limousin P, et al. **Effect of electrode contact location on clinical efficacy of pallidal deep brain stimulation in primary generalised dystonia.** *J Neurol Neurosurg Psychiatry* 2007;78:1314–19 CrossRef Medline
16. Prodoehl J, Yu H, Little DM, et al. **Region of interest template for the human basal ganglia: comparing EPI and standardized space approaches.** *Neuroimage* 2008;39:956–65 CrossRef Medline
17. Keuken MC, Forstmann BU. **A probabilistic atlas of the basal ganglia using 7 T MRI.** *Data Brief* 2015;4:577–82 CrossRef Medline
18. Mayka MA, Corcos DM, Leurgans SE, et al. **Three-dimensional locations and boundaries of motor and premotor cortices as defined by functional brain imaging: a meta-analysis.** *Neuroimage* 2006;31:1453–74 CrossRef Medline
19. Makris N, Goldstein JM, Kennedy D, et al. **Decreased volume of left and total anterior insular lobule in schizophrenia.** *Schizophr Res* 2006;83:155–71 CrossRef Medline
20. Frazier JA, Chiu S, Breeze JL, et al. **Structural brain magnetic resonance imaging of limbic and thalamic volumes in pediatric bipolar disorder.** *Am J Psychiatry* 2005;162:1256–65 CrossRef Medline
21. Desikan RS, Ségonne F, Fischl B, et al. **An automated labeling system for subdividing the human cerebral cortex on MRI scans into gyral based regions of interest.** *Neuroimage* 2006;31:968–80 CrossRef Medline
22. Goldstein JM, Seidman LJ, Makris N, et al. **Hypothalamic abnormalities in schizophrenia: sex effects and genetic vulnerability.** *Biol Psychiatry* 2007;61:935–45 Medline
23. Avants BB, Epstein CL, Grossman M, et al. **Symmetric diffeomorphic image registration with cross-correlation: evaluating automated labeling of elderly and neurodegenerative brain.** *Med Image Anal* 2008;12:26–41 CrossRef Medline
24. Fonov V, Evans AC, Botteron K, et al; Brain Development Cooperative Group. **Unbiased average age-appropriate atlases for pediatric studies.** *Neuroimage* 2011;54:313–27 CrossRef Medline
25. Horn A, Kühn AA. **Lead-DBS: a toolbox for deep brain stimulation electrode localizations and visualizations.** *Neuroimage* 2015;107:127–35 CrossRef Medline
26. Wichmann T, Dostrovsky JO. **Pathological basal ganglia activity in movement disorders.** *Neuroscience* 2011;198:232–44 CrossRef Medline
27. McCairn KW, Iriki A, Isoda M. **Common therapeutic mechanisms of pallidal deep brain stimulation for hypo- and hyperkinetic movement disorders.** *J Neurophysiol* 2015;114:2090–104 CrossRef Medline
28. Yagmurlu K, Vlasak AL, Rhoton AL Jr. **Three-dimensional topographic fiber tract anatomy of the cerebrum.** *Neurosurgery* 2015;11(Suppl 2):274–305; discussion 305 CrossRef Medline
29. Baron MS, Sidibé M, DeLong MR, et al. **Course of motor and associative pallidothalamic projections in monkeys.** *J Comp Neurol* 2001;429:490–501 Medline
30. Severin CM, Young PA, Massapust LC. **Pallidothalamic projections in the rat.** *J Comp Neurol* 1976;166:491–502 CrossRef Medline
31. Gallay MN, Jeanmonod D, Liu J, et al. **Human pallidothalamic and cerebellothalamic tracts: anatomical basis for functional stereotactic neurosurgery.** *Brain Struct Funct* 2008;212:443–63 CrossRef Medline
32. Hashimoto T, Elder CM, Okun MS, et al. **Stimulation of the subthalamic nucleus changes the firing pattern of pallidal neurons.** *J Neurosci* 2003;23:1916–23 Medline
33. Delong MR, Georgopoulos AP, Crutcher MD, et al. **Functional organization of the basal ganglia: contributions of single-cell recording studies.** *Ciba Found Symp* 1984;107:64–82 Medline
34. Plantinga BR, Roebroeck A, Kemper VG, et al. **Ultra-high field MRI post mortem structural connectivity of the human subthalamic nucleus, substantia nigra, and globus pallidus.** *Front Neuroanat* 2016;10:66 CrossRef Medline
35. Perez-Costas E, Melendez-Ferro M, Roberts RC. **Basal ganglia pathology in schizophrenia: dopamine connections and anomalies.** *J Neurochem* 2010;113:287–302 CrossRef Medline
36. Martinez-Gonzalez C, Bolam JP, Mena-Segovia J. **Topographical organization of the pedunculopontine nucleus.** *Front Neuroanat* 2011;5:22 CrossRef Medline
37. Shink E, Sidibé M, Smith Y. **Efferent connections of the internal globus pallidus in the squirrel monkey, II: topography and synaptic organization of pallidal efferents to the pedunculopontine nucleus.** *J Comp Neurol* 1997;382:348–63 Medline
38. Zhang J, Wang ZI, Baker KB, et al. **Effect of globus pallidus internus stimulation on neuronal activity in the pedunculopontine tegmental nucleus in the primate model of Parkinson's disease.** *Exp Neurol* 2012;233:575–80 CrossRef Medline
39. Xiao Y, Fonov V, Chakravarty MM, et al. **A dataset of multi-contrast**

population-averaged brain MRI atlases of a Parkinson's disease cohort. *Data Brief* 2017;12:370–79 CrossRef Medline
40. Detante O, Vercueil L, Thobois S, et al. **Globus pallidus internus stimulation in primary generalized dystonia: a H215O PET study.** *Brain* 2004;127:1899–908 CrossRef Medline
41. Naito A, Kita H. **The cortico-pallidal projection in the rat: an anterograde tracing study with biotinylated dextran amine.** *Brain Res* 1994;653:251–57 CrossRef Medline
42. Rozanski VE, Vollmar C, Cunha JP, et al. **Connectivity patterns of pallidal DBS electrodes in focal dystonia: a diffusion tensor tractography study.** *Neuroimage* 2014;84:435–42 CrossRef Medline
43. Milardi D, Gaeta M, Marino S, et al. **Basal ganglia network by constrained spherical deconvolution: a possible cortico-pallidal pathway?** *Mov Disord* 2015;30:342–49 CrossRef Medline
44. Akkal D, Dum RP, Strick PL. **Supplementary motor area and presupplementary motor area: targets of basal ganglia and cerebellar output.** *J Neurosci* 2007;27:10659–73 CrossRef Medline
45. Hoover JE, Strick PL. **Multiple output channels in the basal ganglia.** *Science* 1993;259:819–21 CrossRef Medline
46. Brücke C, Kempf F, Kupsch A, et al. **Movement-related synchronization of gamma activity is lateralized in patients with dystonia.** *Eur J Neurosci* 2008;27:2322–29 CrossRef Medline
47. Tsang EW, Hamani C, Moro E, et al. **Movement related potentials and oscillatory activities in the human internal globus pallidus during voluntary movements.** *J Neurol Neurosurg Psychiatry* 2012;83:91–97 CrossRef Medline
48. Talakoub O, Neagu B, Udupa K, et al. **Time-course of coherence in the human basal ganglia during voluntary movements.** *Sci Rep* 2016;6:34930 CrossRef Medline
49. Brunenberg EJL, Moeskops P, Backes WH, et al. **Structural and resting state functional connectivity of the subthalamic nucleus: identification of motor STN parts and the hyperdirect pathway.** *PLoS One* 2012;7:e39061 CrossRef Medline
50. Lambert C, Zrinzo L, Nagy Z, et al. **Confirmation of functional zones within the human subthalamic nucleus: patterns of connectivity and sub-parcellation using diffusion weighted imaging.** *Neuroimage* 2012;60:83–94 CrossRef Medline
51. Vanegas-Arroyave N, Lauro PM, Huang L, et al. **Tractography patterns of subthalamic nucleus deep brain stimulation.** *Brain* 2016;139:1200–10 CrossRef Medline
52. Dietz J, Noecker AM, McIntyre CC, et al. **Stimulation region within the globus pallidus does not affect verbal fluency performance.** *Brain Stimul* 2013;6:248–53 CrossRef Medline

Cavitary Plaques in Otospongiosis: CT Findings and Clinical Implications

P. Puac, A. Rodríguez, H.-C. Lin, V. Onofrj, F.-C. Lin, S.-C. Hung, C. Zamora, and M. Castillo

ABSTRACT

BACKGROUND AND PURPOSE: Cavitary plaques have been reported as a manifestation of otospongiosis. They have been related to third window manifestations, complications during cochlear implantation, and sensorineural hearing loss. However, their etiology and clinical implications are not entirely understood. Our purpose was to determine the prevalence, imaging findings, and clinical implications of cavitary plaques in otospongiosis.

MATERIALS AND METHODS: We identified patients with otospongiosis at a tertiary care academic medical center from January 2012 to April 2017. Cross-sectional CT images and clinical records of 47 patients (89 temporal bones) were evaluated for the presence, location, and imaging features of cavitary and noncavitary otospongiotic plaques, as well as clinical symptoms and complications in those who underwent cochlear implantation.

RESULTS: Noncavitary otospongiotic plaques were present in 86 (97%) temporal bones and cavitary plaques in 30 (35%). Cavitary plaques predominated with increasing age (mean age, 59 years; $P = .058$), mostly involving the anteroinferior wall of the internal auditory canal ($P = .003$), and their presence was not associated with a higher grade of otospongiosis by imaging ($P = .664$) or with a specific type of hearing loss ($P = .365$). No patients with cavitary plaques had third window manifestations, and those with a history of cochlear implantation ($n = 6$) did not have complications during the procedure.

CONCLUSIONS: Cavitary plaques occurred in one-third of patients with otospongiosis. Typically, they occurred in the anteroinferior wall of the internal auditory canal. There was no correlation with the degree of otospongiosis, type of hearing loss, or surgical complications. Cavitary plaques tended to present in older patients.

ABBREVIATION: IAC= internal auditory canal

Otospongiosis is an osteodystrophic disorder of the otic capsule that results in acquired hearing loss with a peak onset in the third decade.[1-3] It is believed to originate in cartilaginous remnants within the endochondral layer of the otic capsule, which are replaced by foci of more vascular bone (otospongiosis) that ultimately becomes highly calcified and sclerotic (otosclerosis).[1,2,4-7]

Otospongiosis manifests clinically when the lesion enlarges, encroaches on the stapedial annular ligament, and causes fixation of the stapes with resultant conductive hearing loss. If the lesion progresses to involve the cochlea, the result is irreversible sensorineural hearing loss or mixed hearing loss.

The formation of cavitary plaques in otospongiosis has been reported as a focal low-attenuation notch or diverticulum, most commonly located along the anteroinferior wall of the internal auditory canal (IAC).[1,7-11] Recently, isolated IAC diverticula have been associated with a different pattern of hearing loss than that seen in classic otospongiosis.[8] However, the prevalence of such diverticula or cavitary changes and their clinical implications in the setting of lesion grade or extent is not completely understood. Cavitary plaques are also thought to be a possible cause of "third window lesions," secondary to involvement of the endosteal layer of the bony labyrinth, and previous reports have also suggested

Received September 25, 2017; accepted after revision February 3, 2018.

From the Division of Neuroradiology (P.P., A.R., V.O., S.-C.H., C.Z., M.C.), Department of Radiology, University of North Carolina School of Medicine, Chapel Hill, North Carolina; Radiology Department (H.-C.L.), Cathay General Hospital, Taipei, Taiwan; and Department of Biostatistics and North Carolina Translational and Clinical Sciences Institute (F.-C.L.), University of North Carolina at Chapel Hill, Chapel Hill, North Carolina.

We acknowledge the editorial assistance of the NC Translational and Clinical Sciences Institute, which is supported by the National Center for Advancing Translational Sciences, National Institutes of Health, through grant award No. UL1TR001111.

Please address correspondence to Paulo Puac, MD, MSc, Neuroradiology Research Fellow, Department of Radiology, University of North Carolina School of Medicine, Chapel Hill, CB 7510, Room 2034, Old Infirmary Building, 101 Manning Dr, Chapel Hill, NC 27599-7510; e-mail: puacpaulo@gmail.com

Indicates open access to non-subscribers at www.ajnr.org

Indicates article with supplemental on-line photo.

http://dx.doi.org/10.3174/ajnr.A5613

that they may lead to CSF gushing or electrode misplacement during cochlear implantation.[1,4,7,12]

Therefore, the purpose of this study was the following: 1) to determine the prevalence of cavitary plaques in otospongiosis and correlate them with lesion grade, 2) describe the imaging findings and locations within the temporal bone, and 3) determine the clinical significance in terms of a pattern of hearing loss, third window manifestations, and complications after cochlear implantation.

MATERIALS AND METHODS

The radiology data base of the University of North Carolina was searched for all patients with a clinical diagnosis of otospongiosis who underwent a CT study from January 2012 to April 2017. The study was approved by our institutional review board, and because of its retrospective nature, informed patient consent was waived. Forty-seven patients were included.

Patient Selection

Inclusion criteria were adult patients with imaging and/or clinical findings consistent with unilateral or bilateral otospongiosis. Clinical criteria were a history of progressive hearing loss with pure tone audiometry showing conductive hearing loss with an air-bone gap of >20 dB above a normal adult hearing level and with a perceptive hearing loss of <35 dB above the normal adult hearing level in the range of 0.5, 1, 2, and 4 kHz. Imaging findings included areas of demineralization appearing as radiolucency on CT (otospongiotic plaques) involving the otic capsule, with or without complete or partial obliteration of the oval or round windows.

Exclusion criteria included comorbid middle or inner ear pathology based on clinical history and imaging findings, including cholesteatoma, tympanic membrane perforation, ossicular dislocation, osteogenesis imperfecta, Paget disease, otosyphilis, postsurgical changes, and patients with inconclusive clinical and/or imaging findings of otospongiosis. To analyze the type of hearing loss and third window manifestations, we excluded patients who presented with a concomitant history of Menière disease, semicircular canal dehiscence, enlarged vestibular aqueduct, and perilabyrinthine fistula.

Clinical Findings

Medical charts were reviewed, and we recorded the following data for each patient: 1) age, sex, type of hearing loss, classified as conductive hearing loss, sensorineural hearing loss, and mixed hearing loss; 2) the presence of third window abnormalities defined as sound-induced vertigo, dizziness, nausea, or eye movements (Tullio phenomenon); and 3) cochlear implantation and its possible complications such as CSF gusher and electrode misplacement in cavitary formations.

CT Studies

High-resolution scans of the temporal bones were performed on 128- or 64-slice multidetector CT scanners with 0.6-mm collimation, 0.55 pitch, 320 mAs, and 120 kV(peak); or conebeam CT with 0.6-mm collimation, 140 mAs, and 90 kVp. Axial images parallel to the lateral semicircular canal were obtained. Coronal reformatted images were created perpendicular to the axial images. Images with extensive motion or implant artifacts were excluded from the study. All studies were performed without intravenous contrast administration.

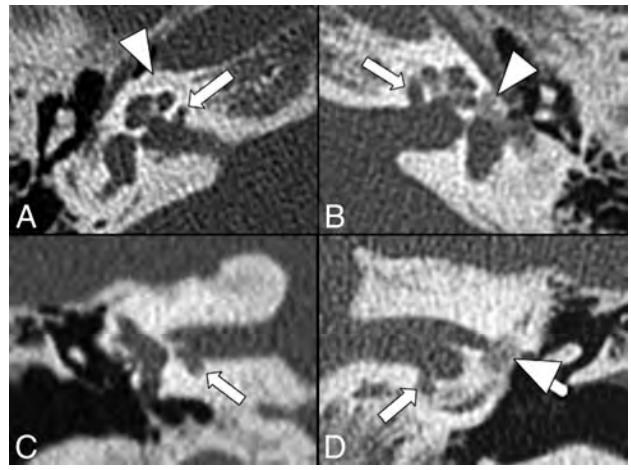

FIG 1. Bilateral cavitary plaques. Axial (*top row*) and coronal (*bottom row*) CT scans show the presence of abnormal CSF-attenuating focal lesions (*arrows*) involving the anterior and inferior walls of the IAC next to the basal turn of the cochlea. Additionally, there are noncavitary plaques (*arrowheads*) around the cochlea on the right (*A*) and at the fissula ante fenestram on the left (*B* and *D*).

Image Evaluation

Eighty-nine temporal bones from 47 patients were analyzed by 1 neuroradiology fellow (P.P.) and verified by 1 neuroradiologist with 3 years of experience reading temporal bone CT images and with a Certificate of Added Qualification in neuroradiology (C.Z.), both blinded to clinical findings. Findings on CT were classified into 2 groups: 1) otospongiotic plaques (noncavitary plaques), and 2) cavitary plaques. Otospongiotic plaques (areas of demineralization appearing as radiolucency on CT) were classified according to the Symons/Fanning classification into the following: grade 0, no findings; grade 1, solely fenestral (fissula ante fenestram), evidence of a thickened stapes footplate, and/or decalcified, narrowed, or enlarged round or oval windows; grade 2, patchy localized cochlear disease (with or without fenestral involvement); and grade 3, diffuse confluent cochlear involvement of the otic capsule (with or without fenestral involvement).[11]

Cavitary plaques were defined as focal, well-delineated, low-attenuating foci similar to CSF (Fig 1). Their location was classified as the following: zone 1 (a region anterior to the oval window), zone 2 (pericochlear region), zone 3 (anteroinferior wall of the IAC), zone 4 (posterior wall of the IAC), and zone 5 (round window) (On-line Figure).

Endosteal involvement was defined as invasion of the cavitary plaque into the endosteal layer of the labyrinth. Communication between IAC cavitary plaques and CSF was determined by lack of a normal bone between the cavity and the IAC (Fig 2).

Hounsfield units from the center of otospongiotic and cavitary plaques were measured by placing ROIs according to the size of the lesion. Studies acquired with conebeam CT were excluded for this analysis. ($n = 5$).

Statistical Analysis

Descriptive statistics were used to determine the prevalence of cavitary plaques in otospongiosis. To account for multiple out-

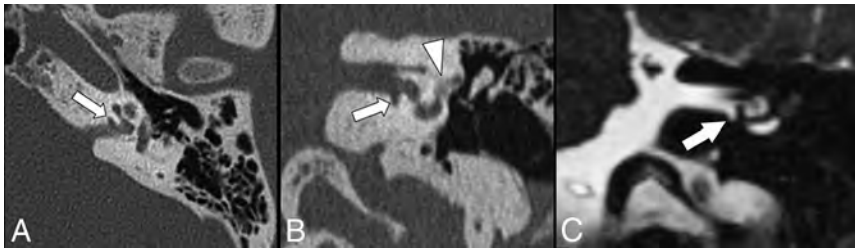

FIG 2. Axial (*A*) and coronal (*B*) CT images show the presence of a cavitary plaque (*arrows*) involving the anterior and inferior walls of the IAC next to the basal turn of the cochlea. Additionally, there is an otospongiotic plaque (*arrowhead*) at the fissula ante fenestram. Coronal CISS MR image (*C*) demonstrates a clear communication between the cavity and CSF of the IAC.

Table 1: Demographic characteristics

Characteristic	Otospongiosis and Cavitary Plaques (*n* = 30)	Otospongiosis Only (*n* = 56)	*P* Value
Median age (yr)	59	51	.058
Temporal bone involvement			.273
Unilateral (No.) (%)	12 (40)	14 (25)	
Bilateral (No.) (%)	18 (60)	42 (75)	
Hounsfield unit	115	953	<.001

Table 2: Location of cavitary plaques in otospongiosis

Location	Cavitary Plaques (*n* = 31)	
	No.	%
IAC	29	93.54
Anteroinferior wall	28	90.34
Posterior wall	1	3.2
Non-IAC	2	6.46
Pericochlear	1	3.2
Fenestral	1	3.2

comes from a patient, we used a generalized linear (logistic) mixed-effects model with a random intercept to determine the association of cavitary plaques with the degree of otospongiosis, type of hearing loss, third window manifestations, and complications during cochlear implantation, as well as relationships between cavitary plaques and the patient's age, sex, and Hounsfield units. The aforementioned independent variables were coded according to their data type. Type III tests for fixed effects were used to determine the overall statistical significance of the variable. *P* values $< .05$ were considered significant. SAS 9.4 (SAS Institute, Cary, North Carolina) was used to generate descriptive statistics as well generalized linear mixed models using PROC GLIMMIX (https://support.sas.com/documentation/cdl/en/statug/63033/HTML/default/viewer.htm#glimmix_toc.htm).

RESULTS

Patient Profile

We identified 47 patients with otospongiosis. The mean patient age was 55 ± 14 years (range, 28–83 years). Twenty-five patients (53%) were women, and 22 (47%) were men.

Of the 47 patients, 42 (89%) had otospongiosis bilaterally, and 5 (11%), unilaterally. Of the 5 patients with unilateral otospongiosis, their contralateral temporal bones were excluded because they had normal audiometry findings and no findings on CT.

Imaging Findings

A total of 89 temporal bones were analyzed. Three had normal CT findings (otospongiosis grade 0), though history and clinical parameters were consistent with otospongiosis. Eighty-six temporal bones had classic imaging findings of otospongiosis (noncavitary plaques) and 30 (35%) of them also presented cavitary plaques. Cavitary plaques were therefore never seen in isolation.

Otospongiotic Plaques

Grade 1 otospongiosis was the most common presentation in 49.4% ($n = 44$) of the temporal bones followed by grade 3 in 29.2% ($n = 26$). Hounsfield units from the center of the otospongiotic plaques were measured in 81 of 86 temporal bones (5 temporal bones with conebeam CT were excluded), resulting in Hounsfield units of 953 ± 278.

Otospongiotic and Cavitary Plaques

From the 30 temporal bones with cavitary plaques, 18 (60%) showed bilateral, and 12 (40%), unilateral cavitary changes ($P = .273$) (Table 1). Regarding the number of cavitary plaques per temporal bone, 96.7% ($n = 29$) of temporal bones had a single cavitary plaque and only 1 (3.3%) had 2 cavitary lesions. Of 31 cavitary plaques, 93.5% ($n = 29$) were in the IACs, and 6.5% ($n = 2$), within the otic capsule ($P = .003$) (Table 2). The anteroinferior wall of the IAC was the most common location for the presence of cavitary plaques (Fig 1).

The presence of cavitary plaques was not associated with a higher grade of otospongiosis by imaging ($P = .664$). Otospongiosis with cavitary changes tended to present in patients older (mean age, 59 ± 11 years) than those without cavities (mean age, 51 ± 15 years), though the difference was not statistically significant ($P = .058$) (Table 1). There was no statistically significant association between the presence of cavitary plaques and sex ($P = .667$).

Of the 29 cavitary plaques located in the IACs, 97% ($n = 28$) showed direct communication with the CSF space of the IAC (Fig 2). Endosteal involvement was seen affecting the basal turn of the cochlea in 3 (10%) temporal bones with cavitary plaques.

The average length and width of the cavitary plaques were 4.44 ± 2.32 and 1.19 ± 0.45 mm, respectively. There was a statistically significant difference in the mean Hounsfield unit value between the noncavitary and cavitary plaques, 953 ± 278 versus 115 ± 75, respectively ($P < .001$).

Clinical Findings

The type of hearing loss was analyzed in 83 of 89 temporal bones (6 temporal bones had an associated history of Menière disease). In the group of patients with cavitary changes ($n = 29$), sensorineural (41.4%) and mixed hearing loss (41.4%) were most common. Mixed hearing loss (51.9%) was the most common type in the group without cavities (Table 3). The presence of cavitary plaques showed no significant association with a specific type of hearing loss ($P = .365$).

Table 3: Hearing loss according to type of otospongiosis

Characteristic	Otospongiosis and Cavitary Plaques	Otospongiosis Only	*P* Value
Type of hearing loss (No.)			.365
Conductive	5 (6%)	13 (15.7%)	
Sensorineural	12 (14.5%)	13 (15.7%)	
Mixed	12 (14.5%)	28 (33.7%)	

None of the temporal bones with otospongiosis, either with or without cavitary changes, had a clinical history of third window manifestations. There were 6 temporal bones with cavitary plaques in patients who underwent cochlear implantation, none of whom had procedural complications such as CSF gusher or misplacement of electrodes into the cavitary plaques.

DISCUSSION

The first report of cavitary plaques in otospongiosis was published by Schuknecht and Kirchner in 1974[13]; they described a case showing a large cavity surrounding the middle and apical turns of the cochlea. After this initial case, cavitary changes were mainly described in reports that included an average of 1–2 cases.[1,7,9,13] An abstract in 2012 reported 32 cases of cavitary changes from a series of 147 temporal bones with a history of hearing loss, in which lesions were referred to as diverticula.[10] However, imaging features were not described, and to the best of our knowledge, a full article with the details of this work has not been published in the English literature.

In 2017, Pippin et al[8] reported a cavitary plaque prevalence of 18% among 66 temporal bones with otospongiosis. Our prevalence was higher at 35%, which could be related to a larger sample of temporal bones with otospongiosis in our study ($n = 86$) as well as possible variations in referral bias at both institutions.

In our study, we identified 31 cavitary plaques among 30 temporal bones, and none of the cavitary plaques were seen in isolation (ie, they were associated with classic findings of otospongiosis in all cases). This observation differs from that of Pippin et al,[8] who reported 57 temporal bones with cavitary plaques as an isolated finding among 807 patients. This difference could be explained by our smaller sample size and our focusing on patients with clinical and/or imaging findings of otospongiosis, whereas Pippin et al analyzed patients regardless of diagnosis. Hoeberigs et al[10] in 2012 reported only 2 temporal bones with isolated cavitary plaques among 222 temporal bones in patients with conductive or mixed hearing loss. However, as mentioned before, this was an abstract, and the details of the study have not been published.

Increased prevalence of cavitary plaques has been reported in patients with greater degrees of otospongiosis by CT (grade 3), suggesting that they may be a manifestation of severe disease.[10] However, in our study, we found that cavitary plaques tended to be more common in grade 1 otospongiosis (16.9%), followed by grade 3 (10.1%), and were not significantly associated with the degree of otospongiosis ($P = .365$). These results suggest that the formation of cavities represents an additional manifestation in the dynamic process of otospongiosis.

The mean age of patients with cavitary plaques (59 ± 11 years) tended to be higher than that of patients with noncavitary plaques (51 ± 15 years) ($P = .058$). A similar outcome was seen by Pippin et al,[8] who found that patients with cavitary plaques were significantly older (61 years of age) than those without cavities (52 years of age). Two growth patterns have been identified in otospongiotic plaques: One grows for a short time and then becomes inactive. The other pattern shows continued growth and progression throughout life.[14] Because most cases of cavitary plaques were seen in patients with a long-standing diagnosis of otospongiosis, it is possible that cavitation may belong to the second growth pattern and present in older individuals, but this possibility remains uncertain.

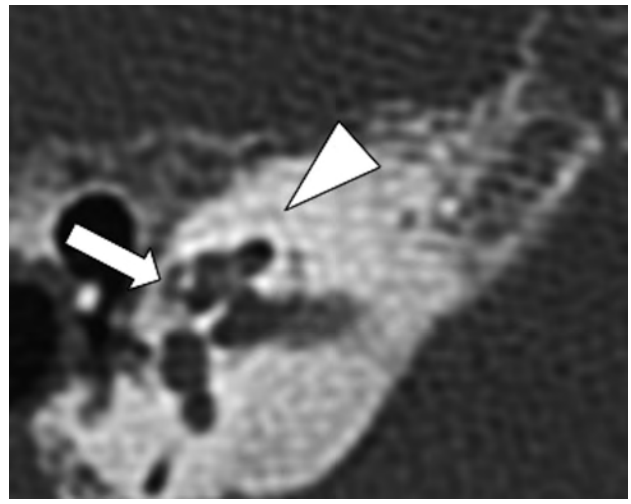

FIG 3. Axial CT scan shows the presence of a cavitary plaque involving the pericochlear region (*arrow*). Note the attenuation of the cavitary plaque, similar to the IAC. Additionally, there are noncavitary otospongiotic plaques surrounding the otic capsule (*arrowhead*).

To assess the location of cavitary plaques, we evaluated the sites within the temporal bone that have been most commonly reported in the literature.[1,7,9,10,15] Our analysis found that the walls of the IAC were the sites most commonly affected by cavitary plaques ($P = .003$), 90.3% involving the anteroinferior wall, and 3.2%, the posterior wall. Involvement of the anteroinferior IAC as the most common location is consistent with reports in the literature.[8,10] In this location, cavitary plaques have been called "cavitary formations," "cavitations," and diverticula or indentations of the IAC.[1,7-10] We found 1 temporal bone with a cavitary plaque involving the posterior wall of the IAC in a patient with advanced otospongiosis (grade 3) and sensorineural hearing loss. However, the preference for this site in this patient is uncertain. Cavitary plaques outside the IAC were seen in 2 instances (Fig 3). These locations are rare and have been previously documented in 4 case reports, most of them identified on histologic analysis.[1,9,16,17]

Cavitary plaques showed low attenuation on CT, similar to that of CSF in the IAC (Fig 1). We found that there was a statistically significant difference in the mean Hounsfield units between the noncavitary plaques and cavitary lesions, 953 ± 278 versus 115 ± 75, respectively ($P < .001$). This difference in Hounsfield units was expected because 96% of cavitary plaques were in apparent communication with the IAC and presumably filled with CSF (Fig 2). This finding was also demonstrated in a patient with cavitary otospongiosis who underwent MR imaging, which serves as an illustrative example (Fig 2*C*). Cavitary plaques may be difficult to evaluate on imaging due to their small size. Therefore, in patients with suspected otospongiosis, it is important to scruti-

nize the anteroinferior wall of the IAC next to the cochlea, which is where cavitary changes are most commonly identified.

Some unrelated disorders affecting the labyrinth can produce third window lesions, resulting in conductive or sensorineural hearing loss, vestibular manifestations (sound and/or pressure-induced vertigo), or a combination.[18,19] Cavitary plaques have been described as a cause of third window lesions when they reach the endosteal margin of the bony labyrinth.[1,16,20] However, this complication is probably rare because 90% of the cavitary plaques in our study did not show extension into the endosteal layer of the cochlea. Three cavitary plaques showed contact with the endosteal margin of the basal turn of the cochlea, but none of them had clinical manifestations of third window phenomena. It is possible that involvement of the endosteal layer in these cases was too mild to result in third window abnormalities.

Pippin et al[8] demonstrated a significant correlation between the presence of cavitary plaques and isolated sensorineural hearing loss. In our study, the presence of cavitary plaques was not statistically associated with a specific type of hearing loss ($P = .365$); however, this finding could be related to our smaller sample size. Also, there was probably an effect of patient selection because their cohort included many patients with cavitary changes but without classic findings of otospongiosis.

Complications of cochlear implantation in patients with otospongiosis are reported to occur in 10%–20% of patients.[21,22] Cavitary plaques as a potential cause of CSF gushing and misplacement of electrode arrays into the pericochlear cavities have been reported in around 4 cases in the literature. Otospongiosis leads to loss of part of the wall of the cochlea, which can result in direct communication between the IAC and the basal turn.[1,15,21,22]

In our patients, we found 6 temporal bones with cavitary plaques that underwent cochlear implantation. These cases showed a discrete layer of intervening bone between the cavitary plaques and the basal turn of the cochlea, and as expected, none of them had any complications related to the operation. The absence of complications in our study, however, could also be explained by the limited number of temporal bones that underwent a cochlear implantation.

The limitations of our study include its retrospective nature, relatively small sample size, and absence of pathologic confirmation because biopsies are not routinely performed during stapedectomy. However, all patients met imaging and/or clinical criteria for otospongiosis. Measurement of Hounsfield units could have also been affected by the small size of the lesions and partial averaging with adjacent bone.

CONCLUSIONS

Cavitary plaques in otospongiosis were seen in one-third of temporal bones, and their most common location was the anteroinferior wall of the IAC next to the cochlea. Cavitary plaques were seen mostly in older patients, and there was no association between them and a greater degree of otospongiosis by imaging or third window manifestations. There were no procedural complications such as CSF gusher or misplacement of electrodes within cavitary plaques during cochlear implantation.

Disclosures: Feng-Chang Lin—*RELATED*: *Grant*: National Institutes of Health, *Comments*: UL1TR001111*; *UNRELATED*: *Employment*: University of North Carolina at Chapel Hill. *Money paid to the institution.

REFERENCES

1. Makarem AO, Hoang TA, Lo WW, et al. **Cavitating otosclerosis: clinical, radiologic, and histopathologic correlations.** *Otol Neurotol* 2010;31:381–84 CrossRef Medline
2. Clayton AE, Mikulec AA, Mikulec KH, et al. **Association between osteoporosis and otosclerosis in women.** *J Laryngol Otol* 2004;118:617–21 Medline
3. Redfors YD, Möller C. **Otosclerosis: thirty-year follow-up after surgery.** *Ann Otol Rhinol Laryngol* 2011;120:608–14 CrossRef Medline
4. Palacios E, Valvassori G. **Cochlear otosclerosis.** *Ear Nose Throat J* 2000;79:494 Medline
5. Wycherly BJ, Berkowitz F, Noone AM, et al. **Computed tomography and otosclerosis: a practical method to correlate the sites affected to hearing loss.** *Ann Otol Rhinol Laryngol* 2010;119:789–94 CrossRef Medline
6. Sanverdi SE, Ozgen B, Dolgun A, et al. **Incomplete endochondral ossification of the otic capsule, a variation in children: evaluation of its prevalence and extent in children with and without sensorineural hearing loss.** *AJNR Am J Neuroradiol* 2015;36:171–75 CrossRef Medline
7. Bou-Assaly W, Mukherji S, Srinivasan A. **Bilateral cavitary otosclerosis: a rare presentation of otosclerosis and cause of hearing loss.** *Clin Imaging* 2013;37:1116–18 CrossRef Medline
8. Pippin XK, Muelleman XT, Hill XJ, et al. **Prevalence of internal auditory canal diverticulum and its association with hearing loss and otosclerosis.** *AJNR Am J Neuroradiol* 2017;38:2167–71 CrossRef Medline
9. Makarem AO, Linthicum FH. **Cavitating otosclerosis.** *Otol Neurotol* 2008;29:730–31 CrossRef Medline
10. Hoeberigs M, Postma A, Waterval J, et al. **Prevalence of anterior internal auditory canal "diverticulum" on high resolution CT in patients with otosclerosis.** In: *Proceedings of the Scientific Assembly and Annual Meeting of the Radiological Society of North America*, Chicago, Illinois. November 25–30, 2012
11. Lee TC, Aviv RI, Chen JM, et al. **CT grading of otosclerosis.** *AJNR Am J Neuroradiol* 2009;30:1435–39 CrossRef Medline
12. Merkus P, van Loon MC, Smit CF, et al. **Decision making in advanced otosclerosis: an evidence-based strategy.** *Laryngoscope* 2011;121:1935–41 CrossRef Medline
13. Schuknecht HF, Kirchner JC. **Cochlear otosclerosis: fact or fantasy.** *Laryngoscope* 1974;84:766–82 Medline
14. Brondbo K, Hawke M, Abel SM, et al. **The natural history of otosclerosis: a correlation of the volume and activity of the otosclerotic lesion with age.** *J Otolaryngol* 1983;12:163–68 Medline
15. Ramsden R, Bance M, Giles E, et al. **Cochlear implantation in otosclerosis: a unique positioning and programming problem.** *J Laryngol Otol* 1997;111:262–65 Medline
16. Richard CC, Linthicum FH Jr. **An unexpected third window in a case of advanced cavitating otosclerosis.** *Otol Neurotol* 2012;33:e47–48 CrossRef Medline
17. Hederstierna C, Cureoglu S, Paparella MM. **Undiagnosed severe cochlear otosclerosis as a cause of profound hearing loss.** *Otol Neurotol* 2013;34:14–15 CrossRef
18. Merchant SN, Rosowski JJ. **Conductive hearing loss caused by third-window lesions of the inner ear.** *Otol Neurotol* 2008;29:282–89 CrossRef Medline
19. Ho ML, Moonis G, Halpin CF, et al. **Spectrum of third window abnormalities: semicircular canal dehiscence and beyond.** *AJNR Am J Neuroradiol* 2017;38:2–9 CrossRef Medline
20. Quesnel AM, Moonis G, Appel J, et al. **Correlation of computed tomography with histopathology in otosclerosis.** *Otol Neurotol* 2013;34:22–28 CrossRef Medline
21. Rotteveel LJ, Proops DW, Ramsden RT, et al. **Cochlear implantation in 53 patients with otosclerosis: demographics, computed tomographic scanning, surgery, and complications.** *Otol Neurotol* 2004;25:943–52 CrossRef Medline
22. Ramsden R, Rotteveel L, Proops D, et al. **Cochlear implantation in otosclerotic deafness.** *Adv Otorhinolaryngol* 2007;65:328–34 Medline

Submandibular Gland Transfer: A Potential Imaging Pitfall

X. Wu, S.S. Yom, P.K. Ha, C.M. Heaton, and C.M. Glastonbury

ABSTRACT

BACKGROUND AND PURPOSE: The Seikaly and Jha submandibular gland transfer surgery is performed to facilitate gland shielding during radiation therapy for head and neck tumors to circumvent radiation-induced xerostomia. It results in an asymmetric postsurgical appearance of the submandibular and submental spaces. Our purpose was to characterize the morphologic and enhancement characteristics of the transferred submandibular gland and identify potential pitfalls in postoperative radiologic interpretation.

MATERIALS AND METHODS: This retrospective study identified patients with head and neck cancer who had undergone the submandibular gland transfer procedure at our institution. Chart reviews were performed to identify relevant oncologic histories and therapies. CT and MR neck imaging was reviewed to characterize morphologic and enhancement characteristics of the pre- and postoperative submandibular glands, as well as interpretive accuracy.

RESULTS: Eleven patients with oropharyngeal and nasopharyngeal squamous cell carcinomas who underwent submandibular gland transfer were identified. The transferred glands were significantly lengthened in the anteroposterior dimension compared with contralateral glands ($P < .001$) and displaced anteriorly and inferiorly within the submandibular and submental spaces. Enhancement patterns of the transferred submandibular glands varied, depending on the time of imaging relative to the operation and radiation therapy. Submandibular gland transfer was acknowledged in the postoperative report in 7/11 cases. Errors in interpretation were present in 2/11 reports.

CONCLUSIONS: After the submandibular gland transfer procedure, the submandibular and submental spaces lose their symmetric appearances as the transferred submandibular glands become lengthened and located more anteriorly and inferiorly, with variable enhancement characteristics. Familiarity with the postsurgical appearance of the transferred submandibular glands is key to accurate imaging interpretation.

ABBREVIATION: SMG = submandibular gland

The Seikaly and Jha submandibular transfer procedure consists of the surgical relocation of the submandibular gland (SMG) to the ipsilateral submental space. The aim of this surgery is to displace the submandibular gland farther away from the highest dose regions of radiation, thereby decreasing the risk of radiation-induced xerostomia.[1-6] Briefly, the procedure begins with a limited level I neck dissection and release of the submandibular gland from its surrounding tissues. As originally described, this is followed by evaluation for retrograde flow in the facial artery and vein supplying the gland and ligation of these vessels if there is sufficient retrograde flow. Alternatively, the gland and supporting vessels can be mobilized sufficiently to allow stretching of the vessels as the gland is repositioned anteriorly. The mylohyoid muscle is then bisected to allow repositioning of the submandibular gland into the submental space, while maintaining its connection with the submandibular duct and ganglion (Fig 1). Once in the submental space, the SMG is anchored deep or sutured superficial to the ipsilateral anterior belly of the digastric muscle.[3,7]

Because this procedure is only performed contralateral to the primary head and neck malignancy, it results in an asymmetric postsurgical appearance of the submandibular and submental spaces, which can lead to diagnostic errors. The confounding postoperative appearance of this transferred submandibular gland has been previously demonstrated on PET/CT imaging.[8] The purpose of this study

Received October 13, 2017; accepted after revision February 3, 2018.

From the Department of Radiology and Imaging Science (X.W.), Emory University, Atlanta, Georgia; and Departments of Radiation Oncology (S.S.Y., C.M.G.), Otolaryngology-Head and Neck Surgery (S.S.Y., P.K.H., C.M.H., C.M.G.), and Clinical Radiology (C.M.G.), University of California, San Francisco, San Francisco, California.

Paper previously presented at: Annual Meeting of the American Society of Head and Neck Radiology, September 16–20, 2017; Las Vegas, Nevada.

Please address correspondence to Xin Wu, MD, Department of Radiology and Imaging Science, Emory University, 1364 Clifton Rd NE, Suite BG 20, Atlanta, GA 30322; e-mail: xin.wu@emory.edu; @CynXinWu

http://dx.doi.org/10.3174/ajnr.A5609

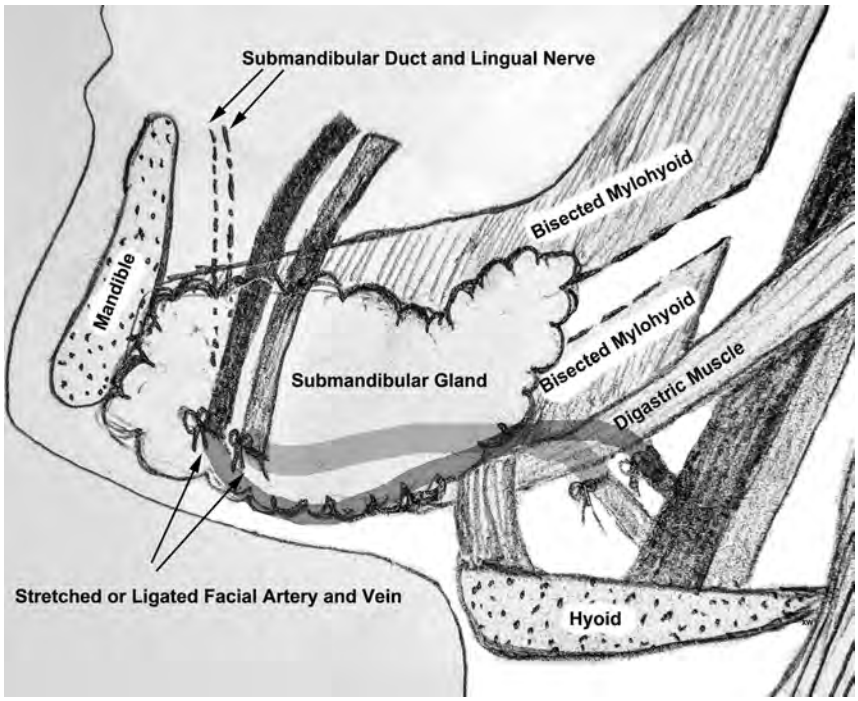

FIG 1. Illustrative schematic demonstrating the key steps in the SMG transfer operation, including mobilization or ligation of the facial artery and vein proximal to the SMG, anterior and inferior translation of the gland into the submental space, and bisection of the mylohyoid muscle to allow repositioning of the submandibular duct and ganglion.[3,7]

was to better characterize the CT and MR imaging findings of the transferred SMG and to identify potential pitfalls in the evaluation of the postsurgical submandibular and submental spaces.

MATERIALS AND METHODS

This institutional review board–approved, Health Insurance Portability and Accountability Act–compliant study reviewed surgical records from University of California, San Francisco, from the past 5 years to identify patients with head and neck cancer who had undergone the submandibular gland transfer procedure. A medical chart review was conducted to identify the patient's primary site of disease and pathology, date of the surgical intervention, description of the surgical intervention (as per the operative report), and dates and dosages of subsequent radiation treatment. Average radiation doses with SDs to the transferred and contralateral SMGs were calculated. Student *t* tests were performed to assess whether the trans-

Table 1: SMG morphologic measurement definitions

Morphologic Measurement	Definition	Direction of Measurement
AP length	As measured between anteriormost border of gland and posteriormost border of SMG	On axial images, perpendicular to axis connecting the mandibular condyles
AP length difference	Difference between the AP lengths of the SMGs by subtraction of the AP length of the contralateral gland from the transferred gland	On axial images, perpendicular to axis connecting the mandibular condyles
Posterior margin difference	Distance between the posteriormost border of the gland and that of the contralateral gland	On axial images, perpendicular to axis formed by connecting the mandibular condyles
Superior margin difference	Distance between the superiormost border of the gland and that of the contralateral gland	On coronal images, perpendicular to axis formed by connecting the mandibular condyles
Anteroinferior margin difference	Distance between the anteroinferior-most border of the gland and that of the contralateral gland	On axial images, perpendicular to axis formed by connecting the mandibular condyles

Note:—AP indicates anteroposterior.

Table 2: Radiation therapy details[a]

Patient No.	Primary Tumor Site	Prescribed Dose to Primary Tumor (Gy)	Prescribed Dose to Involved Neck (Gy)	Mean Dose to SMG on Involved Side (Gy)	Prescribed Dose to Uninvolved Neck (Gy)	Mean Dose to Transferred SMG (Gy)
1	R BOT	60	54	58.64	48	20.45
2	R tonsil	69.96	59.4	61.33	54.12	28.99
3	R tonsil	69.96	59.4	68.8	54.12	43.97
4	R BOT	69.96	59.4	66.01	59.4	41.44
5	R BOT	60	54	60.01	48	44.95
6	L tonsil	66	59.4	66.7	54.12	16.59
7	R tonsil	66	59.4	59.4	54.12	38.8
8	R tonsil	69.96	59.4	72.7	54.12	27.17
9	Nasopharynx	69.96	59.4	61.02	59.4	60.77
Average dose (Gy)		66.87	58.20	63.85	53.93	35.90
SD		4.24	2.38	4.89	4.04	13.88

Note:—R indicates right; BOT, base of tongue; L, left.

[a] Postsurgical radiation dosages for the 9 out of 11 patients who received radiation therapy at our institution following the SMG transfer procedure. Per the Student *t* test, the transferred SMG received a significantly lower radiation dose than the contralateral SMG ($P < .001$).

Table 3: SMG location[a]

	Preoperative (mm)	*P* Value	Postoperative (mm)	*P* Value
Anteroposterior length difference	2.5 (−4–5)	.28	10.5 (−1–17)	<.001
Anteroinferior margin difference	0 (0–0)		13.5 (10–16)	<.001
Posterior margin difference	−1.8 (−9–3)	.10	7.2 (0–16)	<.001
Superior margin difference	0.2 (−3–6)	.79	−7.5 (−15–0)	<.001

[a] Preoperative and postoperative morphologic features of the transferred SMGs, presented as averaged length and location differences between the SMGs in each patient (transferred gland–contralateral gland) followed by ranges of the differences. Positive values indicate anterior and superior directions, respectively. *P* values for significance of length differences are derived from paired pre- and post-*t* tests with a reference value of 0 mm (no difference).

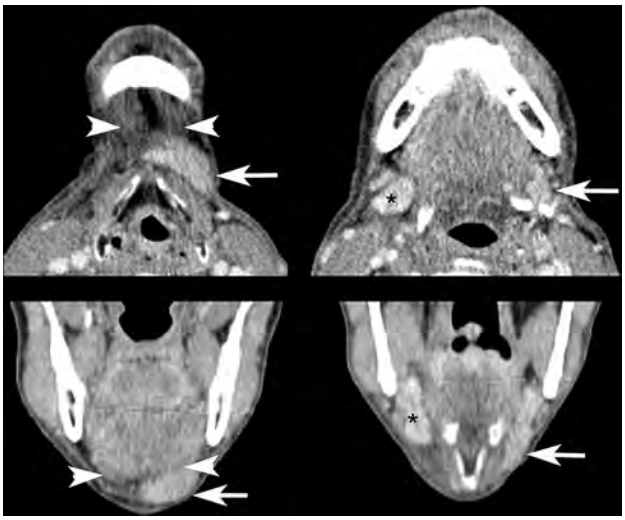

FIG 2. Contrast-enhanced CT images demonstrating the typical asymmetric appearance of the submental and submandibular spaces after SMG transfer. The left transferred SMG (*arrows*) is elongated and displaced inferiorly and anteriorly into the submental space superficial to the anterior belly of the digastric muscle (*arrowheads*), resulting in an asymmetric soft-tissue density in the submental space and diminished soft-tissue volume in the submandibular space relative to the contralateral gland (*asterisks*). Note also edema of surrounding tissues in this patient who was 3 months postchemoradiation with cisplatin and NRG-HN002 (NCT02254278; ClinicalTrials.gov) de-escalation protocol at time of imaging.

ferred SMGs received significantly lower radiation doses relative to the contralateral glands.

The available pre- and postoperative neck CT and MR imaging examinations of these patients were then reviewed to characterize morphologic and enhancement characteristics of the SMGs and key surrounding structures, including the mylohyoid, anterior belly of the digastric, and platysma muscles. Specific morphologic measurements of the submandibular glands were obtained as described in Table 1. Paired pre and post *t* tests were performed to determine whether there was any statistically significant difference in positions between the transferred SMGs and the contralateral glands before and after surgery. Radiology reports were also reviewed for any commentary on the SMGs.

RESULTS

Patient Characteristics

Eleven patients with head and neck malignancies (10 men and 1 woman; ages, 44–64 years) underwent the submandibular transfer procedure at our institution and underwent postoperative contrast-enhanced CT or MR imaging. Eight procedures were performed by 1 surgeon, and 3 were performed by 2 other surgeons. All primary tumors had a histology of squamous cell carcinoma, and the primary subsites were nasopharyngeal in 1 patient and oropharyngeal in 10

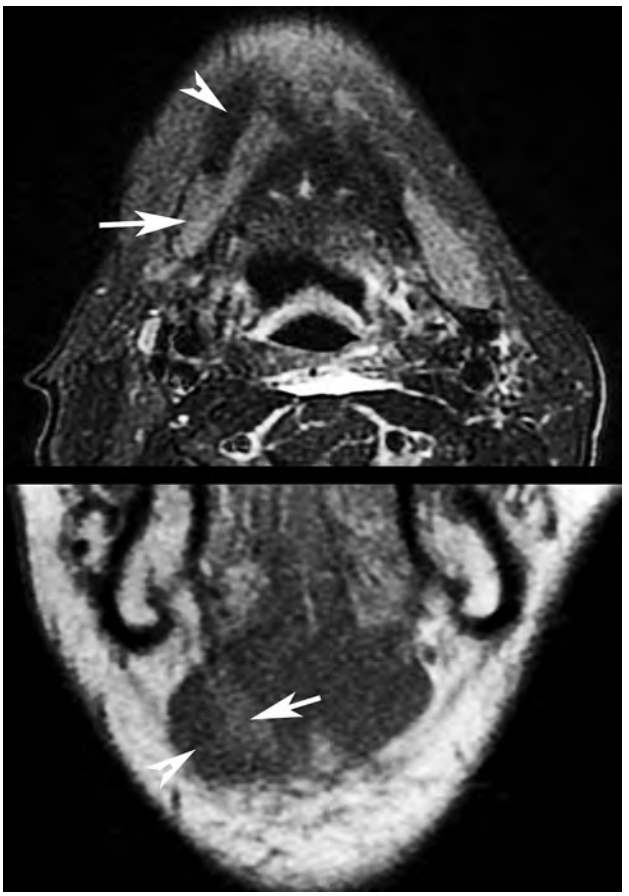

FIG 3. Appearance of SMG (*arrows*) transferred deep to the anterior belly of the digastric muscle (*arrowheads*) on axial T2-weighted, fat-suppressed imaging and coronal T1-weighted imaging. The patient was 2 months postchemoradiation with cisplatin and intensity-modulated radiation therapy at imaging.

patients, with tonsillar primary disease in 7 patients and base of the tongue primary disease in 3 patients. All patients had preoperative neck CT, though 2 patients had only noncontrast CT studies. Two patients also had preoperative MR imaging. Postoperatively, 9 patients underwent contrast-enhanced MR imaging, and 6 patients underwent contrast-enhanced CT. Ten of 11 patients underwent radiation-planning NCCT after the operation.

All patients were treated with chemoradiation with curative intent, and none had preradiation resection of the primary tumor or involved lymph nodes. Two patients underwent radiation treatment at outside institutions; therefore, dosage information was not available for these cases. Dosage information for the remaining patients demonstrated lower dosages to the transferred glands, which received on average 35.90 ± 13.88 Gy, than to the contralateral glands, which received on average 63.85 ± 4.89 Gy (Table 2, $P < .001$).

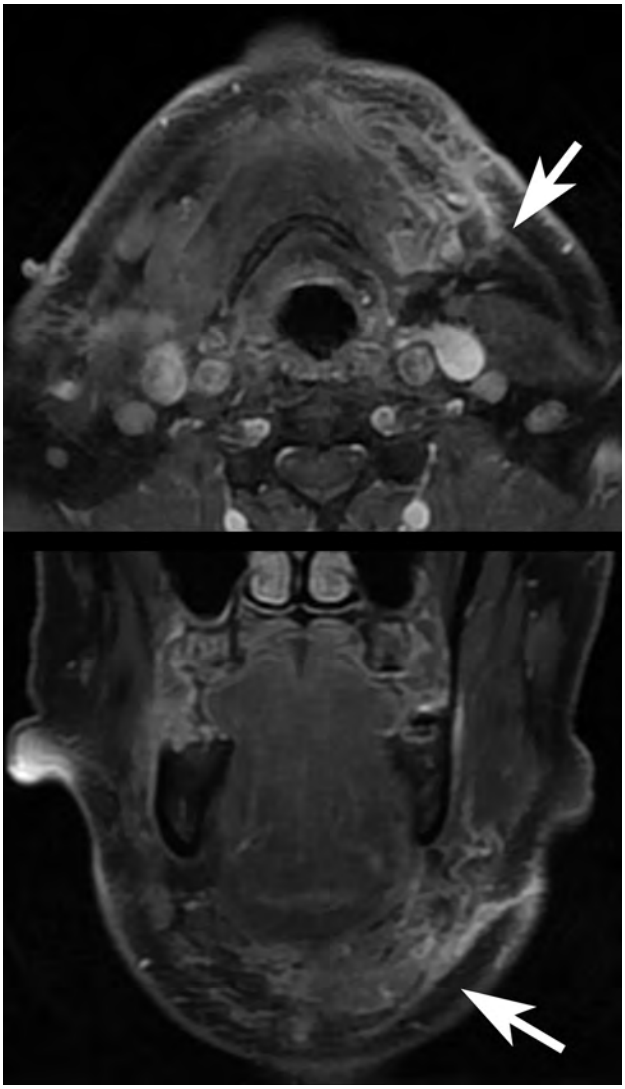

FIG 4. Axial and coronal fat-suppressed postcontrast T1-weighted imaging performed 28 days postoperatively for staging purposes demonstrated platysma enhancement (*arrows*) adjacent to the transferred SMG. The patient had not yet undergone chemoradiation at imaging.

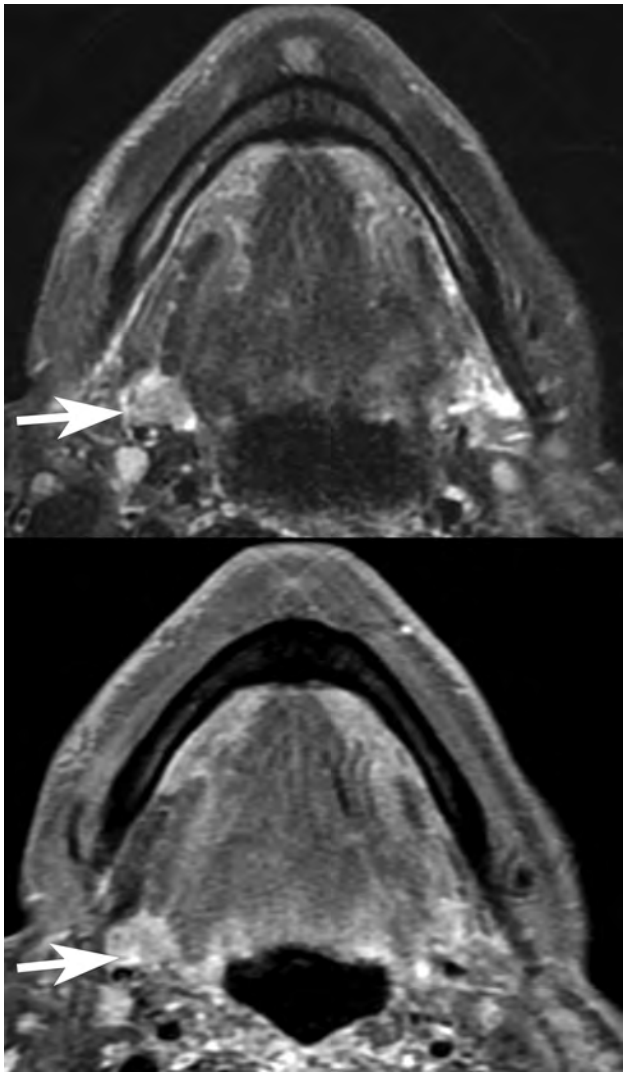

FIG 5. Postoperative asymmetry within the submandibular space results in misinterpretation of the superior aspect of the normal contralateral SMG (*arrows*) as a parapharyngeal mass (axial T2 fat-suppressed and postcontrast imaging). The patient was 2 months postchemoradiation with cisplatin and intensity-modulated radiation therapy at imaging.

SMG Morphology

Preoperatively, there was no significant difference in location or morphology between the bilateral submandibular glands in each patient (Table 3). Specifically, there were no significant differences between the preoperative anteroposterior length differences, anteroposterior locations of the anteroinferior margin of the SMGs, and the posterior and superior margins of the gland to be transferred relative to the contralateral side (all P values $> .05$).

On postoperative imaging, the transferred SMGs were lengthened significantly in the anteroposterior dimension compared with the contralateral glands (Table 3). The transferred SMGs were located more anteriorly within the submandibular and submental spaces, as characterized by the more anterior locations of their anteroinferior and posterior margins (Fig 2). On average, the superior margins of the transferred glands were located inferiorly relative to the contralateral glands.

In 10 of the 11 cases, the submandibular gland was in the subcutaneous tissue superficial to the anterior belly of the digastric muscle; however, in 1 case, it was implanted deep to the ipsilateral anterior belly of the digastric muscle (Fig 3).

SMG CT and MR Imaging Enhancement

On preoperative contrast-enhanced CT, the percentage Hounsfield differences between the target gland and the contralateral gland varied between −18% and 9%, though for all cases except 1, the percentage differences fell below 10%. In 1 exceptional case, there was a percentage difference of −18% between the operative target SMG and the contralateral gland. This patient had bulky enhancing lymph nodes and soft-tissue stranding adjacent to the contralateral gland, suggesting concomitant inflammation or infection.

For the 6 cases that had postoperative contrast-enhanced CT, the transferred gland demonstrated comparable, to slightly decreased enhancement relative to the contralateral gland, ranging from −35% to 9% difference in Hounsfield units.

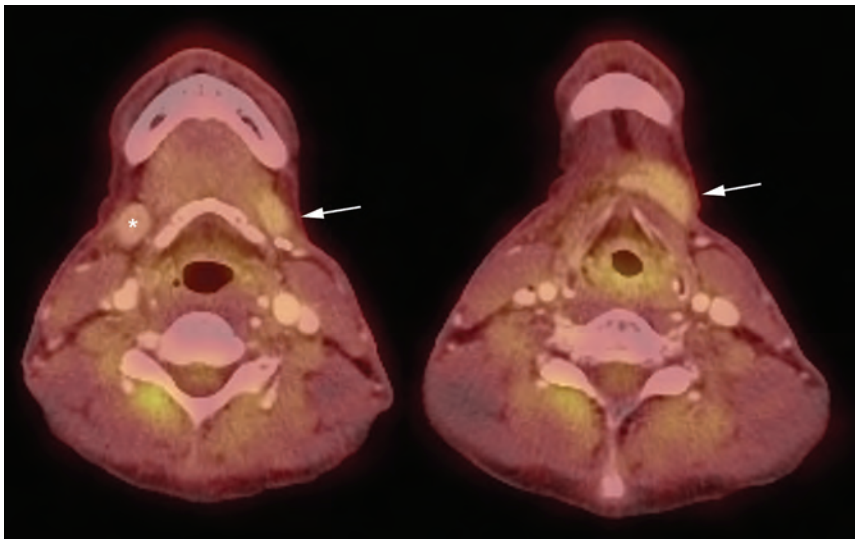

FIG 6. PET/CT images demonstrating mildly increased FDG uptake in the left transferred SMG (*arrows*) compared with the contralateral gland (*asterisk*) 5 months after SMG transfer surgery and 3 months following conclusion of chemoradiation. These findings are congruent with previously published PET findings in a SMG transfer operation and may reflect relatively preserved function in the transferred gland.[8]

On postoperative MR imaging, most of the transferred SMGs demonstrated decreased enhancement compared with the contralateral glands (range, −14 to −1%). The 2 postoperative MRIs that demonstrated increased enhancement (18% and 35% differences) were acquired in the short term, 24 and 28 days postoperatively and before any radiation therapy. Other MRIs were acquired between 52 and 322 days, after the patients had started or undergone radiation therapy.

Additional MR Imaging Findings

For MR imaging examinations performed between 24 and 106 days postoperatively, T2 hyperintense edema was seen in the platysma musculature adjacent to the transferred submandibular gland (5 of 9 cases, Fig 4). For the 4 cases in which MR imaging was performed between 138 and 322 days postoperatively, no edema was evident. Although enhancement and T2 hyperintense signal were noted in the mylohyoid and digastric musculature for some cases, no correlation was noted between the imaging date and the presence or absence of these findings.

Imaging Report Review

For 7 of the 11 cases, the history of submandibular transfer was either provided as a part of the clinical history or acknowledged in the body of the report and presumably had either been recognized or gleaned from the electronic medical record by the radiologist. In one of the cases, the clinical history of submandibular transfer was provided, but the report incorrectly noted that the transferred gland "was not visualized." In 1 of the cases in which the history of submandibular gland transfer was neither provided nor acknowledged, the superior aspect of the contralateral SMG was incorrectly interpreted as a parapharyngeal mass (Fig 5).

DISCUSSION

Our findings demonstrate that while preoperative morphologies, locations, and enhancement characteristics of the SMGs are symmetric, the SMG becomes elongated and translated anteriorly and inferiorly into the submental space after the SMG transfer procedure and may demonstrate differential enhancement patterns. This scenario results in considerable asymmetry in the submandibular and submental spaces, which causes challenges in image interpretation.

SMG ptosis is an age-related phenomenon in which inferior displacement of both submandibular glands results from laxity of the platysma muscle and skin and can be a concern in cosmetic neck rejuvenation.[9] Ptotic SMGs are symmetrically inferiorly displaced within the submandibular space and are not translated anteriorly into the submental space as is the case with a unilaterally transferred SMG.[9] The asymmetric appearance of a transferred SMG and the history of a prior operation distinguish it from ptotic SMGs.

Enhancement of the transferred SMG relative to the contralateral SMG appears to depend on the timing of the study. Increased MR imaging enhancement in the transferred SMG in the immediate postoperative period (24 and 28 days) may reflect reactive hyperemia and correlate with the considerably increased FDG avidity in the transferred gland reported 3 weeks postoperatively in the literature.[8] For all MR imaging examinations performed >52 days from the time of the operation, the transferred SMG demonstrated decreased enhancement relative to the contralateral gland. This may reflect a sequela of altered vascularity, because ligation of the facial artery and vein proximal to the SMG and reliance on retrograde collaterals are components of the transfer procedure.[1] Another cause for differential enhancement may be the different radiation dosages delivered to the SMGs. Increased enhancement of irradiated salivary glands has been well described previously, especially at dosages of >45 Gy.[10,11] The fact that the transferred SMGs received, on average, 35.90 ± 13.88 Gy as opposed to the contralateral glands, which received, on average, 63.85 ± 4.89 Gy, may contribute to these differential enhancement characteristics, especially given that 39 Gy is commonly thought to be a "submandibular gland–sparing" dose due to dose tolerance considerations.[12] Relatively preserved gland function may also explain the mildly increased FDG uptake of the transferred, less irradiated gland compared with the contralateral gland reported in a patient 2 years postoperatively[8] and replicated in a patient in our cohort in a PET/CT examination acquired 5 months after the operation (Fig 6).

Edema of the platysma musculature appears to resolve with increased time after the operation, suggesting that this is a postoperative finding. The lack of correlation between imaging date and the presence or absence of mylohyoid/digastric muscle enhancement and T2 hyperintensity suggest that these findings may reflect denervation changes.

Regardless of whether the clinical history of SMG transfer is provided, the presence of asymmetric soft tissue within the sub-

mandibular and submental spaces can be confusing. Lack of familiarity with the appearance and submental location of the transferred gland may account for the case in which the history of SMG transfer was recognized but the transferred gland was reported as not visualized. Asymmetry of the submandibular spaces may have contributed to the incorrect interpretation of the superior aspect of a contralateral SMG as a parapharyngeal mass because the transferred gland was no longer in its expected location to provide a point of reference.

CONCLUSIONS

Familiarity with the postsurgical appearance of SMG transfer and recognizing the location of the transferred gland and its relationship to the contralateral SMG is important to correctly interpret subsequent neck imaging. Our study demonstrates that after this procedure, there is a loss of SMG symmetric morphology. The transferred gland is located more anteriorly and inferiorly within the submandibular and submental spaces, most frequently superficial to the anterior belly of the digastric musculature. In all except the most immediately postoperative MR imaging examinations (<52 days), the transferred submandibular gland appears to demonstrate less intense enhancement than the native contralateral gland, though T2 signal hyperintensity within the platysma muscle was reliably seen in examinations performed in the first 106 days.

Disclosures: Sue S. Yom—*UNRELATED*: *Consultancy*: BioMimetix Pharmaceutical, Eli Lilly; *Grants/Grants Pending*: Merck, Bristol-Myers Squibb, Genentech*; *Royalties*: UpToDate, Springer; *Travel/Accommodations/Meeting Expenses Unrelated to Activities Listed*: AstraZeneca. Chase M. Heaton—*UNRELATED*: *Consultancy*: OncoSec. Christine M. Glastonbury—*UNRELATED*: *Royalties*: Elsevier-Amirsys, *Comments*: book and chapter royalties. *Money paid to the institution.

REFERENCES

1. Jha N, Seikaly H, McGaw T, et al. **Submandibular salivary gland transfer prevents radiation-induced xerostomia.** *Int J Radiat Oncol Boil Phys* 2000;46:7–11 CrossRef Medline
2. Liu R, Seikaly H, Jha N. **Anatomic study of submandibular gland transfer in an attempt to prevent postradiation xerostomia.** *J Otolaryngol* 2002;31:76–79 CrossRef Medline
3. Seikaly H, Jha N, Harris JR, et al. **Long-term outcomes of submandibular gland transfer for prevention of postradiation xerostomia.** *Arch Otolaryngol Head Neck Surg* 2004;130:956–61 CrossRef Medline
4. Rieger J, Seikaly H, Jha N, et al. **Submandibular gland transfer for prevention of xerostomia after radiation therapy: swallowing outcomes.** *Arch Otolaryngol Head Neck Surg* 2005;131:140–45 CrossRef Medline
5. Jha N, Seikaly H, Harris J, et al. **Phase III randomized study: oral pilocarpine versus submandibular salivary gland transfer protocol for the management of radiation-induced xerostomia.** *Head Neck* 2009;31:234–43 CrossRef Medline
6. Jha N, Harris J, Seikaly H, et al. **A phase II study of submandibular gland transfer prior to radiation for prevention of radiation-induced xerostomia in head-and-neck cancer (RTOG 0244).** *Int J Radiat Oncol Boil Phys* 2012;84:437–42 CrossRef Medline
7. Seikaly H, Jha N, McGaw T, et al. **Submandibular gland transfer: a new method of preventing radiation-induced xerostomia.** *Laryngoscope* 2001;111:347–52 CrossRef Medline
8. Makis W, Ciarallo A, Abikhzer G, et al. **Submandibular salivary gland transfer: a pitfall in head and neck imaging with F-18 FDG PET/CT.** *Clin Nucl Med* 2011;36:712–16 CrossRef Medline
9. Lee MK, Sepahdari A, Cohen M. **Radiologic measurement of submandibular gland ptosis.** *Facial Plast Surg* 2013;29:316–20 CrossRef Medline
10. Saito N, Nadgir RN, Nakahira M, et al. **Posttreatment CT and MR imaging in head and neck cancer: what the radiologist needs to know.** *Radiographics* 2012;32:1261–82; discussion 1282–84 CrossRef Medline
11. Bronstein AD, Nyberg DA, Schwartz AN, et al. **Increased salivary gland density on contrast-enhanced CT after head and neck radiation.** *AJR Am J Roentgenol* 1987;149:1259–63 CrossRef Medline
12. Murdoch-Kinch CA, Kim HM, Vineberg KA, et al. **Dose-effect relationships for the submandibular salivary glands and implications for their sparing by intensity modulated radiotherapy.** *Int J Radiat Oncol Biol Phys* 2008;72:373–82 CrossRef Medline

Characteristic MR Imaging Findings of the Neonatal Brain in RASopathies

M.N. Cizmeci, M. Lequin, K.D. Lichtenbelt, D. Chitayat, P. Kannu, A.G. James, F. Groenendaal, E. Chakkarapani, S. Blaser, and L.S. de Vries

ABSTRACT

BACKGROUND AND PURPOSE: Neuroimaging features in neonates with RASopathies are rarely reported, and to date, there are no neuroimaging studies conducted in this population. Our aim was to investigate the occurrence of supratentorial and posterior fossa abnormalities on brain MRIs of neonates with a RASopathy.

MATERIALS AND METHODS: An observational case-control study of neonates with a confirmed RASopathy was conducted. The presence of an intraventricular and/or parenchymal hemorrhage and punctate white matter lesions and assessments of the splenium of the corpus callosum, gyrification of the cortical gray matter, and enlargement of the extracerebral space were noted. The vermis height, transverse cerebellar diameter, cranial base angle, tentorial angle, and infratentorial angle were measured.

RESULTS: We reviewed 48 brain MR studies performed at 3 academic centers in 3 countries between 2009 and 2017. Sixteen of these infants had a genetically confirmed RASopathy (group 1), and 32 healthy infants were enrolled as the control group (group 2). An increased rate of white matter lesions, extracerebral space enlargement, simplification of the cortical gyrification, and white matter abnormalities were seen in group 1 ($P < .001$, for each). The vermis height of patients was significantly lower, and tentorial and infratentorial angles were significantly higher in group 1 ($P = .01$, $P < .001$, and $P = .001$, respectively).

CONCLUSIONS: Neonates with a RASopathy had characteristic structural and acquired abnormalities in the cortical gray matter, white matter, corpus callosum, cerebellum, and posterior fossa. This study provides novel neuroimaging findings on supratentorial and posterior fossa abnormalities in neonates with a RASopathy.

ABBREVIATIONS: NICU = neonatal intensive care unit; NS = Noonan syndrome; TA = tentorial angle

RASopathies are a family of multisystemic disorders with overlapping phenotypic features affecting approximately 1 in 1000 neonates.[1] These disorders are caused by germline mutations in genes coding for proteins that are part of the RAS/mitogen-activated protein kinase pathway, essential for cell proliferation, differentiation, and senescence. There are >15 genes identified so far in the RAS/mitogen-activated protein kinase signal pathway. Noonan syndrome (NS) is the most common RASopathy, and Noonan-like syndrome, Costello syndrome, cardiofaciocutaneous syndrome, and NS with multiple lentigines (formerly known as LEOPARD syndrome) are other closely related disorders.[2-4] Phenotypic features, associated risks, and severity vary widely, ranging from mild facial features to a lethal combination of congenital anomalies.[2]

The prenatal manifestations of RASopathies are nonspecific and include increased nuchal translucency/cystic hygroma; jugular cysts; hydrops fetalis; pleural/pericardial effusion and ascites; polyhydramnios; cardiac abnormalities, typically a dysplastic pulmonary valve; and hypertrophic cardiomyopathy. Postnatally, they present with craniofacial dysmorphism, respiratory distress, lymphatic dysplasia, cardiac defects, renal anomalies, and hypotonia.[3,5] Neuroimaging features in neonates and infants with RASopathies are rare because in most cases, there is no indica-

Received October 30, 2017; accepted after revision February 5, 2018.

From the Departments of Neonatology (M.N.C., F.G., L.S.d.V.) and Pediatric Radiology (M.L.), Wilhelmina Children's Hospital, University Medical Center Utrecht, Utrecht, the Netherlands; Brain Center Rudolf Magnus (M.N.C., F.G., L.S.d.V.) and Department of Medical Genetics (K.D.L.), University Medical Center Utrecht, Utrecht, the Netherlands; Divisions of Clinical and Metabolic Genetics (D.C., P.K.), Neonatology (A.G.J.), and Neuroradiology (S.B.), Department of Diagnostic Imaging, The Hospital for Sick Children and Department of Paediatrics, University of Toronto, Toronto, Canada; Departments of Obstetrics and Gynecology, Laboratory Medicine, Pathobiology and Molecular Genetics (D.C.), University of Toronto, Toronto, Canada; and Division of Neonatology (E.C.), School of Clinical Sciences, St Michael's Hospital, University of Bristol, Bristol, UK.

Susan Blaser and Linda S. DeVries contributed equally to the article.

Please address correspondence to Linda S. de Vries, MD, PhD, Department Neonatology, KE 04.123.1, Lundlaan 6, 3584 EA Utrecht, the Netherlands; e-mail: l.s.devries@umcutrecht.nl

Indicates article with supplemental on-line table.

http://dx.doi.org/10.3174/ajnr.A5611

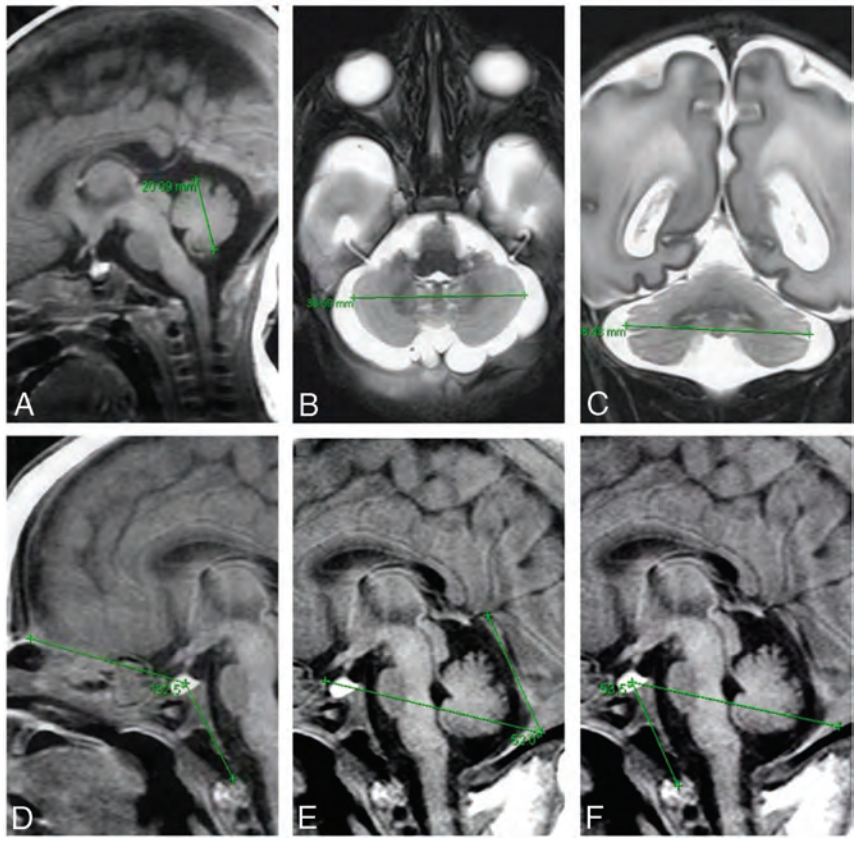

FIG 1. Measurement techniques used in the study. *A*, Preterm neonate, gestational age 35 weeks 6 days. T1-weighted MR image shows measurement of the vermis height from the culmen to the uvular lobule on the midsagittal image. *B* and *C*, Preterm neonate, gestational age 30 weeks 6 days. T2-weighted MR images show the cerebellar diameter measurement at the widest points of the cerebellum on axial and coronal images, respectively. *D*, Preterm neonate, gestational age 33 weeks 4 days. T1-weighted image shows cranial base angle measurement with the fonticulus frontalis used as the anterior landmark; midsella, as the vertex point; and the distal tip of the ossified clivus, as the terminal point. *E*, Measurement of the tentorial angle between the Twining line and a line drawn through tentorium cerebelli with tuberculum sella used as the originating point. *F*, T1-weighted MR image shows measurement of the infratentorial angle, using a line originating from the midsella drawn through the midpoint of the dural reflection of the torcula herophili to the inner cortex, and a line drawn between the midsella and basion.

tion for brain MR imaging. Intracranial abnormalities such as Chiari malformation, syringomyelia, cerebrovascular anomalies, benign external hydrocephalus, craniosynostosis, and posterior fossa abnormalities have been reported in the pediatric and adult literature; however, to date, no observational study was conducted to define the brain abnormalities in patients with a RASopathy.[6-9] We conducted a case-control study to determine the occurrence of supratentorial and posterior fossa abnormalities on brain MRIs in neonates with a RASopathy.

MATERIALS AND METHODS

An observational case-control study of neonates with a genetically confirmed RASopathy and severe clinical symptoms necessitating admission to the neonatal intensive care unit (NICU) at 3 academic centers (Wilhelmina Children's Hospital, University Medical Center Utrecht, the Netherlands; The Hospital for Sick Children, University of Toronto, Canada; and St. Michael's Hospital, University of Bristol, UK) between 2009 and 2017 was conducted. The participating centers have a long-standing practice of incorporating brain MR imaging into the diagnostic process in severely ill neonates during their NICU course. For each neonate with a RASopathy (group 1), 2 healthy neonates with a gestational age of ±7 days were selected for the control group (group 2). Demographic data were extracted from the patients' files and/or hospital data base. A 1:2 case-control ratio was used to increase the statistical power of the analysis.

In the Wilhelmina Children's Hospital, until 2010, brain MR imaging was performed on a 1.5T system (Intera or Achieva; Philips Healthcare, Best, the Netherlands), and the protocol included sagittal T1-weighted images (slice thickness, 5 mm) and axial T2-weighted images (slice thickness, 2–5 mm). Between 2010 and 2017, the brain MR imaging was performed on a 3T system (Achieva; Philips Healthcare), and the recent protocol included conventional sagittal T1-weighted imaging (slice thickness, 3 mm), axial 3D T1-weighted imaging (slice thickness, 2 mm), and axial T2-weighted imaging (slice thickness, 2 mm). The Hospital for Sick Children, Toronto, followed a similar predefined brain MR imaging protocol according to their institutional guidelines during the study period, and the MR imaging studies were all completed without pharmacologic sedation on a 1.5T Avanto scanner (Siemens, Erlangen, Germany) with 3D coronal volumetric T1-weighted and axial fast spin-echo T2-weighted images obtained at both time points. The University of Bristol followed a predefined MR imaging protocol according to their institutional guidelines, and the MR imaging study was performed on a 3T Magnetom Skyra scanner (Siemens) with 3D coronal volumetric T1-weighted and axial T2-weighted images (slice thickness, 3 mm). Diffusion-weighted imaging and susceptibility-weighted imaging were performed for distinguishing ischemic and hemorrhagic lesions. DWI was acquired in the axial plane (slice thickness, 4 mm), and SWI was performed using a 3D gradient-echo sequence with flow compensation. Only the high-quality images suitable for scoring and measurements were included in the study.

MR Imaging Findings and Measurements

MR Imaging Findings. The presence of an intraventricular and/or cerebral parenchymal hemorrhage, cerebellar hemorrhage, and punctate white matter lesions; visual assessment of the corpus callosum for hypoplasia; configuration of the splenium; gyrification of the cortex; and enlargement of the extracerebral space were evaluated by consensus reads.

Clinical characteristics and MRI angle measurements and assessments

	Group 1 (n = 16)	Group 2 (n = 32)	P Value[a]
Gestational age (mean) (wk)	35.6 ± 4.2	37.3 ± 4.5	.1[b]
Postmenstrual age at MRI (mean) (wk)	37.6 ± 4.8	39.8 ± 6.5	.2[b]
Vermis height (mean) (mm)	20.5 ± 4.4	23.7 ± 3.9	.01[be]
Transcerebellar diameter (mean)			
Axial	48.6 ± 9.1	52.3 ± 9.8	.2[b]
Coronal	48.8 ± 9.6	52.7 ± 9.7	.2[b]
Cranial base angle (mean)	130.3° ± 4.0°	134.8° ± 5.3°	.005[ce]
Tentorial angle (mean)	55.4° ± 3.4°	46.6° ± 5.8°	<.001[ce]
Infratentorial angle (mean)	52.2° ± 6.5°	47.7° ± 4.0°	.001[be]
Intraventricular hemorrhage (No.) (%)	8 (47)	0 (0)	<.001[de]
Cerebellar abnormality (No.) (%)	9 (56)	0 (0)	<.001[de]
Hemorrhagic lesion	6 (67)		
Hemorrhagic-cystic lesion	3 (33)		
Enlarged extracerebral space (No.) (%)	13 (81)	0 (0)	<.001[de]
Mild	10 (77)		
Severe	3 (23)		
Delayed cortical gyrification (No.) (%)	12 (75)	0 (0)	<.001[de]
WMI after cerebral hemorrhage (No.) (%)	9 (56)	0 (0)	<.001[de]
Punctate white matter lesion	7 (78)		
Cystic lesion	2 (22)		
Abnormality in DWI (n = 12) (No.) (%)	7 (58)	-	
Focal restriction	6 (86)		
Extensive restriction	1 (14)		
Corpus callosum abnormality (No.) (%)	4 (25)	0 (0)	<.001[de]
Vertical appearance	3 (75)		
Hypoplasia	1 (25)		

Note:—WMI indicates white matter injury.
[a] Adjusted for gestational age as appropriate.
[b] Mann-Whitney U test.
[c] T test.
[d] Fisher exact test.
[e] Significant.

MR Imaging Assessments. The vermis height was measured from the culmen to the uvular lobule on the midsagittal image, with care to avoid including the cerebellar tonsil (Fig 1*A*). The transverse cerebellar diameter was measured on both the coronal and axial views at the widest points of the cerebellum, traversing the dentate nuclei (Fig 1*B*, -*C*). For measurement of the cranial base angle, the fonticulus frontalis was used as the anterior landmark; midsella, as the vertex point; and the distal tip of the ossified clivus, as the terminal point (Fig 1*D*). The tentorial angle (TA) was measured by the angle between the Twining line and a line drawn through tentorium cerebelli. On every measurement, the tuberculum sella was used as the originating point for the TA (Fig 1*E*). The infratentorial angle was measured as the angle between a line originating from the midsella drawn through the midpoint of the dural reflection of torcula herophili to the inner cortex and a line drawn between the midsella and basion (Fig 1*F*).

Two senior neuroradiologists (M.L. and S.B.) with >20 years' experience in reading neonatal MRIs performed and supervised the measurements and assessed the images separately in a blinded fashion on digital PACS systems. To evaluate the interobserver agreement, we assessed 15 studies from 5 random patients and calculated the interclass correlation coefficient for each parameter. For the retrospective data analysis, the ethics committee of the University Medical Center, Utrecht, waived informed consent owing to analysis of anonymous clinical data. The same applied to the control subjects from Toronto. Written parental consent was obtained in Bristol and Toronto for patients.

Statistical Analysis

Statistical analyses of the data were performed using the Statistical Package for the Social Sciences, Version 21.0 (IBM, Armonk, New York). All continuous values were presented as mean ± SD. Categoric values were presented as number and percentage. The Fisher exact test was used to compare categoric variables among groups. The Mann-Whitney U test was used to compare nonparametric variables, and the Student t test was used for the comparison of variables that showed normal distribution. The Pearson correlation coefficient was used to assess the correlation between the continuous variables. The Spearman correlation coefficient was used to search for the correlation among the non-normal variables. To evaluate the reliability of measurements across observers, we calculated the interclass correlation coefficient and classified it as good for 0.8< interclass correlation coefficient <0.9 and excellent for interclass correlation coefficient >0.9. Statistical significance was set at $P < .05$.

RESULTS

We reviewed 48 brain MR imaging studies performed at 3 academic centers between 2009 and 2017. Sixteen of these infants had a genetic diagnosis of a RASopathy (group 1), and 32 healthy neonates were enrolled as the control group (group 2). Eleven (68.7%) neonates in group 1 were diagnosed with NS, while 5 (31.3%) had other RASopathies. Groups were similar in terms of gestational age and postmenstrual age at the date of MR imaging (Table). Molecular genetic testing in all patients included the *BRAF*, *HRAS*, *KRAS*, *MAP2K1*, *MAP2K2*, *PTPN11*, *RAF1*, *RIT1*, *SHOC2*, and *SOS1* genes. Eight of 16 (50%) patients in group 1 had a mutation in the *PTPN11* gene (NS), while there were 3 (18.8%) with a mutation in *HRAS* (Costello syndrome); 1 (6.2%), with *SHOC2* (Noonan-like syndrome); 1 (6.2%), with *SOS1* (NS); 1 (6.2%), with *RAF1* (NS); 1 (6.2%), with *BRAF* (cardiofaciocutaneous syndrome); and 1 (6.2%), with *RIT1* (NS). In 1 patient, the *PTPN11* mutation was paternally inherited; the father was diagnosed with NS with multiple lentigines.

Data regarding white matter injury, intraventricular and cerebellar hemorrhages, and their characteristics are given in the Table. Increased rates of extracerebral space enlargement, simplification of the cortical gyrification, and white matter abnormalities were seen in group 1 (Table and Fig 2). There was a significant difference between the groups in terms of white matter lesions on conventional MR imaging, DWI, and SWI ($P < .001$) (Table). There was 1 (3.1%) neonate in group

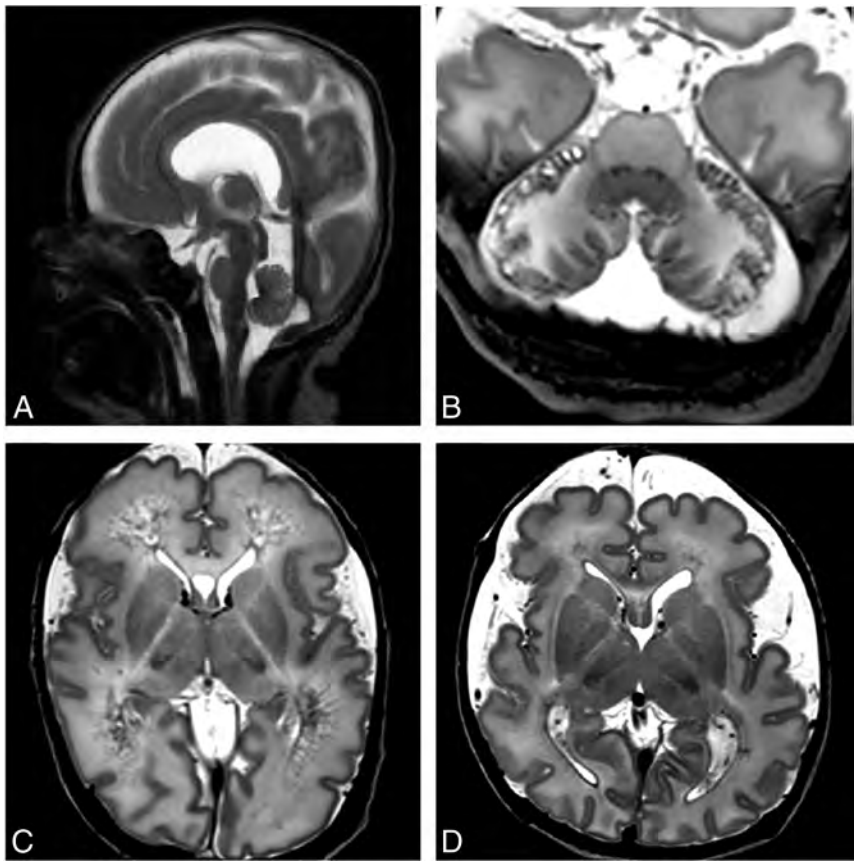

FIG 2. Characteristic MR imaging findings of neonates with a RASopathy. *A*, Preterm neonate, gestational age 28 weeks 6 days, MR imaging performed at postmenstrual age 30 weeks 5 days. T2-weighted midsagittal MR image shows a vertical tentorium and splenium of the corpus callosum. *B*, Preterm neonate, gestational age 34 weeks 2 days. T2-weighted axial MR image demonstrates the presence of hemorrhagic and cystic lesions in the peripheral regions of the cerebellum. *C*, Preterm neonate, gestational age 34 weeks 2 days. T2-weighted axial MR imaging shows a mildly enlarged extracerebral space with severe white matter injury, which evolved into extensive cysts. *D*, Preterm neonate, gestational age 34 weeks. Axial T2-weighted MR image shows a severely enlarged extracerebral space, punctate white matter lesions, and a small amount of blood in the lateral ventricles.

2 who was found to have a Chiari type I malformation. When the neonates in group 1 were categorized according to their mutation type [subgroup 1: *PTPN11* mutation (+), subgroup 2: another type of mutation (+)], there were no differences between the subgroups in terms of white matter injury, intraventricular hemorrhage, cerebellar hemorrhage, extracerebral space enlargement, or gyrification of the cerebral cortex ($P >$ .05 for all parameters).

Angle Measures

The agreement between the neuroradiologists evaluating the images showed an excellent correlation for the measurement of all angles (interclass correlation coefficient = 0.94, 0.96, 0.98 for TA, cranial base angle, and infratentorial angle, respectively). When the groups were compared regarding the cerebellar measurements, the vermis height of the patients in group 1 was significantly lower than that of group 2 ($P = .01$), and vermis height showed a significantly positive correlation with gestational age in both groups ($r = 0.71$; $P < .001$). Although both axial and coronal transverse cerebellar diameters of the cerebellum were reduced in group 1, they were not significantly different across the groups ($P = .2$ for both). Both cerebellar diameters showed a positive correlation with gestational age in the study population ($r = 0.73$, $P < .001$; and $r = 0.74$, $P < .001$, respectively). Tentorial and infratentorial angles were found to be higher in group 1 ($P < .001$ and $P = .001$, respectively) (Table and Fig 3), and the TA showed a negative correlation with vermis height ($r = -0.30$, $P = .03$). After we controlled for gestational age and categorization according to the mutation type, there were no differences between subgroup 1 and subgroup 2 regarding vermis height, TA, cranial base angle, or infratentorial angle ($P > .05$ for all parameters).

Outcome

Ten (62.5%) patients in group 1 died during infancy due to respiratory and cardiac complications, and 7 (70%) of these 10 infants died during their NICU stay due to multiple organ dysfunction. Only one of the surviving infants showed a normal developmental outcome. Characteristics of the patients with a RASopathy and data regarding their clinical features and outcome are given in the On-line Table.

DISCUSSION

This is the first study that describes cranial MR imaging findings in neonates with a RASopathy. We have demonstrated that these neonates had characteristic acquired and structural abnormalities in the posterior fossa, including peripheral cerebellar hemorrhage, vermis hypoplasia, and a steep tentorial configuration compared with healthy controls. Moreover, these neonates also showed an increased incidence of cerebral white matter lesions, enlarged extracerebral spaces, simplification of the cortical folding, and structural corpus callosum abnormalities involving the splenium. Apart from anecdotal pediatric and adult case reports, data on global cerebral abnormalities in neonates with a RASopathy are rare in the literature. Brasil et al[10] reported cerebral abnormalities, including isolated ventriculomegaly, posterior fossa anomalies, and cerebral atrophy in infants with NS. Few studies included cerebral MR imaging, and hypoplastic corpus callosum has only been described once in a patient with RASopathy with a mutation in the *NF1* gene.[11] A vertical position of the splenium of the corpus callosum has also been reported in the literature.[7] We have seen that the splenium of the corpus callosum showed a visually abnormal vertical configuration in 3 of our neonates and was underdeveloped in one. Furthermore, an enlarged extracerebral space, which was previously reported by Gripp et al[7] in 1 patient, and delayed gyrification of the cere-

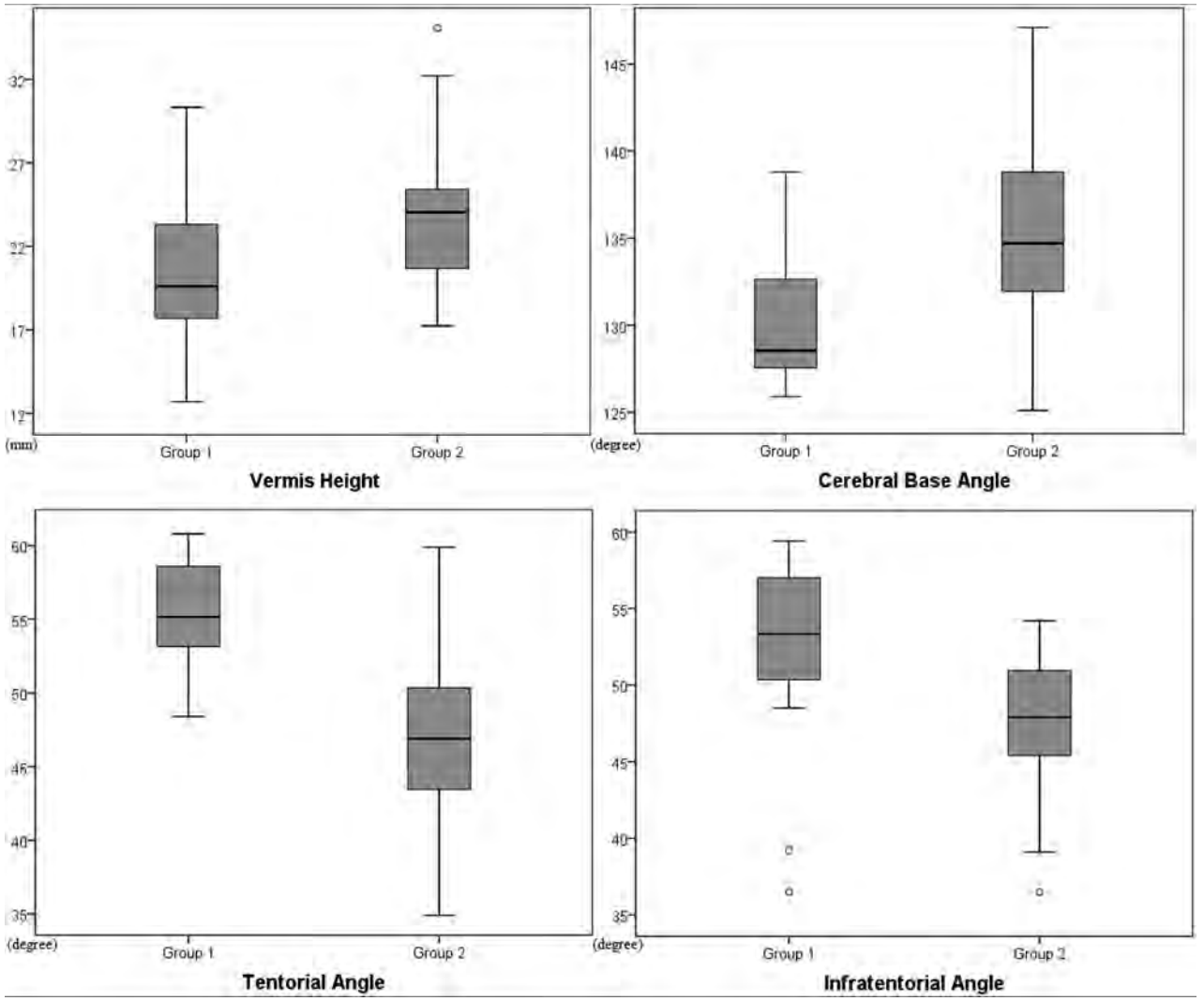

FIG 3. Boxplot graphs show the comparison of the vermis height (*top left*), cranial base angle (*top right*), tentorial angle (*bottom left*), and infratentorial angle (*bottom right*) between infants with a RASopathy and the control group.

bral cortex were present in most of our patients. To the best of our knowledge, these are all novel contributions.

Total brain tissue grows linearly prenatally, and Hüppi et al[12] demonstrated an almost 3-fold increase in the global brain volume between 29 and 41 weeks postconception using volumetric MR imaging measures. The inclination of the fetal tentorium gradually increases during pregnancy, because the rate of the cerebellar growth exceeds the rate of the occipital cerebral growth.[13] However, during postnatal development, the tentorium moves inferiorly while progressively decreasing the TA.[14] We found that the TA of the neonates with a RASopathy was significantly higher than that of healthy controls at similar postmenstrual ages. An increased TA reflects the vertical configuration of the tentorium; however, because we have seen a negative correlation between vermis height and TA, an increased TA in these patients can be explained by the effect of a genetic disorder causing disruption of developmental processes, resulting in a permanent change in the morphology of the cranium with an effect on the growth of other structures, as defined previously.[9,15,16]

Bony structures of the skull base also undergo changes, namely retroflexion of the basicranium in the intrauterine and flexion in the postnatal period. These changes are reflected by an increase in the cranial base angle during fetal development and a subsequent decrease in the postnatal period.[14,17] Any anomaly during the orderly posteroanterior ossification of the cranial structures can interfere with normal formation of the bones and soft tissues and may result in an abnormal configuration.[18,19] The RAS/mitogen-activated protein kinase pathway plays a vital role in regulating components that are critical to normal development, and it is not surprising that a dysregulation in this pathway has deleterious effects on both embryonic and later stages of development, with implications on bony structures and cerebral tissues.[1] It has been shown that patients with NS have various skull anomalies.[3,20] Addissie et al[21] reported a 2-month-old female infant with NS who developed craniosynostosis, and Ueda et al[9] reported a series of 9 infants with a RASopathy and craniosynostosis. It has also been shown that infants with Costello syndrome had bone abnormalities resulting in macrocrania.[5] In the present study, we have demonstrated that the cranial base angles of the infants with RASopathy were markedly depressed, a finding that reflects the abnormal skeletal development of the basicranium. Furthermore, a significantly increased infratentorial angle also

confirms the deviant cranial cavity floor extending posteriorly, as shown in our study. Although the detailed pathophysiologic mechanism remains unknown, we speculate that rather than acquired lesions such as hemorrhages, these bone abnormalities and consequently changed angulations may result in the anomalous formation of the posterior fossa, which, in turn, changes the tentorial configuration.

In recent decades, cumulative evidence has shown that cerebellar function extends beyond sensorimotor control to relate the cerebellum with higher order functions such as attention, language, executive function, and cognition.[22,23] Preterm neonates with cerebellar hemorrhage can develop cognitive impairment, and the vermis is considered especially important for cognitive outcome.[24] Consistent with the literature, we have seen that the cerebellar vermis had an increase in size, as reflected by the increased vermis height, with increasing gestational age. Most interesting, we have found that neonates with a RASopathy had a small vermis compared with controls. Although the cerebellum of the infants in our study showed a trend toward a decreased diameter on coronal and axial planes, this was not statistically significant compared with healthy controls. We might speculate that the disrupting effect of these genetic conditions was more prominent on the central part of the organ, which contains more neural networks than the peripheral parts. Hemorrhages were seen in the peripheral parts of the cerebellum. It is unlikely that these hemorrhages contributed to the hypoplasia of the vermis in these infants because the hemorrhages were of recent onset and the hypoplasia was already present at birth. Further investigation is needed to find whether the hemorrhagic cerebellar lesions and the small vermis, as seen in our patients, can be used in the future as an imaging finding to better predict outcome; however, we would recommend a brain MR imaging in a neonate with a suspected diagnosis of a RASopathy, particularly when the neonatal course is complicated.

The present study has several limitations. First, due to the retrospective design of the study it is difficult to make causal inferences. Second, owing to the rarity of the severe neonatal presentation that requires NICU admission, the number of patients included in the study was relatively small. Finally, because most patients were diagnosed with NS, these results might not be generalizable for all RASopathies; however, NS is the most common type of these closely related disorders in the literature, hence, it is expected to see the same distribution in our cohort. Moreover, we have observed the same characteristic findings, consistently, in every patient in our study regardless of their final genetic diagnosis.

It is of interest that despite a wide range of neurodevelopmental outcomes in children with a RASopathy, no brain MR imaging studies have been performed previously to explore whether these could be explained by differences in brain structure and development. Our data may suggest that early MR imaging could help to better prognosticate outcome. The neonates included in our study were at the severe end of the spectrum because they required admission to a NICU. Thus, further studies are needed on those with a less complicated neonatal course. During the neonatal period, RASopathies can be challenging to diagnose because characteristic morphologic findings may not be fully established and recognition of these neuroimaging findings should facilitate the diagnosis of these conditions.[5] Our study provides novel neuroimaging information that could help neonatologists, neuroradiologists, and geneticists to suspect the diagnosis and be aware of the possible complications during their follow-up. Further studies are warranted to define the exact pattern of injury and malformation in these neonates and correlate their neuroimaging findings with their neurodevelopmental outcome.

CONCLUSIONS

This study provides novel neuroimaging findings on supratentorial and posterior fossa abnormalities in neonates with a RASopathy. These structural and acquired changes in the neonatal brain might prompt the physician to consider the diagnosis of a RASopathy, and we suggest that cranial MR imaging be considered for these patients, especially when the neonatal course is complicated.

Disclosures: Peter Kannu—*UNRELATED*: *Board Membership*: Hypophosphatasia Advisory Board (Alexion). Floris Groenendaal—*UNRELATED*: *Expert Testimony*, *Comments*: payment for expert testimony in cases of perinatal asphyxia*; *Patents (Planned, Pending or Issued)*: 2-iminobiotin, *Comments*: patent on 2-iminobiotin for neuroprotection after perinatal asphyxia*. Susan Blaser—*UNRELATED*: *Royalties*: Amirsys/Elsevier. Linda S. de Vries—*UNRELATED*: *Employment*: University Medical Center in Utrecht, *Comments*: I am a consult neonatologist and receive my salary from the university; *Grants/Grants Pending*: ZonMW (Dutch), *Comments*: grant for which I am co-Principal Investigator*; *Payment for Lectures Including Service on Speakers Bureaus*: cranial ultrasound course in London, *Comments*: I am a speaker at the yearly cranial ultrasound course in London. I receive an honorarium, which is not paid to me but to our neonatal neurology research foundation. The same applies to an electroencephalography meeting organized by Natus Medical this year, for which again my honorarium was paid directly to the foundation*; *Royalties*, *Comments*: I am a coauthor of 2 books for which I receive royalties: Hellström-Westas L, de Vries LS, Rosen I. *An Atlas of Amplitude-Integrated EEGs in the Newborn*. 2nd ed. London: Informa Health; August 2008; and Govaert P, de Vries LS. *An Atlas of Neonatal Brain Sonography*. 2nd ed. (CDM 182-183). London: Mac Keith Press. ISBN: 978-1-898683-56-8, July 2010; *Travel/Accommodations/Meeting Expenses Unrelated to activities listed*, *Comments*: If I am an invited speaker, I usually pay for my flight and get reimbursed for these expenses. *Money paid to the institution.

REFERENCES

1. Rauen KA. **The RASopathies.** *Annu Rev Genomics Hum Genet* 2013; 14:355–69 CrossRef Medline
2. Aoki Y, Niihori T, Inoue S, et al. **Recent advances in RASopathies.** *J Hum Genet* 2016;61:33–39 CrossRef Medline
3. Roberts AE, Allanson JE, Tartaglia M, et al. **Noonan syndrome.** *Lancet* 2013;381:333–42 CrossRef Medline
4. Gelb BD, Roberts AE, Tartaglia M. **Cardiomyopathies in Noonan syndrome and the other RASopathies.** *Prog Pediatr Cardiol* 2015;39: 13–19 CrossRef Medline
5. Myers A, Bernstein JA, Brennan ML, et al. **Perinatal features of the RASopathies: Noonan syndrome, cardiofaciocutaneous syndrome and Costello syndrome.** *Am J Med Genet A* 2014;164A:2814–21 CrossRef Medline
6. Peiris A, Ball MJ. **Chiari (type 1) malformation and syringomyelia in a patient with Noonan's syndrome.** *J Neurol Neurosurg Psychiatry* 1982;45:753–54 CrossRef Medline
7. Gripp KW, Zand DJ, Demmer L, et al. **Expanding the SHOC2 mutation associated phenotype of Noonan syndrome with loose anagen hair: structural brain anomalies and myelofibrosis.** *Am J Med Genet A* 2013;161A:2420–30 CrossRef Medline
8. Hinnant CA. **Noonan syndrome associated with thromboembolic brain infarcts and posterior circulation abnormalities.** *Am J Med Genet* 1995;56:241–24 CrossRef Medline
9. Ueda K, Yaoita M, Niihori T, et al. **Craniosynostosis in patients with RASopathies: accumulating clinical evidence for expanding the phenotype.** *Am J Med Genet* 2017;173:2346–52 CrossRef Medline

10. Brasil AS, Pereira AC, Wanderley LT, et al. **PTPN11 and KRAS gene analysis in patients with Noonan and Noonan-like syndromes.** *Genet Test Mol Biomarkers* 2010;14:425–32 CrossRef Medline
11. Nyström AM, Ekvall S, Stromberg B, et al. **A severe form of Noonan syndrome and autosomal dominant cafe-au-lait spots: evidence for different genetic origins.** *Acta Paediatr* 2009;98:693–98 CrossRef Medline
12. Hüppi PS, Warfield S, Kikinis R, et al. **Quantitative magnetic resonance imaging of brain development in premature and mature newborns.** *Ann Neurol* 1998;43:224–35 CrossRef Medline
13. Moss ML, Noback CR. **Differential growth of the human brain.** *J Comp Neurol* 1956;105:539–51 CrossRef Medline
14. Rehder R, Yang E, Cohen AR. **Variation of the slope of the tentorium during childhood.** *Childs Nerv Syst* 2016;32:441–50 CrossRef Medline
15. Meyer-Marcotty P, Böhm H, Linz C, et al. **Three-dimensional analysis of cranial growth from 6 to 12 months of age.** *Eur J Orthod* 2014;36:489–96 CrossRef Medline
16. Cao H, Alrejaye N, Klein OD, et al. **A review of craniofacial and dental findings of the RASopathies.** *Orthod Craniofac Res* 2017;20: 32–38 CrossRef Medline
17. Jeffery N, Spoor F. **Brain size and the human cranial base: a prenatal perspective.** *Am J Phys Anthropol* 2002;118:324–40 CrossRef Medline
18. Nemzek WR, Brodie HA, Hecht ST, et al. **MR, CT, and plain film imaging of the developing skull base in fetal specimens.** *AJNR Am J Neuroradiol* 2000;21:1699–706 Medline
19. Matras H, Watzek G, Perneczky A. **Cephalometric observations in premature craniosynostosis.** *J Maxillofac Surg* 1977;5:298–303 CrossRef Medline
20. Naficy S, Shepard NT, Telian SA. **Multiple temporal bone anomalies associated with Noonan syndrome.** *Otolaryngol Head Neck Surg* 1997;116:265–67 CrossRef Medline
21. Addissie YA, Kotecha U, Hart RA, et al. **Craniosynostosis and Noonan syndrome with KRAS mutations: expanding the phenotype with a case report and review of the literature.** *Am J Med Genet A* 2015;167A:2657–63 CrossRef Medline
22. Sokolov AA, Miall RC, Ivry RB. **The cerebellum: adaptive prediction for movement and cognition.** *Trends Cogn Sci* 2017;21:313–32 CrossRef Medline
23. Limperopoulos C. **The vulnerable immature cerebellum.** *Semin Fetal Neonatal Med* 2016;21:293–94 CrossRef Medline
24. Stoodley CJ, Limperopoulos C. **Structure-function relationships in the developing cerebellum: evidence from early-life cerebellar injury and neurodevelopmental disorders.** *Semin Fetal Neonatal Med* 2016;21:356–64 CrossRef Medline

Clival Malformations in CHARGE Syndrome

E.S. Mahdi and M.T. Whitehead

ABSTRACT

BACKGROUND AND PURPOSE: CHARGE syndrome is a multisystemic congenital disorder, most commonly including coloboma, heart malformations, choanal atresia, developmental delay, and genital and ear anomalies. The diagnostic criteria for CHARGE syndrome have been refined with time. However, limited reports describe skull base and craniocervical junction abnormalities. Recently, a coronal clival cleft has been identified in association with CHARGE syndrome. The aim of our study was to assess the prevalence of clival pathology in CHARGE syndrome.

MATERIALS AND METHODS: In this retrospective study, the CT/MR imaging data base at a single academic children's hospital was queried for the phrase "CHARGE syndrome" during a 17-year period (2001–2017). Electronic medical records were reviewed to confirm the diagnosis. Images were assessed for skull base anomalies, specifically clival hypoplasia and dysplasia.

RESULTS: The search yielded 42 examinations (21 CTs and 21 MRIs) from 15 distinct patients (mean age, 4.1 ± 5.6 years; range, 2 days to 19 years). CHARGE syndrome diagnosis was confirmed either by clinical and genetic testing ($n = 6$) or by clinical diagnosis only ($n = 9$). A coronal clival cleft was identified in 87% of patients (37 examinations, $n = 13$ patients), either partial (53%) or complete (33%). Clival hypoplasia without clefting was present in all 5 examinations from the remaining 2 patients.

CONCLUSIONS: Clival pathology is universal in CHARGE syndrome. Coronal clival clefts are extremely common, representing a useful additional diagnostic finding. Detection of a clival cleft should alert the radiologist to examine the palate, choana, eyes, ears, and olfactory centers for other signs of CHARGE syndrome.

ABBREVIATIONS: CHARGE = Coloboma of the eye, Heart defects, Atresia of the choanae, Retardation of growth and/or development, Genital and/or urinary abnormalities, and Ear abnormalities and deafness; *CHD7* = chromodomian helicase DNA-binding protein 7

CHARGE syndrome is a rare genetic disorder with widespread malformations. The acronym CHARGE includes coloboma, heart malformation, choanal atresia, retardation of growth and/or development, genital anomalies, and ear anomalies.[1] Across time, there has been refinement of the diagnostic criteria to 3 major (the classic 3*C*'s: choanal atresia, coloboma, semicircular canal hypoplasia) and 5 minor features.[2,3] The prevalence of CHARGE syndrome was estimated to be 1/8500 live births by the Canadian Pediatric Surveillance Program.[4] The discovery of a CHARGE syndrome–associated gene, *CHD7* (chromodomain helicase DNA-binding protein 7, MIM 608892), has greatly assisted syndromic prevalence estimations due to the phenotypic diversity of the disease.[5] Mutations of the *CHD7* gene are present in two-thirds of patients with CHARGE syndrome. Phenotype and genotype correlation are required to better assess this syndrome.[6] The skull base and craniocervical junction abnormalities are often underrecognized in CHARGE syndrome. Detection of these osseous abnormalities should alert the radiologist to examine the palate, choana, eyes, ears, and olfactory centers for other signs of CHARGE syndrome. Recently, a coronal clival cleft has been identified in association with CHARGE syndrome.[7] The aim of our study was to assess the prevalence of clival pathology including clival clefts in patients with CHARGE syndrome.

MATERIALS AND METHODS

Subjects

A retrospective study was performed after institutional review board approval with Health Insurance Portability and Accountability Act compliance. Requirement for informed consent was waived. The imaging data base at a single academic children's hospital was queried for the term "CHARGE syn-

Received November 11, 2017; accepted after revision February 5, 2018.

From the Department of Diagnostic Imaging and Radiology (E.S.M., M.T.W.), Children's National Medical Center, Washington, DC; and George Washington University Hospital (M.T.W.), Washington, DC.

Please address correspondence to Eman S. Mahdi, MD, Department of Radiology, Children's National Health System, 111 Michigan Ave NW, Washington, DC 20010; e-mail: emahdi@childrensnational.org

Indicates article with supplemental on-line table.

http://dx.doi.org/10.3174/ajnr.A5612

drome" provided by the history or by the suspected radiologic findings after filtering by technique (CT and MR imaging) during a 17-year period (2001–2017). Review of the electronic medical records of all patients was performed to confirm the diagnosis and symptomatology. Images were assessed for skull base anomalies, specifically clival hypoplasia/dysplasia and coronal clival cleft.

FIG 1. Midline sagittal spoiled gradient-recalled acquisition T1WI (1.5T MR imaging; TR/TE = 11/5.1 ms; TI = 500 ms; slice thickness = 1.5 mm) from a 3-month-old girl with CHARGE syndrome shows a distinctive complete coronally oriented clival cleft in the basiocciput (*large arrow*). Also note mild thinning of the corpus callosum (*small arrow*), cerebellar vermian hypoplasia, and brain stem volume loss.

Imaging Characteristics

All examinations were of diagnostic quality. MR imaging studies were performed on either 1.5T or 3T scanners (Discovery MR 750 and 450; GE Healthcare, Milwaukee, Wisconsin). Sagittal T1WI, axial T2WI, axial T2 fluid-attenuated inversion recovery imaging, coronal fat-saturated T2WI, and axial DTI with 7 noncollinear directions of encoding were reviewed. Axial T1WI and coronal fat-saturated T1WI of the brain were also performed in 5 MRIs after IV gadolinium administration in 5 different patients (0.1 mmol/kg of either gadoterate meglumine [$n = 2$] or gadopentetate dimeglumine [$n = 3$]). CT images of the head, temporal bone, facial bone, sinuses, and/or cervical spine were acquired on a 16–detector row scanner (GE Healthcare). Studies were reviewed in a blinded manner by a qualified pediatric neuroradiologist (M.T.W.) with >5 years of experience. Imaging studies were qualitatively examined for all visible abnormalities involving the brain, ocular and olfactory systems, temporal bones, cleft lip/palate, and the presence of clival abnormalities.

RESULTS

Characteristics of the Cohort

The search yielded 17 patients with a history or suspected radiologic findings of CHARGE syndrome. Two patients lacking diagnostic confirmation were excluded. The final cohort comprised 42 examinations (21 CTs and 21 MRIs) from 15 patients (mean

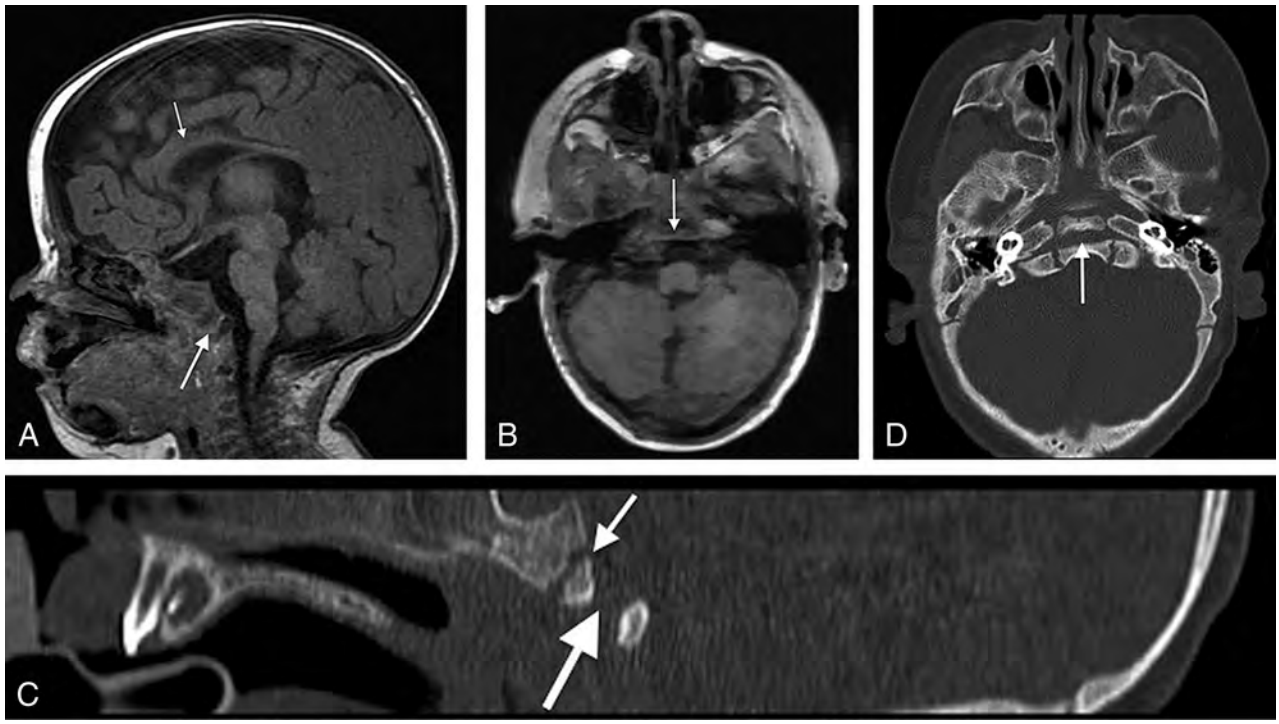

FIG 2. *A*, Midline sagittal spoiled gradient-recalled acquisition T1WI (1.5T MR imaging; TR/TE = 12/5 ms; TI = 500 ms; slice thickness = 2 mm) from a 4-month-old girl with CHARGE syndrome shows a complete coronally oriented clival cleft in the basiocciput (*large arrow*). Also note thinning of the corpus callosum (*small arrow*), cerebellar vermian hypoplasia, and brain stem volume loss. *B*, Axial spoiled gradient-recalled acquisition of the same patient shows a coronally oriented cleft traversing the clivus (*arrow*). Corresponding sagittal (*C*) and axial (*D*) CT images demonstrate the complete cleft (*large arrow*) as distinct from the normal spheno-occipital synchondrosis (*small arrow* in *C*).

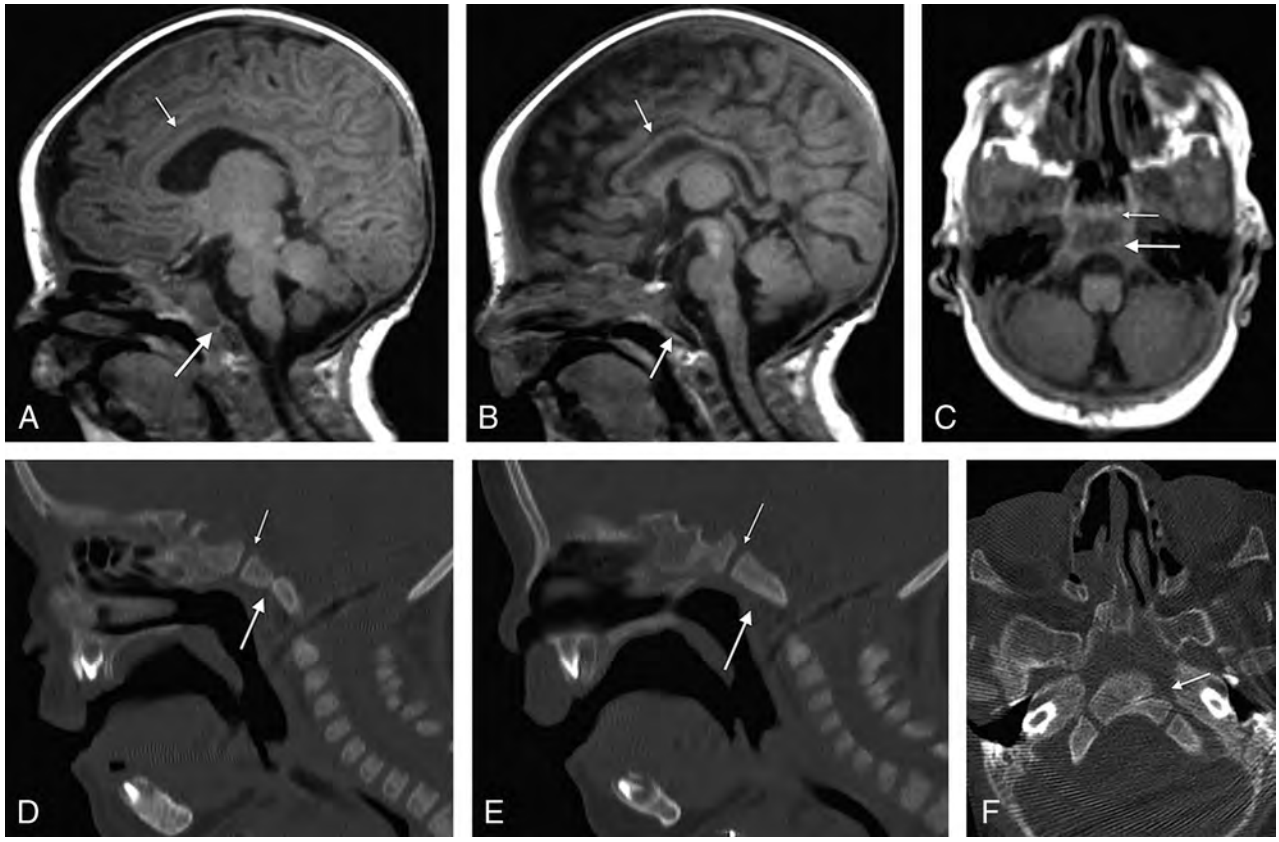

FIG 3. Spoiled gradient-recalled acquisition T1WI (3T MR imaging; TR/TE = 6.6/2.5 ms; TI = 700 ms; slice thickness = 0.63 mm) from a 34-day-old boy with CHARGE syndrome shows a partial (unilateral left side) coronally oriented clival cleft in the basiocciput. *A*, Left parasagittal unilateral clival cleft (*large arrow*), mild thinning of the corpus callosum (*small arrow*), cerebellar vermian hypoplasia, and brain stem volume loss are illustrated. *B*, Right parasagittal image shows a normal appearance of the clivus without clefting, a thin corpus callosum (*small arrow*), and vermian and brain stem hypoplasia. *C*, Axial T1WI of the same patient with a left-sided cleft (*large arrow*) and normal spheno-occipital synchondrosis (*small arrow*). Corresponding sagittal and axial CT images (*D* and *F*) further demonstrate the unilateral left clival cleft (*large arrow*, *D* and *F*) and absence of clival clefting on the contralateral side (*E*). Note normal spheno-occipital synchondrosis (*small arrow*, *D* and *E*).

age, 4.1 ± 5.6 years; range, 2 days to 19 years); 3 patients were older than 11 years at the time of imaging.

Diagnosis of CHARGE syndrome was confirmed by either clinical and genetic testing ($n = 6$) or clinical diagnosis only ($n = 9$).[2,3] Fifty-three percent of the patients were male ($n = 8$).

Clival Imaging Findings

A coronal clival cleft was identified in 87% of patients (37 examinations, $n = 13$ patients), either complete (33%, $n = 5$) (Figs 1 and 2) or partial (53%, $n = 8$) (Fig 3). Clival hypoplasia without clefting was present in all 5 examinations from the remaining 2 patients (On-line Table).[8] Those with a partial cleft were further characterized as having either a unilateral cleft in 25% ($n = 2$) (Fig 3) or bilateral cleft with minimal central fusion in 75% ($n = 6$).

Clival Clefting/Hypoplasia and CHD7 *Mutation*

The clival findings were further stratified according to the *CHD7* mutation. Those with *CHD7* mutation ($n = 6$) had an equal number of complete and partial clival clefts (50%, $n = 3$) of each type. Those with a non-*CHD7*-confirmed clinical diagnosis ($n = 9$) were variable (partial cleft, $n = 5$; complete cleft, $n = 2$; and clival hypoplasia, $n = 2$).

Other imaging features pertinent to the diagnosis of CHARGE syndrome affecting the eye, olfactory apparatus, ears, and brain are classified in the On-line Table.

DISCUSSION

CHARGE syndrome is a systemic disorder with multiorgan involvement. Specific organ abnormalities include cardiac (75%–80%, including atrial septal defect, ventricular septal defect, patent ductus arteriosus, tetralogy of Fallot, atrioventricular canal defect, and double outlet right ventricle),[9] genitourinary (including hypospadias; penile agenesis; bifid scrotum; cryptorchidism; atresia of the vagina, cervix, and uterus; renal hypoplasia; solitary kidney; hydronephrosis; vesicoureteral reflux; and duplex kidneys),[9] ocular (80%, including coloboma of the iris, retina-choroid, and/or disc; and microphthalmos),[9] ear (80%–100%, including external ear dysmorphology; incus hypoplasia; decreased number of cochlear turns; and absent semicircular canals),[9,10] olfactory (100%, including unilateral or bilateral absence or hypoplasia of the olfactory bulbs or sulci),[9,11] choanal atresia (50%–60%),[12] orofacial (15%–20%, including cleft lip/palate),[9] brain (including corpus callosum agenesis; posterior fossa anomalies; cranial nerve dysfunction; and cerebellar vermis hypoplasia),[12,13] and osseous anomalies (skull base and craniocervical junction).[9,8,14] Prenatal diagnosis of CHARGE syndrome has been reported through the finding of *CHD7* mutations on chorionic villus sampling and ultrasonographic findings of hydramnios, choanal atresia, tracheoesophageal fistula, and semicircular canal agenesis.[15,16]

Craniocervical junction abnormalities are common in CHARGE syndrome. Fujita et al[8] demonstrated a high prevalence of basioccipital hypoplasia and basilar invagination in CHARGE syndrome and recommended routine assessment of these anomalies to exclude a life-threatening basilar invagination. Natung et al[14] reported a case of basilar invagination, short clivus, fused cervical vertebrae, and occipitalization of the atlas. A recent case report of a coronal clival cleft has been identified in association with CHARGE syndrome.[7] Recently, Hoch et al[17] described a dorsally angulated clivus with posterior displacement of an ossific density in 7 of 10 patients with CHARGE syndrome. The dominant findings we have described herein, namely partial and complete coronal clival clefting, correspond to the description and imaging depictions that those authors provided and further emphasize the importance of craniocervical junction anomalies in CHARGE syndrome.

The pathogenesis of these anomalies in CHARGE syndrome is not clearly understood. They likely originate in the first trimester, concurrent with other CHARGE malformations.[18] The *CHD7* gene encoding chromodomain helicase DNA-binding protein 7 (*CHD7* protein) may play a role through the assumption of the interaction between the neural crest and somite cells, which are responsible for formation of the basiocciput during development.[19,20]

The clivus is formed from 2 main components, the upper basisphenoid and the lower basiocciput. The 2 are separated by the normal spheno-occipital synchondrosis. The basiocciput is formed from 4 occipital sclerotomes.[19] The clivus reaches the full developmental length by 11 years of age.[21] Clival clefts occur caudal to and distinct from the spheno-occipital synchondrosis, which usually fuses between 12 and 18 years of age.[19] The presence of normal anatomic variants such as clival canal/foramen, fossa navicularis magna, or basilar transverse fissure (Sauser fissure) should not be confused with a clival cleft.[22-24]Although the etiology of coronal clival clefts is unknown, these clefts could be related to incomplete fusion of clival ossification centers, enlarged clival canals (fossa navicularis), or persistence of basilar transverse fissure.[19,22-24]

This study has some limitations by being retrospective and having a relatively small sample size. Despite these limitations, to date, it is the largest study to describe and illustrate clival pathology and clefting in CHARGE syndrome.

CONCLUSIONS

Clival pathology is universal in CHARGE syndrome. Coronal clival clefts are extremely common, representing a useful diagnostic feature and should be considered an additional finding in CHARGE syndrome. The skull base should be scrutinized for these characteristic anomalies. Detection of a clival cleft should alert the radiologist to examine the palate, choana, eyes, ears, and olfactory centers for other signs of CHARGE syndrome.

REFERENCES

1. Pagon RA, Graham JM Jr, Zonana J, et al. **Coloboma, congenital heart disease, and choanal atresia with multiple anomalies: CHARGE association.** *J Pediatr* 1981;99:223–27 CrossRef Medline
2. Verloes A. **Updated diagnostic criteria for CHARGE syndrome: a proposal.** *Am J Med Genet A* 2005;133A:306–08 CrossRef Medline
3. Blake KD, Davenport SL, Hall BD, et al. **CHARGE association: an update and review for the primary pediatrician.** *Clin Pediatr (Phila)* 1998;37:159–73 CrossRef Medline
4. Issekutz KA, Graham JM Jr, Prasad C, et al. **An epidemiological analysis of CHARGE syndrome: preliminary results from a Canadian study.** *Am J Med Genet A* 2005;133A:309–17 CrossRef Medline
5. Vissers LE, van Ravenswaaij CM, Admiraal R, et al. **Mutations in a new member of the chromodomain gene family cause CHARGE syndrome.** *Nat Genet* 2004;36:955–57 CrossRef Medline
6. Sanlaville D, Verloes A. **CHARGE syndrome: an update.** *Eur J Hum Genet* 2007;15:389–99 CrossRef Medline
7. Mahdi E, Whitehead MT. **Coronal clival cleft in CHARGE syndrome.** *Neuroradiol J* 2017;30:574–77 CrossRef Medline
8. Fujita K, Aida N, Asakura Y, et al. **Abnormal basiocciput development in CHARGE syndrome.** *AJNR Am J Neuroradiol* 2009;30:629–34 CrossRef Medline
9. Blake KD, Prasad C. **CHARGE syndrome.** *Orphanet J Rare Dis* 2006;1:34 CrossRef
10. Morimoto AK, Wiggins RH 3rd, Hudgins PA, et al. **Absent semicircular canals in CHARGE syndrome: radiologic spectrum of findings.** *AJNR Am J Neuroradiol* 2006;27:1663–71 Medline
11. Blustajn J, Kirsch CF, Panigrahy A, et al. **Olfactory anomalies in CHARGE syndrome: imaging findings of a potential major diagnostic criterion.** *AJNR Am J Neuroradiol* 2008;29:1266–69 CrossRef Medline
12. Lalani SR, Hefner MA, Belmont JW, et al. **CHARGE syndrome.** In: Adam MP, Ardinger HH, Pagon RA, et al, eds. *GeneReviews*. Seattle: University of Washington; 1993–2018 Medline
13. Yu T, Meiners LC, Danielsen K, et al. **Deregulated FGF and homeotic gene expression underlies cerebellar vermis hypoplasia in CHARGE syndrome.** *Elife* 2013;2:e01305 CrossRef Medline
14. Natung T, Goyal A, Handique A, et al. **Symmetrical chorioretinal colobomata with craniovertebral junction anomalies in CHARGE syndrome: a case report with review of literature.** *J Clin Imaging Sci* 2014;4:5 CrossRef Medline
15. Becker R, Stiemer B, Neumann L, et al. **Mild ventriculomegaly, mild cerebellar hypoplasia and dysplastic choroid plexus as early prenatal signs of CHARGE association.** *Fetal Diagn Ther* 2001;16:280–83 CrossRef Medline
16. Hertzberg BS, Kliewer MA, Lile RL. **Antenatal ultrasonographic findings in the CHARGE association.** *J Ultrasound Med* 1994;13:238–42 CrossRef Medline
17. Hoch MJ, Patel SH, Jethanamest D, et al. **Head and neck MRI findings in CHARGE syndrome.** *AJNR Am J Neuroradiol* 2017;38:2357–63 CrossRef Medline
18. Sanlaville D, Etchevers HC, Gonzales M, et al. **Phenotypic spectrum of CHARGE syndrome in fetuses with CHD7 truncating mutations correlates with expression during human development.** *J Med Genet* 2006;43:211–17 CrossRef Medline
19. Smoker WR. **Craniovertebral junction: normal anatomy, craniometry, and congenital anomalies.** *Radiographics* 1994;14:255–77 CrossRef Medline
20. Nie X. **Cranial base in craniofacial development: developmental features, influence on facial growth, anomaly, and molecular basis.** *Acta Odontol Scand* 2005;63:127–35 CrossRef Medline
21. Krmpotić-Nemanić J, Vinter I, Kelovizć Z, et al. **Postnatal changes of the clivus.** *Ann Anat* 2005;187:277–80 CrossRef Medline
22. Inal M, Muluk NB, Ozveren MF, et al. **The presence of clival foramen through multidetector computed tomography of the skull base.** *J Craniofac Surg* 2015;26:e580–82 CrossRef Medline
23. Beltramello A, Puppini G, El-Dalati G, et al. **Fossa navicularis magna.** *AJNR Am J Neuroradiol* 1998;19:1796–98 Medline
24. Hofmann E, Prescher A. **The clivus: anatomy, normal variants and imaging pathology.** *Clin Neuroradiol* 2012;22:123–39 CrossRef Medline

Noninvasive Assessment of Hemodynamic Stress Distribution after Indirect Revascularization for Pediatric Moyamoya Vasculopathy

D. Tortora, M. Severino, M. Pacetti, G. Morana, M.M. Mancardi, V. Capra, A. Cama, M. Pavanello, and A. Rossi

ABSTRACT

BACKGROUND AND PURPOSE: Indirect revascularization surgery is an effective treatment in children with Moyamoya vasculopathy. In the present study, we hypothesized that DSC-PWI may reliably assess the evolution of CBF-related parameters after revascularization surgery, monitoring the outcome of surgical pediatric patients with Moyamoya vasculopathy. Thus, we aimed to evaluate differences in DSC-PWI parameters, including the hemodynamic stress distribution, in surgical and nonsurgical children with Moyamoya vasculopathy and to correlate them with long-term postoperative outcome.

MATERIALS AND METHODS: Pre- and postoperative DSC parameters of 28 patients (16 females; mean age, 5.5 ± 4.8 years) treated with indirect revascularization were compared with those obtained at 2 time points in 10 nonsurgical patients (6 females; mean age, 6.9 ± 4.7 years). We calculated 4 normalized CBF-related parameters and their percentage variance: mean normalized CBF of the MCA territory, mean normalized CBF of the proximal MCA territory, mean normalized CBF of cortical the MCA territory, and hemodynamic stress distribution. The relationship between perfusion parameters and postoperative outcomes (poor, fair, good, excellent) was explored using 1-way analysis of covariance ($P < .05$).

RESULTS: A significant decrease of the mean normalized CBF of the proximal MCA territory and hemodynamic stress distribution and an increase of the mean normalized CBF of the cortical MCA territory were observed after revascularization surgery ($P < .001$). No variations were observed in nonsurgical children. Postoperative hemodynamic stress distribution and its percentage change were significantly different in outcome groups ($P < .001$).

CONCLUSIONS: DSC-PWI indices show postoperative hemodynamic changes that correlate with clinical outcome after revascularization surgery in children with Moyamoya disease.

ABBREVIATIONS: central nCBF = mean nCBF of the proximal MCA territory; cortical nCBF= mean nCBF of cortical MCA territory; EDAMS = encephalo-duro-arterio-myosynangiosis; EEG = electroencephalography; hdSD = hemodynamic stress distribution; IQ = intelligence quotient; mean nCBF = mean nCBF of all MCA territories; MM = Moyamoya vasculopathy; nCBF = normalized CBF

Moyamoya vasculopathy (MM) is characterized by progressive occlusion of the supraclinoidal internal carotid artery with development of leptomeningeal collaterals. Stenosis of the proximal part of the anterior, middle, and posterior cerebral arteries may be associated.[1,2] These vascular changes result from a wide range of genetic and environmental triggers, either idiopathic (Moyamoya disease) or associated with systemic diseases (Moyamoya syndrome or quasi-Moyamoya disease).[1,3,4] Independent of the underlying causes, the natural history includes occurrence of transient ischemic attacks, ischemic infarcts, or intracerebral hemorrhage. Because medical treatment is not effective in preventing clinical events, patients with compromised cerebral hemodynamics and/or neurologic symptoms may benefit from surgical revascularization.[1,2]

Brain PWI is commonly used to estimate cerebral hemodynamics in patients with MM, depicting regions of decreased cerebral perfusion and cerebrovascular reserve that can improve after revascularization surgery. Nuclear medicine studies, including $H_2[^{15}0]$-PET and iodine 123 iodoamphetamine SPECT, are still considered the criterion standard for evaluating both preoperative cerebral hemodynamic impairment and postoperative perfusion changes in MM.[1,2,5] On the other hand, several studies have

Received December 21, 2017; accepted after revision February 14, 2018.

From the Neuroradiology (D.T., M.S., G.M., A.R.), Neurosurgery (M.P., V.C., A.C., M.P.), and Neuropsychiatry Units (M.M.M.), Istituto Giannina Gaslini, Genoa, Italy.

Domenico Tortora and Mariasavina Severino contributed equally as first authors.

Please address correspondence to Mariasavina Severino, MD, Neuroradiology Unit, Istituto Giannina Gaslini, Via Gerolamo Gaslini, 5, 16147 Genoa, Italy; e-mail: mariasavinaseverino@gaslini.org; @MSavinaSeverino

Indicates article with supplemental on-line tables.

Indicates article with supplemental on-line photos.

http://dx.doi.org/10.3174/ajnr.A5627

demonstrated the efficacy of dynamic susceptibility contrast PWI to depict regions of critically reduced brain perfusion while avoiding radiation exposure.[6-8] Furthermore, the acetazolamide challenge test used to underpin the cerebrovascular reserve is not devoid of potential complications.[9-11] Hence, there has been an effort to find alternative methods for evaluating cerebral hemodynamics in patients with MM.[12-15] In 1996, Kashiwagi et al[12] proposed the ratio of mean CBF values in the lentiform nucleus (central CBF) and cortical MCA territories (cortical CBF) as an index of hemodynamic stress distribution (hdSD) using xenon-enhanced CT.[12] More recently, Schubert et al[14] demonstrated that hdSD could be a more robust parameter than CBF alone for disease assessment in adults with MM. At present, no studies have evaluated the results of indirect revascularization in children with MM using the hdSD obtained with noninvasive PWI techniques.

Here, we hypothesized that DSC-PWI may reliably assess the evolution of CBF-related parameters after revascularization surgery and that hdSD may better correlate with the long-term neurologic outcome of children with MM. To test this hypothesis, we looked for differences of DSC perfusion parameters (including hdSD) among surgical and nonsurgical children with MM evaluated at both an early time point after surgery and last follow-up.

MATERIALS AND METHODS

Our institutional review board approved this retrospective study and parents provided informed consent.

Subjects

We identified 45 consecutive children with MM confirmed at angiography who underwent brain MR imaging and MRA studies at our institution from 2009 to 2016. Inclusion criteria were the following: 1) the presence of DSC-PWI performed at multiple time points, before and after the operation and/or during follow-up (3 patients excluded); 2) good-quality DSC-PWI—that is, unaffected by motion artifacts (4 patients excluded); and 3) available clinical and electroencephalography (EEG) data before and after surgical revascularization (no patients excluded). Patients were categorized into those who underwent indirect revascularization and those without surgical treatment. The indirect revascularization procedures consisted of encephalo-duro-arterio-myosynangiosis (EDAMS), performed as previously described.[16] For the group of patients who underwent EDAMS, we selected PWI performed at 3 consecutive times points: before the operation (time point 1), 3 months after the operation (time point 2), and at last follow-up (time point 3). In the second group of patients, we included 2 PWI studies performed at first examination and last follow-up.

MR Perfusion Techniques

MR imaging was performed on a 1.5T scanner (Achieva; Philips Healthcare, Best, the Netherlands) using an 8-channel head array coil. Uncooperative patients were sedated during the examinations with sevoflurane during spontaneous breathing via a facemask. Brain MR imaging protocol included 3D T1-weighted fast-field echo gradient-recalled, axial FLAIR, T2-weighted, and DWI sequences and 3D TOF MRA. PWI-DSC was performed with a gradient-echo EPI sequence with the following parameters: TR/TE, 2000/60 ms; flip angle, 90°; matrix, 128 × 128; FOV, 240 × 240 mm; section thickness, 5 mm; gap, 0 mm; 28 axial sections. A series of images (10 sections, 50 images per section) was obtained before, during, and after the administration of contrast agent (gadoterate meglumine, 0.5-mmol/mL, 0.2 mL/kg of body weight at 3 mL/s) using a power injector (Spectris MR injector; MedRad, Indianola, Pennsylvania), followed by a 30-mL bolus of saline administered at the same injection rate. Perfusion CBF maps were computed after eliminating the effect of contrast agent recirculation using a γ-variate curve-fitting via commercially available postprocessing software (IB Neuro, Version 2.0; Imaging Biometrics, Elm Grove, Wisconsin).[17]

Perfusion Imaging Analysis

The perfusion analysis was independently performed for each hemisphere at each time point. Because the revascularization procedures were performed in all patients in the MCA territory, the quantitative analysis of perfusion was restricted to this area. In addition, the nontreated hemispheres of patients who underwent unilateral revascularization were excluded from the analysis of nonsurgical hemispheres because it was demonstrated that these may benefit from surgery performed on the contralateral brain.[18] For the quantitative analysis, CBF maps were registered to the Montreal Neurological Institute space through a linear registration process using the FMRIB Linear Image Registration Tool (FLIRT; http://www.fmrib.ox.ac.uk/fsl/fslwiki/FLIRT).[19] An atlas-based segmentation of the MCA, linearly registered in the Montreal Neurological Institute space, was performed for each brain hemisphere, dividing the MCA territory into 3 VOIs: the proximal, the middle, and the distal portions.[20] Subsequently, an additional VOI, including the white and gray matter of both cerebellar hemispheres, was manually drawn for normalization because Moyamoya vasculopathy typically spares cerebellar arteries (On-line Fig 1). The fslmeants function of FSL (http://fsl.fmrib.ox.ac.uk/fsl/fslwiki/Fslutils) was finally used to calculate the mean CBF of each VOI. The normalized CBF (nCBF) values were calculated as the ratio of mean CBF values of each MCA VOI to the mean CBF values of the cerebellum.

Four CBF-related parameters were calculated at rest in surgical and nonsurgical hemispheres: 1) mean nCBF of all MCA territories (mean nCBF); 2) mean nCBF of the proximal MCA territory (central nCBF); 3) mean nCBF of the cortical MCA territory (cortical nCBF), considering both middle and distal MCA portions; and 4) the hemodynamic stress distribution, defined as the ratio of mean CBF in the central versus cortical regions (central nCBF/cortical nCBF).[12] Finally, we calculated the percentage variance of all CBF-related parameters between the selected MR imaging time points. In surgical patients, the percentage variance of all CBF-related parameters between time points 1 and 2 corresponded to an "early percentage variance," while the percentage variance between time points 1 and 3 was considered a "late percentage variance."

Clinical Outcome

The neurologic outcome in the 28 surgical patients was evaluated on the basis of the following: 1) resolution or improvement of neurologic symptoms, 2) absence of new ischemic events (transient ischemic attack and/or stroke), 3) stability or improvement of the global intelligence quotient (IQ) score at neuropsycholog-

Table 1: Comparison of CBF-related parameters between 2 time points in surgical and nonsurgical brain hemispheres

Index	Surgical				Nonsurgical			
	Before Operation	Last Follow-Up	% Variance	*P*[a]	First MRI	Last Follow-Up	% Variance	*P*[a]
Central nCBF (mean)	1.806 ± 1.001	1.107 ± 0.835	−33.8%	<.001[b]	1.820 ± 0.916	1.856 ± 0.863	10%	.732
Cortical nCBF (mean)	1.224 ± 0.693	2.811 ± 2.298	152.1%	<.001[b]	1.328 ± 0.663	1.363 ± 0.612	12.1%	.627
Mean nCBF	1.515 ± 0.814	1.959 ± 1.474	47.4%	.081	1.574 ± 0.777	1.610 ± 0.725	11%	.765
hdSD (mean)	1.515 ± 0.364	0.454 ± 0.239	−68.8%	<.001[b]	1.359 ± 0.233	1.342 ± 0.241	−1.2%	.117

[a] Significance level of paired *t* test analysis used to compare CBF-related parameters at 2 time points.
[b] Significant.

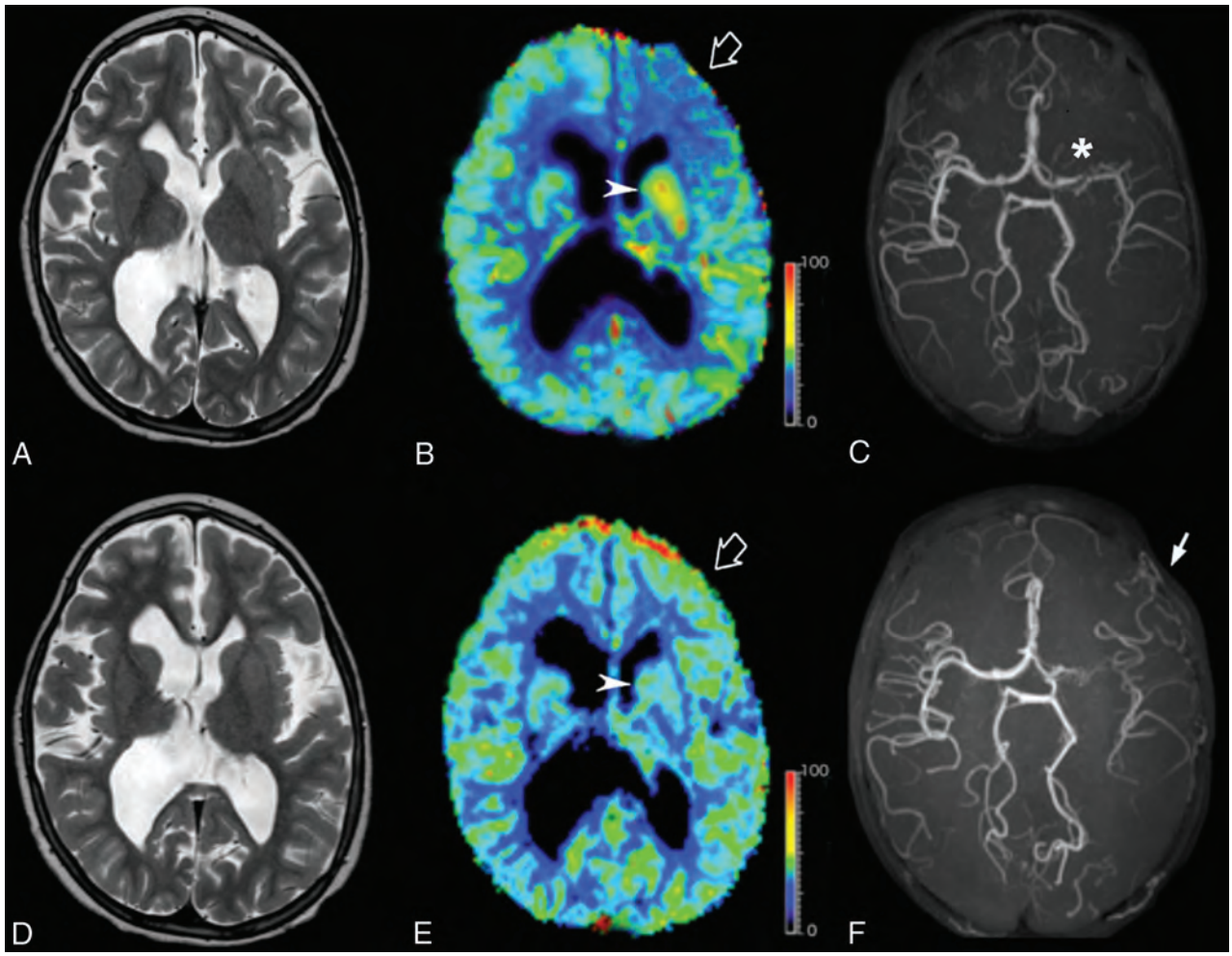

FIG 1. Representative T2-weighted images (*A* and *D*), DSC-CBF (*B* and *E*), and noncontrast MR angiography (*C* and *F*) of pre- (*A–C*) and postoperative (*D–F*) images in a 10-year-old patient with left Moyamoya disease (*asterisk*) treated with surgical indirect revascularization (EDAMS) (*white arrow*). The *empty arrow* indicates the left frontal region with reduced CBF values before the operation (*B*). DSC-PWI acquired 36 months after left EDAMS shows an improvement in CBF in the left frontal lobe (*empty arrow*, *E*). *Arrowheads* indicate preoperative hyperperfusion of the proximal MCA region (*B*) that returns to normal at postoperative PWI (*E*). The color scale unit of the CBF map is mL/100 mg/min.

ical evaluations, and 4) resolution or improvement of EEG abnormalities. Patients were assigned to 1 of the following 4 categories by the same blinded neurologist at the last outpatient visit: 4, excellent (preoperative symptoms totally gone without fixed neurologic deficits and EEG abnormalities and improved global IQ score); 3, good (symptoms totally gone with persistent EEG abnormalities and stable or improved global IQ score); 2, fair (persistent symptoms and EEG abnormalities but with decreased frequency and stable or decreased global IQ score); and 1, poor (unchanged or worsened symptoms and EEG abnormalities and decreased global IQ score).[7]

Statistical Analysis

A paired *t* test was used to compare the mean CBF-related parameters evaluated by DSC between the first and the last MR imaging time points. A 1-way analysis of covariance was used to test statistically significant differences of CBF-related parameters between surgical and nonsurgical hemispheres controlling for age, sex, side of revascularization, and time interval between MR imaging examinations.

The Jonckheere-Terpstra test was used to test trends in CBF-related parameters evaluated both in the earlier and later stages after the operation, with outcome categories. Perfusion parame-

Table 2: Relation between CBF-related parameters and clinical outcome in surgical patients

Index	Time Point	Clinical Outcome (mean)			P^a
		Fair	Good	Excellent	
Central nCBF	TP1	2.222 ± 1.146	1.175 ± 1.111	2.008 ± 0.742	.728
	TP2	2.038 ± 1.123	1.049 ± 0.975	1.649 ± 0.694	.933
	TP3	1.631 ± 1.012	0.806 ± 0.825	1.806 ± 1.001	.813
Early % variance central nCBF	TP1 vs TP2	−9.512 ± 12.011	−4.185 ± 16.081	−16.081 ± 15.109	.090
Late % variance central nCBF	TP1 vs TP3	−29.024 ± 24.023	−18.371 ± 32.163	−43.941 ± 30.218	<.090
Cortical nCBF	TP1	1.718 ± 0.682	0.760 ± 0.729	1.306 ± 0.535	.967
	TP2	2.157 ± 0.951	1.178 ± 0.974	2.697 ± 1.623	.177
	TP3	2.359 ± 1.310	1.451 ± 1.195	3.717 ± 2.668	.098
Early % variance cortical nCBF	TP1 vs TP2	21.931 ± 25.817	85.478 ± 65.899	113.672 ± 15.733	.046[b]
Late % variance cortical nCBF	TP1 vs TP3	30.784 ± 46.941	146.324 ± 119.817	197.586 ± 203.151	.047[b]
Mean nCBF	TP1	1.970 ± 0.777	0.968 ± 0.917	1.657 ± 0.622	.626
	TP2	2.097 ± 0.886	1.114 ± 0.967	2.173 ± 1.129	.185
	TP3	1.995 ± 0.942	1.129 ± 0.980	2.403 ± 1.685	.196
Early % variance mean nCBF	TP1 vs TP2	4.919 ± 19.287	31.057 ± 14.137	32.989 ± 17.349	.168
Late % variance mean nCBF	TP1 vs TP3	−1.797 ± 34.718	48.936 ± 62.703	63.780 ± 102.328	.123
hdSD	TP1	1.406 ± 0.588	1.521 ± 1.296	1.550 ± 0.313	.989
	TP2	1.073 ± 0.480	0.822 ± 0.179	0.694 ± 0.222	.003[b]
	TP3	0.772 ± 0.323	0.515 ± 0.161	0.310 ± 0.056	<.001[b]
Early % variance hdSD	TP1 vs TP2	−24.016 ± 9.812	−45.013 ± 11.767	−53.801 ± 16.003	<.001[b]
Late % variance hdSD	TP1 vs TP3	−44.676 ± 4.101	−65.555 ± 10.516	−79.054 ± 6.043	<.001[b]

Note:—TP1 indicates time point 1, before the operation; TP2, time point 2, three months after the operation; TP3, time point 3, last follow-up after the operation; Early % variance, percentage variance between TP1 and TP2; Late % variance, percentage variance between TP1 and TP3.

[a] Significance level of the Jonckheere-Terpstra test used to test whether there was a statistically significant trend between CBF-related parameters and clinical outcome categories.

[b] Significant.

ters that survived the latter test were considered independent variables of a 1-way analysis of covariance to evaluate the relationship with clinical outcome (dependent variable); results of this analysis were corrected for confounding effects of age, sex, and duration of clinical follow-up. Moreover, estimated marginal means of the selected perfusion parameters were used to obtain Sidak-corrected post hoc comparisons. Statistical analysis was performed using commercially available software (SPSS, Version 21.0 for Windows; IBM, Armonk, New York), and a significant *P* value was set at .05.

RESULTS

Patients

Thirty-eight of 45 patients with MM satisfied the inclusion criteria (18 females; mean age at clinical onset, 6 ± 1.8 years; range, 6 months to 16.3 years). The first group was composed of 28 children who underwent indirect revascularization (16 females; mean age at clinical onset, 5.5 ± 4.8 years; range, 6 months to 10 years). Bilateral revascularization was performed in 10, and unilateral revascularization, in 18 patients. The second group included 10 patients with bilateral MM who did not undergo surgical synangiosis (6 females; mean age at clinical onset, 6.9 ± 4.7 years; range, 1–14 years). Thus, 38 surgical hemispheres (ie, 20 from bilateral surgery and 18 from unilateral surgery) and 20 nonsurgical hemispheres were included in the study. Overall, we analyzed 84 DSC-PWIs for surgical patients (28 performed at each time point) and 20 DSC-PWIs for nonsurgical patients (10 performed at each time point). In the first patient group, the mean period between preoperative PWI and the operation (time point 1) was 4.5 days (range, 1–15 days). The mean period between the operation and the first postoperative PWI (time point 2) was 3.1 ± 0.5 months (range, 2.6–3.6 months), and the mean period between the operation and the last postoperative PWI (time point 3) was 38.5 ± 25 months (range, 13.5–63.5 months). No significant difference in the interval between the first and the last MR imaging studies was observed between the 2 groups ($P = .246$). On-line Table 1 summarizes the clinical-radiologic data of the 38 patients, including MRA findings.

DSC Perfusion Imaging

The mean values of CBF-related parameters evaluated by DSC-PWI at the first MR imaging study and at the last follow-up are reported in Table 1. In surgical hemispheres, significant reduction of the central nCBF and a significant increase of cortical nCBF were noticed at last follow-up ($P < .001$) (Fig 1 and On-line Fig 2). Moreover, a significant reduction of the hdSD index was observed in surgical hemispheres ($P < .001$). No variations of CBF-related parameters were observed in nonsurgical hemispheres ($P > .05$). The 1-way analysis of covariance showed a significant effect of surgical revascularization on central nCBF ($P = .005$), cortical nCBF ($P = .011$), the hdSD index ($P < .001$), and the hdSD percentage age variation ($P < .001$) after controlling for age, sex, and the time interval between MR imaging examinations (On-line Table 2).

Relation between Perfusion MR Imaging Data and Clinical Outcomes

At the last outpatient visit, 14/28 surgical children had an excellent outcome; 7/28, a good outcome; and 7/28, a fair outcome. No patients had a new stroke or intracranial hemorrhage during the interval between the MR imaging studies. Table 2 shows results of the Jonckheere-Terpstra test. A significant trend toward better outcome was observed in patients who had lower hdSD values at time point 2 ($P = .003$) and time point 3 ($P < .001$), higher early ($P < .001$) and late ($P < .001$) percentage decreases in hdSD indices, and higher early ($P = .046$) and late ($P = .047$) percentage

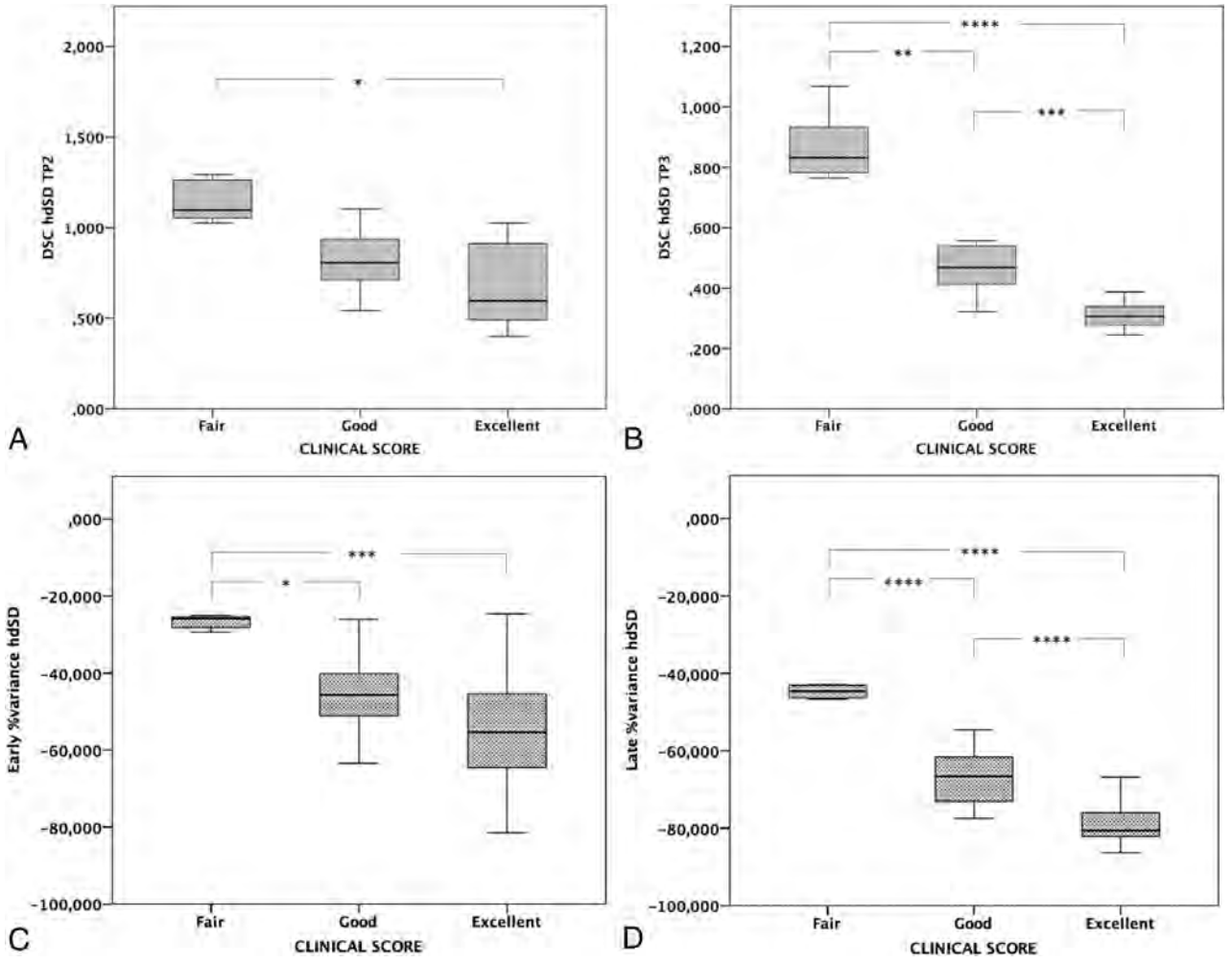

FIG 2. The relation between change in DSC hdSD values and clinical outcomes 3 months after revascularization (time point 2 [TP2], *A*) and at last follow-up (time point 3 [TP3], *B*). The relation between the percentage variation of DSC hdSD and clinical outcomes 3 months after the operation (early percentage variation, *C*) and at last follow-up (late percentage variation, *D*). Note that these perfusion indices are significantly different in the 3 clinical outcome categories, especially when comparing excellent and good versus fair categories. The "poor" category was not included in the graphs because no surgical patients had poor clinical outcome. *Three asterisks* indicate $P < .001$; *2 asterisks*, $P = .001$; *1 asterisk*, $P = .01$.

increases in cortical nCBF. Of these, only hdSD at time point 2, hdSD at time point 3, early percentage variance of hdSD, and late percentage variance of hdSD remained significantly different in the clinical outcome categories after covariance analysis (Fig 2 and On-line Table 3).

DISCUSSION

In this study, we demonstrated that nCBF in the central and cortical MCA territories and the hdSD index obtained with DSC-PWI may be used to noninvasively evaluate postsurgical variations of brain perfusion in children with MM. We found a significant reduction of central nCBF and hdSD and a significant increase of cortical nCBF in surgical hemispheres, while no relative perfusion changes were observed in the hemispheres of nonsurgical patients with Moyamoya disease. Most interesting, hdSD was a more robust parameter for postsurgical assessment than central nCBF and cortical nCBF. These results confirm and expand the initial observations on xenon CT by Kashiwagi et al,[12] reporting a significant reduction of the hdSD index in the surgical hemispheres of 4 children with MM, and by Takahashi et al,[13] showing postsurgical hdSD reduction in 3 adult patients who underwent a bypass operation and in 1 who underwent indirect revascularization. The variations of these CBF-related parameters correspond well to the pathologic mechanisms of MM and postsurgical hemodynamic changes. In the initial phases of the disease, collateral networks of dilated vessels at the base of the brain attempt to compensate for the hypoperfusion of the peripheral cortical territories. This attempt generates an abnormal arterial pressure gradient between deep and superficial brain regions, corresponding to a high hdSD. After the operation, progressive superficial angiogenesis and arteriogenesis at the site of indirect revascularization restore an adequate cortical CBF through the external carotid artery system, with reduction of central nCBF related to the regression of the MM vessels in the basal ganglia. Perfusion gradient redistribution through the newly formed pial circulation thus determines significant reduction of the hdSD.[3,7,15,21]

Most interesting, hdSD at the last MR imaging evaluation and postoperative variations of hdSD obtained with DSC-PWI were related to postoperative outcome after controlling for age, sex,

and the duration of clinical follow-up. These perfusion indices were significantly different in the 4 clinical outcome categories at the last follow-up point (average, 38.5 months after the operation). Patients with a higher percentage decrease of hdSD after the operation experienced resolution or improvement of neurologic symptoms and EEG anomalies and improved cognitively. In 2015, Takahashi et al[13]demonstrated that cortical CBF after acetazolamide load and hdSD at rest reflected ischemic symptoms of adult patients with MM, suggesting that these parameters could be used as ischemic symptom markers in this vasculopathy.

Notably, we found that reduction of hdSD at 3 months after the operation correlated with an excellent outcome at last follow-up, thus representing a potential early postoperative prognostic marker in pediatric patients with MM. This finding is relevant because hdSD may provide the advantage of noninvasively identifying patients with MM at higher risk for suboptimal clinical outcome after a revascularization operation, thereby helping select which patients require closer clinical-radiologic follow-up and additional surgical interventions. Indeed, repeat revascularization procedures are clinically effective in preventing future ischemic events and can be safely performed in patients who are clinically symptomatic and have inadequate collateral vessels following indirect procedures.[22,23] Therefore, we suggest that early hdSD variations may play a role in the selection of patients who require further revascularization procedures.[24] However, future investigations performed on larger cohorts of surgical patients with MM, focusing on the comparison between hdSD and cerebrovascular reserve, are awaited to confirm this preliminary observation.

There are some limitations to our study, including its retrospective design and the relatively small number of patients. Moreover, masks created for measuring CBF in the MCA territory could include subarachnoid spaces in addition to the brain parenchyma. This feature can affect the CBF measurements and could be a confounder because some patients could have more CSF included in the mask than others. Moreover, we did not evaluate the cerebrovascular reserve, and DSC MR imaging was not compared with PET or SPECT perfusion studies because they were not available for all patients. Considering that even surgical hemispheres may have benefited from the operation performed on the contralateral brain, another limit derives from the potential overestimation of the perfusion improvement in the hemispheres of patients with bilateral revascularization. Indeed, we could not separately estimate the direct effect of the revascularization on the first surgical hemisphere from the indirect effect due to the subsequent revascularization procedure on the contralateral hemisphere. Finally, another limitation of this study was the lack of a direct comparison of CBF-related parameters between patients with MM and healthy controls. However, for ethical reasons, we do not administer contrast media in patients with normal brain MR imaging findings.

CONCLUSIONS

CBF in the central and cortical MCA territories and hdSD obtained with DSC may be used to noninvasively evaluate postsurgical variations of brain perfusion in children with MM. Postsurgical hdSD variations correlate well with clinical outcome, even when assessed shortly after the operation, thus being a promising tool for monitoring and predictive purposes. The relative noninvasiveness of PWI makes this technique better suited for studying brain hemodynamics in the pediatric population compared with radiation-exposing techniques. Further investigations testing the same perfusion indices obtained with even less invasive perfusion techniques, such as arterial spin-labeling MR perfusion, could potentially reduce the need for contrast material administration in these patients.

Disclosures: Mattia Pacetti—*UNRELATED*: *Employment*: Istituto Giannina Gaslini Children's Hospital, *Comments*: employed as a neurosurgeon.

REFERENCES

1. Kuroda S, Houkin K. **Moyamoya disease: current concepts and future perspectives.** *Lancet Neurol* 2008;7:1056–66 CrossRef Medline
2. Scott RM, Smith ER. **Moyamoya disease and Moyamoya syndrome.** *N Engl J Med* 2009;360:1226–37 CrossRef Medline
3. Tortora D, Severino M, Accogli A, et al. **Moyamoya vasculopathy in PHACE syndrome: six new cases and review of the literature.** *World Neurosurg* 2017;108:291–302 CrossRef Medline
4. Hu J, Luo J, Chen Q. **The susceptibility pathogenesis of Moyamoya disease.** *World Neurosurg* 2017;101:731–41 CrossRef Medline
5. Lee M, Zaharchuk G, Guzman R, et al. **Quantitative hemodynamic studies in Moyamoya disease: a review.** *Neurosurg Focus* 2009;26:E5 CrossRef Medline
6. Kim SK, Wang KC, Oh CW, et al. **Evaluation of cerebral hemodynamics with perfusion MRI in childhood Moyamoya disease.** *Pediatr Neurosurg* 2003;38:68–75 CrossRef Medline
7. Yun TJ, Cheon JE, Na DG, et al. **Childhood Moyamoya disease: quantitative evaluation of perfusion MR imaging—correlation with clinical outcome after revascularization surgery.** *Radiology* 2009;251:216–23 CrossRef Medline
8. Lee SK, Kim DI, Jeong EK, et al. **Postoperative evaluation of Moyamoya disease with perfusion-weighted MR imaging: initial experience.** *AJNR Am J Neuroradiol* 2003;24:741–47 Medline
9. Ogasawara K, Tomitsuka N, Kobayashi M, et al. **Stevens-Johnson syndrome associated with intravenous acetazolamide administration for evaluation of cerebrovascular reactivity: case report.** *Neurol Med Chir (Tokyo)* 2006;46:161–63 CrossRef Medline
10. Saito H, Ogasawara K, Suzuki T, et al. **Adverse effects of intravenous acetazolamide administration for evaluation of cerebrovascular reactivity using brain perfusion single-photon emission computed tomography in patients with major cerebral artery steno-occlusive diseases.** *Neurol Med Chir (Tokyo)* 2011; 51:479–83 CrossRef Medline
11. Gallerani M, Manzoli N, Fellin R, et al. **Anaphylactic shock and acute pulmonary edema after a single oral dose of acetazolamide.** *Am J Emerg Med* 2002;20:371–72 CrossRef Medline
12. Kashiwagi S, Yamashita T, Katoh S, et al. **Regression of Moyamoya vessels and hemodynamic changes after successful revascularization in childhood Moyamoya disease.** *Acta Neurol Scand Suppl* 1996; 93:85–88 CrossRef Medline
13. Takahashi S, Tanizaki Y, Kimura H, et al. **Hemodynamic stress distribution reflects ischemic clinical symptoms of patients with Moyamoya disease.** *Clin Neurol Neurosurg* 2015;138:104–10 CrossRef Medline
14. Schubert GA, Czabanka M, Seiz M, et al. **Perfusion characteristics of Moyamoya disease: an anatomically and clinically oriented analysis and comparison.** *Stroke* 2014;45:101–06 CrossRef Medline
15. Laiwalla AN, Kurth F, Leu K, et al. **Evaluation of encephaloduroarteriosynangiosis efficacy using probabilistic independent component analysis applied to dynamic susceptibility contrast perfusion MRI.** *AJNR Am J Neuroradiol* 2017;38:507–14 CrossRef Medline
16. Kinugasa K, Mandai S, Kamata I, et al. **Surgical treatment of Moyamoya disease: operative technique for encephalo-duro-arterio-**

myo-synangiosis, its follow-up, clinical results, and angiograms. *Neurosurgery* 1993;32:527–31 CrossRef Medline
17. Ostergaard L, Sorensen AG, Kwong KK, et al. **High resolution measurement of cerebral blood flow using intravascular tracer bolus passages, Part II: experimental comparison and preliminary results.** *Magn Reson Med* 1996;36:726–36 CrossRef Medline
18. Yun TJ, Paeng JC, Sohn CH, et al. **Monitoring cerebrovascular reactivity through the use of arterial spin labeling in patients with Moyamoya disease.** *Radiology* 2016;278:205–13 CrossRef Medline
19. Jenkinson M, Beckmann CF, Behrens TE, et al. **FSL**. *Neuroimage* 2012;62:782–90 CrossRef Medline
20. Mutsaerts HJ, van Dalen JW, Heijtel DF, et al. **Cerebral perfusion measurements in elderly with hypertension using arterial spin labeling.** *PLoS One* 2015;10:e0133717 CrossRef Medline
21. Nakamura M, Imai H, Konno K, et al. **Experimental investigation of encephalomyosynangiosis using gyrencephalic brain of the miniature pig: histopathological evaluation of dynamic reconstruction of vessels for functional anastomosis—laboratory investigation.** *J Neurosurg Pediatr* 2009;3:488–95 CrossRef Medline
22. Pandey P, Steinberg GK. **Outcome of repeat revascularization surgery for Moyamoya disease after an unsuccessful indirect revascularization: clinical article.** *J Neurosurg* 2011;115:328–36 CrossRef Medline
23. Hayashi T, Shirane R, Tominaga T. **Additional surgery for postoperative ischemic symptoms in patients with Moyamoya disease: the effectiveness of occipital artery-posterior cerebral artery bypass with an indirect procedure—technical case report.** *Neurosurgery* 2009;64:E195–96; discussion E196 CrossRef Medline
24. Fujimura M, Niizuma K, Endo H, et al. **Quantitative analysis of early postoperative cerebral blood flow contributes to the prediction and diagnosis of cerebral hyperperfusion syndrome after revascularization surgery for Moyamoya disease.** *Neurol Res* 2015;37:131–38 CrossRef Medline

Volumetric Brain MRI Study in Fetuses with Congenital Heart Disease

H. Olshaker, R. Ber, D. Hoffman, E. Derazne, R. Achiron, and E. Katorza

ABSTRACT

BACKGROUND AND PURPOSE: It is well-established that a high prevalence of infants with congenital heart defects surviving to childhood have neurodevelopmental abnormalities. The etiology is not clear. In this study, we aimed to find prenatal neuroanatomic changes in fetuses with congenital heart disease to better understand the pathophysiology behind these sequelae.

MATERIALS AND METHODS: A retrospective study of 46 fetal brain MR imaging scans was performed at a tertiary medical center during a 4-year period. Clinical data were collected from electronic medical charts. Volumes of the supratentorial brain, right hemisphere, left hemisphere, and cerebellum were measured using a semiautomated method and were compared with the normal growth percentiles.

RESULTS: We found that cerebellar volume and the cerebellar-supratentorial volume ratio were significantly lower among fetuses with congenital heart disease. Supratentorial and hemisphere volumes showed no difference between groups. This difference was not observed in fetuses with septation defects.

CONCLUSIONS: Fetuses with congenital heart disease have smaller cerebellar volumes than healthy fetuses. Additional research is needed to assess this finding as a radiologic marker for long-term outcome.

ABBREVIATIONS: CHD = congenital heart disease; CV = cerebellar volume; HLHS = hypoplastic left heart syndrome; LHV = left hemisphere volume; ICC = intraclass correlation coefficient; RHV = right hemisphere volume; STV = supratentorial brain volume; TGA = transposition of the great arteries

Congenital heart diseases (CHDs), which affect approximately 0.9% of all births, are abnormalities of the heart present at birth. Once a life-threatening condition, today most CHDs are corrected or palliated in infancy, enabling these children to reach adulthood. However, a considerable proportion of the surviving children show neurodevelopmental abnormalities.[1]

Studies were made to further understand these sequelae and found that neonates with CHD have a high prevalence of anatomic and functional neurologic abnormalities.[2-19] The etiology of the abnormalities is unknown, and it is presumed to be multifactorial, both from a shared genetic background and as a secondary outcome. One of the leading hypotheses is damaged oxygen supply to the brain,[3,5,6,15,18,20] either because of reduced cerebral oxygen saturation or from the disturbed circulation, both derived from the heart defect.

To investigate this hypothesis, a few biometric studies have been performed. Miller et al[7] used preoperative MR imaging to evaluate and compare several parameters indicative of cerebral maturation and oxidative stress between fetuses with and without hypoplastic left heart syndrome (HLHS) and transposition of the great arteries (TGA). They found significant changes in both CHD groups compared with controls. Also supporting the hypoxemia hypothesis, Mahle et al[4] used MR imaging to show that neonates with a variety of CHDs had ischemic lesions in the form of periventricular leukomalacia and infarcts as well as elevated lactate levels before surgery. Kaltman et al[6] examined the cerebrovascular blood flow in fetuses with right- and left-sided obstructive congenital heart diseases using a Doppler echocardiogram. They showed differences in middle cerebral and umbilical artery resistance in fetuses with CHD compared with normal values. These changes may result from a primary unknown etiology or can represent a functioning autoregulatory mechanism of the brain vasculature reacting to hypoxia.

Our objective was to compare volumetric measurements of different structures in the fetal brain between healthy fetuses and those with CHD using a new 3D MR imaging method. We hy-

Received December 23, 2017; accepted after revision February 14, 2018.

From the Antenatal Diagnostic Unit (H.O., R.B., D.H., R.A., E.K.), Department of Obstetrics and Gynecology, Chaim Sheba Medical Center, Tel-Hashomer, Israel; and Sackler School of Medicine (H.O., R.B., D.H., E.D., R.A., E.K.), Tel Aviv University, Tel Aviv, Israel.

Please address correspondence to Olshaker Hagar, MD, Antenatal Diagnostic Unit, Department of Obstetrics and Gynecology, Chaim Sheba Medical Center, Tel-Hashomer, 52621 Ramat Gan, Israel; e-mail: hagar.olshaker@gmail.com

http://dx.doi.org/10.3174/ajnr.A5628

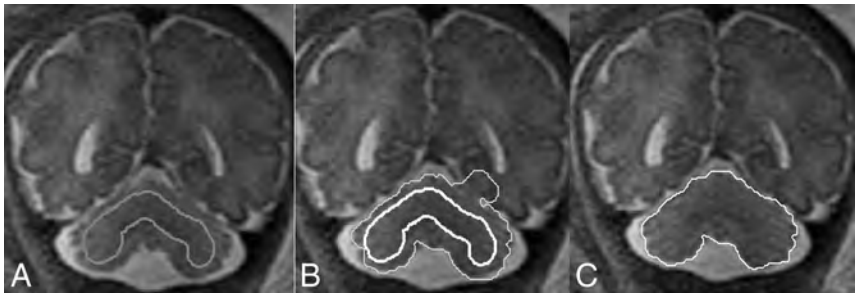

FIG 1. *A*, The initial contour drawn manually on the midcoronal slice. *B*, Converged contour automatically propagated by a level-set-based active contour algorithm. *C*, The contour after manual adjustment.

pothesized that brain volume would be smaller in the CHD group compared with healthy controls.

MATERIALS AND METHODS

Subjects

The subjects of this retrospective study were women who underwent MR imaging scans in the third trimester of pregnancy for fetal evaluation after a suspected CHD. Scans were obtained between 2011 and 2014 at the tertiary Chaim Sheba medical center. Performing MR imaging is now the routine practice in fetuses with suspected CHD, used for structural and biometric 2D examination of the brain. An estimated diagnosis of CHD was made during pregnancy and was made final after postnatal tests.

The measurements were compared with percentile tables derived from healthy fetuses in a previous study.[21] Measurements and calculation methods in the current and the aforementioned study are identical and are described below.

MR Imaging

This study was based on the routine fetal MR imaging procedure performed in our institution. Fetal brain MR imaging was performed using a 1.5T system (Optima scanner; GE Healthcare, Milwaukee, Wisconsin). Single-shot fast spin-echo T2-weighted sequences in 3 orthogonal planes were obtained using a half-Fourier technique (NEX = 0.53) with the following parameters: section thickness = 3 or 4 mm, no gap, flexible coil (8-channel cardiac coil). FOV was determined by the size of the fetal head, with a range of 24 × 24 cm to 30 × 30 cm, acquisition time = 40–45 seconds, matrix = 320/224, TE = 90 ms, TR = 1298 ms, pixel bandwidth = 122 Hz/pixel. Specific absorption rate values were between 1.1 and 1.7 W/kg.[22]

Measurements

All measurements were obtained in the coronal plane. For each fetus, we measured 6 structures: the supratentorial brain, right and left cerebral hemispheres, right and left lateral ventricles, and cerebellum. Of the volumes measured, 5 structures were assessed in the study: supratentorial brain volume (STV), right hemisphere volume (RHV), left hemisphere volume (LHV), cerebellar volume (CV), and the ratio between the cerebellar volume and the supratentorial volume (CV/STV). Measurements were used as follows:

Supratentorial Brain. For measurement of the supratentorial brain volume, we included the parenchyma of the frontal, parietal, occipital, and temporal lobes (including the third ventricle) and excluded the lateral ventricles (measured separately and subtracted), brain stem, cerebellum, and fourth ventricle. Anterior, posterior, superior, and lateral boundaries were defined as the outer edge of the cerebral cortex. The inferior border matched the cortex and an imaginary line crossing the brain stem between the edges of the tentorium cerebelli.

Hemispheres. The left and right hemisphere volumes were measured separately using the same lateral boundaries with the longitudinal fissure as a medial boundary.

Cerebellum. Cerebellar hemispheres were drawn with the cerebellar peduncles and vermis. Brain stem and the fourth ventricle were excluded.

Delineation was made by a semiautomated algorithm implemented using Matlab computing environment (MathWorks, Natick, Massachusetts). In this method, the first step includes tracing the ROI manually in the brain parenchyma of the midcoronal slice through cursor-guided freehand traces. On the basis of the intensity of the pixels included in the initial contour, the contour is then automatically propagated by a level-set-based active contour algorithm until convergence into a new, more accurate contour. The next step is forward and backward propagation, starting at the midcoronal slice, achieving contours automatically for every slice. Each new contour is based on the previous one; with a prefixed downsized volume for every slice. When it is completed, the user can manually adjust the resulted contour to achieve maximal accuracy (Fig 1). The volume is computed as the total number of voxels enclosed by the contours multiplied by the size of the voxel.[21]

The reliability of the semiautomated method was assessed. Interobserver variability was tested comparing measurements of 15 fetuses made by 2 independent observers. Intraobserver variability was checked by 1 observer who measured a sample of 15 fetuses twice. The intraclass correlation coefficient (ICC) was calculated. Medium agreement is defined as $0.4 < ICC < 0.6$; good agreement, as $0.6 < ICC < 0.8$; and very good agreement, as $ICC > 0.8$.[14]

Statistics

Our main purpose was to see whether our sample was different from the normal population. The sample size of 46 was estimated to give a power of 80%, with $\alpha = .05$, to assess an average difference of 0.6% between our study groups.

Fetal brain volumes (STV, RHV, LHV, CV, CV/STV) from the CHD group were assigned to percentiles according to the normal fetal brain volume distribution; then, using a *t* test, the mean was compared with a population with a mean of 50. For each structure that was measured, fetuses were also classified into 4 categories according to their percentiles: <15%, 15%–50%, 50%–85%, and >85%. They were then compared with expected values from normal distributions using the χ^2 test. Statistical

Table 1: Demographic characteristics of the CHD group

Characteristic	
Male (No.) (%)	19 (59%)
Gestational age at MRI (wk)	
Median	32.1
Interquartile range	32–34
Gestational age at birth (wk)	
Median	39
Interquartile range	38–40
Mother's age (yr)	
Median	31
Interquartile range	28–34
Birth weight percentile	
Median	46
Interquartile range	31.2–69.7
Birth weight percentile <10th (No.) (%)	3 (6.5%)
Apgar score at 5 min <7 (No.) (%)	5 (11%)

analysis was performed using SPSS Statistics for Windows, Version 23.0 (IBM, Armonk, New York).

To see whether there was a difference among different types of congenital heart defects, we subdivided the group of CHDs into 3 subgroups according to a division by Bruneau in 2008.[23] Thirty-six of 46 fetuses fell into 1 of 3 subcategories: cyanotic heart disease ($n = 19$), left-sided obstruction defects ($n = 9$), and septation defects ($n = 8$). The groups' means were compared to each other and to the normal population using a *t* test.

We also addressed the effect of brain pathology on the volume measurements. As described in the "Results" section, some fetuses were diagnosed with various brain pathologies according to the official MR imaging report. To understand whether there is a difference in the measured volumes between fetuses with and without brain pathology, we subdivided the CHD group into 2 subgroups according to the official MR imaging report: group A for fetuses with a diagnosed brain pathology ($n = 11$) and group B for fetuses without one ($n = 35$). For each structure measured, we then performed a comparison between the percentile distributions of the 2 groups using a *t* test for equal variances. A result of no difference between the groups would mean that brain pathology has no impact on the volume measurements.

RESULTS

Clinical Characteristics of the Study Population

Fifty-six fetuses with CHD were identified; 10 cases were excluded due to lack of sufficient information. Demographic details on the CHD group are shown in Table 1. Of the whole CHD group, 2 pregnancies were terminated due to parental decisions. Nuchal translucency was obtained in 39 of 46 pregnancies (85%) and had abnormal findings in 3 (8%). Thirty-three of 46 (72%) had undergone amniocentesis; one had abnormal findings (3%). One of 46 fetuses (2%) was diagnosed with intrauterine growth restriction on fetal ultrasound. Diagnosis of heart defects was determined according to postnatal imaging for 44 of 46 fetuses and according to the prenatal echocardiography for the 2 pregnancies that were terminated. Diagnoses are shown in Table 2. More than half of the fetuses had >1 defect.

Table 2: CHD types[a]

CHD (No.) (%)	
HLHS	4 (8.6%)
AS	1 (2.1%)
COA	3 (6.5%)
Interrupted aortic arch	2 (4.3%)
MS	2 (4.3%)
TOF	3 (6.5%)
Absent pulmonary valve	2 (4.3%)
PS	2 (4.3%)
Tricuspid atresia	1 (2.1%)
Epstein anomaly	1 (2.1%)
TR	8 (17.3%)
TGA	11 (23%)
VSD	16 (34.7%)
ASD	6 (13%)
PI	2 (4.3%)
Fetuses with >1 CHD	24 (52.1%)

Note:—AS indicates aortic stenosis; COA, coarctation of the aorta; MS, mitral stenosis; TOF, tetralogy of Fallot; PS, pulmonic stenosis; TR, tricuspid regurgitation; VSD, ventricular septal defect; ASD, atrial septal defect; PI, pulmonary insufficiency.

[a] Defects not specified in this table include but are not limited to partial defects, azygous and vena cava abnormalities, and situs abnormalities. Some fetuses had only one of these defects, and some had combined defects.

Table 3: Interobserver reliability of measurements expressed as ICCs

	Interobserver		Intraobserver	
Volume	ICC	95% CI	ICC	95% CI
STV	0.98	0.94–0.99	0.98	0.94–0.99
RHV	0.96	0.96–0.99	0.99	0.98–0.99
LHV	0.61	−0.15–0.87	0.92	0.8–0.97
CV	0.89	0.69–0.97	0.75	0.37–0.9

Table 4: Fetal brain pathology according to the official MRI report

Report (No.) (%)	
Pathology	11 (23.9%)
Cortical pathology	4 (9.3%)
Ventricle pathology	5 (10.8%)
Corpus callosum pathology	2 (4.3%)
Extra-axial findings	3 (6.5%)
Unclear findings	1 (2.3%)

Variability Assessment Results

Estimations are shown in Table 3. Volumetric estimations show between good and very good interobserver and intraobserver reliability.

Official MR Imaging Report

In 10 of 46 fetuses (22%), brain fetal MR imaging demonstrated variable findings. The brain pathologies are shown in Table 4.

Volumetric MR Imaging Measurements and Analysis

Analysis of the comparison among different brain structures using a *t* test is shown in Table 5. For each brain structure measured, subjects were divided according to their percentiles in relation to the normal distribution. One fetus had STV below the third percentile, 2 had RHV below the third percentile, 2 had LHV below the third percentile, 19 (41%) had CV below the third percentile, and in 21 (46%) fetuses, the CV/STV ratio was below the third percentile. Distributions are shown in Fig 2, and χ^2 *P* values are given for each structure. Results show that the cerebellar volume is significantly lower in the CHD group compared with healthy

fetuses ($P < .005$, Table 5), as well as the ratio between the cerebellum and the supratentorial brain ($P < .005$). We did not find any differences in other structures measured.

When analyzing the different types of defects, we found a significantly smaller cerebellar volume in the cyanotic heart disease group compared with healthy fetuses and the same for the group of left-sided heart obstruction defects. However, we did not find any difference between the septation defects group and healthy fetuses. This group had defects such as atrial septal defect and ventricular septal defect.

Analysis of the effect of brain pathology on volume measurements was also made. For each structure, we compared the percentile distribution between groups A and B and found no difference between the groups. We infer that the existence of a brain pathology diagnosis has no impact on those measurements.

Table 5: Comparison between the CHD and reference groups using a *t* test analysis

	Mean	SD	Significance[a]
STV	48.36	32.87	.73
RHV	52.78	30.54	.53
LHV	54.91	31.13	.29
CV	22.64	29.8	<.05
CV/STV	19.55	27.66	<.05

[a] Two-tailed test value.

DISCUSSION

In our study, we attempted to investigate brain volume disturbances in fetuses with CHD. While our results do not show lower volumes of the RHV, LHV, and STV among fetuses with CHD, we did find a significant decrease in CV and in CV/STV compared with healthy fetuses. When analyzing the CHD type, we found that this difference did not exist in septal defects.

Our study adds evidence to increasing reports on brain growth and volume disturbances in fetuses with CHD. Limperopoulos et al[11] used 3D MR imaging and MR spectroscopy to compare brain volumes and metabolism between healthy fetuses and those with CHD. They found progressively smaller total brain volumes in the CHD group compared with controls. Masoller et al[17] also studied brain volumes in fetuses with CHD and found a reduction in brain volume compared with fetuses without CHD. Our results are not comparable with theirs because we measured different structures; we divided the total brain volume into supratentorial and infratentorial structures. This division enabled us to reveal

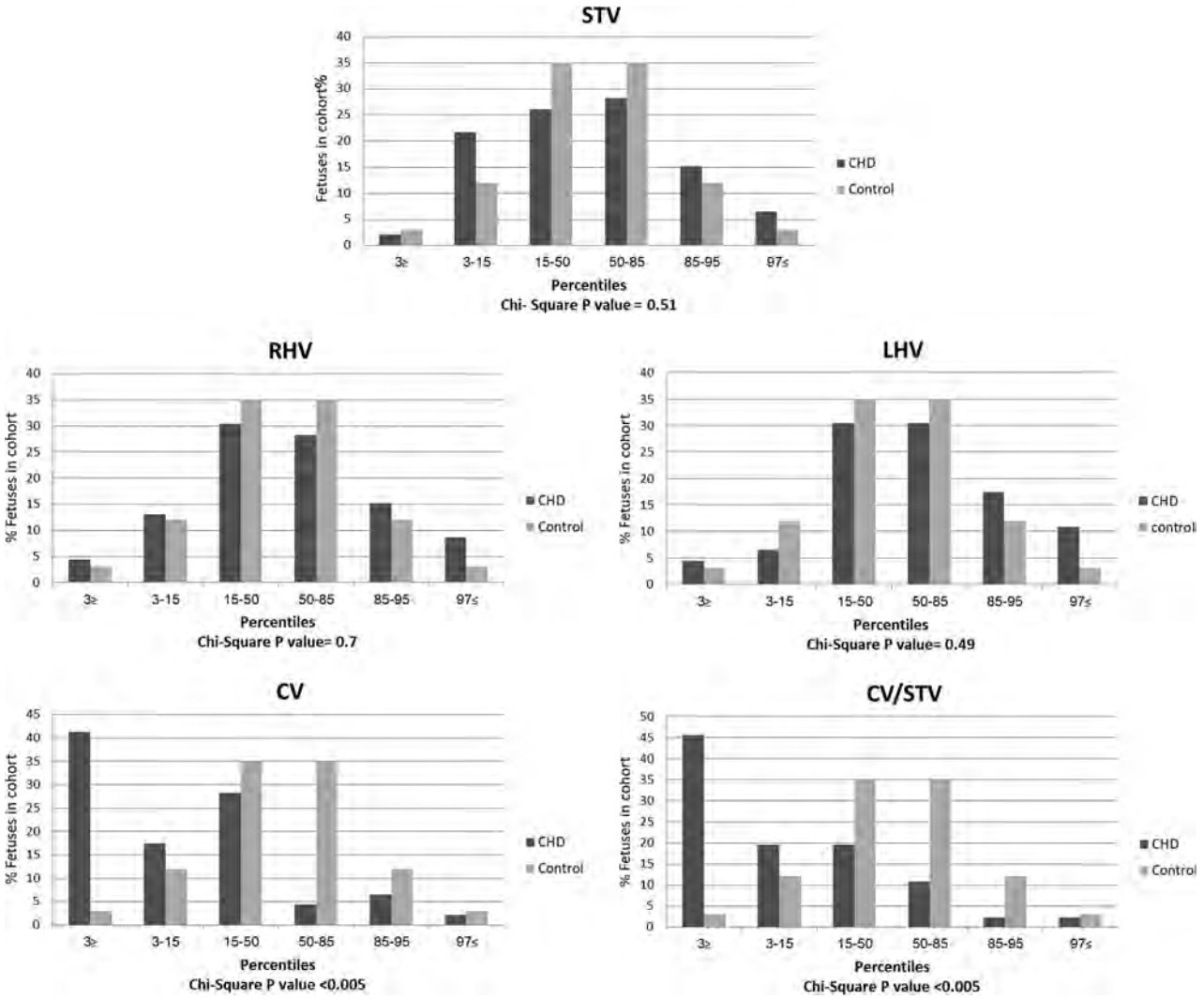

FIG 2. Brain volumes of the CHD group distributed by percentiles derived from the reference group: STV, RHV/LHV, and CV.

that in fact, the cerebellum was the major contributor to the significant decrease in volume.

This finding is congruent with the findings of a recent study by Wong et al,[19] who used MR imaging to measure the cerebellum of fetuses with CHD in 3 planes. They found a significant decrease in the sagittal vermis height in the CHD group versus controls. Vermian hypoplasia was also reported by Brossard-Racine et al[24] as one of the possible findings in MR imaging of fetuses with CHD. Zeng et al[16] used ultrasound to evaluate volumes of different structures in the brains of fetuses with CHD. They found a reduction in all brain volumes in fetuses with CHD, yet in their study, the reduction was larger in the frontal lobes than in the cerebellum. Ortinau et al[13] also evaluated different brain structure volumes using 2D measurements in 3 cross-sections. They found that fetuses with CHD had smaller frontal, parietal, cerebellar, and brain stem measurements than healthy controls. In accord with Zeng et al, they also found that the frontal lobes showed the greatest alteration in growth.

Fetal cerebellar volumes were studied in different diseases. A volumetric MR imaging study on fetuses with intrauterine growth restriction demonstrated a reduction in cerebellar volume compared with other brain structures.[22] A cerebellar growth restriction was also demonstrated in preterm fetuses.[25] Most interesting, both of these conditions are associated with hypoxemia.[26,27] Studies in sheep showed that a prolonged period of placental insufficiency, resulting in fetal hypoxemia, can affect the growth of the cerebellum, with a reduction in cell number and size.[28,29] The cerebellum is considered particularly vulnerable to the negative effects of an insult due to its rapid growth during gestation.[30] Cerebellar injury is associated with a broad spectrum of functional neurodevelopmental sequelae, including cognitive, language, behavioral, and social deficits as well as the well-known motor effect attributed to cerebellar injuries.[31] Children with CHD exhibit a range of disabilities in these areas[1]; hence, cerebellar injury is a relatively less recognized but possibly important cause of neurodevelopmental delay in children with CHD.

Another aspect of the contribution of our study is that so far, results on brain volume reduction mainly focused on HLHS and TGA.[2,6,8-10,20] In our study, we demonstrated these effects in various types of CHD because our cohort comprised only 4 cases of HLHS (~9%) and 9 cases of TGA (~20%). Masoller et al[18] addressed this question and compared the fetal neurodevelopment between 2 groups of fetuses with CHD divided according to the expected blood supply to the brain, with group A containing only HLHS, TGA, critical aortic stenosis, and hypoplastic aortic arch. They found that both groups had significant abnormal neurodevelopment (including brain volumes) compared with healthy control fetuses, but a linear tendency across the 3 subgroups was observed, with CHD group A fetuses showing more pronounced differences.[18] When we tried to find differences among the types of CHD, we found that only defects considered mild such as atrial septal defect and ventricular septal defect do not affect the volume, while all the others do.

The presence of preoperative brain abnormalities in fetuses with CHD is well-established, showing disturbances in metabolism, blood flow, growth, and maturation. There is growing evidence that hypoxia is a major mechanism. This theory is based on the hypothesis that circulatory disturbances, especially occurring in HLHS and TGA, disrupt the oxygen supply to the brain and thus impact its growth and maturation. In healthy neonates, blood is oxygenated in the lungs and flows to the body through the left ventricle and aorta. In certain defects, this circulation is disturbed. For example, in HLHS, blood does not flow to the body through the left ventricle because it is hypoplastic, and in TGA, the left ventricle is connected to the lungs. In both defects, the neonate is dependent on the fetal shunts (foramen ovale, ductus arteriosus, or a ventricular septal defect) and pumps blood to the body using the right ventricle. Under those conditions, tissue oxygen supply is compromised, first due to inefficient circulatory architecture, and secondly due to systemic delivery of deoxygenated blood.

We acknowledge some limitations of this study. First, normal curves were derived from healthy fetuses undergoing MRI for suspected fetal abnormalities, allowing for a possible selection bias in the reference group. Lack of women with healthy pregnancies for reference is a common limitation in this research field.[32,33] Another limitation is a lack of postnatal follow-up to assess whether findings are associated with neurodevelopmental outcomes.

CONCLUSIONS

We found that fetuses with CHD have smaller CV and CV/STV than healthy fetuses. Although further research is needed to assess the extent of damage among the different CHD types and to investigate the association with neurodevelopmental sequelae, this finding can provide deeper insight into the pathophysiology of the neurodevelopmental sequelae of children with CHD and influence important decision-making.

REFERENCES

1. Marino BS, Lipkin PH, Newburger JW, et al; American Heart Association Congenital Heart Defects Committee, Council on Cardiovascular Disease in the Young, Council on Cardiovascular Nursing, and Stroke Council. **Neurodevelopmental outcomes in children with congenital heart disease: evaluation and management—a scientific statement from the American Heart Association.** *Circulation* 2012; 126:1143–72 CrossRef Medline
2. Glauser TA, Rorke LB, Weinberg PM, et al. **Congenital brain anomalies associated with the hypoplastic left heart syndrome.** *Pediatrics* 1990;85:984–90 Medline
3. Kurth CD, Steven JL, Montenegro LM, et al. **Cerebral oxygen saturation before congenital heart surgery.** *Ann Thorac Surg* 2001;72: 187–92 CrossRef Medline
4. Mahle WT, Tavani F, Zimmerman RA, et al. **An MRI study of neurological injury before and after congenital heart surgery.** *Circulation* 2002;106:I109–14 Medline
5. Donofrio MT, Bremer YA, Schieken RM, et al. **Autoregulation of cerebral blood flow in fetuses with congenital heart disease: the brain sparing effect.** *Pediatr Cardiol* 2003;24:436–43 CrossRef Medline
6. Kaltman JR, Di H, Tian Z, et al. **Impact of congenital heart disease on cerebrovascular blood flow dynamics in the fetus.** *Ultrasound Obstet Gynecol* 2005;25:32–36 CrossRef Medline
7. Miller SP, McQuillen PS, Hamrick S, et al. **Abnormal brain development in newborns with congenital heart disease.** *N Engl J Med* 2007; 357:1928–38 CrossRef Medline
8. Shillingford AJ, Ittenbach RF, Marino BS, et al. **Aortic morphometry and microcephaly in hypoplastic left heart syndrome.** *Cardiol Young* 2007;17:189–95 CrossRef Medline

9. Hinton RB, Andelfinger G, Sekar P, et al. **Prenatal head growth and white matter injury in hypoplastic left heart syndrome.** *Pediatr Res* 2008;64:364–69 CrossRef Medline
10. Licht DJ, Shera DM, Clancy RR, et al. **Brain maturation is delayed in infants with complex congenital heart defects.** *J Thorac Cardiovasc Surg* 2009;137:529–36; discussion 536–37 CrossRef Medline
11. Limperopoulos C, Tworetzky W, McElhinney DB, et al. **Brain volume and metabolism in fetuses with congenital heart disease: evaluation with quantitative magnetic resonance imaging and spectroscopy.** *Circulation* 2010;121:26–33 CrossRef Medline
12. McQuillen PS, Goff DA, Licht DJ. **Effects of congenital heart disease on brain development.** *Prog Pediatr Cardiol* 2010;29:79–85 CrossRef Medline
13. Ortinau C, Beca J, Lambeth J, et al. **Regional alterations in cerebral growth exist preoperatively in infants with congenital heart disease.** *J Thorac Cardiovasc Surg* 2012;143:1264–70 CrossRef Medline
14. Dimitropoulos A, McQuillen PS, Sethi V, et al. **Brain injury and development in newborns with critical congenital heart disease.** *Neurology* 2013;81:241–48 CrossRef Medline
15. Masoller N, Martinez JM, Gómez O, et al. **Evidence of second-trimester changes in head biometry and brain perfusion in fetuses with congenital heart disease.** *Ultrasound Obstet Gynecol* 2014;44:182–87 CrossRef Medline
16. Zeng S, Zhou QC, Zhou JW, et al. **Volume of intracranial structures on three-dimensional ultrasound in fetuses with congenital heart disease.** *Ultrasound Obstet Gynecol* 2015;46:174–81 CrossRef Medline
17. Masoller N, Sanz-Cortés M, Crispi F, et al. **Mid-gestation brain Doppler and head biometry in fetuses with congenital heart disease predict abnormal brain development at birth.** *Ultrasound Obstet Gynecol* 2016;47:65–73 CrossRef Medline
18. Masoller N, Sanz-Cortés M, Crispi F, et al. **Severity of fetal brain abnormalities in congenital heart disease in relation to the main expected pattern of in utero brain blood supply.** *Fetal Diagn Ther* 2016;39:269–78 CrossRef Medline
19. Wong A, Chavez T, O'Neil S, et al. **Synchronous aberrant cerebellar and opercular development in fetuses and neonates with congenital heart disease: correlation with early communicative neurodevelopmental outcomes, initial experience.** *AJP Rep* 2017;7:e17–27 CrossRef Medline
20. Sakazaki S, Masutani S, Sugimoto M, et al. **Oxygen supply to the fetal cerebral circulation in hypoplastic left heart syndrome: a simulation study based on the theoretical models of fetal circulation.** *Pediatr Cardiol* 2015;36:677–84 CrossRef Medline
21. Ber R, Hoffman D, Hoffman C, et al. **Volume of structures in the fetal brain measured with a new semiautomated method.** *AJNR Am J Neuroradiol* 2017;38:2193–98 CrossRef Medline
22. Polat A, Barlow S, Ber R, et al. **Volumetric MRI study of the intrauterine growth restriction fetal brain.** *Eur Radiol* 2017;27:2110–18 CrossRef Medline
23. Bruneau BG. **The developmental genetics of congenital heart disease.** *Nature* 2008;451:943–48 CrossRef Medline
24. Brossard-Racine M, du Plessis AJ, Vezina G, et al. **Prevalence and spectrum of in utero structural brain abnormalities in fetuses with complex congenital heart disease.** *AJNR Am J Neuroradiol* 2014;35:1593–99 CrossRef Medline
25. Limperopoulos C, Soul JS, Gauvreau K, et al. **Late gestation cerebellar growth is rapid and impeded by premature birth.** *Pediatrics* 2005;115:688–95 CrossRef Medline
26. du Plessis AJ, Volpe JJ. **Perinatal brain injury in the preterm and term newborn.** *Curr Opin Neurol* 2002;15:151–57 CrossRef Medline
27. Ferrazzi E, Bulfamante G, Mezzopane R, et al. **Uterine Doppler velocimetry and placental hypoxic-ischemic lesion in pregnancies with fetal intrauterine growth restriction.** *Placenta* 1999;20:389–94 CrossRef Medline
28. Biran V, Verney C, Ferriero DM. **Perinatal cerebellar injury in human and animal models.** *Neurol Res Int* 2012;2012:858929 CrossRef Medline
29. Mallard EC, Rees S, Stringer M, et al. **Effects of chronic placental insufficiency on brain development in fetal sheep.** *Pediatr Res* 1998;43:262–70 Medline
30. Volpe JJ. **Cerebellum of the premature infant: rapidly developing, vulnerable, clinically important.** *J Child Neurol* 2009;24:1085–104 CrossRef Medline
31. Limperopoulos C, Robertson RL, Sullivan NR, et al. **Cerebellar injury in term infants: clinical characteristics, magnetic resonance imaging findings, and outcome.** *Pediatr Neurol* 2009;41:1–8 CrossRef Medline
32. Hatab MR, Kamourieh SW, Twickler DM. **MR volume of the fetal cerebellum in relation to growth.** *J Magn Reson Imaging* 2008;27:840–45 CrossRef Medline
33. Clouchoux C, Kudelski D, Gholipour A, et al. **Quantitative in vivo MRI measurement of cortical development in the fetus.** *Brain Struct Funct* 2012;217:127–39 CrossRef Medline

Postnatal Brain Growth Assessed by Sequential Cranial Ultrasonography in Infants Born <30 Weeks' Gestational Age

R. Cuzzilla, A.J. Spittle, K.J. Lee, S. Rogerson, F.M. Cowan, L.W. Doyle, and J.L.Y. Cheong

ABSTRACT

BACKGROUND AND PURPOSE: Brain growth in the early postnatal period following preterm birth has not been well described. This study of infants born at <30 weeks' gestational age and without major brain injury aimed to accomplish the following: 1) assess the reproducibility of linear measures made from cranial ultrasonography, 2) evaluate brain growth using sequential cranial ultrasonography linear measures from birth to term-equivalent age, and 3) explore perinatal predictors of postnatal brain growth.

MATERIALS AND METHODS: Participants comprised 144 infants born at <30 weeks' gestational age at a single center between January 2011 and December 2013. Infants with major brain injury seen on cranial ultrasonography or congenital or chromosomal abnormalities were excluded. Brain tissue and fluid spaces were measured from cranial ultrasonography performed as part of routine clinical care. Brain growth was assessed in 3 time intervals: <7, 7–27, and >27 days' postnatal age. Data were analyzed using intraclass correlation coefficients and mixed-effects regression.

RESULTS: A total of 429 scans were assessed for 144 infants. Several linear measures showed excellent reproducibility. All measures of brain tissue increased with postnatal age, except for the biparietal diameter, which decreased within the first postnatal week and increased thereafter. Gestational age of ≥28 weeks at birth was associated with slower growth of the biparietal diameter and ventricular width compared with gestational age of <28 weeks. Postnatal corticosteroid administration was associated with slower growth of the corpus callosum length, transcerebellar diameter, and vermis height. Sepsis and necrotizing enterocolitis were associated with slower growth of the transcerebellar diameter.

CONCLUSIONS: Postnatal brain growth in infants born at <30 weeks' gestational age can be evaluated using sequential linear measures made from routine cranial ultrasonography and is associated with perinatal predictors of long-term development.

ABBREVIATIONS: AHW = anterior horn width; BPD = biparietal diameter; BW = birth weight; CCL = corpus callosum length; cUS = cranial ultrasonography; GA = gestational age; NEC = necrotizing enterocolitis; PMA = postmenstrual age; PNA = postnatal age; TEA = term-equivalent age; TCD = transcerebellar diameter

Preterm infants are at risk of long-term neurodevelopmental impairment related to perinatal brain injury and altered brain maturation.[1,2] The optimal technique and timing of neuroimaging for identifying high-risk infants is under debate.[3] While early and sequential cranial ultrasonography (cUS) can be reliably used to detect major brain injury, it is less sensitive than MR imaging for the more prevalent, diffuse white matter injury associated with preterm birth.[1,4,5] Nonetheless, cUS remains the most widely used neuroimaging technique for preterm infants because it is readily available, easily repeatable, and sensitive enough for detecting most major pathology.

In the absence of overt brain injury and where MR imaging is not accessible, there is a need to improve the prognostic utility of cUS, to better understand why some preterm infants without major brain injury seen on cUS later develop motor and cognitive impairments.[1,6] Most infants born preterm have at least 1 early and 1 later neonatal cUS scan, affording an opportunity to quan-

Received October 26, 2017; accepted after revision March 5, 2018.

From the Victorian Infant Brain Studies research group (R.C., A.J.S., K.J.L., L.W.D., J.L.Y.C.), Murdoch Childrens Research Institute, Melbourne, Australia; Departments of Obstetrics and Gynaecology (R.C., S.R., L.W.D., J.L.Y.C.), Paediatrics (K.J.L., L.W.D.), and Physiotherapy (A.J.S.), University of Melbourne, Melbourne, Australia; Neonatal Services (R.C., A.J.S., S.R., L.W.D., J.L.Y.C.), The Royal Women's Hospital, Melbourne, Australia; and Department of Paediatrics (F.M.C.), Imperial College, London, UK.

This study was funded by grants from the National Health and Medical Research Council (project grant 1024516; Career Development Fellowship 1108714; Centre for Clinical Research Excellence 546519; Centre for Research Excellence 1060733, and Senior Research Fellowship 628371). The Murdoch Childrens Research Institute is supported by the Operational Infrastructure Support Program of the Victorian Government.

Please address correspondence to Rocco Cuzzilla, MD, Neonatal Services, The Royal Women's Hospital, 20 Flemington Rd, Parkville 3052 Victoria, Australia; e-mail: rocco.cuzzilla@thewomens.org.au

Indicates open access to non-subscribers at www.ajnr.org

Indicates article with supplemental on-line table.

http://dx.doi.org/10.3174/ajnr.A5679

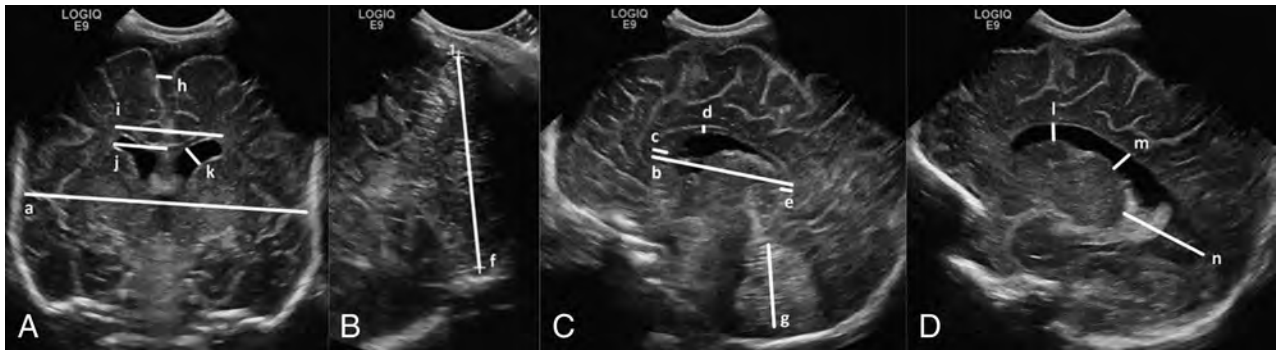

FIG 1. Cranial ultrasonography linear measures: images through the anterior fontanel in the coronal plane at the level of foramina of Monro (*A*) and the sagittal (*C*) and parasagittal (*D*) planes, and an image through the mastoid fontanel in the coronal plane posterior to the fourth ventricle (*B*). Brain tissue: biparietal diameter (a), corpus callosum length (b), corpus callosum genu width (c), corpus callosum body height (d), corpus callosum splenium width (e), transcerebellar diameter (f), and vermis height (g). Fluid spaces: interhemispheric distance (h), ventricular width (i), ventricular index (j), anterior horn width (k), anterior horn height (l), ventricular midbody width (m), and thalamo-occipital distance (n).

tify early brain growth as a potential marker of long-term development that has not been fully exploited.[7]

Linear measures of brain tissue and fluid spaces made from neonatal cUS have been associated with neurodevelopmental outcomes in preterm children.[8,9] However, only 2 studies have evaluated early postnatal brain growth using sequential cUS.[9,10] In a study of 140 infants born at <29 weeks' gestational age (GA), Roelants et al[10] reported normative data for the growth of the corpus callosum length (CCL) and corpus callosum–fastigium length with respect to postmenstrual age (PMA), but they did not relate brain growth with postnatal age (PNA). The study of 61 very-low-birth-weight infants by Anderson et al[9] found that slower growth of the CCL between 2 and 6 weeks' PNA was predictive of motor delay and cerebral palsy at 2 years; however, this study included infants with major brain injury.

To explore further the usefulness of cUS in assessing brain growth in preterm infants without major brain injury, we aimed to achieve the following: 1) assess the reproducibility of linear measures of brain tissue and fluid spaces made from cUS, 2) evaluate brain growth with respect to PNA using sequential cUS linear measures from birth to term-equivalent age (TEA), and 3) explore the associations between perinatal variables and postnatal brain growth measured by cUS.

MATERIALS AND METHODS

Study Participants

One hundred forty-nine infants born at <30 weeks' GA at The Royal Women's Hospital, Melbourne, Australia, between January 2011 and December 2013, were recruited into a prospective longitudinal study of neuroimaging, neurobehavior, and long-term development.[11] Infants with congenital or chromosomal anomalies known to affect neurodevelopment were excluded. For the current study, 5 infants with major preterm brain injury detected on cUS were also excluded, including infants with grades III or IV intraventricular hemorrhage, posthemorrhagic ventricular dilation, and cystic periventricular leukomalacia, leaving 144 infants for analysis.[12,13] The study received institutional approval from the Human Research Ethics Committee of the hospital, and written informed consent was obtained from parents of all participants.

Cranial Ultrasonography

cUS was performed as part of routine clinical care using a Logiq 9 Ultrasound System and an 8-MHz broadband curvilinear transducer (GE Healthcare, Milwaukee, Wisconsin). Standard images were acquired through the anterior fontanel (5 images in different coronal planes, an image in the midsagittal plane, and 2 images in different parasagittal planes both on the left and right) and the mastoid fontanel (1 image in the coronal plane). As per local protocol for the surveillance of preterm brain injury, infants born at <30 weeks' GA were scanned on, or around, days 7, 28, and 60 PNA. Infants born at <28 weeks' GA were also scanned on, or around, day 1 PNA. Additional scans were performed depending on clinical need. The current study included all neonatal scans performed from birth to TEA (<42 weeks' PMA).

Nineteen linear measures of brain tissue and fluid spaces were explored on the basis of potential clinical importance, ease of recognition of anatomic landmarks on standard imaging planes, and evaluation of their reproducibility (Fig 1). A neonatologist (R.C.) blinded to the clinical course of study participants and with 4 years' experience in performing cUS obtained measurements using electronic calipers on stored digital images (Synapse; Fujifilm Medical Company, Minato-Ku, Japan). Thirty scans (7%) were randomly selected to assess the reproducibility of the linear measures. Measurements were made by the same observer (R.C.) twice, at least 1 month apart, and once by another observer (S.R.) with 20 years' experience in performing cUS.

Perinatal Predictors of Long-Term Neurodevelopment

Perinatal variables were chosen a priori on the basis of their known associations with brain injury and long-term neurodevelopmental outcomes following preterm birth.[14] These included GA at birth (determined by first-trimester ultrasonography when available or by menstrual history), birth weight SD score (BW *z* score), sex, multiple gestations, chorioamnionitis (confirmed by placental histology), antenatal corticosteroids (any number of doses of betamethasone) and magnesium sulfate (for maternal or fetal indications), bronchopulmonary dysplasia (defined by oxygen requirement at 36 weeks' PMA), postnatal corticosteroids, confirmed sepsis (blood or CSF culture–positive and the use of antibiotics for ≥5 days) and/or necro-

tizing enterocolitis (NEC; defined by stage II or higher modified Bell criteria), and low-grade intraventricular hemorrhage (grades I or II) seen on cUS (defined by Papile classification).[13,15]

Data Analysis

Data were analyzed using STATA, Version 13.1 (StataCorp, College Station, Texas). Intra- and interobserver agreement was assessed by the intraclass correlation coefficient. Linear measures with both intra- and interobserver intraclass correlation coefficients of >0.80 were considered for inclusion in further analyses. Brain growth (or rate of change) with respect to PNA was assessed using mixed-effects linear regression fitted to all the sequential measurements from all individuals, with PNA as the time variable and a random effect for an individual fitted with an unstructured covariance matrix. The model included a random effect to account for multiple measurements for each infant, with a fixed effect of time. First, overall brain growth was assessed from birth to TEA using a single time variable. Brain growth was then assessed within 3 time intervals to reflect the timing of our routine cUS by fitting separate effects of time in the periods <7, 7–27, and >27 days' PNA. Analyses were repeated with adjustment for GA, BW *z* score, and sex. Associations between perinatal variables and brain growth with respect to PNA (fitting a single effect of time from birth to TEA) were explored separately by including an interaction between the perinatal variable and PNA in the mixed-effects linear regression model. Continuous variables were dichotomized for this analysis: GA group (<28 weeks or 28–29 weeks) and BW *z* score group (<−2 or ≥−2 SDs from the mean). Analyses were repeated with adjustment for GA, BW *z* score, and sex, with the exception that GA and the BW *z* score were not adjusted for when exploring the effect of the GA group and BW *z* score group, respectively. Measurements of the left and right anterior horn widths (AHWs) included the germinal layer hemorrhage when present. Consequently, all analyses involving the AHW were restricted to infants without an ipsilateral intraventricular hemorrhage, to eliminate the influence of the germinal layer hemorrhage on the generalizability of results with respect to rates of change of the AHW with PNA.

Table 1: Infant characteristics

Perinatal Variable	Summary (*N* = 144 Infants)
Gestational age (mean) (SD) (wk)	27.7 (1.5)
Birth weight (mean) (SD) (g)	1017 (259)
Small for gestational age, birth weight <−2 SDs (No.) (%)	16 (11)
Female (No.) (%)	75 (52)
Multiple gestations (No.) (%)	64 (44)
Cesarean delivery (No.) (%)	106 (74)
Antenatal corticosteroids (No.) (%)	134 (93)
Antenatal magnesium sulfate (No.) (%)	103 (72)
Respiratory distress from birth (No.) (%)	141 (98)
Surfactant (No.) (%)	91 (63)
Duration of positive pressure ventilation (median) (25th–75th centile) (days)	19 (0–96)
Duration of supplemental oxygen (median) (25th–75th centile) (days)	19 (4–56)
Bronchopulmonary dysplasia[a] (No.) (%)	46 (32)
Postnatal corticosteroids (No.) (%)	18 (13)
Intraventricular hemorrhage, grades I or II (No.) (%)	25 (17)
Retinopathy of prematurity (No.) (%)	32 (22)
Sepsis confirmed[b] (No.) (%)	20 (14)
NEC (No.) (%)	17 (12)
Sepsis confirmed and/or NEC (No.) (%)	31 (22)
Survived to discharge home (No.) (%)	139 (97)

[a] Defined by oxygen requirement at 36 weeks' postmenstrual age.
[b] Blood or CSF culture–positive and use of antibiotics for ≥5 days.

Table 2: Reproducibility of cranial ultrasonography linear measures

Linear Measure	Intraobserver		Interobserver	
	ICC	95% CI	ICC	95% CI
Brain tissue				
Biparietal diameter	0.98	0.95–0.99	0.97	0.94–0.99
Corpus callosum length	0.99	0.97–0.99	0.98	0.95–0.99
Corpus callosum genu width	0.78	0.53–0.90	0.38	−0.04–0.69
Corpus callosum body height	0.74	0.52–0.87	0.58	0.27–0.78
Corpus callosum splenium width	0.80	0.56–0.92	0.21	−0.22–0.58
Transcerebellar diameter	0.99	0.98–0.99	0.98	0.96–0.99
Vermis height	0.91	0.82–0.96	0.81	0.62–0.91
Fluid spaces				
Interhemispheric distance	0.98	0.96–0.99	0.98	0.95–0.99
Anterior horn width, left	0.94	0.87–0.97	0.91	0.81–0.96
Anterior horn width, right	0.96	0.90–0.98	0.95	0.89–0.98
Ventricular index, left	0.85	0.70–0.93	0.85	0.69–0.93
Ventricular index, right	0.63	0.32–0.82	0.59	0.26–0.80
Ventricular width	0.87	0.72–0.94	0.89	0.76–0.95
Anterior horn height, left	0.86	0.72–0.94	0.76	0.53–0.88
Anterior horn height, right	0.92	0.82–0.96	0.78	0.55–0.90
Ventricular midbody height, left	0.73	0.49–0.87	0.47	0.11–0.72
Ventricular midbody height, right	0.81	0.61–0.91	0.52	0.18–0.75
Thalamo-occipital distance, left	0.93	0.81–0.97	0.80	0.52–0.93
Thalamo-occipital distance, right	0.92	0.80–0.97	0.62	0.22–0.84

Note:—ICC indicates intraclass correlation coefficient.

RESULTS

Characteristics of the 144 infants included in the current study are presented in Table 1. In the 144 infants, 429 scans were performed from birth to TEA. The mean number of scans per infant was 3 (range, 1–8). For the 77 infants born at <28 weeks' GA, 291 scans were assessed (mean, 3.8; range, 1–8 per infant), and 138 scans for the 67 infants born at ≥28 weeks' GA (mean, 2.1; range, 1–6 per infant). Almost two-thirds (n = 272; 63%) of the scans were performed at <28 days' PNA, but most infants had scans up to 33 weeks' PMA.

Intra- and Interobserver Reproducibility

Intra- and interobserver intraclass correlation coefficients are shown in Table 2. Eight linear measures, 4 of brain tissue (biparietal diameter [BPD], CCL, transcerebellar diameter [TCD], and vermis height) and 4 reflecting fluid spaces (interhemispheric distance, left and right AHWs, and ventricular width), had intraclass correlation coefficients of >0.8 both between and within observers and were used to evaluate brain growth.

Brain Growth with Respect to Postnatal Age

There was evidence that all linear measures of brain tissue increased with PNA, before and after adjustment for GA, BW *z* score, and sex, overall and within the 3 time intervals, except for the BPD, which decreased within the first postnatal week (Fig 2 and On-line Table). Faster rates of growth of the BPD, TCD, and vermis height were observed after 27 days' PNA compared with 7–27 days' PNA; however, the rate of growth of the CCL more than halved after 27 days' PNA compared with 7–27 days' PNA (Fig 2 and On-line Table).

Rates of change of linear measures of fluid spaces were variable within the first postnatal week, with little evidence of an association between linear measures and PNA (Fig 2 and On-line Table). The interhemispheric distance and ventricular width increased after the first postnatal week, with faster rates of change after 27 days' PNA (1.5 and 2.7 times, respectively) compared with 7–27 days' PNA. Although the rates of change for the AHW appeared to decrease with successive time intervals, there was little statistical evidence of an association between the AHW and PNA, except for the right AHW between 7 and 27 days' PNA.

Associations between Perinatal Variables and Postnatal Brain Growth

There was strong evidence of associations between many of the perinatal variables and brain growth with respect to PNA, which remained after adjustment for GA, BW *z* score, and sex (Table 3). Infants born at 28–29 weeks' GA showed slower growth of the BPD and ventricular width than infants born at <28 weeks' GA. Postnatal corticosteroid administration was associated with slower growth of the CCL, TCD, and vermis height, and bronchopulmonary dysplasia was associated with slower growth of the CCL and TCD. Infants with a BW *z* score < -2 SDs below the mean showed slower growth of the CCL than infants with BW ≥ -2 SDs below the mean. Sepsis and/or NEC and antenatal corticosteroid administration were associated with slower growth of the TCD.

DISCUSSION

In this study of early postnatal brain growth in infants born at <30 weeks' GA and without major brain injury, several linear measures of brain tissue and fluid spaces were reliably made from routine clinical cUS scans. Most linear measures of brain tissue increased with PNA, but rates of change were more variable for the fluid spaces. Several perinatal variables related to long-term development were associated with postnatal brain growth. Bronchopulmonary dysplasia and postnatal corticosteroid administration were associated with slower growth of the CCL and TCD, and postnatal corticosteroid administration was also associated with slower growth of the vermis height. Sepsis and/or NEC were associated with slower growth of the TCD.

Measurements of brain growth for use in clinical practice should be simple to obtain and reproducible. The cUS linear measures explored in this study had well-defined anatomic landmarks on standard imaging planes obtained during routine clinical care, and several showed excellent intra- and interobserver reproducibility, as also shown by others.[8,10,16,17]

Although cUS affords an opportunity to make sequential measurements from birth, there are limited published data relating to postnatal brain growth in preterm infants. To our knowledge, this study is the first to describe the growth of the BPD in the early postnatal period following preterm birth using sequential cUS. We speculate that the decreasing size of the BPD in the first postnatal week found in the current study may relate to a reduction in brain-water in the immediate postnatal days rather than deformational changes in head shape.[18] Growth of the BPD between 7 and 27 days was slower (1.30 mm/week PNA) than after the first 27 days (2.17 mm/week PNA), from which time postnatal growth of the BPD approximates to expected fetal growth (2.10 mm/week PMA) as reported from cross-sectional data by Kurmanavicius et al.[19] Higher GA at birth related to slower growth of the BPD from birth to TEA, in keeping with normative data for fetal growth of the BPD that demonstrates a slowing of growth with increasing PMA.[19,20] However, infants born at <30 weeks' GA have smaller brains at TEA than term-born controls, and most are likely to have slower rates of brain growth immediately after birth than normally expected in utero.[20,21]

In the current study, CCL growth was relatively constant from birth to 27 days' PNA but slowed by half thereafter. Similarly, Anderson et al[9] showed that postnatal growth of the CCL in very-low-birth-weight infants approximated fetal growth (1.4–1.89 mm/week PMA) within the first 2 postnatal weeks but subsequently slowed to approximately half of that expected.[22,23] Moreover, the current study found that a BW *z* score of < -2 SDs was associated with slower CCL growth from birth to TEA, a finding consistent with that of Roelants et al.[10]

The TCD measured in the fetus, or the neonate in the first postnatal days, is a reliable marker of GA, even with fetal growth restriction, small- and large-for-gestational age fetuses, and multiple gestations (1.25–1.89 mm/week PMA).[24-27] Cross-sectional preterm MR imaging studies have reported cerebellar size, but our study is the first to report postnatal growth of the TCD in preterm infants using sequential cUS.[20,28] Similar to fetal growth patterns, TCD growth in the current study progressively increased between time intervals. Unlike the TCD, the vermis height increased with PNA at a relatively constant rate of change from birth to TEA, approximating fetal growth (0.55 mm/week PMA).[29]

Bronchopulmonary dysplasia and postnatal corticosteroids were associated with slower CCL and TCD growth with PNA, and postnatal corticosteroid administration was also related to slower growth of the vermis height. Tam et al[30] reported a similar association between postnatal corticosteroids, a marker of severe bronchopulmonary dysplasia, and impaired cerebellar growth in very preterm infants using serial MR imaging between 32 weeks' PMA and TEA. In another MR imaging study of very preterm infants scanned at TEA and 7 years, Thompson et al[31] reported an association between postnatal corticosteroids and delayed maturation of the posterior corpus callosum, a region that develops later in gestation and contributes to corpus callosum length. In the current study, sepsis and/or NEC were related to slower growth of the TCD. Sepsis and/or NEC have been associated with preterm white matter injury at TEA, but their relationship with brain growth and maturation in the early postnatal period remains unclear.[32] The relationship between antenatal corticoste-

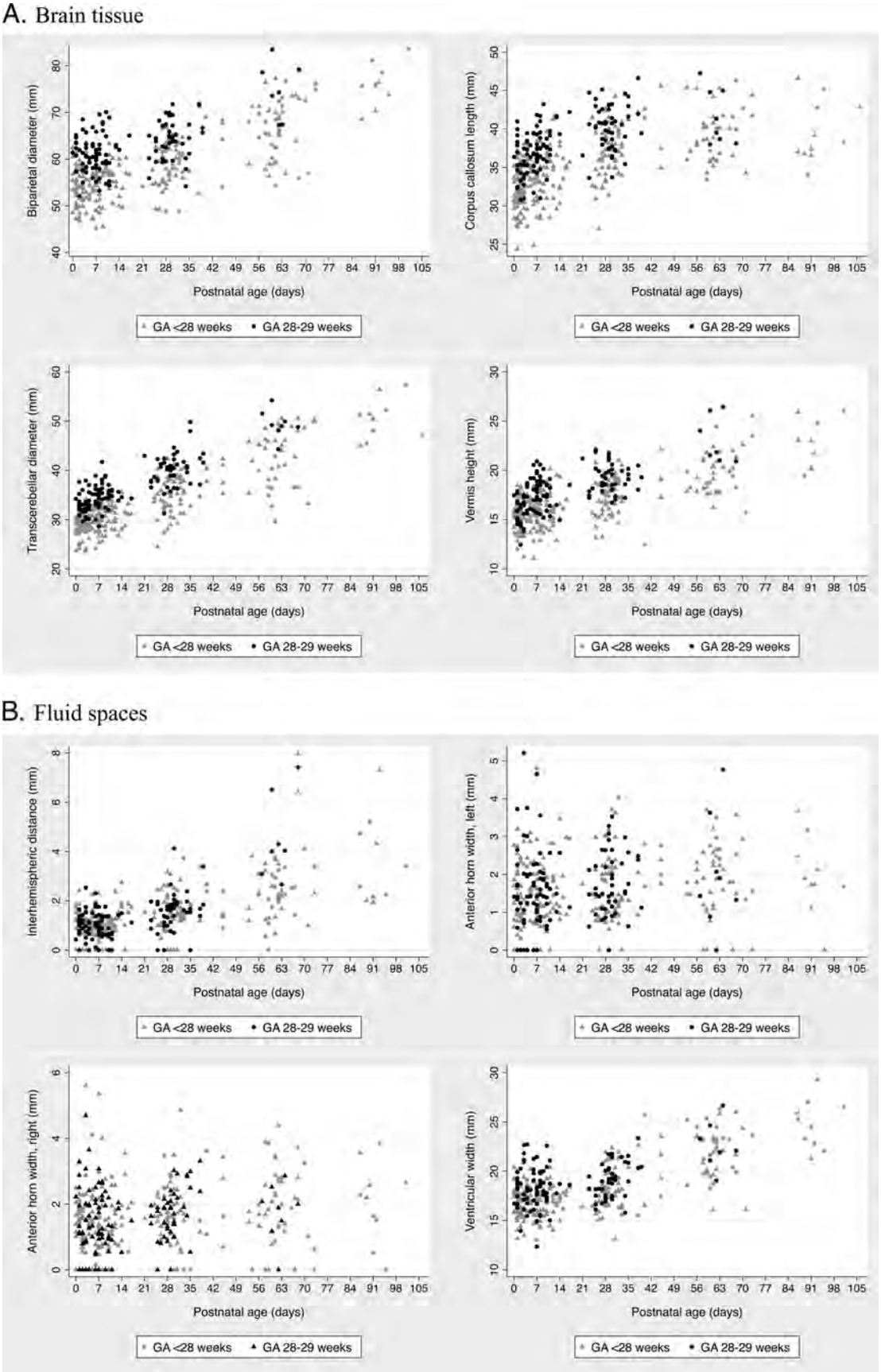

FIG 2. Cranial ultrasonography linear measures with respect to postnatal age. *A*, Brain tissue. *B*, Fluid spaces.

Table 3: Associations between perinatal variables and postnatal brain growth

Perinatal Variable	Adjusted[a] Growth (mm/week PNA) β	95% CI	Interaction Term[b] (*P* Value)
Biparietal diameter			
GA			
<28 weeks	1.88	1.71–2.05	.002
≥28 weeks	1.29	0.96–1.62	
Corpus callosum length			
BW *z* score			
≥−2 SD	0.91	0.84–0.98	.045
<−2 SD	0.73	0.57–0.89	
Postnatal corticosteroids			
No	0.92	0.85–1.00	.046
Yes	0.77	0.63–0.90	
Bronchopulmonary dysplasia			
No	0.98	0.88–1.07	.01
Yes	0.81	0.73–0.89	
Transcerebellar diameter			
Antenatal corticosteroids			
No	2.26	1.81–2.70	.023
Yes	1.73	1.63–1.83	
Postnatal corticosteroids			
No	1.84	1.74–1.95	<.001
Yes	1.41	1.22–1.61	
Bronchopulmonary dysplasia			
No	1.89	1.75–2.02	.008
Yes	1.63	1.49–1.76	
Sepsis/NEC			
No	1.82	1.71–1.93	.016
Yes	1.55	1.36–1.74	
Vermis height			
Postnatal corticosteroids			
No	0.63	0.58–0.69	.011
Yes	0.49	0.39–0.59	
Ventricular width			
GA			
<28 weeks	0.64	0.57–0.71	.004
≥28 weeks	0.41	0.27–0.55	

[a] Adjusted for gestational age, birth weight *z* score, and sex.
[b] *P* value for the interaction between the perinatal variable and postnatal age.

roid exposure and slower TCD growth reported here is novel and needs to be replicated in future studies.

Liao et al[33] and Levene[34] reported serial measurements of the ventricular index in preterm infants from birth to 6 weeks' and 6 months' PNA, respectively, and found rates of change like those in the current study for the ventricular width (the sum of left and right ventricular indices). We found that lower GA was related to a faster rate of change in the ventricular width, possibly resulting from a greater burden of diffuse cerebral white matter injury in the less mature infants leading to greater ex vacuo dilation. Rates of change for the AHW with respect to PNA were variable and increased little after the first postnatal week, as also reported in other studies.[33-36]

A major strength of the current study is its use of simple and reproducible linear measures obtained from standard cUS performed as part of routine clinical care. We use the mastoid fontanel for cerebellar imaging and TCD measurement, a reliable approach that is not technically difficult.[37] Our study, however, has several limitations. We used routine clinical scans timed to detect major preterm brain injury. There is, therefore, an inherent bias in our study cohort because the smaller, less mature infants were more likely to have had a greater burden of brain injury and, subsequently, a greater number of scans for monitoring the progression of any overt findings. It is also likely that these infants had more comorbidities and longer periods of hospitalization. In our neonatal unit, infants who no longer need tertiary-level care are transferred to nontertiary hospitals from as early as 32 weeks' PMA. The more mature infants in our cohort, unless they were very sick, were likely to have had fewer scans, limited to the early days and weeks after birth. However, the mixed-effects model used allows for different infants having different numbers of scans.

The cohort used in the current study will have developmental assessments throughout childhood, which will allow the relationships between sequential cUS linear measures of early postnatal brain growth and neurodevelopment in later childhood to be determined in the future.

CONCLUSIONS

Brain growth in infants born at <30 weeks' GA can be assessed using simple and reproducible linear measures made on sequential cUS. Several perinatal variables already shown to be related to long-term development, including GA, BW *z* score, bronchopulmonary dysplasia, postnatal corticosteroids, and sepsis and/or NEC, were associated with early postnatal brain growth. Further research is needed to evaluate the usefulness of brain growth, as evaluated using sequential cUS linear measures, as a marker of long-term neuro developmental outcome.

ACKNOWLEDGMENTS

We acknowledge Merilyn Bear, Emma McInnes, Brenda Argus, Bernice Mills, and Nicole van der Linden for their input into recruitment of infants and their families for this study.

Disclosures: Rocco Cuzzilla—*UNRELATED*: *Employment*: The Royal Women's Hospital, Melbourne, *Comments*: This is my clinical employer. Alicia J. Spittle—*RELATED*: *Grant*: National Health and Medical Research Council, *Comments*: Career Development Fellowship ID 1108714. Katherine J. Lee—*RELATED*: *Grant*: National Health Medical Research Council, *Comments*: Career Development Fellowship ID 1127984. Sherlyle Rogerson—*UNRELATED*: *Payment for Lectures Including Service on Speakers Bureaus*: GE Webinar lectures, *Comments*: paid for 1 webinar lecture on cranial ultrasound (November 2016). Frances M. Cowan—*UNRELATED*: *Employment*: Chelsea and Westminster Hospital, *Comments*: teaching and reviewing neonatal brain imaging; *Payment for Lectures Including Service on Speakers Bureaus*: Imperial College London Symposium, *Comments*: remuneration for teaching a 3-day course on cranial ultrasound. Lex W. Doyle—*RELATED*: *Grant*: National Health and Medical Research Council of Australia, *Comments*: Centre of Research Excellence grant.* Jeanie L.Y. Cheong—*RELATED*: *Grant*: National Health and Medical Research Coun-

cil, *Comments*: Career Development Fellowship ID 1141354; *UNRELATED*: *Employment*: The Royal Women's Hospital, Melbourne, *Comments*: This is my clinical employer. *Money paid to the institution.

REFERENCES

1. Woodward LJ, Anderson PJ, Austin NC, et al. **Neonatal MRI to predict neurodevelopmental outcomes in preterm infants.** *N Engl J Med* 2006;355:685–94 CrossRef Medline
2. De Vries LS, Van Haastert IL, Rademaker KJ, et al. **Ultrasound abnormalities preceding cerebral palsy in high-risk preterm infants**. *J Pediatr* 2004;144:815–20 Medline
3. Plaisier A, Raets MM, Ecury-Goossen GM, et al. **Serial cranial ultrasonography or early MRI for detecting preterm brain injury?** *Arch Dis Child Fetal Neonatal Ed* 2015;100:F293–300 CrossRef Medline
4. Leijser LM, de Bruïne FT, van der Grond J, et al. **Is sequential cranial ultrasound reliable for detection of white matter injury in very preterm infants?** *Neuroradiology* 2010;52:397–406 CrossRef Medline
5. Miller SP, Cozzio CC, Goldstein RB, et al. **Comparing the diagnosis of white matter injury in premature newborns with serial MR imaging and transfontanel ultrasonography findings.** *AJNR Am J Neuroradiol* 2003;24:1661–69 Medline
6. Laptook AR, O'Shea TM, Shankaran S, et al. **Adverse neurodevelopmental outcomes among extremely low birth weight infants with a normal head ultrasound: prevalence and antecedents.** *Pediatrics* 2005;115:673–80 CrossRef Medline
7. Ment LR, Bada HS, Barnes P, et al. **Practice parameter: neuroimaging of the neonate: report of the Quality Standards Subcommittee of the American Academy of Neurology and the Practice Committee of the Child Neurology Society.** *Neurology* 2002;58:1726–38 CrossRef Medline
8. Fox LM, Choo P, Rogerson SR, et al. **The relationship between ventricular size at 1 month and outcome at 2 years in infants less than 30 weeks' gestation.** *Arch Dis Child Fetal Neonatal Ed* 2014;99:F209–14 CrossRef Medline
9. Anderson NG, Laurent I, Woodward LJ, et al. **Detection of impaired growth of the corpus callosum in premature infants.** *Pediatrics* 2006;118:951–60 CrossRef Medline
10. Roelants, JA, Koning, IV, Raets MM, et al. **A new ultrasound marker for bedside monitoring of preterm brain growth.** *AJNR Am J Neuroradiol* 2016;37:1516–22 CrossRef Medline
11. Spittle AJ, Thompson DK, Brown NC, et al. **Neurobehaviour between birth and 40 weeks' gestation in infants born <30 weeks' gestation and parental psychological wellbeing: predictors of brain development and child outcomes.** *BMC Pediatr* 2014;14:111 CrossRef Medline
12. de Vries LS, Eken P, Dubowitz LM. **The spectrum of leukomalacia using cranial ultrasound.** *Behav Brain Res* 1992;49:1–6 CrossRef Medline
13. Papile LA, Burstein J, Burstein R, et al. **Incidence and evolution of subependymal and intraventricular hemorrhage: a study of infants with birth weights less than 1,500 gm.** *J Pediatr* 1978;92:529–34 CrossRef Medline
14. Doyle LW, Cheong JL, Burnett A, et al; Victorian Infant Collaborative Study Group. **Biological and social influences on outcomes of extreme-preterm/low-birth weight adolescents.** *Pediatrics* 2015;136:e1513–20 CrossRef Medline
15. Bell MJ, Ternberg JL, Feigin RD, et al. **Neonatal necrotizing enterocolitis: therapeutic decisions based upon clinical staging.** *Ann Surg* 1978;187:1–7 CrossRef Medline
16. Hagmann CF, Robertson NJ, Acolet D, et al. **Cerebral measurements made using cranial ultrasound in term Ugandan newborns.** *Early Hum Dev* 2011;87:341–47 CrossRef Medline
17. Anderson NG, Laurent I, Cook N, et al. **Growth rate of corpus callosum in very premature infants.** *AJNR Am J Neuroradiol* 2005;26:2685–90 Medline
18. Williams J, Hirsch NJ, Corbet AJ, et al. **Postnatal head shrinkage in small infants.** *Pediatrics* 1977;59:619–22 Medline
19. Kurmanavicius J, Wright EM, Royston P, et al. **Fetal ultrasound biometry, 1: head reference values.** *Br J Obstet Gynaecol* 1999;106:126–35 CrossRef Medline
20. Bouyssi-Kobar M, du Plessis AJ, McCarter R, et al. **Third trimester brain growth in preterm infants compared with in utero healthy fetuses.** *Pediatrics* 2016;138. pii: e20161640 CrossRef Medline
21. Nguyen The Tich S, Anderson PJ, Shimony JS, et al. **A novel quantitative simple brain metric using MR imaging for preterm infants.** *AJNR Am J Neuroradiol* 2009;30:125–31 CrossRef Medline
22. Achiron R, Achiron, A. **Development of the human fetal corpus callosum: a high-resolution, cross-sectional sonographic study.** *Ultrasound Obstet Gynecol* 2001;18:343–47 CrossRef Medline
23. Malinger G, Zakut, H. **The corpus callosum: normal fetal development as shown by transvaginal sonography.** *AJR Am J Roentgenol* 1993;161:1041–43 CrossRef Medline
24. Imamoglu EY, Gursoy T, Ovali F, et al. **Nomograms of cerebellar vermis height and transverse cerebellar diameter in appropriate-for-gestational-age neonates.** *Early Hum Dev* 2013;89:919–23 CrossRef Medline
25. Chavez MR, Ananth CV, Smulian JC, et al. **Fetal transcerebellar diameter measurement for prediction of gestational age at the extremes of fetal growth.** *J Ultrasound Med* 2007;26:1167–71; quiz 1173–74 Medline
26. Chavez MR, Ananth CV, Kaminsky LM, et al. **Fetal transcerebellar diameter measurement for prediction of gestational age in twins.** *Am J Obstet Gynecol* 2006;195:1596–600 CrossRef Medline
27. Davies MW, Swaminathan M, Betheras FR. **Measurement of the transverse cerebellar diameter in preterm neonates and its use in assessment of gestational age.** *Australas Radiol* 2001;45:309–12 CrossRef Medline
28. Kyriakopoulou V, Vatansever D, Davidson A, et al. **Normative biometry of the fetal brain using magnetic resonance imaging.** *Brain Struct Funct* 2017;222:2295–307 CrossRef Medline
29. Zalel Y, Seidman DS, Brand N, et al. **The development of the fetal vermis: an in-utero sonographic evaluation.** *Ultrasound Obstet Gynecol* 2002;9:136–39 Medline
30. Tam EW, Chau V, Ferriero DM, et al. **Preterm cerebellar growth impairment after postnatal exposure to glucocorticoids.** *Sci Transl Med* 2011;3:105ra105 CrossRef Medline
31. Thompson DK, Inder TE, Faggian N, et al. **Corpus callosum alterations in very preterm infants: perinatal correlates and 2 year neurodevelopmental outcomes.** *Neuroimage* 2012;59:3571–81 CrossRef Medline
32. Shah DK, Doyle LW, Anderson PJ, et al. **Adverse neurodevelopment in preterm infants with postnatal sepsis or necrotizing enterocolitis is mediated by white matter abnormalities on magnetic resonance imaging at term.** *J Pediatr* 2008;153170–75, 175.e1 CrossRef Medline
33. Liao MF, Chaou WT, Tsao LY, et al. **Ultrasound measurement of the ventricular size in newborn infants.** *Brain Dev* 1986;8:262–68 CrossRef Medline
34. Levene MI. **Measurement of the growth of the lateral ventricles in preterm infants with real-time ultrasound.** *Arch Dis Child* 1981;56:900–04 CrossRef Medline
35. Sondhi V, Gupta G, Gupta PK, et al. **Establishment of nomograms and reference ranges for intra-cranial ventricular dimensions and ventriculo-hemispheric ratio in newborns by ultrasonography.** *Acta Paediatr* 2008;97:738–44 CrossRef Medline
36. Perry RN, Bowman ED, Murton LJ, et al. **Ventricular size in newborn infants.** *J Ultrasound Med* 1985;4:475–77 CrossRef Medline
37. da Graca AL, Cardoso KR, da Costa JM, et al. **Assessment of gestational age using cerebellar measurements at cranial ultrasound: what is the best approach?** *Early Hum Dev* 2013;89:1–5 CrossRef Medline

Altered White Matter Microstructure in the Corpus Callosum and Its Cerebral Interhemispheric Tracts in Adolescent Idiopathic Scoliosis: Diffusion Tensor Imaging Analysis

C. Xue, L. Shi, S.C.N. Hui, D. Wang, T.P. Lam, C.-B. Ip, B.K.W. Ng, J.C.Y. Cheng, and W.C.W. Chu

ABSTRACT

BACKGROUND AND PURPOSE: Neural system was one of the important contributors to the etiopathogenesis of adolescent idiopathic scoliosis; additionally, the morphology of corpus callosum interconnecting both hemispheres of the brain was found to be altered morphologically. Our aim was to evaluate and compare the microstructural changes of the corpus callosum and its interhemispheric white matter fiber tracts interconnecting both cerebral hemispheres in patients with adolescent idiopathic scoliosis and matched controls using diffusion tensor imaging.

MATERIALS AND METHODS: Brain DTI was performed in 69 patients with adolescent idiopathic scoliosis (female, right thoracic/thoracolumbar curve) and 40 age-matched controls without adolescent idiopathic scoliosis (female). 2D and 3D segmentation of the corpus callosum were performed using a region-growing method, and the corpus callosum was further divided into 6 regions, including the rostrum, genu, anterior and posterior midbodies, isthmus, and splenium. The laterality index was calculated to quantify the asymmetry of the corpus callosum. Interhemispheric fiber tractography were performed using the Brodmann atlas.

RESULTS: 2D ROI analysis revealed reduced fractional anisotropy in the genu and splenium ($P = .075$ and $P = .024$, respectively). Consistently reduced fractional anisotropy on the left sides of the genu and splenium was also found in 3D ROI analysis ($P = .03$ and $P = .012$, respectively). The laterality index analysis revealed a pseudo-right lateralization of the corpus callosum in adolescent idiopathic scoliosis. Interhemispheric fibers via the splenium interconnecting Brodmann 3, 1, and 2; Brodmann 17; and Brodmann 18 (corresponding to the primary somatosensory cortex and primary and secondary visual cortices) were also found to have reduced fractional anisotropy ($P \leq .05$).

CONCLUSIONS: Reduced fractional anisotropy was found in the genu and splenium of the corpus callosum and corresponding interhemispheric fiber tracts interconnecting the somatosensory and visual cortices via the splenium. Our results are suggestive of altered white matter microstructure within the brain of those with adolescent idiopathic scoliosis, which could be related to abnormal brain maturation during adolescence in adolescent idiopathic scoliosis and could possibly explain the previously documented somatosensory function impairment and visuo-oculomotor dysfunction in this condition.

ABBREVIATIONS: AIS = adolescent idiopathic scoliosis; CC = corpus callosum; FA = fractional anisotropy; LI = laterality index

Adolescent idiopathic scoliosis (AIS) is the most common form of scoliosis that causes 3D structural deformities of the spine, which affect approximately 4% of teenagers during puberty. AIS has been reported to involve impaired balance control,[1] possibly due to a combination of disruptive somatosensory[2] and visuo-oculomotor and vestibular[3] functions. Multiple studies have repeatedly shown evidence of disturbed somatosensory function in AIS, with a higher percentage of abnormal cortical somatosensory-evoked potentials compared with healthy controls.[1,2]

Apart from the neurophysiologic dysfunction, the neuromorphologic changes in AIS have been documented by various imaging studies with changes in the cord[4,5] and brain, including low cerebellar tonsils,[6] abnormalities in white matter density,[7] cerebral cortical thickness,[8] and corpus callosum (CC) morphology.[9,10] Asymmetries in the cerebral hemispheres[7,9,11] and vestibular apparatus[12] were also found in AIS. The neural system is proposed as one of the important contributors to the etiopathogenesis of AIS.[13]

Received September 22, 2017; accepted after revision February 14, 2018.

From the Departments of Imaging and Interventional Radiology (C.X., L.S., S.C.N.H., D.W., C.-B.I., W.C.W.C.) and Orthopedics and Traumatology (T.P.L., B.K.W.N., J.C.Y.C.), Prince of Wales Hospital, The Chinese University of Hong Kong, Shatin, New Territories, Hong Kong.

This work was supported, in part, by grants from the Research Grants Council of the Hong Kong Special Administrative Region (Project No. 14206716 and SEG_CUHK02) and the Fondation Yves Cotrel de l'Institut de France.

Please address correspondence to Dr Lin Shi for technical issues and W.C.W. Chu for clinical issues, Department of Imaging and Interventional Radiology, Prince of Wales Hospital, The Chinese University of Hong Kong, Sha Tin, N.T., Hong Kong SAR; e-mail: shilin@cuhk.edu.hk (L. Shi); winniechu@cuhk.edu.hk (W.C.W. Chu)

Indicates open access to non-subscribers at www.ajnr.org

http://dx.doi.org/10.3174/ajnr.A5634

Diffusion tensor imaging visualizes water diffusion of white matter fiber tracts.[14] The fractional anisotropy (FA) value is commonly applied to interpret the altered microstructure of these tracts.[14] It is highly sensitive to microstructural changes and could be used to reflect microstructural integrity such as fiber density, axonal diameter, and myelination of white matter.

A previous DTI study of the spinal cord and hindbrain showed lower FA values in the medulla oblongata and cervical spinal cord.[4] Another DTI study by Joly et al[15] found a significant decrease in FA values in the midbody of the CC, which possibly suggests abnormal brain development in AIS.

The objective of this study was to use the DTI technique in a larger subject cohort to investigate whether there is any difference in white matter microstructure within the brain between AIS and matched controls using a 3D approach. The ROI was focused on the CC because it is the largest fiber bundle and connector between the 2 cerebral hemispheres.

MATERIALS AND METHODS

Subjects

The research protocol was approved by the Clinical Research Ethics Committee of the institution and was conducted in compliance with the principles of the Declaration of Helsinki. Written informed consent was obtained from all subjects. Subjects with AIS and healthy controls (age- and sex-matched) were prospectively recruited for DTI from January 2012 to December 2014. Patients with AIS were recruited from our outpatient clinic, while the healthy controls were recruited from local schools. All participants were right-handed Chinese female adolescents 12–18 years of age. Inclusion criteria of patients with AIS were typical scoliosis curves convex to the right side. They were carefully assessed clinically to rule out other known associated causes of scoliosis and any neurologic abnormalities. Healthy controls were screened by experienced orthopedic surgeons to exclude minor scoliosis. Exclusion criteria of all subjects were a history of head or back injury, developmental delay, or psychiatric illness.

MR Imaging Acquisition

All subjects underwent MR imaging using a 3T scanner (Achieva TX series; Philip Healthcare, Best, the Netherlands) equipped with an 8-channel sensitivity encoding head coil. For the suppression of eddy current artifacts, brain sensitivity encoding–DTI was acquired using a single-shot EPI sequence with the following parameters: TR = 8667 ms, TE = 60 ms, FOV = 224 × 224 mm^2, flip angle = 90°, NEX = 1, matrix = 112 × 109, sections = 70, section thickness = 2 mm, no interslice gap with an in-plane image resolution = 2 × 2 mm. Thirty-two directions of diffusion gradients with b-values of 1000 s/mm^2 and 1 B_0 volume were collected. Conventional T1-weighted images of the brain for mapping were obtained using a 3D fast-field echo imaging sequence with following parameters: TR = 18 ms, TE = 2.4 ms, FOV = 210 × 210 mm^2, flip angle = 30°, NEX = 1, matrix = 232 × 232, sections = 200.

MR Image Preprocessing

The FMRIB Software Library (FSL; http://www.fmrib.ox.ac.uk/fsl)[16] was used to perform eddy current correction and head motions correction by registering each data point to the first $b=0$ image with affine transformation. Nonbrain tissues were also excluded using the FSL Brain Extraction Tool (http://fsl.fmrib.ox.ac.uk/fsl/fslwiki/BET).[16] After the preprocessing methods, all data were manually checked to exclude any errors.

Voxelwise Statistical Analysis

For voxelwise statistical analysis, the Tract-Based Spatial Statistics (TBSS; http://fsl.fmrib.ox.ac.uk/fsl/fslwiki/TBSS) pipeline available in FSL 5.0.9 was performed.[17] First, FA maps from all participants were smoothed using Gaussian filters with the full width at half maximum of 6 mm and aligned into a 1-mm^3 FA template created by aligning every FA image to every other one using the FMRIB Nonlinear Registration Tool (FNIRT; http://fsl.fmrib.ox.ac.uk/fsl/fslwiki/FNIRT). Second, the mean FA image was calculated from all normalized FA images and thinned to create a mean FA skeleton, which represented the centers of all tracts common to the group. Finally, the skeleton was set to have an FA threshold of 0.2 (FA ≥ 0.2) to ensure that gray matter regions were excluded from the analyses. Resulting skeletonized data were fit into voxelwise cross-subject statistics. The FSL Randomise method (https://fsl.fmrib.ox.ac.uk/fsl/fslwiki/Randomise) was used with threshold-free cluster enhancement at a P value $< .05$ to compare the data and correct the multiple comparisons.

ROI Analysis

After we obtained the FA maps, a 2D segmentation of the CC was performed manually in the midsagittal plane as shown in Fig 1*A*, followed by a 3D segmentation of the same region semiautomatically using a region-growing method in the FA maps by ITK-SNAP 2.4 (www.itksnap.org).[18] For consistency, all 3D segmented CCs consisted of 15 slices on either side of the midlines and the midline image (ie, 31 slices in total), which incorporated the main bulk of CCs as illustrated in Fig 1*B*. All segmented CCs were manually checked for correctness. Regional segmentation of CCs was performed on the basis of the template defined by Witelson,[19] which included the rostrum, genu, anterior midbody, posterior midbody, isthmus, and splenium from an anterior-to-posterior direction. 3D segmentation was further divided into left (LHS) and right (RHS) sides, with the midsagittal line acting as the dividing line. The laterality index (LI)[20] was calculated by the following formula:

$$LI = \frac{Mean\ FA_{\mathrm{LHS}} - Mean\ FA_{\mathrm{RHS}}}{Mean\ FA_{\mathrm{LHS}} + Mean\ FA_{\mathrm{RHS}}}.$$

The laterality index shows left hemispheric lateralization by the value ≥+0.1, while the value ≤−0.1 indicates rightward asymmetry. Values between +0.1 and −0.1 represent bilateral lateralization.[20]

DTI Tractography Analysis

DSI Studio (http://dsi-studio.labsolver.org/)[21] was used to process the corrected diffusion-weighted images for fiber tractography analysis. To measure and quantify the fiber tracking from the left to right hemisphere of the brain, we applied the Brodmann atlas,[22] and the midsagittal line was used as the middle line to separate the atlas into left and right sides. The Brodmann atlas was

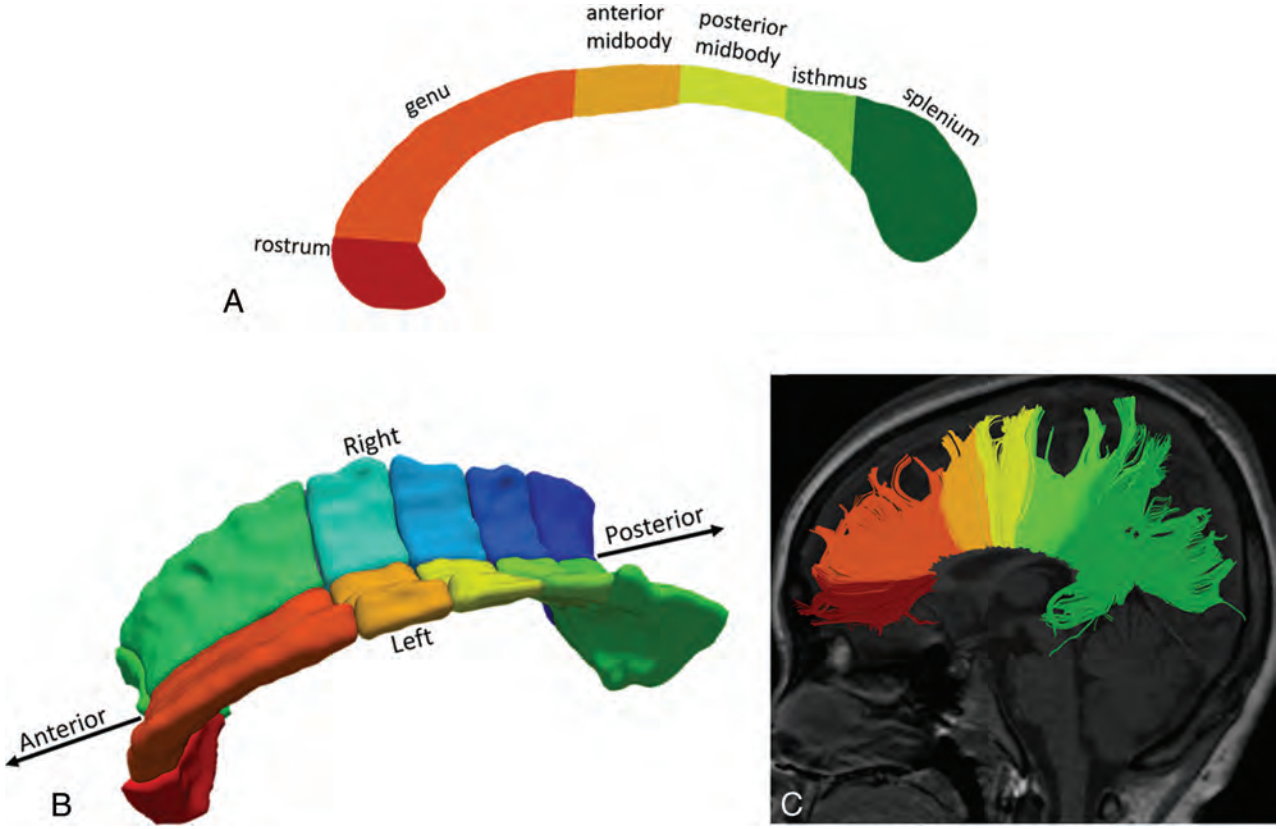

FIG 1. Subdivision of the CC based on the Witelson template[19] in the midsagittal view in 2D segmentation (*A*), 3D segmentation (*B*), and fiber tractography (*C*).

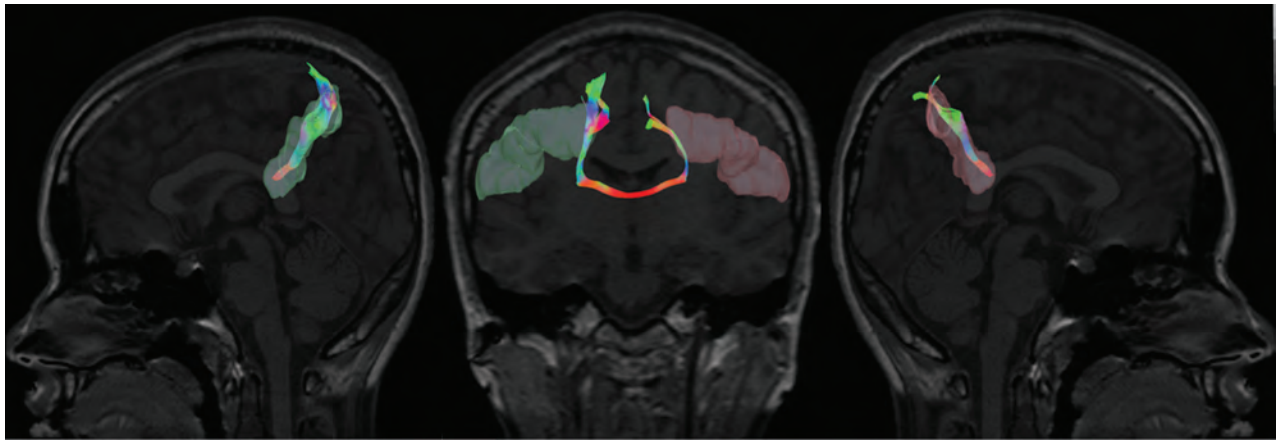

FIG 2. Illustration of the interhemispheric tract with the ROIs (left and right Brodmann 2) selected from the Brodmann atlas.

then registered nonlinearly to the subject space using the statistical parametric mapping (SPM software; http://www.fil.ion.ucl.ac.uk/spm/software/spm12) nonlinear registration algorithm. For each tract, left and right ROIs were placed to establish the tract network with the following cutoffs and thresholds: FA threshold = 0.15; angular threshold = 70,[23] only limited to fibers passing through the CC as shown in Fig 2.

Statistics

The FA maps in the AIS group were compared with those in the control groups using an independent *t* test. One-way ANOVA was performed to compare mean FA values among the control and AIS groups with different levels of severity (ie, mild, moderate, and severe) with Bonferroni as a post hoc analysis. The level of statistical significance was defined at $P \leq .05$. False discovery rate correction was used for multiple comparison corrections.

RESULTS

Participant Characteristics

Sixty-nine right-handed patients with AIS (female; mean age, 14.5 ± 2.2 years; mean Cobb angle, 33.55° ± 13.9°) and 40 age-matched right-handed healthy controls (female; mean age, 14.6 ± 1.04 years) were recruited. The AIS group consisted of 65 patients with a dominant right thoracic curve and 4 patients with a dom-

Table 1: Demographics of subjects with AIS with different curve severities and healthy controls

	AIS				
	Mild	Moderate	Severe	Overall	Controls
Cobb angle	13°–19°	20°–39°	40°–79°	13°–79°	–
Age (range) (mean) (yr)	12.2–16.4 (13.3)	11.3–16.7 (14.6)	12.7–16.4 (14.9)	11.3–16.7 (14.5)	12.6–16.4 (14.6)
No. of subjects	9 AIS (9 RT)	43 AIS (40 RT, 3 RTL)	17 AIS (16 RT, 1 RTL)	69 AIS (65 RT, 4 RTL)	40

Note:—RT indicates right thoracic; RTL, right thoracolumbar.

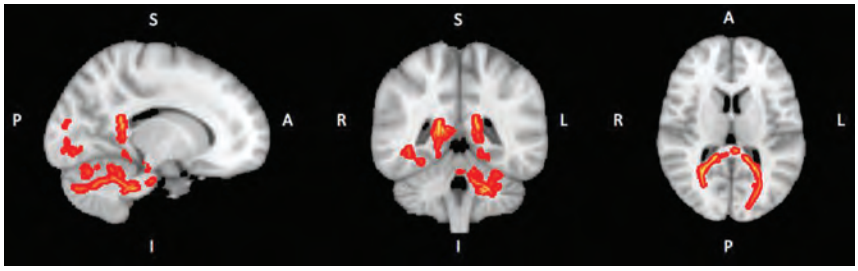

FIG 3. Results of voxelwise statistical analysis using the TBSS pipeline. The *red lines* show the lower FA value in the voxels in the subject with AIS compared with control subjects. S indicates superior; I, inferior; R, right; L, left; P, posterior; A, anterior.

inant right thoracolumbar curve. Their demography is shown in Table 1.

The 69 patients with AIS were further divided into 3 groups based on the severity of their scoliosis curve defined by the Cobb angle as follows: mild group (n = 9, Cobb angle = 13°–19°); moderate group (n = 43, Cobb angle = 20°–39°); and severe group (n = 17, Cobb angle = 40°–79°).[5] T1- and T2-weighted images were reviewed by an experienced radiologist (W.C.W.C.), and no structural brain abnormality was found in any subject.

Voxel-Based Analysis

Using the TBSS analysis implemented in FSL, we found no significant lower FA (P = .438) between the 2 groups voxelwise, even though slightly lower mean FAs were found in the splenium of patients (Fig 3).

2D ROI Analysis of the Corpus Callosum

The summary of FA values at different regions of the CC from 2D analysis is shown in Fig 4. Significantly lower mean FA values in patients with AIS were found in the genu (uncorrected P = .025) and splenium (uncorrected P = .004). Compared with different scoliosis severities, significantly lower FA values were found only in the splenium (corrected P = .02), while a marginal difference (corrected P = .069) of lower FA values was observed in the genu when we compared the control with the moderate group. After multiple comparison correction, significantly reduced FA values were persistently found in the splenium of patients with AIS (corrected P = .024). The overall summary is shown in Table 2.

3D ROI Analysis of the Corpus Callosum

Using 3D segmentation, we performed analysis of the CC in detail with data obtained from the whole region instead of only 1 midsagittal slice in 2D. We also conducted the left-right comparison, which was not performed in the previous 2D study.[15]

FA values were compared between the left and right sides of the CC, summarized in Fig 5 and Table 3. Lower FA values were found significantly on the left side of splenium (corrected P = .012) and in the left genu (corrected P = .03). Comparisons among different severities of AIS revealed significantly lower FA values on the left side of the splenium (corrected P = .048) and genu (corrected P = .012) in the moderate group. FA values from the left side of the splenium (corrected P = .078) also showed a trend toward lower values in the severe group.

The LI assessed lateralization of the brain. Comparison between controls and patients with AIS is shown in Fig 6 and Table 4. Results indicated that LI values in different regions of the CC of both those with AIS and controls fell between +0.1 and −0.1, compatible with bilateral lateralization in both subject groups, however, with a significantly lower LI in the splenium of the corpus callosum (corrected P = .012) and in the genu (corrected P = .03) of those with AIS. The above findings reflected significant interhemispheric FA asymmetry of the CC with reduced FA on the left side (pseudo-right lateralization) in AIS compared with controls. This pseudo-right lateralization was also significant (corrected $P < .05$) when comparing controls with the moderate AIS group.

DTI Tractography Analysis

The mean FA values of all the resulting tracts were extracted and compared between patients with AIS and controls. Significantly lower FA values were only observed in Brodmann 3, 1, and 2, with mean FA values of 0.517 (AIS) versus 0.53 (controls) (P = .045), which reflect the primary somatosensory cortex; Brodmann 17 with mean FA values of 0.567 (AIS) versus 0.581 (controls) (P = .027); and Brodman 18 with mean FA values 0.571 (AIS) versus 0.582 (controls) (P = .038), which are correlated with the primary visual cortex (V1) and secondary visual cortex (V2), correspondingly, in AIS. When we compared patients with AIS with different severities, lower FA values were also detected in Brodmann 17 with a mean FA value of 0.563 (P = .007) and Brodmann 18 with a mean FA value of 0.5693 (P = .029) in moderate cases.

DISCUSSION

The corpus callosum is known as the largest white matter fiber bundle connecting both hemispheres of the brain.[24] Different segments of the CC are connected to different cerebral regions[24] as shown in Fig 1*C*. Topographic organization of the CC is supported by various studies[25,26] in patients with surgical resection of callosal lesions: Anterior callosal axons transfer motor information between frontal lobes, while posterior fibers crossing the posterior midbody, isthmus, and splenium transfer somatic sensory, auditory, and visual information.[26]

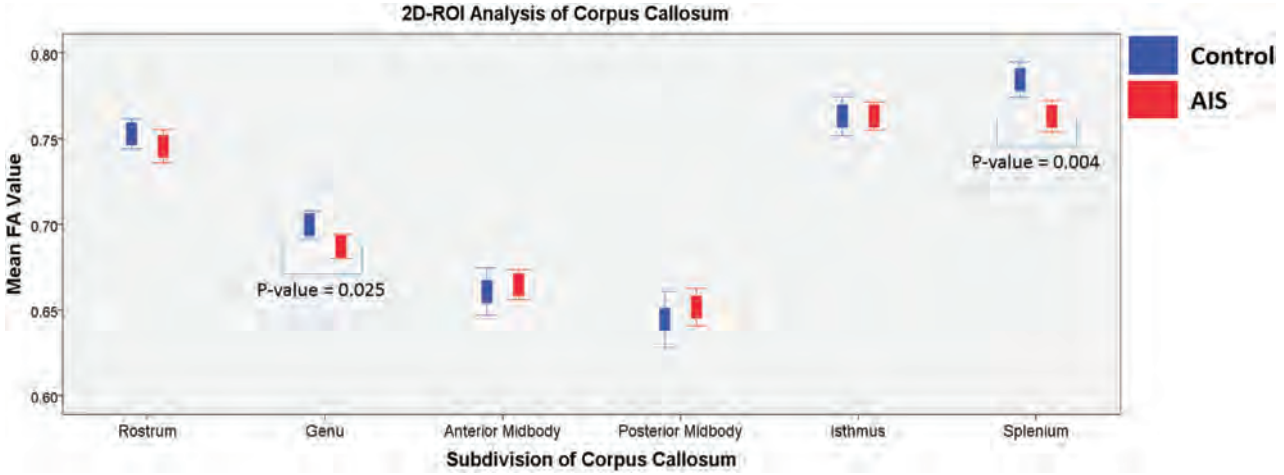

FIG 4. Summary of FA values of each subdivision of the corpus callosum divided by the Witelson template[19] in the 2D segmentation ROI analysis. Blue represents controls, and red represents patients with AIS.

Table 2: Descriptive statistics of the FA comparison between controls and patients with AIS in 2D segmentation[a]

	Controls	AIS	*P* Value (Uncorrected)	*P* Value (Corrected)[b]
Rostrum	0.7528 ± 0.02735	0.7455 ± 0.04039	.31	.62
Genu	0.6997 ± 0.02552	0.6870 ± 0.02955	.025	.08
Anterior midbody	0.6607 ± 0.04330	0.6647 ± 0.0366	.61	.73
Posterior midbody	0.6445 ± 0.05131	0.6516 ± 0.04586	.46	.68
Isthmus	0.7630 ± 0.03550	0.7631 ± 0.03340	.99	.99
Splenium	0.7845 ± 0.03228	0.7630 ± 0.03855	.004	.02

[a] Data are means unless otherwise indicated.
[b] *P* value after multiple comparison correction.

In our 2D ROI analysis, significantly lower FA values were found in the genu and splenium. In 3D ROI analysis, significantly lower FA values at the left genu and left splenium were consistently found as in the 2D ROI analysis, while in the study of Joly et al,[15] lower FA values were found in the midbody. The above apparent discrepancies could be partially explained by different templates used in dividing the CC. The genu in this study overlapped the anterior midbody in the study of Joly et al. Hence, both studies were basically in agreement; however, an additional area of lower FA value was found in the splenium of patients with AIS in the current study, which might be partially explained by differences in subject recruitment. Our study included a larger number of patients with AIS with major right thoracic curves while in the study of Joly et al, subjects predominantly had major thoracolumbar curves.

The genu of the CC provides interconnection to the prefrontal cortex, premotor cortex, and supplementary motor area.[24] Caille et al[25] studied patients without epilepsy with resection of different portions of the anterior CC, showing that motor coordination transfer occurred at the level of the middle portion of the genu. Our study showed a significantly lower FA value and reduced laterality index in the genu of patients with AIS, which concurs with previous fMRI findings about an abnormal activation in the supplementary motor area and a significantly higher interhemispheric asymmetry index in the premotor cortex and supplementary motor area in patients with AIS.[27]

Our tractography analysis found lower FA values in the fibers passing through the splenium and interconnecting primary somatosensory cortex (Brodmann 3, 1, and 2) and the primary and secondary visual cortices (Brodmann 17 and 18) in patients with AIS. Fabri et al[28] performed an fMRI study in a human subject who had undergone resection of the CC (callosotomy) in 2 stages and concluded that integrity of the posterior body of the CC/splenium was required for normal interhemispheric transfer of somatosensory input to activate the related cerebral cortex. In the current study, we found significantly lower FA values on the left side of the splenium after multiple corrections. Our findings correspond with the clinical observation of somatosensory-evoked-potential dysfunction in AIS.[1,2,29] According to the study of Fabri et al,[28] for subjects with an intact posterior body of the CC, peripheral somatosensory stimulation leads to activation of both contralateral and ipsilateral somatosensory areas and the posterior parietal cortex; however, if the posterior half and splenium of the CC was damaged, activation could only be observed in the contralateral cortex. In this study, lower FA was found on the left side, which corresponded to the reported somatosensory-evoked-potential abnormalities[29] found over the right cerebral cortex in patients with AIS with a typical right thoracic scoliotic curve.

Other reported studies have provided evidence that transfer of visual[30,31] information between the hemispheres occurs in the splenium. Our finding of reduced FA values in fibers interconnecting the visual cortex coincides with findings of a previous study in which smaller brain volume closely related to the visual cortex was found in patients with AIS.[9] Moreover, visually impaired children have been shown to have a higher risk of spinal deformity.[32]

What is the possible link between such alterations of the CC and scoliosis development in AIS? The human brain develops extensively during adolescence, with maturation of the CC continuing until early adulthood,[33] characterized by both myelination and axonal pruning; hence, development of the brain could be reflected by FA values in DTI because it reveals information

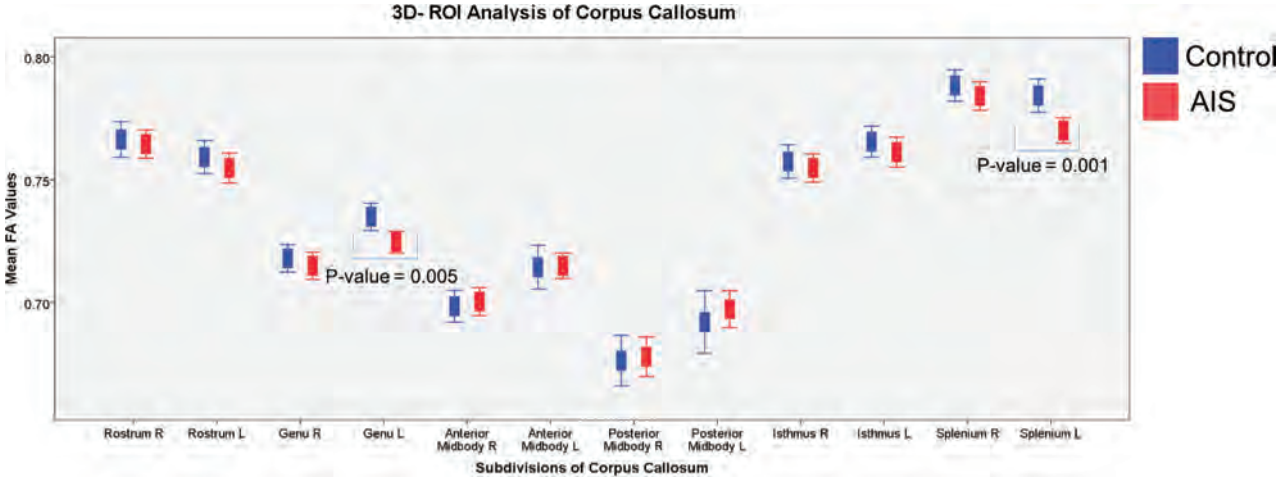

FIG 5. Summary of the mean FA values on the right and left of 3D segmentation of the CC for each subdivision according to the Witelson template[19] in controls and patients with AIS.

Table 3: Descriptive statistics of the FA comparison between controls and patients with AIS in 3D segmentation[a]

	Controls		AIS		*P* Value (Uncorrected)		*P* Value (Corrected)[b]	
	LH	RH	LH	RH	LH	RH	LH	RH
Rostrum	0.7592 ± 0.02106	0.7664 ± 0.02260	0.7548 ± 0.02522	0.7645 ± 0.02396	.33	.69	1	.83
Genu	0.7349 ± 0.01735	0.7180 ± 0.0175	0.7246 ± 0.01843	0.7073 ± 0.02316	.005[c]	.47	.03[c]	.94
Anterior midbody	0.7144 ± 0.02782	0.6985 ± 0.02027	0.7150 ± 0.02142	0.7004 ± 0.02379	.91	.67	.91	.90
Posterior midbody	0.6921 ± 0.03998	0.6764 ± 0.03216	0.6973 ± 0.03141	0.6780 ± 0.03358	.48	.81	.82	.88
Isthmus	0.7655 ± 0.01978	0.7574 ± 0.02134	0.7612 ± 0.02547	0.7548 ± 0.02395	.36	.56	.87	.85
Splenium	0.7842 ± 0.02128	0.7883 ± 0.01990	0.7701 ± 0.02154	0.7841 ± 0.02404	.001[c]	.34	.012[c]	1

Note:—LH indicates left-hand side; RH, right-hand side.

[a] Data are means unless otherwise indicated.

[b] *P* value after multiple comparison correction.

[c] Statistically significant ($P < .05$).

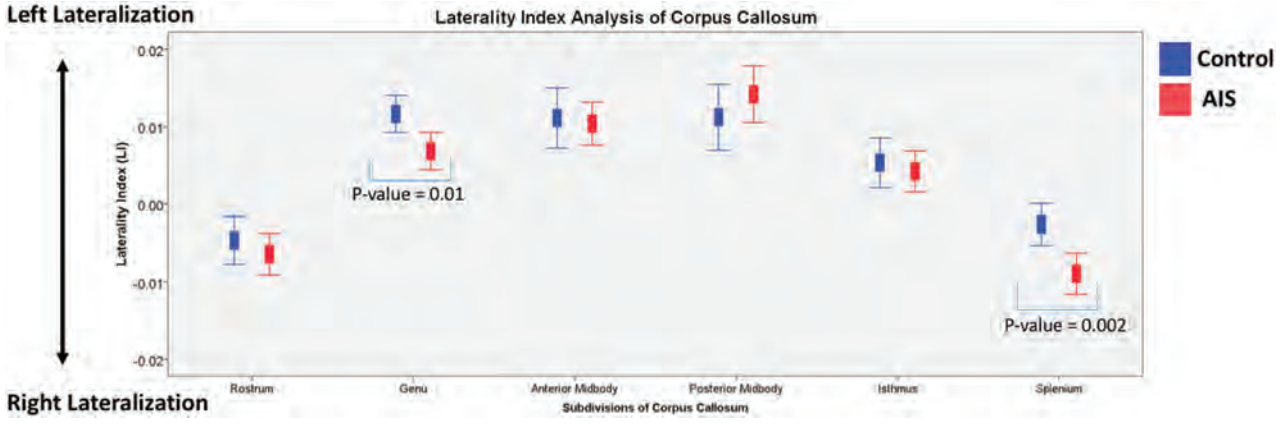

FIG 6. The laterality index of the CC for both patients with AIS (red) and controls (blue). The laterality index was calculated by the following formula: $LI = (Mean\ FA_{LHS} - Mean\ FA_{RHS}) / (Mean\ FA_{LHS} + Mean\ FA_{RHS})$.

about the homogeneity of water diffusion. Different regions of the CC mature at different pubertal stages.[34] Both the genu and splenium become more mature and thicker, reaching 90% of maximal thickness in earlier puberty,[34] which coincides with the typical period for the onset of the scoliotic curve in AIS. Burwell et al[35] have formulated a collective model of the pathogenesis of AIS, which is a neuro-osseous timing of the maturation system operating in a child's internal world during growth and maturation. Burwell et al have suggested that AIS progresses as the neural system fails to maintain a balance of postural equilibrium to control asymmetric growth of a rapidly enlarging and moving adolescent spine. In line with the above theory, we hypothesize that the brain maturation process, including the maturation of the genu and splenium in AIS, might be interrupted during the rapid growing period of adolescence when onset and/or progression of the scoliotic curve occurs. Our finding has suggested that there are alterations of white matter in the CC reflected by lower FA values. These alterations are also in agreement with previously reported morphologic changes of the CC by MR imaging.[9,10]

Furthermore, we found reduced FA on the left side of the CC

Table 4: Descriptive statistics of the laterality index comparison between controls and patients with AIS[a]

	Controls	AIS	*P* Value (Uncorrected)	*P* Value (Corrected)[b]
Rostrum	−0.0047 ± 0.00965	−0.0064 ± 0.01120	.41	.61
Genu	0.0116 ± 0.00750	0.0068 ± 0.01001	.01[c]	.03[c]
Anterior midbody	0.0111 ± 0.01220	0.0104 ± 0.01156	.76	.76
Posterior midbody	0.0112 ± 0.01331	0.0142 ± 0.01521	.31	.61
Isthmus	0.00053 ± 0.01001	0.0042 ± 0.01101	.60	.72
Splenium	−0.00026 ± 0.00848	−0.009 ± 0.01108	.002[c]	.012[c]

[a] Data are means unless otherwise indicated.
[b] *P* value after multiple comparison correction.
[c] Statistically significant ($P < .05$).

involving the genu and splenium in patients with AIS with a dominant right convex scoliotic curve. These observations might not be just a casual phenomenon but could have implications related to underlying spinal asymmetry. The pseudo-right lateralization of the CC might be part of the known generalized asymmetry of many functions and structures proposed in AIS, such as cerebral hemisphere asymmetries,[7,9,11] vestibular apparatus asymmetries,[12] extraspinal left-right skeletal length asymmetries, and proximodistal lower limb disproportions (allometry),[35] though the exact mechanism and clinical significance (whether it is related to primary etiopathogenesis or is a secondary consequence of AIS) is not certain.

One of the limitations of this study is the unequal number of subjects in the mild, moderate, and severe groups of AIS, with most subjects belonging to moderate group. This is the genuine distribution of AIS in the daily clinical setting and probably explains why a significant difference is consistently observed in the moderate group only, while the other subgroups, though showing similar trends, have not reached the significance level. For future studies, a concerted effort of multiple centers with recruitment of more patients with mild and severe AIS would be useful to further investigate the relationship between those alterations in the CC and the effect on scoliosis curve severity.

The neuropsychologic dysfunctions of AIS are usually subclinical, though they can be elicited by specific tests; however, these tests are sophisticated and expensive and have not been included in this study, which is another limitation. Examples of these specific tests, however, have been well-documented in the published literature, which include video-oculography for visuo-oculomotor dysfunction[3] and electromyographic analysis for gait[36] in AIS.

Although there is a significant FA difference in the CC and related cerebral regions, reflecting white matter microstructural changes, the FA values derived from DTI do not involve non-Gaussian properties of biologic tissues and intravoxel fiber crossings,[37] which may interfere with FA value accuracy. Diffusional kurtosis imaging, which involves more sophisticated calculations, can overcome the limitations by eliminating some confounding factors. Future studies using the more advanced diffusional kurtosis imaging might be useful to further validate our DTI findings.

CONCLUSIONS

Reduced FA was found in the genu and splenium in patients with AIS compared with matched controls on both 2D and 3D segmentation analysis. There was corresponding reduction of FA in fibers interconnecting the primary somatosensory cortex and visual cortex, passing through the splenium in patients with AIS. Furthermore, relatively reduced FA was also observed on the left side of the above regions of the CC in patients with AIS presenting with a typical right scoliotic curve. The above microstructural changes of the white matter fiber tracts might be related to the documented somatosensory function impairment and visuo-oculomotor dysfunction in AIS.

REFERENCES

1. Lao ML, Chow DH, Guo X, et al. **Impaired dynamic balance control in adolescents with idiopathic scoliosis and abnormal somatosensory evoked potentials.** *J Pediatr Orthop* 2008;28:846–49 CrossRef Medline
2. Guo X, Chau WW, Hui-Chan CW, et al. **Balance control in adolescents with idiopathic scoliosis and disturbed somatosensory function.** *Spine* 2006;31:E437–40 CrossRef Medline
3. Lion A, Haumont T, Gauchard GC, et al. **Visuo-oculomotor deficiency at early-stage idiopathic scoliosis in adolescent girls.** *Spine* 2013;38:238–44 CrossRef Medline
4. Kong Y, Shi L, Hui SC, et al. **Variation in anisotropy and diffusivity along the medulla oblongata and the whole spinal cord in adolescent idiopathic scoliosis: a pilot study using diffusion tensor imaging.** *AJNR Am J Neuroradiol* 2014;35:1621–27 CrossRef Medline
5. Chu WC, Man GC, Lam WW, et al. **Morphological and functional electrophysiological evidence of relative spinal cord tethering in adolescent idiopathic scoliosis.** *Spine* 2008;33:673–80 CrossRef Medline
6. Chu WC, Man GC, Lam WW, et al. **A detailed morphologic and functional magnetic resonance imaging study of the craniocervical junction in adolescent idiopathic scoliosis.** *Spine* 2007;32:1667–74 CrossRef Medline
7. Shi L, Wang D, Chu WC, et al. **Volume-based morphometry of brain MR images in adolescent idiopathic scoliosis and healthy control subjects.** *AJNR Am J Neuroradiol* 2009;30:1302–07 CrossRef Medline
8. Wang D, Shi L, Chu WC, et al. **Abnormal cerebral cortical thinning pattern in adolescent girls with idiopathic scoliosis.** *Neuroimage* 2012;59:935–42 CrossRef Medline
9. Liu T, Chu WC, Young G, et al. **MR analysis of regional brain volume in adolescent idiopathic scoliosis: neurological manifestation of a systemic disease.** *J Magn Reson Imaging* 2008;27:732–36 CrossRef Medline
10. Wang D, Shi L, Chu WC, et al. **A comparison of morphometric techniques for studying the shape of the corpus callosum in adolescent idiopathic scoliosis.** *Neuroimage* 2009;45:738–48 CrossRef Medline
11. Goldberg CJ, Dowling FE, Fogarty EE, et al. **Adolescent idiopathic scoliosis and cerebral asymmetry: an examination of a nonspinal perceptual system.** *Spine (Phila Pa 1976)* 1995;20:1685–91 CrossRef Medline
12. Chu WC, Shi L, Wang D, et al. **Variations of semicircular canals orientation and left-right asymmetry in adolescent idiopathic scoliosis (AIS) comparing with normal controls: MR morphometry study using advanced image computation techniques.** *Research into Spinal Deformities 6* 2008;140:333 CrossRef
13. Cheng JC, Castelein RM, Chu WC, et al. **Adolescent idiopathic scoliosis.** *Nat Rev Dis Primers* 2015;1:15030 CrossRef Medline
14. Beaulieu C. **The basis of anisotropic water diffusion in the nervous system: a technical review.** *NMR Biomed* 2002;15:435–55 CrossRef Medline

15. Joly O, Rousie D, Jissendi P, et al. **A new approach to corpus callosum anomalies in idiopathic scoliosis using diffusion tensor magnetic resonance imaging.** *Eur Spine J* 2014;23:2643–49 CrossRef Medline
16. Jbabdi S, Sotiropoulos SN, Savio AM, et al. **Model-based analysis of multishell diffusion MR data for tractography: how to get over fitting problems.** *Magn Reson Med* 2012;68:1846–55 CrossRef Medline
17. Smith SM, Jenkinson M, Johansen-Berg H, et al. **Tract-based spatial statistics: voxelwise analysis of multi-subject diffusion data.** *Neuroimage* 2006;31:1487–505 CrossRef Medline
18. Yushkevich PA, Piven J, Hazlett HC, et al. **User-guided 3D active contour segmentation of anatomical structures: significantly improved efficiency and reliability.** *Neuroimage* 2006;31:1116–28 CrossRef Medline
19. Witelson SF. **Hand and sex differences in the isthmus and genu of the human corpus callosum: a postmortem morphological study.** *Brain* 1989;112(Pt 3):799–835 CrossRef Medline
20. Sreedharan RM, Menon AC, James JS, et al. **Arcuate fasciculus laterality by diffusion tensor imaging correlates with language laterality by functional MRI in preadolescent children.** *Neuroradiology* 2015; 57:291–97 CrossRef Medline
21. Yeh FC, Verstynen TD, Wang Y, et al. **Deterministic diffusion fiber tracking improved by quantitative anisotropy.** *PLoS One* 2013;8: e80713 CrossRef Medline
22. Brodmann K. *Vergleichende Lokalisationslehre der Grosshirnrinde in ihren Prinzi-pen Dargestellt auf Grund des Zellenbaus.* Leipzig: Barth-Verlag; 1909
23. Hecke WV. **DTI in neurosurgical planning.** In: Van Hecke W, Emsell L, Sunaert S. *Diffusion Tensor Imaging.* New York: Springer-Verlag; 2016:291–306
24. Hofer S, Frahm J. **Topography of the human corpus callosum revisited: comprehensive fiber tractography using diffusion tensor magnetic resonance imaging.** *Neuroimage* 2006;32:989–94 CrossRef Medline
25. Caille S, Sauerwein HC, Schiavetto A, et al. **Sensory and motor interhemispheric integration after section of different portions of the anterior corpus callosum in nonepileptic patients.** *Neurosurgery* 2005;57:50–59; discussion 50–59 CrossRef Medline
26. Fabri M, Pierpaoli C, Barbaresi P, et al. **Functional topography of the corpus callosum investigated by DTI and fMRI.** *World J Radiol* 2014; 6:895–906 CrossRef Medline
27. Domenech J, Garcia-Marti G, Marti-Bonmati L, et al. **Abnormal activation of the motor cortical network in idiopathic scoliosis demonstrated by functional MRI.** *Eur Spine J* 2011;20:1069–78 CrossRef Medline
28. Fabri M, Polonara G, Del Pesce M, et al. **Posterior corpus callosum and interhemispheric transfer of somatosensory information: an fMRI and neuropsychological study of a partially callosotomized patient.** *J Cogn Neurosci* 2001;13:1071–79 CrossRef Medline
29. Chau WW, Chu WC, Lam TP, et al. **Anatomical origin of abnormal somatosensory evoked potential (SEP) in adolescent idiopathic scoliosis with different curve severity and correlation with cerebellar tonsillar level determined by MRI.** *Spine (Phila Pa 1976)* 2016;41: E598–604 CrossRef Medline
30. Gazzaniga MS, Freedman H. **Observations on visual processes after posterior callosal section.** *Neurology* 1973;23:1126–30 CrossRef Medline
31. Clarke S, Maeder P, Meuli R, et al. **Interhemispheric transfer of visual motion information after a posterior callosal lesion: a neuropsychological and fMRI study.** *Exp Brain Res* 2000;132:127–33 CrossRef Medline
32. Catanzariti JF, Salomez E, Bruandet JM, et al. **Visual deficiency and scoliosis.** *Spine* 2001;26:48–52 CrossRef Medline
33. Pujol J, Vendrell P, Junqué C, et al. **When does human brain development end? Evidence of corpus callosum growth up to adulthood.** *Ann Neurol* 1993;34:71–75 CrossRef Medline
34. Chavarria MC, Sanchez FJ, Chou YY, et al. **Puberty in the corpus callosum.** *Neuroscience* 2014;265:1–8 CrossRef Medline
35. Burwell RG, Dangerfield PH, Freeman BJ. **Etiologic theories of idiopathic scoliosis: somatic nervous system and the NOTOM escalator concept as one component in the pathogenesis of adolescent idiopathic scoliosis.** *Stud Health Technol Inform* 2008;140: 208–17 Medline
36. Mahaudens P, Mousny M. **Gait in adolescent idiopathic scoliosis: kinematics, electromyographic and energy cost analysis.** *Stud Health Technol Inform* 2010;158:101–06 Medline
37. Veraart J, Poot DH, Van Hecke W, et al. **More accurate estimation of diffusion tensor parameters using diffusion kurtosis imaging.** *Magn Reson Med* 2011;65:138–45 CrossRef Medline

CSF Pressure Change in Relation to Opening Pressure and CSF Volume Removed

B. Griffith, T. Capobres, S.C. Patel, H. Marin, A. Katramados, and L.M. Poisson

ABSTRACT

BACKGROUND AND PURPOSE: Idiopathic intracranial hypertension is a complex neurologic disorder resulting from increased intracranial pressure. Our aim was to determine whether a correlation exists between the CSF pressure-volume relationship, specifically the craniospinal elastance and pressure-volume index, in patients with idiopathic intracranial hypertension and whether opening pressure affects this relationship.

MATERIALS AND METHODS: Lumbar punctures performed for suspected idiopathic intracranial hypertension from 2006 to 2017 were identified. Opening and closing pressures, CSF volume removed, and clinical diagnosis of idiopathic intracranial hypertension were obtained from the medical records. The craniospinal elastance (pressure change per milliliter of CSF removed) and pressure-volume index were calculated, and the Pearson correlation coefficients between both the craniospinal elastance and pressure-volume index and opening pressure were determined. Linear regression models of craniospinal elastance and the pressure-volume index and interaction terms with opening pressure were assessed for covariate influence on this association.

RESULTS: One hundred sixteen patients were included in the final analysis. The mean craniospinal elastance according to opening pressure group was 0.52 ± 0.18 for <20 cm H_2O, 0.57 ± 0.20 for 20–29 cm H_2O, 0.91 ± 0.28 for 30–39 cm H_2O, and 1.20 ± 0.25 for ≥40 cm H_2O. There was a positive linear association between opening pressure and craniospinal elastance with a 0.28 cm H_2O/mL increase in craniospinal elastance (standard error = 0.03, $P < .001$) for every 10 cm H_2O increase in opening pressure. Of the covariables analyzed, only age older than 50 years and total volume of CSF removed affected this association.

CONCLUSIONS: As opening pressure increases, the craniospinal elastance increases in a linear fashion while the pressure-volume index decreases. Further studies are needed to determine whether these changes relate to the underlying pathophysiology of idiopathic intracranial hypertension or simply represent established CSF volume pressure dynamics.

ABBREVIATIONS: BMI = body mass index; ΔP/ΔV = pressure change per milliliter of CSF removed; E_{cs} = craniospinal elastance; ICP = intracranial pressure; IIH = idiopathic intracranial hypertension; LP = lumbar puncture; OP = opening pressure; PVI = pressure-volume index

Idiopathic intracranial hypertension (IIH) is a complex neurologic disorder resulting from increased intracranial pressure (ICP). Although the definite etiology of IIH is not known, disturbed CSF homeostasis, primarily due to impaired CSF absorption, and decreased craniospinal compliance have been implicated as possible causes of the elevated intracranial pressure.[1,2]

Although various criteria are needed to establish the diagnosis of IIH, documentation of an elevated ICP by lumbar puncture (LP) is required regardless of the criteria used.[3,4] In addition to helping establish the diagnosis of IIH, the pressure and volume parameters acquired during the LP offer insight into the fluid dynamics of the craniospinal system. Specifically, pressure and volume changes can be used to determine craniospinal elastance (E_{cs}), which represents the change in ICP per change in volume of CSF removed (ΔP/ΔV). In addition, the pressure-volume index (PVI) of the craniospinal system can be calculated. PVI represents the calculated volume required to raise the ICP by a factor of 10 and is directly proportional to the compliance of the CSF space.[5]

However, despite the frequency with which LPs are performed in patients with IIH, no well-defined relationship has been established between the CSF volume removed and the change in ICP in patients with IIH, and the few publications to date have shown varying results. One prior study evaluating patients younger than 22 years of age with suspected IIH found that ICP decreased by 1 cm H_2O for every 0.91 mL of CSF removed if the maximum

Received November 2, 2017; accepted after revision February 24, 2018.

From the Departments of Radiology (B.G., T.C., S.C.P., H.M.), Neurology (A.K.), and Public Health Sciences (L.M.P.), Henry Ford Health System, Detroit, Michigan.

Please address correspondence to Brent Griffith, MD, Department of Radiology, K3, Henry Ford Hospital, 2799 West Grand Blvd, Detroit, MI 48202; e-mail: brentg@rad.hfh.edu; @BrentDGriffith

http://dx.doi.org/10.3174/ajnr.A5642

change in pressure was <15 cm H_2O.[6] An additional study of 41 patients with IIH found that for every 1 mL of CSF removed, the closing pressure decreased by approximately 1.5 cm H_2O.[7] However, neither of these studies accounted for changes in this relationship based on opening pressure (OP). More recently, Chisholm et al[8] assessed E_{cs} and PVI in patients with and without a diagnosis of IIH and found that there was a statistically significant association of both increased E_{cs} and decreased PVI in patients with IIH. However, that study included only 20 patients with IIH.[8]

The primary purpose of this study was to evaluate pressure-volume relationships in a large series of patients with IIH undergoing LP, specifically E_{cs} and PVI, as well as whether these relationships are affected by the initial opening pressure. These findings will be helpful in future studies assessing differences in patients with and without IIH.

MATERIALS AND METHODS

Lumbar Punctures

This study was approved by the institutional review board. The imaging data base at our institution was searched for LPs performed between February 2006 and May 2017 with any of the following search terms: "idiopathic intracranial hypertension," "IIH," and "pseudotumor." This search yielded 304 LPs. The imaging records were reviewed to determine the OPs and closing pressures, volume of CSF removed, use of procedural sedation (usually performed by using a combination of up to 100 mcg of fentanyl and 5 mg of midazolam [Versed], which is titrated to patient comfort) and a decubitus-versus-prone positioning.

Pressure measurements and CSF volume removed were used to determine pressure change (ΔP, centimeter H_2O) and pressure change per milliliter of CSF removed (ΔP/ΔV). LPs without all the required documentation and those performed with the patient in the prone position were excluded from analysis, resulting in 245 remaining lumbar punctures.

Patients

Patient charts for the remaining 245 LPs were reviewed to identify patient age, sex, body mass index (BMI), race/ethnicity, clinical diagnosis of IIH either before or following the LP, and the presence of CSF shunts at the time of the LP. Patients with CSF shunts and those without a clinical diagnosis of IIH were excluded. The clinical diagnosis of IIH was based on chart review and documentation of a diagnosis of IIH in the medical records. Specific clinical criteria used for establishing the diagnosis of IIH could not be determined due to the retrospective nature of the study. Additionally, in those patients with multiple LPs, only the first LP was included in the final analysis. The final study group included 116 patients.

Statistical Analysis

Calculation of craniospinal elastance (E_{cs}) was performed according to established relationships (ΔP/ΔV)[8,9] using OP, closing pressure (CP), and CSF volume removed (mL_{CSF}):

$$E_{cs} = OP - CP / mL_{CSF}.$$

Calculation of the pressure-volume index (PVI), which represents the calculated volume required to raise the ICP by a factor of 10, was performed according to the previously established equation using the same pressure and volume data:

$$PVI = mL_{CSF} / \log_{10}(OP / CP).$$

Continuous variables were summarized by median and range. Categoric variables were summarized by count and percentage. Analysis of variance, with post hoc 2-sample *t* tests, was used to compare means between groups. A χ^2 test was used to assess associations among categoric variables. Pearson correlation coefficients, with 95% CIs, were estimated to express the correlation between CSF ΔP and OP either in total or within subsets of patients.

Linear regression models of CSF ΔP were developed using OP, age (continuous or categoric), BMI (continuous or categoric), race (black or white), and sedation (yes or no) as potential predictors. Interaction terms with OP were used to determine whether a covariate (as continuous or categoric) had an influence on the association between OP and CSF ΔP. Sums of squares from nested models were used to construct *F* tests to assess the contribution of additional variables to the model.

RESULTS

Patient Demographics

The study population included 116 patients; 109 (94.0%) were female and 7 (6.0%) were male with a median age of 33.5 years. In the 109 patients declaring race, 70 (64.2%) were black and 39 (35.8%) were white.

Craniospinal Elastance in Relation to OP

For purposes of assessing craniospinal elastance (E_{cs}) as a function of OP, patients were first categorized into 1 of 4 groups (OP of <20, 20–29, 30–39, and ≥40 cm H_2O), depending on the OP (Fig 1*A*). The mean E_{cs} ($E_{cs\text{-}mean}$) according to the OP group was 0.52 ± 0.18 for an OP of <20 cm H_2O, 0.57 ± 0.20 for an OP of 20–29 cm H_2O, 0.91 ± 0.28 for an OP of 30–39 cm H_2O, and 1.20 ± 0.25 for an OP of ≥40 cm H_2O (Fig 1*A*). A 1-way analysis of variance of $E_{cs\text{-}mean}$ by group indicates that there was a statistically significant difference among the 4 groups (*F* test, $P < .001$). Additionally, there were significant differences in $E_{cs\text{-}mean}$ between any 2 groups (*t* test, $P < .005$), except for the 2 lowest groups (<20 and 20–29 cm H_2O).

When the OP was analyzed as a continuous measure rather than by group, there was a positive linear association between OP and E_{cs} (Fig 1*B*). Specifically, when the E_{cs} was regressed on OP, it was estimated that for every 10 cm H_2O increase in OP, there was a 0.28 cm H_2O/mL increase in E_{cs} (standard error = 0.03, *F* test, $P < .001$). This finding demonstrated a moderately strong correlation, with the Pearson coefficient = 0.70 (95% CI, 0.59–0.78). With the predicted values from the linear regression of E_{cs} regressed on OP, the expected ΔV/ΔP relationship was estimated, demonstrating an exponential relationship with OP (Fig 1*C*). Specifically, at higher OPs, the volume of CSF required to be removed to achieve a similar change in pressure decreases with increasing OP.

Pressure-Volume Index in Relation to OP

For assessing the pressure-volume index as a function of OP, patients were again categorized into the same 4 OP groups (Fig 2*A*). The mean PVI per milliliter of CSF removed according to the OP

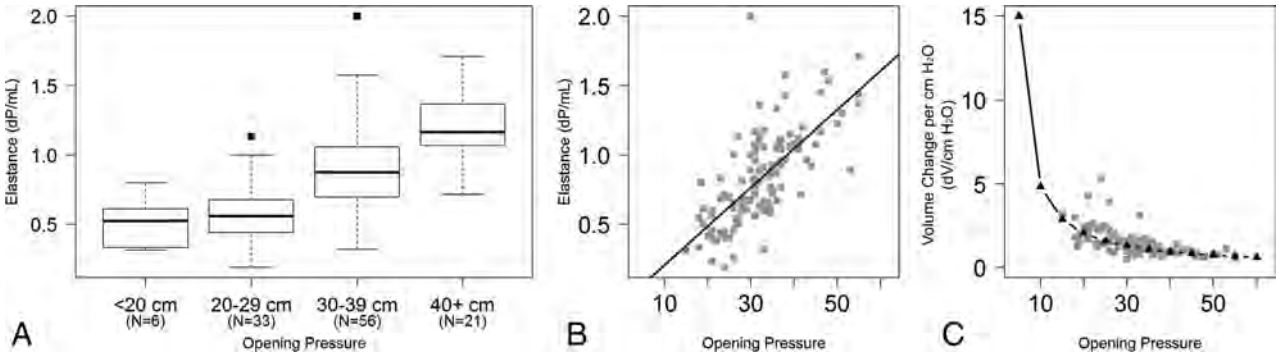

FIG 1. *A*, Boxplots depict the distribution of craniospinal elastance by increasing opening pressure. *B*, Scatterplot demonstrates E_{cs} as a function of opening pressure using opening pressure as a continuous measure. The black line represents the linear regression model. *C*, Scatterplot demonstrates the inverse of elastance, which demonstrates the nonlinear relationship between the volume of CSF required to change the intracranial pressure as the opening pressure changes.

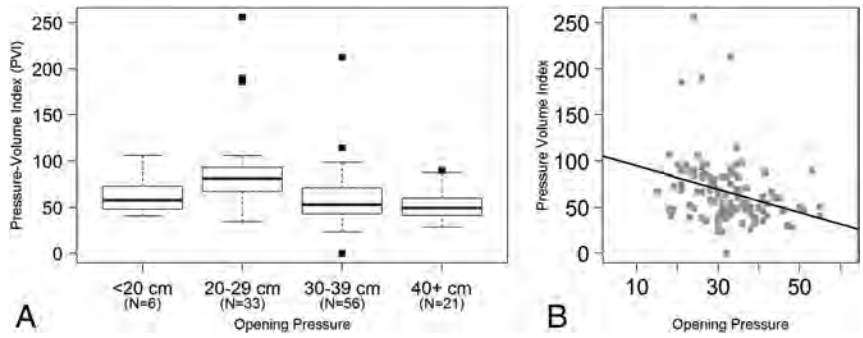

FIG 2. *A*, Boxplots depict the distribution of the pressure-volume index by increasing opening pressure. *B*, Scatterplot demonstrates PVI as a function of opening pressure using opening pressure as a continuous measure. The solid line represents the linear regression model.

group was 63.89 ± 24.08 for an OP of <20 cm H_2O, 87.05 ± 44.62 for an OP of 20–29 cm H_2O, 59.79 ± 30.21 for an OP of 30–39 cm H_2O, and 51.97 ± 15.74 for an OP of ≥40 cm H_2O (Fig 2*A*). A 1-way analysis of variance of PVI by group indicated that there was a statistically significant difference among the 4 groups (*F* test, $P < .001$). On further analysis, the significance was due to an increased mean in the 20–29 cm H_2O group compared with the 2 higher OP groups (*t* test, $P < .001$).

When the PVI was analyzed as a continuous measure rather than by group, there was a negative linear association between OP and PVI (Fig 2*B*). Specifically, PVI decreased by 1.25 for every 1 unit increase in OP (Fig 2*B*, solid line, standard error = 0.37, $P = .001$, adjusted $R^2 = 0.08$). This finding demonstrated a significant negative correlation, with a Pearson coefficient of −0.30 (95% CI, −0.46 to −0.13).

Covariable Analysis

E_{cs} and PVI in relation to OP were also assessed within each of the 4 covariate groups analyzed in this study: age, BMI, race/ethnicity, and use of procedural sedation (Table). Total CSF volume removed was also assessed as a covariable.

Age. The relationship between E_{cs} and OP was not constant with age (*F* test of interaction $P = .03$). To examine this relationship, patients were grouped by age (younger than 30 years, 30–39 years, 40–49 years, and 50 years and older). It was estimated that for every 10 cm H_2O increase in OP, there was a 0.27 to 0.34 cm H_2O/mL increase in E_{cs} for the groups younger than 50 years of age, which was consistent with the overall relationship (Table). There was evidence of a diminished relationship between OP and E_{cs} for patients 50 years and older, with only a 0.10 cm H_2O/mL increase in E_{cs} (coefficient *t* statistic, $P = .01$). Likewise, the relationship between PVI and OP was not constant with age (*F* test of interaction, $P = .04$). Patients were again grouped by age, as was done for E_{cs}. It was estimated that for every 10 cm H_2O increase in OP, there was a 10.5 to 20.1 point decrease in PVI for the groups younger than 50 years of age, which was consistent with the overall relationship (Table). There was evidence of a positive relationship between OP and PVI for patients 50 years and older with a 10.6 point increase in PVI per 10 cm H_2O increase in OP (coefficient *t* statistic, $P = .02$). To assess whether these relationships were independent of OP, we evaluated for evidence of a correlation between age and OP or ΔP and found no evidence of a correlation (Pearson coefficient with OP = −0.14; 95% CI, −0.31–0.043; Pearson coefficient with ΔP = −0.06; 95% CI, −0.24–0.12).

BMI. BMI was recorded for 74 of the 116 cases in this study, and the median BMI was 42.0 kg/m^2. There was no evidence that BMI has any influence on the relationship between E_{cs} and OP (*F* test of the interaction model, $P = .91$; *F* test of the main-effects model, $P = .13$). There was no evidence that BMI has any influence on the relationship between PVI and OP (*F* test of the interaction model, $P = .84$; *F* test of the main-effects model, $P = .39$). Cases without a recorded BMI had higher mean OP and ΔP than those modeled here (*t* test, $P = .03$ and $P = .004$, respectively).

Race. There was no evidence that race has any influence on the relationship between E_{cs} and OP (*F* test of the interaction model, $P = .85$; *F* test of the main-effects model, $P = .82$). There was no evidence that race has any influence on the relationship between PVI and OP (*F* test of the interaction model, $P = .93$; *F* test of the main-effects model, $P = .71$).

Sedation. There was no evidence that sedation has any influence on the relationship between E_{cs} and OP (*F* test of the interaction

E_{cs} and PVI for covariate groups[a]

	No.	E_{cs}		PVI	
		Slope ± SEM	Correlation Coefficient	Slope ± SEM	Correlation Coefficient
Age group (yr)					
Younger than 30	39	0.34 ± 0.04	0.89 (0.79–0.94)	−20.1 ± 5.9	−0.48 (−0.69 to −0.20)
30–39	44	0.27 ± 0.05	0.67 (0.47–0.81)	−13.0 ± 7.0	−0.35 (−0.58 to −0.06)
40–49	24	0.28 ± 0.06	0.59 (0.25–0.80)	−10.5 ± 8.5	−0.24 (−0.59 to −0.18)
50 and older[b]	9	0.10 ± 0.08	0.31 (−0.44–0.81)	10.6 ± 11.7	0.20 (−0.54 to 0.76)
BMI group (kg/m^2)					
< 30	8	0.44 ± 0.14	0.57 (−0.23–0.91)	−19.1 ± 19.6	−0.62 (−0.92 to 0.14)
30–39	20	0.20 ± 0.07	0.60 (0.21–0.82)	−2.7 ± 9.3	−0.11 (−0.53 to 0.35)
40–49	34	0.29 ± 0.05	0.79 (0.62–0.89)	−16.4 ± 6.3	−0.33 (−0.60 to 0.01)
≥50	12	0.20 ± 0.08	0.67 (0.16–0.90)	−1.6 ± 10.5	−0.08 (−0.63 to 0.51)
Race group					
Black	70	0.27 ± 0.04	0.69 (0.54–0.80)	−12.5 ± 5.3	−0.32 (−0.52 to −0.10)
White	39	0.28 ± 0.04	0.66 (0.44–0.81)	−11.8 ± 6.2	−0.24 (−0.52 to 0.08)
Procedural sedation group					
Yes	46	0.28 ± 0.05	0.60 (0.37–0.76)	−19.0 ± 6.5	−0.32 (−0.56 to −0.04)
No	70	0.28 ± 0.03	0.77 (0.66–0.85)	−10.2 ± 4.5	−0.34 (−0.53 to −0.11)
CSF volume removed (mL)					
<20	27	0.38 ± 0.06	0.64 (0.34–0.82)	−14.0 ± 10.3	−0.27 (−0.59 to 0.12)
20.0–24.9	27	0.37 ± 0.05	0.79 (0.59–0.90)	−8.6 ± 8.8	−0.18 (−0.53 to 0.21)
25.0–29.9	30	0.38 ± 0.05	0.87 (0.75–0.94)	−18.3 ± 8.7	−0.53 (−0.75 to −0.21)
≥30	32	0.29 ± 0.04	0.90 (0.80–0.95)	−18.9 ± 6.2	−0.41 (−0.67 to −0.08)

Note:—SEM indicates standard error of the mean.

[a] The slope indicates the average change in the measure for a 1 cm H_2O change in opening pressure. The Pearson correlation coefficient reflects the correlation between the measure and opening pressure.

[b] Comparing 50 years and older with younger than 30 years ($P = .01$), 30–39 years ($P = .09$), and 40–49 years ($P = .08$).

model, $P = .97$; F test of the main-effects model, $P = .84$). There was no evidence that sedation has any influence on the relationship between PVI and OP (F test of the interaction model, $P = .27$; F test of the main-effects model, $P = .11$).

Volume Removed. There was some evidence that the volume of CSF removed influenced the slope of the linear relationship between opening pressure and E_{cs} across all patients (F test of the interaction model, $P = .04$). It was estimated that the increase in E_{cs} with every 10 cm H_2O increase in OP is diminished by 0.068 points for every additional 10 mL removed (Table). To examine whether this relationship holds when linearity constraints are not in place, we grouped patients by volume removed (<20 mL, 20.0–24.9 mL, 25–29.9 mL, and ≥30 mL quartiles). The interaction model did not show a significant change in slope across groups (F test of interaction model, $P = .42$). As a significant main effect (F test of the main effects model, $P < .0001$), volume removed modified the intercept of the line, which would be expected because both volume of CSF removed and E_{cs} increase as the OP increases. There was evidence that the volume of CSF removed influenced only the intercept of the linear relationship between OP and PVI across all patients (F test of the interaction model, $P = .77$; F test of the main effects, $P = .02$). This finding was not retained within the quartiles of volume removed (F test of the interaction model, $P = .80$; F test of the main effects, $P = .12$).

DISCUSSION

The results of this study demonstrate a clear relationship between change in ICP following LP and OP. Specifically, as the OP increases, the pressure change per milliliter of CSF removed (craniospinal elastance) increases in a linear fashion (Fig 1*B*). This linear relationship was present not only when comparing OP groups, but it also demonstrated a moderately strong correlation when considering OP as a continuous variable. When we assessed whether other potential factors, specifically age, BMI, race, use of procedural sedation, and total volume of CSF removed, may affect this relationship, only age older than 50 years and total volume of CSF removed were found to have any significant interaction. The interaction with age older than 50 years, though small, showed a decrease in average E_{cs} as the OP increased. Similarly, there was a decrease in the strength of the relationship between E_{cs} and OP as the volume of CSF removed increased, though this effect was removed when volumes were categorized into groups.

Because of the increasing craniospinal elastance at higher OPs, the volume of CSF required to be removed to achieve a similar change in pressure ($\Delta V/\Delta P$) decreases as the OP increases. In other words, the CSF volume (ΔV) required to be removed to cause a 1 unit change in CSF pressure is much smaller at higher OPs than at lower OPs. When this relationship between $\Delta V/\Delta P$ is plotted against OP, a monoexponential relationship between ΔV and ΔP becomes evident (Fig 1*C*).

Similar to the E_{cs}, the pressure-volume index, which represents the calculated volume required to raise the ICP by a factor of 10, also demonstrated a linear relationship with OP, though negative, which would be expected because PVI is a measure of system compliance and thus would be expected to decrease as OP increases. As with E_{cs}, there was again a difference noted for patients older than 50 years of age.

Three prior studies have investigated change in ICP according to CSF volume removed in patients with IIH. The largest of those, however, only evaluated patients younger than 22 years of age with suspected IIH. That study found that ICP decreased by 1 cm H_2O for every 0.91 mL of CSF removed if the maximum change in pressure was <15 cm H_2O.[6] However, if the ΔP was beyond 15 cm H_2O, the relationship was no longer statistically significant. In

addition, the study did not take into account the effect of differences in OP. The second study found that for every 1 mL of CSF removed, the closing pressure decreased by approximately 1.5 cm H_2O.[7] However, that study assessed only 41 patients with preexisting diagnoses of IIH and, like the first study, did not account for the effect of different OPs. A more recent study by Chisholm et al[8] assessed E_{cs} and PVI in a group of 20 patients with IIH and 29 patients without IIH and found a statistically significant association of both increased E_{cs} and decreased PVI in patients with IIH. That study did note the direct correlation between OP and E_{cs} but found no effect of OP on PVI.

Elastance is a fundamental property of the craniospinal system. In the present study, craniospinal elastance was found to increase in a linear fashion as OP increased (Fig 1*B*). This linear correlation between E_{cs} and OP is then responsible for the monoexponential shape of the volume-pressure curve (Fig 1*A*). These findings are expected. In fact, in 1975, Marmarou et al[5] demonstrated a similar relationship in experiments performed on cats. That study found that at low initial pressure levels, large increases in fluid volume resulted in relatively small increases in ICP.[5] In contrast, at high initial pressures, the compliance of the system is reduced and small volume additions resulted in larger increases in pressure.[5] When plotted on a linear axis, the volume-pressure curve in that study was found to be exponential, with the slope ($\Delta V/\Delta P$) decreasing as the pressure increased.[5] Although our study looked at the inverse of this volume-pressure curve relationship, with fluid being removed from the system rather than added, our findings support this monoexponential volume-pressure model.

In 1979, Avezaat et al[9] performed a similar study in anesthetized and ventilated dogs at changing ventricular fluid pressures. That study assessed the volume-pressure response, which is defined as the immediate change in ICP resulting from a uniform change in ventricular CSF volume and is also a measure of intracranial elastance.[9] Most interesting, in contrast to the mono-exponential volume-pressure model described by Marmarou et al,[5] Avezaat et al[9] actually described 3 distinct zones in this relationship. In zone 1, the volume-pressure response, or elastance, increased linearly with the ventricular fluid pressures, which would be in accordance with the monoexponential model described by Marmarou et al.[5] However, in zone 2, the volume-pressure response leveled off or even decreased, and finally, at the advanced stage of cerebral compression, zone 3, the volume-pressure response started to rise again, but more rapidly than during zone 1.[9] The study concluded that the exponential volume-pressure model is valid for a restricted ICP range only and theorized that the breakpoint in the monoexponential relationship may relate to failure of autoregulation, given the role that intracranial hemodynamics play in determining ICP.[9] Although the findings of our study fit the monoexponential model put forth by Marmarou et al,[5] it would be difficult to say for certain that the different zones identified by Avezaat et al[9] do not exist because these changes may take place outside the physiologic range of CSF pressures seen in patients with IIH.

The other interesting finding in this study is the effect of older age on E_{cs} and PVI, a finding only seen in patients older than 50 years of age. Although the cause for this interaction cannot be ascertained from this study, it is possible that age-related brain volume loss counteracts the effect of increasing OP, thereby dampening the effect on ΔP. However, with only 9 patients older than 50 years of age, these relationships require further study for validation.

Of course, because this study assessed only patients with IIH, it is not possible to assess whether these findings are due to pathophysiologic changes associated with IIH or simply reflect the expected changes in the normal craniospinal system as the pressure of the system increases. To that end, 1 recently published study similar to this one compared measures of elastance and PVI in patients with and without IIH.[8] That study found that patients with IIH had higher elastance and lower PVI and suggested that this increased elastance may contribute to the pathophysiology of IIH. However, that study was much smaller, including only 20 patients with IIH, making comparison between the 2 groups more difficult, given the influence that OP has on these parameters. That study also found that PVI was independent of OP. However, in this study, although the strength of the correlation was less, there was a negative linear association between PVI and OP.

The greatest limitation of our study is that only opening and closing pressures were obtained. As a result, while the value obtained for E_{cs} is ascribed to a single OP, in fact, this value is likely continuously changing as fluid is being removed and the ICP is decreasing. Thus, the E_{cs} calculated for higher OPs is likely blunted by an averaging effect from the E_{cs} as fluid is being removed at lower pressures. This feature likely accounts for the effect that the volume of CSF removed had on the relationship between E_{cs} and OP, with the increase in E_{cs} for every 10 cm H_2O increase in OP diminished by 0.068 points for every additional 10 mL removed. It is thus possible that the true E_{cs} may actually be higher than this study suggests at higher OPs. Thus, a confirmatory study measuring pressure change at multiple time points during the removal of CSF would be of value.

The lack of data points at lower OPs is also a limitation, thus requiring an estimation for $\Delta V/\Delta P$ at low OPs based on the slope of the E_{cs}. The study was also limited by its retrospective nature. Because a clinical diagnosis of IIH was determined by chart review, it is possible that some patients were inappropriately included or excluded. An additional limitation was the inclusion of patients undergoing treatment for IIH. While patients with CSF shunts were excluded and only the first LPs were included when multiple LPs were available, some patients were likely receiving pharmacologic treatment for IIH at the time of the LP. This might explain the small number of patients with a clinical diagnosis of IIH, but normal CSF OPs. In addition, while the measurement and documentation of CSF pressures and volume of CSF removed are objective by nature, techniques vary by proceduralist, which could add a degree of variability to the results.

CONCLUSIONS

This study demonstrates the effect of OP on craniospinal system fluid dynamics, specifically E_{cs} and PVI, in patients with IIH undergoing LP. Recent studies suggest that these dynamics differ in patients with IIH, which may provide insight into the disease pathogenesis. However, further studies comparing the results of this study with similar measurements in patients without IIH are

needed to determine whether these changes reflect expected variations due to normal changes in craniospinal elastance or may be related to pathophysiologic changes in IIH.

REFERENCES

1. Tain RW, Bagci AM, Lam BL, et al. **Determination of cranio-spinal canal compliance distribution by MRI: methodology and early application in idiopathic intracranial hypertension.** *J Magn Reson Imaging* 2011;34:1397–404 CrossRef Medline
2. Alperin N, Ranganathan S, Bagci AM, et al. **MRI evidence of impaired CSF homeostasis in obesity-associated idiopathic intracranial hypertension.** *AJNR Am J Neuroradiol* 2013;34:29–34 CrossRef Medline
3. Friedman DI, Liu GT, Digre KB. **Revised diagnostic criteria for the pseudotumor cerebri syndrome in adults and children.** *Neurology* 2013;81:1159–65 CrossRef Medline
4. Headache Classification Committee of the International Headache Society. **The International Classification of Headache Disorders, 3rd edition (beta version).** *Cephalalgia* 2013;33:629–808 CrossRef Medline
5. Marmarou A, Shulman K, LaMorgese J. **Compartmental analysis of compliance and outflow resistance of the cerebrospinal fluid system.** *J Neurosurg* 1975;43:523–34 CrossRef Medline
6. McLaren SH, Monuteaux MC, Delaney AC, et al. **How much cerebrospinal fluid should we remove prior to measuring a closing pressure?** *J Child Neurol* 2017;32:356–59 CrossRef Medline
7. Fiorito-Torres F, Rayhill M, Perloff M. **Idiopathic intracerebral hypertension (IIH)/pseudotumor: removing less CSF is best.** *Neurology* 2014;82(10 Suppl):I9-1.006
8. Chisholm JT, Sudhakar P, Alhajeri AN, et al. **Intracranial elastance is increased in idiopathic intracranial hypertension.** *Eur J Neurol* 2017; 24:1457–63 CrossRef Medline
9. Avezaat CJ, van Eijndhoven JH, Wyper DJ. **Cerebrospinal fluid pulse pressure and intracranial volume-pressure relationships.** *J Neurol Neurosurg Psychiatry* 1979;42:687–700 CrossRef Medline

Brian C. Bowen, MD, PhD

It is with sadness that I am writing to inform the members of the ASNR of the death of our colleague Brian Bowen, MD, PhD (1946–2018).

Brian grew up in Southern California and graduated from Stanford University, where he majored in Chemical Engineering; subsequently, he obtained a PhD in Chemistry from the University of California, San Diego. Brian then entered the PhD-to-MD program at the University of Miami School of Medicine and graduated in 1983. Following a radiology residency and a fellowship in MR imaging at Mount Sinai Medical Center, Miami Beach, he was a neuroradiology fellow at the University of Miami/Jackson Memorial Hospital. Thereafter, he became a full-time faculty member, rising to the rank of Professor of Radiology.

Brian was an outstanding radiologist, teacher, and researcher and made major contributions to the field of MR imaging, among which were the development of MR images used in spectroscopy and techniques for the evaluation of spinal vascular malformations using MRA. He was held in high esteem by the radiology community both nationally and internationally; his contributions to the field were widely recognized, resulting in his election as President of the American Society of Spine Radiology (2006).

In this short communication, it is not possible to do justice to Brian's many accomplishments. Brian's work ethic, his contributions to the science of radiology, and his devotion to education were remarkable.

Brian is survived by his former wife Ana Campo, MD, and his 2 children, Katherine and Christopher.

Robert M. Quencer, MD
University of Miami School of Medicine
Miami, Florida

http://dx.doi.org/10.3174/ajnr.A5683

Multisociety Consensus Quality Improvement Revised Consensus Statement for Endovascular Therapy of Acute Ischemic Stroke

From the American Association of Neurological Surgeons (AANS), American Society of Neuroradiology (ASNR), Cardiovascular and Interventional Radiology Society of Europe (CIRSE), Canadian Interventional Radiology Association (CIRA), Congress of Neurological Surgeons (CNS), European Society of Minimally Invasive Neurological Therapy (ESMINT), European Society of Neuroradiology (ESNR), European Stroke Organization (ESO), Society for Cardiovascular Angiography and Interventions (SCAI), Society of Interventional Radiology (SIR), Society of NeuroInterventional Surgery (SNIS), and World Stroke Organization (WSO)

D. Sacks, B. Baxter, B.C.V. Campbell, J.S. Carpenter, C. Cognard, D. Dippel, M. Eesa, U. Fischer, K. Hausegger, J.A. Hirsch, M.S. Hussain, O. Jansen, M.V. Jayaraman, A.A. Khalessi, B.W. Kluck, S. Lavine, P.M. Meyers, S. Ramee, D.A. Rüfenacht, C.M. Schirmer, and D. Vorwerk

ABBREVIATIONS: ASPECTS = Alberta Stroke Program Early Computed Tomography Score; EVT = endovascular therapy; mRS = modified Rankin Scale; mTICI = modified thrombolysis in cerebral infarction; NIHSS = National Institutes of Health Stroke Scale; QI = quality improvement; SAH = subarachnoid hemorrhage; SICH = symptomatic intracranial hemorrhage; SITS-MOST = Safe Implementation of Thrombolysis in Stroke Monitoring Study; TICI = thrombolysis in cerebral infarction; TIMI = thrombolysis in myocardial infarction; TPA = tissue plasminogen activator

Endovascular therapy (EVT) for acute ischemic stroke in selected patients has recently been proved effective in several clinical trials, and the widespread adoption of thrombectomy into routine clinical practice has begun. However, these acute stroke services are resource-intensive, including advanced cerebral imaging and highly trained multidisciplinary hospital teams rapidly responding to emergency activation. Despite the previous acceptance of intravenous fibrinolysis for acute ischemic stroke and the development of designated stroke centers,[1] ischemic stroke remains a leading cause of adult death and disability.[2] Many patients are not candidates for fibrinolysis, and intravenous therapy is relatively ineffective for severe strokes as a result of large cerebral artery occlusions. Moreover, it is uncertain if the benefits of endovascular stroke treatment in the trial setting can be generalized to clinical care provided by hospitals and teams of varying training, experience, and case volume. In other medical disciplines, rapid technologic advancement required guidelines to utilize these tools effectively and responsibly.[3] Quality-improvement (QI) metrics for the outcomes of endovascular ischemic stroke treatment were published by a multisociety, multispecialty, international consensus group in 2013.[4] These QI metrics have been accepted at a national level in Great Britain and Ireland[5] but have yet to be included into stroke center accreditation requirements in the United States. Subsequent to the publication of the prior QI guidelines, eight randomized trials and several meta-analyses of EVT have been published.[6-20] These randomized trials have established EVT as standard of care when available,[5,21-23] and provide additional data on which to update the metrics and bench-

From the Department of Interventional Radiology (D.S.), The Reading Hospital and Medical Center, West Reading, Pennsylvania; Department of Radiology (B.B.), Erlanger Medical Center, Chattanooga, Tennessee; Departments of Medicine and Neurology (B.C.V.C.), Melbourne Brain Centre at the Royal Melbourne Hospital, University of Melbourne, Parkville, Victoria, Australia; Department of Radiology (J.S.C.), West Virginia University, Morgantown, West Virginia; Department of Diagnostic and Therapeutic Neuroradiology (C.C.), Centre Hospitalier Universitaire de Toulouse, Hôpital Purpan, Toulouse, France; Department of Neurology (D.D.), Erasmus University Medical Center, Rotterdam, the Netherlands; Department of Radiology (M.E.), University of Calgary, Calgary, Alberta, Canada; Department of Neurology (U.F.), Inselspital-Universitätsspital Bern, Bern, Switzerland; Department of Radiology (K.H.), Klagenfurt State Hospital, Klagenfurt am Wörthersee, Austria; Neuroendovascular Program, Department of Radiology (J.A.H.), Massachusetts General Hospital, Boston, Massachusetts; Cerebrovascular Center, Neurological Institute (M.S.H.), Cleveland Clinic, Cleveland, Ohio; Department of Radiology and Neuroradiology (O.J.), Klinik für Radiologie und Neuroradiologie, Kiel, Germany; Departments of Diagnostic Imaging, Neurology, and Neurosurgery (M.V.J.), Warren Alpert School of Medicine at Brown University, Rhode Island Hospital, Providence, Rhode Island; Department of Surgery (A.A.K.), University of California San Diego Health, San Diego, California; Interventional Cardiology (B.W.K.), Heart Care Group, Allentown, Pennsylvania; Departments of Neurological Surgery and Radiology (S.L.), Columbia University Medical Center/New York–Presbyterian Hospital, New York, New York; Departments of Radiology and Neurological Surgery (P.M.M.), Columbia University College of Physicians and Surgeons, New York, New York; Interventional Cardiology, Heart and Vascular Institute (S.R.), Ochsner Medical Center, New Orleans, Louisiana; Neuroradiology Division (D.A.R.), Swiss Neuro Institute–Clinic Hirslanden, Zürich, Switzerland; Department of Neurosurgery and Neuroscience Center (C.M.S.), Geisinger Health System, Wilkes-Barre, Pennsylvania; and Diagnostic and Interventional Radiology Institutes (D.V.), Klinikum Ingolstadt, Ingolstadt, Germany.

B.B. receives personal fees from Penumbra (Alameda, California), Medtronic (Dublin, Ireland), Stryker (Fremont, California), and Pulsar Vascular (Los Gatos, California) and has a patent (US8622992) issued to Advanced Catheter Therapies (Chattanooga, Tennessee). C.C. receives personal fees from MicroVention (Tokyo, Japan), Stryker, Medtronic, and Balt (Montmorency, France). D.D. receives grants from the Dutch Heart Foundation, AngioCare (Eemnes, the Netherlands), Medtronic/Covidien/ev3 (Dublin, Ireland), Medac/Lamepro (Breda, the Netherlands), Penumbra, Top Medical/Concentric (New York, New York), and Stryker. U.F. receives grants from the SWIFT DIRECT study and personal fees from Medtronic. J.A.H. receives personal fees from Medtronic, Globus (Audubon, Pennsylvania), and Codman Neuro (Raynham, Massachusetts). C.M.S. receives grants from the National Institutes of Health/National Institute of Neurological Disorders and Stroke, Medtronic, and Penumbra and personal fees from Toshiba (Otawara, Japan) and ExpertiCas (Southport, Connecticut) and is a stockholder in Neurotechnology Investors (Palo Alto, California). None of the other authors have identified a conflict of interest.

Table E1 is available online at www.jvir.org/cms/attachment/2119125784/2089482678/mmc1.xlsx.

This article was previously published in the *Journal of Vascular and Interventional Radiology*. The articles are identical except for minor stylistic and spelling differences in keeping with each journal's style. The *JVIR* article should be used when citing this article in a journal. ©SIR, 2018 *J Vasc Interv Radiol* 2018; 29:441–53. http://doi.org/10.1016/j.jvir.2017.11.026

Please address correspondence to David Sacks, MD, Interventional Radiology, Reading Hospital, 6th and Spruce Streets, West Reading, PA 19612-6052; e-mail: david.sacks@towerhealth.org

Table 1: mTICI revascularization scale scores[30,31,113]

Score	Description
0	No perfusion, complete obstruction; no flow past occlusion of "major" vessel
1	Perfusion past initial obstruction but limited distal branch filling with little/slow distal perfusion
2a	Partial perfusion: <50% of "major" vascular territory perfused (eg, filling and complete perfusion through one M2 division)
2b	Partial perfusion: ≥50% of major vascular territory is filled, but there is not complete and normal perfusion of entire territory
3	Complete or full perfusion with filling of all distal branches

Note:—mTICI indicates modified thrombolysis in cerebral infarction.

marks of the previous paper.[4] Therefore, it is now appropriate to revise the prior QI document based on new evidence.

Revision of this QI consensus statement remains focused on processes of care and patient outcomes. Other documents address standards for physician training[24,25] and recommendations for patient selection and treatment methods.[5,23] As in the previous guidelines, it is intended that these benchmarks be used in a quality-improvement program to assess and improve processes and outcomes in acute stroke revascularization. The benchmarks provide the consensus process and outcome consensus measures called for by the Stroke Treatment Academic Industry Roundtable (STAIR) IX for the next generation of endovascular trials.[26] The benchmarks may also be suitable for accreditation of stroke intervention programs. Most of the metrics apply to the role of the interventional physician, regardless of specialty or particular board certification, but comprehensive stroke care requires a broad multidisciplinary process involving care that ranges from emergency dispatch of paramedics through acute hospital care and posttreatment subacute rehabilitation. Therefore, although it is not the intention of this document to assess in detail the quality of facilities, some of the metrics also apply to institutional policies and procedures for stroke care.

MATERIALS AND METHODS

A literature search was conducted by using Ovid and EMBASE from 2012 (from the last date of the literature search for the first publication of these metrics)[4] to October 2015 by using article titles that included the following: (acute ischemic stroke OR cerebrovascular accident OR stroke) AND (intra-arterial OR intra-arterial OR endovascular OR angioplasty OR stent OR stent retriever OR mechanical thrombectomy OR thrombolysis OR tissue plasminogen activator [TPA] OR TPA OR urokinase OR streptokinase OOR TPA OR urokinaseR alteplase OR tenecteplase). Additional articles were then solicited from writing group members. An evidence table (Table E1, available on-line at www.jvir.org/cms/attachment/2119125784/2089482678/mmc1.xlsx) was constructed by using articles that were randomized controlled trials, registries, or case series of at least 100 patients, and some case series of less than 100 patients were included if the series provided uniquely useful data. From the evidence table, metrics were chosen that were believed to be important markers of quality of care. Thresholds for metrics were then chosen by consensus of the writing group based on review of the evidence table. Consensus was defined as 80% of the writing group. If consensus was not achieved during discussion, a modified Delphi process was used to obtain consensus.[27] If consensus was not achieved after the modified Delphi process, a threshold was not chosen. The evidence table was then updated by using the same search terms in February 2017 at the time of completion of the draft of the document to allow updating of the metrics if appropriate.

Standards for developing clinical practice guidelines were reviewed.[28] It was determined that most of these standards were not applicable for this document that updates quality benchmarks for processes and outcomes of care rather than creating recommendations for types of patient care. For this reason, this revision has been changed to a consensus statement rather than a guideline.

DEFINITIONS

Measures and metrics will depend on the definition of a good outcome or a complication and the time at which patients are assessed for these outcomes, as many patients show gradual improvement following an ischemic stroke. Numerous trials have used varying definitions for similar concepts. The definitions used in this document were derived from review of these trials and then consensus of the writing group.

Ischemic Central Nervous System Infarction. A uniformly accepted simple definition of central nervous system infarction remains elusive. A successful multidisciplinary attempt arrived at a definition as follows[29]:

Central nervous system infarction is defined as brain, spinal cord, or retinal cell death due to ischemia, based on:

1. Pathological, imaging, or other objective evidence of cerebral, spinal cord, or retinal focal ischemic injury in a defined vascular distribution; or
2. Clinical evidence of cerebral, spinal cord, or retinal focal ischemic injury based on symptoms persisting at least 24 hours or until death, and other etiologies excluded.

Door-to-Event Time. The term "door" is used to determine the time of onset of medical care, as in "door to time of CT imaging." It is defined as the time of arrival in the emergency department for an outpatient or the time first discovered to have a stroke for an inpatient. When patients are transferred, "door" refers to the arrival (ie, registration) time at the receiving facility.

Time to Thrombus. Time to thrombus is considered to represent the start of endovascular lytic infusion or first placement of a mechanical device in the target vessel.

Successful Revascularization. Successful revascularization is considered to represent modified thrombolysis in cerebral infarction (mTICI)[30,31] grade 2b or 3 flow through the previously occluded vessel segment (Table 1).

Symptomatic Intracranial Hemorrhage. Symptomatic intracranial hemorrhage (SICH) is a parenchymal hematoma type II (per the Safe Implementation of Thrombolysis in Stroke Monitoring Study [SITS-MOST] definition)[32] or subarachnoid hemorrhage

Table 2: mRS Scores[35]

Score	Description
0	No symptoms
1	No significant disability: able to carry out all usual activities despite some symptoms
2	Slight disability: able to look after own affairs without assistance but unable to carry out all previous activities
3	Moderate disability: requires some help but able to walk unassisted
4	Moderately severe disability: unable to attend to own bodily needs without assistance and unable to walk unassisted
5	Severe disability: requires constant nursing care and attention, bedridden, incontinent
6	Dead

Note:—mRS indicates modified Rankin Scale.

(SAH) with neurologic deterioration leading to an increase in National Institutes of Health Stroke Scale (NIHSS) score >4 or leading to death within 36 hours of treatment. Because of the risk of vessel perforation during endovascular procedures, SAH has been added as a cause of intracranial hemorrhage to the SITS-MOST SICH definition.[33]

This definition is similar to that used in the recent randomized trials of EVT.[7,11,15] Several of the authors of those trials have joined others in proposing a new definition of SICH.[34] These new definitions have not yet been validated on a larger scale, adopted in stroke trials, or applied to the outcomes of the recent randomized trials. Therefore, the original definition of SICH is maintained in the present revision of the consensus statement and modified to include any intracranial hemorrhage associated with a decrease in NIHSS score >4 or death within 24 hours of the end of the revascularization procedure.[20]

Good Clinical Outcome. A good clinical outcome is a measure of neurologic functional with a score of 0–2 on the modified Rankin Scale (mRS; Table 2)[35] assessed 90 days after treatment. This does not exclude clinically significant benefit in patients in whom an mRS score of 2 is not achieved.

INDICATIONS AND CONTRAINDICATIONS

EVT for acute ischemic stroke with large vessel occlusion is established in guidelines as the standard of care.[22,36] If the patient is also eligible for intravenous TPA, this drug should be administered as a "bridging" strategy in parallel without delaying thrombectomy. Waiting to assess "response" to TPA is strongly discouraged,[22] as clinical improvement may not indicate recanalization. The rate of TPA-induced recanalization before thrombectomy (performed without delay) was <10% in recent randomized trials.[11,13,20] Proceeding directly to thrombectomy (ie, direct thrombectomy) should be performed in appropriate candidates with a contraindication to TPA, including risk of hemorrhage or when >4.5 hours have elapsed since stroke onset.

Indications and contraindications for EVT are based on subgroup analyses of randomized trials and case series. Clinical trials tend to have more restrictive criteria, whereas case series represent more of a "real-world" experience. Potential selection criteria are based on stroke severity, time (ie, duration of symptoms), imaging, clot location, age, and comorbidities.

Stroke Severity. Clinical trials have set variable NIHSS score limits for eligibility, often requiring ≥6, 8, or 10 points. The Multicenter Randomized Clinical Trial of Endovascular Treatment for Acute Ischemic Stroke in the Netherlands (MR CLEAN) trial had a minimum NIHSS score of 2 and Extending the Time for Thrombolysis in Emergency Neurologic Deficits-Intra-Arterial (EXTEND-IA) had no NIHSS score limits, but, given the requirement for large vessel occlusion, few patients with NIHSS scores <6 were enrolled.[37] Individual patient data meta-analysis of five positive randomized trials[14] demonstrated highly consistent treatment effects across the NIHSS score spectrum, at least for NIHSS scores ≥6. Data from observational studies have demonstrated an important incidence of large vessel occlusion in patients with clinically mild stroke and a propensity for these patients to later experience neurologic deterioration.[38] The risk/benefit in patients with low NIHSS scores therefore needs to be carefully considered, and future studies have to address whether endovascular procedures are beneficial in patients with mild symptoms and proximal vessel occlusion. There are no data supporting an upper limit on stroke severity.

Time. Most trials of intra-arterial lytic agents and mechanical revascularization devices have historically required start of treatment within 6 or 8 hours[39-42] for anterior-circulation strokes. The strongest evidence for EVT is for treatment commenced within 6 hours.[14,43] More rapid time to reperfusion has been linked to improved clinical outcomes and is therefore an important consideration in patient selection.[43-45] A few patients in recent trials were treated at 6–8 hours in the Randomized Trial of Revascularization with Solitaire FR Device versus Best Medical Therapy in the Treatment of Acute Stroke Due to Anterior Circulation Large Vessel Occlusion Presenting within Eight Hours of Symptom Onset (REVASCAT) trial[15] and at 6–12 hours in the Endovascular Treatment for Small Core and Anterior Circulation Proximal Occlusion with Emphasis on Minimizing CT to Recanalization Times (ESCAPE) trial.[13] Individual patient data meta-analysis suggests significant benefit to at least 7 hours, 18 minutes.[46] Observational studies have suggested that patients presenting at later time points with favorable imaging findings still benefit from reperfusion,[47] and this was confirmed in the DWI or CTP Assessment with Clinical Mismatch in the Triage of Wake-Up and Late Presenting Strokes Undergoing Neurointervention with Trevo (DAWN) trial,[48] which used clinical-core mismatch criteria to select patients 6–24 hours after the "last known well" time. In the DAWN trial,[48] independent functional outcome occurred in 48.6% of patients who underwent endovascular treatment versus 13.1% of control patients ($P < .0001$) with similar revascularization success as 0–6-hour thrombectomy trials and no variation in treatment effect between the 6- to 12-hour and 12- to 24-hour treatment windows. Other randomized trials in extended time windows are ongoing.[49,50] Vertebrobasilar occlusions have been treated at extended times, sometimes more than 24–48 hours after symptom onset.[51,52] This is partly because of the traditional definition of onset as the last known well time. Patients with basi-

lar artery occlusion may have prodromal mild symptoms in 60% of cases before the development of severe deficits.[53] The Basilar Artery International Cooperation Study (BASICS) registry[53] advocated using time of severe deficit (ie, likely moment of occlusion) and found that good outcome with reperfusion beyond 9 hours of that time was extraordinarily rare.[53] Randomized trials in patients with basilar artery occlusion are ongoing.[54,55]

Imaging. Noncontrast CT has been an essential component of patient selection in randomized trials of intravenous and endovascular revascularization for treatment of acute stroke.[1,7,11,13,15,20,39-41,56] Absolute noncontrast CT contraindications to endovascular treatment are similar to those for intravenous thrombolytic agents and include the presence of acute intracranial hemorrhage or a significant established infarct.[1]

Infarct size can be approximated on noncontrast CT by using the Alberta Stroke Program Early CT Score (ASPECTS).[57,58] However, the score is not closely related to infarct volume or functional eloquence and has variable interrater agreement, particularly early after stroke onset. In recent randomized trials, there was clear benefit in patients with ASPECTS 6–8 and 9/10. Relatively few patients with ASPECTS 0–5 were included in the trials. The benefit in this group appeared to be of lesser magnitude, but a clinically meaningful benefit could not be excluded.[14] Patients with ASPECTS 3–5 will be evaluated in a randomized trial.[59]

The hyperdense middle cerebral artery sign can alert clinicians to the presence of a large vessel occlusion. This sign has a high degree of sensitivity if thin (~1-mm) slices are reconstructed and good specificity if clearly asymmetric compared with the contralateral artery.[60] Clot length on noncontrast CT of more than 8 mm has been associated with lower recanalization rates after intravenous TPA,[61] but this is not absolute,[62] and none of the positive randomized trials considered clot length in determining eligibility. The Randomized, Concurrent Controlled Trial to Assess the Penumbra System's Safety and Effectiveness in the Treatment of Acute Stroke (THERAPY) trial that used this criterion was neutral.[18] There is evidence that occult anterograde flow can be associated with TPA-induced recanalization even in the presence of a long thrombus.[63]

The target vessel occlusion should be established by using noninvasive angiography (CT or MR imaging), as practiced in all the positive randomized trials. This also provides information on proximal arterial pathology and catheter access. CT angiography has also been used to grade the quality of collateral flow. However, there is potential for standard single early-phase acquisitions to underestimate late-arriving collateral flow and therefore exclude patients who may benefit. Dynamic angiography derived from CT perfusion or multiphase CT angiography acquisitions avoids this pitfall.[64]

Many centers use CT perfusion to improve diagnostic sensitivity and provide an estimate of tissue viability, which is closely related to the quality of collateral blood flow. A large volume of ischemic core (eg, >70 mL) on CT perfusion is certainly associated with a worse prognosis, but whether this alters treatment effect within 6 hours of stroke onset is yet to be clarified. Some case series have suggested a benefit of reperfusion even in patients with a large ischemic core >100 mL.[65] Analysis of the MR CLEAN trial did not reveal treatment effect heterogeneity between cases of <70 and >70-mL core, although the absolute probability of independent functional outcome in those with a core >70 mL was only 8%.[66] Rather than excluding patients from treatment as a result of a large ischemic core, the presence of favorable imaging may be useful in deciding to pursue treatment in patients with otherwise less favorable clinical characteristics. Estimation of ischemic core volume by using CT perfusion combined with age and NIHSS score in clinical-core mismatch was shown to identify patients who benefit from thrombectomy in the extended time window of 6–24 hours in the DAWN trial.[48]

MR imaging with diffusion imaging, with or without perfusion imaging, is increasingly used in some centers. There are some logistic challenges of safety screening and rapid access to MR scanners that have to be overcome to avoid relevant delays in treatment. However, in the high-performing centers in the Solitaire With the Intention For Thrombectomy as PRIMary Endovascular treatment (SWIFT PRIME trial),[44] there was no significant difference in arrival to randomization time according to image technique (ie, CT versus MR imaging), suggesting that MR-related delay is not inevitable. Uncertainties regarding whether core volume is truly treatment effect-modifying or simply prognostic apply, as discussed with CT perfusion.[65] It is also important to note that measured perfusion lesion volumes vary between processing software programs and the thresholds used to estimate ischemic core may vary with time.[67]

Clot Location. The randomized trials demonstrated clear benefit in internal carotid artery terminus and M1 (ie, first segment of middle cerebral artery) occlusion, with or without tandem occlusion in the cervical carotid artery.[10,14] Arterial occlusions arising more proximally are associated with poorer outcomes. Most notably, "T-lesions" have the poorest outcomes among anterior-circulation strokes.[68,69] Proximal M1 occlusions have worse outcomes than distal M1 occlusions as a result of occlusion of lenticulostriate arteries and basal ganglia infarction, with an increased risk of reperfusion hemorrhage.[70] More distal M2 occlusions were less common among trial patients, and a clear benefit was not demonstrated, although there was no significant heterogeneity in treatment effect observed. Many patients with M2 occlusions were assessed as having M1 occlusions at the site and reclassified as having M2 occlusions by the core laboratory, leading to a predominance of larger, more proximal occlusions. Some case-control studies have suggested that benefit persists in M2 occlusions, with similar safety as M1 occlusions.[71] Basilar artery occlusion was not included in the recent trials, in some cases because of perceived lack of equipoise and in others because of concerns regarding excessive heterogeneity. The BASICS trial[54] is ongoing, but many sites regard the dismal prognosis if untreated and the clear improvement associated with recanalization as sufficient grounds to treat. EVT for occlusions in the anterior cerebral artery, M3/4 segments, and posterior cerebral artery has not been systematically studied. More distal vessels are smaller and more tortuous, which potentially increases procedural risk, and the smaller territory at risk and increased efficacy of TPA reduces the benefit. Further device development may alter this balance in the future.

Age. Although increased age is associated with a worse prognosis after stroke in general, the recent trials have clearly demonstrated a treatment effect in patients aged >80 years of at least the same magnitude as in younger patients. Indeed, there is a significant mortality benefit in elderly patients, with 20% absolute risk reduction (number needed to treat = 5).[10,14] Importantly, the trials included only patients with independent premorbid function, regardless of age, and the potential quality-of-life benefit for patients with significant comorbidities needs to be weighed in clinical practice. Prestroke dementia before endovascular reperfusion has been linked with a low probability of achieving a good clinical outcome.[72] Some trials have therefore excluded patients aged >80 years.[73] Older patients may also have tortuous arterial access, which can complicate the procedure.

Medical Comorbidities. Most contraindications to intravenous thrombolysis do not apply to EVT. Overall, mechanical thrombectomy (with or without intravenous TPA) has a similar risk of SICH compared with TPA alone.[10,14] There are relatively limited data on the safety of EVT in patients with markedly abnormal coagulation (eg, International Normalized Ratio >3.0 or current use of novel or direct oral anticoagulant agents), and risks and benefits need to be considered on an individual basis.

The criteria chosen to select patients for treatment will affect outcomes. Patients at higher risk are more likely to do poorly with or without treatment, but selection of only patients at low risk will deny clinical benefit to a large number of severely ill patients. Because published selection criteria vary, there is no single "correct" list of inclusion and exclusion criteria. The American Heart Association has published class I recommendations for EVT patient selection,[22] but 40%–50% of patients are now being treated outside of these class I recommendations.[74,75] Based on published data and the desired ratio of benefit to risk, each institution will need to create and follow its own indications and contraindications.

Metric 1: At least 90% of patients who meet the institutional selection criteria (ie, indications/contraindications) should be treated with endovascular therapy.

PROCESS AND OUTCOMES METRICS

In general, previously published endovascular stroke therapy metrics[76] were designed to measure aggregate performance of hospital or clinical outcomes. They were neither designed nor intended to define individual physician performance. In contrast, this document provides requirements for performance criteria for the individual practitioner and the facility. The purpose of these metrics is to define the minimum standards for EVT in acute ischemic stroke patients. It is recognized that a concerted team effort is required to ensure efficient workflow, timely EVT, and safe, effective care.

The recent endovascular trials have reiterated the importance of appropriate patient selection and procedural performance such as timely and more complete revascularization to improve the likelihood of achieving a good clinical outcome. This paradigm is based on selecting patients with potentially salvageable ischemic penumbra. A noncontrast head CT/MR study and vascular imaging such as CT/MR angiography will demonstrate areas of established infarct and presence of a proximal large vessel occlusion, respectively, and provide vital information to select patients for endovascular therapy.

Data Collection

From a quality-assurance perspective, endovascular therapy for acute ischemic stroke differs slightly from other areas in which quality initiatives, morbidity, and mortality discussions focus on specific events in which errors in care or complications occurred. The measure of benefit from endovascular stroke therapy is not based on single or isolated cases, but rather is expressed as a percentage of aggregated patients treated who can function independently at 3 months. This has also been measured by using shift analysis in the recent endovascular trials.[77] As demonstrated in those trials, clinical benefit from EVT is dependent on delivery of high-quality care in a timely manner at the institutional level by a dedicated team.

As such, performance metrics from large aggregates of patients treated by endovascular means are compared versus performance standards in clinical trials in which benefits were demonstrated, recognizing that patients may be treated outside trial inclusion criteria on a case-by-case basis. This requires all patients' procedural, process, and clinical outcomes to be entered into a data base, trial, or registry.[24,76,78-80] Without the denominator of "all patients," measures of success and percentage descriptors are meaningless. These data allow comparison of metrics against benchmarks for individual operator performance, risk-adjusted clinical outcomes, and individual and institutional process measures.

As stated in a prior document concerning Comprehensive Stroke Centers,[76] it is advantageous to collect data in a standardized fashion to avoid redundant efforts. Data collection tools such as multicenter registries will serve as useful benchmarks and will facilitate an ongoing process of constant evaluation. Multicenter registries are recommended over institutional registries because of the ability to serve as a benchmark against other institutions. There are numerous examples of such data-collection tools for treatment of acute ischemic stroke.[78,80-82] A recent publication looking at trends in endovascular therapy and clinical outcomes within the Get With The Guidelines–Stroke registry[83] demonstrates the utility of strict data collection within well-maintained nationwide data base systems.

Data collection for EVT is closely tied in with the process already in place for patients who are eligible for intravenous thrombolytic therapy and starts with documentation of time of onset and the time the patient arrives at the "door." This could mean (*i*) the door of a primary stroke center, where data collection should ideally start, or, (*ii*) in cases being transferred to an endovascular center, the time of registration at the center that receives the patient. The detailed time metrics will be discussed in the next section. Data collection, especially time points, should be as inclusive as possible, with subsequent metrics being reported by combining multiple elements. The mandatory threshold for collection of the minimum defined elements is 100%.

Data concerning demographic characteristics are used to identify various patient subgroups, whereas other data points are pertinent for risk adjustment and are necessary for evaluation of pro-

cedural and clinical outcomes. These would include factors specific to the individual case, such as location of occlusion and time from onset, as well as demographic factors specific to patient subgroups, such as age, race, and sex. Ancillary data such as prognostic factors pertaining to comorbidity, stroke severity, and imaging parameters may help in risk- and severity-adjusted analysis to adjust for variability in case mix. Collection of these data points is necessary for an appropriate evaluation of patient risk factors and also for study of institutional factors that could influence overall patient outcomes and have a bearing on evaluation of operator performance.

At a minimum, these data should include age, sex, premorbid mRS score, NIHSS score, location of occlusion, various time points and intervals described in the subsequent sections, blood pressure, blood glucose level at presentation, and presence of atrial fibrillation. Specific data-collection metrics for EVT have already been included in national guidelines.[22,23,36] Other data elements may be helpful and may become evident with further research, such as radiation exposure and contrast agent dose.

Metric 2: 100% of patients have the required minimum process and outcomes data entered into an institutional or national data base, trial, or registry.

Time Intervals

Emergency endovascular stroke treatment is one of the most complex multidisciplinary functions a medical institution chooses to undertake. Reperfusion treatment (intravenous or endovascular) achieved within the shortest period of time is widely accepted as a prerequisite for optimal clinical outcomes.[45,84,85]

Subgroup analyses from several trials[43,86,87] have shown that treatment delays resulted in significant decrease in the likelihood of a good outcome of endovascular stroke therapy. Analysis of the pooled data of 5 endovascular trials[46] confirmed this: every 1-hour delay in time from onset to arterial puncture results in a 5.3% shift in the direction of more disability on the mRS.

There are many steps from stroke onset to completion of treatment, and optimal and timely execution of each of these steps is necessary to achieve the stated goal. Numerous opportunities exist to minimize the time needed for each step from the time of the acute stroke to patient arrival to the hospital and then until reperfusion is achieved.

Process improvement for emergency stroke treatment should be an ongoing component of all stroke systems of care and should focus on all the tasks and activities in this complex sequence of events. These data are then used for quality assessment/assurance and process improvement and therefore directly relate to the eventual clinical outcome of the patients being treated by the team. To judge satisfaction of these performance goals in regard to expeditious delivery of care, time points and intervals are the units of measurement.

At a minimum, the time points and intervals specified in this document should be tracked in all cases. Institutions may choose to measure additional time points. The more time points that are recorded, the more exactly deficiencies might be identified; however, this may prove onerous to document from a resource perspective. For instance, delays in obtaining a CT scan may result from delay in ordering the study, delay in response by CT staff (eg, multiple other procedures being requested at the same time), or delay related to transportation.

Acknowledgment of the critical importance of time to reperfusion for obtaining favorable outcomes in myocardial reperfusion treatments has led to the formation of initiatives such as "Door to Balloon: An Alliance of Quality" for patients with ST-segment elevation myocardial infarction. The key was achievement of a door-to-balloon time of $<$90 minutes for at least 75% of patients presenting directly to the treating hospital by using various strategies identified through research, resulting in dramatic reductions in times.[88,89]

The impressive results in shortening the time to myocardial reperfusion for acute myocardial infarction obtained by such initiatives provided an impetus for launching similar initiatives related to intravenous TPA for stroke.[90] The Joint Commission has set a more ambitious goal of 80% of patients treated within 1 hour for primary stroke centers.[91] The experience in reducing door-to-needle times reported by the group from Helsinki[92] suggests that, with simple strategies, median door-to-needle times of 30 minutes or even less can be achieved. Because of the need for neurologic assessment and imaging in addition to the emergency medicine and interventional components, acute stroke patients referred for EVT require more time for initiation of treatment than patients with ST-segment elevation myocardial infarction. Although rapid-response mechanisms aiming to result in initiation of revascularization therapies within the minimum amount of time can be modeled according to the myocardial infarction experience, it should be recognized that acute stroke treatment, especially EVT, requires a far more complex infrastructure. Notwithstanding that, it is clear that, similar to the cardiology model, major improvements in door-to-treatment time need to take place to increase the proportion of favorable outcomes for patients treated with EVT for acute stroke.[93]

Since the early years of endovascular stroke treatment, various time metrics have been reported, with a trend toward overall improvement in times. These were initially reported on the basis of case series,[94,95] with newer metrics from registries,[96,97] earlier device trials,[98,99] and recent randomized controlled trials.[10] These reports focused on median onset-to-groin puncture times ranging from 200 minutes in the latest randomized trials[10] to 277 minutes in registry data.[97] Recent trial data[10] have also reported various components of these times, breaking them down into intervals that include patient arrival times and imaging times. In the ESCAPE trial,[13] the authors reported a median time from imaging to arterial puncture of 51 minutes and a median time from imaging to reperfusion of 84 minutes. The median imaging-to-puncture time in the SWIFT PRIME trial[20] was 57 minutes. The Highly Effective Reperfusion evaluated in Multiple Endovascular Stroke trials (HERMES) meta-analysis of treatment times from five recent large endovascular trials[46] reported better clinical outcomes with faster treatment times, with median door-to-imaging time of 19 minutes, imaging-to-puncture time of 76 minutes, and puncture-to-reperfusion time of 44 minutes in the entire cohort.

The endovascular trials represent optimal results based on study site and patient selection. Many of the endovascular trials included only study sites with a proved ability to respond rapidly,

excluded patients with carotid dissections or internal carotid artery–origin occlusions, and excluded patients who could not be treated rapidly. However, the reported times in recent trials did include time taken for patient randomization. These rapid responses have not been uniformly achieved in other trials, registries, or case series.[18,100-102] Nevertheless, the time intervals in this consensus statement are intended to be achievable with good practice as centers become proficient at routinely performing endovascular therapies, and provide a benchmark for QI in current clinical practice. Moreover, many of the conditions and findings that, in the past, could have complicated decision-making, such as older age, extracranial carotid obstruction, vessel tortuosity, requirement for penumbral imaging, and requirement for general anesthesia, did not negatively influence treatment effect and should not delay the decision for treatment. The treatment of more complex cases than were included in the trials may prolong treatment times but should not prolong the time to arterial puncture.

As a general approach to setting metrics for care processes, we used data from the HERMES collaboration.[46] The 75th-percentile times (ie, slowest quartile) are considered minimum benchmarks, and the 25th-percentile times (ie, fastest quartile) from that study are considered achievable by the best centers with high volumes and good resource infrastructure. The metrics are intended to be used for measurements such that centers will progressively become faster and improve times from minimum acceptable to ideal.

The times reported in the following sections apply to anterior circulation occlusions, as vertebrobasilar occlusions were excluded in the recent randomized trials. These metrics should be applicable regardless of the time of the day and regardless of whether the patient presents on a weekday versus a weekend.[103] These metrics represent maximum recommended times. Because of ample evidence that, the shorter the time to reperfusion, the higher the likelihood of a favorable outcome, all centers should strive to initiate endovascular therapy within the shortest possible time frame. Although intravenous TPA administration should not represent a justification for excessive delays in initiation of endovascular therapy, it is acknowledged that intravenous thrombolysis may be associated with some delays in initiation of endovascular therapy.

Door to Imaging. Most hospitals will use CT-based imaging, but some hospital protocols may use MR imaging as the first imaging study. The use of CT angiography or MR angiography for vascular imaging is considered the standard of care for endovascular treatment based on recent trials and should be incorporated into the imaging protocol. Indeed, previously published guidelines on imaging in acute stroke patients[104] recommend that noninvasive vascular imaging be routinely performed, and it is recognized that the use of advanced multimodal imaging does not delay treatment times.[105] Regardless of the choice of technique based on institutional preferences, imaging should be started as quickly as feasible. Because of the difficulty in defining exactly when an order might have been entered in the system, this document is in agreement with the American Stroke Association recommendations that these time intervals be measured from arrival to start of imaging, which will also include vascular imaging. Interpretation of imaging is done in parallel and usually at the scanner by the treating team, and the time needed to interpret the scans and make a decision will be part of the overall time from the start of imaging to arterial puncture. In the HERMES meta-analysis,[46] the fastest 25% of cases had imaging initiated by 12 minutes, and 75% of patients had imaging initiated within 30 minutes.

Metric 3: 75% of patients being evaluated for revascularization should have imaging initiated within 30 minutes from time of arrival. At the best of centers with high volumes and an established resource infrastructure, this is expected to be achieved in 12 minutes.

Imaging to Puncture. The largest amount of time from door to revascularization comes from the steps from door to puncture rather than puncture to revascularization, and most endovascular treatment decisions are made after imaging. Therefore, the largest opportunities to reduce delays and improve outcomes will come from reducing imaging-to-puncture times. The recommended time from start of imaging to arterial puncture is 50 minutes or less. This is in keeping with the time intervals reported in the recent endovascular trials, which had a fastest 25th percentile of 51 minutes,[46] and it is the consensus of the writing group that this time metric is necessary, achievable, and consistent with the improvement in door-to-balloon times that have been achieved for acute myocardial infarction. The recent trials also reported that 75% of patients had an imaging-to-puncture time of no more than 110 minutes. For patients transferred from another site whose imaging does not need to be repeated, it is expected that door-to-puncture times can be reduced by 30 minutes.

Metric 4: 75% of patients treated with endovascular therapy should have an imaging-to-puncture time of 110 minutes or less. At the best of centers with high volumes and an established resource infrastructure, this is expected to be achieved in 50 minutes or less.

Metric 5: For patients transferred from another site in whom imaging is not repeated, 75% of patients being treated should have a door-to-puncture time of 80 minutes or less.

Imaging-to-Thrombus Time. Previous versions of this document have included imaging-to-thrombus time as a metric. This is no longer believed to be a necessary time point for measurement as a result of inaccuracies of measurement and inconsistent practice in documenting the same.

Puncture Time to Reperfusion. This metric assesses the efficiency of the interventional physician and team. Given the rapid advancements in endovascular treatment modalities, these recommendations are likely to change. In the Mechanical Embolus Removal in Cerebral Ischemia registry,[41] the largest prospective endovascular data base to date reflecting procedural outcomes across a large variety of stroke centers in the United States, the median time from groin puncture to the end of the procedure was 90 minutes. Newer technologies such as "stentrievers" have been noted to achieve significantly shorter procedural times (median of approximately 50 minutes).[46]

Although time to final angiography is easily measured, it may be variable depending on the need to perform thrombolysis of peripheral-branch occlusions after recanalization of the proximal occlusion, as more complete revascularization is likely to lead to

improved clinical outcomes, albeit at some increased procedural risk. The time metric described here for successful reperfusion represents the time to first reach an mTICI grade ≥2b. Additional time, if required to achieve complete revascularization, ie, mTICI grade 3, is not reflected in this metric. Recent trials have published their time intervals, and, by doing so, set new expectations. Median time from groin puncture to reperfusion in the SWIFT PRIME trial[20] was 24 minutes (interquartile range, 18–33 minutes). The median puncture-to-reperfusion time in the HERMES collaboration[46] was 44 minutes (interquartile range, 27–64.5 minutes). Generally, we recommend that procedure times not exceed 60 minutes as in the recent trials, and the reperfusion target should be to reach mTICI grade ≥2b.[20] This threshold is further clarified in the following section on recanalization/reperfusion.

Metric 6: In 70% of patients, mTICI grade ≥2b should be reached ideally within 60 minutes of arterial puncture.

Recanalization/Reperfusion

Revascularization is key to improving outcomes with endovascular stroke therapy. Recanalization of the occluded vessel and reperfusion of the distal capillary bed are measures of revascularization, and, although intimately linked, are not necessarily interchangeable. Of the two measures, reperfusion of the distal capillary bed is most linked with clinical outcome.[106] Reperfusion can be assessed by using CT or MR perfusion imaging. On angiography, crude assessment of reperfusion can be made by assessing blood flow into the distal bed, but this does not necessarily correlate with reperfusion on a microcirculatory level.[106] Although advances have been made in perfusion assessment in the angiographic suite,[107] this assessment is not readily available at the present time. Therefore, most interventionalists will rely on a combination of recanalization and reperfusion to assess revascularization.

Revascularization can be assessed in a number of ways, including the thrombolysis in cerebral infarction (TICI) scale,[108] the thrombolysis in myocardial infarction (TIMI) scale,[109,110] the Mori reperfusion scale,[111] the Qureshi scale,[112] and the Arterial Occlusive Lesion score,[113] among others. No direct comparisons of the revascularization scales in terms of their predictive ability for final infarct volume exist, but, through expert comparison of scales, the stroke and interventional community favors the use of the TICI scale.[114,115] In a comparison of TIMI versus TICI scales, TICI was found to be superior to TIMI. The mTICI scale (Table 1) shifted the definition of a grade of 2b to reperfusion of >50% rather than >66% of the distal territory,[31] and mTICI grade 2b/3 was used as the definition of procedural success in most successful endovascular trials. This is the scale recommended for future studies.[30] A further refinement to the TICI scale introduced a new category of 2c to define angiographic revascularization of >90% and <100% of the distal territory.[116] However, the clinical applicability of TICI grade 2c has not been validated in larger prospective trials. Nevertheless, the higher the recanalization and reperfusion grade, the better the outcome, with particularly improved outcomes seen with grades of 2b or higher[116] and the best outcomes seen with TICI grade 3 revascularization.[117]

Compared with earlier studies,[9,17] the positive clinical trials of endovascular stroke therapy showed vastly improved revascularization rates, with mTICI grade 2b/3 rates ranging from 58.7% to 88.0%,[7,11,13,15,20] and the HERMES meta-analysis[14] found an mTICI grade 2b/3 rate of 71%. The THERAPY trial[18] reported an mTICI grade 2b/3 rate of 73%. This was assessed with the use of core laboratory adjudication in most studies, and it has been shown that local sites tend to overestimate the degree of reperfusion compared with a core laboratory.[99] Postmarket registries have found mTICI grade ≥2b rates of 70.9%–73.9%, but no central adjudication was performed.[97,118,119] Based on this, an mTICI grade ≥2b rate of 70% seems a reasonable number for all acute ischemic strokes treated. Only moderate agreement exists between raters for the TICI scale, even though agreement is substantial when the scale is dichotomized into successful (ie, TICI grade 2b/3) or unsuccessful outcomes (ie, TICI grade 0, 1, or 2a).[120]

In terms of technical success of procedures, it is also important to note the presence of distal embolization and embolization to new territory.[31] The ultimate goal of revascularization is to improve patient outcomes. However, there is a risk that persistent attempts to recanalize an occlusion may lead to more complications. The combined metrics for SICH, revascularization, and mRS scores of 0–2 measure these risks and benefits.

Metric 7: The mTICI scale should be the primary scale used to assess angiographic reperfusion.

Metric 8: At least 70% of patients should have mTICI grade 2b/3 (ie, >50%) reperfusion for all clot locations.

Postprocedural CT/MR Imaging

Postprocedural imaging is necessary to identify acute SAH or parenchymal hematoma, differentiate intraparenchymal hemorrhage from contrast staining, define the overall extent of new stroke, and identify other findings. Although there is no evidence that this improves clinical outcomes, there is consensus based on European guidelines that postprocedural imaging is required.[121] CT or MR imaging within 36 hours after intervention should be performed in all stroke patients.[7,11,15,20] Although some patients may receive CT or MR imaging immediately after the procedure, imaging performed the next day provides additional valuable information. It is recognized that there are certain circumstances that might render follow-up imaging difficult or impossible to perform. Therefore, the threshold for this imaging is 90%, acknowledging that a goal of 100% is desired.

Metric 9: At least 90% of patients should have a brain CT or MR imaging examination within 36 hours of the end of the procedure.

SICH

The most common major risk of endovascular treatment of acute ischemic stroke is SICH. As defined by individual studies, the incidences of SICH following endovascular revascularization range from 2% to 10% for combined intravenous and intra-arterial thrombolytic trials[9,12,39,122] and from 1% to 8% for EVT trials.[7,11,13,20,121] Several definitions have been used, as described in the National Institute of Neurological Disorders and Stroke trial,[1] the SITS-MOST[33] and INSTOR registries,[78] and European regis-

tries such as SITS-Thrombectomy,[32,81] MR CLEAN[82] (Netherlands), and the Heidelberg Bleeding Classification.[34]

SAH is a unique complication of endovascular therapy and is not typically seen with intravenous therapy with TPA alone. Intraprocedural SAH caused by arterial perforation can be rapidly fatal, but has been described as being asymptomatic in as many as 16% of patients treated with mechanical thrombectomy without perforation.[123]

The definition chosen for SICH in this document is based on that used by the SWIFT PRIME trial[20] and includes any intracranial hemorrhage with neurologic deterioration leading to an increase in NIHSS score >4 or leading to death within 24 hours of treatment.

SICH is not only an "end-result" evaluation of clinical judgment in the realm of patient selection and technical skill, but also a reflection of timing, procedural execution, and expeditious completion of the task. For these reasons, tracking of SICH is mandatory.

Metric 10: 100% of cases with SICH are reviewed (see "Quality Improvement").

Metric 11: No more than 10% of treated patients should develop SICH.

Embolization of New Territory

Embolization of previously unaffected territories and embolization as a result of clot fragmentation within the treated territory can occur during endovascular treatment. Distal embolization within the treated territory is different from embolization of new territory and has been reported in 16% of patients treated with endovascular thrombolysis and 35% of patients treated with thrombectomy, without decreasing the likelihood of a favorable outcome.[124,125] Embolization of new territory has been reported in 5%–9% of patients treated in the recent EVT trials[7,13,20] and may cause new areas of symptomatic infarct or require additional treatment of previously unaffected vessels.

Metric 12: No more than 10% of patients should have embolization of new territory.

Death within 72 Hours of Treatment

Death within 72 hours of stroke is typically not a result of the stroke itself. The authors clearly acknowledge that every case is unique and that each instance needs to be reviewed in its entirety with the understanding that there are circumstances (eg, myocardial infarction) that lead to death in the short term and are unrelated to operator factors. Death soon after a procedure in and of itself does not imply or indicate a quality problem. However, all deaths within 72 hours are a trigger for review.

Metric 13: 100% of cases of death within 72 hours of the end of the procedure are reviewed.

Clinical Outcomes

Ultimately, the goal of endovascular stroke therapy is to limit the size and extent (ie, severity) of stroke, improve the clinical outcome of the patient, and prevent long-term disability. By convention, these outcomes are commonly assessed by using various functional grading systems: during initial hospitalization, stroke is commonly assessed based on changes in the NIHSS score, and then, often at 90 days, by using the mRS. Clinical outcomes of stroke revascularization are multifactorial, depending on factors intrinsic to the patient such as pre-existing cerebral artery collateral vessels, procedural factors such as time to revascularization and completeness of revascularization, as well as the patient's response to a host of interventions in intensive care and then rehabilitation. Among specific patient factors, higher admission NIHSS scores and age were shown in the HERMES meta-analysis[14] to portend worse outcomes with medical or endovascular therapy. Other medical comorbidities such as underlying cardiac disease, hypertension, and diabetes mellitus all play a role in outcomes. From a procedural standpoint, higher rates of recanalization are associated with improved outcomes. A key component of any interventional stroke program is tracking of clinical outcomes. To that end, we propose that a discharge NIHSS score be documented on all patients, and that all patients are contacted and evaluated to obtain an mRS score at 90 days. Early improvement in NIHSS score may function as a surrogate marker of outcome in situations in which an mRS score cannot be obtained.[126,127] Although it is ideal to assess the patient in person, this may not always be possible, and telephone assessment of mRS score is a reasonable alternative that is well validated.[128] We understand that some patients may be lost to follow-up by 90 days.

Metric 14: All treated patients have a documented NIHSS score 20–36 hours after treatment and at discharge. Attempts are made to contact and document a follow-up mRS score at 90 days (evaluated in person or via telephone) on all treated patients. At least 90% of treated patients have documented 90-day mRS score.

Determining a single threshold level of "good clinical outcome" for all patient populations is difficult because of the heterogeneity of treated patients and the absence of comprehensive data. Individual centers, for example, may have a more elderly patient population or patients with later presentations. The incidences of patients with an mRS score of 0–2 at 90 days in the recent randomized controlled endovascular trials ranged from 33% (MR CLEAN)[7] to 71% (EXTEND-IA),[11] with an overall aggregate rate of 46% in the HERMES trial.[14] Similarly, the THERAPY[18] and Trial and Cost Effectiveness Evaluation of Intra-arterial Thrombectomy in Acute Ischemic Stroke (THRACE)[8] trials reported 38% and 53% rates of mRS score 0–2 at 90 days, respectively, and, in the per-protocol population of the Pragmatic Ischemic Thrombectomy Evaluation (PISTE) trial,[129] 57% of the endovascular group reached an mRS score of 0–2 at 90 days.

The major trials focused on stroke patients with large artery occlusions, specifically internal carotid terminus or proximal middle cerebral (ie, M1) arteries. However, some patients with severe stroke have occlusions at other locations. Patients with isolated M2 branch occlusions may be reasonable candidates for EVT, but, in general, the natural history of stroke in these patients is better than those with more proximal occlusions.[130] Although there are no randomized data showing a benefit for thrombectomy in basilar artery occlusions, these are often treated at many centers.[131] Several studies have specifically reported worse outcomes for patients who did not meet the trial inclusion criteria or

the current American Heart Association level IA recommendations.[22] Gratz et al[119] reported 30% versus 57% incidences of mRS score of 0–2 for high-risk patients versus standard-risk patients. Similarly, Goyal et al[75] reported 39% versus 47% incidences of mRS score of 0–2 for patients not meeting versus meeting AHA level I recommendations.

One must take prestroke functional status into account when setting a threshold for 90-day mRS score for good outcome. Most patients in the recent randomized trials had an mRS score of 0/1 at baseline. As described in the "Indications" section, this is not to imply that EVT be withheld for those who do not have an mRS score of 0/1, but that any outcome threshold needs to account for prestroke functional status.

Multicenter registries have reported results with modern thrombectomy in more heterogeneous groups of patients, including patients with vertebrobasilar and M2 clot locations as well as tandem lesions. The registries include the German Register on Revascularization in Ischemic Stroke Patients (REVASK) registry (n = 1, 107 patients, 40% mRS score 0–2 at 90 days),[132] the Catalonia stroke registry (n = 536 patients, 43% mRS score 0–2 at 90 days),[118] the North American Solitaire registry (n = 354 patients, 42% mRS score 0–2 at 90 days),[133] and the Madrid registry (n = 479, 54% mRS score 0–2 at 90 days).[131] The Dutch MR CLEAN registry[134] reported a 41% incidence of mRS score 0–2 at 90 days in a group of 1,321 patients. Compared with the randomized trials, the registries will include some patients at higher risk (ie, basilar occlusions), some at lower risk (ie, M2 occlusions), and some biased data, as the data are not adjudicated, likely leading to better reported outcomes. However, this is likely to be similar to the experiences of hospitals using the metrics of this document.

Clinical acumen is needed to determine the risk versus benefit of treatment based on published trial and registry data and personal experience. The AHA has created level I recommendations[22] for patient selection based on current randomized trials. However, we expect these recommendations to evolve as results from trials address "wake-up" strokes, prolonged time from symptom onset, basilar artery occlusions, large infarct size, and "mothership" versus "drip-and-ship" cases.[48,49,54,55,59,135]

We propose a single threshold for clinical outcomes for all treated patients regardless of whether they would have been candidates for most recent trials or meet the AHA level I recommendations. This is consistent with the heterogeneity of current clinical practice in which nearly half of treated patients do not meet the AHA recommendations.[75] This document does not advocate for or against treating patients outside of the randomized trial or AHA level I recommendations, but suggests a threshold that recognizes the common practice of treating such patients. The threshold of a 30% incidence of mRS score of 0–2 at 90 days is lower than those of the recent randomized trials and registries based on the experience that "off-trial" patients are more likely to be at higher risk for poor outcomes[75,119] and the belief that the published registry results may not reflect the most current trends in patient selection. It is important to note that, although achieving an mRS score of 0–2 is an important goal, it is not the only marker of a favorable outcome after endovascular therapy. Some patients may have important clinical benefit with an mRS score shift from 4/5 down to 3. However, mRS score shift analysis requires a control group comparison, which is not useful as a quality metric. This suggested threshold should not dissuade centers from treating individual patients if they believe there is a potential benefit from the procedure. Given the multiple factors that influence outcomes, centers are encouraged to benchmark their outcomes against those from a similar patient population.

The clinical outcome threshold of this document is intended to prompt internal review of the endovascular stroke program. It is not designed to constitute a standard for reimbursement from payers, or for accreditation purposes. Local patient factors such as overall medical comorbidities and time from symptom onset to treatment should be taken into account when reviewing any single institution's performance. This is especially true in those patients who have a greater degree of prestroke disability or other comorbidities that may have excluded them from the recent randomized trials, but for whom treatment may be warranted.

Metric 15: Of all treated patients, at least 30% are independent (ie, mRS score 0–2) at 90 days after treatment.

QUALITY IMPROVEMENT

Ongoing Quality Improvement

As EVT of acute ischemic stroke becomes a mainstream offering at many centers, an endovascular-specific multidisciplinary QI process should be established in all programs offering this treatment.[24,25] These endovascular cases, similar to trauma cases, require complex processes of care. These processes go beyond the clinical and technical skills of the operators themselves and should be monitored in a continuous and ongoing fashion.

A peer-review committee at the local hospital should be formed that involves personnel from the several backgrounds that have expertise in stroke care as well as a vested interest in quality of care and outcomes. This committee should provide an open and transparent forum for process and case review. Transparency will optimize confidence in the process, which should have a positive impact on patient care. Although there may be potential for conflict or disagreement among various participants, it is vital that the process be viewed as a nonpolitical, nonpunitive instrument for care process improvement.

Specifically within the United States, in keeping with standards established under the Health Care Quality Improvement Act of 1986 (42 USC §11101 et seq.), peer-review meetings and minutes are generally protected from legal inquiry in most states as long as the review is conducted under the auspices of the facility QI program. The Health Care Quality Improvement Act established standards for professional review actions. Although this protection is not absolute, if a professional review body meets these standards, neither the professional review body nor any person acting as a member or staff to the body will be liable for damages under most federal or state laws with respect to the action.[136-139] All associated QI documents should include routine annotation that establishes the purpose of the document and that its content is protected under applicable federal or state law. The program should operate under the local facility umbrella established for all facility QI and peer-review initiatives.

Table 3: Endovascular therapy quality improvement case review triggers and process metrics

Indications for Endovascular Treatment
- Metric 1: At least 90% of patients who meet the institution selection criteria (indications/contraindications) should be treated with endovascular therapy.

Data Collection
- Metric 2: 100% of patients have the required minimum process and outcomes data entered into an institutional or national data base, trial, or registry.

Key Time Intervals

Door to imaging
- Metric 3: 75% of patients being evaluated for revascularization should have imaging initiated within 30 minutes from time of arrival. At the best of centers with high volumes and an established resource infrastructure, this is expected to be achieved in 12 minutes.

Imaging to puncture
- Metric 4: 75% of patients treated with endovascular therapy should have an imaging-to-puncture time of 110 minutes or less. At the best of centers with high volumes and an established resource infrastructure, this is expected to be achieved in 50 minutes or less.
- Metric 5: For patients transferred from another site and in whom imaging is not repeated, 75% of patients being treated should have a door-to-puncture time of 80 minutes or less.

Puncture to revascularization
- Metric 6: In 70% of patients, mTICI score ≥2b should be reached ideally within 60 minutes of arterial puncture.

Outcome Metrics

Recanalization/reperfusion
- Metric 7: The mTICI scale should be the primary scale used to assess angiographic reperfusion.
- Metric 8: At least 70% of patients should have an mTICI score ≥2b/3 (>50% reperfusion) for all clot locations.

Postprocedure CT/MR Imaging
- Metric 9: At least 90% of patients should have a brain CT or MR imaging within 36 hours of the end of the procedure.

SICH
- Metric 10: 100% of cases with SICH are reviewed.
- Metric 11: No more than 10% of treated patients should develop SICH.

Embolization of new territory
- Metric 12: No more than 10% of patients should have embolization of new territory.

Death within 72 hours of treatment
- Metric 13: 100% of cases of death within 72 hours of the end of the procedure are reviewed.

Clinical Outcomes
- Metric 14: All treated patients have a documented NIHSS score at discharge. Attempts are made to contact and document a follow-up mRS score at 90 days (evaluated in person or via telephone) on all treated patients. At least 90% of treated patients have a documented 90-day mRS score.
- Metric 15: Of all treated patients, at least 30% are independent (ie, mRS score 0–2) at 90 days after treatment.

Note:—mRS indicates modified Rankin Scale; mTICI, modified thrombolysis in cerebral infarction; NIHSS, National Institutes of Health Stroke Scale; SICH, symptomatic intracranial hemorrhage.

Peer Review Team

It is recommended that, under the oversight of the stroke team medical director, a predetermined multidisciplinary subgroup consisting of medical personnel with familiarity and expertise in endovascular therapy be established to address issues specifically relating to endovascular treatment. Although a stroke neurologist is generally in the best overall position to objectively assess overall process deficiencies and outcomes, for technical and procedural issues, an interventionalist perspective must be considered. Ideally, the endovascular oversight team should be directed by a highly qualified and unbiased physician such as a noninterventional vascular neurologist. Depending on the institution, the endovascular QI peer group could include a variable combination of interventionalists, vascular neurologists, cerebrovascular neurosurgeons, intensivists, and diagnostic neuroradiologists. Additional members might include hospital representative(s) from the quality assurance/improvement or risk management departments, as well as possibly the stroke coordinator or other data personnel and secretarial support staff.

Review Process

The endovascular QI meeting should occur at least quarterly, and, depending on volume, may need to occur more frequently to provide adequate assessment and review. There should be review of every case in centers with volumes <50 cases per year and review of every case in which the parameters are outside the benchmarks (eg, prolonged time to puncture, failure of reperfusion, prolonged time to reperfusion) or in which a complication occurs (eg, SICH, embolization of new territory, or death within 72 hours). As noted earlier in the section on data collection, all cases should be entered into a trial, data base, or registry with national participation.[24,25,76] In the United States, Medicare is functioning under the Medicare Access and Children's Health Insurance Program Reauthorization Act of 2015,[140] which seeks to align disparate quality programs through Qualified Clinical Data Registries. This approach is in keeping with our aforementioned recommendation for data collection and quality control.[141,142]

The interventionalist who performed the specific case under review should be present to offer his/her observations and perspective. The focused endovascular peer review should routinely include assessment of technical factors such as device choice, supplemental lytic agent infusion, and equipment inventory assessment. Process elements such as on-call notification, timing (ie, door-to-imaging and imaging-to-arterial puncture times), procedure table setup, and overall communication should also receive routine attention. Performance review is not limited to the treating endovascular physician, but should also include the emergency department, neurology and neurointensive care personnel,

interventional technologists, nursing staff, and other related service areas as indicated. Information concerning transfer from and communication with referring primary stroke centers before and after return to the primary center, complications, and 90-day functional outcome should also be routinely discussed and benchmarked.

Triggers for Review

Any event that might affect quality should be reviewed. Specific triggers for endovascular review include unmet process benchmarks, death, and symptomatic postprocedural hemorrhage. Some complications or process delays may be unavoidable, whereas others may reflect significant errors in judgment or process deficiencies. A determination must be made if the patient was harmed. Process problems such as delays or inadequate communication increase the risk of harm. Therefore, complications and events that increase the risk of poor outcomes need to be reviewed as a means of improving quality. There must also be differentiation between clearly procedure-related complications (eg, perforation and/or dissection, distal dislodgment of thrombus that remains unreachable, embolization of new territory, and immediate SICH following the procedure) and those that might be related to the primary ischemic event itself (eg, infarction, cerebral edema, and hemorrhagic transformation). Predisposing underlying vascular disease and comorbidities must also be considered.

Physicians who choose to treat sicker patients may have poorer outcomes and may not meet established benchmarks. These cases should not be considered in isolation, as a poor outcome does not necessarily indicate that such physicians are providing a lower quality of care, but rather that they have a different patient mix than the trials that were used to create the benchmarks.[7,8,10,11,13-15,18,20,143-145] Adjusting for risk and severity may be helpful in assessing local outcomes compared with other institutions and benchmarks. Endovascular QI case review triggers and key process metrics are summarized in Table 3.

In addition to these morbidity and mortality markers, it is incumbent on the institution and the quality-assurance/improvement and peer-review committee to also assess the "good outcomes." A certain percentage of good outcomes are necessary for there to be sufficient benefit to the overall patient population. This document also defines minimal recanalization rates as well as improved clinical outcomes that should be attained.

Performance and Process Improvement

The committee should be equipped to deal with poor performance in a supportive, constructive, and collegial manner. In cases in which negative trends and deficiencies become apparent, improvement may require individual mentoring, additional education, or supplemental training. Endovascular stroke QI review of problematic cases should generate a specific course of action to remedy recognized problems and prevent future occurrences. Individual assignments should be tracked, with accountability reports scheduled for subsequent meetings. Further, process improvement is a continuing activity that, along with individual performance improvement, will significantly impact clinical outcomes.[146]

ACKNOWLEDGMENTS

The authors thank Zachary Zhang, MD (Rochester General Hospital, Rochester, New York), for assistance creating the evidence table and formatting the document; and Sean A. Kennedy, MD (University of Toronto, Toronto, Ontario), and Ajinkya Desai, MD (Rochester General Hospital, Rochester, New York), for assistance creating the evidence table.

REFERENCES

1. National Institute of Neurological Disorders and Stroke rt-PA Stroke Study Group. **Tissue plasminogen activator for acute ischemic stroke.** *N Engl J Med* 1995;333:1581–87 CrossRef Medline
2. Mozaffarian D, Benjamin EJ, Go AS, et al; American Heart Association Statistics Committee and Stroke Statistics Subcommittee. **Heart disease and stroke statistics–2015 update: a report from the American Heart Association.** *Circulation* 2015;131:e29–322 CrossRef Medline
3. Gibson CM, Pride YB, Frederick PD, et al. **Trends in reperfusion strategies, door-to-needle and door-to-balloon times, and in-hospital mortality among patients with ST-segment elevation myocardial infarction enrolled in the National Registry of Myocardial Infarction from 1990 to 2006.** *Am Heart J* 2008;156:1035–44 CrossRef Medline
4. Sacks D, Black CM, Cognard C, et al; American Society of Neuroradiology, Canadian Interventional Radiology Association, Cardiovascular and Interventional Radiological Society of Europe, Society for Cardiovascular Angiography and Interventions, Society of Interventional Radiology, Society of NeuroInterventional Surgery, European Society of Minimally Invasive Neurological Therapy, Society of Vascular and Interventional Neurology. **Multisociety consensus quality improvement guidelines for intraarterial catheter-directed treatment of acute ischemic stroke, from the American Society of Neuroradiology, Canadian Interventional Radiology Association, Cardiovascular and Interventional Radiological Society of Europe, Society for Cardiovascular Angiography and Interventions, Society of Interventional Radiology, Society of NeuroInterventional Surgery, European Society of Minimally Invasive Neurological Therapy, and Society of Vascular and Interventional Neurology.** *J Vasc Interv Radiol* 2013;24:151–63 CrossRef Medline
5. White PM, Bhalla A, Dinsmore J, et al. **Standards for providing safe acute ischaemic stroke thrombectomy services (September 2015).** *Clin Radiol* 2017;72:175.e1–9 CrossRef Medline
6. Badhiwala JH, Nassiri F, Alhazzani W, et al. **Endovascular thrombectomy for acute ischemic stroke: a meta-analysis.** *JAMA* 2015;314:1832–43 CrossRef Medline
7. Berkhemer OA, Fransen PS, Beumer D, et al. **A randomized trial of intraarterial treatment for acute ischemic stroke.** *N Engl J Med* 2015;372:11–20 CrossRef Medline
8. Bracard S, Ducrocq X, Mas JL, et al; THRACE investigators. **Mechanical thrombectomy after intravenous alteplase versus alteplase alone after stroke (THRACE): a randomised controlled trial.** *Lancet Neurol* 2016;15:1138–47 CrossRef Medline
9. Broderick JP, Palesch YY, Demchuk AM, et al; Interventional Management of Stroke (IMS) III Investigators. **Endovascular therapy after intravenous t-PA versus t-PA alone for stroke.** *N Engl J Med* 2013;368:893–903 CrossRef Medline
10. Campbell BC, Hill MD, Rubiera M, et al. **Safety and efficacy of Solitaire stent thrombectomy: individual patient data meta-analysis of randomized trials.** *Stroke* 2016;47:798–806 CrossRef Medline
11. Campbell BC, Mitchell PJ, Kleinig TJ, et al; EXTEND-IA Investigators. **Endovascular therapy for ischemic stroke with perfusion-imaging selection.** *N Engl J Med* 2015;372:1009–18 CrossRef Medline
12. Ciccone A, Valvassori L, Nichelatti M, et al; SYNTHESIS Expansion Investigators. **Endovascular treatment for acute ischemic stroke.** *N Engl J Med* 2013;368:904–13 CrossRef Medline

13. Goyal M, Demchuk AM, Menon BK, et a; ESCAPE Trial Investigators. **Randomized assessment of rapid endovascular treatment of ischemic stroke.** *N Engl J Med* 2015;372:1019–30 CrossRef Medline
14. Goyal M, Menon BK, van Zwam WH, et al; HERMES collaborators. **Endovascular thrombectomy after large-vessel ischaemic stroke: a meta-analysis of individual patient data from five randomised trials.** *Lancet* 2016;387:1723–31 CrossRef Medline
15. Jovin TG, Chamorro A, Cobo E, et al; REVASCAT Trial Investigators. **Thrombectomy within 8 hours after symptom onset in ischemic stroke.** *N Engl J Med* 2015;372:2296–306 CrossRef Medline
16. Kennedy SA, Baerlocher MO, Baerlocher F, et al. **Meta-analysis of local endovascular therapy for acute ischemic stroke.** *J Vasc Interv Radiol* 2016;27:307–21.e2 CrossRef Medline
17. Kidwell CS, Jahan R, Gornbein J, et al; MR RESCUE Investigators. **A trial of imaging selection and endovascular treatment for ischemic stroke.** *N Engl J Med* 2013;368:914–23 CrossRef Medline
18. Mocco J, Zaidat OO, von Kummer R, et al; THERAPY Trial Investigators. **Aspiration thrombectomy after intravenous alteplase versus intravenous alteplase alone.** *Stroke* 2016;47:2331–38 CrossRef Medline
19. Prabhakaran S, Ruff I, Bernstein RA. **Acute stroke intervention: a systematic review.** *JAMA* 2015;313:1451–62 CrossRef Medline
20. Saver JL, Goyal M, Bonafe A, et al; SWIFT PRIME Investigators. **Stent-retriever thrombectomy after intravenous t-PA vs. t-PA alone in stroke.** *N Engl J Med* 2015;372:2285–95 CrossRef Medline
21. NICE Interventional Procedure Guidance. Mechanical clot retrieval for treating acute ischaemic stroke. Interventional procedures guidance (IPG548), February 2016. http://www.nice.org.uk/guidance/ipg548. Accessed April 10, 2016
22. Powers WJ, Derdeyn CP, Biller J, et al; American Heart Association Stroke Council. **2015 American Heart Association/American Stroke Association Focused Update of the 2013 Guidelines for the Early Management of Patients with Acute Ischemic Stroke Regarding Endovascular Treatment: A Guideline for Healthcare Professionals from the American Heart Association/American Stroke Association.** *Stroke* 2015;46:3020–35 CrossRef Medline
23. Wahlgren N, Moreira T, Michel P, et al; ESO-KSU, ESO, ESMINT, ESNR and EAN. **Mechanical thrombectomy in acute ischemic stroke: consensus statement by ESO-Karolinska Stroke Update 2014/2015, supported by ESO, ESMINT, ESNR and EAN.** *Int J Stroke* 2016;11:134–47 CrossRef Medline
24. Connors JJ 3rd, Sacks D, Black CM, et al; Society of Interventional Radiology. **Training guidelines for intra-arterial catheter-directed treatment of acute ischemic stroke: a statement from a special writing group of the Society of Interventional Radiology.** *J Vasc Interv Radiol* 2009;20:1507–22 CrossRef Medline
25. Lavine SD, Cockroft K, Hoh B, et al. **Training Guidelines for Endovascular Ischemic Stroke Intervention: An International Multi-Society Consensus Document.** *AJNR Am J Neuroradiol* 2016;37:E31–34 CrossRef Medline
26. Jovin TG, Albers GW, Liebeskind DS; STAIR IX Consortium. **Stroke treatment academic industry roundtable: the next generation of endovascular trials.** *Stroke* 2016;47:2656–65 CrossRef Medline
27. Fink A, Kosecoff J, Chassin M, et al. **Consensus methods: characteristics and guidelines for use.** *Am J Public Health* 1984;74:979–83 CrossRef Medline
28. Institute of Medicine (U.S.) Committee on Standards for Developing Trustworthy Clinical Practice Guidelines. Graham R, Mancher M, Wolman DM, et al, eds. *Clinical Practice Guidelines We Can Trust.* Washington, DC: National Academies Press; 2011: xxxiv
29. Sacco RL, Kasner SE, Broderick JP, et al; American Heart Association Stroke Council, Council on Cardiovascular Surgery and Anesthesia, Council on Cardiovascular Radiology and Intervention, Council on Cardiovascular and Stroke Nursing, Council on Epidemiology and Prevention, Council on Peripheral Vascular Disease, Council on Nutrition, Physical Activity and Metabolism. **An updated definition of stroke for the 21st century: a statement for healthcare professionals from the American Heart Association/American Stroke Association.** *Stroke* 2013;44:2064–89 CrossRef Medline
30. Wintermark M, Albers GW, Broderick JP, et al. **Acute stroke imaging research roadmap II.** *Stroke* 2013;44:2628–39 CrossRef Medline
31. Zaidat OO, Yoo AJ, Khatri P, et al; Cerebral Angiographic Revascularization Grading (CARG) Collaborators, STIR Revascularization working group, STIR Thrombolysis in Cerebral Infarction (TICI) Task Force. **Recommendations on angiographic revascularization grading standards for acute ischemic stroke: a consensus statement.** *Stroke* 2013;44:2650–63 CrossRef Medline
32. Wahlgren N, Ahmed N, Eriksson N, et al; Safe Implementation of Thrombolysis in Stroke-MOnitoring STudy Investigators. **Multivariable analysis of outcome predictors and adjustment of main outcome results to baseline data profile in randomized controlled trials: Safe Implementation of Thrombolysis in Stroke-Monitoring Study (SITS-MOST).** *Stroke* 2008;39:3316–22 CrossRef Medline
33. Wahlgren N, Ahmed N, Davalos A, et al; SITS-MOST investigators. **Thrombolysis with alteplase for acute ischaemic stroke in the Safe Implementation of Thrombolysis in Stroke-Monitoring study (SITS-MOST): an observational study.** *Lancet* 2007;369:275–82 CrossRef Medline
34. von Kummer R, Broderick JP, Campbell BC, et al. **The Heidelberg Bleeding Classification: classification of bleeding events after ischemic stroke and reperfusion therapy.** *Stroke* 2015;46:2981–86 CrossRef Medline
35. van Swieten JC, Koudstaal PJ, Visser MC, et al. **Interobserver agreement for the assessment of handicap in stroke patients.** *Stroke* 1988;19:604–07 CrossRef Medline
36. Casaubon LK, Boulanger JM, Blacquiere D, et al; Heart and Stroke Foundation of Canada Canadian Stroke Best Practices Advisory Committee. **Canadian Stroke Best Practice Recommendations: Hyperacute Stroke Care Guidelines, Update 2015.** *Int J Stroke* 2015;10:924–40 CrossRef Medline
37. Campbell BC, Donnan GA, Lees KR, et al. **Endovascular stent thrombectomy: the new standard of care for large vessel ischaemic stroke.** *Lancet Neurol* 2015;14:846–54 CrossRef Medline
38. Coutts SB, Modi J, Patel SK, et al; Calgary Stroke Program. **CT/CT angiography and MRI findings predict recurrent stroke after transient ischemic attack and minor stroke: results of the prospective CATCH study.** *Stroke* 2012;43:1013–17 CrossRef Medline
39. Furlan A, Higashida R, Wechsler L, et al. **Intra-arterial prourokinase for acute ischemic stroke: the PROACT II study—a randomized controlled trial. Prolyse in Acute Cerebral Thromboembolism.** *JAMA* 1999;282:2003–11 CrossRef Medline
40. Penumbra Pivotal Stroke Trial Investigators. **Penumbra pivotal stroke trial: the penumbra pivotal stroke trial—safety and effectiveness of a new generation of mechanical devices for clot removal in intracranial large vessel occlusive disease.** *Stroke* 2009;40:2761–68 CrossRef Medline
41. Smith WS, Sung G, Saver J, et al; Multi MERCI Investigators. **Mechanical thrombectomy for acute ischemic stroke: final results of the Multi MERCI trial.** *Stroke* 2008;39:1205–12 CrossRef Medline
42. Tarr R, Hsu D, Kulcsar Z, et al. **The POST trial: initial post-market experience of the Penumbra system: revascularization of large vessel occlusion in acute ischemic stroke in the United States and Europe.** *J Neurointerv Surg* 2010;2:341–44 CrossRef Medline
43. Fransen PS, Berkhemer OA, Lingsma HF, et al. **Time to Reperfusion and Treatment Effect for Acute Ischemic Stroke: a randomized clinical trial.** *JAMA Neurol* 2016;73:190–96 CrossRef Medline
44. Goyal M, Jadhav AP, Bonafe A, et al; SWIFT PRIME investigators. **Analysis of workflow and time to treatment and the effects on outcome in endovascular treatment of acute ischemic stroke: results from the SWIFT PRIME randomized controlled trial.** *Radiology* 2016;279:888–97 CrossRef Medline
45. Khatri P, Abruzzo T, Yeatts SD, et al; IMS I and II Investigators. **Good clinical outcome after ischemic stroke with successful revascularization is time-dependent.** *Neurology* 2009;73:1066–72 CrossRef Medline

46. Saver JL, Goyal M, van der Lugt A, et al; HERMES Collaborators. **Time to treatment with endovascular thrombectomy and outcomes from ischemic stroke: a meta-analysis.** *JAMA* 2016;316:1279–88 CrossRef Medline
47. Lansberg MG, Cereda CW, Mlynash M, et al; Diffusion and Perfusion Imaging Evaluation for Understanding Stroke Evolution 2 (DEFUSE 2) Study Investigators. **Response to endovascular reperfusion is not time-dependent in patients with salvageable tissue.** *Neurology* 2015;85:708–14 CrossRef Medline
48. Nogueira R, Jovin T. **Clinical mismatch in the triage of wake up and late presenting strokes undergoing neurointervention with Trevo (DAWN).** *N Engl J Med* 2018;378:11–21
49. POSITIVE Stroke Clinical Trial. https://clinicaltrials.gov/ct2/show/NCT01852201?term=positive+stroke+trial&rank=1. Accessed February 12, 2016
50. Endovascular Therapy Following Imaging Evaluation for Ischemic Stroke 3 (DEFUSE 3). https://clinicaltrials.gov/ct2/show/NCT02586415. Accessed February 12, 2016
51. Brandt T, von Kummer R, Müller-Küppers M, et al. **Thrombolytic therapy of acute basilar artery occlusion: variables affecting recanalization and outcome.** *Stroke* 1996;27:875–81 CrossRef Medline
52. Lin DD, Gailloud P, Beauchamp NJ, et al. **Combined stent placement and thrombolysis in acute vertebrobasilar ischemic stroke.** *AJNR Am J Neuroradiol* 2003;24:1827–33 Medline
53. Schonewille WJ, Wijman CA, Michel P, et al; BASICS study group. **Treatment and outcomes of acute basilar artery occlusion in the Basilar Artery International Cooperation Study (BASICS): a prospective registry study.** *Lancet Neurol* 2009;8:724–30 CrossRef Medline
54. Basilar Artery International Cooperation Study (BASICS). https://clinicaltrials.gov/ct2/show/NCT01717755?term=basics+stroke+trial&rank=1. Accessed April 11, 2017
55. Basilar Artery Occlusion Chinese Endovascular Trial. https://clinicaltrials.gov/ct2/show/NCT02737189?term=best+stroke+trial&rank=2. Accessed April 11, 2017
56. Hacke W, Kaste M, Fieschi C, et al. **Randomised double-blind placebo-controlled trial of thrombolytic therapy with intravenous alteplase in acute ischaemic stroke (ECASS II): Second European-Australasian Acute Stroke Study Investigators.** *Lancet* 1998;352:1245–51 CrossRef Medline
57. Barber PA, Demchuk AM, Zhang J, et al. **Validity and reliability of a quantitative computed tomography score in predicting outcome of hyperacute stroke before thrombolytic therapy: ASPECTS Study Group—Alberta Stroke Programme Early CT Score.** *Lancet* 2000;355:1670–74 CrossRef Medline
58. Pexman JH, Barber PA, Hill MD, et al. **Use of the Alberta Stroke Program early CT score (ASPECTS) for assessing CT scans in patients with acute stroke.** *AJNR Am J Neuroradiol* 2001;22:1534–42 Medline
59. Efficacy and Safety of Thrombectomy in Stroke with Extended Lesion and Extended Time Window (Tension). https://clinicaltrials.gov/show/NCT03094715. Accessed April 11, 2017
60. Riedel CH, Zoubie J, Ulmer S, et al. **Thin-slice reconstructions of nonenhanced CT images allow for detection of thrombus in acute stroke.** *Stroke* 2012;43:2319–23 CrossRef Medline
61. Riedel CH, Zimmermann P, Jensen-Kondering U, et al. **The importance of size: successful recanalization by intravenous thrombolysis in acute anterior stroke depends on thrombus length.** *Stroke* 2011;42:1775–77 CrossRef Medline
62. Rohan V, Baxa J, Tupy R, et al. **Length of occlusion predicts recanalization and outcome after intravenous thrombolysis in middle cerebral artery stroke.** *Stroke* 2014;45:2010–17 CrossRef Medline
63. Ahn SH, d'Esterre CD, Qazi EM, et al. **Occult anterograde flow is an under-recognized but crucial predictor of early recanalization with intravenous tissue-type plasminogen activator.** *Stroke* 2015;46:968–75 CrossRef Medline
64. Menon BK, d'Esterre CD, Qazi EM, et al. **Multiphase CT angiography: a new tool for the imaging triage of patients with acute ischemic stroke.** *Radiology* 2015;275:510–20 CrossRef Medline
65. Gilgen MD, Klimek D, Liesirova KT, et al. **Younger stroke patients with large pretreatment diffusion-weighted imaging lesions may benefit from endovascular treatment.** *Stroke* 2015;46:2510–16 CrossRef Medline
66. Borst J, Berkhemer OA, Roos YB, et al; MR CLEAN investigators. **Value of computed tomographic perfusion-based patient selection for intra-arterial acute ischemic stroke treatment.** *Stroke* 2015;46:3375–82 CrossRef Medline
67. d'Esterre CD, Boesen ME, Ahn SH, et al. **Time-dependent computed tomographic perfusion thresholds for patients with acute ischemic stroke.** *Stroke* 2015;46:3390–97 CrossRef Medline
68. Barreto AD, Albright KC, Hallevi H, et al. **Thrombus burden is associated with clinical outcome after intra-arterial therapy for acute ischemic stroke.** *Stroke* 2008;39:3231–35 CrossRef Medline
69. Lin R, Vora N, Zaidi S, et al. **Mechanical approaches combined with intra-arterial pharmacological therapy are associated with higher recanalization rates than either intervention alone in revascularization of acute carotid terminus occlusion.** *Stroke* 2009;40:2092–97 CrossRef Medline
70. Shi ZS, Loh Y, Walker G, et al; MERCI and Multi-MERCI Investigators. **Clinical outcomes in middle cerebral artery trunk occlusions versus secondary division occlusions after mechanical thrombectomy: pooled analysis of the Mechanical Embolus Removal in Cerebral Ischemia (MERCI) and multi MERCI trials.** *Stroke* 2010;41:953–60 CrossRef Medline
71. Coutinho JM, Liebeskind DS, Slater LA, et al. **Mechanical thrombectomy for isolated M2 occlusions: a post hoc analysis of the STAR, SWIFT, and SWIFT PRIME studies.** *AJNR Am J Neuroradiol* 2016;37:667–72 CrossRef Medline
72. Busl KM, Nogueira RG, Yoo AJ, et al. **Prestroke dementia is associated with poor outcomes after reperfusion therapy among elderly stroke patients.** *J Stroke Cerebrovasc Dis* 2013;22:718–24 CrossRef Medline
73. Khatri P, Hill MD, Palesch YY, et al; Interventional Management of Stroke III Investigators. **Methodology of the Interventional Management of Stroke III Trial.** *Int J Stroke* 2008;3:130–37 CrossRef Medline
74. Bhole R, Goyal N, Nearing K, et al. **Implications of limiting mechanical thrombectomy to patients with emergent large vessel occlusion meeting top tier evidence criteria.** *J Neurointerv Surg* 2017;9:225–28 CrossRef Medline
75. Goyal N, Tsivgoulis G, Frei D, et al. **A multicenter study of the safety and effectiveness of mechanical thrombectomy for patients with acute ischemic stroke not meeting top-tier evidence criteria.** *J Neurointerv Surg* 2018;10:10–16 CrossRef Medline
76. Leifer D, Bravata DM, Connors JJ 3rd, et al; American Heart Association Special Writing Group of the Stroke Council, Atherosclerotic Peripheral Vascular Disease Working Group, Council on Cardiovascular Surgery and Anesthesia, Council on Cardiovascular Nursing. **Metrics for measuring quality of care in comprehensive stroke centers: detailed follow-up to Brain Attack Coalition comprehensive stroke center recommendations: a statement for healthcare professionals from the American Heart Association/American Stroke Association.** *Stroke* 2011;42:849–77 CrossRef Medline
77. Saver JL, Gornbein J. **Treatment effects for which shift or binary analyses are advantageous in acute stroke trials.** *Neurology* 2009;72:1310–15 CrossRef Medline
78. Interventional Stroke Therapy Outcomes Registry (INSTOR). http://www.strokeregistry.org. Accessed July 19, 2016
79. Meyers PM, Schumacher HC, Alexander MJ, et al; Wrting Group for American Academy of Neurology, American Association of Neurological Surgeons Cerebrovascular Section, Society of Neurointerventional Surgery and Society of Vascular and Interventional Neurology. **Performance and training standards for endovascular ischemic stroke treatment.** *J Stroke Cerebrovasc Dis* 2009;18:411–15 CrossRef Medline

80. Schwamm LH, Fonarow GC, Reeves MJ, et al. **Get With the Guideline: Stroke is associated with sustained improvement in care for patients hospitalized with acute stroke or transient ischemic attack.** *Circulation* 2009;119:107–15 CrossRef Medline
81. SITS-Thrombectomy registry. http://www.sitsinternational.org/registries/sits-thrombectomy/. Accessed August 12, 2016
82. MR CLEAN-R Registry. http://www.mrclean-trial.org. Accessed August 12, 2016
83. Menon BK, Saver JL, Goyal M, et al. **Trends in endovascular therapy and clinical outcomes within the nationwide Get With The Guidelines-Stroke registry.** *Stroke* 2015;46:989–95 CrossRef Medline
84. Hacke W, Donnan G, Fieschi C, et al; ATLANTIS Trials Investigators, ECASS Trials Investigators, NINDS rt-PA Study Group Investigators. **Association of outcome with early stroke treatment: pooled analysis of ATLANTIS, ECASS, and NINDS rt-PA stroke trials.** *Lancet* 2004;363:768–74 CrossRef Medline
85. Lansberg MG, Schrooten M, Bluhmki E, et al. **Treatment time-specific number needed to treat estimates for tissue plasminogen activator therapy in acute stroke based on shifts over the entire range of the modified Rankin Scale.** *Stroke* 2009;40:2079–84 CrossRef Medline
86. Menon BK, Sajobi TT, Zhang Y, et al. **Analysis of workflow and time to treatment on thrombectomy outcome in the Endovascular Treatment for Small Core and Proximal Occlusion Ischemic Stroke (ESCAPE) randomized, controlled trial.** *Circulation* 2016; 133:2279–86 CrossRef Medline
87. Ribo M, Molina CA, Cobo E, et al; REVASCAT Trial Investigators. **Association between time to reperfusion and outcome is primarily driven by the time from imaging to reperfusion.** *Stroke* 2016;47: 999–1004 CrossRef Medline
88. Bradley EH, Curry LA, Webster TR, et al. **Achieving rapid door-to-balloon times: how top hospitals improve complex clinical systems.** *Circulation* 2006;113:1079–85 CrossRef Medline
89. Krumholz HM, Bradley EH, Nallamothu BK, et al. **A campaign to improve the timeliness of primary percutaneous coronary intervention: Door-to-Balloon—An Alliance for Quality.** *JACC Cardiovasc Interv* 2008;1:97–104 CrossRef Medline
90. Fonarow GC, Smith EE, Saver JL, et al. **Improving door-to-needle times in acute ischemic stroke: the design and rationale for the American Heart Association/American Stroke Association's target—stroke initiative.** *Stroke* 2011;42:2983–89 CrossRef Medline
91. Mitka M. **Reducing door-to-needle time for tPA use remains an elusive goal in stroke care.** *JAMA* 2011;305:1288–89 CrossRef Medline
92. Meretoja A, Strbian D, Mustanoja S, et al. **Reducing in-hospital delay to 20 minutes in stroke thrombolysis.** *Neurology* 2012;79: 306–13 CrossRef Medline
93. Rai AT, Smith MS, Boo S, et al. **The 'pit-crew' model for improving door-to-needle times in endovascular stroke therapy: a Six-Sigma project.** *J Neurointerv Surg* 2016;8:447–52 CrossRef Medline
94. Costalat V, Machi P, Lobotesis K, et al. **Rescue, combined, and stand-alone thrombectomy in the management of large vessel occlusion stroke using the Solitaire device: a prospective 50-patient single-center study: timing, safety, and efficacy.** *Stroke* 2011;42: 1929–35 CrossRef Medline
95. Miley JT, Memon MZ, Hussein HM, et al. **A multicenter analysis of "time to microcatheter" for endovascular therapy in acute ischemic stroke.** *J Neuroimaging* 2011;21:159–64 CrossRef Medline
96. Sun CH, Ribo M, Goyal M, et al. **Door-to-puncture: a practical metric for capturing and enhancing system processes associated with endovascular stroke care, preliminary results from the rapid reperfusion registry.** *J Am Heart Assoc* 2014;3:e000859 CrossRef Medline
97. Zaidat OO, Castonguay AC, Gupta R, et al. **North American Solitaire Stent Retriever Acute Stroke Registry: post-marketing revascularization and clinical outcome results.** *J Neurointerv Surg* 2014; 6:584–88 CrossRef Medline
98. Nogueira RG, Lutsep HL, Gupta R, et al; TREVO 2 Trialists. **Trevo versus Merci retrievers for thrombectomy revascularisation of large vessel occlusions in acute ischaemic stroke (TREVO 2): a randomised trial.** *Lancet* 2012;380:1231–40 CrossRef Medline
99. Saver JL, Jahan R, Levy EI, et al. **Solitaire flow restoration device versus the Merci Retriever in patients with acute ischaemic stroke (SWIFT): a randomised, parallel-group, non-inferiority trial.** *Lancet* 2012;380:1241–49 CrossRef Medline
100. Abilleira S, Ribera A, Dávalos A, et al; Catalan Stroke Code and Reperfusion Consortium. **Functional outcome after primary endovascular therapy or IV thrombolysis alone for stroke: an observational, comparative effectiveness study.** *Cerebrovasc Dis* 2014;38: 328–36 CrossRef Medline
101. Goyal M, Almekhlafi MA, Fan L, et al. **Evaluation of interval times from onset to reperfusion in patients undergoing endovascular therapy in the Interventional Management of Stroke III trial.** *Circulation* 2014;130:265–72 CrossRef Medline
102. van Heerden J, Yan B, Churilov L, et al. **Picture-to-puncture time in acute stroke endovascular intervention: are we getting faster?** *J Neurointerv Surg* 2015;7:564–68 CrossRef Medline
103. Nikoubashman O, Probst T, Schürmann K, et al. **Weekend effect in endovascular stroke treatment: do treatment decisions, procedural times, and outcome depend on time of admission?** *J Neurointerv Surg* 2017;9:336–39 CrossRef Medline
104. Latchaw RE, Alberts MJ, Lev MH, et al; American Heart Association Council on Cardiovascular Radiology and Intervention, Stroke Council, and the Interdisciplinary Council on Peripheral Vascular Disease. **Recommendations for imaging of acute ischemic stroke: a scientific statement from the American Heart Association.** *Stroke* 2009;40:3646–78 CrossRef Medline
105. McTaggart RA, Ansari SA, Goyal M, et al; Standards and Guidelines Committee of the Society of NeuroInterventional Surgery (SNIS). **Initial hospital management of patients with emergent large vessel occlusion (ELVO): report of the standards and guidelines committee of the Society of NeuroInterventional Surgery.** *J Neurointerv Surg* 2017;9:316–23 CrossRef Medline
106. Cho TH, Nighoghossian N, Mikkelsen IK, et al. **Reperfusion within 6 hours outperforms recanalization in predicting penumbra salvage, lesion growth, final infarct, and clinical outcome.** *Stroke* 2015;46:1582–89 CrossRef Medline
107. Struffert T, Deuerling-Zheng Y, Engelhorn T, et al. **Feasibility of cerebral blood volume mapping by flat panel detector CT in the angiography suite: first experience in patients with acute middle cerebral artery occlusions.** *AJNR Am J Neuroradiol* 2012;33:618–25 CrossRef Medline
108. Higashida RT, Furlan AJ, Roberts H, et al; Technology Assessment Committee of the American Society of Interventional and Therapeutic Neuroradiology, Technology Assessment Committee of the Society of Interventional Radiology. **Trial design and reporting standards for intra-arterial cerebral thrombolysis for acute ischemic stroke.** *Stroke* 2003;34:e109–37 CrossRef Medline
109. TIMI Study Group. **The Thrombolysis in Myocardial Infarction (TIMI) trial: Phase I findings.** *N Engl J Med* 1985;312:932–36 Medline
110. Chesebro JH, Knatterud G, Roberts R, et al. **Thrombolysis in Myocardial Infarction (TIMI) Trial, Phase I: a comparison between intravenous tissue plasminogen activator and intravenous streptokinase—clinical findings through hospital discharge.** *Circulation* 1987;76:142–54 CrossRef Medline
111. Mori E, Yoneda Y, Tabuchi M, et al. **Intravenous recombinant tissue plasminogen activator in acute carotid artery territory stroke.** *Neurology* 1992;42:976–82 CrossRef Medline
112. Qureshi AI. **New grading system for angiographic evaluation of arterial occlusions and recanalization response to intra-arterial thrombolysis in acute ischemic stroke.** *Neurosurgery* 2002;50: 1405–14; discussion 1414–15 Medline
113. Khatri P, Neff J, Broderick JP, et al; IMS-I Investigators. **Revascularization end points in stroke interventional trials: recanalization**

versus reperfusion in IMS-I. *Stroke* 2005;36:2400–03 CrossRef Medline
114. Gerber JC, Miaux YJ, von Kummer R. **Scoring flow restoration in cerebral angiograms after endovascular revascularization in acute ischemic stroke patients.** *Neuroradiology* 2015;57:227–40 CrossRef Medline
115. Zaidat OO, Lazzaro MA, Liebeskind DS, et al. **Revascularization grading in endovascular acute ischemic stroke therapy.** *Neurology* 2012;79(13 Suppl 1):S110–16 CrossRef Medline
116. Almekhlafi MA, Mishra S, Desai JA, et al. **Not all "successful" angiographic reperfusion patients are an equal validation of a modified TICI scoring system.** *Interv Neuroradiol* 2014;20:21–27 CrossRef Medline
117. Kleine JF, Wunderlich S, Zimmer C, et al. **Time to redefine success? TICI 3 versus TICI 2b recanalization in middle cerebral artery occlusion treated with thrombectomy.** *J Neurointerv Surg* 2017;9:117–21 CrossRef Medline
118. Abilleira S, Cardona P, Ribo M, et al; Catalan Stroke Code and Reperfusion Consortium. **Outcomes of a contemporary cohort of 536 consecutive patients with acute ischemic stroke treated with endovascular therapy.** *Stroke* 2014;45:1046–52 CrossRef Medline
119. Gratz PP, Jung S, Schroth G, et al. **Outcome of standard and high-risk patients with acute anterior circulation stroke after stent retriever thrombectomy.** *Stroke* 2014;45:152–58 CrossRef Medline
120. Gaha M, Roy C, Estrade L, et al. **Inter- and intraobserver agreement in scoring angiographic results of intra-arterial stroke therapy.** *AJNR Am J Neuroradiol* 2014;35:1163–69 CrossRef Medline
121. Fiehler J, Cognard C, Gallitelli M, et al. **European Recommendations on Organisation Of Interventional Care in Acute Stroke (EROICAS).** *Int J Stroke* 2016;11:701–16 CrossRef Medline
122. Ogawa A, Mori E, Minematsu K, et al; MELT Japan Study Group. **Randomized trial of intraarterial infusion of urokinase within 6 hours of middle cerebral artery stroke: the middle cerebral artery embolism local fibrinolytic intervention trial (MELT) Japan.** *Stroke* 2007;38:2633–39 CrossRef Medline
123. Yoon W, Jung MY, Jung SH, et al. **Subarachnoid hemorrhage in a multimodal approach heavily weighted toward mechanical thrombectomy with Solitaire stent in acute stroke.** *Stroke* 2013;44:414–19 CrossRef Medline
124. Herial N, Qureshi M, Khan A, et al. **Arterial reocclusion and distal embolization during endovascular treatment using new generation stent retrievers in acute ischemic stroke patients.** *Neurology* 2015;84(14 Suppl P4):299
125. Janjua N, Alkawi A, Suri MF, et al. **Impact of arterial reocclusion and distal fragmentation during thrombolysis among patients with acute ischemic stroke.** *AJNR Am J Neuroradiol* 2008;29:253–58 CrossRef Medline
126. Kerr DM, Fulton RL, Lees KR; VISTA Collaborators. **Seven-day NIHSS is a sensitive outcome measure for exploratory clinical trials in acute stroke: evidence from the Virtual International Stroke Trials Archive.** *Stroke* 2012;43:1401–03 CrossRef Medline
127. Sajobi TT, Menon BK, Wang M, et al; ESCAPE Trial Investigators. **Early trajectory of stroke severity predicts long-term functional outcomes in ischemic stroke subjects: results from the ESCAPE trial (Endovascular Treatment for Small Core and Anterior Circulation Proximal Occlusion with Emphasis on Minimizing CT to Recanalization Times).** *Stroke* 2017;48:105–10 CrossRef Medline
128. Janssen PM, Visser NA, Dorhout Mees SM, et al. **Comparison of telephone and face-to-face assessment of the modified Rankin Scale.** *Cerebrovasc Dis* 2010;29:137–39 CrossRef Medline
129. Muir KW, Ford GA, Messow CM, et al; PISTE Investigators. **Endovascular therapy for acute ischaemic stroke: the Pragmatic Ischaemic Stroke Thrombectomy Evaluation (PISTE) randomised, controlled trial.** *J Neurol Neurosurg Psychiatry* 2017;88:38–44 CrossRef Medline
130. Khan M, Goddeau RP Jr, Zhang J, et al. **Predictors of outcome following stroke due to isolated M2 occlusions.** *Cerebrovasc Dis Extra* 2014;4:52–60 CrossRef Medline
131. Alonso de Leciñana M, Kawiorski MM, Ximénez-Carrillo Á, et al; Madrid Stroke Network. **Mechanical thrombectomy for basilar artery thrombosis: a comparison of outcomes with anterior circulation occlusions.** *J Neurointerv Surg* 2017;9:1173–78 CrossRef Medline
132. Minnerup J, Wersching H, Teuber A, et al; REVASK Investigators. **Outcome after thrombectomy and intravenous thrombolysis in patients with acute ischemic stroke: a prospective observational study.** *Stroke* 2016;47:1584–92 CrossRef Medline
133. Nogueira RG, Zaidat OO, Castonguay AC, et al. **Rescue thrombectomy in large vessel occlusion strokes leads to better outcomes than intravenous thrombolysis alone: a 'real world' applicability of the recent trials.** *Interv Neurol* 2016;5:101–10 CrossRef Medline
134. Jansen I, Mulder M, Goldhoorn RJ, et al; on behalf of the MRCLEAN-Registry investigators (www.mrclean-trial.org). **MR CLEAN registry: a post-trial multicenter registry of intra-arterial treatment for acute ischemic stroke in the Netherlands.** In: *Proceedings of the International Stroke Conference,* February 21–24, 2017; Houston, Texas
135. Direct Transfer to an Endovascular Center Compared to Transfer to the Closest Stroke Center in Acute Stroke Patients with Suspected Large Vessel Occlusion (RACECAT). https://clinicaltrials.gov/ct2/show/NCT02795962. Accessed April 11, 2017
136. Legal Protections for Peer Review H-375.962: American Medical Association. https://searchpf.ama-assn.org/SearchML/searchDetails.action?uri=%2FAMADoc%2FHOD.xml-0-3167.xml. Accessed May 31, 2012
137. The Health Care Quality Improvement Act of 1986 (HCQIA), 42 USC §11101 et seq.
138. Suydam S, Liang BA, Anderson S, et al. **Patient safety data sharing and protection from legal discovery.** In: Henriksen K, Battles JB, Marks ES, Lewin DI, eds. *Advances in Patient Safety: From Research to Implementation* (*Volume 3: Implementation Issues). Advances in Patient Safety.* Rockville: Agency for Healthcare Research and Quality, 2005. https://www.ncbi.nlm.nih.gov/books/NBK20558/. Accessed January 20, 2018
139. Willner RB. Health Care Quality Improvement Act (HCQIA) of 1986. What is it? Why was it established? Is it working? http://www.peerreview.org/articles/HCQIQ.htm. Accessed May 31, 2012
140. H. R. 2—114th Congress: Medicare Access and CHIP Reauthorization Act of 2015. http://www.congress.gov/bill/114th-congress/house-bill/2. Accessed April 24, 2017
141. Hirsch JA, Harvey HB, Barr RM, et al. **Sustainable growth rate repealed, MACRA revealed: historical context and analysis of recent changes in Medicare physician payment methodologies.** *AJNR Am J Neuroradiol* 2016;37:210–14 CrossRef Medline
142. Hirsch JA, Leslie-Mazwi TM, Patel AB, et al. **MACRA: background, opportunities and challenges for the neurointerventional specialist.** *J Neurointerv Surg* 2016;8:868–74 CrossRef Medline
143. Berkhemer OA, Jansen IG, Beumer D, et al; MR CLEAN Investigators. **Collateral status on baseline computed tomographic angiography and intra-arterial treatment effect in patients with proximal anterior circulation stroke.** *Stroke* 2016;47:768–76 CrossRef Medline
144. Hussein HM, Georgiadis AL, Vazquez G, et al. **Occurrence and predictors of futile recanalization following endovascular treatment among patients with acute ischemic stroke: a multicenter study.** *AJNR Am J Neuroradiol* 2010;31:454–58 CrossRef Medline
145. Kim JT, Jahan R, Saver JL; SWIFT Investigators. **Impact of glucose on outcomes in patients treated with mechanical thrombectomy: a post hoc analysis of the Solitaire flow restoration with the intention for thrombectomy study.** *Stroke* 2016;47:120–27 CrossRef Medline
146. Institute of Medicine (US) Committee on Quality of Health Care in America; Kohn LT, Corrigan JM, Donaldson MS, editors. *To Err is Human: Building a Safer Health System.* Washington DC: National Academies Press; 2000

Targeting the Clot in Acute Stroke

Recent stroke trials have undeniably shown that thrombectomy is not just a safe method for treating acute stroke but also can extend the accepted time window considerably.[1,2] While most imaging techniques have rightly focused on first detecting hemorrhage or other sources of potential stroke mimics or the eventuality of cerebral hypoperfusion amenable to restoration through vascular techniques, very little research has focused on the thrombus itself. This is strange because it is the thrombus that has been the target of both pharmaceutical and interventional therapies because it is known to be the cause of the event. Imaging techniques such as CT perfusion and MR perfusion readily document the presence or absence of areas of perturbed perfusion that may be larger or smaller than expected, but these techniques would require a successful neuroprotective agent to fulfill their promises as techniques for full revascularization.

Currently, imaging needs to just demonstrate the absence of a hemorrhagic event and the presence of a clot for a decision to proceed to the angiography room. While the large-scale implementation of clot extraction using interventional techniques has allowed major advances with major improvement in clinical outcomes with fewer hemorrhages, selecting the right device for the right occlusion type will play a more important role. On the one hand, as has been the case with aneurysm treatment-planning, probably the clot location and thus its orientation will have an impact on the choice of catheters; it is also possible that looking at the clot itself and trying to deduce its composition could be helpful for deciding which patients undergo which therapy. Indeed, if a clot is more calcific, more fibrinous, or contains more blood cells, the management types may differ because the consistency will have an impact on retrieval and eventually on distal migration that might occur during the procedure. While in vitro studies may indeed be helpful to determine clot composition, determining the exact morphology and consistency of the clot will be necessary.

Indeed, some data are also available for MR imaging with the susceptibility vessel sign,[3] which demonstrates high erythrocyte content. Using modern CT techniques may be a way to further characterize these clots: Indeed, CT is, currently, the preferred technique of choice for the first evaluation of a patient with stroke, due to its sensitivity for hemorrhage.[4] The dense artery sign is a well-established sign of acute occlusion that corresponds to the presence of an occluding clot. The morphology and direction of the clot and the associated vessel morphology can be assessed by CTA; however, more exact information on clot composition might be extracted by further evaluation of the imaging characteristics of the clot.[5,6] Indeed, relatively simple measures of density could be helpful, but it may be difficult to differentiate high density due to red blood hemoglobin content from calcific changes. Therefore, additional measurements such as postcontrast images to assess eventual porosity or investigate calcification with dual-energy CT could quickly provide additional findings to help show clot composition that would guide an improved choice for thrombectomy-device selection. As with any imaging technique chosen to assess stroke, this will only provide another part of the information needed and is not a solution but could provide insight into clot composition to guide therapy. Also, as with most other imaging techniques, it should not interfere by prolonging unnecessary imaging time and thus time to therapeutic decision.

REFERENCES

1. Jovin TG, Chamorro A, Cobo E, et al; REVASCAT Trial Investigators. **Thrombectomy within 8 hours after symptom onset in ischemic stroke**. *N Engl J Med* 2015;372:2296–306 CrossRef Medline
2. Nogueira RG, Jadhav AP, Haussen DC, et al; DAWN Trial Investigators. **Thrombectomy 6 to 24 hours after stroke with a mismatch between deficit and infarct.** *N Engl J Med* 2018;378:11–21 CrossRef Medline
3. Liu H, Mei W, Huang Y, et al. **Susceptibility vessel sign predicts poor clinical outcome for acute stroke patients untreated by thrombolysis.** *Exp Ther Med* 2017;14:5207–13 CrossRef Medline
4. Bouchez L, Sztajzel R, Vargas MI, et al. **CT imaging selection in acute stroke.** *Eur J Radiol* 2017;96:153–61 CrossRef Medline
5. Bouchez L, Lovblad KO, Kulcsar Z. **Pretherapeutic characterization of the clot in acute stroke.** *J Neuroradiol* 2016;43:163–66 CrossRef Medline
6. Bouchez L, Altrichter S, Pellaton A, et al. **Can clot density predict recanalization in acute ischemic stroke treated with intravenous tPA?** *Clinical and Translational Neuroscience* 2017;1:1–6 CrossRef

K.-O. Lövblad
Division of Diagnostic and Interventional Neuroradiology
Geneva University Hospitals
Geneva, Switzerland

http://dx.doi.org/10.3174/ajnr.A5600

Consensus Needed for Noncontrast CT Markers in Intracerebral Hemorrhage

We read with interest the article by Ng et al, in which the authors investigated associations between the "swirl sign" and hematoma growth. Ng et al found that patients positive for the swirl sign demonstrated larger hemorrhage volumes and higher odds of subsequent hemorrhage expansion (HE).[1]

As the authors mention, accurately predicting HE is key for targeting those patients at higher risk of this ominous outcome, hence deemed to be most likely to benefit from expansion-targeted treatment such as intensive blood pressure lowering or hemostatic treatment. Consequently, acute imaging biomarkers associated with HE have been the subject of intense research effort. In this context, the article by Ng et al would have thus benefited from a more complete and comprehensive account of the relevant literature in the field. As it stands, references beyond the spot sign are only seldom, if at all, cited in the current article.

Indeed, the first convincing evidence of a relationship between hemorrhage heterogeneity and intracerebral hemorrhage (ICH) outcome came as early as 2008.[2] After that, a number of studies investigated several aspects of acute intracerebral hemorrhage using noncontrast CT to look for HE and outcome, coining a new term for each of those particular aspects ("black hole sign," "island sign," "satellite sign," "blend sign," "density heterogeneity scale," and so forth).[2] One downside of giving a different name to each individual sign in the literature is that it may gray out their potential translation in clinical practice by a profusion of potentially overlapping sets of findings. For instance, because the black hole sign represents a subcategory of the swirl sign and because an important degree of heterogeneity should characterize the presence of all "swirls" and "black holes," the relative value of each of these findings is very hard to evaluate pragmatically.[2]

There is little remaining doubt that ICH heterogeneity based on noncontrast CT is associated with more frequent hemorrhagic expansion and poorer clinical outcome. However, there is considerable overlap between different noncontrast CT predictors of HE, with lack of consensus on the diagnostic criteria to identify these markers. Hence, future research should aim to homogenize the ever-growing terminology of signs predicting HE, analyzing whether they ought to be used for patient selection in ICH trials and validation studies. Because one of the common features of these markers is the presence of a hypodense area within the hyperdense acute hematoma, their simplest descriptive characterization (eg, "presence of hypodense area encapsulated in the hematoma, with no contact with the hemorrhage margin") is the most replicable and straightforward way of assessing hemorrhage heterogeneity. In fact, in a cohort of 1029 patients, we found that the presence of any hypodensity was strongly associated with ICH expansion[3] and outcome[4] and that dividing these hypodensities into their various aspects (corresponding to the above-mentioned markers, including the swirl sign investigated by Ng et al) did not change their predictive ability for HE, independent of power issues.[3]

In a large post hoc analysis of patients enrolled in the Antihypertensive Treatment of Acute Cerebral Hemorrhage II (ATACH-II) randomized controlled trial, there was no evidence that patients with these markers, hypothesized to be at the highest risk of expansion, specifically benefited from intensive blood pressure reduction aimed at limiting hemorrhage growth.[5] These and other findings reinforce the notion that these individual markers may not be sufficient, sensitive, or calibrated enough to identify target patients for such therapies with high sensitivity and specificity.

While there is hope of finding better acute therapeutic approaches for patients with ICH, harmonizing nomenclature terminology, scales, and assessment methods is the way forward.

REFERENCES

1. Ng D, Churilov L, Mitchell P, et al. **The CT swirl sign is associated with hematoma expansion in intracerebral hemorrhage.** *AJNR Am J Neuroradiol* 2018;39:232–37 CrossRef Medline
2. Boulouis G, Morotti A, Charidimou A, et al. **Noncontrast computed tomography markers of intracerebral hemorrhage expansion.** *Stroke* 2017;48:1120–25 CrossRef Medline
3. Boulouis G, Morotti A, Brouwers HB, et al. **Association between hypodensities detected by computed tomography and hematoma expansion in patients with intracerebral hemorrhage.** *JAMA Neurol* 2016;73:961–68 CrossRef Medline
4. Boulouis G, Morotti A, Brouwers HB, et al. **Noncontrast computed tomography hypodensities predict poor outcome in intracerebral hemorrhage patients.** *Stroke* 2016;47:2511–16 CrossRef Medline
5. Morotti A, Boulouis G, Romero JM, et al; ATACH-II and NETT investigators. **Blood pressure reduction and noncontrast CT markers of**

http://dx.doi.org/10.3174/ajnr.A5604

intracerebral hemorrhage expansion. *Neurology* 2017;89:548–54
CrossRef Medline

G. Boulouis
Department of Neuroradiology
Institut National de la Santé et de la Recherche Médicale Unite Mixte de Recherche 894
Centre Hospitalier Sainte-Anne, Université Paris-Descartes
Paris, France
Department of Neurology, Hemorrhagic Stroke Research Program
Massachusetts General Hospital Stroke Research Center, Harvard Medical School
Boston, Massachusetts
A. Charidimou
Department of Neurology, Hemorrhagic Stroke Research Program
Massachusetts General Hospital Stroke Research Center, Harvard Medical School
Boston, Massachusetts
A. Morotti
Stroke Unit
Istituto Di Ricovero e Cura a Carattere Scientifico Mondino Foundation
Pavia, Italy

Increasing the Accuracy of Optic Nerve Measurement Using 3D Volumetry

We read with much interest the article by Hoffmann et al in the February 2018 issue of the *American Journal of Neuroradiology* regarding the measurement of the optic nerve using MR imaging on pediatric patients. The authors provided values for optic nerve sizes correlated with the ages of enrolled children.

However, despite stating in their introduction that the use of new volumetric methods with thin-cut images could help obtain accurate measurements, they provided only 2D measurements of the optic nerve using 2D sequences, which are less accurate and reproducible than volumetric data.[1] Volumetry is dependent on neither orbital morphology nor volume nor on the disposition and course of the optic nerve. Optic nerves are flexible structures with a unique orbital fixed anchor point at the apex. Thus, they easily stretch or become lax in their orbital portion, especially in the case of orbital diseases such as optic neuropathy or optic nerve tumors. Intraorbital portion length varies among individuals. Optic nerves may have a tortuous or stretched path in the case of intracranial hyper- or hypotension, respectively. Therefore, 2D measurements obtained from 2 fixed distances at 3 and 7 mm posterior to the lamina cribrosa in the axial plane as performed in this article vary so much among individuals that the authors' conclusions could be questioned.

Moreover, the measurements of the optic nerve in the coronal plane are inaccurate due to the oblique course of the nerve. The use of coronal acquisitions orthogonal to the nerve is mandatory to provide accurate measurements. Thus, coronal diameters are probably overestimated in this article. Some authors suggest measuring the mean cross-sectional area of the intraorbital portion of each optic nerve,[2] but volumetric measurements are better and more accurate.[3]

The use of STIR sequences is also questionable because this sequence has the disadvantage of producing a high signal from CSF, obscuring the edge of the optic nerve and, consequently, blocking a clear image of the optic nerve sheath. The optic nerves were reported to be about 20% greater than with a FLAIR sequence.[2]

Thus, the measurements of the optic nerve provided in this article should be used with caution.

To correct these weaknesses and provide the most accurate measurements of the optic nerve, we advise developing a prospective study with the same MR imaging acquisitions on the same MR imaging device for all patients, preferably using high-field MR imaging (3T or more), including 3D high-spatial-resolution sequences with inframillimetric slices without gaps. Fat- and CSF-saturated sequences with high signal and contrast-to-noise ratio should be used. Acquisition time should remain short to avoid kinetic artifacts. Patients should be advised to look at a fixed point in the MR imaging to avoid eye movement, which may modify the course of the optic nerve.

Automatic or semiautomatic volumetry can be easily performed on many posttreatment software packages. In a routine radiologic setting, image postprocessing with quantitative analysis can be achieved rapidly (10 minutes) by experienced radiologists.[1,3] Volumetry has been widely validated in neurologic and orbital studies and is reproducible.[1,4]

Finally, we agree with the authors that there is a need to establish a standardized method for the measurement of the optic nerve on MR imaging, but we believe that volumetric measurements should be made including the entire volume of the optic nerve starting from the papilla and ending at the point of convergence of the extraocular muscles at the tendinous ring of the orbital apex,[1] or ending at the chiasma, to provide accurate and reproducible measurements.

REFERENCES

1. Hoffmann J, Schmidt C, Kunte H, et al. **Volumetric assessment of optic nerve sheath and hypophysis in idiopathic intracranial hypertension.** *AJNR Am J Neuroradiol* 2014;35:513–18 CrossRef Medline
2. Hickman SJ, Brex PA, Brierley CM, et al. **Detection of optic nerve atrophy following a single episode of unilateral optic neuritis by MRI using a fat-saturated short-echo fast FLAIR sequence.** *Neuroradiology* 2001;43:123–28 CrossRef Medline
3. Agid R, Farb RI, Willinsky RA, et al. **Idiopathic intracranial hypertension: the validity of cross-sectional neuroimaging signs.** *Neuroradiology* 2006;48:521–27 CrossRef Medline
4. Maresky HS, Ben Ely A, Bartischovsky T, et al. **MRI measurements of the normal pediatric optic nerve pathway.** *J Clin Neurosci* 2018;48:209–13 CrossRef Medline

A. Lecler
J. Savatovsky
Department of Radiology
C. Lamirel
Department of Ophthalmology
Fondation Ophtalmologique Adolphe de Rothschild
Paris, France

http://dx.doi.org/10.3174/ajnr.A5625

REPLY:

We would like to thank Drs Lecler, Savatovsky, and Lamirel for taking the time to read and comment on our article and propose valuable suggestions.

As noted by Drs Lecler, Savatovsky, and Lamirel, the volumetric method is the technique expected to yield the most accurate measurements with a high reproducibility, should the same software be used. However, although made more accessible with automated techniques, 3D measurements remain time-consuming and require specific software; they are thus not commonly obtained in everyday clinical practice. Despite being less accurate, 2D measurements have the advantages of being more widely used in clinical practice and easily performed, and thus are of higher clinical relevance than 3D ones, which are more likely to be reserved for research purposes.

Our study, therefore, tried to find a balance of accuracy, reproducibility, and practicality in a clinical setting. We do agree that a prospective study taking into account all the commenters' suggestions with additional 3D sequences of the orbit would be very valuable because 3D measurements of the optic nerve (ON) have not been reported yet, to our knowledge. It would be interesting to examine volumetric measurements of the optic nerve and correlate them with the more accessible 2D measurements in a future study. The only article that performed volumetric measurements that was cited in the comment letter did not measure the ON proper but rather the ON sheath in idiopathic intracranial hypertension, which would further increase the gap between the ON diameter and the ON sheath diameter.[1]

Dr Lecler and colleagues also highlighted an important point to consider with respect to the flexibility of the optic nerve structures and how the intraorbital portion length may vary, especially in orbital/optic nerve diseases. Being aware of such variability and given that our study aimed at providing normative data of the ON in the pediatric age group, we included only orbital MRIs with normal findings and excluded patients with diseased optic pathways, systemic diseases, and tumors.

Our main study objective was to provide normative data of pediatric ON measurements that would be easily reproducible in a clinical setting. We therefore excluded measurements considered difficult to reproduce, mainly cases with tortuous or oblique ONs; this feature explains the different number of measurements reported for each cut in Table 2. Measurements were performed similarly in all patients in the axial and coronal planes obtained perpendicular to the long axis of the nerve and thus were considered reproducible. Furthermore, the reproducibility of the measurements was documented by the results of the interrater correlation. The ON measurements were obtained by 2 raters with different levels of expertise, yet still yielded good agreement, with a high interrater correlation coefficient of 0.842.

We used STIR or T1 inversion recovery sequences to conduct our measurements. These sequences are excellent in differentiating the ON from the surrounding CSF, and we therefore found no difficulty defining the edge of the ON. On the other hand, the FLAIR sequence mentioned by Dr Lecler and colleagues is useful in assessing ON abnormal signal in optic neuropathy, but it seems less useful for detecting ON atrophy as concluded by Boegel et al.[2]

The suggestion to fixate the eyes during scanning to avoid eye movements seems valid for our older study group; however, eye fixation could not be controlled in the younger population in which MR imaging was mostly performed under sedation. We do believe that our reported 2D normative ON measurements in the pediatric age group would be a valuable aid to the neuroradiologist, neuro-ophthalmologist, and pediatric ophthalmologist in an everyday clinical setting.

http://dx.doi.org/10.3174/ajnr.A5647

REFERENCES

1. Hoffmann J, Schmidt C, Kunte H, et al. **Volumetric assessment of optic nerve sheath and hypophysis in idiopathic intracranial hypertension.** *AJNR Am J Neuroradiol* 2014;35:513–18 CrossRef Medline
2. Boegel KH, Tyan AE, Iyer VR, et al. **Utility of coronal contrast-enhanced fat-suppressed FLAIR in the evaluation of optic neuropathy and atrophy.** *Eur J Radiol Open* 2017;4:13–18 CrossRef Medline

C.E. Al-Haddad
Department of Ophthalmology
M.G. Sebaaly
Department of Diagnostic Radiology
American University of Beirut Medical Center
Beirut, Lebanon
R.N. Tutunji
Department of Diagnostic Radiology
American University of Beirut Medical Center
Beirut, Lebanon
Donders Institute for Brain, Cognition and Behaviour
Department of Cognitive Neuroscience
Radboud University Medical Centre
Nijmegen, the Netherlands
C.J. Mehanna
Department of Ophthalmology
S.R. Saaybi
Department of Pediatrics
A.M. Khamis
Clinical Research Institute
R.G. Hourani
Department of Diagnostic Radiology
American University of Beirut Medical Center
Beirut, Lebanon

On-line Table 1: First author's institution origin in American neuroscience literature from 1997 to 2017

Year, Field	% American	% Asian[a]	Most Frequent Non-American Country
1997			
Neurology	50.77	7.69	Canada
Neurosurgery	56.67	20	Japan
Neuroradiology	57.58	15.15	Japan
1998			
Neurology	53.57	7.14	Germany, Italy
Neurosurgery	58.62	10.34	Germany, Japan
Neuroradiology	66.67	5.88	UK
1999			
Neurology	34.15	12.2	Canada, UK, Germany, Japan
Neurosurgery	50	18.76	Japan
Neuroradiology	23.91	17.39	Germany, Japan
2000			
Neurology	47.83	17.39	Japan
Neurosurgery	46.15	7.69	Canada, UK
Neuroradiology	52.94	20.58	Italy, Japan, Korea
2001			
Neurology	37.84	0	Germany
Neurosurgery	25	22	Japan
Neuroradiology	45.71	14.28	France, Japan
2002			
Neurology	46.67	6.66	UK
Neurosurgery	48.57	22.86	Japan
Neuroradiology	58.06	12.91	Japan
2003			
Neurology	57.41	1.85	UK
Neurosurgery	57.50	10	Canada, Japan
Neuroradiology	45.83	8.33	Germany, France
2004			
Neurology	50.82	6.56	France
Neurosurgery	56.76	18.92	Japan
Neuroradiology	37.50	18.74	Japan
2005			
Neurology	50.98	3.92	Germany, France, Italy, Israel
Neurosurgery	56.25	21.88	Japan
Neuroradiology	43.75	20.32	Japan
2006			
Neurology	44.90	8.16	Canada
Neurosurgery	60.61	6.06	Canada, Germany
Neuroradiology	33.33	24.06	France, Japan
2007			
Neurology	50.82	8.2	the Netherlands
Neurosurgery	43.24	21.62	Japan
Neuroradiology	60.87	13.03	UK, Japan
2008			
Neurology	56.67	1.67	France, the Netherlands, Sweden
Neurosurgery	45.71	11.43	Germany
Neuroradiology	36.73	18.36	the Netherlands
2009			
Neurology	54.72	1.89	UK, Germany
Neurosurgery	50.00	6.52	Canada
Neuroradiology	40.63	17.19	UK, Japan
2010			
Neurology	40.38	7.69	UK, Germany, the Netherlands
Neurosurgery	66.67	2.08	France, Germany
Neuroradiology	39.53	18.61	Japan
2011			
Neurology	56.36	1.82	France
Neurosurgery	45.83	20.84	Japan
Neuroradiology	33.33	15.55	Germany
2012			
Neurology	45.31	4.68	UK
Neurosurgery	52.86	18.57	Canada
Neuroradiology	28	30	Germany

Continued on next page

On-line Table 1: Continued

Year, Field	% American	% Asian[a]	Most Frequent Non-American Country
2013			
Neurology	42.86	4.08	UK
Neurosurgery	56.25	16.66	Japan
Neuroradiology	36	18	Canada
2014			
Neurology	37.74	13.2	Germany
Neurosurgery	60.47	4.65	France, Turkey, Australia
Neuroradiology	37.97	7.61	Germany
2015			
Neurology	45.10	1.96	UK, Germany
Neurosurgery	40.00	17.77	Canada, Italy, Japan
Neuroradiology	23.21	32.15	China
2016			
Neurology	31.67	10	UK
Neurosurgery	55.36	17.86	China
Neuroradiology	22.81	14.02	Germany
2017			
Neurology	38.60	10.52	Italy, Japan
Neurosurgery	53.70	11.11	Canada, Germany
Neuroradiology	45.16	12.9	China
Total			
Neurology	46.79	6.52	UK
Neurosurgery	51.98	14.77	Japan
Neuroradiology	40.38	16.84	Japan

[a] Asian countries included China, Japan, South Korea, Thailand, Taiwan, and Singapore.

On-line Table 2: Comparison of average number of citations between American and non-American authors

Year, Field	Average American Citations	Average Non-American Citations
1997		
Neurology	233.42	85.96
Neurosurgery	86.41	97.38
Neuroradiology	110.63	55.64
1998		
Neurology	160.53	152.26
Neurosurgery	74.58	100
Neuroradiology	78	96.70
1999		
Neurology	77.92	198.37
Neurosurgery	71.25	58.06
Neuroradiology	284	170
2000		
Neurology	200.90	144.83
Neurosurgery	170.58	67.85
Neuroradiology	110.11	110.43
2001		
Neurology	174.14	175.73
Neurosurgery	82.77	95.62
Neuroradiology	103.43	120.26
2002		
Neurology	118	100.04
Neurosurgery	116.88	56.77
Neuroradiology	124.72	126.76
2003		
Neurology	136.83	115.47
Neurosurgery	101.30	96.29
Neuroradiology	68.59	100.07
2004		
Neurology	132.09	81.53
Neurosurgery	66.23	45.37
Neuroradiology	115.44	58.36
2005		
Neurology	166.69	109.32
Neurosurgery	77.44	38.07
Neuroradiology	144.92	139.25
2006		
Neurology	218.72	93.51
Neurosurgery	79.95	43.92
Neuroradiology	52.94	70.77
2007		
Neurology	121.45	152.23
Neurosurgery	67.75	45.28
Neuroradiology	81.78	49.05
2008		
Neurology	114	74.73
Neurosurgery	48.62	41.57
Neuroradiology	98.61	80.06
2009		
Neurology	103.86	93.08
Neurosurgery	42.17	28.95
Neuroradiology	54.23	65.89
2010		
Neurology	55.71	56.32
Neurosurgery	53.87	34.87
Neuroradiology	41.05	33.57
2011		
Neurology	65.06	95.41
Neurosurgery	41.86	32.84
Neuroradiology	38.86	32.96
2012		
Neurology	62.68	68.42
Neurosurgery	32.29	36.42
Neuroradiology	36.92	31.72
2013		
Neurology	83.23	45.96
Neurosurgery	28.44	18.76
Neuroradiology	29.61	25.87
2014		
Neurology	31.3	27.51
Neurosurgery	18.65	17.76
Neuroradiology	20.96	26.75
2015		
Neurology	24.47	23.89
Neurosurgery	11.66	11.88
Neuroradiology	11.84	13.79
2016		
Neurology	9.78	8.63
Neurosurgery	7.41	6.88
Neuroradiology	7	6.04
2017		
Neurology	1.31	2.05
Neurosurgery	2.27	1.88
Neuroradiology	0.82	1.08
Total		
Neurology	113.05	85.25
Neurosurgery	53.24	42.79
Neuroradiology	73.62	60.85

On-line Table 2: Continued

On-line Table: Demographic and clinical characteristics of the patient cohort

Pt. ID	Age (yr)	Sex	Pathology	Therapy Type	Total Prebevacizumab Operations	Prebevacizumab Surgical Extent	*IDH1* Status	*MGMT* Status	*EGFR* Amplification	Steroid Dose Prebevacizumab (mg/day)[c]	Steroid Dose Postbevacizumab (mg/day)[c]	PFS (mo)	OS (mo)	Malignant Transformation
1	49	M	GBM[a]	BEV + CARBO	3[b]	GTR				6	12	3.94	4.46	
2	63	F	GBM[a]	BEV + TMZ	2	STR				0	0	7.75	11.89	
3	58	F	GBM	BEV + irinotecan	1	STR		U	N	1	1	1.38	3.06	
4	59	F	GBM	MONO	1	GTR	WT	U		4	4	4.17	5.02	
5	56	M	GBM	BEV + CARBO	1	STR				2	2	3.58	7.68	
6	73	M	GBM	MONO	1	GTR				2	2	3.02	11.63	
7	53	F	GBM	BEV + CCNU	2	GTR				1	1	7.43	9.85	
8	65	M	GBM	BEV + CCNU	3	STR	WT		Y	2	2	6.44	6.89	
9	61	M	GBM	BEV + CCNU	2[b]	STR	WT			0	4	11.73	11.79	
10	36	M	AO[a]	MONO	2	STR	WT	U	N	2	2	5.16	6.89	Y
11	54	M	GBM	BEV + dasatinib	1	GTR			N	1	8	1.54	1.54	
12	65	M	GBM	MONO	2	GTR	WT	U	N	6	6	7.1	8.08	
13	49	F	GBM	BEV + dasatinib	1	STR	WT		N	16	2	2.66	4.59	
14	34	M	GBM[a]	BEV + CARBO	2	STR				2	6	3.61	7.52	
15	60	F	GBM	MONO	1	STR			N	4	4	11.47	13.56	
16	53	M	GBM	MONO	2	STR	WT		Y	2	2	0.92	2.95	
17	63	M	GBM	MONO	1	GTR	WT	U	Y	8	2	6.24	6.80	
18	62	M	AO	BEV + irinotecan	5	STR	MUT	M	N	4	8	3.45	4.86	Y
19	49	M	AA	MONO	2	STR	WT		Y	0	0	19.32	19.31	Y
20	46	M	GBM	BEV + single CCNU	4	GTR	WT	U	Y	4	2	5.13	8.60	
21	45	M	GBM[a]	BEV + CCNU	2	STR	MUT	U	N	1	2	2.53	4.27	
22	33	F	AA	MONO	1	STR	MUT		N	0	4	1.84	17.57	
23	61	M	GBM	BEV + CCNU	1	GTR	WT			6	6	1.58	2.26	
24	31	F	GBM[a]	MONO	2	GTR			N	2/1 QOD	2/1 QOD	2.37	2.37	
25	65	M	GBM	MONO	2	STR	WT	U	Y	8	8	6.69	6.69	
26	74	M	GBM	MONO	1	GTR	WT	M	Y	6	6	4.3	4.41	
27	66	M	GBM	BEV + TMZ	1	STR				6	1.75	2.69	4.23	
28	53	M	GBM	MONO	1	STR				0	8	5.85	6.21	
29	37	M	GBM	BEV + TMZ	2	STR				0	0	2.99	9.92	
30	59	M	GBM[a]	BEV + CARBO	2	STR			Y	1	1.5	0.99	3.38	
31	61	F	GBM	BEV + CARBO	2[b]	STR	WT		Y	0[d]	16	12.85	23.55	
32	58	F	GBM	MONO	2	GTR			N	0	0	5.29	7.72	
33	67	M	GBM	MONO	1	GTR				2	1.5	2.1	5.09	

Note:—Pt. ID indicates Patient Identification; AO, anaplastic oligodendroglioma; AA, anaplastic astrocytoma; BEV, bevacizumab; CARBO, carboplatin; TMZ, temozolomide; MONO, monotherapy; CCNU, lomustine; WT, wild type; MUT, mutant; U, unmethylated; M, methylated; QOD, every other day; Y, yes; N, no.

[a] Pathologic diagnosis at time of recurrence.

[b] Patient received an additional operation after bevacizumab treatment.

[c] Dexamethasone (Decadron) dosage during time of MRI.

[d] Prednisone 60 mg/day for 5 days, no dexamethasone (Decadron).

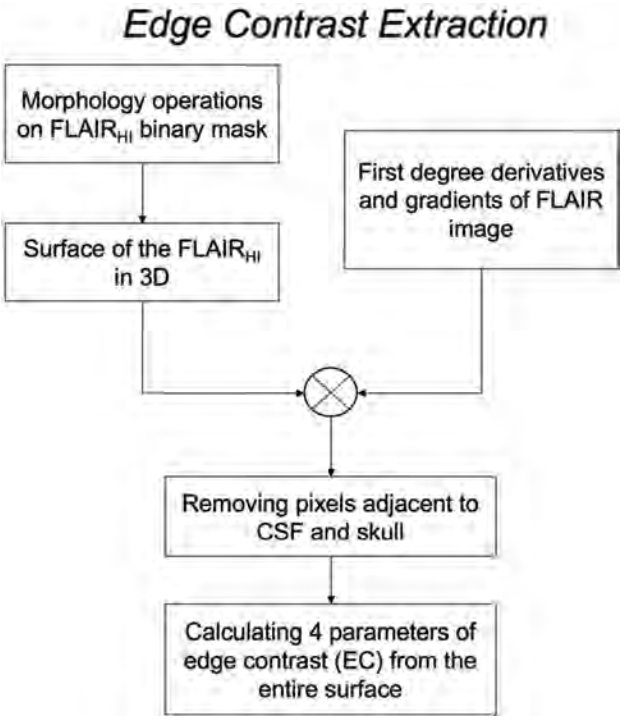

ON-LINE FIG 1. Flowchart of edge contrast extraction.

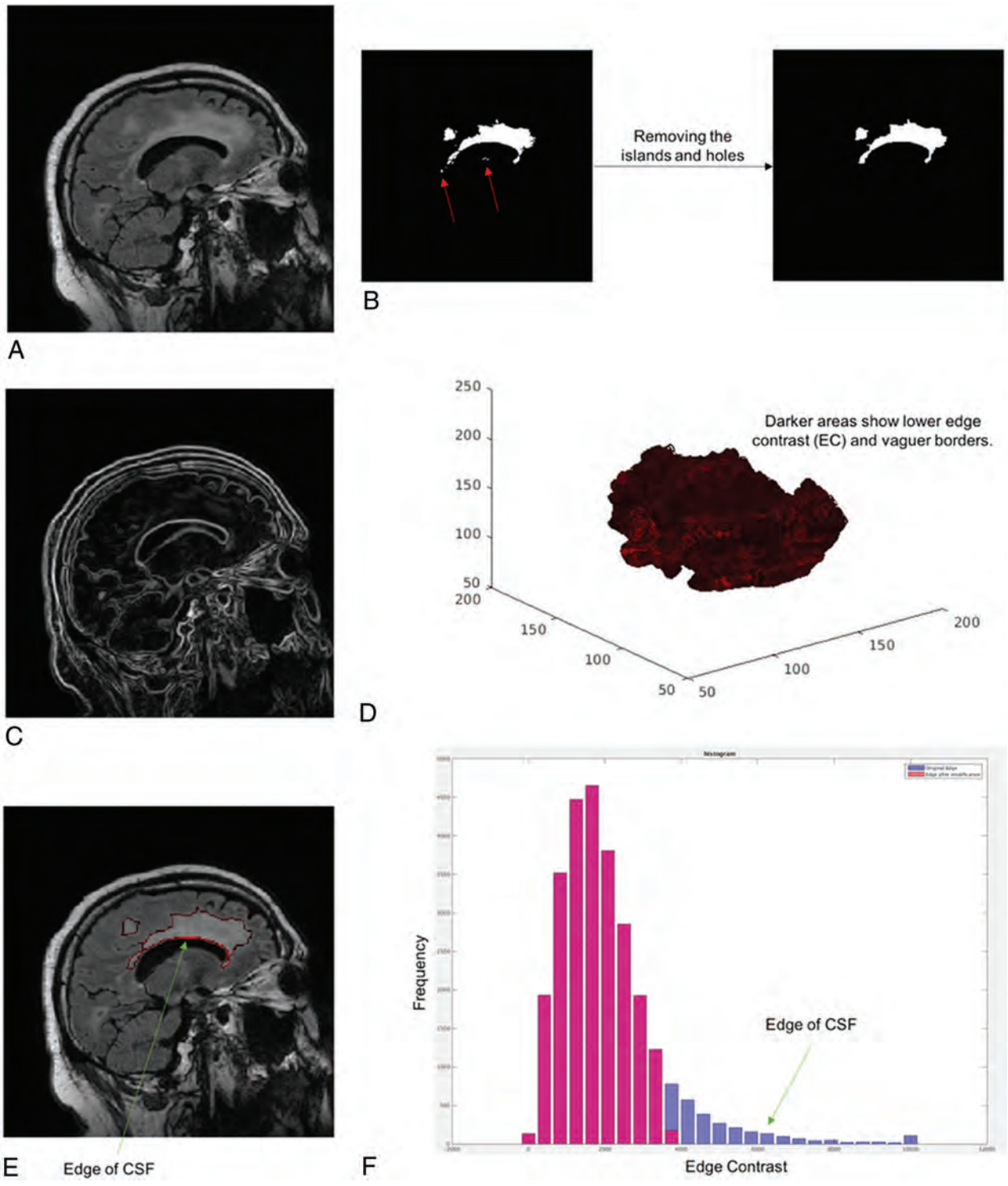

ON-LINE FIG 2. The outcome of processing steps. *A*, FLAIR with a hyperintense mass. *B*, The morphology preprocessing on the hyperintense mask and cleaning the mask by removing the islands and holes. *C*, 3D gradient image of FLAIR. *D*, 3D of the hyperintense mass in which the dark intensity indicates low EC. *E*, The overlap of the hyperintense gradient with the cleaned mask. *F*, The cleaned edges next to CSF.

On-line Table 1: Characteristics of the study population of radionecrosis

No.	Age (yr)	Sex	Origin	Location	Area (cm)	$T1_{5min}$ (ms)	$T1_{60min}$ (ms)	$T1_{differ}$ (ms)	Dose (Gy)	rCBV
1	56	Female	Lung	Occipital	3.24	1144.89	871.05	−273.84	15	1.16
2	48	Female	Lung	Cerebellum	2.31	899.17	961.02	61.85	18	1.18
3	53	Male	DT	Cerebellum	2.14	1058.66	875.97	−182.69	15	1.2
4[a]	72	Female	Lung	BG	1.75	1016.39	827.55	−188.84	21	0.86
5	58	Female	Lung	Parietal	0.86	857.93	496.47	−361.46	24	1.05
6	67	Male	Skin	Parietal	0.69	765.92	678.77	−87.15	24	1.12
7	61	Female	Lung	Frontal	2.52	679.11	604.96	74.15	18	0.66
8	73	Male	Lung	Occipital	1.68	934.36	785.82	−175.54	21	0.83
9[a]	56	Female	Breast	Occipital	1.27	1034.6	770.94	263.66	21	0.92
10	57	Male	DT	Frontal	1.83	1122.11	785.36	−336.75	21	2.24
11	50	Female	Lung	Parietal	3.5	1038.51	930.87	−107.64	15	1.08
12	62	Female	Breast	Cerebellum	2.48	1431.2	1048.12	−383.08	18	0.76
13	65	Female	Lung	Brain stem	2.12	742.84	809.64	66.80	18	1.73
14[a]	52	Male	Lung	Temporal	1.22	846.72	723.4	−123.32	21	0.97
15	69	Female	Lung	Occipital	3.84	1224.35	885.25	−39.10	15	1.49
16	57	Female	Skin	Parietal	1.61	980.76	690.69	290.07	21	1.24
17	74	Male	Lung	Occipital	2.46	1154.23	875.42	−278.81	18	1.12
18	54	Male	Kidney	Cerebellum	1.78	885.76	572.68	−313.08	21	0.87
19	52	Male	Lung	Frontal	1.22	740.56	621.45	−119.11	24	1.43
20	61	Male	Lung	Occipital	1.34	838.34	754.72	−83.62	21	0.56
21	63	Female	Lung	Occipital	1.92	1180.57	1040.87	−139.7	21	1.35
22	46	Female	Breast	Frontal	3.59	700.73	574.76	125.97	15	1.61
23	80	Male	Skin	BG	2.78	1043.31	956.63	−86.68	18	0.62
24[a]	58	Male	Lung	Parietal	2.18	819.64	721.99	−97.65	18	0.92
25	61	Male	Kidney	Temporal	2.32	929.34	978.25	48.91	18	1.44
26	73	Female	Lung	Frontal	1.64	549.4	566.54	17.14	21	1.31
27	48	Female	Breast	Temporal	2.75	876.39	857.46	−18.93	18	0.58
28[a]	68	Male	Lung	Occipital	2.45	837.06	692.34	−144.72	18	1.27
29	38	Male	Lung	Cerebellum	2.28	1042.92	1129.78	86.86	18	1.34

Note:—DT indicates digestive tract; BG, basal ganglia.
[a] Histopathologic diagnosis was performed.

On-line Table 2: Characteristics of the study population of tumor recurrence

No.	Age (yr)	Sex	Origin	Location	Area (cm)	$T1_{5min}$ (ms)	$T1_{60min}$ (ms)	$T1_{differ}$ (ms)	Dose (Gy)	rCBV
1	75	Male	Lung	Frontal	3.57	698.87	774.29	75.42	15	2.87
2[a]	54	Female	DT	Frontal	3.46	457.38	765.01	307.63	15	2.33
3	70	Male	Kidney	Occipital	4.02	1329.58	1462.9	133.32	15	2.87
4	48	Male	Lung	Parietal	1.15	683.42	626.42	−57.00	21	2.44
5	48	Male	Lung	Frontal	1.62	539.18	1039.3	500.12	21	2.15
6	59	Female	Skin	Cerebellum	1.86	922.02	1142.69	220.67	21	2.25
7[a]	66	Female	Lung	BG	0.64	1165.44	1717.84	552.4	24	2.52
8	50	Male	DT	Cerebellum	1.23	1263.92	1414.07	150.15	21	4.46
9	77	Female	Breast	Parietal	2.34	568.56	905.96	337.4	18	1.37
10	62	Male	Lung	Brain stem	2.47	942.66	1161.95	219.29	18	2.08
11	64	Female	Lung	BG	0.99	946.17	1160.32	214.15	24	2.89
12	55	Female	Breast	Occipital	2.74	774.32	1023.62	249.3	18	2.65
13[a]	59	Male	Lung	Parietal	3.35	867.16	1123.93	256.77	18	3.13
14	40	Female	Breast	Frontal	3.86	845.08	897.68	52.6	15	1.32
15	59	Female	Lung	Temporal	3.32	822.02	930.9	108.88	18	1.75
16	72	Male	DT	Frontal	1.73	914.37	883.31	−31.06	21	1.09
17	57	Female	Lung	Frontal	1.96	394.14	567.76	173.62	21	4.78
18	46	Female	Breast	Cerebellum	1.33	822.57	1042.98	220.41	24	3.37
19	55	Female	Lung	Occipital	2.56	568.23	719.73	151.5	18	2.76
20	41	Male	Lung	Cerebellum	1.82	504.42	773.86	44.21	21	3.68
21[a]	53	Male	Lung	Parietal	2.48	817.41	847.93	30.52	18	1.45
22	52	Female	Lung	Temporal	4.32	622.67	1025.32	402.65	15	3.45
23	61	Female	DT	Parietal	3.66	923.65	1166.96	243.31	15	3.08
24	80	Male	Lung	Frontal	2.74	516.7	664.44	147.74	18	4.6
25[a]	58	Male	Lung	Parietal	2.49	668.16	688.28	20.12	18	2.57
26	70	Female	Kidney	Cerebellum	3.25	1134.46	1456.32	321.86	18	2.29
27	55	Male	Lung	Parietal	2.67	777.82	980.94	203.12	21	2.19

Note:—DT indicates digestive tract; BG, basal ganglia.
[a] Histopathologic diagnosis was performed.

On-line Table 1: Kurtosis and conventional diffusion metric values in the solid region of the tumor and the contralateral NAWM[a]

Region	MK	AK	RK	FA	MD	ADC
LGMs	0.88 (0.81∼0.94)	0.80 (0.72∼0.85)	0.93 (0.85∼0.99)	0.20 (0.14∼0.30)	1.44 (1.14∼1.55)	0.73 (0.67∼0.82)
HGMs	1.02 (0.91∼1.08)	0.90 (0.81∼0.96)	1.08 (0.97∼1.16)	0.19 (0.16∼0.29)	1.32 (1.12∼1.44)	0.63 (0.60∼0.71)
NAWM	1.01 (0.98∼1.05)	0.85 (0.83∼0.87)	1.10 (1.08∼1.15)	0.36 (0.35∼0.38)	1.42 (1.14∼1.54)	0.60 (0.59∼0.63)
P value	.001	.001	.001	.925	.116	.003

Note:—NAWM indicates normal-appearing white matter.
[a] Data are medians, with interquartile ranges in parentheses.

On-line Table 2: Interobserver variability in measurements of meningiomas

Region/Metrics	Intraclass Correlation Coefficient, 95% CI for Interobserver
Solid region of the tumor	
MK	0.983, 0.969–0.990
AK	0.979, 0.963–0.989
RK	0.957, 0.923–0.976
MD	0.984, 0.971–0.991
FA	0.993, 0.987–0.996
ADC	0.801, 0.603–0.892
NAWM	
MK	0.986, 0.975–0.992
AK	0.929, 0.873–0.961
RK	0.907, 0.833–0.948
MD	0.947, 0.905–0.971
FA	0.827, 0.688–0.904
ADC	0.984, 0.970–0.991

Note:—NAWM indicates normal-appearing white matter.

On-line Table 3: Comparisons of AUCs among normalized MK, AK, RK, FA, MD, and ADC (part 1)

Comparison	Statistic	MK-AK	MK-RK	MK-FA	MK-MD	MK-ADC
LGMs-HGMs	*P*	.683	.221	.002[a]	.038[a]	.135
	Z	0.409	1.223	3.101	2.080	1.496

Note:—AUC indicates area under the curve.
[a] Significant.

On-line Table 4: Comparisons of AUCs among normalized MK, AK, RK, FA, MD, and ADC (part 2)

Comparison	Statistic	AK-RK	AK-FA	AK-MD	AK-ADC	RK-FA
LGMs-HGMs	*P*	.740	<.001[a]	.076	.204	.007[a]
	Z	0.332	3.533	1.776	1.271	2.712

Note:—AUC indicates area under the curve.

[a] Significant.

On-line Table 5: Comparisons of AUCs among normalized MK, AK, RK, FA, MD, and ADC (part 3)

	Statistic	RK-MD	RK-ADC	FA-MD	FA-ADC	MD-ADC
LGMs-HGMs	*P*	.197	.456	.021[a]	.019[a]	.771
	Z	1.289	0.746	2.303	2.340	0.291

Note:—AUC indicates area under the curve.

[a] Significant.

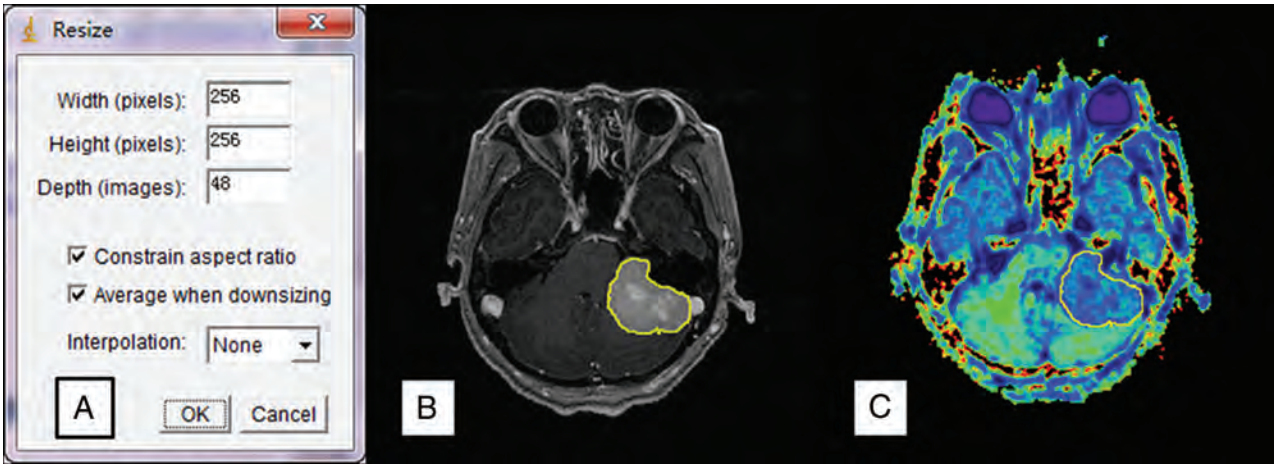

ON-LINE FIGURE. Protocols for resizing the enhanced T1 FSPGR image to match the DKI metric maps. *A*, The slice number of enhanced T1 FSPGR should be changed to 48 without interpolation. *B*, The ROI was semiautomatically delineated in the enhanced T1 FSPGR image. *C*, Finally, the ROI was copied to the DKI metric maps.

On-line Table: MRI planimetry and MRPI data[a]

	Controls *n* = 15	PSP *n* = 24	CBD *n* = 9	MSA (Total) *n* = 19	MSA-C *n* = 10	MSA-P *n* = 9	PD *n* = 18	*P* Value
Surfaces (mm^2)								
Midbrain	143.7 (21.1)	92.2 (21.3)	119.7 (12.0)	141.3 (18.6)	141.5 (18.1)	141.1 (20.3)	148.3 (25.5)	<.001[b]
Pons	546.5 (43.9)	495.9 (62.5)	509.9 (39.5)	448.7 (97.3)	379.8 (55.6)	525.2 (72.9)	578.4 (76.2)	<.001[b]
CC	625.3 (114.8)	558.5 (102.0)	489.1 (90.8)	571.2 (53.0)	570.1 (32.6)	572.4 (71.5)	592.1 (81.2)	.006[b]
$CC_{P\text{-}A\ grad}$	295.1 (70.3)	262.2 (70.2)	199.5 (58.6)	269.6 (36.5)	267.3 (37.0)	272.1 (38.3)	262.4 (42.7)	.03[b]
Surface ratios and MRPI								
Pons/CC	0.87 (0.81–0.97)	0.90 (0.83–0.93)	0.97 (0.90–1.18)	0.78 (0.57–0.90)	0.64 (0.57–0.78)	0.90 (0.83–1.04)	0.94 (0.87–1.10)	.002[c]
Midbrain/pons	0.25 (0.23–0.29)	0.18 (0.16–0.21)	0.24 (0.21–0.26)	0.32 (0.27–0.37)	0.35 (0.32–0.48)	0.27 (0.23–0.32)	0.26 (0.22–0.29)	<.001[c]
Midbrain /CC	0.24 (0.05)	0.17 (0.05)	0.25 (0.05)	0.25 (0.05)	0.25 (0.04)	0.25 (0.06)	0.25 (0.05)	<.001[b]
Midbrain/$CC_{P\text{-}A\ grad}$	0.52 (0.12)	0.38 (0.15)	0.64 (0.20)	0.54 (0.10)	0.55 (0.13)	0.52 (0.07)	0.58 (0.14)	<.001[b]
MRPI	8.6 (1.7)	16.2 (3.3)	10.7 (2.6)	6.2 (2.4)	4.7 (1.7)	7.9 (2.1)	9.9 (1.8)	<.001[b]

[a] All data are presented as mean (SD) or median (25th–75th quartile).

[b] ANCOVA.

[c] Kruskal-Wallis test.

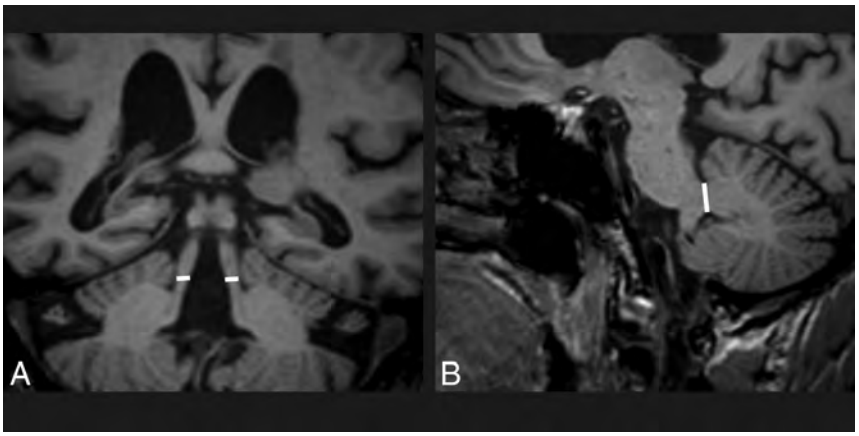

ON-LINE FIG 1. Superior cerebellar peduncle measurement in a coronal T1-weighted image (*A*). Middle cerebellar peduncle measurement in a parasagittal T1-weighted image (*B*).

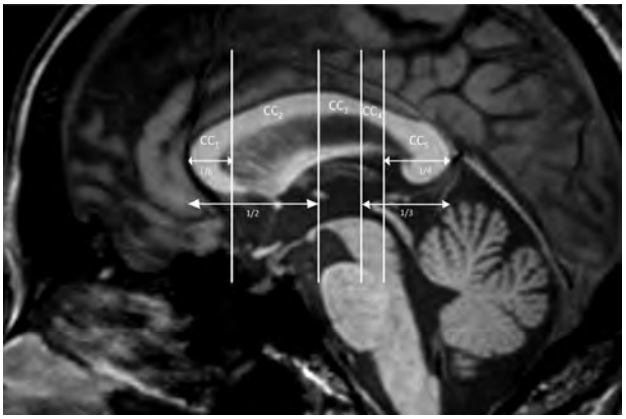

ON-LINE FIG 2. Corpus callosum subsections. CC_1 indicates the prefrontal cortex; CC_2, the premotor and supplementary motor cortex; CC_3, the primary motor cortex; CC_4, the primary sensory cortex; and CC_5, the temporal, parietal, and occipital cortex.

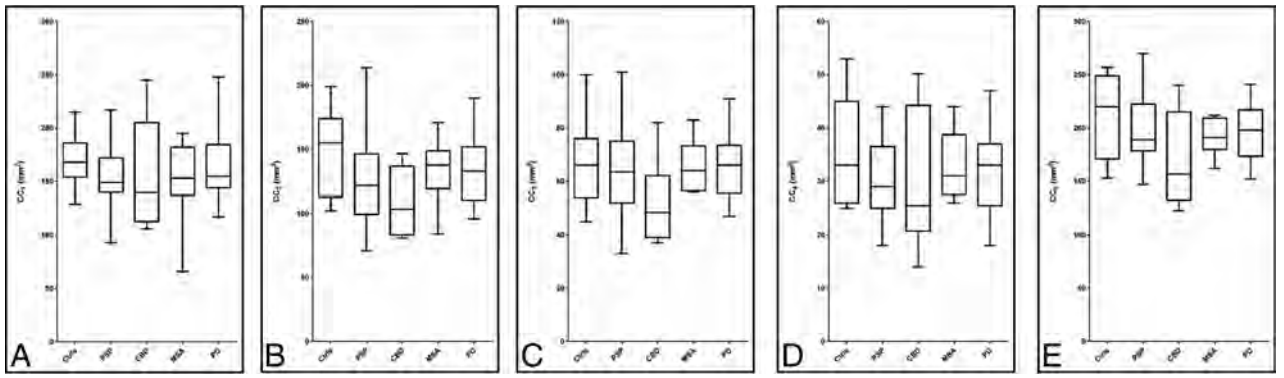

ON-LINE FIG 3. Boxplot diagrams of corpus callosum subsection surfaces. *A,* CC_1 indicates the prefrontal cortex. *B,* CC_2, the premotor and supplementary motor cortex. *C,* CC_3, the primary motor cortex. *D,* CC_4, the primary sensory cortex. *E,* CC_5, the temporal, parietal, and occipital cortices. Ctrls indicates controls.

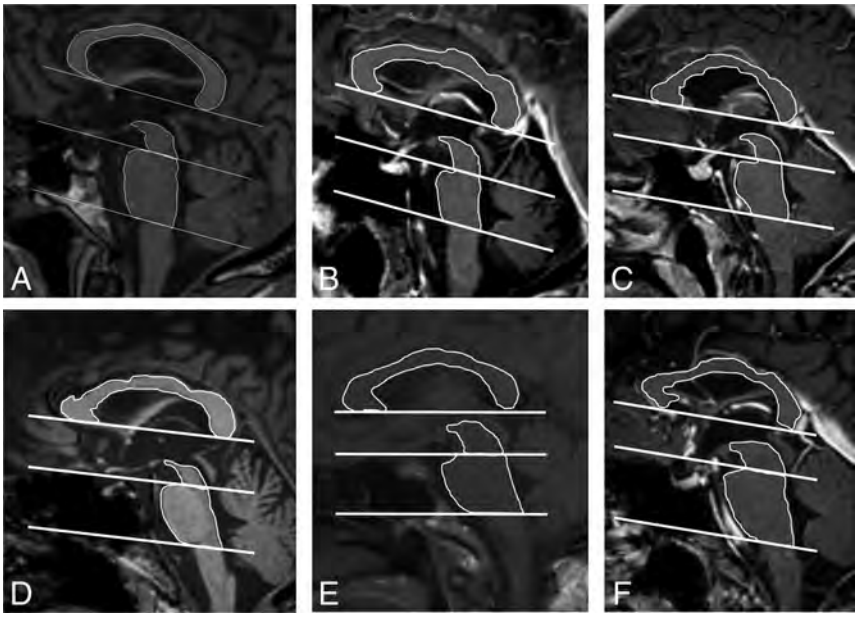

ON-LINE FIG 4. Representative midsagittal T1-weighted images with planimetry traces of patients with CBD (*A*), MSA-C (*B*), MSA-P (*C*), PSP (*D*), PD (*E*), and healthy controls (*F*).

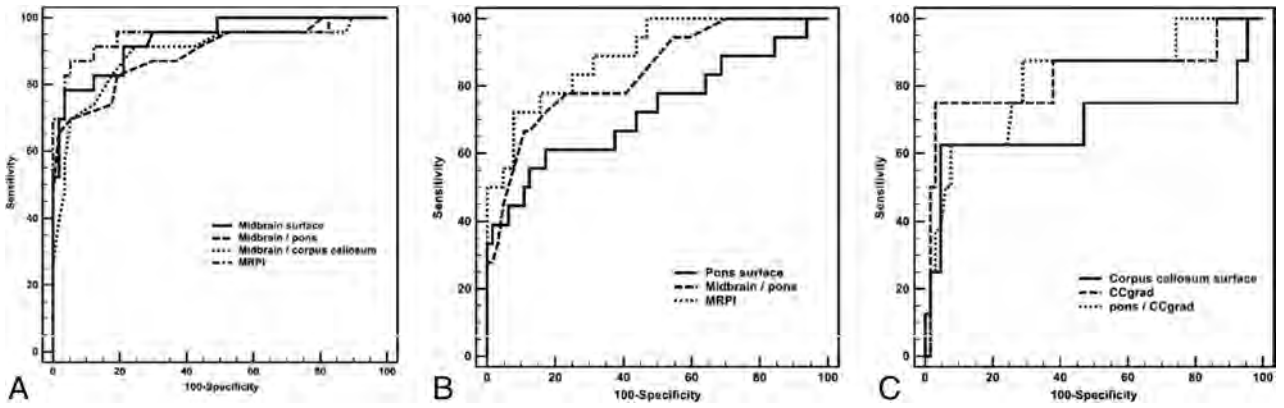

ON-LINE FIG 5. Receiver operating characteristic curve diagrams of the most potent imaging markers for PSP (*A*), MSA (*B*), and CBD (*C*).

On-line Table 1: Sequence parameters used for this study

	GE DV750 (8-Channel Head Coil)	Siemens Skyra (32-Channel Head Coil)
GM-DIR		
Sequence	Cube DIR	SPACE IR
Voxel dimensions (mm)	0.98 × 0.98 × 1.0	1.0 × 1.0 × 1.0
TR (ms)	5000	7500
TE (ms)	400	325
TI (ms)	640/2740	800/3600
Flip angle	90°	120°
Phase acceleration	1.5	2.0
Slice acceleration	1.5	None
Echo-train length	84	220
Scan time (min:sec)	9:38	8:32
WM-DIR		
Sequence	Cube DIR	SPACE IR
Voxel dimensions (mm)	0.98 × 0.98 × 1.0	1.02 × 1.02 × 1.0
TR (ms)	5000	7500
TE (ms)	13	319
TI (ms)	725/2500	450/3000
Flip angle	90°	120°
Phase acceleration	2.0	2.0
Slice acceleration	2.0	None
Echo-train length	72	221
Scan time (min:sec)	7:18	6:32
MPRAGE		
Sequence	IRP-FSPGR	MPRAGE
Voxel dimensions (mm)	0.98 × 0.98 × 1.07	1.0 × 1.0 × 1.0
TR (ms)	7	2200
TE (ms)	3	1.88
TI (ms)	900	900
Flip angle	8°	9°
Phase acceleration	None	None
Slice acceleration	None	None
Echo-train length	1	1
Scan time (min:sec)	9:17	6:05

Note:—SPACE indicates sampling perfection with application-optimized contrasts by using different flip angle evolution; IR, inversion-recovery; IRP, inversion-recovery prepped; FSPGR, fast-spoiled gradient recalled.

On-line Table 2: Subject-level rim lesion results

Characteristic	MS (*n* = 107)	Total PC (*n* = 36)	*P*	Definite PC (*n* = 26)	*P*	Indeterminate PC (*n* = 10)	*P*
No. of lesions/subject			.22		.77		.04
Median (IQR)	20 (10–42)	20 (6–34)		24 (8–38)		10 (4–27)	
Range	3–151	1–103		1–103		1–39	
Lesion volume (cm^3)/subject			.79		.56		.12
Median (IQR)	2.6 (0.9–5.5)	2.1 (0.8–5.8)		2.7 (1.1–8.6)		1.4 (0.6–2.6)	
Range	0.1–43.0	0.1–35.6		0.1–35.6		0.1–6.4	
Volume (mm^3)/lesion			.08		.10		.39
Median (IQR)	62 (42–87)	48 (33–73)		48 (33–66)		48 (31–77)	
Range	15–497	19–822		21–230		19–822	
Rim lesions/subject			<.001		<.001		<.001
Median (IQR)	5 (2–13)	0 (0–0)		0 (0–0)		1 (1–1)	
Range	0–62	0–2		0–0		0–2	
Rim lesions/subject (No.) (%)			<.001		<.001		<.001
0	3 (3)	28 (78)		26 (100)		2 (20)	
1	10 (9)	7 (19)		0		7 (70)	
2	16 (15)	1 (3)		0		1 (10)	
3	6 (6)	0		0		0	
4	15 (14)	0		0		0	
5–10	25 (23)	0		0		0	
11–20	16 (15)	0		0		0	
>20	16 (15)	0		0		0	
Fraction lesions with rims			<.001		<.001		.001
Median (IQR)	0.33 (0.19–0.47)	0.00 (0–0)		0.00 (0.0–0.0)		0.06 (0.03–0.11)	
Range	0.00–0.82	0.00–1.00		0.0–0.0		0.00–1.00	

On-line Table 3: Lesion distribution and odds ratios for any-versus-no rims after accounting for age, sex, total number of lesions, and median lesion size

Region	Total Lesions (%)		Rim Lesions (%)		Single ROI Models[a]		Multiple ROI Models[b]	
	MS	Total PC	MS	Total PC	OR (95% CI)	*P*	OR (95% CI)	*P*
All regions	3211	893	1120	9	120 (31–463)	<.001	–	–
Infratentorial	160 (5%)	10 (1%)	82 (7%)	0	25 (2–309)	.01	24 (1–414)	.03
Juxtacortical	1001 (31%)	344 (39%)	392 (35%)	3 (33%)	45 (11–191)	<.001	12 (2–60)	.003
Periventricular	925 (29%)	107 (12%)	510 (46%)	6 (67%)	16 (5–48)	<.001	16 (3–73)	<.001
Deep WM	1125 (35%)	432 (48%)	136 (12%)	0	79 (9–735)	<.001	16 (1–252)	.05

[a] Single-ROI models are based on an overall analysis and 4 separate region-specific analyses.

[b] Multiple-ROI model is one model that includes the rim count for each region as separate predictors.

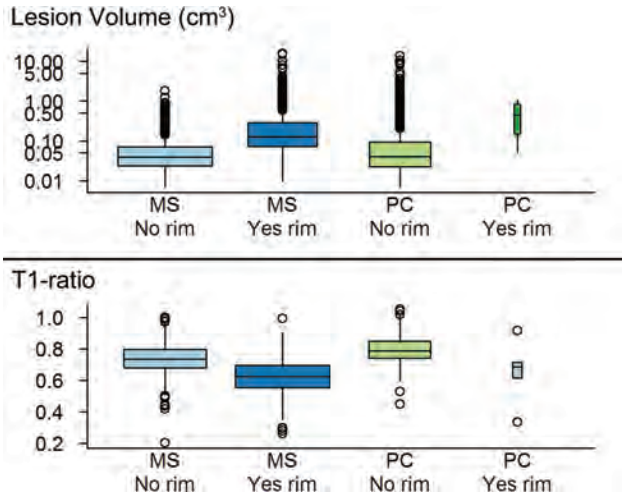

ON-LINE FIGURE. Lesion volumes and T1 ratio data in subjects with MS and PCs, stratified by the presence ("yes" rim) or absence ("no" rim) of rims. In general, lesions with rims tended to be larger (note the logarithmic scale of lesion volume), which makes sense because these rims could not be detected on lesions of only a few pixels in diameter. Lesions with rims also tended to have a lower T1 ratio, supporting our premise that rims probably arise from the opposed magnetization artifacts.

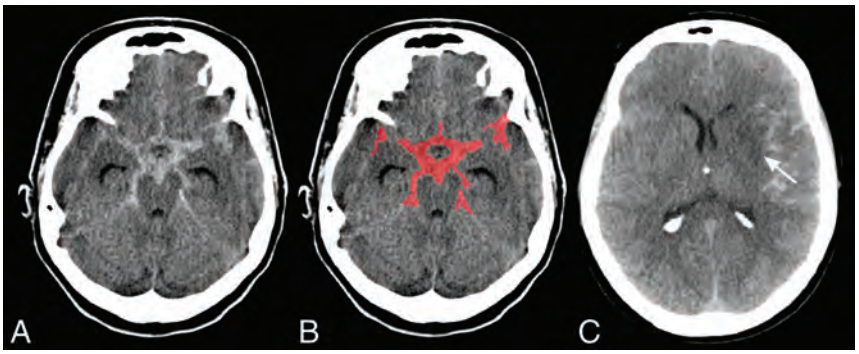

ON-LINE FIGURE. *A*, Axial slice of a baseline noncontrast CT scan of a patient with aSAH due to a ruptured middle cerebral artery aneurysm prior to developing signs of DCI. *B*, Quantified 34-mL cisternal blood. *C*, Axial slice of a noncontrast CT scan of the same patient 4 days after ictus with clinical signs of DCI after a successful coiling procedure without thromboembolic complications. This image shows a hypodensity in the left middle cerebral artery territory indicative of recent ischemia.

On-line Table: Baseline characteristics of the studied groups[a]

Baseline Characteristics	All	Group A (OTT ≤6 hr)	Group B (OTT > 6 hr)	*P* (A vs B)
No.	93	64 (68.8)	29 (31.2)	–
Age (mean) (yr)	61.6 ± 13.8	62.4 ± 12.8	60 ± 16.1	.44
Sex (male)	64 (68.8)	44 (68.8)	20 (69.0)	.98
Atrial fibrillation	22 (23.7)	16 (25.0)	6 (20.7)	.65
Diabetes	13 (14.0)	9 (14.1)	4 (13.8)	1.00
Hypertension	62 (66.7)	47 (73.4)	15 (51.7)	.04
Hyperlipidemia	11 (11.8)	7 (10.9)	4 (13.8)	.96
Current smoking	25 (26.9)	18 (28.1)	7 (24.1)	.80
Current drinking	16 (17.2)	11 (17.2)	5 (17.2)	1.00
History of stroke or TIA	15 (16.1)	13 (20.3)	2 (6.9)	.19
Coronary artery disease	11 (11.8)	9 (14.1)	2 (6.9)	.52
Baseline measurements				
Baseline glucose (mean) (mmol/L)[b]	7.1 ± 2.5	6.9 ± 2.4	7.5 ± 2.7	.34
Baseline SBP (mean) (mm Hg)	139.9 ± 20.6	140.5 ± 21.5	138.8 ± 18.6	.72
Baseline TC (mean) (mmol/L)[c]	4.5 ± 1.0	4.4 ± 1.1	4.6 ± 0.9	.36
Admission NIHSS score (median) (IQR)	7 (5–8)	6 (4–8)	7 (5–8)	.49
Collateral score 0–1	28 (30.1)	21 (32.8)	7 (24.1)	.40
ASPECTS (median) (IQR)[d]	9 (8–10)	9 (8–10)	10 (9–10)	.09
Intravenous thrombolysis	26 (28.0)	18 (28.1)	8 (27.6)	.96
Occlusion site				.33
ACA	0 (0)	0 (0)	0 (0)	
MCA M1	56 (60.2)	35 (54.7)	21 (72.4)	
MCA M2	12 (12.9)	10 (15.6)	2 (6.9)	
ICA	9 (9.7)	8 (12.5)	1 (3.5)	
Tandem	16 (17.2)	11 (17.2)	5 (17.2)	
Etiology				.01
Cardioembolic	30 (32.3)	23 (35.9)	7 (24.1)	
Large-vessel atherosclerosis	52 (55.9)	38 (59.4)	14 (48.3)	
Other/undetermined	11 (11.8)	3 (4.7)	8 (27.6)	
Procedure				.15
Mechanical thrombectomy	79 (85.0)	56 (87.5)	23 (79.3)	
Balloon + stent implantation	3 (3.2)	3 (4.7)	0 (0)	
Stent implantation	3 (3.2)	2 (3.1)	1 (3.5)	
Balloon	8 (8.6)	3 (4.7)	5 (17.2)	
mTICI				.46
0–2a	9 (9.7)	4 (6.2)	5 (17.2)	
2b–3	84 (90.3)	60 (93.8)	24 (82.8)	
OTT (mean) (min)	328.2 ± 181.7	237.0 ± 89.0	529.4 ± 172.5	<.001
PTR (mean) (min)	87.6 ± 44.3	86.0 ± 47.0	91.1 ± 37.9	.61

Note:—mTICI indicates modified TICI; IQR, interquartile range; OTT, onset to treatment; ACA, anterior cerebral artery; SBP, systolic blood pressure; PTR, puncture to reperfusion; TC, total cholesterol.

[a] Results are shown as number (%) unless stated otherwise.

[b] Missing data in 4 patients.

[c] Missing data in 4 patients.

[d] Missing data in 3 patients.

On-line Table: Clinical outcome

Patient No.	Age (yr)	Procedure Year	Pretreatment NIHSS	Intracranial Occlusion Site	Thrombectomy Method	TICI Score	mRS at 3 Months
1	47	2010	19	M1	Stent retriever	3	2
2	73	2010	22	ICA-T	Stent retriever	2a	4
3	53	2011	15	M1	Stent retriever	3	3
4	61	2011	36	ICA-T	Stent retriever	3	2
5	64	2011	3	ICA-T	Stent retriever	2a	1
6	45	2012	18	M1	Stent retriever	2a	1
7	45	2012	19	M1	Stent retriever	3	2
8	57	2012	14	M1	Stent retriever	2b	0
9	62	2013	9	M1	Stent retriever	2b	2
10	57	2013	18	M1	Stent retriever	2b	3
11	56	2013	17	ICA-T	Stent retriever	2a	6
12	41	2013	21	M2	Stent retriever	2a	4
13	39	2014	2	M1	Stent retriever	2b	0
14	34	2014	17	M1	Stent retriever	3	1
15	61	2014	24	M1	Stent retriever	2b	6
16	30	2010	15	M1	Stent retriever	2a	0
17	65	2010	20	M1	Stent retriever	3	4
18	57	2010	25	M1	Stent retriever	2a	6
19	72	2011	12	ICA-T	Stent retriever	2b	0
20	44	2011	8	M2	Stent retriever	3	2
21	63	2011	20	M1	Stent retriever	3	2
22	58	2011	19	ICA-T	Stent retriever	0	4
23	51	2011	13	M1	Stent retriever	3	1
24	56	2012	16	M1	Stent retriever	3	2
25	50	2012	18	ICA-T	Stent retriever	0	4
26	46	2012	21	M1	Stent retriever	3	1
27	60	2012	17	M1	Stent retriever	2a	0
28	57	2012	21	M1	Stent retriever	2b	1
29	47	2012	15	M1	Stent retriever	0	5
30	52	2012	14	ICA-T	Stent retriever	2b	0
31	39	2012	17	M1	Stent retriever	3	1
32	51	2013	18	M1	Stent retriever	2b	2
33	38	2013	21	M1	Stent retriever	3	0
34	52	2013	24	M1	Stent retriever	3	2

Note:—ICA-T indicates internal carotid terminus.

On-line Table 1: Summary of patients and aneurysm characteristics

Sex/Age (yr)	Vascular Risk Factors	Other Intracranial Aneurysms	Aneurysm Location	Aneurysm Size (mm) (Width × Height × Neck)	Aneurysm Characteristics	Parent Artery (Diameter, mm)	Covered Branch Vessels (Diameter, mm/Origin)
1) F/68	Hypertension, smoking	No	L MIFA	6 × 5 × 3	U	P:1.7 D:1.5	0.6/from the sac
2) F/77	Hypertension	No	R FP	4 × 3 × 2	U	P:1.5 D:1.5	0.7/from the neck
3) F/58	Smoking	No	R AIFA	5 × 3 × 4	U (recanalization after coiling)	P:3 D:2.9	1.7/from the neck
4) M/50	Hypertension, smoking	No	L CM	6 × 7 × 4	Subacute R	P:2.5 D:2.3	0.9/from the neck
5) M/74	Hypertension, smoking	No	1) L CM 2) L distal peric (SPA division)	1) 7 × 9 × 4 2) 4 × 3 × 3	U	1) P:2.9 D:2.1 2) P:2 D:2	1) 2.5/from the neck 2) 1.4/ from the sac
6) F/62	Familial history of intracranial aneurysms	No	1) L CM 2) R FP	1) 2 × 3 × 1 2) 2 × 3 × 1	U	1) P:1.9 D:2.1 2) P:2.2 D:2	1) 0.9/from the neck 2) 0.7/from the neck
7) F/47	Smoking	No	R CM	4 × 3 × 3	Previously R (coiled in the acute phase)	P:1.9 D:1.4	1.2/from the artery
8) M/71	No	No	R CM	4 × 3 × 3	Previously R (coiled in the acute phase)	P:2 D:1.5	1.7/from the neck
9) F/68	Smoking	No	R CM	5 × 3 × 2	Previously R (coiled in the acute phase)	P:1.8 D:1.2	1.2/from the neck
10) F/53	No	No	L AIFA	3 × 2 × 1	Previously R (coiled in the acute phase)	P:1.8 D:1.7	1/from the artery
11) F/40	Hypertension	U PcomA aneurysm	R CM	3 × 3 × 3	U	P:1.6 D:1.7	0.8/from the neck
12) F/67	Hypertension, smoking	R PCA aneurysm	L CM	2 × 2 × 2	U	P:1.5 D:1.2	1.2/from the artery
13) F/55	Hypertension, smoking	R MCA aneurysm	L CM	3 × 4 × 3	U	P:1.7 D:1.4	0.6/from the neck
14) M/70	Hypertension, smoking	No	R CM	2 × 2 × 2	U	P:1.8 D:1.7	1.1/from the neck
15) M/53	Hypertension	No	R OF and FP	3 × 2 × 3	Previously R (coiled in the acute phase)	P:1.9 D:1.6	0.6 and 0.8/from the neck and sac

Note:—MIFA indicates middle internal frontal artery; FP, frontopolar; AIFA, anterior internal frontal artery; CM, callosomarginal; SPA, superior parietal artery; OF, orbitofrontal; U, unruptured; R, ruptured or right; PcomA, posterior communicating artery; PCA, posterior cerebral artery; peric, pericallosal artery; D, distal portion of the artery; P, proximal portion of the artery; L, left.

On-line Table 2: Summary of treatment, patient outcome, and follow-up results

Pt No.	Stent Type and Size (mm)	Intra- and Periprocedural Complications	Long-Term Complications	Angiographic Outcome of Covered Vessel	Aneurysm Occlusion (OKM) before/after Treatment	Aneurysm Occlusion (OKM) during Follow-Up	mRS Pretreatment/mRS during Follow-Up	Radiologic Follow-Up (mo)
1	PED 2.5 × 12	No	No	Normal	A2/B3	D	mRS 1/mRS 1	14
2	PED 2.5 × 16	No	No	Slow flow and narrowing	A2/B2	D	mRS 2/mRS 2	24
3	PED 2.5 × 14	No	No	Normal	A1/A2	D	mRS 0/mRS 0	14
4	PED 2.5 × 14	No	No	Normal	A3/B3	D	mRS 2/mRS 2	16
5	PED 25 × 14 + 25 × 20 (telescopic)	Transient L leg weakness 24 hr after treatment (small basal ganglia infarct due to insufficient platelet inhibition)	No	Normal	1) A2/B2 2) A1/B3	1) B2 2) C2	mRS 2/mRS 2	10
6	PED 2.75 × 16 (right) + 2.5 × 14 (Left)	No	No	Normal	1) A1/B2 2) A1/B2	1) B2 2) D	mRS 0/mRS 0	5 12
7	PED 2.5 × 14	No	No	Slow flow and narrowing	A1/A2	D	mRS 1/mRS 1	12
8	FRED Jr 2.5 × 18	No	NA	Normal	A1/A1	D	mRS 2/mRS 2	12
9	PED 2.5 × 14	No	No	Normal	A1/A3	D	mRS 1/mRS 1	12
10	PED 2.5 × 12	No	No	Normal	A1/A2	D	mRS 2/mRS 2	12
11	Silk 2 × 15	Severe L hemiparesis due to stent thrombosis 10 days after treatment (discontinuation of antiplatelet therapy)	NA	Stent thrombosis and occlusion of the branch	A1/A2	NA	mRS 0/mRS 4	3
12	PED 25 × 12	No	No	Normal	A1/A3	B3	mRS 1/mRS 1	6
13	FRED Jr 2.5 × 18	R hemiparesis due to stent thrombosis 12 hr after treatment	No	Slow flow and narrowing	A1/B3	D	mRS 0/mRS 1	10
14	Silk 2 × 15	No	No	Normal	A1/A1	D	mRS 1/mRS 1	13
15	Silk 2 × 15	No	No	Normal	A1/A1	D	mRS 1/mRS 1	13

Note:—NA indicates not applicable; Pt, patient; L, left; R, right.

On-line Table 3: Summary studies reporting flow-diversion treatment of distal anterior cerebral artery aneurysms

Study Name	Study Design	No. of Men/Mean Age (yr)	No. and Location of Distal ACA An	Mean Aneurysm Size/Type	No. of FDs/Type of FDs	Unruptured/Previously Ruptured	Previous Treatments	Angiographic Result	Patency of Covered Branches	Treatment-Related Complications	Mean Follow-Up
Pistocchi et al,[13] 2012	P single center	NA	3 Pericallosal	6.8 mm/2 saccular +1 fusiform	3/Silk (2.5–20) (2 × 2.5–15)	3/0	Previously coiled (recurrence)	1 Complete occlusion[a]	Patency of covered pericallosal artery[b]	No	12-mo DSA
Martínez-Galdámez et al,[10] 2015	R multicenter	NA/70	1 Pericallosal	7.4 mm/saccular	1/PED (3 × 16)	1 Unruptured	No	Residual	Patency of covered pericallosal artery	No	6-mo DSA
Puri et al,[14] 2016	R single center	1 M/61.5	2 Pericallosal	2.7 mm/saccular	2/PED (2.5 × 10) (2.5 × 12)	1/1	1 Previously coiled	2 Complete occlusions	1 Asymptomatic frontopolar branch stenosis	No	12-mo DSA
Lin et al,[9] 2016	–	2 M/36.7	2 A2 2 A3	NA/2 dissecting +2 saccular	4/PED	3/1 Ruptured dissecting aneurysm	1 Coiling +1 clipping	4 Complete occlusions	NA	No	10-mo DSA
Clarençon et al,[6] 2017	R single center	NA	2 A2 A3	5.4 mm/saccular	NA	1/1	1 Previously coiled	1 Complete 1 Near-complete occlusion	1 Asymptomatic narrowing of covered pericallosal artery	No	12-mo DSA
Nossek et al,[12] 2017	Pro DB	2 M/61	1 A2 3 A2A3 1 A3	5.5 mm/2 fusiform +3 saccular	6/PED (2 × 2.5–14) (2 × 2.5–16) (2.5–10) (2.75–10)	4/1	1 Previously coiled	5 Complete occlusions	1 Asymptomatic branching vessel occlusion (2 overlapping PEDs)	No	11-mo DSA
Dabus et al,[7] 2017	R multicenter	NA/66	6 A2	6.7 mm/NA	NA/PED	4/2	2 Previously coiled	1 Complete +1 near-complete +2 incomplete occlusion	NA	No	10-mo DSA
Vachhani et al,[15] 2016	Case report	1 F/12	1 Pericallosal	6.2 mm/fusiform	2/PED (2.5–20) (2.75–20)	1 Unruptured	No	Complete occlusion	NA	No	12-mo MRA
De Macedo Rodrigues et al,[8] 2017	R multicenter	2 M/60	7 Pericallosal	4.3 mm/saccular	7/PED (3 × 2.5–12) (2 × 2.5–16) (2.5–10) (2.5–20)	6/1	1 Previously coiled	5 Complete +1 near-complete[c]	3 Asymptomatic narrowing of callosomarginal artery	No	6-mo DSA (7 patients)/ 12-mo DSA (3 patients)
Möhlenbruch et al,[11] 2017	P multicenter	4 M/57	10 A2 A3	5.8 mm/9 saccular +1 fusiform	10 FRED (4 × 25–20) (2 × 25–13) (30–21) (25–26) (30–14) (25–08)	9/1	1 Previously coiled	5 Complete occlusions +3 near-complete +1 incomplete[e]	Transient acute stenosis of covered branching vessel	Acute stenosis of covered branching vessel regressed after IV tirofiban	12 mo DSA

Note:—An indicates aneurysm; FDs, flow diverters; Pro DB, prospective database; P, prospective; R, retrospective; NA, not applicable.

[a] Pistocchi et al[13]: 2 patients available during follow-up.

[b] One patient available during follow-up.

[c] De Macedo Rodrigues et al[8]: 6 patients available during follow-up.

[d] Dabus et al[7]: 4 patients available during follow-up.

[e] Möhlenbruch et al[11]: 9 patients available during follow-up.

On-line Table 1: SNR and CNR of the different (precontrast-only) scan variants[a]

	T1WI VISTA (Variant 1)	PD_W VISTA (Variant 2)[f]	T1WI VIRTA (Variant 3)[g]	T1WI VIRTA (Variant 4)	T1WI VISTA (Variant 5)[h]	T1WI VISTA (Variant 6)	T1WI VIRTA (Variant 7)
SNR_{tissue}[b]	15.8 ± 0.9	31.8 ± 2.5	27.9 ± 1.8	43.4 ± 3.4	25.5 ± 2.2	21.2 ± 1.6	45.3 ± 3.6
$SNR_{carotid\ vessel\ wall}$[c]	8.2 ± 0.4	21 ± 1.8	14 ± 0.5	27.3 ± 2.1	16.1 ± 1.8	10.4 ± 0.4	21.4 ± 2.8
$SNR_{basilar\ vessel\ wall}$	6.1 ± 0.6	15.3 ± 2.9	11 ± 1.9	21.2 ± 5.9	11.8 ± 1.9	7.9 ± 0.7	15.2 ± 2.8
$SNR_{suprasellar\ CSF}$	6.9 ± 0.5	17.8 ± 3.2	12.2 ± 0.8	24.3 ± 1.1	13.8 ± 0.9	8.7 ± 1.0	16.6 ± 2.1
$SNR_{pontine\ CSF}$	2.5 ± 0.4	10 ± 3.9	5.9 ± 1.9	12.8 ± 5.4	7.7 ± 2.7	3.7 ± 1.1	10.8 ± 2.6
SNR_{blood}	2.5 ± 0.2	4.4 ± 0.8	3.4 ± 0.4	4.2 ± 1.1	3.3 ± 0.8	2.5 ± 0.7	4.7 ± 1.1
$CNR_{carotid\ vessel\ wall–CSF}$[d]	1.3 ± 0.6	3.2 ± 2.3	1.8 ± 0.4	3.0 ± 1.9	2.2 ± 1.1	1.7 ± 1.2	4.8 ± 1.5
$CNR_{basilar\ vessel\ wall–CSF}$[e]	3.6 ± 0.4	5.3 ± 1.7	5.1 ± 2.0	8.4 ± 3.9	5.2 ± 0.9	4.1 ± 1.5	4.4 ± 1.6
$CNR_{carotid\ vessel\ wall–blood}$[c]	5.7 ± 0.4	16.6 ± 0.9	10.6 ± 0.8	23.1 ± 2.7	12.7 ± 1.5	8 ± 0.9	16.7 ± 2.5

[a] Data are mean and SD calculated in 5 subjects (precontrast).
[b] Tissue ROI is located at the left orbital gyri.
[c] The mean of the left and right distal intracranial internal carotid arteries.
[d] Suprasellar CSF is used as a reference.
[e] Pontine CSF is used as a reference.
[f] Adjusted from Qiao et al.[19]
[g] Currently used in our clinic.
[h] Adjusted from Qiao et al[19] with a shorter TR.

On-line Table 2: SNRs and CNRs of the pre- and postcontrast scan variants 3 and 7 with the remaining comparisons[a]

	Precontrast		Postcontrast				
	T1WI VIRTA (Variant 3)[f]	T1WI VIRTA (Variant 7)	T1WI VIRTA (Variant 3)[f]	T1WI VIRTA (Variant 7)	*P* Value[g] (Pre 3–Post 3)	*P* Value[g] (Pre 7–Post 7)	*P* Value[h] Any Combination
SNR_{tissue}[b]	28.0 ± 1.8	40.5 ± 3.4	27.9 ± 1.3	42.4 ± 2.8	.721	.047	.000[i]
$SNR_{carotid\ vessel\ wall}$[c]	15.3 ± 1.4	20.8 ± 2.7	17.2 ± 0.9	26.4 ± 4.0	.009	.005[i]	.000[i]
$SNR_{basilar\ vessel\ wall}$	13.0 ± 1.4	15.9 ± 1.7	13.4 ± 2.4	19.2 ± 1.8	.241	.017	.000[i]
$SNR_{suprasellar\ CSF}$	9.1 ± 2.0	11.9 ± 2.2	11.3 ± 0.7	14.1 ± 2.4	.005[i]	.047	.000[i]
$SNR_{pontine\ CSF}$	5.9 ± 2.1	8.0 ± 2.0	6.5 ± 1.8	11.2 ± 2.6	.114	.009	.000[i]
SNR_{blood}	3.6 ± 0.6	5.4 ± 1.2	3.8 ± 0.5	6.3 ± 1.4	.508	.047	.000[i]
$SNR_{pituitary\ gland}$	23.0 ± 3.4	33.4 ± 4.7	33.3 ± 3.5	49.5 ± 6.7	.005[i]	.005[i]	.000[i]
$CNR_{carotid\ vessel\ wall–CSF}$[d]	6.1 ± 1.6	9.0 ± 1.5	6.0 ± 0.7	12.3 ± 3.6	.799	.013	.000[i]
$CNR_{basilar\ vessel\ wall–CSF}$[e]	7.2 ± 1.4	7.9 ± 1.4	7.0 ± 2.0	8.0 ± 1.9	.878	.878	.279
$CNR_{carotid\ vessel\ wall–blood}$[c]	11.6 ± 1.3	15.5 ± 2.9	13.5 ± 1.0	20.1 ± 3.8	.005[i]	.007[i]	.000[i]

[a] Data are mean and SD calculated in 10 subjects.
[b] Tissue ROI is located at the left orbital gyri.
[c] The mean of the left and right distal intracranial internal carotid arteries.
[d] Suprasellar CSF is used as reference.
[e] Pontine CSF is used as reference
[f] Currently used in our clinic.
[g] Post hoc analyses were performed using a Wilcoxon signed rank test with a Bonferroni correction applied to determine the specific differences among the variants.
[h] A Friedman test was conducted to test for differences across the multiple vessel wall images.
[i] Statistically significant ($P < .008$).

On-line Table 3: All detected vessel wall lesions in the 10 subjects

Vessel Wall Segment	Proximal or Distal	Concentric or Eccentric	Contrast Enhancement
Subject 1			
Left vertebral artery	P	C	+
Left vertebral artery	D	E	+
Right vertebral artery	P	C	+
Basilar artery	P	E	+
Basilar artery	D	E	−
Left PCA (P1 segment)	–	C	−
Subject 2			
Right ICA	D	C	−
Left vertebral artery	D	E	+
Right vertebral artery	D	E	−
Subject 3			
Left vertebral artery	P	C	+
Right vertebral artery	P	C	+
Basilar artery	P	E	−
Subject 4			
Left ICA	D	C	−
Left vertebral artery	P	C	+
Right vertebral artery	P/D	C	−
Subject 5	–	–	
Subject 6	–	–	
Subject 7	–	–	
Subject 8	–	–	
Subject 9			
Left vertebral artery	P	C	+
Subject 10			
Left ICA	P/D	C	+
Left MCA (M1 segment)	P/D	C	+
Left MCA (M2 segment)	P	C	+

Note:—C indicates concentric; E, eccentric; D, distal; P, proximal; PCA, posterior cerebral artery; –, no lesions detected.

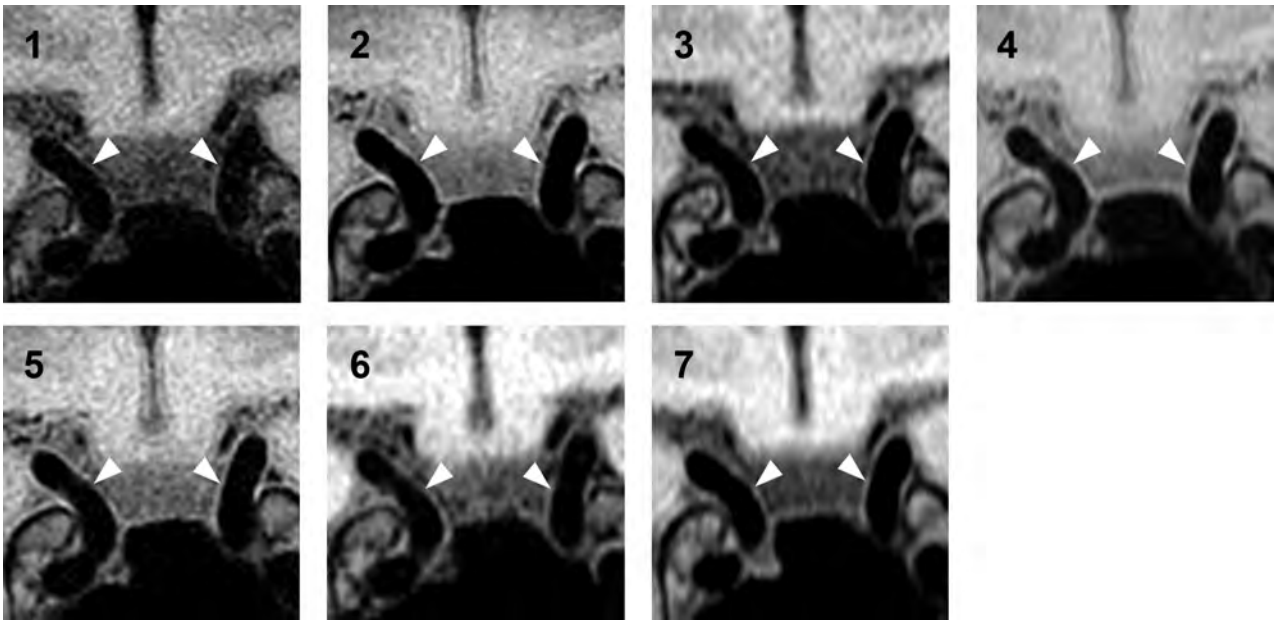

ON-LINE FIG 1. Sample images in the coronal plane of the 7 different scan variants performed at 3T (precontrast, in the order of decreasing scan duration). Both distal intracranial internal carotid arteries (*white arrowheads*) are depicted in all images, surrounded by CSF and brain parenchyma. *1*, T1WI VISTA variant 1 (8:24 minutes). *2*, Proton density–weighted VISTA variant 2 (7:50 minutes), adjusted from Qiao et al.[19] *3*, T1WI VIRTA variant 3 (6:42 minutes). *4*, T1WI VIRTA variant 4 (6:01 minutes). *5*, T1WI VISTA variant 5 (5:52 minutes), adjusted from Qiao et al[19] with a shorter TR. *6*, T1WI VISTA variant 6 (5:49 minutes). *7*, T1WI VIRTA variant 7 (4:39 minutes).

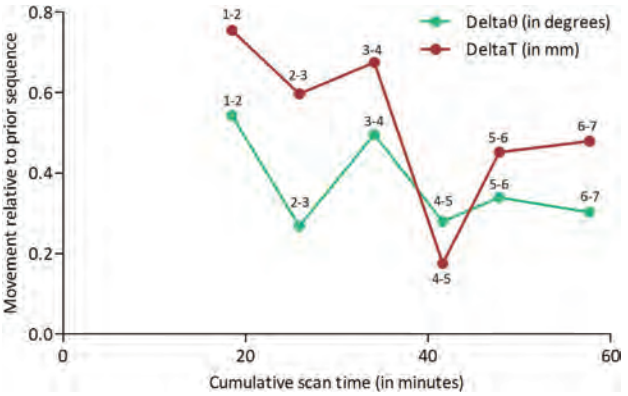

ON-LINE FIG 2. The degree of movement during the acquisition time expressed as ΔRotation (in degrees) and ΔTranslation (in millimeters) among all consecutively acquired vessel wall sequences. Each vessel wall sequence is compared with the prior acquired sequence according to the scan protocol (consecutively, variants 2, 5, 3, 4, 7, 1, and 6; Table 1). The mean registration parameters are calculated for 5 subjects. The ΔRotation and ΔTranslation parameters were calculated as $\sqrt{(X\text{-axis}^2 + Y\text{-axis}^2 + Z\text{-axis}^2)}$. Across time, there was no increase in motion in the later scheduled sequences.

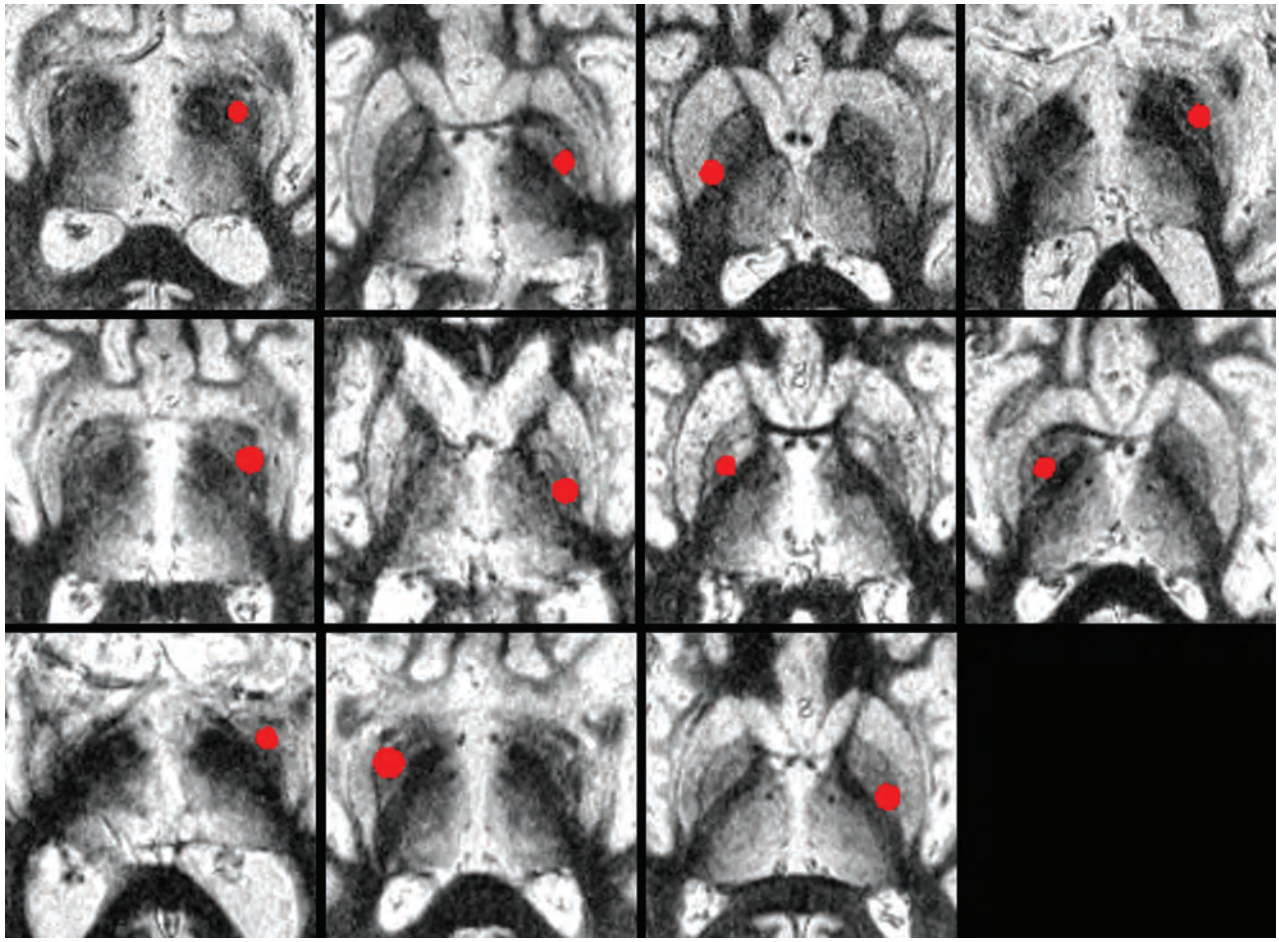

ON-LINE FIGURE. Axial fast gray matter acquisition T1 inversion recovery image for all 11 patients illustrating the volume of tissue activated (red) in the native space of the patient.

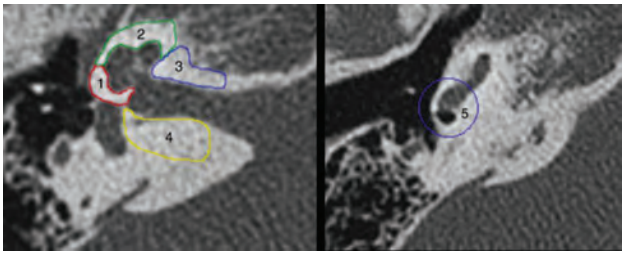

ON-LINE FIGURE. Cavitary plaque location. Fenestral (zone 1), pericochlear (zone 2), anteroinferior wall of the IAC (zone 3), posterior wall of the IAC (zone 4), and round window (zone 5).

On-line Table: Characteristics of the patients with a RASopathy, their clinical features, and outcome

Case	GA (wk)	Disorder	Genetic Mutation	Antenatal Findings	Respiratory System	Cardiac Findings	Other Postnatal Findings	Outcome
1	$37^{3/7}$	NS	*PTPN11*	Hydrops fetalis, pleural effusion	Severe respiratory distress	HCM	Chylothorax	Died in the neonatal period
2	$28^{5/7}$	NLS	*SHOC2*	Polyhydramnios	Severe respiratory distress	HCM	Necrotizing enterocolitis	Died in the neonatal period
3	$34^{0/7}$	NS	*RAF1*	Polyhydramnios, pyelectasis, talipes equinovarus	Severe respiratory distress	HCM	–	Died at 1.5 mo
4	$34^{2/7}$	NS	*SOS1*	Polyhydramnios, cystic hygroma, pyelectasis	Mild respiratory distress	HCM	–	Developed West syndrome, severe cognitive delay, visual impairment and cerebral palsy
5	$29^{0/7}$	NS	*PTPN11*	Polyhydramnios	Severe respiratory distress	–	Chylothorax	Died in the neonatal period
6	$40^{3/7}$	NS	*PTPN11*	–	Severe respiratory distress	ASD	Multiple skeletal dysplasias	Severe cognitive delay
7	$38^{3/7}$	NS	*PTPN11*	–	Severe respiratory distress	HCM, valvular pulmonary stenosis	Chylothorax	Severe cognitive delay
8	$40^{4/7}$	NS	*PTPN11*	–	Mild respiratory distress	HCM	JMML	Died at 6 mo
9	$32^{0/7}$	NS	*PTPN11*	–	Severe respiratory distress	HCM, PPHN	HIE	Osteofibrous dysplasia of the lower extremities, failure to thrive, ND within normal range
10	$40^{2/7}$	CFCS	*BRAF*	–	–	ASD	Congenital CMV infection	Generalized developmental delay, visual impairment
11	$36^{2/7}$	NS	*RIT1*	Hydrops fetalis, pleural effusion	Severe respiratory distress	SVT	HIE, chylothorax, chronic renal failure	Died at 3.5 mo
12	$34^{0/7}$	CS	*HRAS*	–	Severe respiratory distress	HCM, VSD, chaotic atrial ectopia, tachycardia	Multiple cardiac arrests	Died at 8.5 mo
13	$39^{2/7}$	NS	*PTPN11*	–	–	HCM, ASD	Myeloproliferative disorder	ADHD, severe autism spectrum disorder
14	$36^{6/7}$	CS	*HRAS*	Polyhydramnios, adrenal hemorrhage, skeletal dysplasia	Meconium aspiration syndrome	PPHN, SVT, severe hypotension	HIE, multiple skeletal dysplasias	Died at 6 mo
15	$38^{6/7}$	NS	*PTPN11*	–	Severe respiratory distress	HCM, complete AVSD	Chylothorax	Died in the neonatal period
16	$28^{6/7}$	CS	*HRAS*	–	Severe respiratory distress	HCM, arrhythmia, hypotension	Chylothorax, chylascites, small bowel volvulus	Died in the neonatal period

Note:—ADHD indicates attention deficit/hyperactivity disorder; ASD, atrial septal defect; AVSD, atrioventricular septal defect; CFCS, cardiofaciocutaneous syndrome; CS, Costello syndrome; GA, gestational age; HCM, hypertrophic cardiomyopathy; HIE, hypoxic-ischemic encephalopathy; JMML, juvenile myelomonocytic leukemia; NLS, Noonan-like syndrome disorder with loose anagen hair; PPHN, persistent pulmonary hypertension of the newborn; SVT, supraventricular tachycardia; VSD, ventricular septal defect; CMV, cytomegalovirus; ND, neurodevelopment.

On-line Table: Neurologic imaging of CHARGE syndrome

Patient	Patient Age	Method of Diagnosis	Clivus	Eye	Olfactory	Temporal Bone	Brain
1	32 days, 73 days	Clinical and genetic	CCC	ASH, Co	OTH	CH, SCCH, CAH, IACH, CNH	CVL, CVH, BH
2	4 mo, 8 mo, 14 mo	Clinical	CCC	Hypotelorism	OTH	SCCH	CVL, CVH, BH
3	30 days, 34 days, 63 days, 84 days, 5 mo	Clinical	PCC	WNL	OTH	CH, SCCH	CVL, CVH, BH
4	2 days, 3 mo	Clinical	PCC	Co, ONH	OTH	CH, SCCH, CAH, IACH, CNH	Frontoparietal chronic infarct; CVL, CVH, BH
5	4 mo, 10 mo, 13 mo, 6 yr	Clinical	PCC	Co, ONH	OTH	SCCH, CNH, VH	CVL, BH
6	3 mo	Clinical	CCC	Co	WNL	SCCH	CVH, BH
7	5 mo, 8 mo, 10 mo	Clinical	PCC	ONH	OTH	IACH, CNH, CH, CAH, SCCH, VH	CVH, BH
8	8 mo, 13 mo, 15 mo, 3 yr	Clinical and genetic	PCC	WNL	OTH	CH, SCCH, VH	Bifrontal encephalomalacia, BH
9	6 yr	Clinical	PCC	Co, Microphthalmos	OTH	SCCH, VH	CVH, BH
10	9 yr, 18 yr, 19 yr	Clinical and genetic	PCC	Co, ONH	OTH	SCCH, CH	CVL and pachygyria/lissencephaly, heterotopia
11	11 yr	Clinical and genetic	CCC	Co, PHPV	OTH	SCCH	CVL, BH
12	30 mo, 34 mo	Clinical and genetic	PCC	WNL	OTH	SCCH, CNH	WNL
13	12 yr, 14 yr, 15 yr	Clinical and genetic	CCC	WNL	OTH	CH, SCCH, VH	WNL
14	1 mo, 3 mo	Clinical	H	Dacryocystocele	?	CH, SCCH, VH	Multiple acute/subacute cerebral infarcts; BH
15	10 yr	Clinical	H	WNL	OTH	CH, SCCH, VH	CVL, cerebellar atrophy, BH

Note:—CCC indicates complete clival cleft; PCC, partial clival cleft; H, clival hypoplasia; ONH, optic nerve hypoplasia; ASH, anterior segment hypoplasia; Co, coloboma; OTH, olfactory tract hypoplasia; CH, cochlear hypoplasia; SCCH, semicircular canal hypoplasia; CAH, cochlear aperture hypoplasia; IACH, internal auditory canal hypoplasia; CNH, cochlear nerve hypoplasia or absent; VH, vestibular hypoplasia; CVL, cerebral volume loss; CVH, cerebellar vermis hypoplasia; BH, brain stem hypoplasia; WNL, within normal limits; ?, unknown; PHPV, persistent hyperplastic primary vitreous.

On-line Table 1: Clinical-radiologic data of the 38 patients included in the study[a]

Patient No.	Sex	Age at Clinical Onset (yr)	Symptoms	Side	Suzuki Classification	Surgical Procedure	Age Time Point 1 (yr)	Age Time Point 2 (yr)	Interval between Time Points (mo)	Postoperative Outcome	MRA Outcome
1	M	1	Right hemiparesis	Left	III	EDAMS	1	5	53	Excellent	↓ Deep CV and ↑ Pial CV
				Right	II	EDAMS	1	5	47		↓ Deep CV and ↑ Pial CV
2	F	2	Aphasia, hypotonia	Left	III	EDAMS	2	4	15	Fair	↑ Pial CV
3	F	4	Central retinal artery occlusion	Left	III	EDAMS	4	8	36	Excellent	↑ Pial CV
				Right	III	EDAMS	4	8	43		↓ Deep CV
4	F	13	Right hemiparesis	Left	II	EDAMS	13	17	35	Excellent	↓ Deep CV and ↑ Pial CV
				Right	III	EDAMS	13	17	50		↓ Deep CV and ↑ Pial CV
5	M	11	TIA, right facial nerve deficit	Left	IV	EDAMS	11	14	38	Good	↑ Pial CV
				Right	III	EDAMS	11	14	41		↑ Pial CV
6	M	6	TIA	Right	III	EDAMS	6	7	12	Fair	Unchanged
7	M	1	Seizure	Left	III	EDAMS	1	3	22	Good	↑ Pial CV
				Right	II	EDAMS	1	3	27		↓ Deep CV and ↑ Pial CV
8	M	5	TIA, headache	Left	III	EDAMS	5	6	11	Fair	↓ Deep CV
9	F	7	Headache	Left	III	EDAMS	7	10	36	Good	↓ Deep CV and ↑ Pial CV
10	F	13	Right hemiparesis	Left	III	EDAMS	13	18	52	Excellent	↓ Deep CV and ↑ Pial CV
				Right	III	EDAMS	13	18	48		↓ Deep CV and ↑ Pial CV
11	F	8	TIA	Right	IV	EDAMS	8	9	11	Fair	↓ Deep CV
12	F	1	Seizure	Right	III	EDAMS	1	6	62	Excellent	↓ Deep CV and ↑ Pial CV
				Left	III	EDAMS	1	6	58		↓ Deep CV and ↑ Pial CV
13	F	1	Seizure	Right	IV	EDAMS	1	2	5	Fair	Unchanged
14	M	1	Headache	Left	III	EDAMS	1	2	5	Excellent	↓ Deep CV
15	F	2	Seizure	Right	II	EDAMS	1	2	5	Excellent	↑ Pial CV
16	M	13	Right hemiparesis	Right	III	EDAMS	13	18	64	Excellent	↓ Deep CV and ↑ Pial CV
				Left	III	EDAMS	13	18	57		↓ Deep CV and ↑ Pial CV
17	F	1	TIA	Left	IV	EDAMS	1	4	36	Excellent	↓ Deep CV and ↑ Pial CV
18	F	1	Headache	Left	II	EDAMS	1	2	14	Excellent	↓ Deep CV and ↑ Pial CV
19	M	1	Headache	Left	III	EDAMS	1	3	30	Fair	↓ Deep CV
20	F	11	TIA/seizure	Left	IV	EDAMS	11	16	56	Good	↑ Pial CV
21	F	12	Headache	Right	III	EDAMS	12	15	43	Good	↓ Deep CV
				Left	III	EDAMS	12	15	40		↑ Pial CV
22	M	1	Headache	Left	II	EDAMS	1	2	11	Excellent	↓ Deep CV and ↑ Pial CV
23	F	12	Left hemiparesis	Left	IV	EDAMS	12	15	42	Excellent	↓ Deep CV and ↑ Pial CV
24	F	6	TIA, headache	Left	II	EDAMS	6	8	18	Good	↑ Pial CV
25	M	1	Quadriplegia	Right	II	EDAMS	1	4	33	Good	↓ Deep CV and ↑ Pial CV
				Left	II	EDAMS	1	4	33		↑ Pial CV
26	M	1	TIA	Left	III	EDAMS	1	1	5	Fair	Unchanged
27	F	1	TIA	Left	III	EDAMS	1	2	11	Excellent	↓ Deep CV and ↑ Pial CV
28	F	1	Headache	Right	III	EDAMS	1	1	5	Excellent	↓ Deep CV
29	M	10	Mild headache	Right	II	–	10	14	52	–	↑ Deep CV
				Left	II	–	10	14	52		Unchanged
30	F	13	Drug-responsive seizure	Right	II	–	13	17	41	–	Unchanged
				Left	II	–	13	17	41		↑ Deep CV
31	F	5	Mild headache	Right	III	–	5	8	35	–	Unchanged
				Left	II	–	5	8	35		Unchanged
32	F	2	Drug-responsive seizure	Right	III	–	2	3	12	–	Unchanged
				Left	III	–	2	3	12		Unchanged
33	M	14	Drug-responsive seizure	Right	II	–	14	15	15	–	↑ Deep CV
				Left	I	–	14	15	15		↑ Deep CV
34	F	3	Mild headache	Right	I	–	3	6	36	–	Unchanged
				Left	II	–	3	6	36		Unchanged
35	F	1	Mild headache	Right	II	–	1	5	52	–	Unchanged
				Left	I	–	1	5	52		Unchanged
36	M	3	Mild headache	Right	II	–	3	7	41	–	↑ Deep CV
				Left	I	–	3	7	41		Unchanged
37	M	8	Mild headache	Right	II	–	8	11	35	–	↑ Deep CV
				Left	II	–	8	11	35		↑ Deep CV
38	F	10	Mild headache	Right	II	–	10	11	12	–	Unchanged
				Left	I	–	10	11	12		Unchanged

Note:—CV indicates collateral vessels; –, not operated; ↑, increased; ↓, decreased.

[a] The Moyamoya vasculopathy is classified, according to the Suzuki classification, into 6 stages based on the findings of conventional angiography: I, stenosis of the intracranial bifurcation of the internal carotid artery; II, first appearance of Moyamoya vessels (dilation of the intracerebral arteries); III, increase of Moyamoya vessels (disappearance of the middle cerebral and anterior cerebral arteries); IV, minimization of Moyamoya vessels (disappearance of the middle cerebral and anterior cerebral arteries); V, shrinking of Moyamoya vessels (disappearance of the intracerebral arteries); and VI, disappearance of Moyamoya vessels and dominance of collateral circulation from only the external carotid system.

On-line Table 2: Comparison of DSC CBF-related parameters at first MRI and at last follow-up between surgical and nonsurgical brain hemispheres

Index	Surgical		Nonsurgical		P^a
Central nCBF (mean)	Before the operation	1.806 ± 1.001	First MRI	1.820 ± 0.916	.969
	Last follow-up	1.107 ± 0.835	Last follow-up	1.856 ± 0.863	.005[b]
% Variance central nCBF		−33.8%		10%	<.001[b]
Cortical nCBF (mean)	Before the operation	1.224 ± 0.693	First MRI	1.328 ± 0.663	.772
	Last follow-up	2.811 ± 2.298	Last follow-up	1.363 ± 0.612	.011[b]
% Variance cortical nCBF		152.1%		12.1%	.001[b]
Mean nCBF	Before the operation	1.515 ± 0.814	First MRI	1.574 ± 0.777	.921
	Last follow-up	1.959 ± 1.474	Last follow-up	1.610 ± 0.725	.334
% Variance mean nCBF		47.4%		11%	.121
hdSD (mean)	Before the operation	1.515 ± 0.364	First MRI	1.359 ± 0.233	.173
	Last follow-up	0.454 ± 0.239	Last follow-up	1.342 ± 0.241	<.001[b]
% Variance hdSD		−68.8%		−1.2%	<.001[b]

[a] Significance level of 1-way analysis of covariance used to compare CBF-related parameters in surgical and nonsurgical brain hemispheres.
[b] Significant.

On-line Table 3: Pairwise post hoc comparisons of CBF-related parameters that were different for clinical outcome categories

Perfusion Index	(I) Clinical Category	(J) Clinical Category	Mean Difference (I - J)	SD	P^a	95% Confidence Interval	
						Lower Limit	Upper Limit
DSC hdSD TP2	Fair	Good	0.191	0.129	.380	−0.133	0.514
		Excellent	0.361	0.119	.014[b]	0.062	0.661
	Good	Fair	−0.191	0.129	.380	−0.514	0.133
		Excellent	0.171	0.099	.255	−0.078	0.419
	Excellent	Fair	−0.0361	0.119	.014[b]	−0.661	−0.062
		Good	−0.171	0.099	.255	−0.419	0.078
DSC hdSD TP3	Fair	Good	0.22	0.074	.017[b]	0.032	0.407
		Excellent	0.455	0.069	<.001[b]	0.282	0.629
	Good	Fair	−0.22	0.074	.017[b]	−0.407	−0.032
		Excellent	0.236	0.057	.001[b]	0.092	0.379
	Excellent	Fair	−0.455	0.069	<.001[b]	−0.629	−0.282
		Good	−0.236	0.057	.001[b]	−0.379	−0.092
Early DSC % variance hdSD	Fair	Good	18.766	7.026	.035[b]	1.096	36.436
		Excellent	27.578	6.513	.001[b]	11.196	43.959
	Good	Fair	−18.766	7.026	.035[b]	−36.436	−1.096
		Excellent	8.812	5.398	.300	−4.764	22.388
	Excellent	Fair	−27.578	6.513	.001[b]	−43.959	−11.196
		Good	−8.812	5.398	.300	−22.388	4.764
Late DSC % variance hdSD	Fair	Good	19.552	3.677	<.001[b]	10.303	28.801
		Excellent	33.275	3.409	<.001[b]	24.7	41.849
	Good	Fair	−19.552	3.677	<.001[b]	−28.801	−10.303
		Excellent	13.723	2.825	<.001[b]	6.616	20.829
	Excellent	Fair	−33.275	3.409	<.001[b]	−41.849	−24.7
		Good	−13.723	2.825	<.001[b]	−20.829	−6.616
Early DSC % variance cortical nCBF	Fair	Good	−42.236	44.024	.718	−152.959	68.487
		Excellent	−72.700	40.814	.232	−175.348	29.948
	Good	Fair	42.236	44.024	.718	−68.487	152.959
		Excellent	−30.464	33.825	.755	−115.537	54.608
	Excellent	Fair	72.700	40.814	.232	−29.948	175.348
		Good	30.464	33.825	.755	−54.608	115.537
Late DSC % variance cortical nCBF	Fair	Good	−76.792	80.044	.718	−278.107	124.523
		Excellent	−132.182	74.207	.232	−318.815	54.451
	Good	Fair	76.792	80.044	.718	−124.523	278.107
		Excellent	−55.39	61.501	.755	−210.067	99.288
	Excellent	Fair	132.182	74.207	.232	−54.451	318.815
		Good	55.39	61.501	.755	−99.288	210.067

[a] Comparisons were made using a 1-way analysis of covariance, and the Sidak correction for multiple comparisons was applied.
[b] Significant.

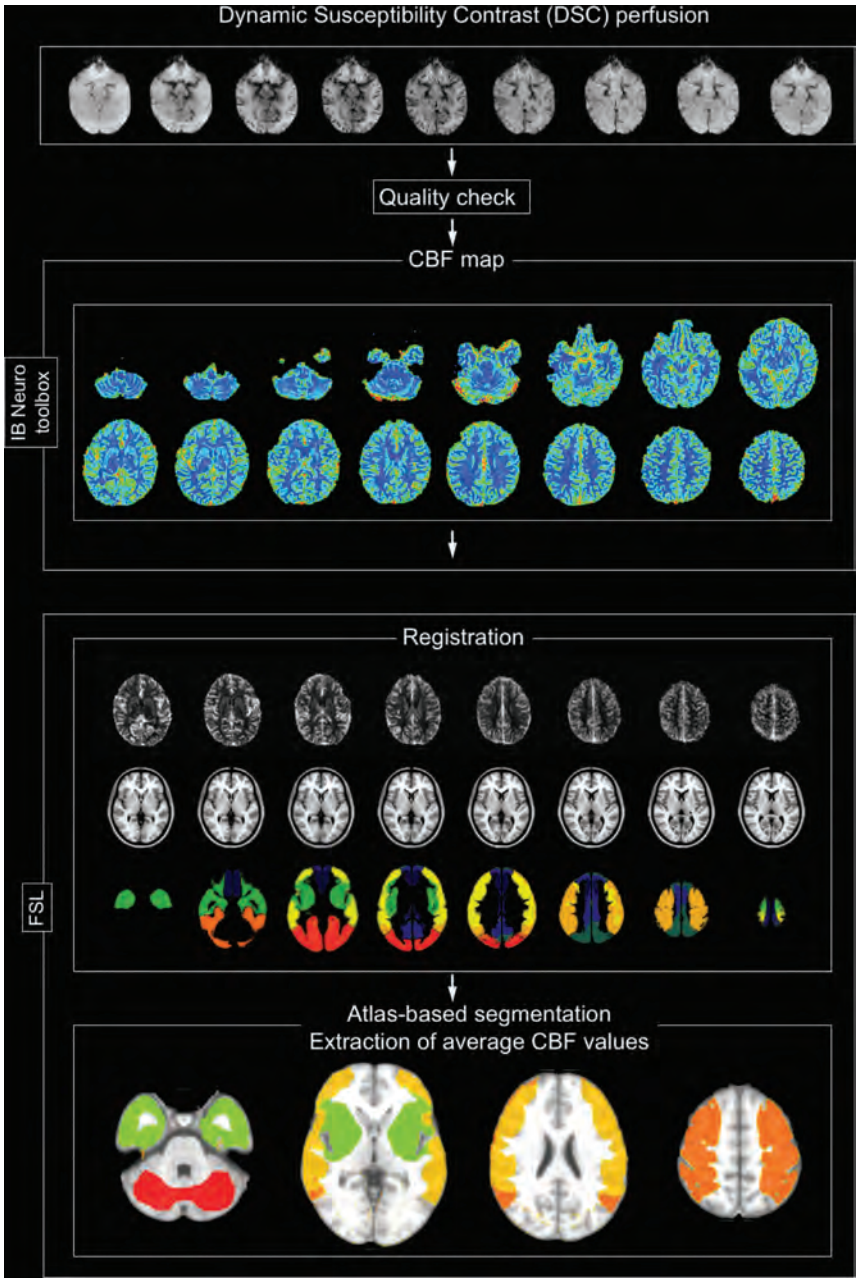

ON-LINE FIG 1. Flowchart of the pipeline used for DSC-PWI data analysis. The last row of images shows the automated determination of VOIs in the MCA territories overlaid on anatomic T1-weighted images. The average normalized CBF value determined from the green VOI corresponds to the central nCBF (proximal MCA territory). The average nCBF values determined from the yellow and orange VOIs correspond to the cortical nCBF (middle and distal MCA regions). The average CBF value determined from the red VOI at the cerebellar level is used for normalization.

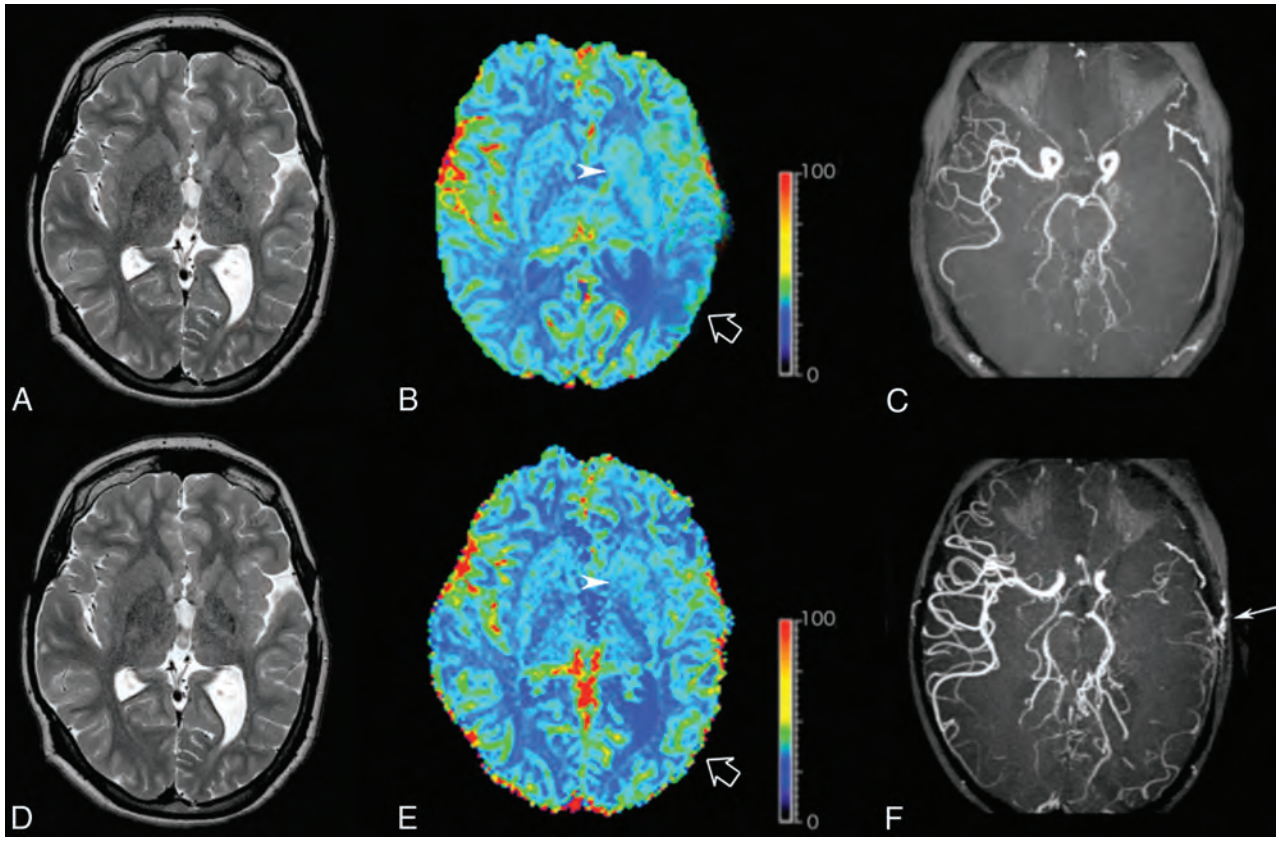

ON-LINE FIG 2. Representative T2-weighted images (*A* and *D*), DSC-CBF (*B* and *E*), and noncontrast MR angiography (*C* and *F*) of pre- (*A–C*) and postoperative (*D–F*) images in a 12-year-old patient with left Moyamoya disease treated with surgical indirect revascularization (EDAMS) (*white arrow*). The *empty arrow* indicates the left temporal region with reduced values of CBF before the operation (*B*). DSC-PWI acquired 42 months after left EDAMS shows improvement in CBF in the left temporal lobe (*empty arrow*, *E*). *Arrowheads* indicate preoperative hyperperfusion of the proximal MCA region (*B*), which returns to normal at postoperative PWI (*E*). The color scale unit of the CBF map is mL/100 mg/min.

On-line Table: Brain growth with postnatal age

Postnatal Age	Unadjusted Growth (mm/week PNA)			Adjusted[a] Growth (mm/week PNA)		
	β	95% CI	*P* Value[b]	β	95% CI	*P* Value[b]
Biparietal diameter						
Birth to TEA	1.50	1.37–1.63	<.001	1.54	1.41–1.66	<.001
<7 days	−0.36	−2.15–1.43	.69	−2.01	−3.66–0.36	.017
7–27 days	1.30	0.90–1.70	<.001	1.30	0.93–1.66	<.001
>27 days	1.98	1.69–2.26	<.001	2.17	1.94–2.40	<.001
Corpus callosum length						
Birth to TEA	0.91	0.84–0.97	<.001	0.89	0.83–0.96	<.001
<7 days	1.04	0.02–2.06	.045	0.99	0.06–1.92	.038
7–27 days	1.10	0.83–1.36	<.001	1.09	0.84–1.33	<.001
>27 days	0.45	0.33–0.58	<.001	0.50	0.38–0.62	<.001
Transcerebellar diameter						
Birth to TEA	1.81	1.72–1.91	<.001	1.76	1.66–1.85	<.001
<7 days	1.93	0.92–2.95	<.001	1.22	0.34–2.11	.007
7–27 days	1.73	1.35–2.10	<.001	1.52	1.13–1.90	<.001
>27 days	2.01	1.82–2.19	<.001	2.03	1.86–2.20	<.001
Vermis height						
Birth to TEA	0.60	0.54–0.65	<.001	0.59	0.54–0.65	<.001
<7 days	0.83	0.10–1.55	.026	0.52	−0.17–1.22	.141
7–27 days	0.51	0.28–0.74	<.001	0.46	0.26–0.67	<.001
>27 days	0.58	0.44–0.73	<.001	0.71	0.60–0.83	<.001
Interhemispheric distance						
Birth to TEA	0.22	0.19–0.26	<.001	0.22	0.18–0.26	<.001
<7 days	−0.04	−0.32–0.24	.788	−0.04	−0.33–0.24	.773
7–27 days	0.19	0.10–0.28	<.001	0.19	0.10–0.28	<.001
>27 days	0.27	0.18–0.36	<.001	0.29	0.21–0.36	<.001
Anterior horn width, left[c]						
Birth to TEA	0.09	0.06–0.13	<.001	0.10	0.07–0.14	<.001
<7 days	0.42	−0.26–1.09	.229	0.53	−0.15–1.20	.125
7–27 days	0.11	0.01–0.21	.038	0.11	0.01–0.21	.034
>27 days	0.05	−0.02–0.11	.143	0.06	−0.002–0.12	.059
Anterior horn width, right[c]						
Birth to TEA	0.09	0.05–0.12	<.001	0.09	0.06–0.13	<.001
<7 days	−0.04	−0.37–0.28	.791	−0.04	−0.37–0.28	.788
7–27 days	0.20	0.08–0.32	.001	0.20	0.08–0.32	.001
>27 days	0.05	−0.02–0.12	.173	0.06	−0.01–0.13	.096
Ventricular width						
Birth to TEA	0.58	0.52–0.65	<.001	0.59	0.52–0.65	<.001
<7 days	1.05	−0.27–2.37	.118	0.57	−0.67–1.82	.368
7–27 days	0.27	0.07–0.47	.007	0.30	0.10–0.49	.003
>27 days	0.75	0.62–0.88	<.001	0.80	0.66–0.93	<.001

Note:—β indicates regression coefficient (rate of change of the linear measure per week postnatal age).

[a] Adjusted for gestational age, birth weight *z* score, and sex.

[b] *P* value reflects strength of the evidence for an association between the linear measure and postnatal age.

[c] Restricted to infants without an ipsilateral intraventricular hemorrhage.